Transient Boiling and Two-Phase Flow Problems Associated with Nuclear Reactor Safety(Dissertation_全文)

AUTHOR(S):

Kataoka, Isao

TRANSIENT BOILING AND TWO-PHASE FLOW PROBLEMS ASSOCIATED WITH NUCLEAR REACTOR SAFETY

ISAO KATAOKA

INSTITUTE OF ATOMIC ENERGY
KYOTO UNIVERSITY

TRANSIENT BOILING AND TWO-PHASE FLOW PROBLEMS ASSOCIATED WITH NUCLEAR REACTOR SAFETY

ISAO KATAOKA

INSTITUTE OF ATOMIC ENERGY
KYOTO UNIVERSITY

ACKNOWLEDGEMENTS

I would like to express my deep appreciation to Professor A. Sakurai for his guidance and support throughout this work. I would also like to thank Associate Professor A. Serizawa at the Department of Nuclear Engineering, Kyoto University for his guidance, cooperation and valuable discussions during this investigation. A part of this work (Chapter I) was carried out with him while he was at the Institute of Atomic Energy. I would also like to express my sincere appreciation to Dr. M. Ishii at Argonne National Laboratory, U.S.A. for his guidance and support during my stay and investigaion in U.S.A. The works on two-phase flow in this study were carried out with him while I was engaged in nuclear reactor safety research at Argonne National Laboratory under the auspices of the U.S. Nuclear Regulatory Commission.

Thanks are also due to Associate Professor M. Shiotsu and Mr. K. Hata for their assistance during the experiments described in Chapter I.

The helpful discussions and suggestions of Professor I. Michiyoshi at the Department of Nuclear Engineering, Kyoto University are deeply appreciated. The valuable discussions of Drs. N. Zuber, Y. Y. Hsu, and M. Young of U.S. Nuclear Regulatory Commision in Chapters III through VI are greatly appreciated.

I am also thankful to Mr. K. Mishima at the Research Reactor Institute, Kyoto University for his coorperation in a part of this work (Chapter III).

ABSTRACT

The transient boiling and two-phase flow phenomena are quite important in evaluating thermohydraulic aspects of nuclear reactor safety. In this study, some problems on these phenomena have been investigated both experimentally and analytically. The main objectives of this study are to provide the basic knowledge of transient boiling and two-phase flow necessary to the reactor safety analyses. The problems investigated here cover a wide range of operational conditions; from slow to fast transient, from low to high steam quality, and from local to overall characteristic of boiling and two-phase flow. The problems concern various phases of nuclear reactor accidents such as reactivity accident, large break LOCA (loss of coolant accident) and small break LOCA. The results obtained here will be utilized in analysing these accidents numerically coupled with a large scale computor code. Some of the results will also contribute to designing integrated facilities which simulate a prototype reactor (LOFT, Semiscale, etc.).

In a reactivity initiated accident where excessive reactivity is inserted into a nuclear reactor, the reactor power increases exponentially with time. The heat transfer processes under this circumstance are unsteady ones. They include transient boiling and non-boiling heat transfer under forced convective conditions. These subjects have been studied in Chapter I and II.

In Chapter I, described are the experimental works that have been carried out on transient forced convective boiling phenomena using thin platinum wires located

parallel to the water flow. The effects of subcooling, velocity, pressure and heater size on transient boiling heat transfer coefficients and maximum heat fluxes have been studied for exponential heat increase with periods up to 5 millisecond. The experimental correlation for transient maximum heat flux was presented in collaboration with dimensional analysis of forced convective transient boiling.

In Chapter II, the transient non-boiling heat transfer coefficient under forced convection condition has been analysed for exponentially increasing heat flux. When the power transient accident occurs in a pressurized water reactor or in a liquid metal cooled reactor, the heat transfer process in an initial stage is considered to be a transient non-boiling forced convective heat transfer. Therefore, in analysing the problem associated with the reactivity accident, the knowledge of the transient non-boiling heat transfer is also indispensable. The boundary layer approximation was applied to this problem. Approximate but simple analytic solutions for transient non-boiling heat transfer coefficient have been obtained for laminar and turbulent flow over a wide range of Prandtl number. For an exponentially increasing heat flux, transient heat transfer coefficients attain asymptotic values and these values were correlated by one dimensionless parameter including heat flux increasing rate.

Another important phase of a reactor accident is loss of coolant accident (LOCA) and subsequent rewetting and quenching phenomena of the reactor core. In this case, a large amount of vapor is generated and high quality two-phase flows are often encountered. One of the most important flow regimes under these circumstances is annular dispersed flow.

Therefore, the knowledge of hydrodynamic and heat transfer of annular dispersed flow is indispensable for analysing LOCA and subsequent phenomena. Chapters III through V deal with these subjects.

In Chapter III, average droplet size and its distribution have been investigated for annular dispersed flow of relatively low viscosity fluids. Based on the mechanistic modelling of droplet generation in annular dispersed flow, the correlation for average droplet size and its distribution have been presented in collaboration with experimental data of droplet size distribution by various reseachers. The correlation predicts a wide range of experimental data considerably well. The droplet size is an important factor in evaluating the heat transfer in annular two-phase flow and post CHF heat transfer.

In Chapter IV, the entrainment rate has been studied for both entrance and developed region of annular dispersed flow. The knowledge of entrainment rate is indispensable for an accurate analysis of annular dispersed flow. There are several mechanisms for the occurrence of entrainment. Among those, shearing-off of roll wave crests by highly turbulent streaming gas flow is basically a dominant mechanism. Based on this mechanism and in collaboration with experimental data, a correlation for the entrainment rate has been developed. Along with the correlations for entrainment fraction and droplet deposition coefficient previously developed, the present correlation predicts experimental data of entrainment in entrance and developed region very well. It also enables the prediction of entrainment under various initial conditions. This entrainment rate correlation , coupled with two-fluid model formulation of annular dispersed flow, can be a useful tool for detailed analyses of transient, steady,

entrance and developed region of the annular dispersed flow.

In Chapter V, droplet entrainment from stagnant liquid by bursting or splashing of vapor bubbles has been studied. This subject is particularly important for the analyses for of reflooding and rewetting in a reactor core where liquid flow rate is small. The droplets from the stagnant liquid are carried away by vapor stream and play a dominant role in cooling the unwetted surface of the reactor core. Using various experimental data and based on detailed mechanistic modelling of droplet generation and its motion, the correlation for the amount of entrained droplets from stagnant liquid has been developed in terms of vapor velocity, distance from pool surface and system pressure. The results indicate that there are three regions for pool entrainment, i.e. near surface region, momentum controlled region and deposition controlled region. The present correlation predicts the experimental data over a wide range of of vapor velocity, system pressure and distance from pool surface.

As stated above, various two-phase flow phenomena associated with nuclear reactor safety have been investigated by integrated facilities which simulate prototype plants. In designing such scaled facilities and in analysing the results obtained from these facilities, it is necessary to have reliable scaling criteria for two-phase flow. Due to the complexity of two-phase flow phenomena, it is not easy to obtain such criteria compared to single phase flow. However, this subject is another important application of two-phase flow research and it is carried out in the final chapter of this thesis.

In Chapter VI, the scaling criteria for two-phase flow have been developed using drift flux model formulation of two-phase flow. In this chapter, natural circulation system has been analysed since it

has become one of the most important problems in current nuclear reactor safety associated with small break LOCA and subsequent pump trip.

After some simplifications and approximations, practical scaling criteria have been obtained. Based on this criteria, preliminary assesments for existing scaled model (LOFT) were carried out for the possibility of simulating natural circulation in typical PWR plants.

TABLE OF CONTENTS

		Page
Acknowledgements		i
Abstract		iii
Introduction		1
Chapter I.	Forced Convective Boiling Heat Transfer under Power Transients	
I.1	Introduction	9
I.2	Experimental Apparatus and Procedures	12
I.3	Results and Discussions	14
I.3.1	Steady State Performances	14
I.3.1.a	Non-Boiling Heat Transfer	15
I.3.1.b	Nucleate Boiling Heat Transfer	16
I.3.1.c	Maximum Heat Flux	17
I.3.2	Transient Performances	21
I.3.2.a	Transient Non-Boiling Heat Transfer	21
I.3.2.b	Transient Boiling Heat transfer	23
I.3.2.c	Transient Maximum Heat Flux	25
I.4	Conclusions	29
Chapter II.	Analysis of Transient Forced Convective Heat Transfer by Boundary Layer Approximation	
II.1	Introduction	113

II.2	Basic Equations	115
II.3	Laminar Flow for Pr << 1 (Slug Flow)	117
II.4	Laminar Flow for Pr >> 1	121
II.5	Laminar Flow for Pr ≃ 1	123
II.6	Turbulent Flow for Pr << 1	126
II.7	Turbulent Flow for Pr >> 1	126
II.8	Turbulent Flow for Pr ≃ 1	129
II.9	Comparison with Experimental Data	134
II.10	Conclusions	135

Chapter III.. Generation and Size Distribution of Droplet in Gas Liquid Two-Phase Flow

III.1	Introduction	155
III.2	Droplet Generation Mechanism	157
III.3	Droplet Generation by Entrainment	160
III.4	Mean Droplet Size and Size Distribution	164
III.5	Conclusions	169

Chapter IV. Entrainment Rate in Annular Two-Phase Flow

IV.1	Introduction	193
IV.2	Previous Works	194
IV.3	Basic Equation for Entrainment Rate	197
IV.4	Entrainment Rate Correlation	200
IV.5	Entrainment Rate in Entrance Region	205

IV.5.1 General Formulation of Entrainment Rate 205

IV.5.2 Entrance Effect and Experimental Data 208

IV.5 Conclusions 213

Chapter V. Mechanistic Modeling and Correlation for Pool Entrainment Phenomena

V.1 Introduction 255

V.2 Previous Works 256

V.3 Basic Equations 261

V.4 Droplet Diameter Distribution and Entrainment Rate at Interface 263

V.5 Droplet Velocity at Interface 267

V.6 Maximum Height of Rising Droplet 273

V.7 Correlation for Entrainment Amount 276

V.8 Entrainment Amount in Momentum Controlled Regime 280

V.9 Entrainment Amount in Deposition Controlled Regime 284

V.10 Entrainment Amount Near Surface Region 286

V.11 Conclusions 288

V.12 Supplementary Remarks on Application to Practical Cases 291

Chapter VI. Scaling Criteria for LWR's under Single Phase and Two-Phase Natural Circulation

VI.1 Introduction 331

VI.2 Single Phase Similarity Law 332

VI.2.1 Similarity Parameter for Single Phase Natural Convection 332

VI.2.2 General Similarity Laws 336

VI.2.3 Scale Model with Same Fluid 341

VI.2.4 Sample Calculations (Real Time Scale) 344

VI.3 Two-Phase Similarity Laws 345

VI.3.1 Basic Formulation for Two-Phase Natural Circulation 345

VI.3.2 Steady State Formulation for Two-Phase Flow 349

VI.3.3 Similarity Criteria for Two-Phase Flow 352

VI.3.4 Scale Model with Same Fluid 354

VI.3.5 Sample Calculations 357

VI.4 Conclusions 358

Summary and Conclusions 370

INTRODUCTION

The safety of a nuclear reactor has been a problem of great importance for these decades in view of its societal, environmental and technical importance. To evaluate the safety of a nuclear reactor, the starting point is to have an accurate knowledge of various phenomena in the nuclear reactor system under accidental conditions. Some of the most important aspects of nuclear reactor accidents are the thermohydraulic behaviours of reactor coolant, initiated by power, pressure and flow transients. They involve various types of two-phase flow and boiling phenomena under both steady and unsteady conditions. Therefore, research efforts have been concentrated to these phenomena. These researches have been carried out using large integrated facilities which simulate nuclear reactor systems (LOFT, Semiscale etc.) and also using laboratory size facilities in which separate effects of various thermohydraulic behaviours can be studied in detail.

Various types of boiling and two-phase flow phenomena encountered in nuclear reactor accidents can be categorized into three groups depending on the ratio between the length and the diameter of the flow passage involved in momentum and heat transfer. One denotes this ratio by ℓ/d_{he} where ℓ is the length and d_{he} is the heated equivalent diameter of the flow passage.

When the ℓ/d_{he} is small, boiling heat transfer and burnout occur in small steam quality two-phase flow. The flow regime is usually bubbly or slug flow. Under such situations, the boiling phenomena are localized. Therefore, the heat transfer coefficient and burnout heat flux do not depend on the heated length ℓ. In this case, the burnout heat flux is

high.

The boiling phenomena under very rapid transients are assumed to occur at low steam quality and localized, because in such transients heat transfer process changes so rapidly that the upstream condition can not affect the downstream phenomena.

One of the most important cases of the rapid transients in a nuclear reactor is the power transient where the reactor power increases exponentially with time due to excessive reactivity insertion in the reactor core. The accurate knowledge of the transient boiling heat transfer and burnout heat flux under such a rapid power increase is indispensable for the safety evaluation of a nuclear reactor.

In view of this, the problem on the boiling under rapid power increase (exponential increase) has been investigated in Chapter I. The small ℓ/d_{he} values were adopted in the experiment in order to simulate the localized and low steam quality boiling phenomena. Rapidly increasing heat generation rate in the platinum wires was realized using a large capacity power amplifier and a high speed analog computor.

In relation to the transient boiling under rapid power increase, non-boiling transient heat transfer becomes another important problem. Because, under the rapid transients, heat is transferred by transient non-boiling heat transfer mechanism up to a considerably high heat flux until the transient boiling commences. In view of this, the problem on the non-boiling heat transfer under rapid heat flux increases (exponential increase) has been investigated analytically in Chapter II.

Based on the boundary layer approximation, the overall understandings

of the transient non-boiling heat transfer have been made possible. The results obtained in this chapter are also useful in a natural circulation problem in the entire nuclear system which is dealt with in Chapter VI.

The second category of the transient boiling and two-phase flow phenomena corresponds to a larger ℓ/d_{he} value. In this case, the boiling heat transfer and burnout occur in high steam quality two-phase flow. The flow regime is usually annular or annular dispersed flow. The burnout heat flux under this condition is relatively low. Furthermore, the boiling heat transfer coefficient and burnout heat flux (in this case, often called dryout heat flux) are considerably affected by the steam quality at the outlet which reflects the integrated effects of the entire heated length. Therefore, they depend on the length of the heated section. These phenomena are often observed in a slow transient boiling. Under such a circumstance, the boiling heat transfer and dryout heat flux are determined by the liquid film flow rate at the heated surface, the droplet flow rate in the core flow and droplet size and its distribution. Therefore, in Chapters III through V, the problems on the hydrodynamics of the annular and annular diapersed flow have been analysed. In Chapter III, the mean droplet size and its distribution are analysed and the correlations for these parameters have been developed. In Chapter IV, the droplet entrainment rate from the liquid film at the wall and the deposition rate of the droplets to the wall have been analysed. These entrainment and deposition rates determine the film flow rate and the droplet flow rate under both transient and steady state conditions.

While Ghapters III and IV are involved in the annular dispersed flow with a positive liquid flow rate, Chapter V deals with the dispersed flow

under zero liquid flow rate (in a stagnant liquid pool). The droplet flow rate from the stagnant liquid pool is analysed in this chapter.

The results obtained in these three chapters enable accurate calculations of the boiling phenomena under annular and annular dispersed flow for a wide range of liquid flow rate. These calculations are indispensable for the evaluation of loss of coolant accidents with large and small breaks, loss of flow accidents and subsequent rewetting and reflooding phenomena in the nuclear reactors.

The annular dispersed flow hydrodynamics analysed in Chapters III and IV are of practical importance in an early stage of LOCA and reflooding. In this stage the liquid flow rate or reflooding velocity are positive values (flowing upward) and cocurrent annular dispersed flow is the main flow regime involved.

On the other hand, the pool entrainment analysed in Chapter V are important in a later stage of the LOCA and reflooding phenomena. In this stage, the reflooding velocity is assumed to be considerably low. Then liquid phase can be regarded as a stagnant pool. The droplet amount entrained from the free surface of the stagnant liquid pool by the streaming vapor flow plays an important role in the assesment of coolability of the regions not yet covered by water.

The last category of the transient boiling and two-phase flow phenomena corresponds to an extremely large ℓ/d_{he}. In this category, ℓ covers the entire system of a nuclear reactor. The understanding of the phenomena in this category is very important in analysing the overall characteristics of the nuclear reactor under accidental conditions.

Practically, when one evaluates the coolability of a nuclear re-

actor core by natural circulation cooling, treatment of transient heat transfer and two-phase flow throughout the entire loop of the reactor is indespensable. This is because in natural circulation, the driving force is determined by the density difference between the hot and cold sections throughout the entire loop. The importance of natural circulation cooling has been recognized since the accident of Three Mile Island Power Plant.

In view of these, the final chapter (Chapter Ⅵ) of this thesis is devoted to the natural circulation problem. The scaling criteria for the natural circulation under single and two-phase flow have been developed based on the basic formulations of the phenomena. Of cource, the results obtained in the previous chapters are closely related to this analysis. The knowledge of the non-boiling transient heat transfer (Chapter Ⅱ) can be used in the single phase natural circulation and the knowledges of the transient boiling and two-phase flow (Chapter I, Ⅲ-Ⅴ) are necessary to the two-phase natural circulation. The results obtained in this chapter can be used in designing a model plant which simulates a prototype power plant. They are also needed in interpreting the experimental data obtained in the model facilities.

CHAPTER I

FORCED CONVECTIVE BOILING HEAT TRANSFER UNDER POWER TRANSIENTS

I.1 INTRODUCTION

One of the most important phases of nuclear reactor transients is a power transient where the reactor power increases exponentially with time due to an excessive reactivity in the reactor core. When such a transient occurs, the temperature of the fuel surface increases rapidly and then transient boiling occurs. Further increase of the power will result in a transition from nucleate boiling to film boiling (transient burnout). Therefore, in evaluating the behavior of reactor coolant and fuel temperature in a reactivity accident, it is quite important to know the forced convective transient boiling heat transfer process for exponetial power increases.

Usually, the steam quality of a two-phase flow in normal operating conditions of a nuclear reactor is very low. Furthermore, under the rapid power increase, the transient boiling process is considered to be a local phenomenon. This means the phenomena are determined only by the local conditions and not dependent on the integrated effects of the upstream conditions.

Therefore, the boiling and two-phase flow phenomena under the reactivity accident in a nuclear reactor correspond to the phenomena with a small length to diameter ratio, ℓ/d_{he} (ℓ; heater length, d_{he}; heated equivalent diameter of a flow passage), where the boiling phenomena are localized and occur in a low quality two-phase flow.

In view of these, in this chapter, the transient boiling phenomena under exponential power increase have been studied experimentally, using small ℓ/d_{he} heaters and under low steam quality conditions.

There have been two groups of works on the transient boiling heat transfer associated with reactivity accident in a nuclear reactor. In the first group, the overall characteristics of the transient boiling and two-phase flow have been investigated using nuclear reactors. The typical ones are the SPERT and BORAX experiments. In these experiments, the reactivity accidents were artificially realized.

The second group corresponds to the out-of-pile experiments of which objectives are to clarify the basic mechanisms of the transient boiling.

Several experimental works on transient boiling heat transfer have been conducted in stagnant water at atmospheric pressure. Rosenthal *et al.* [1], Hall *et al.* [2] and Sakurai *et al.* [3] carried out experiments with exponential power increase. Cole [4], Hayashi *et al.* [5,6], Lurie *et al.* [7] and Sato *et al.* [8,9] with step power increase. Tachibana *et al.* [10,11] with linear power increase. In these experiments, quantitative knowledge of the transient non-boiling heat transfer coefficient and the transient maximum heat flux were obtained to some extent, but the range of experimental conditions was limited and the data were insufficient to give physical insight into the mechanisms involved. In particular, the effects of experimental variables on transient burnout characteristics were not made clear.

At elevated pressures up to 2.1 MPa, Sakurai *et al.* [12,13] carried out a series of transient pool boiling experiments with exponential power increase. They presented experimental correlations for transient incipient boiling superheat, transient departure from nucleate boiling and maximum heat fluxes including the effect of pressure.

Meanwhile, few works have been reported on transient boiling heat transfer under forced convection. Johnson *et al.* [14,15] conducted

experiments for transient forced convective boiling with an exponential power increase over a wide range of experimental variables, but the data of their experiments show considerable scatter and fail to give quantitative information about the effects of period, velocity, pressure and subcooling on the transient boiling characteristics. In Martenson's experiment [16], the flow channel was so narrow (0.18 cm gap) that bubbles generated on the heater would interact violently with the outer wall and make the phenomena more complicated. Only a few data for transient maximum heat flux are reported in his paper. Aoki *et al.* [17] studied flow and boiling characteristics under transient conditions using an annular passage with the inner tube heated exponentially with time. As in Martenson's experiment [16], the annular flow passage was narrow (0.15 cm gap), and the system pressure was limited to nearly atmospheric.

Thus little is known about transient boiling characteristics under forced convection. As for transient maximum heat flux, knowledge is still limited, particularly about the effects of period, velocity, pressure, subcooling and heater size, not to mention the mechanisms involved.

As is well known, various flow patterns exist in flow boiling and heat transfer characteristics are more or less affected by them. It is therefore necessary to study transient boiling taking these effects into consideration. In fact, a change of flow pattern along the flow direction, which is often encountered, makes transient boiling phenomena much more complicated.

Since the purpose of this chapter is to clarify fundamental aspects of transient boiling under forced convection, the experimental setup was designed in such a way that there might be no change of flow pattern and

no direct interaction between the outer tube wall and vapor bubbles [18]. Under these flow conditions, effects of exponential period, velocity, subcooling, pressure and heater size were studied on transient boiling heat transfer.

I. 2 EXPERIMENTAL APPARATUS AND PROCEDURES

Figure 1 shows a schematic diagram of the experimental apparatus used in this work. Distilled and deionized water (specific resistivity was more than 5 MΩ-cm) is circulated by a pump (at a flow rate up to 300 L/min.) and heated to the desired temperature level in a preheater. The flow rate is controlled by a flow regulating valve and measured by a turbine flow meter. Water and steam are separated in a separator & expansion tank, steam being then collected in condensers. A cooler is used to cool down circulating water to the desired temperature if necessary. The test loop is made of stainless steel with a quartz glass window to allow visual observation. The test section is a round tube, 1425 mm long and 38 mm in inner diameter. Water flows upward in this test section. The test loop is pressurized by steam in experiments at zero subcooling and by compressed air in those at subcooled conditions.

Figure 2 shows a cross-sectional view of the heated section. The heater element is a platinum wire of diameter 0.8, 1.2 and 1.5 mm and length 3.93, 7.12 and 10.04 cm. It is soldered to silver-coated copper electrodes at both ends, and located along the centerline of the flow channel at a position 1200 mm downstream from the test section inlet. Potential taps (0.2 mm diam platinum wires) are soldered at positions about

10 mm from both ends of platinum wire heater. Mean temperature and heat flux are measured between these potential taps so as to exclude end effects of the heater. The details of the experimental apparatus are are reported elsewhere [18].

The power supply and data processing systems are essentially the same as those used in transient pool boiling experiments performed by Sakurai *et al.*. The details are referred to Ref.[12,19]. A power amplifier controlled by a high speed analog computer supplies direct current to the test heater. The analog computer computes the instantaneous power generation rate in the heater and compares it with the reference value, $Q_0 \exp(t/\tau)$. Thus, the computer controls the output of the power apmlifier so that the two values (heat generation rate and the reference value) are equal. In this way, exponentially increasing heat input is supplied to the heater. The analog computer also computes the instantaneous mean temperature of the heater and cuts off the power supply to the heater when the calculated mean temperature reaches a preset value. This procedure prevents the heater from actual burnout. The power amplifier consists of 800 power transistors in parallel and can supply 2000 amperes at 40 volts. The heat generation rate in the heater is calculated from the measured voltage differnce between the potential taps of the heater and the current measured using a Manganin standard resistance. The instantaneous mean temperature of the heater is calculated from the unbalanced voltage of a double bridge circuit including the heater. Instantaneous surface heat flux is then obtained from the following equation for a given heat generation rate.

$$q = \frac{1}{4} Qd - \frac{1}{4} C_p \rho_s d \frac{dT_m}{dt} \quad . \tag{1}$$

On the other hand, the instantaneous surface temperature of the heater is obtained by solving numerically the following conduction equation for a given heat generation rate with a given surface heat flux as a boundary condition

$$\lambda_s \frac{1}{r} \frac{\partial}{\partial r}\left(r \frac{\partial T}{\partial r}\right) + Q = C_p \rho_s \frac{\partial T}{\partial t} \quad . \tag{2}$$

An on-line data processing system was used. The unbalanced voltage of the double bridge circuit including the heater, and the voltage differences between the potential taps of the heater and across the standard resistance were fed to the digital computer through an A-D converter. The fastest sampling speed of the A-D converter was 20 μs per channel.

I. 3 RESULTS AND DISCUSSION

I.3.1. Steady State Performances

Before considering transient boiling heat transfer, it is important to know the steady-state boiling and non-boiling characteristics with the same heaters under the same flow conditions. Steady-state experiments were therefore carried out prior to transient experiments. The effects of velocity, subcooling, pressure and heater size on the non-boiling heat transfer coefficient, the nucleate boiling heat transfer coefficient and the maximum heat flux were studied at steady state. The results indicated that when the exponential period was larger than 5 sec, the rate of heat input increase was so slow that heat transfer coefficients and maximum heat flux did not depend upon the exponential period. Therefore, experiments with exponential periods of 5 - 10 sec can be practically regarded as steady-state experiments.

I.3.1.a. Non-Boiling Heat Transfer

As shown in Fig.2, the heaters used in this experiment were thin platinum wires located at the center of the pipe parallel to its axis. To the present authors' knowledge, there can be found neither theoretical nor experimental results for the turbulent heat transfer coefficient of such a heat transfer configuration. Therefore, it is necessary to determine experimentally the non-boiling heat transfer coefficient for the heaters and flow geometry used in these experiments. At the same time, the hydrodynamic aspects around the heater must be known. These knowledges will become necessary in analysing boiling phenomena. The velocity distributions just upstream of the heater were measured with a Pitot tube. Results indicated that fully-developed flows were established and velocity distributions were approximated by the 1/7 power law. Flow disturbances caused by the electrodes supporting the heater were visualized by introducing very small air bubbles into the flow as tracers. It was found that the electrodes produced no serious effects on the flow around the heater.

The non-boiling heat transfer coefficient varied approximately as the 0.7 power of the velocity and increased with increasing water temperature and with decreasing heater length. Effects of heater diameter on heat transfer coefficient could not be seen over the range of the heater size of this experiment. Data for pressure ranging from 0.143 to 1.503 MPa, liquid subcooling from 70 to 0 K (liquid temperature from 313 to 461 K), velocity from 0.39 to 4.04 m/s, heater diameter from 0.8 to 1.5 mm and heater length from 4 to 10 cm, are presented in nondimensional form in Fig.3. Heater length was used as a characteristic length. Physical

properties were taken at film temperature. Experimental data are correlated by Eq.(3) within ±15 % deviations

$$Nu = 0.2411\ Re^{0.7}Pr^{0.35} \qquad (3)$$

I.3.1.b. Nucleate Boiling Heat Transfer

Figure 4 shows typical trends of the steady state boiling curves obtained in this experiment. Figure 4(a) represents the effect of pressure. In the fully-developed nucleate boiling region, the boiling curve shifts toward the left as pressure increases. Thus, the boiling heat transfer coefficient($q/\Delta T_{sat}$) increases with increasing pressure. Figure 4(b) shows the effect of subcooling, indicating that the fully-developed nucleate boiling curve is almost independent of the liquid subcooling. Figure 4(c) shows the effect of velocity. No significant such an effect can be seen on the fully-developed nucleate boiling curves almost over a velocity range of 0 to 4.04 m/s. Figure 4(d) shows the effect of heater diameter and Fig. 4(e) the effect of heater length. As shown in these figures, the heater diameter and heater length have little effects on the boiling curves within the limited heater size range of this experiment.

The fully-developed boiling curve was expressed in the form of $q \propto (\Delta T_{sat})^n$. The exponent 'n' was about 3 to 4 regardless of experimental conditions. It is generally said that, in fully-developed nucleate boiling region, forced convective boiling curve almost coincides with the extrapolation of the pool boiling curve [20]. This was the case in this experiment as shown in Fig.4(c). Kutateladze [21] presented a nondimensional correlation for pool boiling heat transfer coefficient, that is,

$$Nu_B = 7.0 \times 10^{-4}\ P^{*0.7}\ Re_B^{0.7}\ Pr^{0.35}\ , \qquad (4)$$

where

$$Nu_B = \frac{q}{\Delta T_{sat}} \frac{\sqrt{\frac{\sigma}{g(\rho_l-\rho_v)}}}{\lambda_l}\ , \quad Re_B = \frac{q}{H_{fg}\rho_v} \frac{\sqrt{\frac{\sigma}{g(\rho_l-\rho_v)}}}{\nu_l}\ , \quad P^* = \frac{P}{\sqrt{\sigma g(\rho_l-\rho_v)}}.$$

Figure 5 is a representation of the experimental heat transfer coefficient in fully-developed nucleate boiling in $Nu_B/Re_B^{0.7}$ vs. $P^{*0.7}\ Pr^{0.35}$ diagram. The regression is given by

$$Nu_B = 10.0 \times 10^{-4}\ P^{*0.7}\ Re_B^{0.7}\ Pr^{0.35}\ . \qquad (5)$$

The fully-developed nucleate boiling heat transfer coefficient obtained in this work was about 40 % higher than Kutateladze's correlation.

I.3.1.c. Maximum Heat Flux

Figures 6 through 10 demonstrate a complete set of the experimental steady state maximum heat flux obtained in this work. The solid lines except those in Fig.10 represent the empirical correlation, Eq.(10), which will be discussed later. Figures 6 and 7 show the effects of velocity and subcooling on the steady state maximum heat flux for the 1.2 mm diam and 7 cm long heater. Results show the steady state maximum heat flux increases with increasing velocity, subcooling and pressure. At constant pressure, it increases approximately as the 0.2 power of the velocity over the velocity range of 0.39 to 4.04 m/s. Figure 8(a) shows the results with the 0.8 mm diam and 7 cm long heater. Figures 8(b) and (c) with the 1.5 mm diam and 7 cm long heater. As is the case with 1.2 mm diam heater, the maximum heat flux increases with increasing subcooling, velocity and pressure.

In Fig.9(a) is shown the effect of heater diameter on the maximum heat flux. The maximum heat flux slightly increases with decreasing heater diameter. This tendency is noticeable at higher velocity and larger inlet subcooling. Figure 9(b) is the effect of heater length on the maximum heat flux over a heater length range of 3.93 to 10.04 cm, showing the maximum heat flux does not depend upon the heater length.

Figure 10 shows the effect of subcooling on the steady state maximum heat flux for the 1.2 mm diam, 7 cm long heater at a velocity of 2.67 m/s over a pressure range of 0.143 to 1.503 MPa. At each pressure, the steady state maximum heat flux increases with subcooling. The slope in the higher subcooling range (40 ~ 70 K) is steeper than that in the lower subcooling range(0 ~ 40 K). This tendency is noticeable at lower system pressures. A similar trend was observed at velocity other than 2.67 m/s.

Recently, Katto [22] correlated successfully a variety of forced convective maximum heat flux data for annuli with $l/d_{he} > 10$ by the following equations

$$q_{max} = q_{max,0} \left(1 + K \frac{\Delta H_i}{H_{fg}} \right), \tag{6}$$

$$\frac{q_{max,0}}{GH_{fg}} = f\left(\frac{\rho_l}{\rho_g}, \frac{\sigma\rho_l}{G^2 l}, \frac{l}{d_{he}} \right). \tag{7}$$

In the present work, l/d_{he} is very small (0.033 ~ 0.083), so that it may not be appropriate to apply Eqs.(6) & (7) to the present case. However, a similar approach may be adapted to correlate the present maximum heat flux data. In this approach, the heater length, l, in Eq.(7) was taken place by the Laplace coefficient $l_0 = \sqrt{\frac{\sigma}{g(\rho_l - \rho_v)}}$, because the maximum heat flux did not show the dependence on heater length as shown in Fig.9(b).

The value of K in Eq.(6) was determined by least squares fitting, using the present experimental data over a subcooling range of 0 to 70 K. The result is given by

$$K = 0.03648 \left(\frac{l_0}{d_{he}} \right)^{-0.20} \left(\frac{\rho_v}{\rho_l} \right)^{-0.79} + \varepsilon \quad , \tag{8-1}$$

where $\varepsilon = 0$ ($\Delta T_{sub} = 0 \sim 40$ K)

$$= 0.00808 \left(\frac{\rho_v}{\rho_l} \right)^{-1.09} \frac{\Delta H_i - \Delta H_{i40}}{\Delta H_i} \quad (\Delta T_{sub} = 40 \sim 70 \text{ K}) \quad . \tag{8-2}$$

In this experiment, d_{he} ranged from 1805 to 963 mm for heater diameter from 0.8 to 1.5 mm.

On the other hand, $q_{max,0}$ in Eq.(6) is given by Eq.(9), by using least squares fitting

$$\frac{q_{max,0}}{GH_{fg}} = 0.3740 \left(\frac{\rho_v}{\rho_l} \right)^{0.66} \left(\frac{\sigma \rho_l}{G^2 l_0} \right)^{0.40} \quad . \tag{9}$$

By substituting Eqs.(8) and (9) into Eq.(6), we have

$$\frac{q_{max}}{GH_{fg}} = 0.3740 \left(\frac{\rho_v}{\rho_l} \right)^{0.66} \left(\frac{\sigma \rho_l}{G^2 l_0} \right)^{0.40}$$

$$\times \left[1 + \left\{ 0.03648 \left(\frac{l_0}{d_{he}} \right)^{-0.20} \left(\frac{\rho_v}{\rho_l} \right)^{-0.79} + \varepsilon \right\} \frac{\Delta H_i}{H_{fg}} \right] \quad , \tag{10}$$

where ε is given by Eq.(8-2) and is a small contribution (15 % at most). A comparison of Eq.(10) with the present steady state maximum heat flux data is made in Fig.11 in $\frac{q_{max}}{GH_{fg}}$ vs. $(\frac{\rho_v}{\rho_l})^{0.66}(\frac{\sigma \rho_l}{G^2 l_0})^{0.40}(1+K\frac{\Delta H_i}{H_{fg}})$ diagram. The data scatter around Eq.(10) within ±10 % error bands.

Borishansky *et al.* [23] reported steady state maximum heat flux under forced convection in an annular passage whose geometry is similar to that in our experiment. In their experiment, a 3 mm o.d., 7.2 cm long heater is located

in a 19 mm i.d. tube with water and ethyl alcohol flowing at velocities up to 2.5 m/s at atmospheric pressure($1/d_{he}$=0.61). Figure 12 shows a comparison of the present correlation, Eq.(10), with their data. Except for the case of water with 46.6 K subcooling, Eq.(10) satisfactorily agrees with their data.

Equation(10) is originally derived for the experimental data at velocity higher than 0.39 m/s and, therefore, it may not be applied to those at lower velocity or stagnant condition. Measurements were made of the steady state maximum heat flux at zero flow and zero subcooling (hereafter called $q_{max,st00}$). Figure 13 shows $q_{max,st00}$ in $\frac{q_{max}}{H_{fg}\rho_v}$ vs. $\{\frac{\sigma g(\rho_l-\rho_v)}{\rho_v^2}\}^{1/4}$ diagram. In this figure, the open circle represents the value of $q_{max,st00}$ obtained by extrapolating non-zero flow and non-zero subcooling data at $U \to 0$ and $\Delta T_{sub} \to 0$. The straight line in this figure represents the Kutateladze's correlation of maximum heat flux for saturated pool boiling [21], which is given by

$$\frac{q_{max,st00}}{H_{fg}\rho_v} = 0.16 \left\{ \frac{\sigma g(\rho_l-\rho_v)}{\rho_v^2} \right\}^{1/4} . \qquad (11)$$

Agreement was quite good between Kutateladze's correlation and the present data.

Under forced convection, there are several different burnout mechanisms suggested for different flow patterns [24]. Under the particular flow condition of this experiment and of Borishansky *et al.* (small heater diameters, short heater lengths), quality change along the heater is small and burnout quality is low. Therefore, it is likely that steady burnout is caused not by dryout of liquid film flow but by bubble coalescence and vapor blanketting near the heater surface.

Visual observations were made of steady state boiling to provide a better understanding of burnout phenomen.

Photo 1 shows some boiling aspects at pressure 0.143 MPa, velocity 1.35 m/s, subcooling 10 K and nearly maximum heat flux. It can be seen that small bubbles generated on the heater coalesce to form larger bubbles as flow goes downstream (upper side of this photo). It is also observed that these larger bubbles further coalesce and vapor blankets appear around the heater surface.

I.3.2. Transient Performances

I.3.2.a. Transient Non-Boiling Heat Transfer

During a period from the initiation of heating to the boiling inception, heat is transferred to water by transient non-boiling heat transfer. Analytical or experimental works have been presented by Chambré *et al.* [25] and Soliman *et al.* [26] for transient non-boiling heat transfer under forced convection with exponential heat input to flat plates. Chambré *et al.* assumed a slug flow model where the velocity profile is uniform, while Soliman *et al.* took into consideration the boundary layer over a flat plate and compared the result with experiments. Both analyses predicted that the transient non-boiling heat transfer coefficient had initially a decreasing tendency with time, t, and attained an asymptotic value for $\frac{t}{\tau} \geq \frac{l}{\tau U}$ where t is the time elapsed from the initiation of heating.

The present experiment showed a trend similar to those predicted by the above analyses. Figure 14 shows the variation of transient non-boiling heat transfer coefficients with time for velocity 1.35 m/s, water temperature 316 K and period from 10 ms to 5 s using 1.2 mm diam and 7 cm

long heater. The transient non-boiling heat transfer coefficient initially decreases with time and attains an asymptotic value approximately by $\frac{t}{\tau} = 3$. The transient heat transfer coefficient maintains the asymptotic value until boiling occurs. In this figure, are also presented the theoretical or asymptotic values calculated by Eq.(13) which will appear later in this section. Particular attention should be paid to these asymptotic values of the heat transfer coefficient (therefore the heat transfer coefficient means hereafter its asymptotic value in this section). As shown in Fig.14, the heat transfer coefficient increases with decreasing period. The present experiment also showed that the heat transfer coefficient increased with an increase in velocity and heater length for constant period. However, the heater diameter had little effect on the transient non-boiling heat transfer coefficient within the limited range of heater diameters tested in the present work(0.8 ~ 1.5 mm diam).

Figure 15 represents the experimental data in Nu_{tr}/Nu_{st} vs. $\tau U/l$ diagram, where Nu_{tr} is the Nusselt number associated with the transient non-boiling heat transfer coefficient and Nu_{st} is associated with the steady state coefficient (see Nomenclature). The data are correlated by Eq.(12) within $\pm$20%.

$$\frac{Nu_{tr}}{Nu_{st}} = 1 + 0.1448 \left(\frac{\tau U}{l} \right)^{-0.97} . \qquad (12)$$

Figure 15 also presented a comparison between the present data and an analytical equation obtained based on a slug flow model, Eq.(13), for exponential heat input to a cylindrical wire for $\frac{t}{\tau} \geq \frac{l}{\tau U}$ whose heat capacity can be neglected

$$\frac{Nu_{tr}}{Nu_{st}} = \frac{\frac{4}{3\sqrt{\pi}} (1-\xi) \sqrt{\frac{l}{\tau U}}}{(1- \frac{1}{2} \frac{\tau U}{l}) \mathrm{erf} \sqrt{\frac{l}{\tau U}} + \sqrt{\frac{\tau U}{\pi l}} \exp(- \frac{l}{\tau U}) - \frac{8}{3} \xi \sqrt{\frac{\tau U}{\pi l}} \{1- \frac{\tau U}{l} + \frac{\tau U}{l} \exp(- \frac{l}{\tau U})\}} , \qquad (13\text{-}1)$$

where

$$\xi = \frac{3}{8}\sqrt{\pi}\left(\frac{l}{d}\right)\frac{1}{\sqrt{RePr}} \quad . \tag{13-2}$$

Here, Nu_{st} is derived theoretically and is given by

$$Nu_{st} = \frac{3}{4}\sqrt{\pi}\,\frac{1}{1-\xi}\sqrt{RePr} \quad . \tag{14}$$

Equations(13) and (14) are derived in the same manner as Chambré's treatment; by consulting the textbook by Carslaw and Jaeger [27] (see Appendix). Equation (13-1) reduces to Chambré's equation for a flat plate with $\xi = 0$. Under the present experimental conditions, ξ ranged from 0.021 to 0.079. In this range of ξ, ξ had little effect on Nu_{tr}/Nu_{st} in Eq.(13-1) (therefore, in Fig.15 the curve for $\xi = 0.079$ indicates representative of the present experiment).

It is noted in Fig.15 that Eq.(13-1) predicts well the experimental trends, though the model cannot reflect quantitatively the experimental tendencies in Nu_{tr} and Nu_{st} (compare, for example, Eq.(14) with Eq.(3)). More strict models are needed to take into account the effects of heat capacity and flow structure such as the turbulence and the velocity field around a thin wire.

I.3.2.b. Transient Boiling Heat Transfer

Typical examples of steady state and transient boiling curves are demonstrated in Figs.16 through 18. Figure 16(a) shows results for the 1.2 mm diam, 7 cm long heater at pressure 0.396 MPa, subcooling 10 K and velocity 1.35 m/s. The exponential period of power increase ranges from 10 s(steady state) to 5 ms. For each period, the transient boiling curve

shifts towards higher wall superheat than the steady state boiling curve (the solid curve in the figures) for a certain time after commencement of boiling. At higher heat flux, the transient boiling curve coincides with the steady state boiling curve and/or its extrapolation. This type of transient boiling is called "A-type" transient boiling in this paper. Most of the transient boiling achieved in the present work was A-type.

However, as can be seen in Fig.16(b), results indicated that the transient boiling curves did not coincide with the steady state boiling curve and/or its extrapolation for the period smaller than 14 ms with 0.8 mm diam heater. On these particular boiling curves, the wall superheat remains higher than that on steady state boiling curve and/or its extrapolation until the maximum heat flux is reached. This type of transient boiling curve is called 'B-type' here.

B-type boiling was observed in the following conditions. For 0.8 mm diam, 7 cm long heater: pressure lower than 0.396 MPa, subcooling lower than 30 K and period smaller than 14 ms. For 1.2 mm diam, 7 cm long heater: pressure lower than 0.143 MPa, subcooling lower than 10 K and period smaller than 30 ms. For 1.5 mm diam, 7 cm long heater it was not observed. For 1.2 mm diam, 10 cm long heater it was observed for pressures lower than 0.396 MPa, subcooling lower than 30 K and periods smaller than 14 ms. For 1.2 mm diam, 4 cm long heater it was not observed.

In a nuclear reactor, the system pressure is usually more than 0.4 MPa. Therefore, from a practical point of view, A-type boiling which was mostly observed in the high pressure range is important. In view of this a primary concern is directed to A-type boiling.

As mentioned above, the transient boiling curve had a portion where the wall superheat shifts to the right of the steady state boiling curve. A similar phenomenon is reported to have been observed in pool boiling of water [13].

I.3.2.c Transient Maximum Heat Flux

Figures 19 through 27 are correlative representations of the experimental transient maximum heat flux vs. exponential period. Solid lines in these figures represent an empirical correlation, Eq.(17) and will be discussed later. The boundary between A-type and B-type boilings is also indicated in some of these figures by dot-dash-line. Unless boundaries are indicated in the figure, A-type boiling is meant. Effects of period, pressure, subcooling, velocity and heater size on the transient maximum heat flux will be discussed individually.

Effect of exponential period on transient maximum heat flux is given in Fig.26(a) for 0.8 mm diam, 7 cm long heater at pressure 0.396 MPa, subcooling 30 K and velocity from 1.35 to 4.04 m/s. In this figure, the right hand side of the dot-dash-line is a region of A-type transient boiling and the left hand side a region of B-type. In the A-type region, the transient maximum heat flux increases with decreasing period at constant velocity, whereas, in the B-type region, the transient maximum heat flux decreases with the period and then increases.

Effects of velocity, subcooling and pressure are seen in Figs.26(a), (b) and (c), respectively. Results thus indicate that the transient maximum heat flux increases as the period is decreased and, for a constant period it increases with increasing velocity, subcooling and pressure.

Figures 27(a) and (b) show the effects of heater diameter and heater length, respectively. In these representations, arrow marks indicate the transition between A-type and B-type boilings. As far as A-type boiling is concerned, it may be concluded that the transient maximum heat flux has an increasing tendency with heater diameter but is independent of heater length for a constant period.

As stated in previous section, the boiling curves encountered in the present experiment were mostly A-type, and B-type boiling was exceptional. A-type maximum heat flux will be discussed below in more detail.

As shown in the figures, the dependences of the transient maximum heat flux on velocity, subcooling, pressure, heater diameter and length observed in A-type boiling were similar both quantitatively and qualitatively to those of the steady state maximum heat flux. Therefore, the difference between the transient maximum heat flux and the steady state maximum heat flux seems to be useful in correlating the transient maximum heat flux. In fact, the difference between the transient maximum heat flux and steady state flux varied approximately as the -0.6 power of the period over the pressure, velocity, subcooling and heater sizes ranges of this experiment. Taking this into account, the following dimensional analysis will be adopted.

As stated in section 3.1.c., the steady state maximum heat flux is expressed in the form of five nondimensional groups, $\frac{q}{GH_{fg}}$, $\frac{\rho_v}{\rho_l}$, $\frac{\sigma\rho_l}{G^2 l_0}$, $\frac{l_0}{d_{he}}$ and $\frac{\Delta H_i}{H_{fg}}$. By applying dimensional analysis to the case of transient maximum heat flux, we obtain another nondimensional group, $\frac{\tau_0 G}{\rho_l l_0}$ in addition to the above five, where τ_0 is a characteristic time specifying

the transient maximum heat flux. It might be possible to assume exponential period, τ, for τ_0 for exponentially increasing heat generation. We further assume the following nondimensional expression for the transient maximum heat flux because the transient maximum heat flux approaches the steady state maximum heat flux at the period for exponential power increase being infinity

$$\frac{q_{max,tr} - q_{max,st}}{GH_{fg}} = C \left(\frac{\rho_v}{\rho_l} \right)^a \left(\frac{\sigma\rho_l}{G^2 l_0} \right)^b \left(\frac{l_0}{d_{he}} \right)^c \left(\frac{\Delta H_i}{H_{fg}} \right)^d \left(\frac{\tau G}{\rho_l l_0} \right)^e \quad (15)$$

The experimental data for A-type boiling were used to determine a ~ e in Eq.(15). This showed that $(q_{max,tr} - q_{max,st})$ had little dependence on $\left(\frac{l_0}{d_{he}} \right)$ and $\left(\frac{\Delta H_i}{H_{fg}} \right)$, i.e. c and d are zero. a, b and e have been determined by least squares fitting, giving

$$\frac{q_{max,tr} - q_{max,st}}{GH_{fg}} = 0.2038 \left(\frac{\rho_v}{\rho_l} \right)^{0.52} \left(\frac{\sigma\rho_l}{G^2 l_0} \right)^{0.19} \left(\frac{\tau G}{\rho_l l_0} \right)^{-0.63} \quad (16)$$

Figure 28 shows plots of the transient maximum heat flux in terms of $\left(\frac{q_{max,tr} - q_{max,st}}{GH_{fg}} \right)\left(\frac{\rho_v}{\rho_l} \right)^{-0.52}\left(\frac{\sigma\rho_l}{G^2 l_0} \right)^{-0.19}$ vs. $\left(\frac{\tau G}{\rho_l l_0} \right)$ for subcooling from 0 to 40 K, velocity from 1.35 to 4.04 m/s, pressure from 0.143 to 1.503 MPa, heater diameter from 0.8 to 1.5 mm and heater length from 3.93 to 10.04 cm and for A-type boiling. The data lie within ±30 % of Eq.(16).

By substituting Eq.(10) into Eq.(16), we finally obtain Eq.(17) for the transient maximum heat flux

$$\frac{q_{max,tr}}{GH_{fg}} = 0.3740 \left(\frac{\rho_v}{\rho_l} \right)^{0.66} \left(\frac{\sigma\rho_l}{G^2 l_0} \right)^{0.40} \times \left[1 + \{0.03648 \left(\frac{l_0}{d_{he}} \right)^{-0.20} \left(\frac{\rho_v}{\rho_l} \right)^{-0.79} \pm \varepsilon\} \frac{\Delta H_i}{H_{fg}} \right] + 0.2038 \left(\frac{\rho_v}{\rho_l} \right)^{0.52} \left(\frac{\sigma\rho_l}{G^2 l_0} \right)^{0.19} \left(\frac{\tau G}{\rho_l l_0} \right)^{-0.63} \quad (17)$$

where ε is given by Eq.(8-2)

$$\varepsilon = 0 \quad (\Delta T_{sub} \approx 0 \sim 40 \text{ K})$$

$$= 0.00808 \left(\frac{\rho_v}{\rho_l} \right)^{-1.09} \frac{\Delta H_i - \Delta H_{i40}}{\Delta H_i} \quad (\Delta T_{sub} = 40 \sim 70 \text{ K})$$

Figure 29 shows a comparison of Eq.(17) with the experimental data. Over the experimental range of this work, the measured maximum heat flux for A-type boiling lies within ±20 % of that calculated.

Equation(16) can be rewritten as

$$\frac{q_{max,tr} - q_{max,st}}{q_{max,st00}} = 1.274 \left(\frac{\rho_v}{\rho_l} \right)^{-0.30} \left[\frac{\tau \left\{ \frac{\sigma g(\rho_l - \rho_v)}{\rho_v^2} \right\}^{\frac{1}{4}}}{l_0} \right]^{-0.63}, \quad (18)$$

where $q_{max,st00}$ is given by Eq.(11). For water at pressures from 0.1 to 5 MPa, Eq.(18) can be approximated for practical uses by

$$\frac{q_{max,tr} - q_{max,st}}{q_{max,st00}} = 0.083 \, \tau^{-0.63}, \quad (19)$$

where τ is in sec. Equation(19) correlates the present data accurately as Eq.(16).

As stated in section *3.1.c.*, under the flow conditions of this experiment, it is considered that burnout is caused by bubble coalescence and vapor blanketting. Even at steady state maximum heat flux, the transition to film boiling, and the resulting heater overheat occurs over a certain(though very short) time period. This is partly because the heater possesses finite heat capacity, and partly because it takes certain time for hydrodynamic instability to grow and for the liquid layer under the vapor blanket to vaporize. In the case of the transient power increase, a similar process is assumed to occur for A-type boiling,where the transient boiling curve coincides with the steady state boiling curve and/or its extrapolation. Under such circum-

stances, after the heat flux reaches the steady state maximum heat flux, it will continue to increase for a time duration needed for the growth of hydrodynamic instability and the evaporation of liquid layer under vapor blanket.

The present study gives quantitative information about forced convective transient boiling heat transfer with fine wires. However, much remains to be studied. The mechanisms of forced convective transient boiling phenomena need to be clarified based on more detailed observations of flow characteristics and bubble behavior under transient conditions.

I. 4 CONCLUSIONS

Forced convective transient boiling heat transfer for exponential heat input using platinum wire heaters were studied. And the following conclusions are drawn.

(1) The steady state non-boiling heat transfer coefficient is correlated within ±15 % by Eq.(3), where the heater length, ℓ, appears as a characteristic length instead of diameter.

(2) The steady state heat transfer coefficient in fully-developed nucleate boiling region was 40 % higher than Kutateladze's prediction.

(3) The steady state maximum heat flux increased with increasing velocity, pressure and subcooling and with decreasing heater diameter. The steady state maximum heat flux is correlated by Eq.(10) within ±10 % errors. Equation(10) agrees well with Borishansky *et al.*'s data for water and ethyl alcohol.

(4) The transient non-boiling heat transfer coefficient increased with

decreasing period and increased with an increase in velocity and heater length for constant period. The transient non-boiling heat transfer coefficient is correlated by Eq.(12) within ±20 % . Equation(13), an analytical correlation obtained based on slug flow model, predicts the experimental trends.

(5) Two types of transient boiling were observed. In A-type boiling, the transient boiling curve coincided at higher heat flux with the steady state boiling curve and/or its extrapolation. In B-type boiling, the wall superheat remained higher than that on the steady state boiling curve and/or its extrapolation until the maximum heat flux was reached. Under most of the experimental conditions tested, A-type boiling was observed.

(6) In A-type boiling, the transient maximum heat flux increased with decreasing period and with increasing pressure, velocity and subcooling. The difference between the transient maximum heat flux and the steady state flux varied approximately as the -0.6 power of the period over the pressure, velocity, subcooling and heater size ranges of this experiment.

(7) The nondimensional correlation for the transient maximum heat flux, Eq.(17), is presented for A-type boiling. Equation(17) correlates experimental data within ±20 % . For water at pressures from 0.1 to 5 MPa, Eq.(15) can be approximated by Eq.(18).

NOMENCLATURE

a ~ e	exponents in Eq.(15);
C	constant in Eq.(15);
C_p	specific heat of platinum;
d	heater diameter;
d_{he}	heated equivalent diameter ($=(D^2-d^2)/d$);
D	diameter of test section;
g	acceleration due to gravity;
G	mass velocity;
H_{fg}	latent heat of vaporization;
ΔH_i	enthalpy of inlet subcooling;
ΔH_{i40}	enthalpy of 40 K inlet subcooling;
K	parameter for the effect of inlet subcooling;
ℓ	heater length;
ℓ_0	Laplace coefficient ($= \sqrt{\frac{\sigma}{g(\rho_\ell-\rho_v)}}$);
n	exponent;
Nu	Nusselt number ($=\alpha\ell/\lambda_\ell$);
Nu_B	boiling Nusselt number defined in Eq.(4);
Nu_{st}	steady state non-boiling Nusselt number ($=\alpha_{st}\ell/\lambda_\ell$);
Nu_{tr}	transient non-boiling Nusselt number ($=\alpha_{tr}\ell/\lambda_\ell$);
P	pressure;
P*	nondimensional pressure defined in Eq.(4);
Pr	Prandtl number;
q	heat flux;
q_{max}	maximum heat flux;

$q_{max,0}$ maximum heat flux at zero subcooling;

$q_{max,st}$ steady state maximum heat flux;

$q_{max,st00}$ steady state maximum heat flux at zero flow and zero subcooling;

$q_{max,tr}$ transient maximum heat flux;

Q heat generation rate per unit volume;

r radial position;

R radius of test section;

Re Reynolds number ($=UL/\nu_l$);

Re_B boiling Reynolds number defined in Eq.(4);

t time;

T temperature;

T_m mean temperature of heater;

T_{sat} saturation temperature;

ΔT_{sat} wall superheat ($=T_w-T_{sat}$);

ΔT_{sub} inlet subcooling;

T_w wall temperature;

u local liquid velocity;

U mean liquid velocity;

Greek symbols

α heat transfer coefficient;

α_{st} steady state non-boiling heat transfer coefficient;

α_{tr} transient non-boiling heat transfer coefficient;

ε parameter for the effect of inlet subcooling defined in Eq.(8-1);

λ	thermal conductivity;
ν	dynamic viscosity;
ρ	density;
σ	surface tension;
τ	exponential period of power increase;
τ_0	characteristic time;

Subscripts

l	liquid;
v	vapor;
s	solid(platinum);

Physical properties were taken at saturation temperatures unless otherwise indicated.

REFERENCES

1. Rosenthal,M.W., "An experimental study of transient boiling", *Nucl. Sci. Engng* 2, 640-656 (1957); also M. W. Rosenthal and R. L. Miller, ORNL-2294 (1957).

2. Hall,W.B. and Harrison,W.C.,ı,"Transient boiling of water at atmospheric pressure", *Proceedings of the Third International Heat Transfer Conference*, Chicago (1966).

3. Sakurai,A., Mizukami,K. and Shiotsu,M., "Experimental studies on transient boiling heat transfer and burnout", *Proceedings of the Fourth International Heat Transfer Conference*, Paris (1970).

4. Cole,R., "Investigation of transient pool boiling due to sudden large power surge", NACA Technical Note 3885 (1956).

5. Hayashi,S., Iwazumi,T.,Wakabayashi,J., Sakurai,A., Aoki,H. and Kitamura,M., "Experimental study of the temperature overshoot and the delay time of the transient boiling", *J. Atomic Energy Soc. Japan* 2, 736-741 (1960) (in Japanese).

6. Hayashi,S.,Sakurai,A. and Iwazumi,T., "Transient heat transfer in heterogeneous water reactor (I)", *J. Atomic Energy Soc. Japan* 5, 403-411 (1963) (in Japanese).

7. Lurie,H. and Johnson,H.A., "Transient pool boiling of water on vertical surface with a step in heat generation", *J. Heat Transfer* 84, 217-224 (1962).

8. Sato,T.,Michiyoshi,I.,Takeuchi,K. and Kondo,K.,"Experimental studies of the burnout under the boiling I", *Trans. J.S.M.E.* 27, 722-730 (1961) (in Japanese).

9. Sato,T., Michiyoshi,I. and Takeuchi,K.,"Studies of the burnout under the boiling II", *Trans. J.S.M.E.* 27, 1817-1822 (1961) (in Japanese).

10. Tachibana,F., Akiyama,M. and Kawamura,H.,"Heat transfer and critical heat flux in transient boiling (I)", *J. Nucl. Sci. Technol.* 5, 117-126 (1968).

11. Kawamura,H., Tachibana,F. and Akiyama,M.,"Heat transfer and DNB heat flux in transient boiling,"*Proceedings of the Fourth International Heat Transfer Conference*, Paris (1970).

12. Sakurai,A. and Shiotsu,M.,"Transient pool boiling heat transfer, part 1", *J. Heat Transfer* 99, 547-553 (1977).

13. Sakurai,A. and Shiotsu,M.,"Transient pool boiling heat transfer, part 2", *J. Heat Transfer* 99, 554-560 (1977).

14. Johnson,H.A., Shrock,V.E. *et al.* , Reactor heat transients project, University of California, Berkeley, USAEC, TID 4500 Reports: SAN 1001 (1961) to SAN 1013 (1966).

15. Johnson,H.A., "Transient boiling heat transfer to water", *Int. J. Heat Mass Transfer* 14, 67-82 (1971).

16. Martenson,A.J.,"Transient boiling in small rectangular channels", WAPID-T-1290 (1963).

17. Aoki,S., Kozawa,Y. and Iwasaki,H.,"Boiling and burnout phenomena under transient heat input", *Trans. J.S.M.E.* 41, 2950-2959 (1975) (in Japanese).

18. Serizawa,A. and Sakurai,A., unpublished work (1973).

19. Sakurai,A., Shiotsu,M. and Hata,K.,"Transient boiling caused by rapid depressurization from initial nonboiling state", *Multiphase Transport; Fundamental, Reactor Safety, Applications, edited by T. N. Veziroglu*, Vol. 2, 724-747, Hemisphere Pub. Co., Washington D.C. (1980).

20. McAdams,W.H., *Heat Transmission, Third edition*, McGraw-Hill, New York

(1954).

21. Kutateladze,S.S., *Heat Transfer in Condensation and Boiling*, AEC-tr-3770 (1959).

22. Katto,Y., "Generalized correlations of critical heat flux for uniformly heated annuli," *Int. J. Heat Mass Transfer* 22, 575-584 (1979).

23. Borishansky,V.M. and Fokin,B.S., " Onset of heat transfer crisis with unsteady increase in heat flux," *Heat Transfer-Soviet Research* 1, 27-55 (1969).

24. Tong,L.S. and Hewitt,G.F., "Overall viewpoint of flow boiling CHF mechanism," ASME Paper 72-HT-54 (1972).

25. Johnson,H.A. and Chambré,P.L., "Slug conduction solution for exponential heat generation in a thin flat plate," USAEC Report SAN-1009 (1963), (quoted from USAEC Report SAN-1013 (1963)).

26. Soliman,M. and Johnson,H.A., "Transient heat transfer for forced convection flow over a flat plate of appreciable thermal capacity and containing an exponential time-dependent heat source," *Int. J. Heat Mass Transfer* 11, 27-38 (1968).

27. Carslaw,H.S. and Jaeger,J.C., *Conduction of Heat in Solids, Second edition*, Oxford Univ. Press, Oxford (1959).

APPENDIX

Consider a semi-infinite rod (radius r_0) in a parallel flow(in z direction) with uniform velocity, U, in lateral direction (slug flow assumption).

The governing equation for $r \geqq r_0$ is

$$\frac{\partial\theta}{\partial t} + U\frac{\partial\theta}{\partial z} = a\left(\frac{1}{r}\frac{\partial\theta}{\partial r} + \frac{\partial^2\theta}{\partial r^2}\right), \tag{A-1}$$

where $\theta = T - T_0$, T_0 is bulk temperature of the fluid and a is thermal diffusivity of the fluid.

In case that the surface heat flux increases exponentially with time for $t \geqq 0$, the initial and boundary conditions are

$$\begin{aligned}
&\theta = 0 \quad \text{for } t \leqq 0,\ z \geqq 0 \text{ and } r \geqq r_0 , \\
&\theta = 0 \quad \text{for } t \geqq 0,\ z \geqq 0 \text{ and } r \to \infty , \\
&-\lambda\frac{\partial\theta}{\partial r} = q_0 \exp(\omega t) \quad \text{for } t \geqq 0,\ z \geqq 0 \text{ and } r = r_0 .
\end{aligned} \tag{A-2}$$

By using double Laplace transformation, we have from Eq.(A-1)

$$s\bar{\theta} + pU\bar{\theta} = a\left(\frac{1}{r}\frac{\partial\bar{\theta}}{\partial r} + \frac{\partial^2\bar{\theta}}{\partial r^2}\right), \tag{A-3}$$

where $\bar{\theta}$ is Laplace transform of θ,and s and p are parameters for t and z respectively. Solution to Eq.(A-3) satisfying the initial and boundary conditions given by Eq.(A-2), is then

$$\bar{\theta} = \frac{q_0 K_0\left(\sqrt{\frac{s+Up}{a}}\, r\right)}{\lambda p(s-\omega)\sqrt{\frac{s+Up}{a}}\, K_1\left(\sqrt{\frac{s+Up}{a}}\, r_0\right)} , \tag{A-4}$$

where K_0 and K_1 are modified Bessel functions of the second order of zero and first orders respectively.

For large t and small z the inverse Laplace transformation of Eq.(A-4) is

obtained by consulting a text book by Carslaw and Jaeger [27] and is given by

$$\frac{\theta\lambda}{q_0\exp(\omega t)} = \frac{1}{2}\left(\frac{r_0}{r}\right)^{\frac{1}{2}}\left(\frac{\kappa}{\alpha}\right)^{\frac{1}{2}}\{\exp(-(r-r_0)\sqrt{\alpha/\kappa})\ \mathrm{erfc}\left(\frac{r-r_0}{2\sqrt{\kappa z}} - \sqrt{\alpha z}\right)$$

$$- \exp((r-r_0)\sqrt{\alpha/\kappa})\ \mathrm{erfc}\left(\frac{r-r_0}{2\sqrt{\kappa z}} + \sqrt{\alpha z}\right)\}$$

$$- \frac{1}{2}\left(\frac{r_0}{r}\right)^{\frac{1}{2}}\left(\frac{\kappa}{\alpha}\right)\frac{3r+r_0}{8rr_0}\{\exp(-(r-r_0)\sqrt{\alpha/\kappa})\ \mathrm{erfc}\left(\frac{r-r_0}{2\sqrt{\kappa z}} - \sqrt{\alpha z}\right)$$

$$+ \exp((r-r_0)\sqrt{\alpha/\kappa})\ \mathrm{erfc}\left(\frac{r-r_0}{2\sqrt{\kappa z}} + \sqrt{\alpha z}\right)\}$$

$$+ \left(\frac{r_0}{r}\right)^{\frac{1}{2}}\left(\frac{\kappa}{\alpha}\right)\frac{3r+r_0}{8rr_0}\exp(-\alpha z)\ \mathrm{erfc}\left(\frac{r-r_0}{2\sqrt{\kappa z}}\right) , \qquad \text{(A-5)}$$

where $\alpha = \omega/U$ and $\kappa = a/U$.

At $r = r_0$ this equation reduces to

$$\frac{\theta\lambda}{q_0\exp(\omega t)} = \left(\frac{\kappa}{\alpha}\right)^{\frac{1}{2}}(1 - \mathrm{erfc}\sqrt{\alpha z}) - \frac{1}{2r_0}\left(\frac{\kappa}{\alpha}\right)\{1 - \exp(-\alpha z)\} . \qquad \text{(A-6)}$$

The mean heat transfer coefficient, h_m, averaged over $z = 0 \sim \ell$ is defined as

$$h_m = \frac{q_0\exp(\omega t)}{\frac{1}{\ell}\int_0^{\ell}\theta dz} . \qquad \text{(A-7)}$$

By substituting Eq.(A-6) into Eq.(A-7)

$$\mathrm{Nu}(\equiv \mathrm{Nu}_{tr}) = \frac{\sqrt{\mathrm{RePr}}\sqrt{\frac{\ell}{\tau U}}}{(1-\frac{1}{2}\frac{\tau U}{\ell})\mathrm{erf}\sqrt{\frac{\ell}{\tau U}} + \sqrt{\frac{\tau U}{\pi\ell}}\exp(-\frac{\ell}{\tau U}) - (\frac{\ell}{d})\sqrt{\frac{\tau U}{\mathrm{RePr}\,\ell}}\{1-\frac{\tau U}{\ell} + \frac{\tau U}{\ell}\exp(-\frac{\ell}{\tau U})\}} , \qquad \text{(A-8)}$$

where $\mathrm{Nu} = h_m\ell/\lambda$, $\mathrm{Pr} = \nu/a$, $\tau = 1/\omega$ and $d = 2r_0$.

With $\tau \to \infty$, Eq.(A-8) reduces to

$$\mathrm{Nu}(\equiv \mathrm{Nu}_{st}) = \frac{3}{4}\sqrt{\pi}\ \frac{1}{1-\xi}\ \sqrt{\mathrm{RePr}} , \qquad \text{(A-9)}$$

where $\xi = \frac{3}{8}\sqrt{\pi}\ (\frac{\ell}{d})\ \frac{1}{\sqrt{\mathrm{RePr}}}$.

From Eq.(A-8) and Eq.(A-9), we have

$$\frac{Nu_{tr}}{Nu_{st}} = \frac{\frac{4}{3\sqrt{\pi}}(1-\xi)\sqrt{\frac{\iota}{\tau U}}}{(1-\frac{1}{2}\frac{\tau U}{\iota})\mathrm{erf}\sqrt{\frac{\iota}{\tau U}} + \sqrt{\frac{\tau U}{\pi \iota}}\exp(-\frac{\iota}{\tau U}) - \frac{8}{3}\xi\sqrt{\frac{\tau U}{\pi \iota}}\{1-\frac{\tau U}{\iota} + \frac{\tau U}{\iota}\exp(-\frac{\iota}{\tau U})\}} \quad (A-9)$$

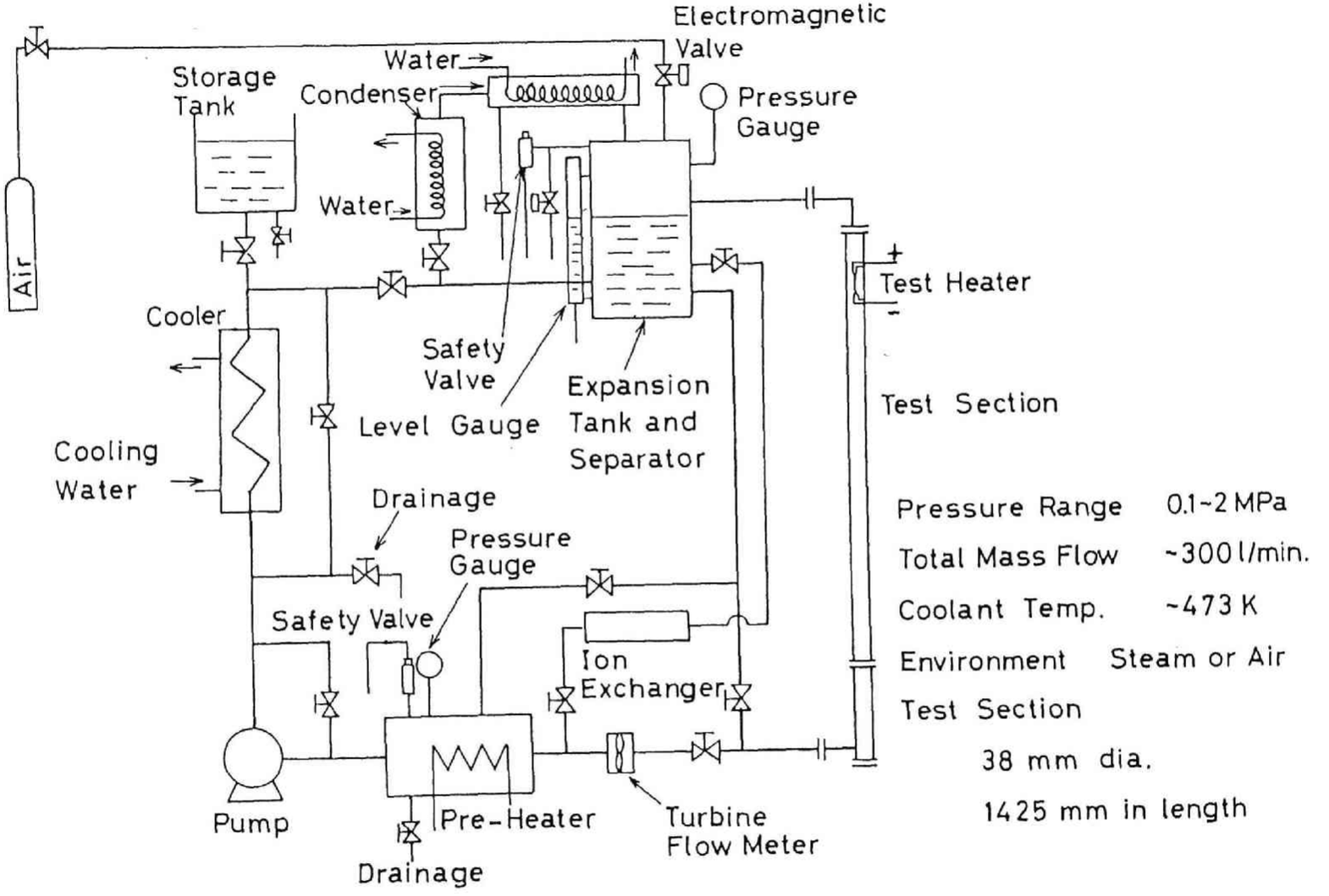

Fig.1 Schematic diagram of the experimental apparatus.

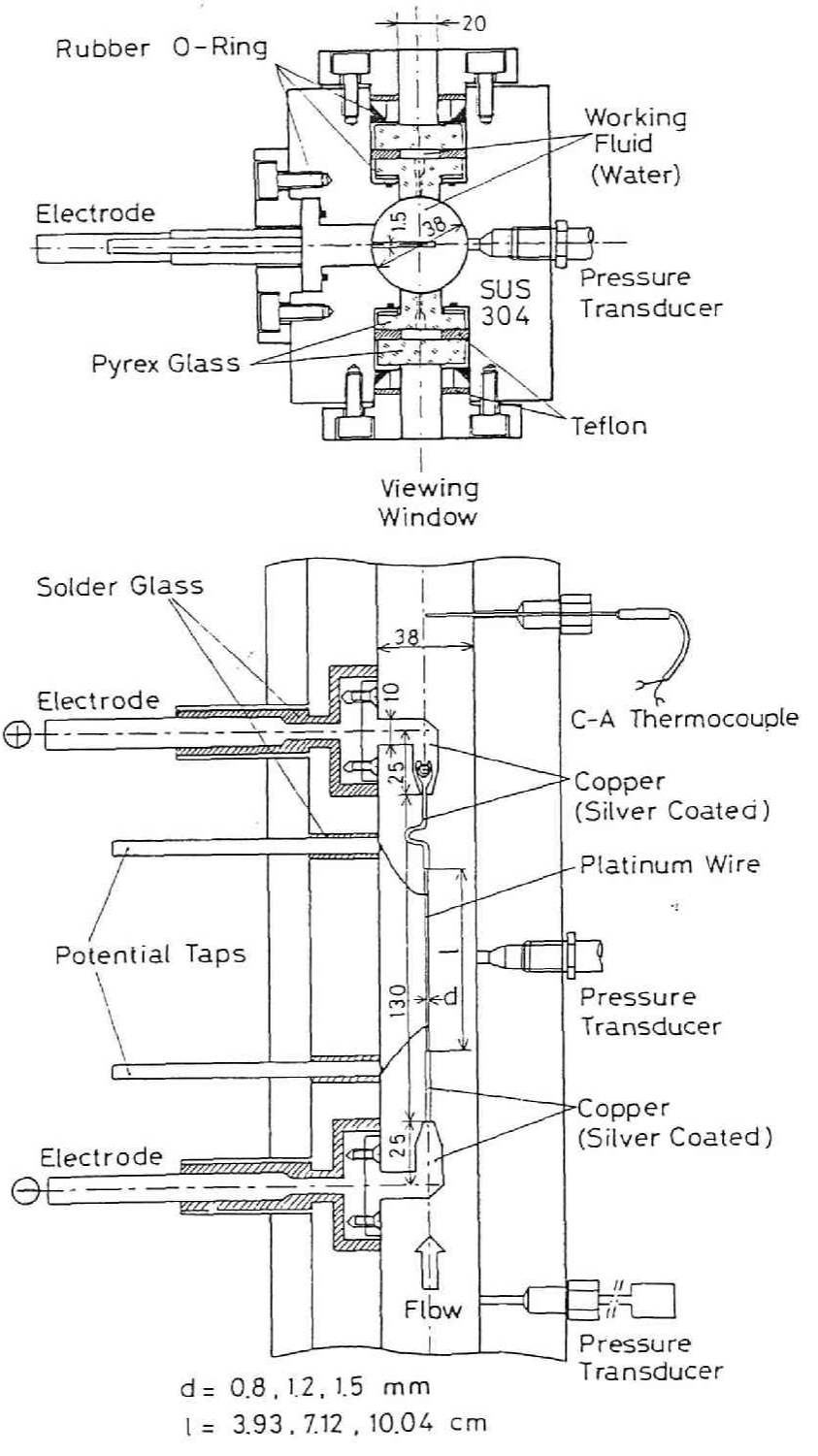

Fig.2 Cross-sectional views of the heated section.

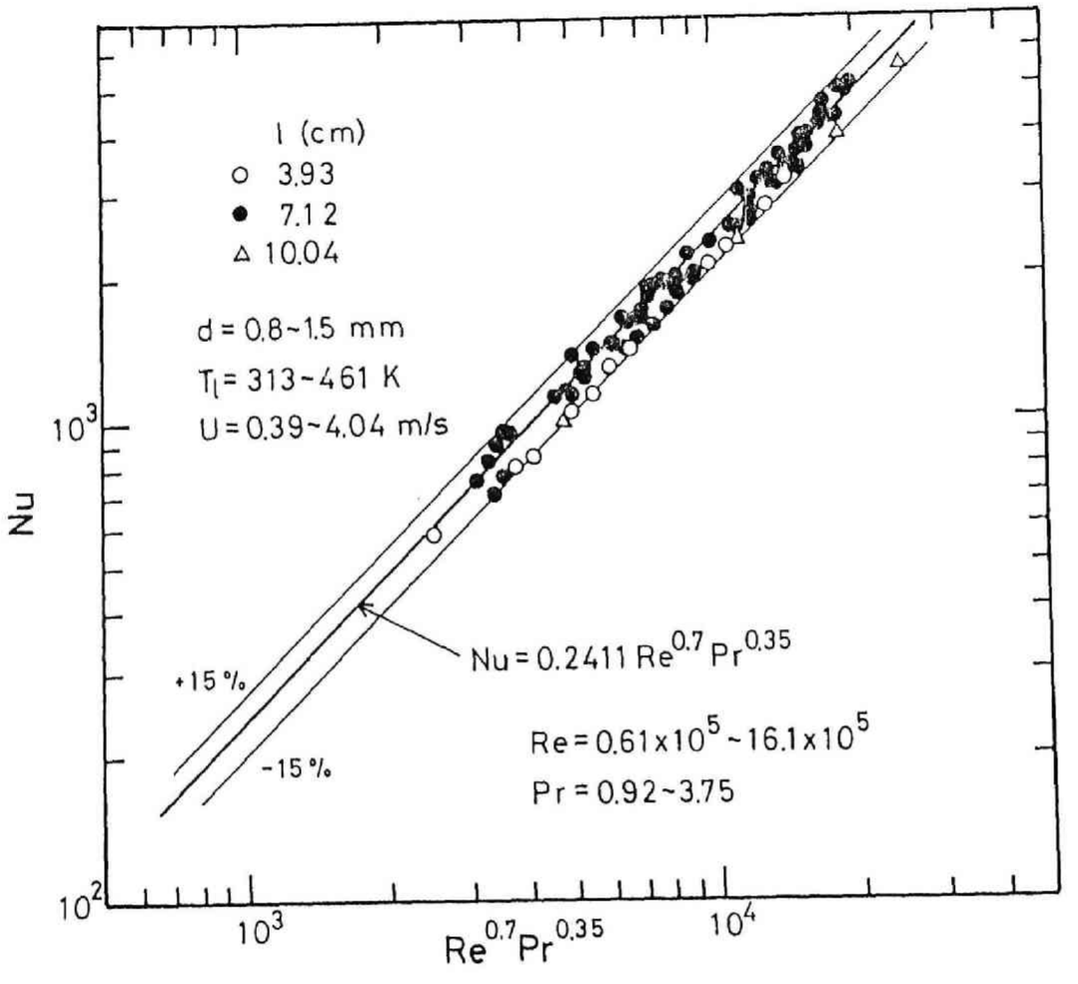

Fig.3 Comparative representation of steady state non-boiling heat transfer coefficient.

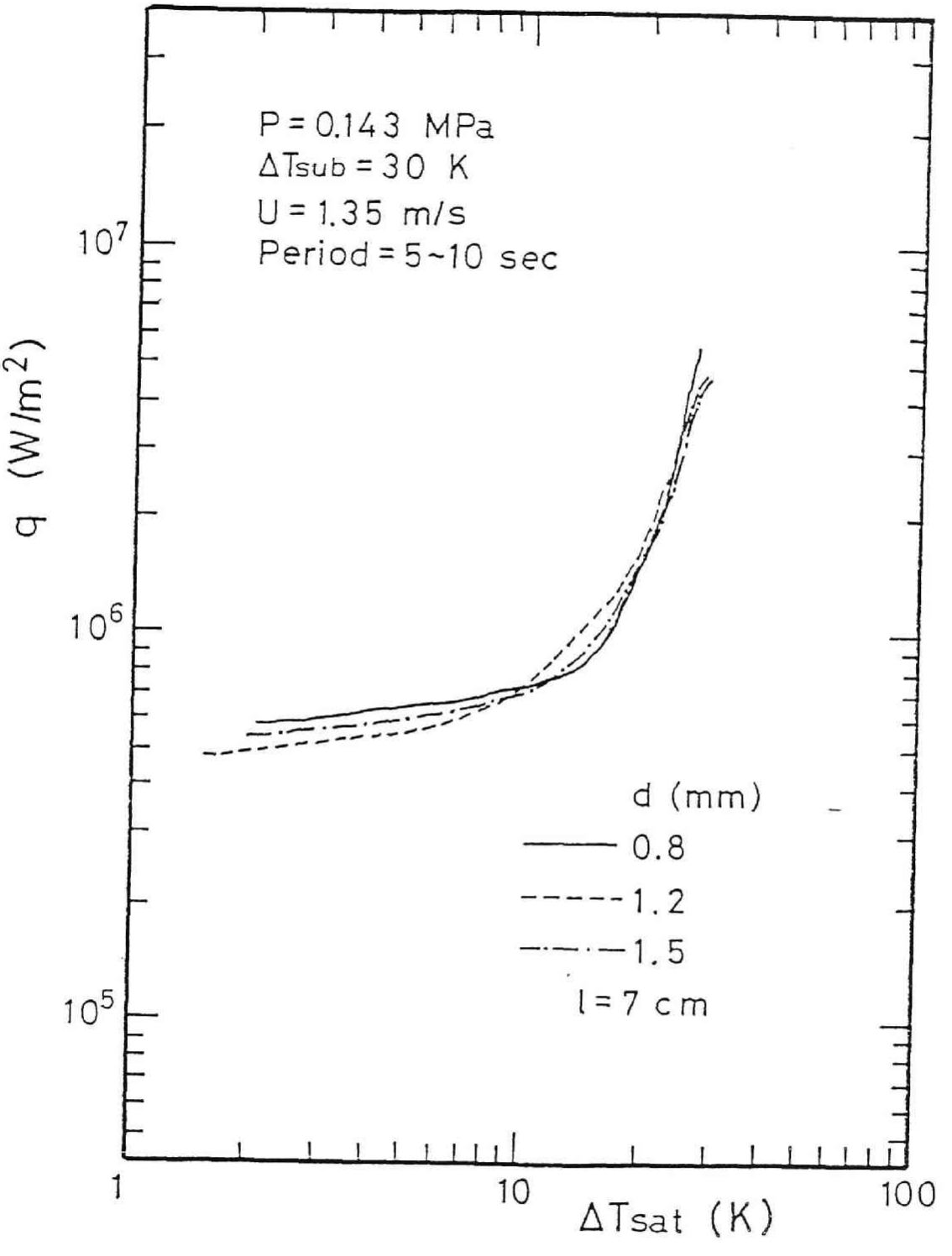

Fig.4(a) The effect of heater diameter on steady state boiling curve

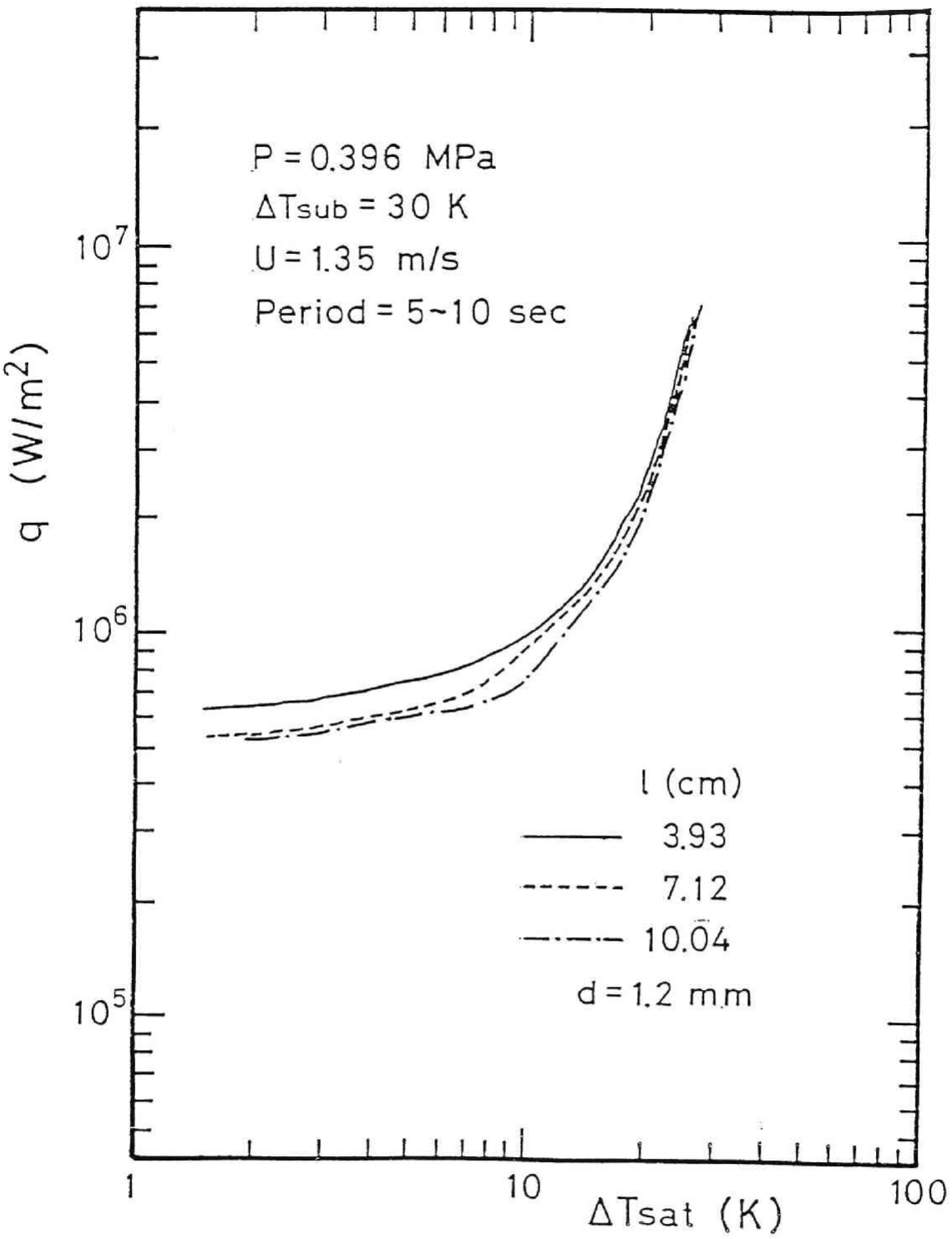

Fig.4(b) The effect of heater length on steady state boiling curve

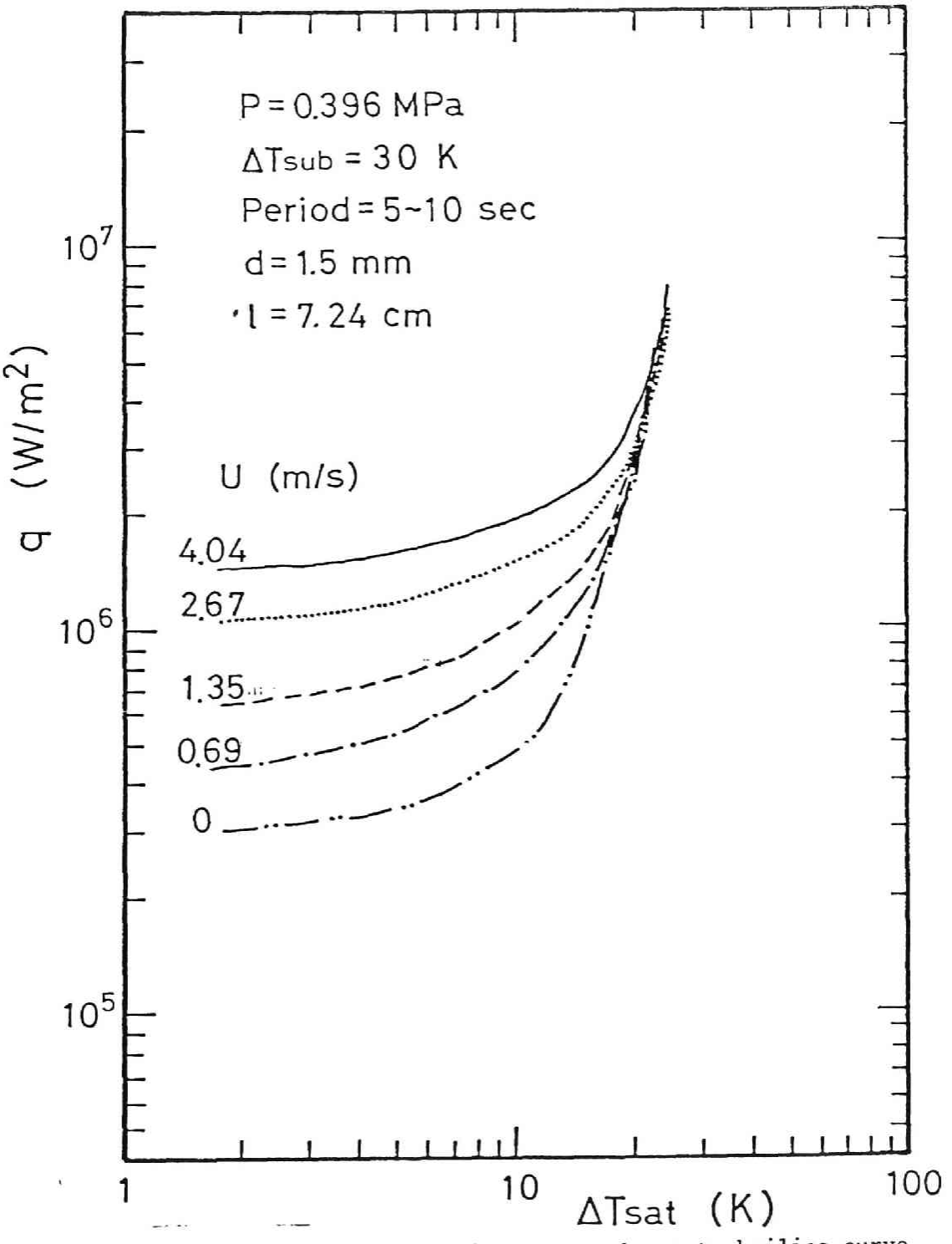

Fig.4(c) The effect of velocity on steady state boiling curve

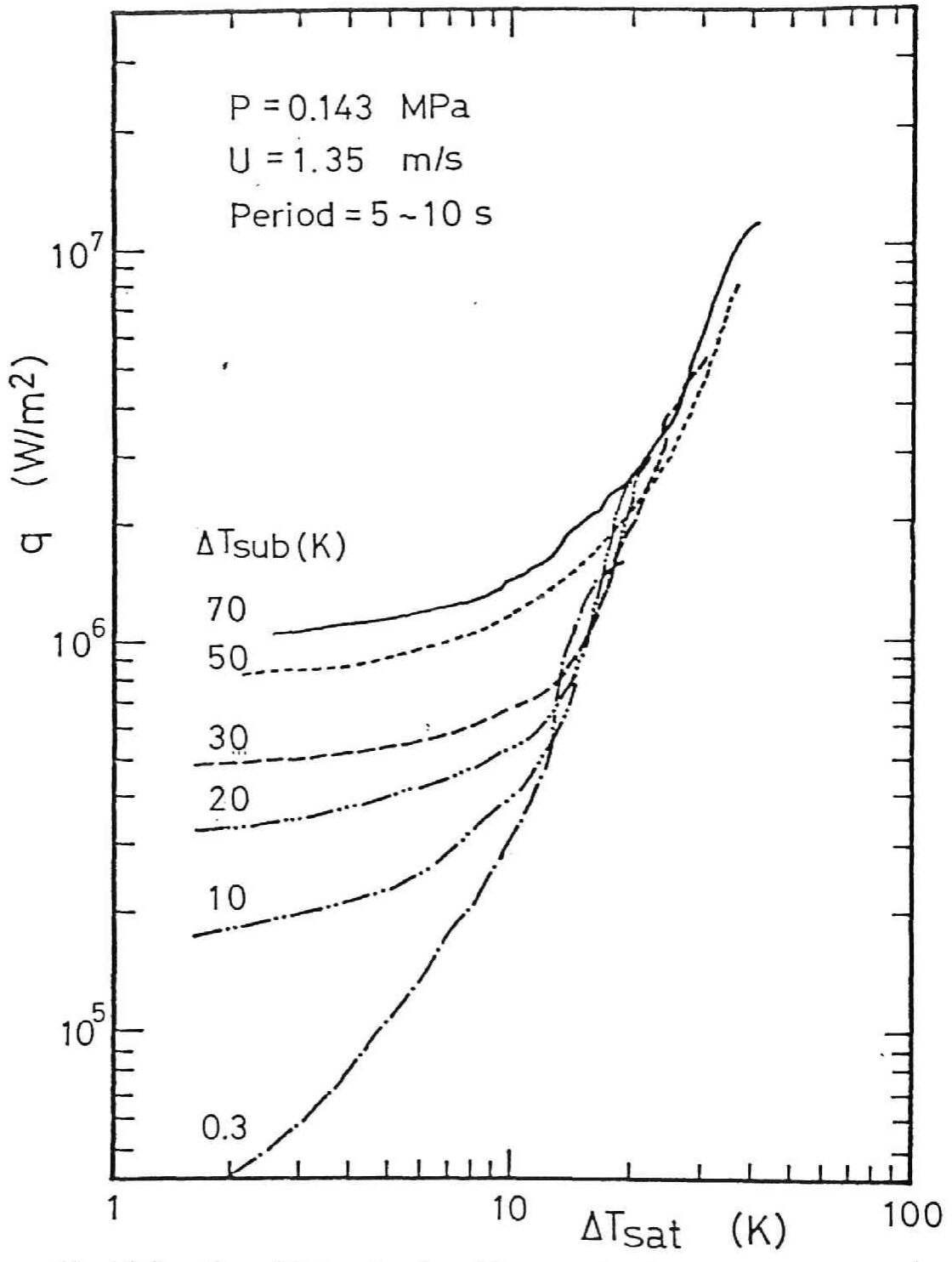

Fig.4(d) The effect of subcooling on steady state boiling curve

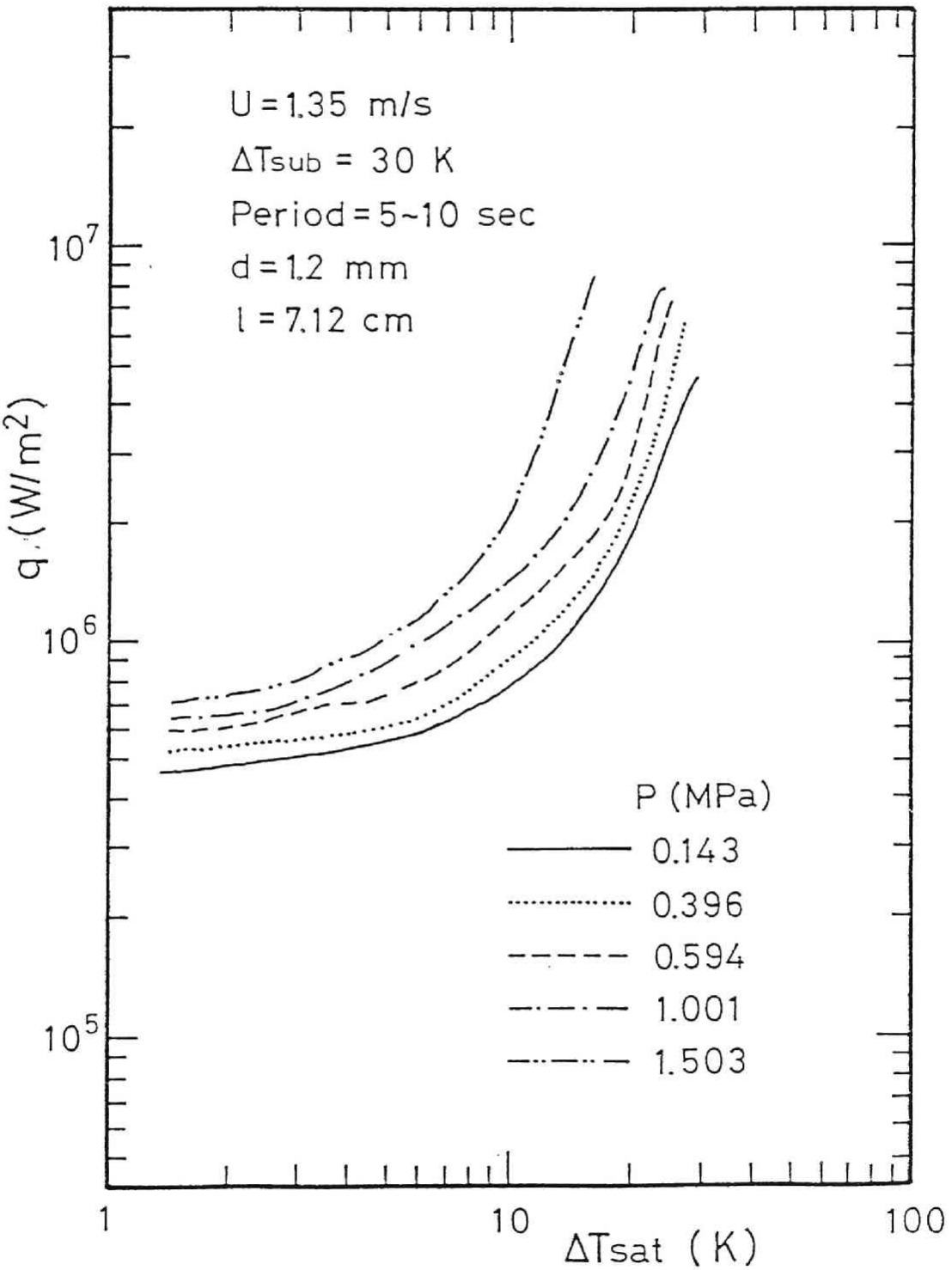

Fig.4(e) The effect of pressure on steady state boiling curve

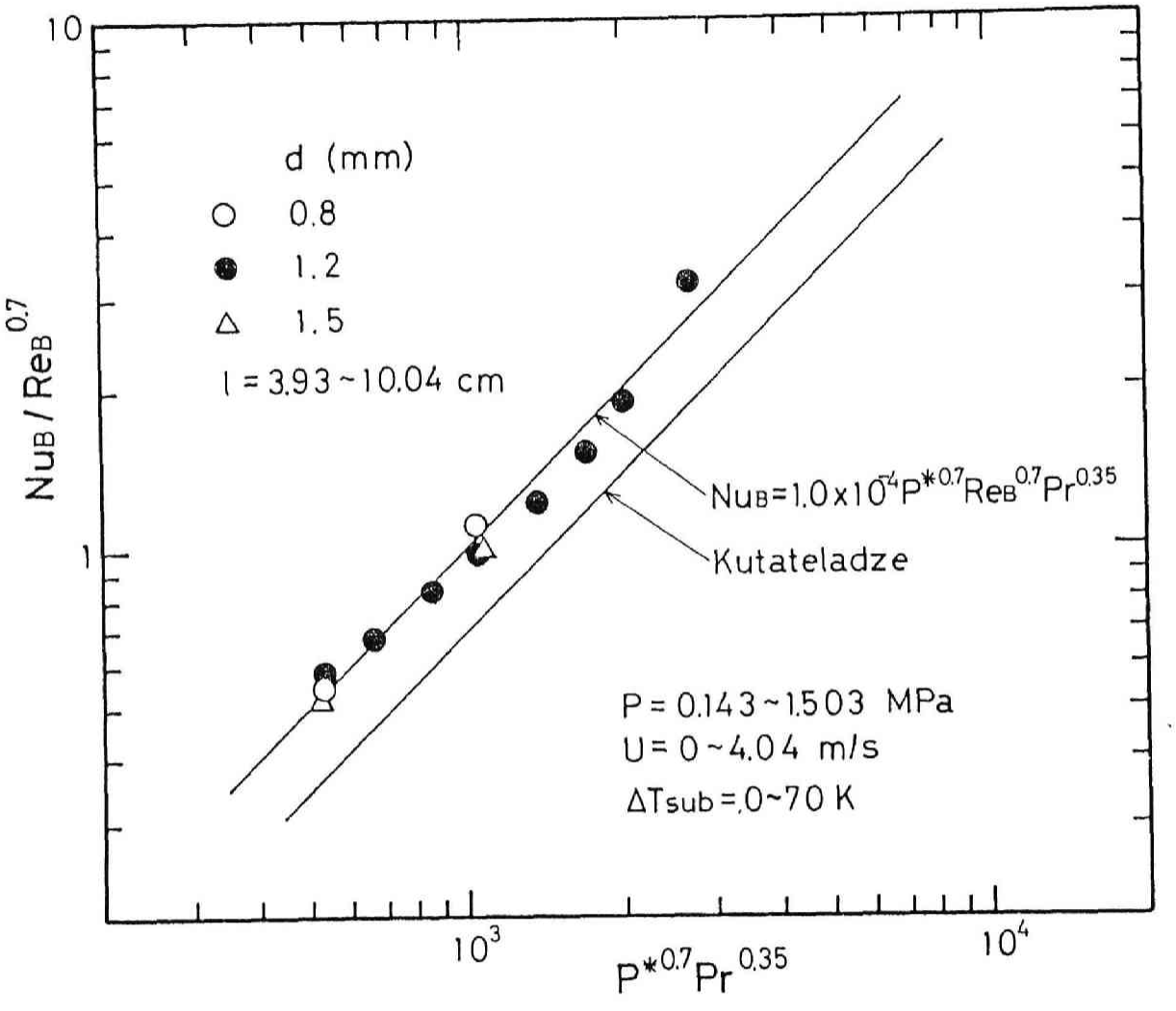

Fig.5 Comparative representation of steady state boiling heat transfer coefficient.

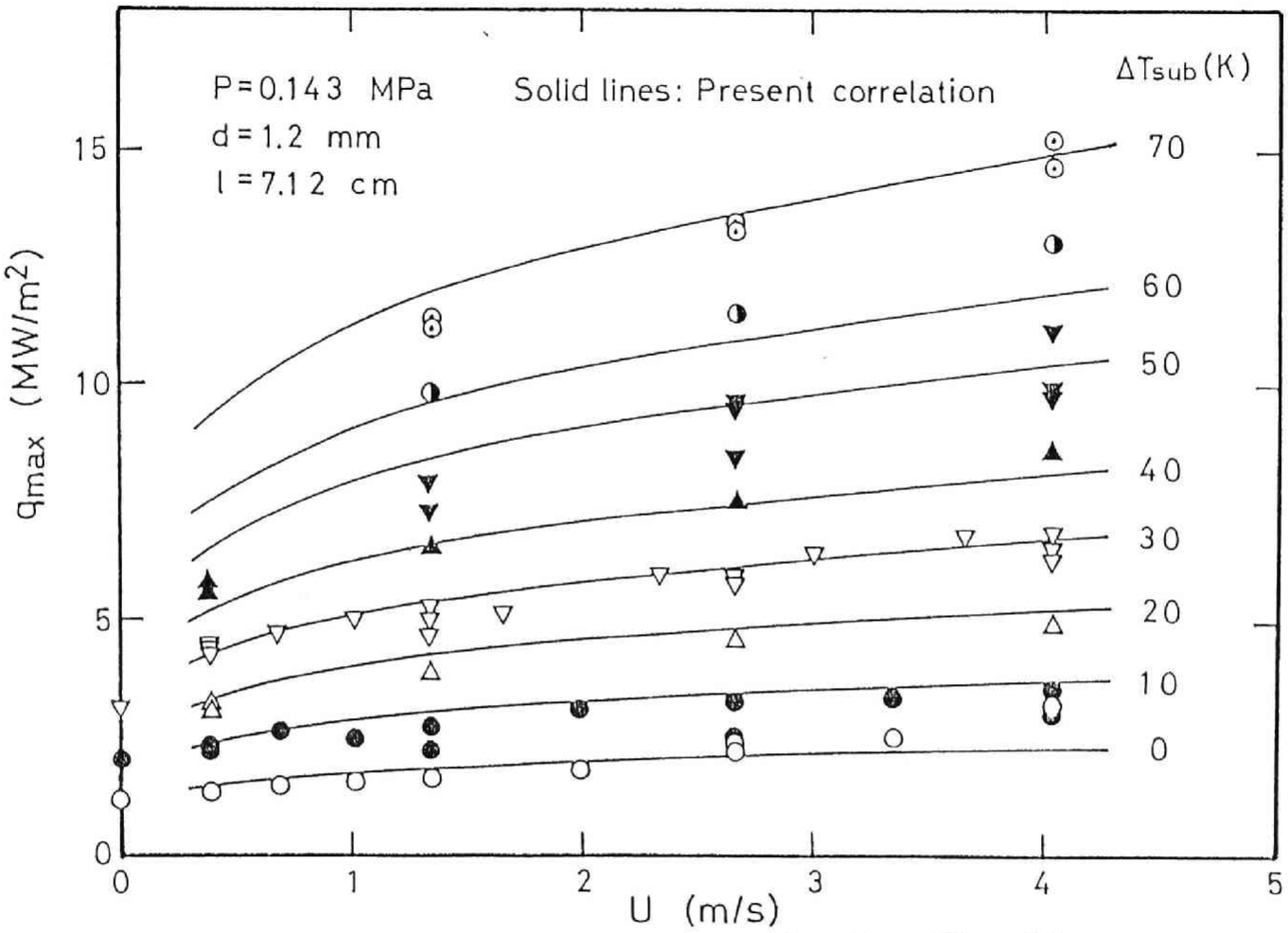

Fig.6(a) The variation of steady state maximum heat flux with velocity and subcooling at 0.143 MPa (1.2 mm diam heater)

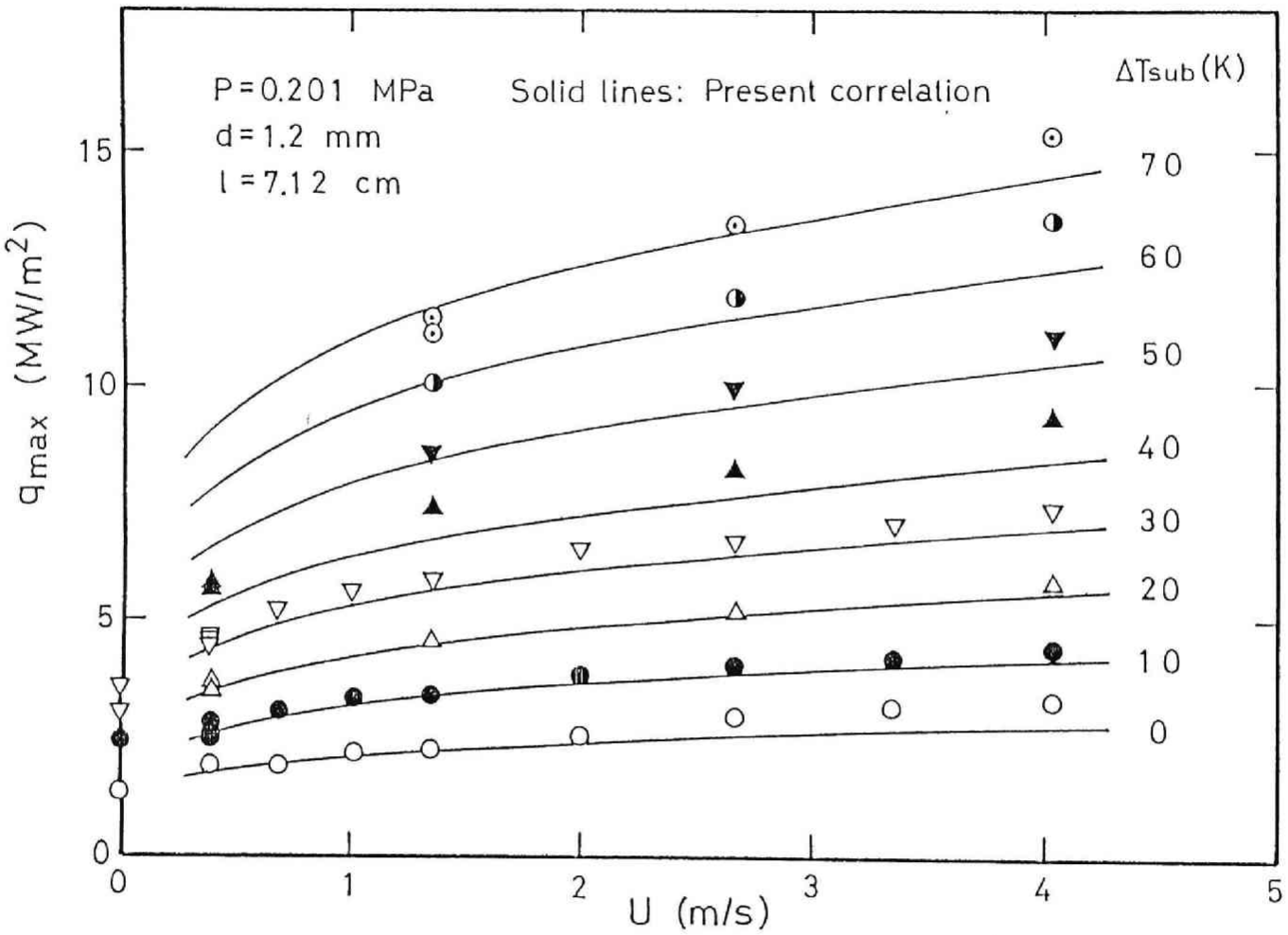

Fig.6(b) The variation of steady state maximum heat flux with velocity and subcooling at 0.201 MPa (1.2 mm diam heater)

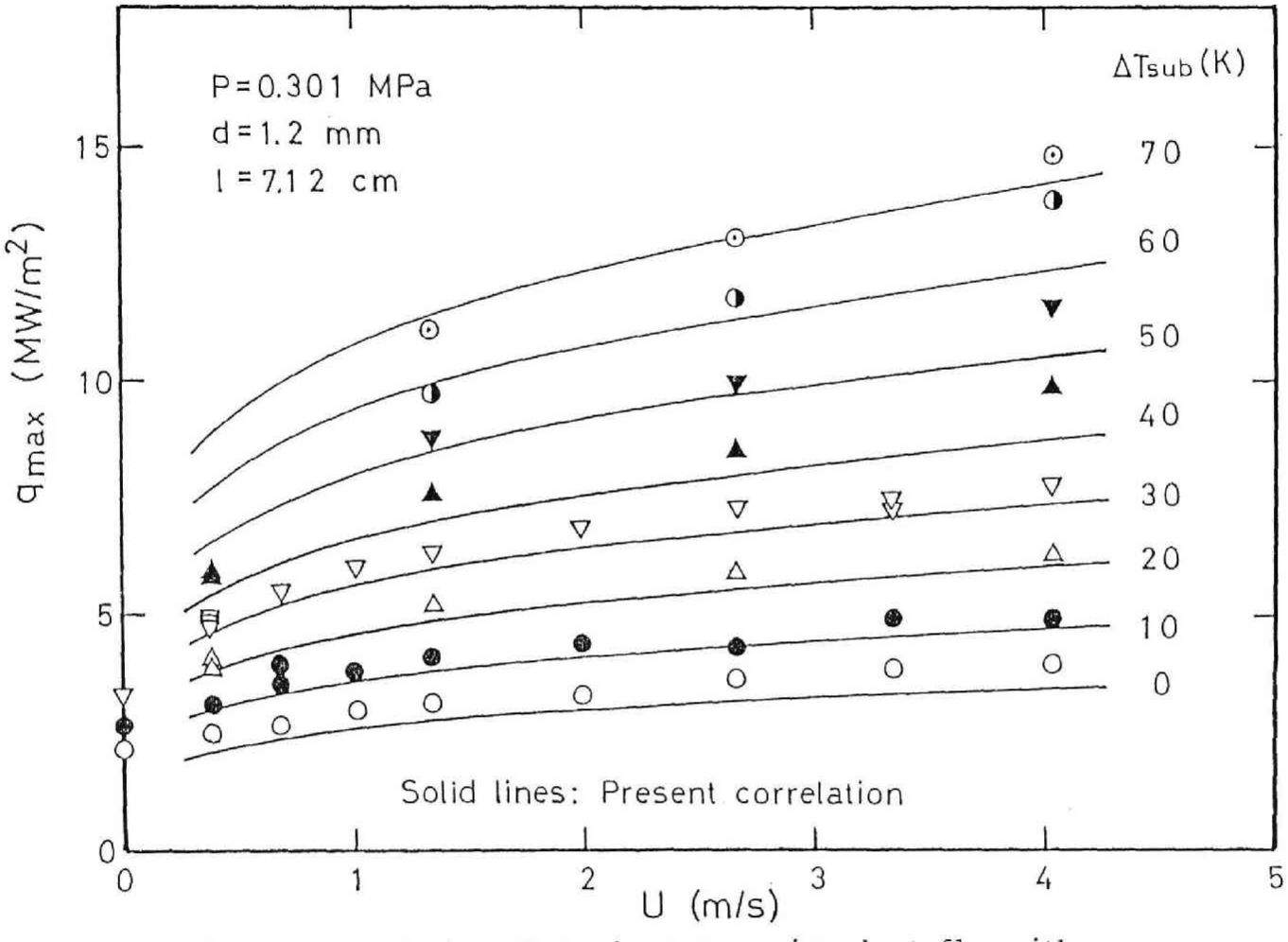

Fig.6(c) The variation of steady state maximum heat flux with velocity and subcooling at 0.301 MPa (1.2 mm diam heater)

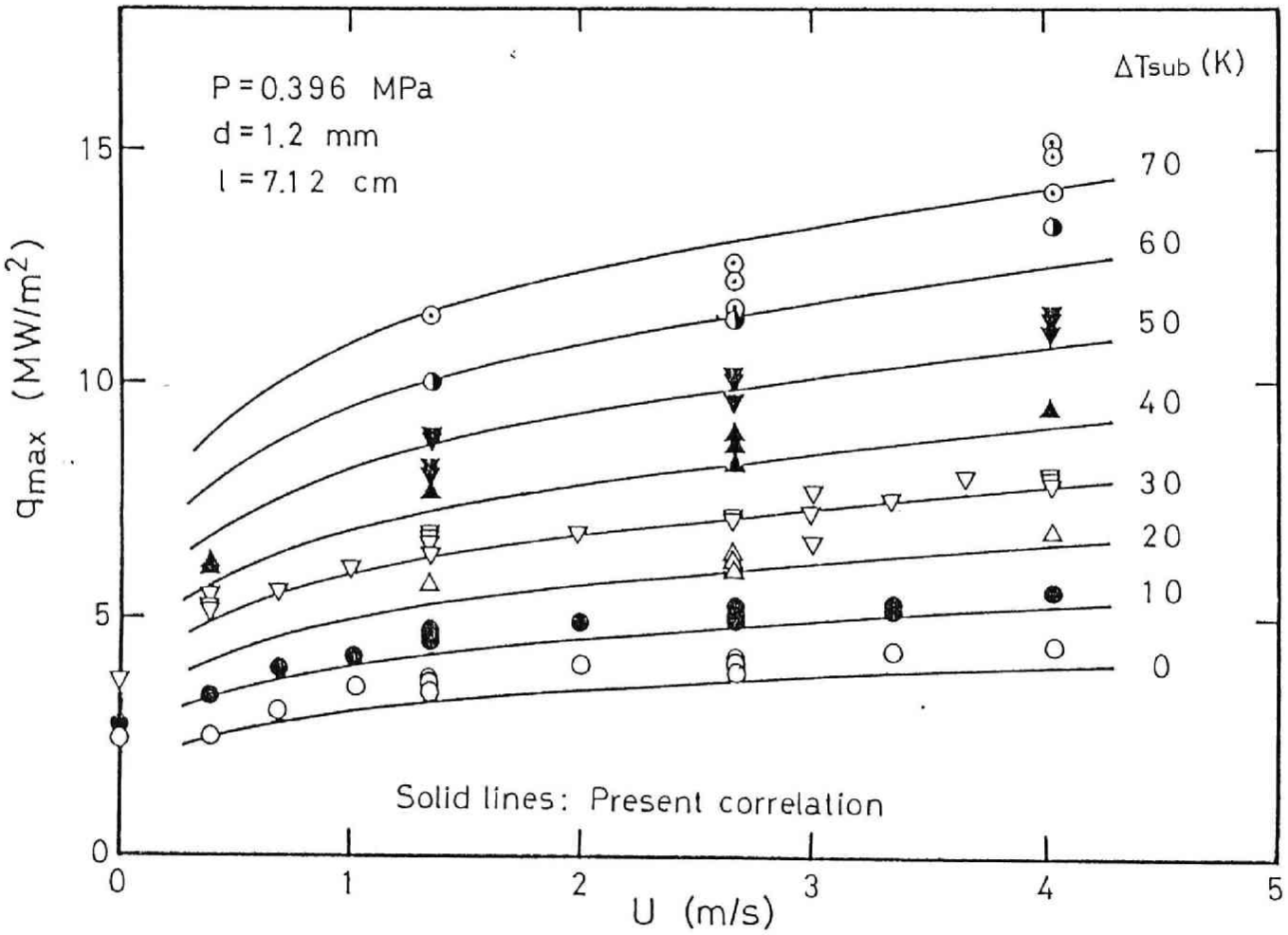

Fig.6(d) The variation of steady state maximum heat flux with velocity and subcooling at 0.396 MPa (1.2 mm diam heater)

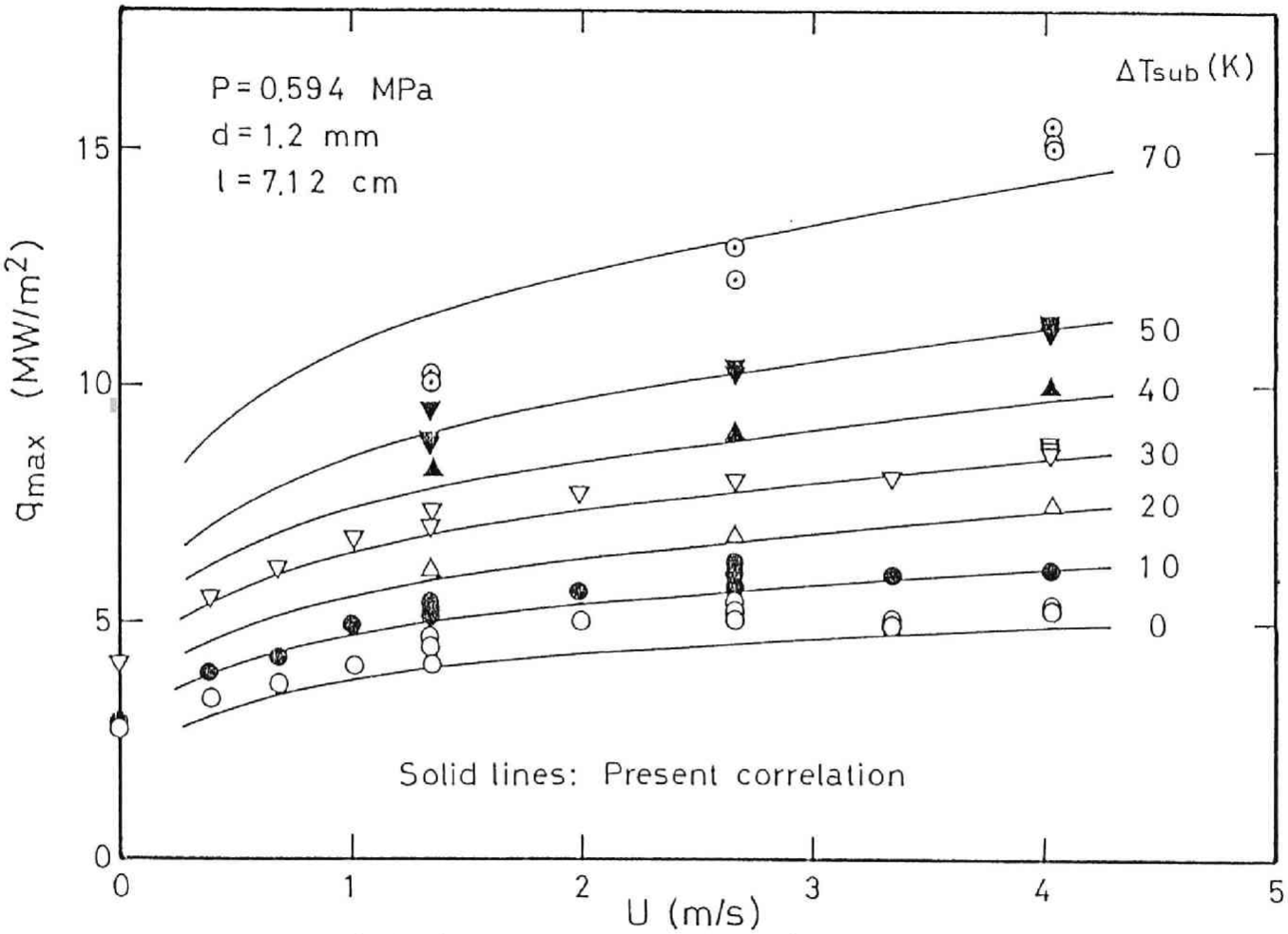

Fig.7(a) The variation of steady state maximum heat flux with velocity and subcooling at 0.594 MPa (1.2 mm diam heater)

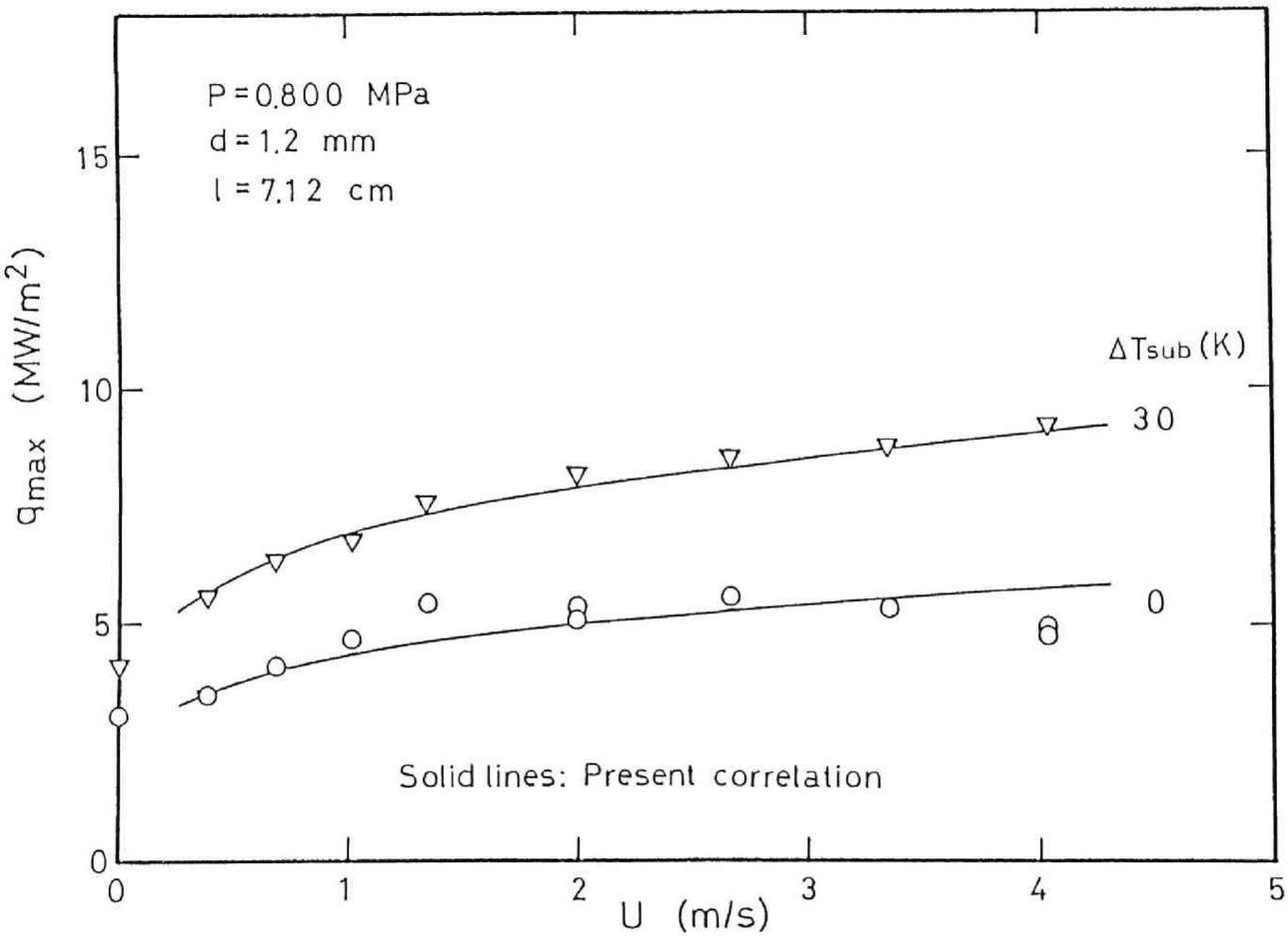

Fig.7(b) The variation of steady state maximum heat flux with velocity and subcooling at 0.800 MPa (1.2 mm diam heater)

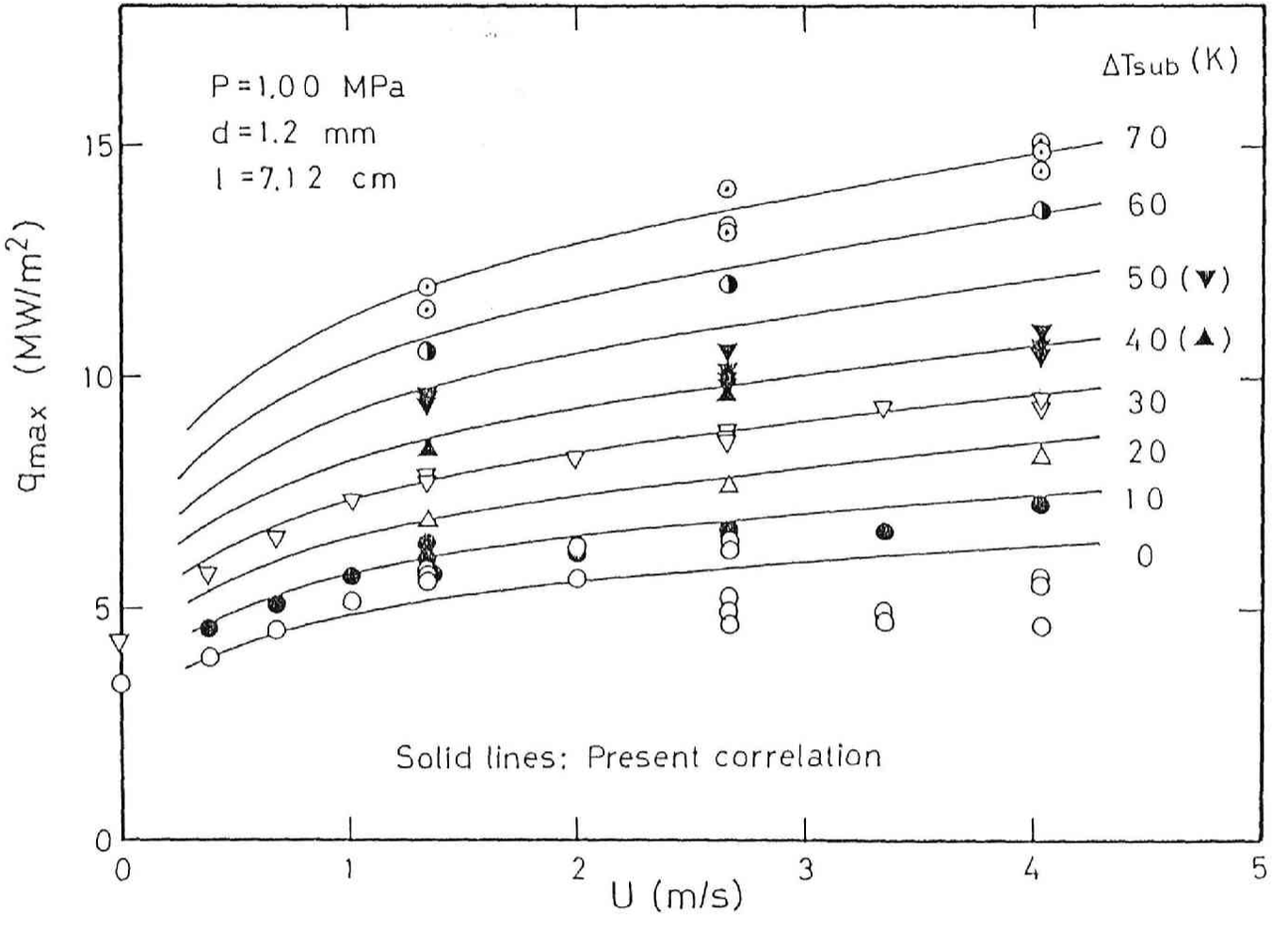

Fig.7(c) The variation of steady state maximum heat flux with velocity and subcooling at 1.00 PMa (1.2 mm diam heater)

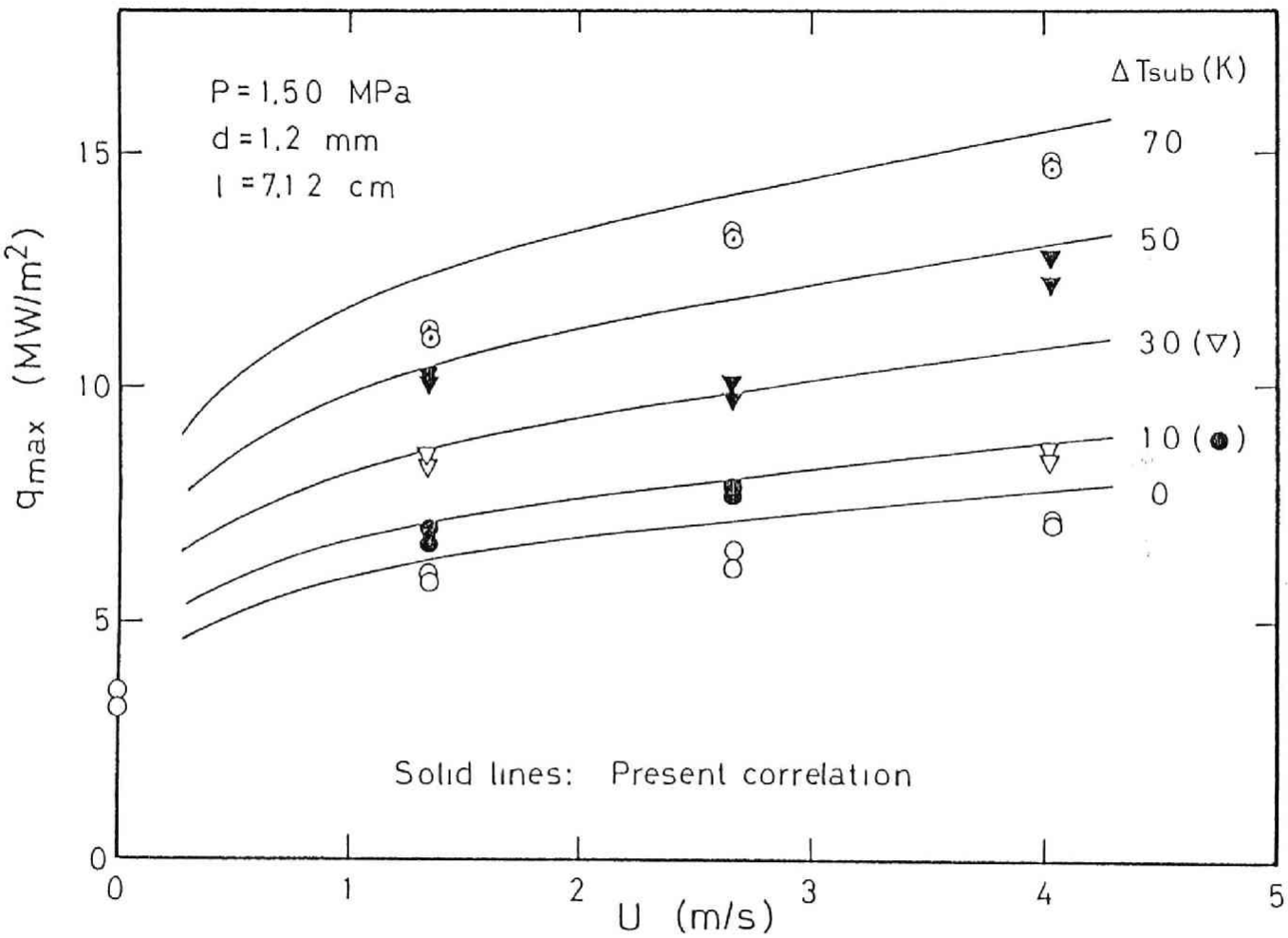

Fig.7(d) The variation of steady state maximum heat flux with velocity and subcooling at 1.50 MPa (1.2 mm diam heater)

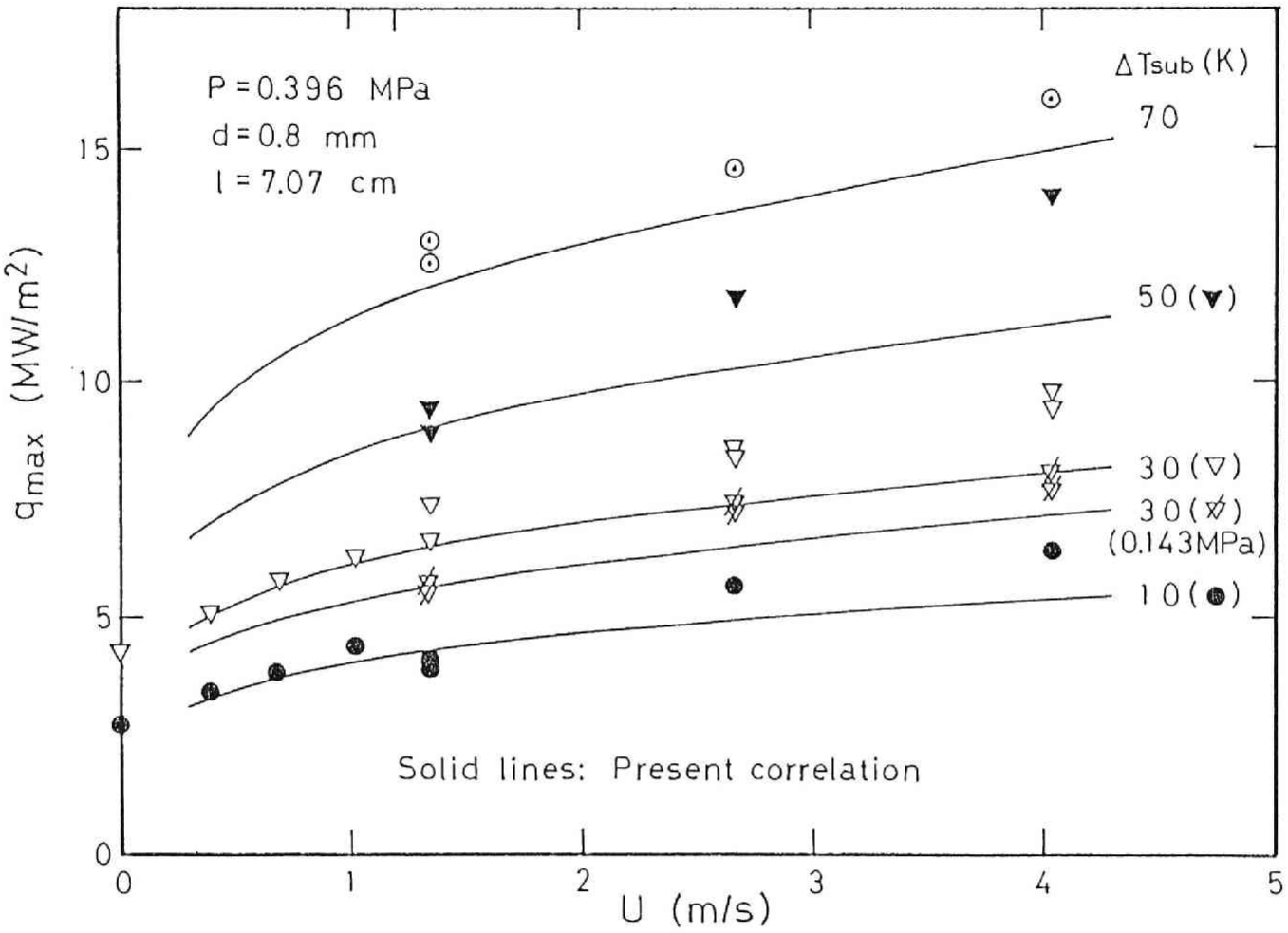

Fig.8(a) The variation of steady state maximum heat flux with velocity and subcooling at 0.396 MPa (0.8 mm diam heater)

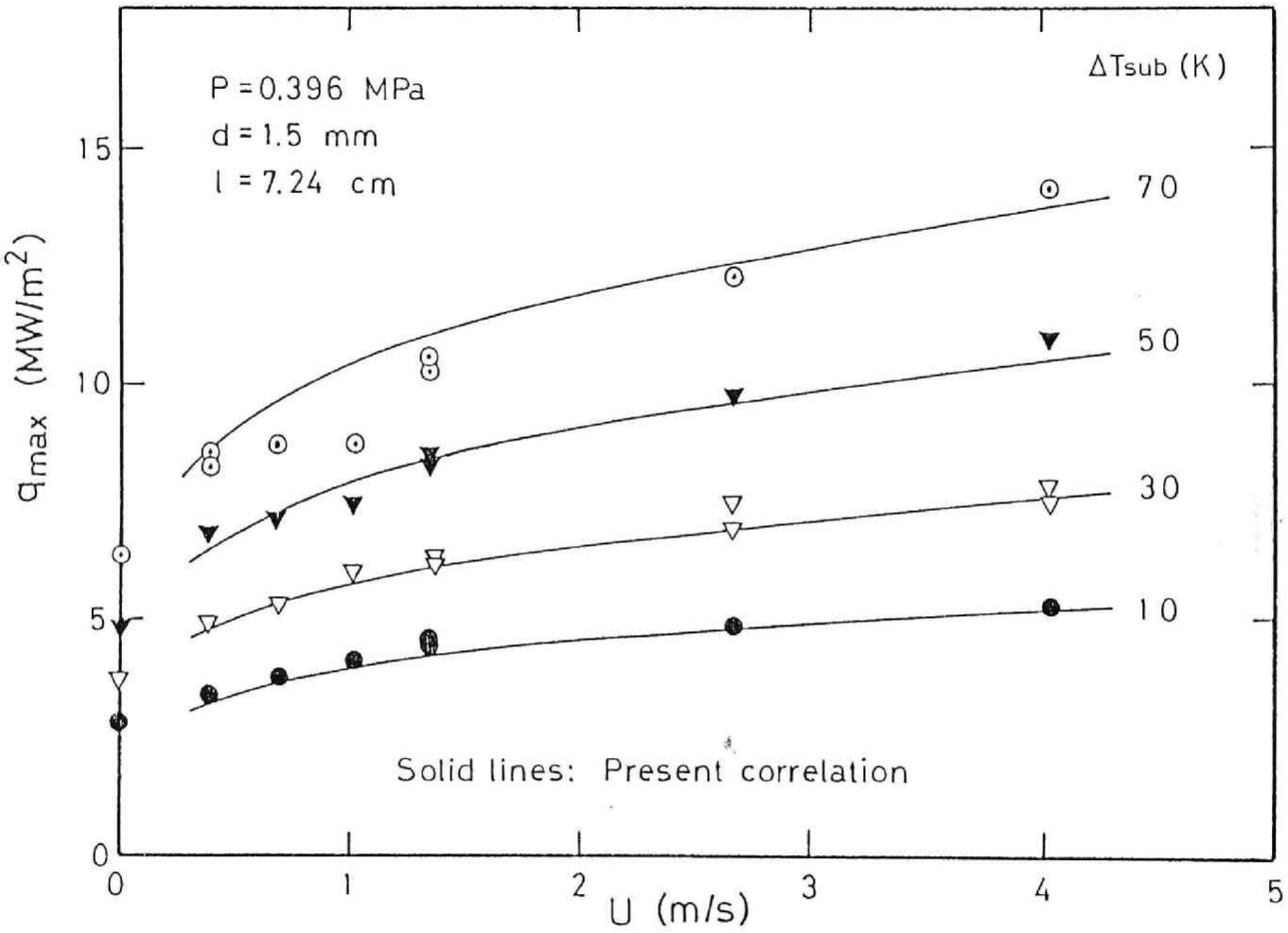

Fig.8(b) The variation of steady state maximum heat flux with velocity and subcooling at 0.396 MPa (1.5 mm diam heater)

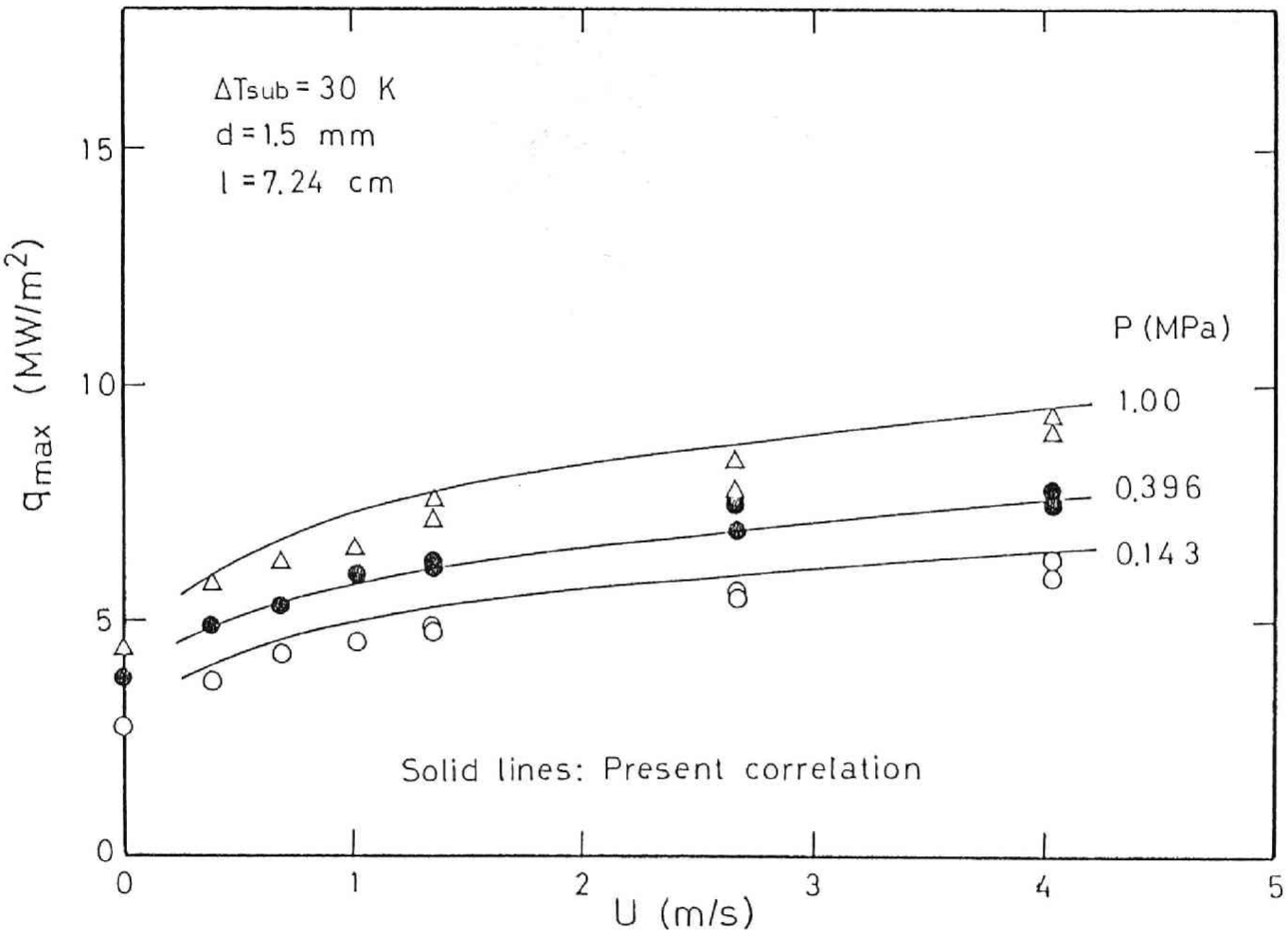

Fig.8(c) The variation of steady state maximum heat flux with velocity and pressure at 30 K subcooling (1.5 mm diam heater)

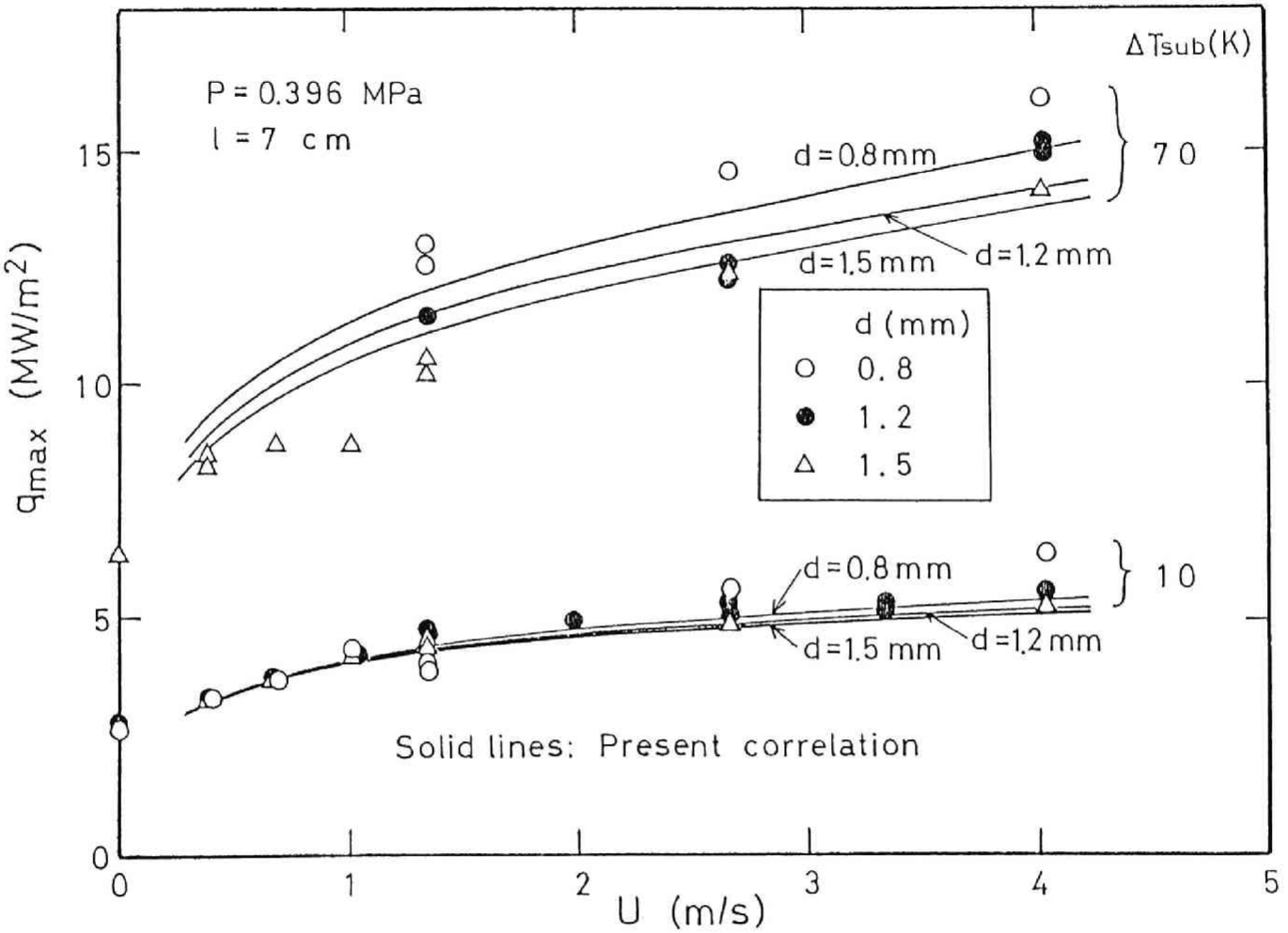

Fig.9(a) The effect of heater diameter on steady state maximum heat flux

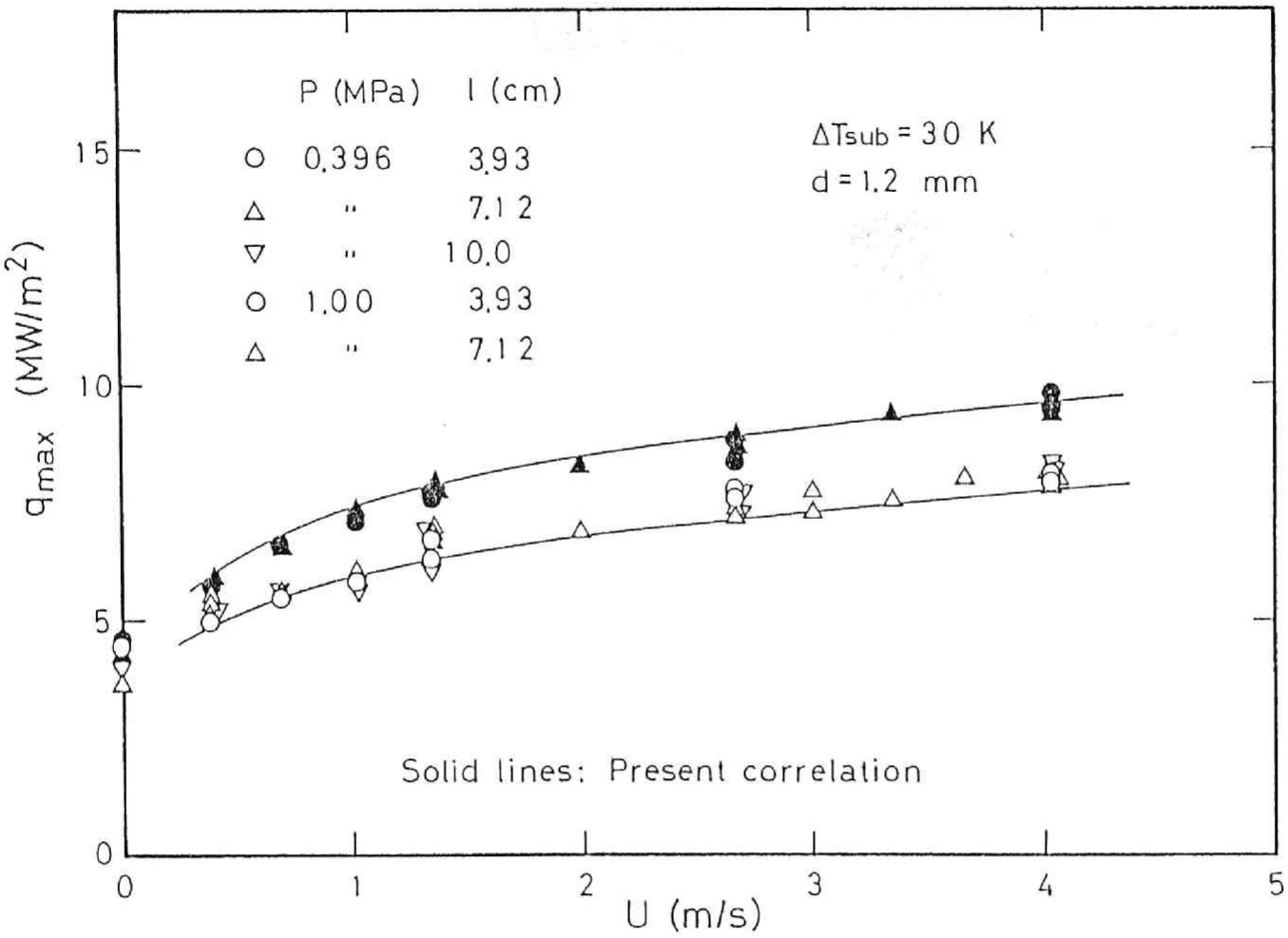

Fig.9(b) The effect of heater length on steady state maximum heat flux

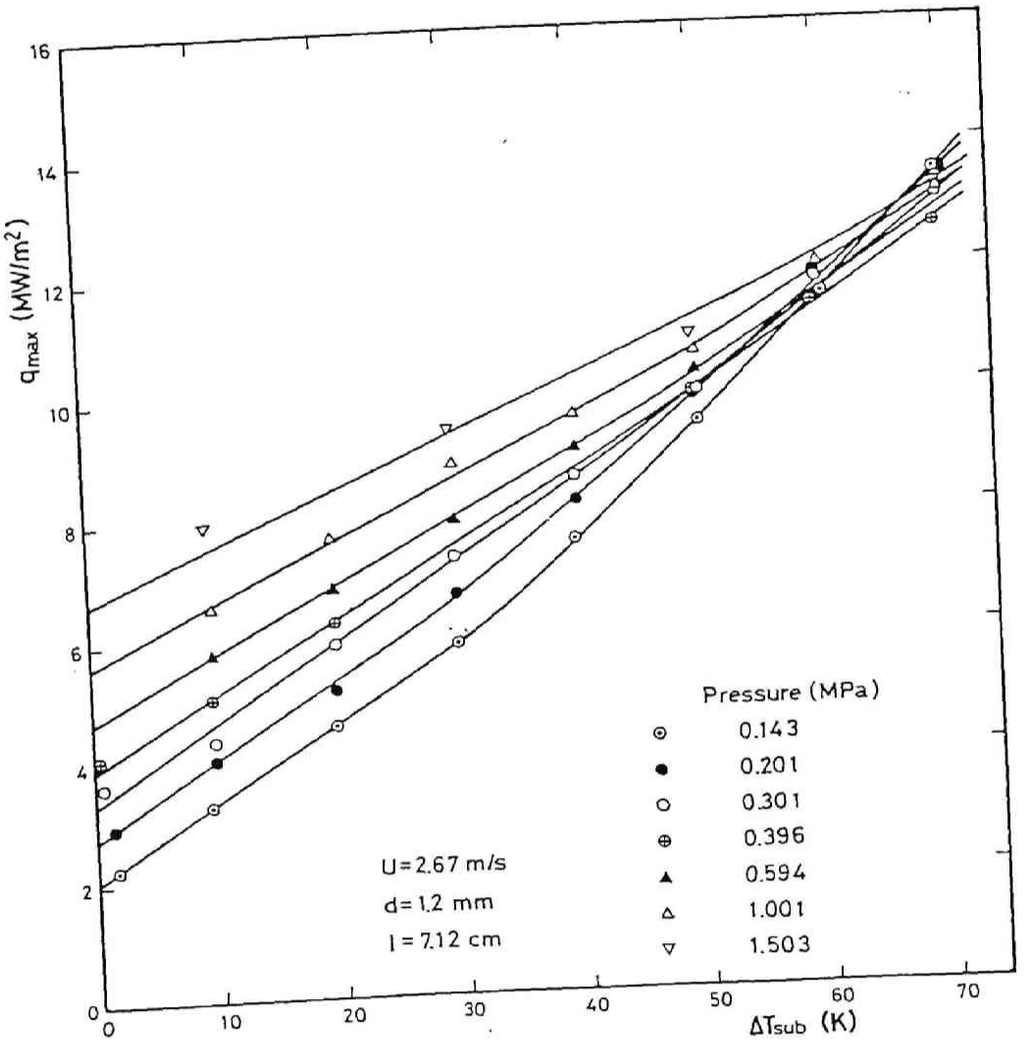

Fig.10 The variation of steady state maximum heat flux with subcooling and pressure.

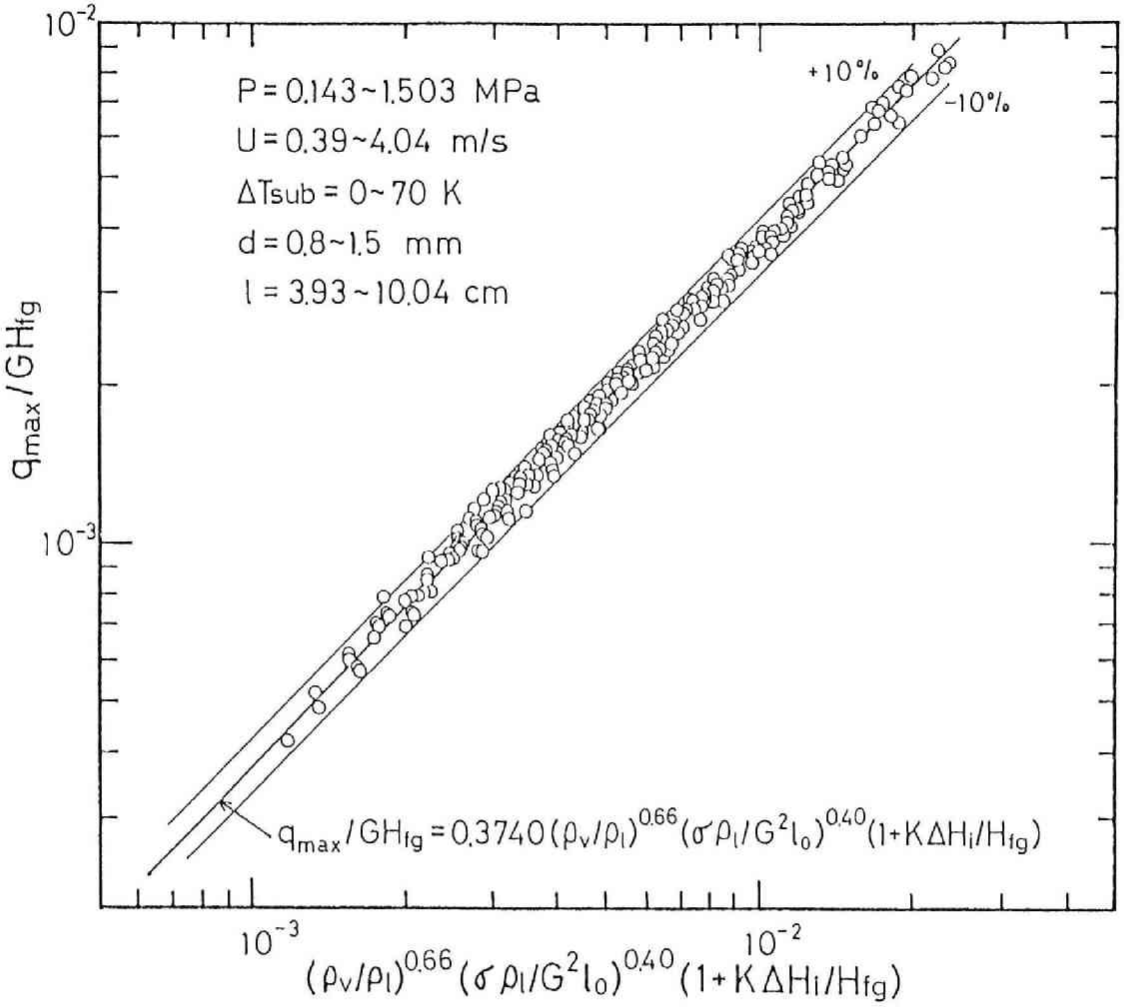

Fig.11 Comparative representation of steady state maximum heat flux.

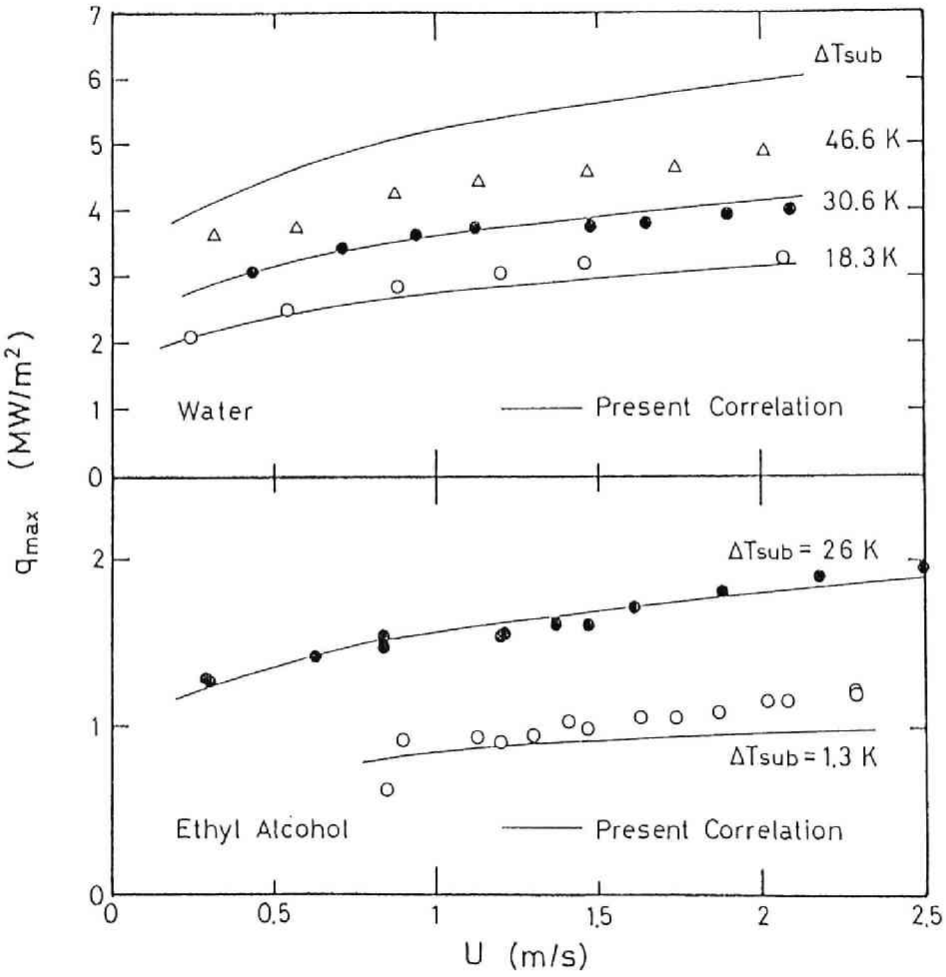

Fig.12 Comparison of Eq.(10) with the experimental data of Borishansky *et al.*.

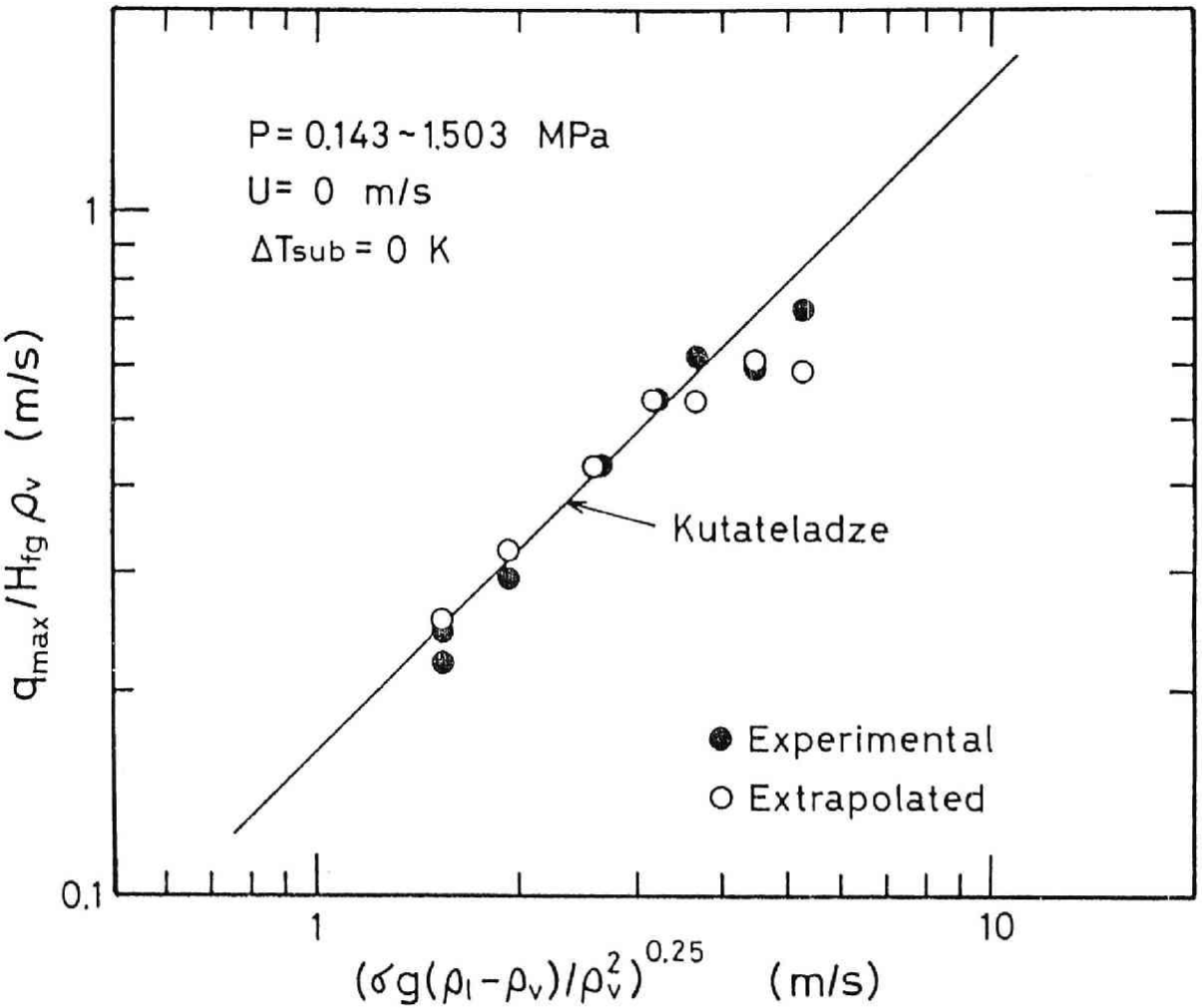

Fig.13 Comparative representation of steady state maximum heat flux at zero flow and zero subcooling.

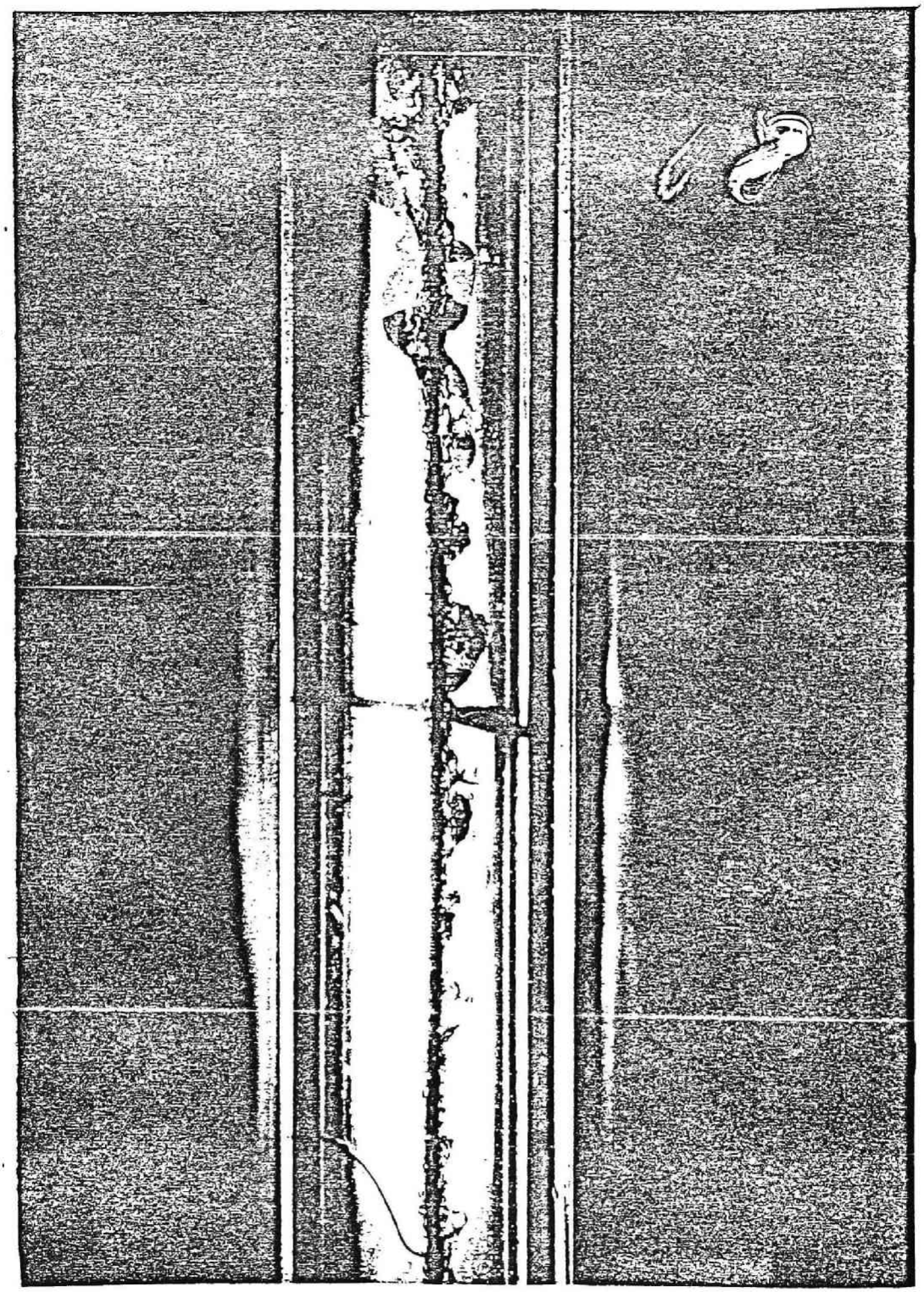

Photo.1 Steady state boiling at nearly maximum heat flux.

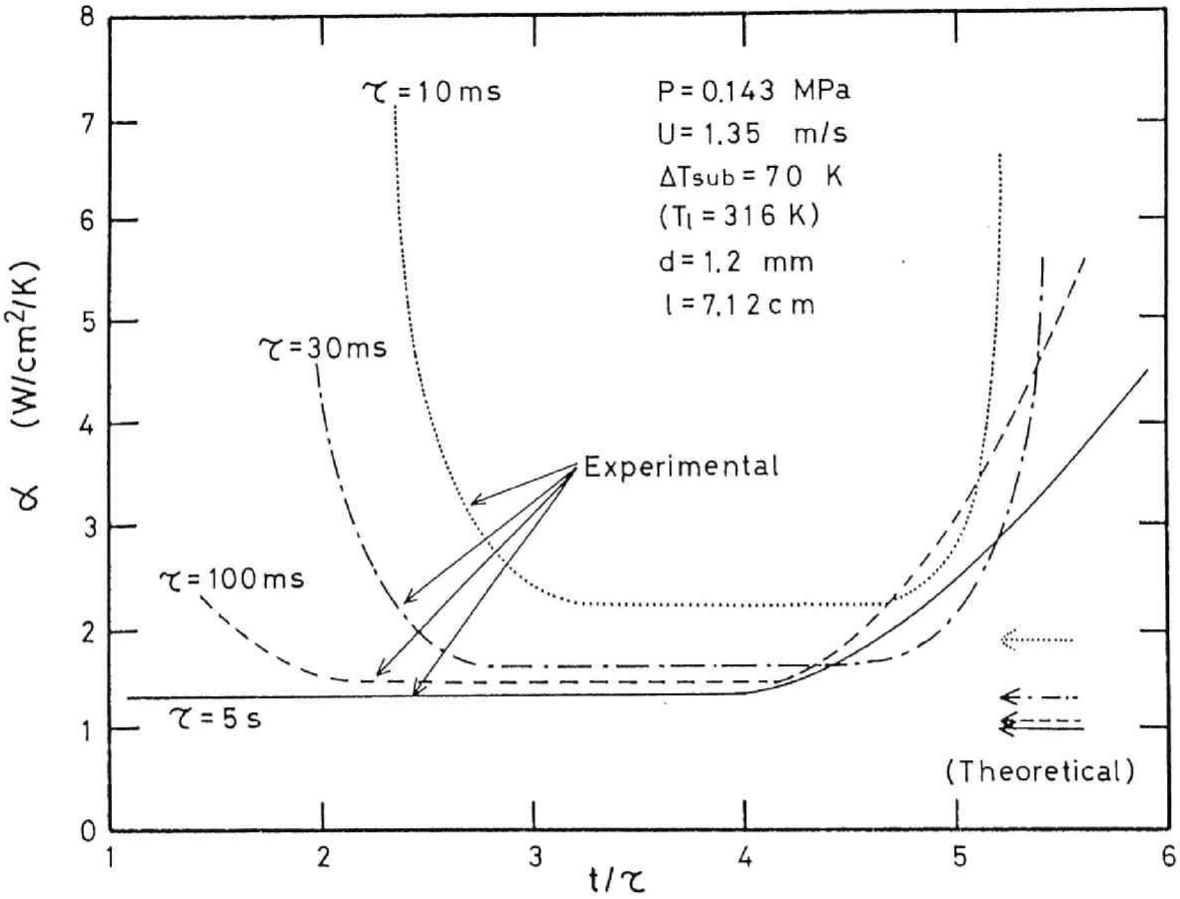

Fig.14 Transient non-boiling heat transfer coefficient.

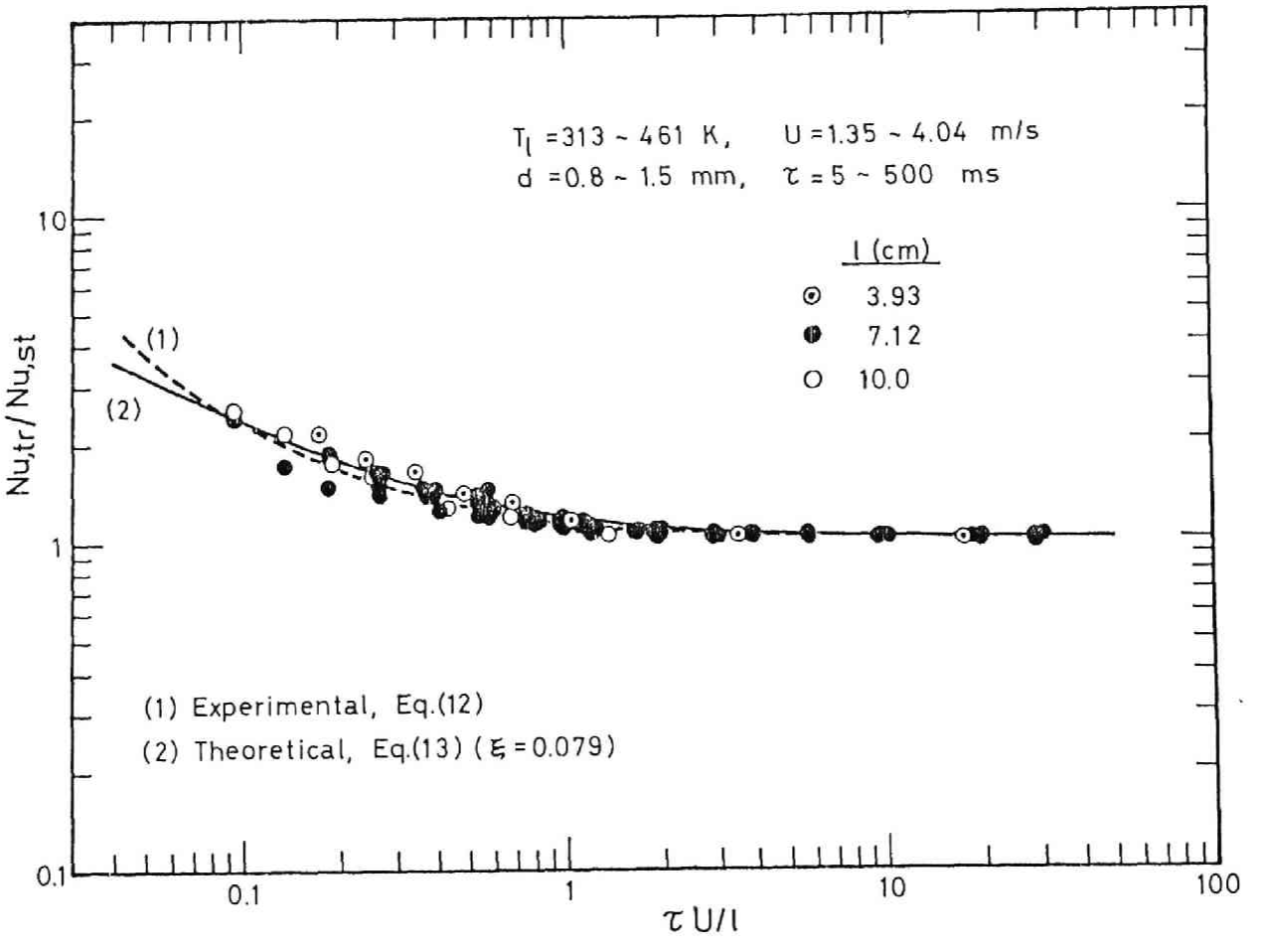

Fig.15 Comparative representation of transient non-boiling heat transfer coefficient.

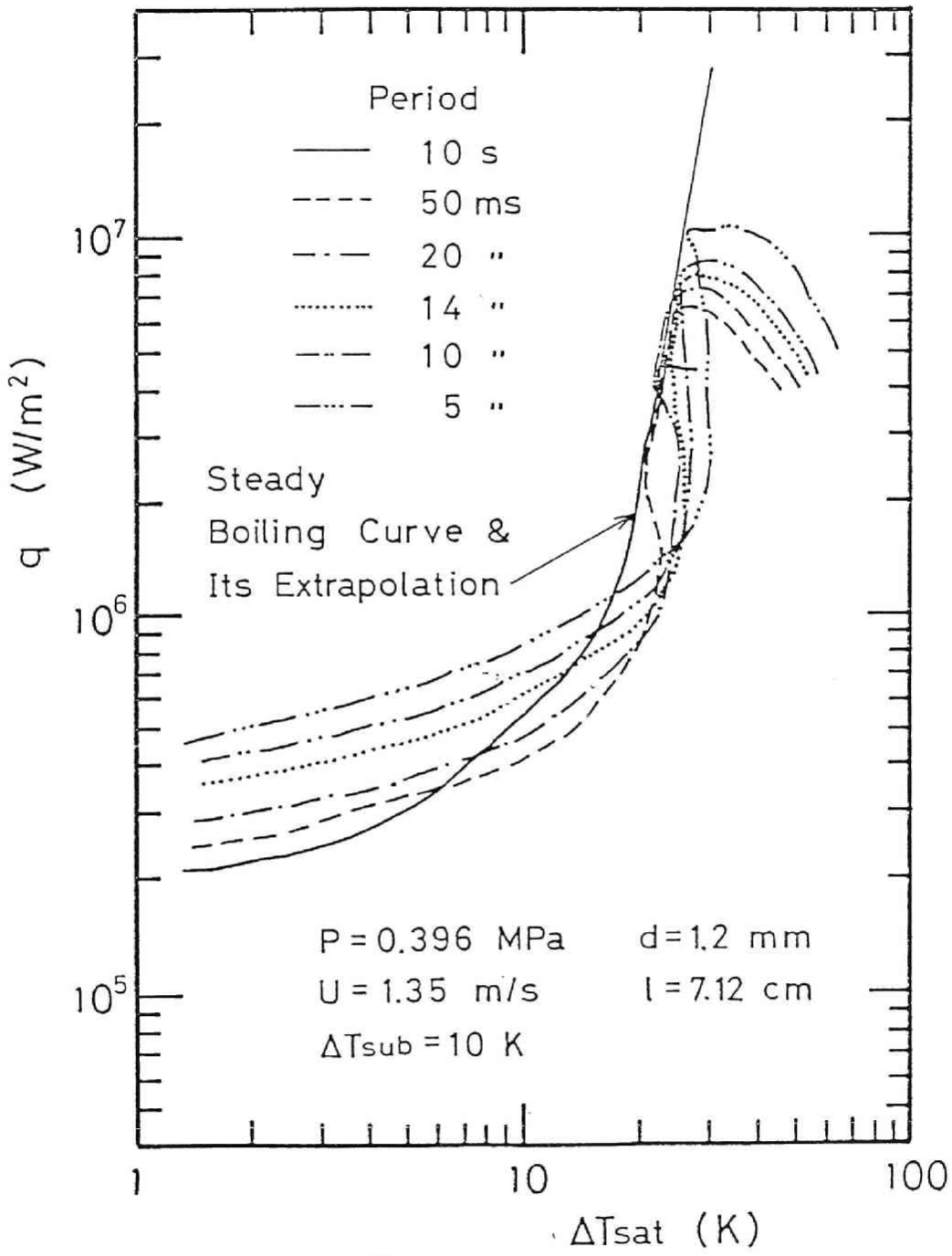

Fig.16(a) The effect of period on transient boiling curve at 0.396 MPa, 1.35 m/s and 10 K subcooling (1.2 mm diam heater)

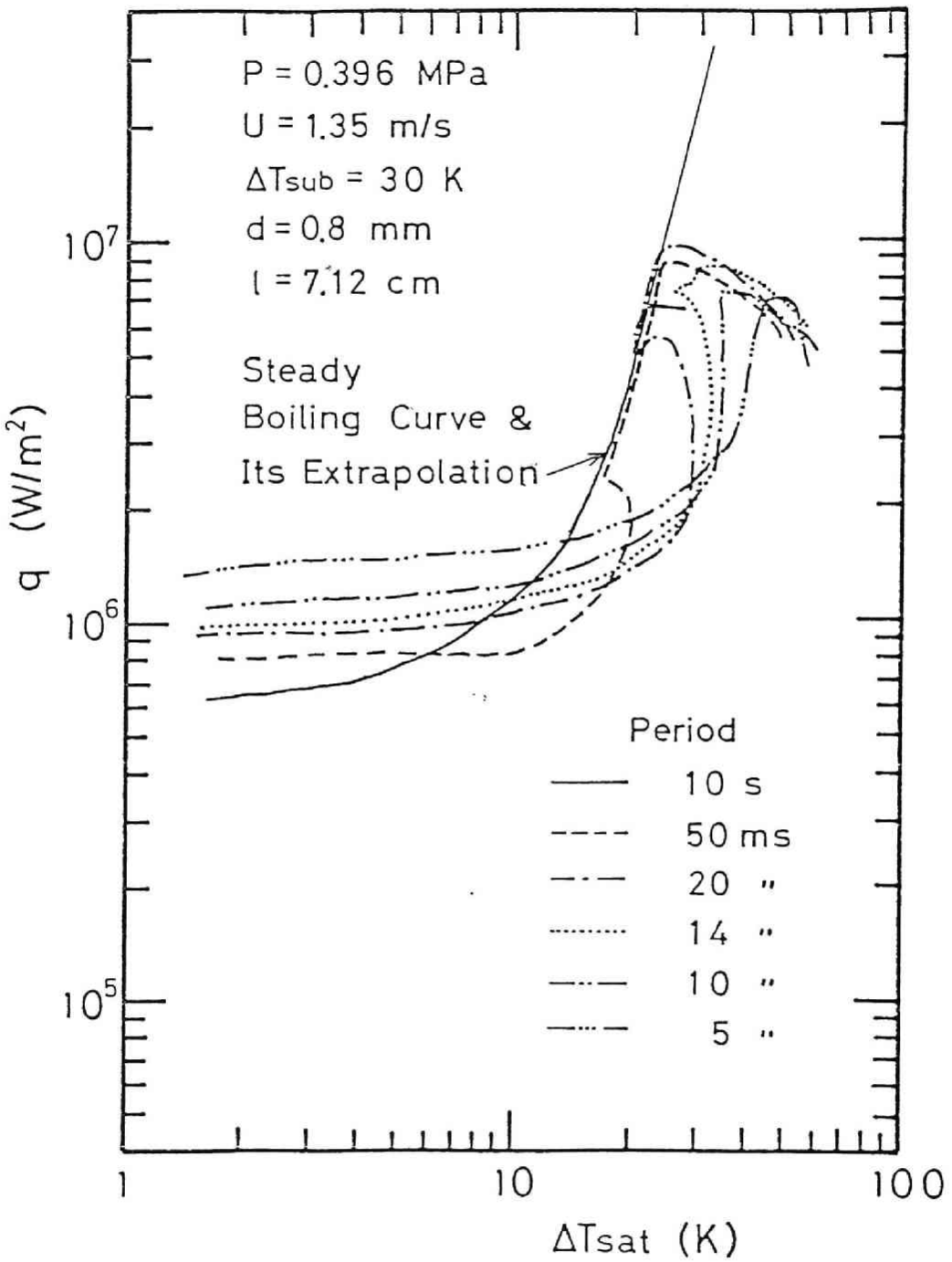

Fig.16(b) The effect of period on transient boiling curve at 0.396 MPa, 1.35 m/s and 30 k subcooling (0.8 mm diam heater)

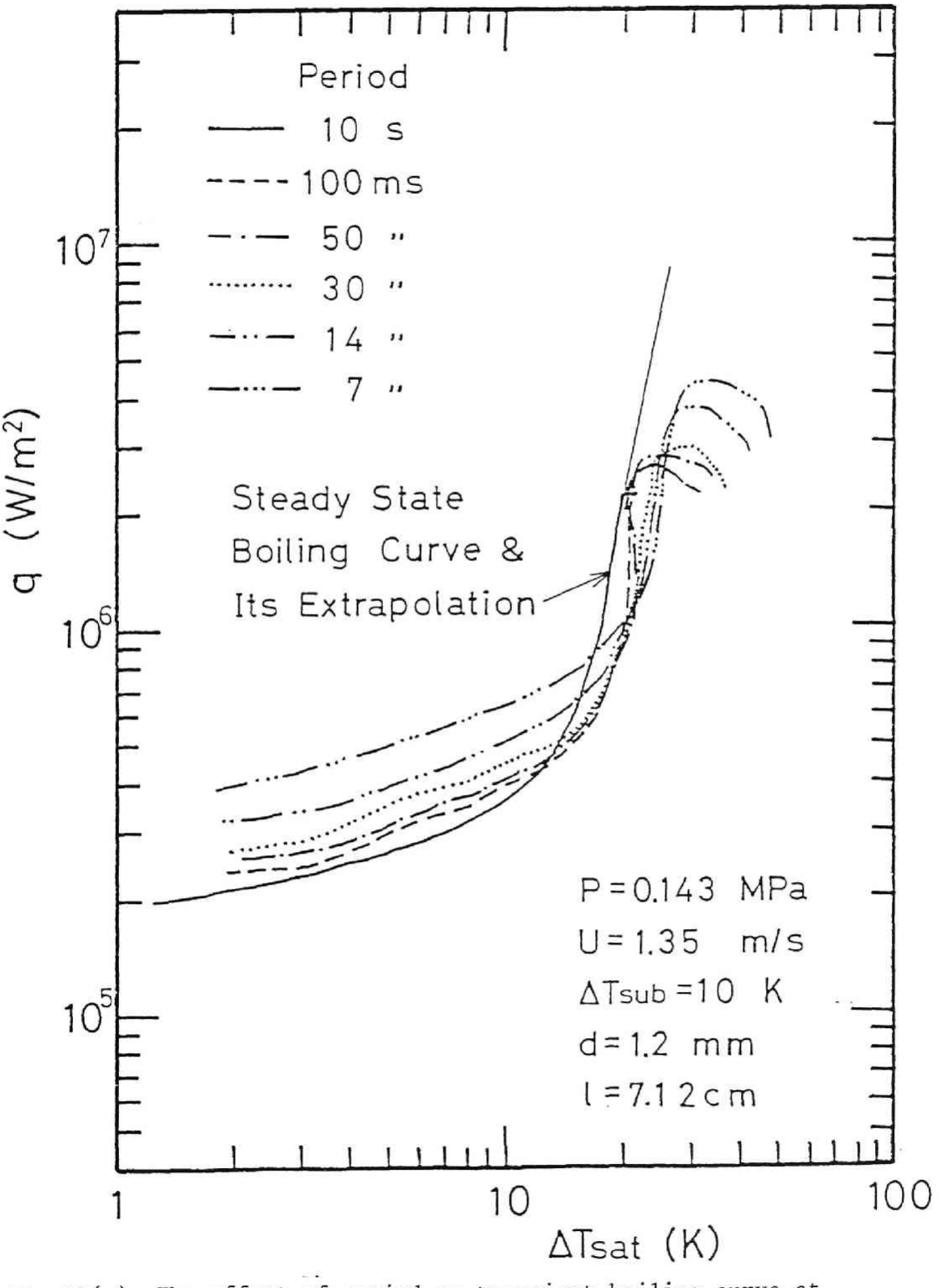

Fig.17(a) The effect of period on transient boiling curve at 0.143 MPa, 1.35 m/s and 10 K subcooling (1.2 mm diam heater)

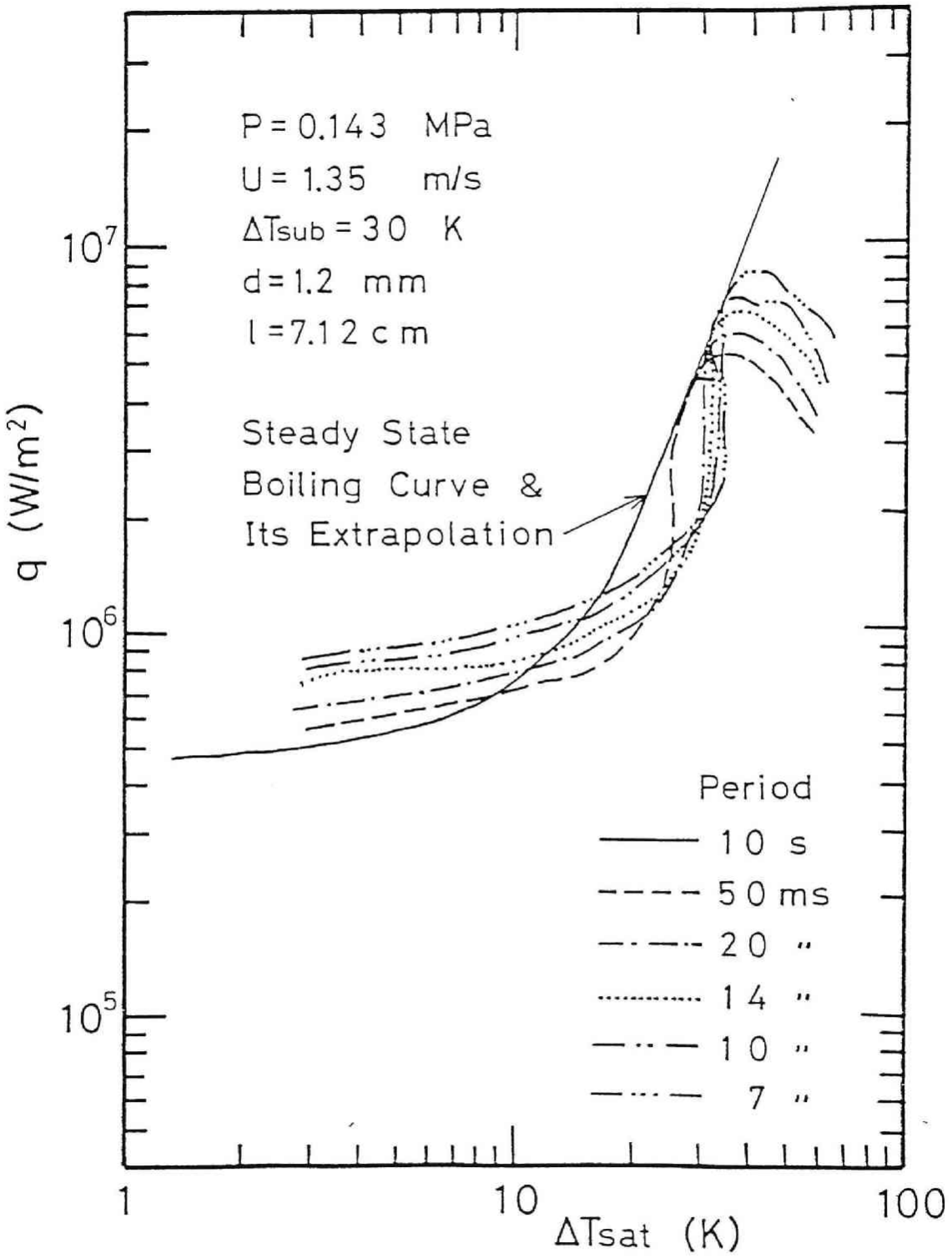

Fig.17(b) The effect of period on transient boiling curve at 0.143 MPa, 1.35 m/s and 30 K subcooling (1.2 mm diam heater)

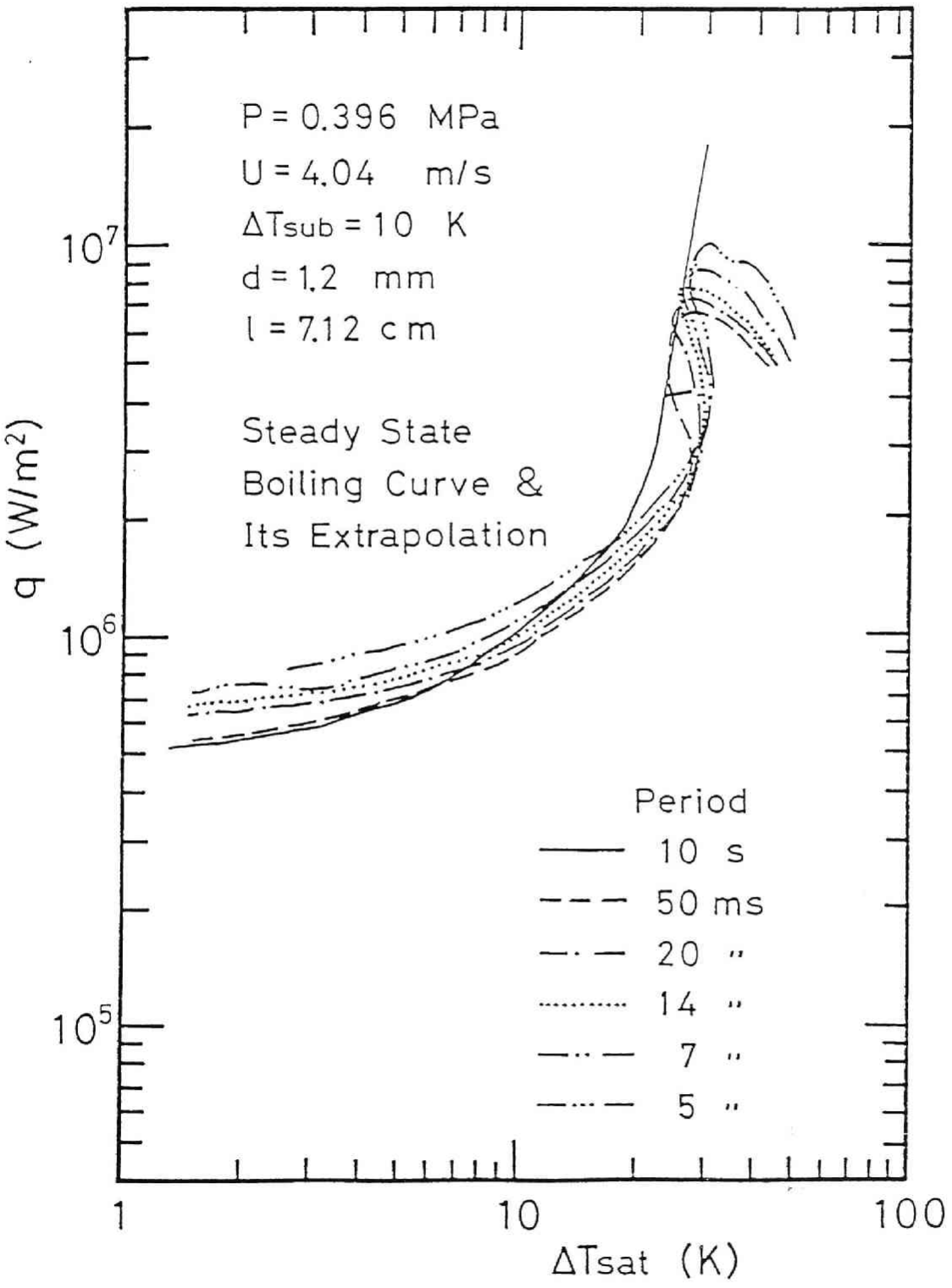

Fig.17(c) The effect of period on transient boiling curve at 0.396 MPa, 4.04 m/s and 10 K subcooling (1.2 mm diam heater)

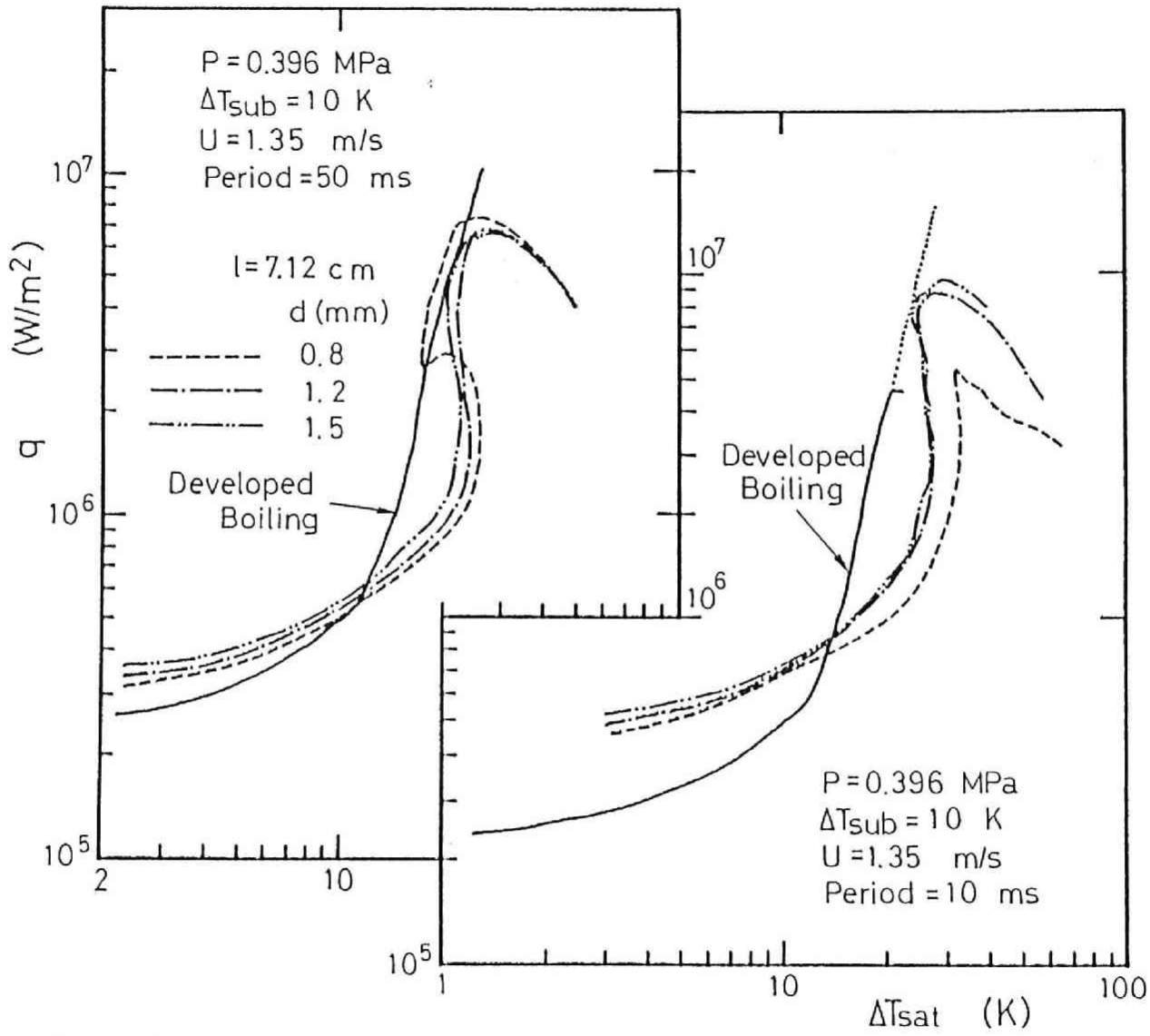

Fig.18(a) The effect of heater diameter on transient boiling curve

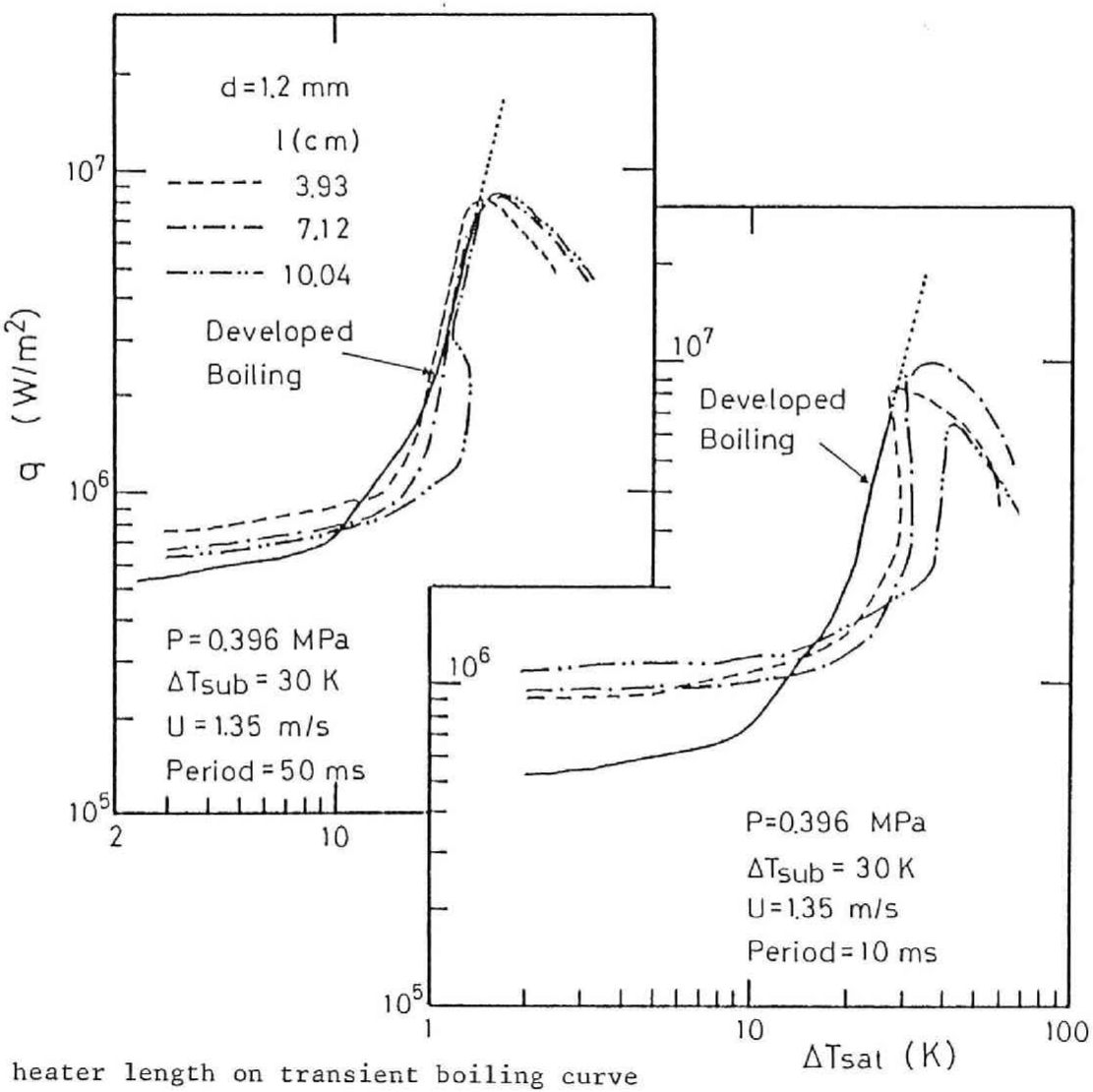

Fig.18(b) The effect of heater length on transient boiling curve

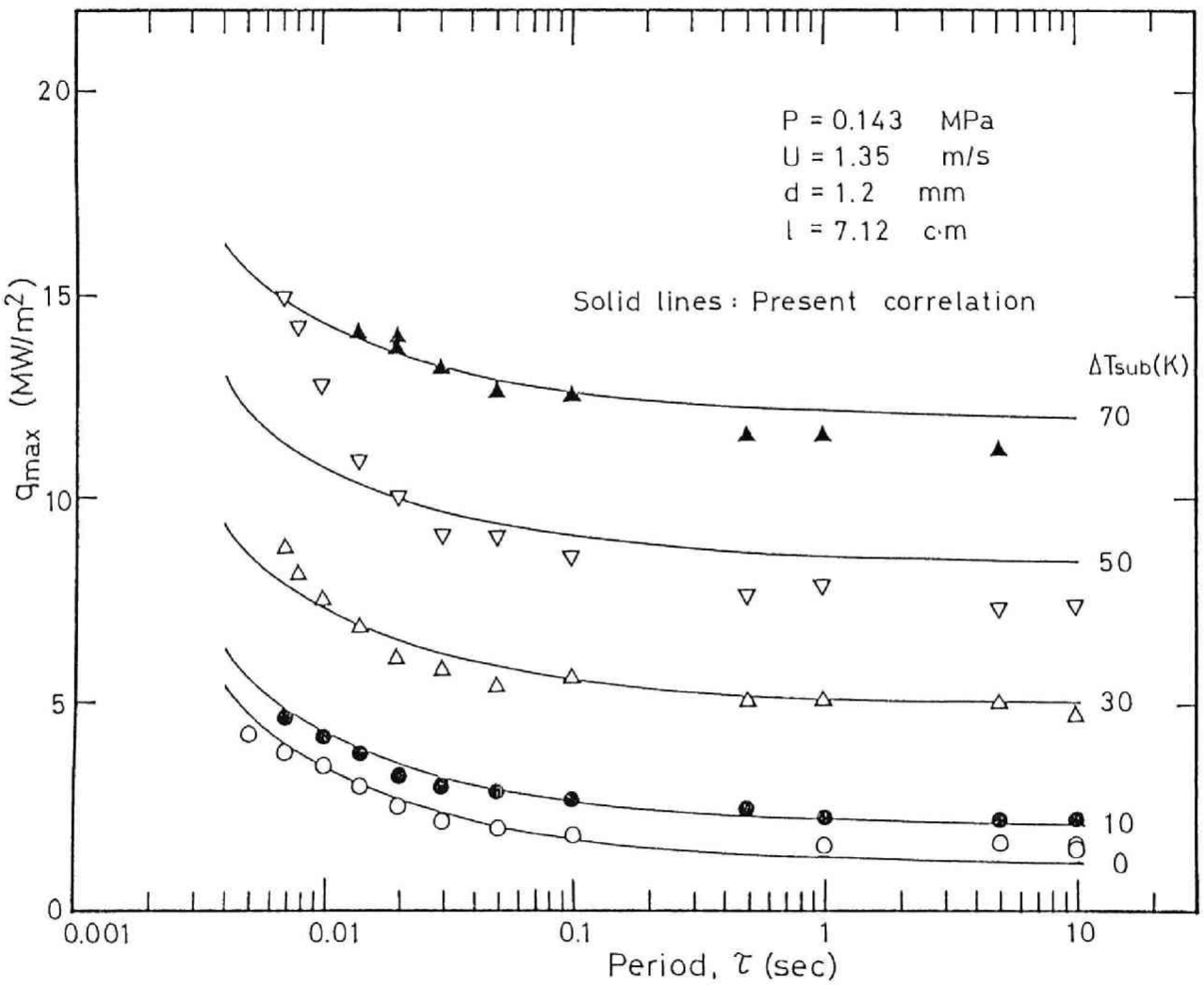

Fig.19(a) The variation of transient maximum heat flux with period and subcooling at 0.143 MPa and 1.35 m/s (1.2 mm diam heater)

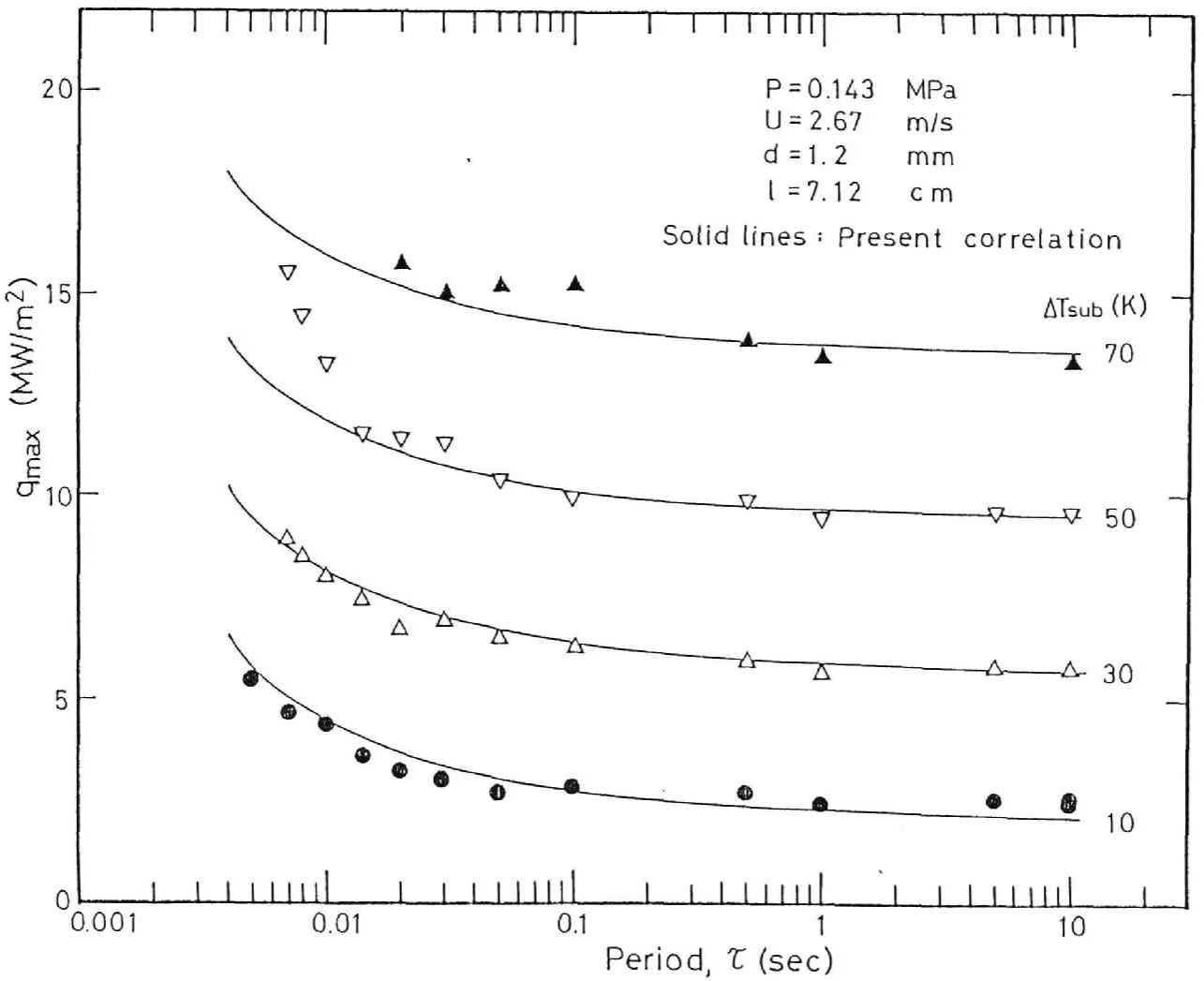

Fig.19(b) The variation of transient maximum heat flux with period and subcooling at 0.143 MPa and 2.67 m/s (1.2 mm diam heater)

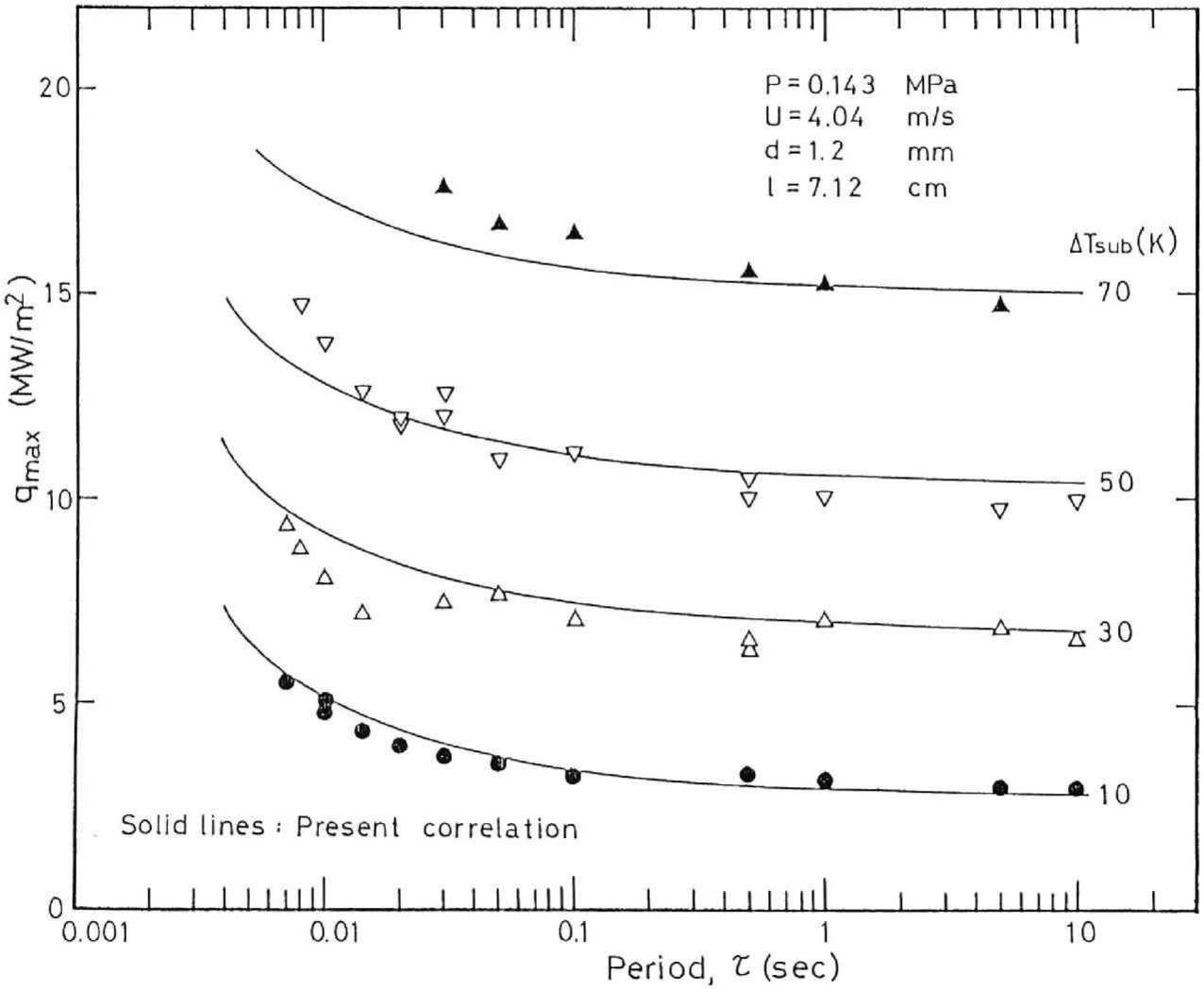

Fig.19(c) The variation of transient maximum heat flux with period and subcooling at 0.143 MPa and 4.04 m/s (1.2 mm diam heater)

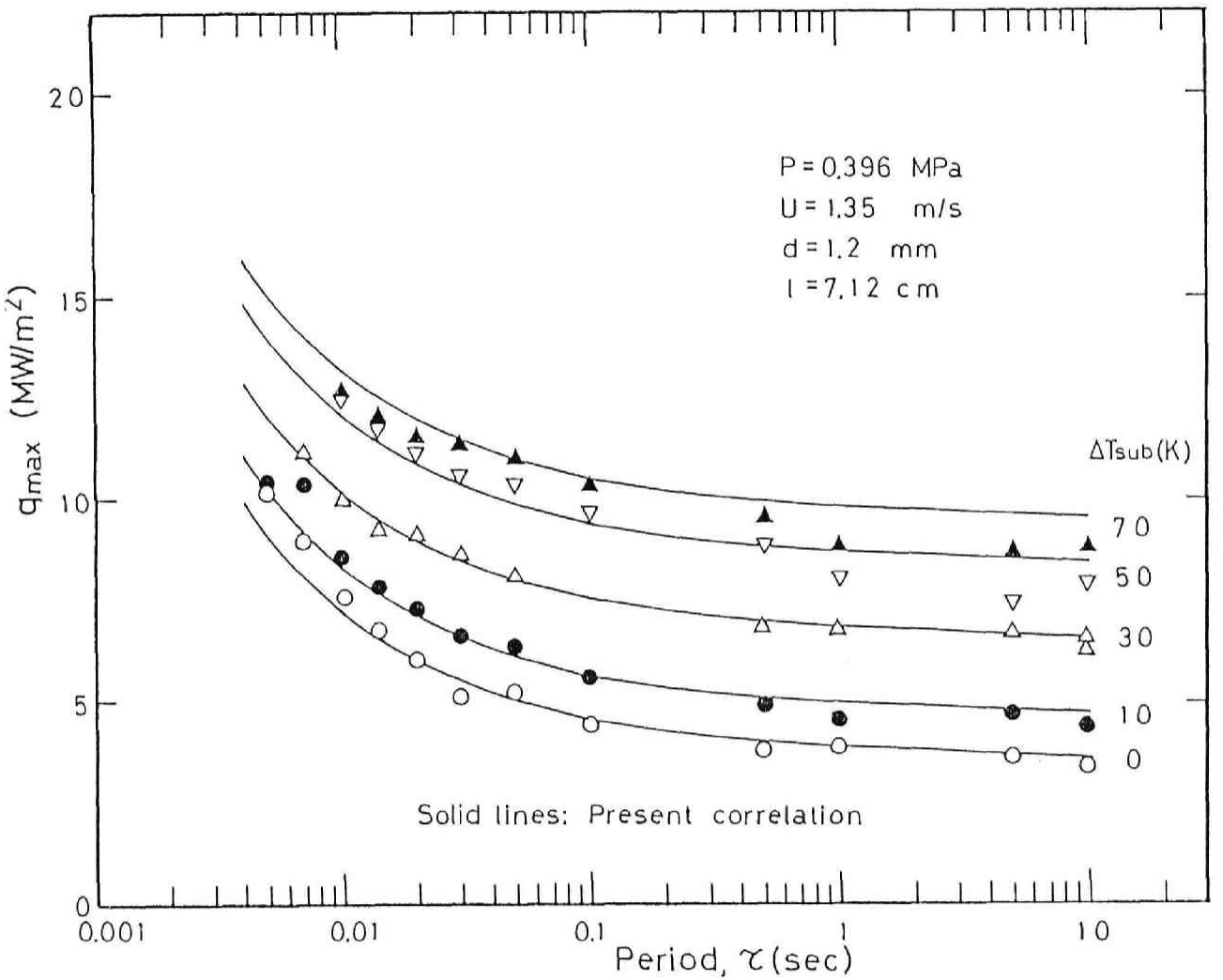

Fig.19(d) The variation of transient maximum heat flux with period and subcooling at 0.396 MPa and 1.35 m/s (1.2 mm diam heater)

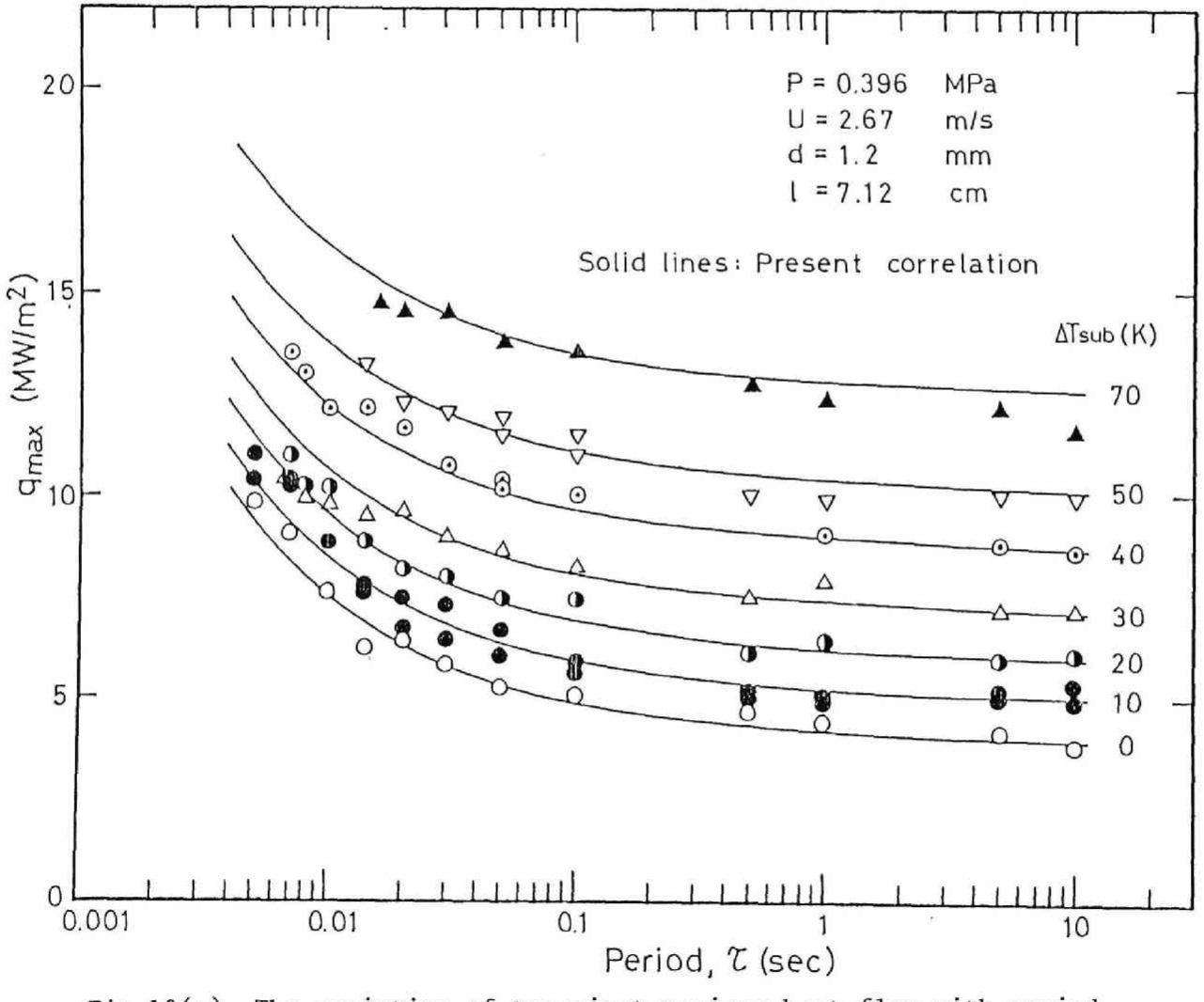

Fig.19(e) The variation of transient maximum heat flux with period and subcooling at 0.396 MPa and 2.67 m/s (1.2 mm diam heater)

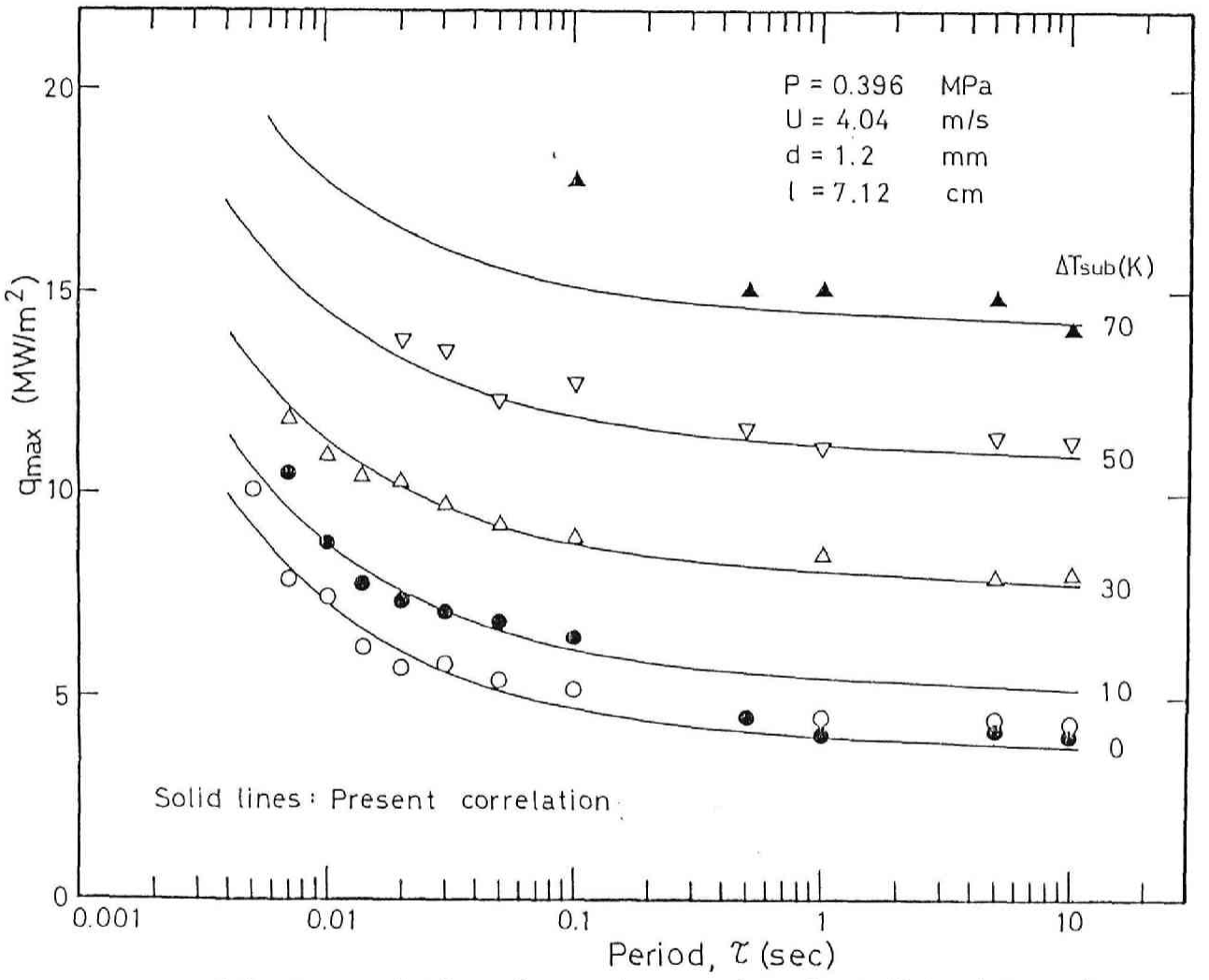

Fig.19(f) The variation of transient maximum heat flux with period and subcooling at 0.396 MPa and 4.04 m/s (1.2 mm diam heater)

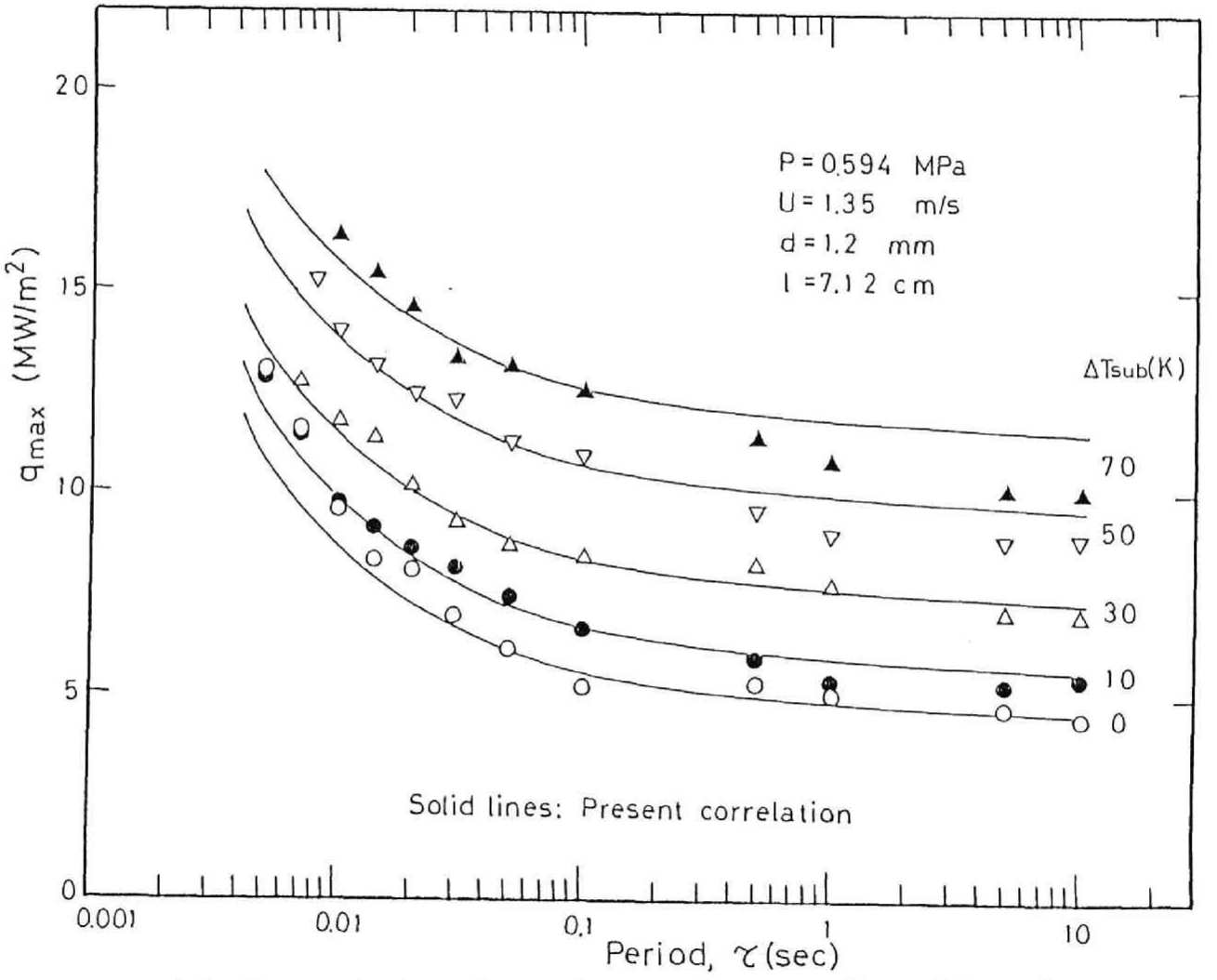

Fig.20(a) The variation of transient maximum heat flux with period and subcooling at 0.594 MPa and 1.35 m/s (1.2 mm diam heater)

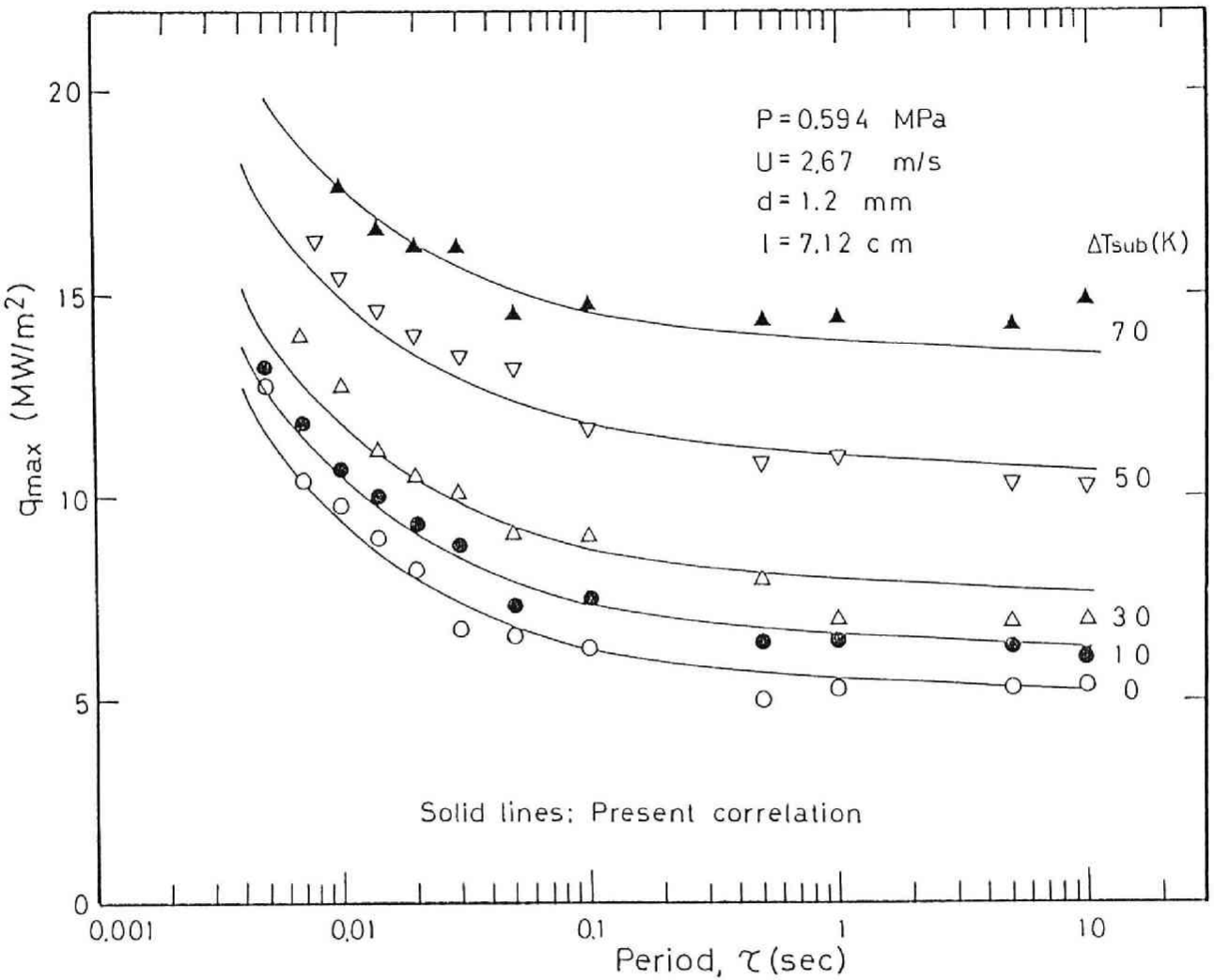

Fig.20(b) The variation of transient maximum heat flux with period and subcooling at 0.594 MPa and 2.67 m/s (1.2 mm diam heater)

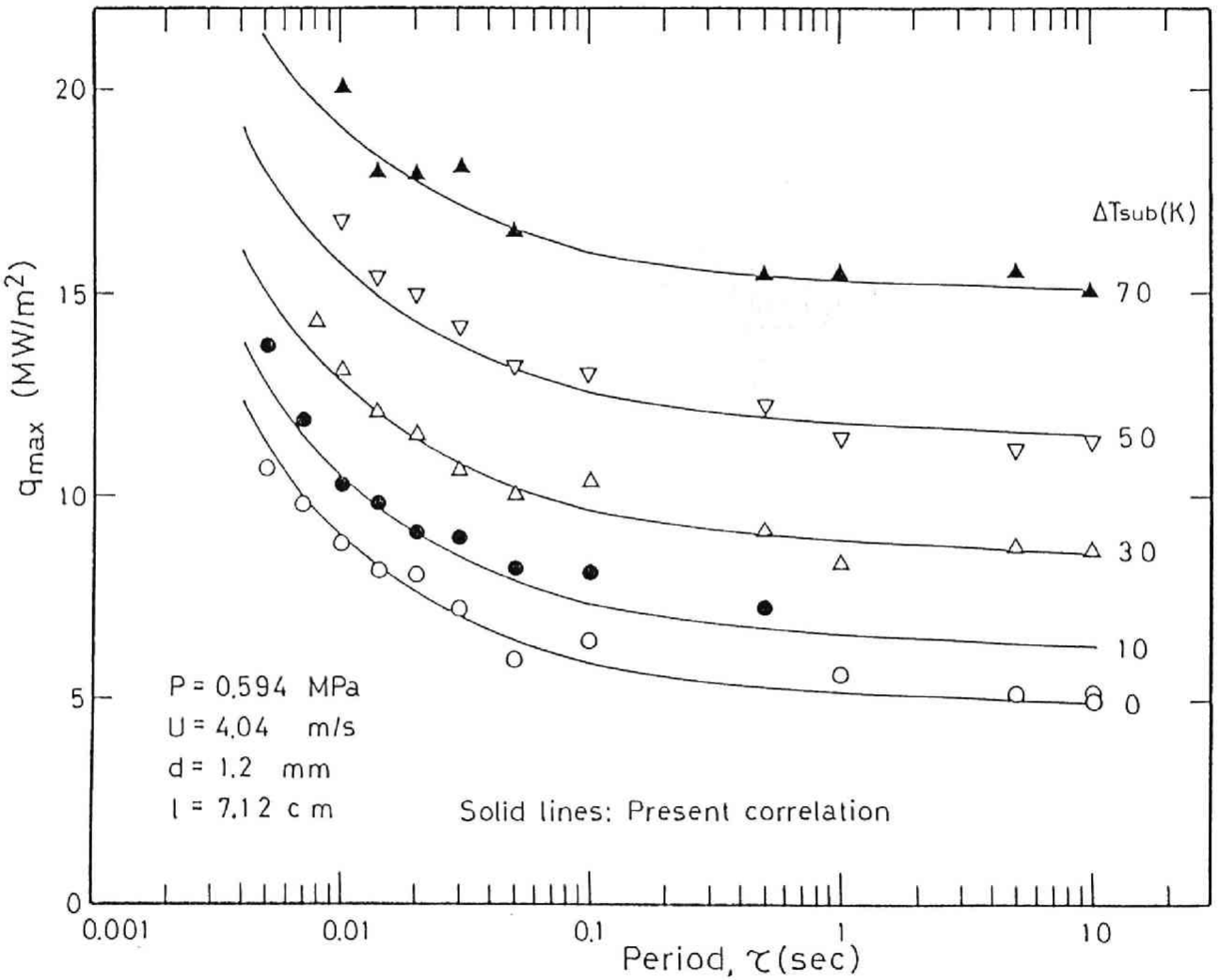

Fig.20(c) The variation of transient maximum heat flux with period and subcooling at 0.594 MPa and 4.04 m/s (1.2 mm diam heater)

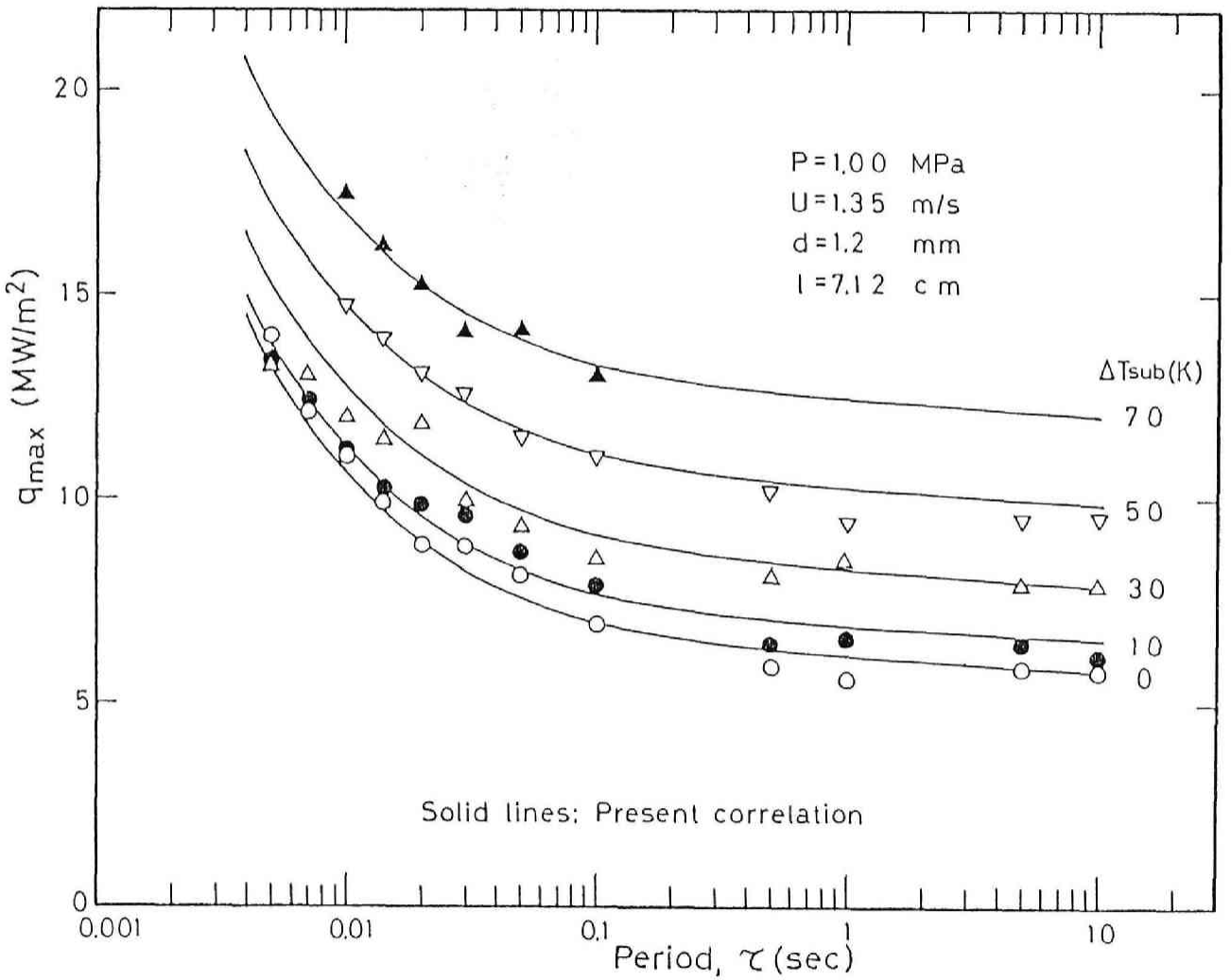

Fig.20(d) The variation of transient maximum heat flux with period and subcooling at 1.00 MPa and 1.35 m/s (1.2 mm diam heater)

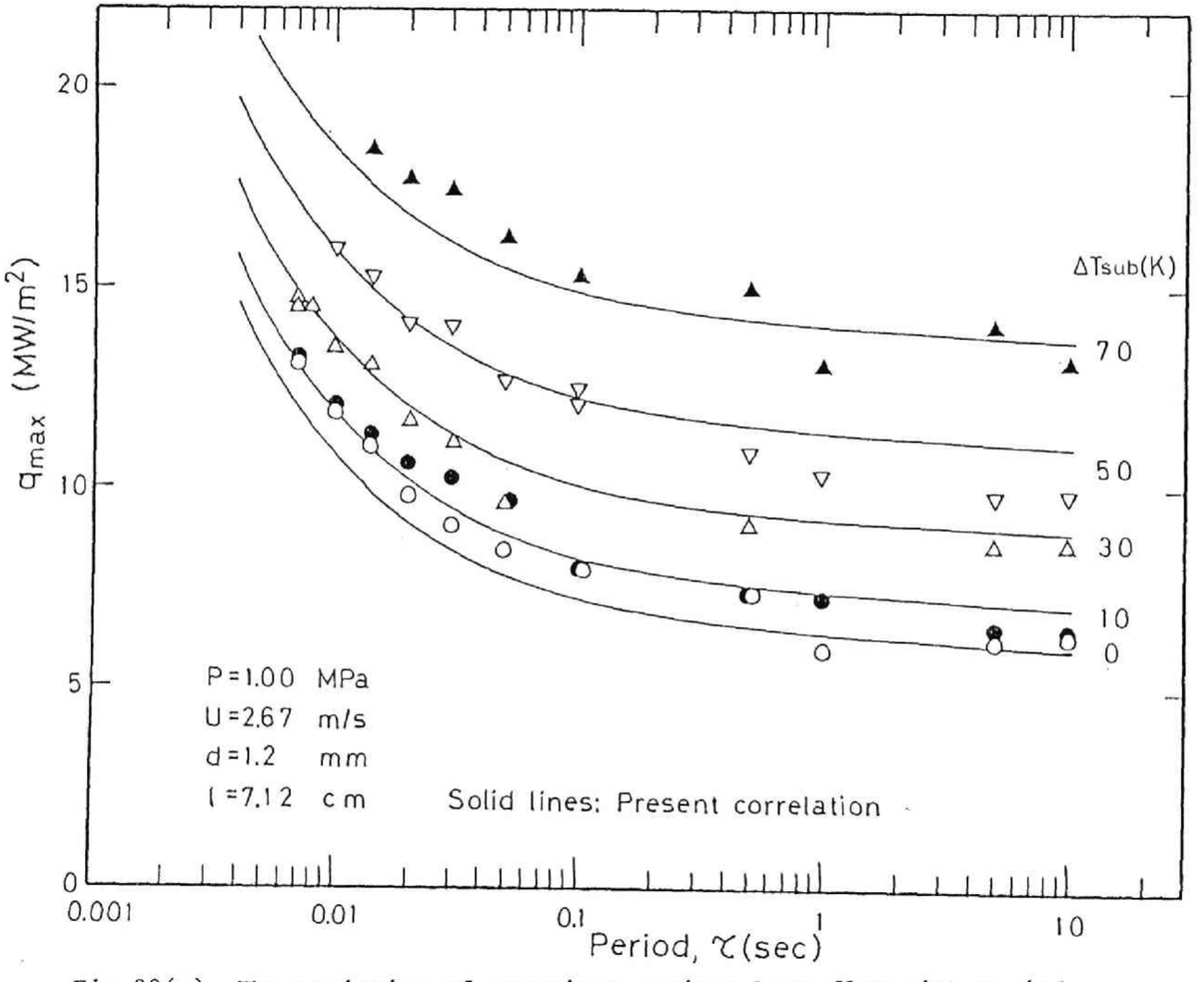

Fig.20(e) The variation of transient maximum heat flux with period and subcooling at 1.00 MPa and 2.67 m/s (1.2 mm diam heater)

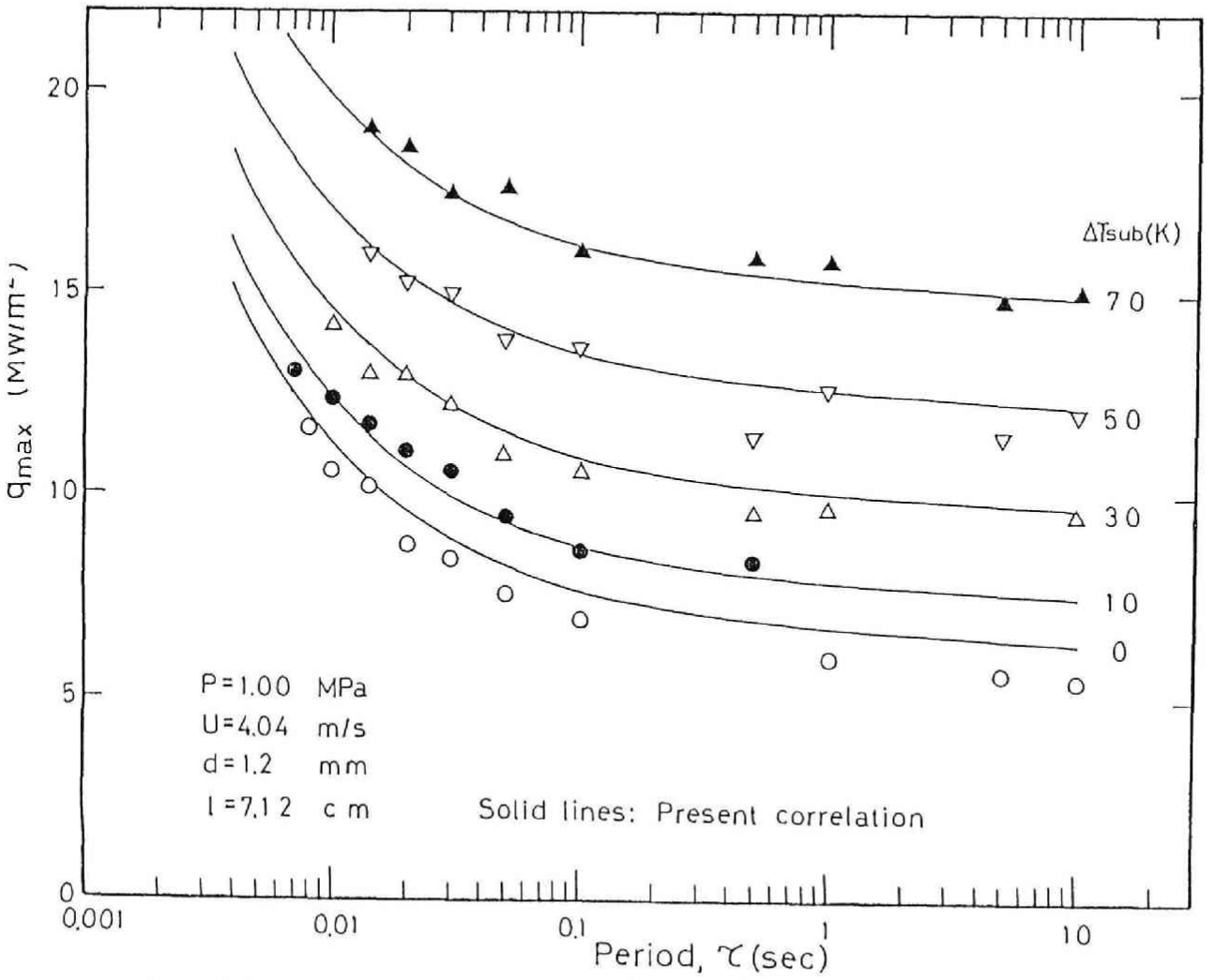

Fig.20(f) The variation of transient maximum heat flux with period and subcooling at 1.00 MPa and 4.04 m/s (1.2 mm diam heater)

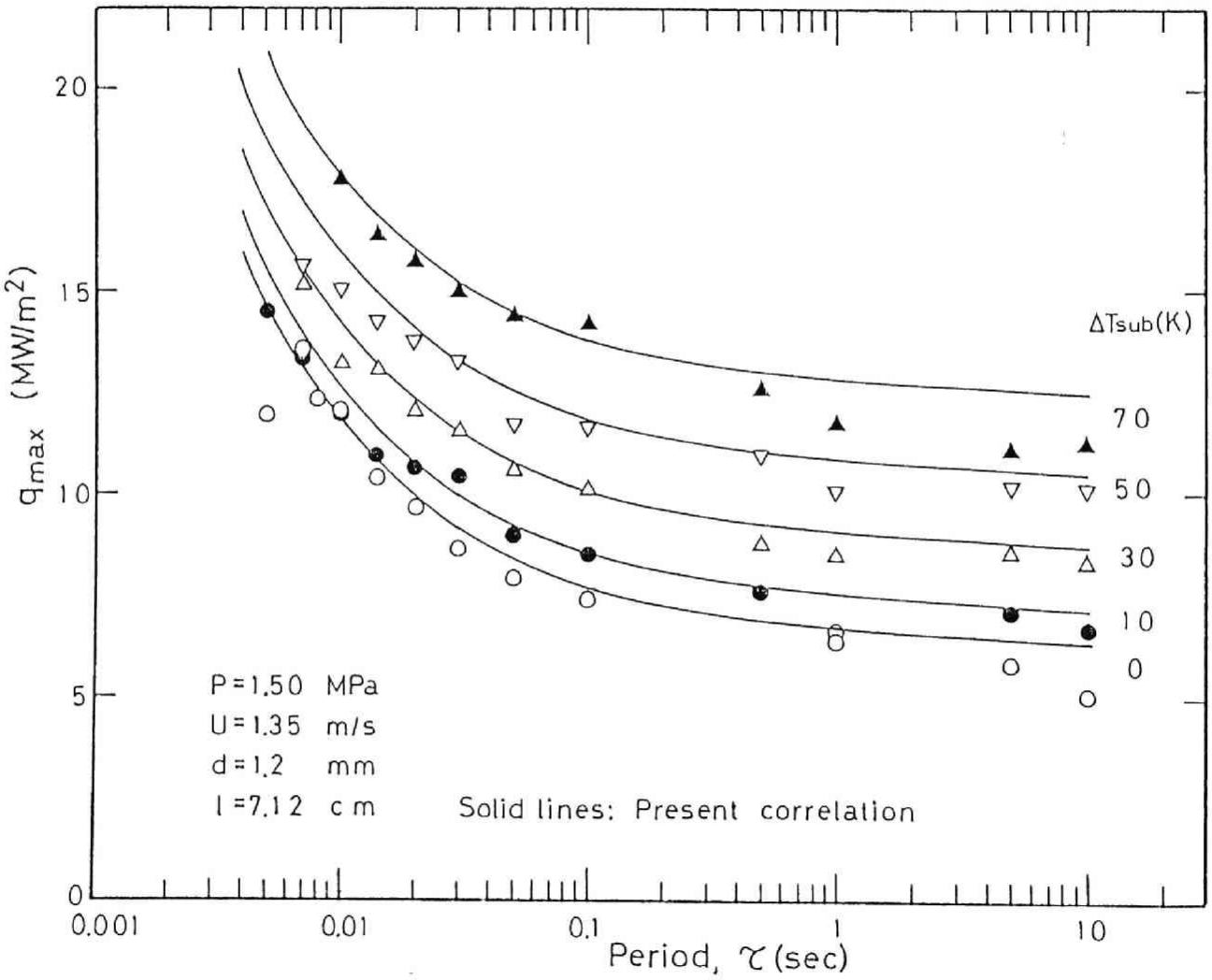

Fig.21(a) The variation of transient maximum heat flux with period and subcooling at 1.50 MPa and 1.35 m/s (1.2 mm diam heater)

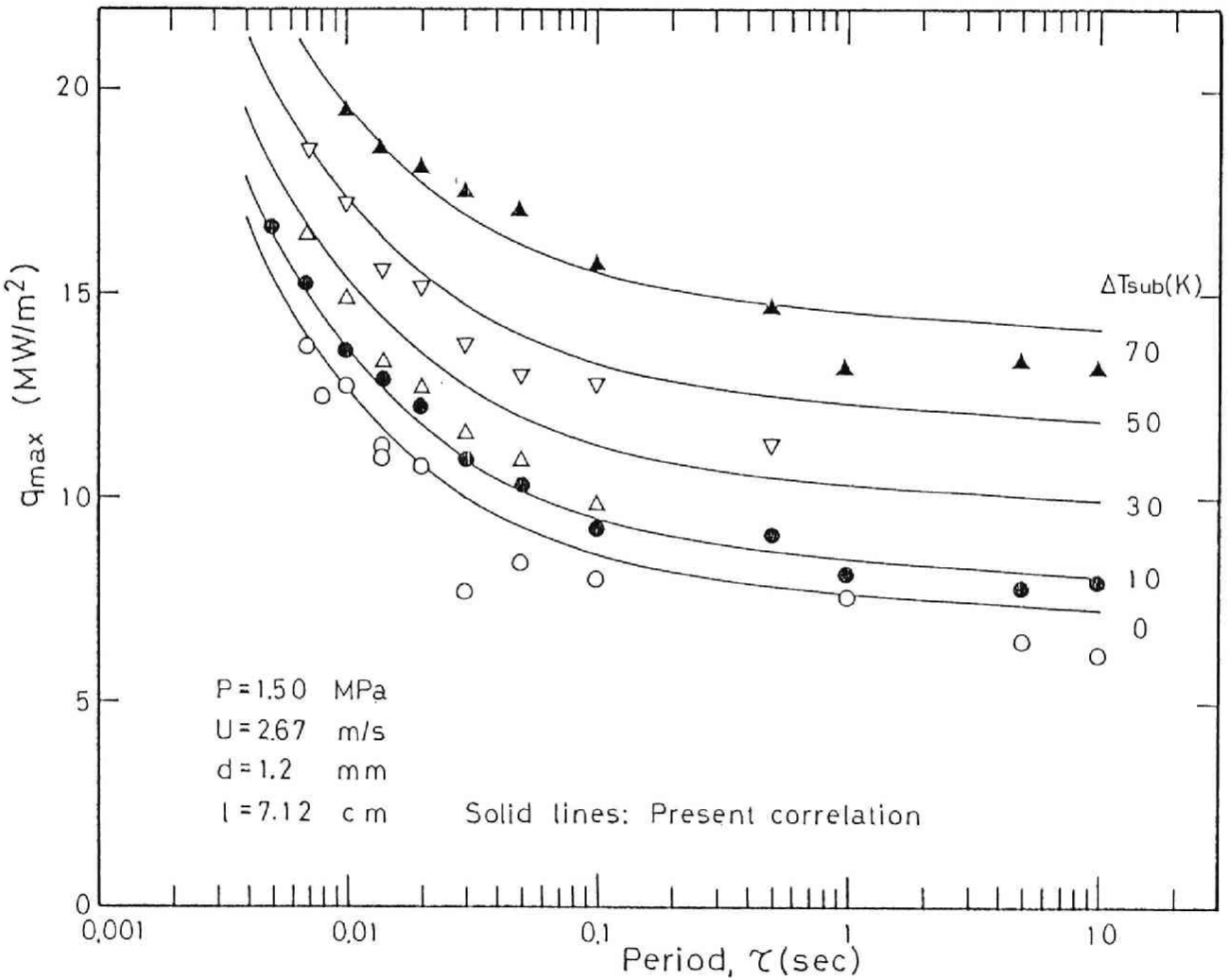

Fig.21(b) The variation of transient maximum heat flux with period and subcooling at 1.50 MPa and 2.67 m/s (1.2 mm diam heater)

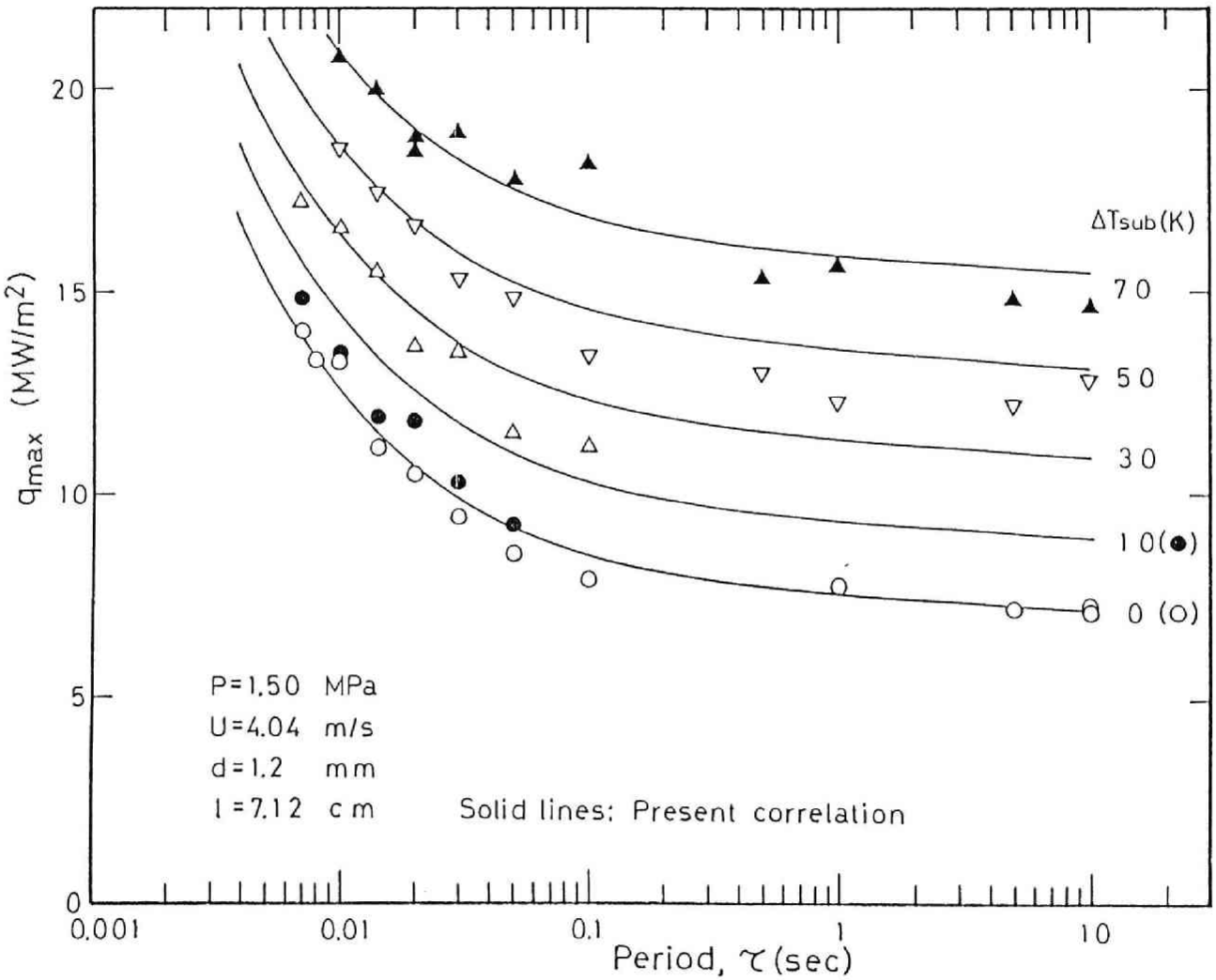

Fig.21(c) The variation of transient maximum heat flux with period and subcooling at 1.50 MPa and 4.04 m/s (1.2 mm diam heater)

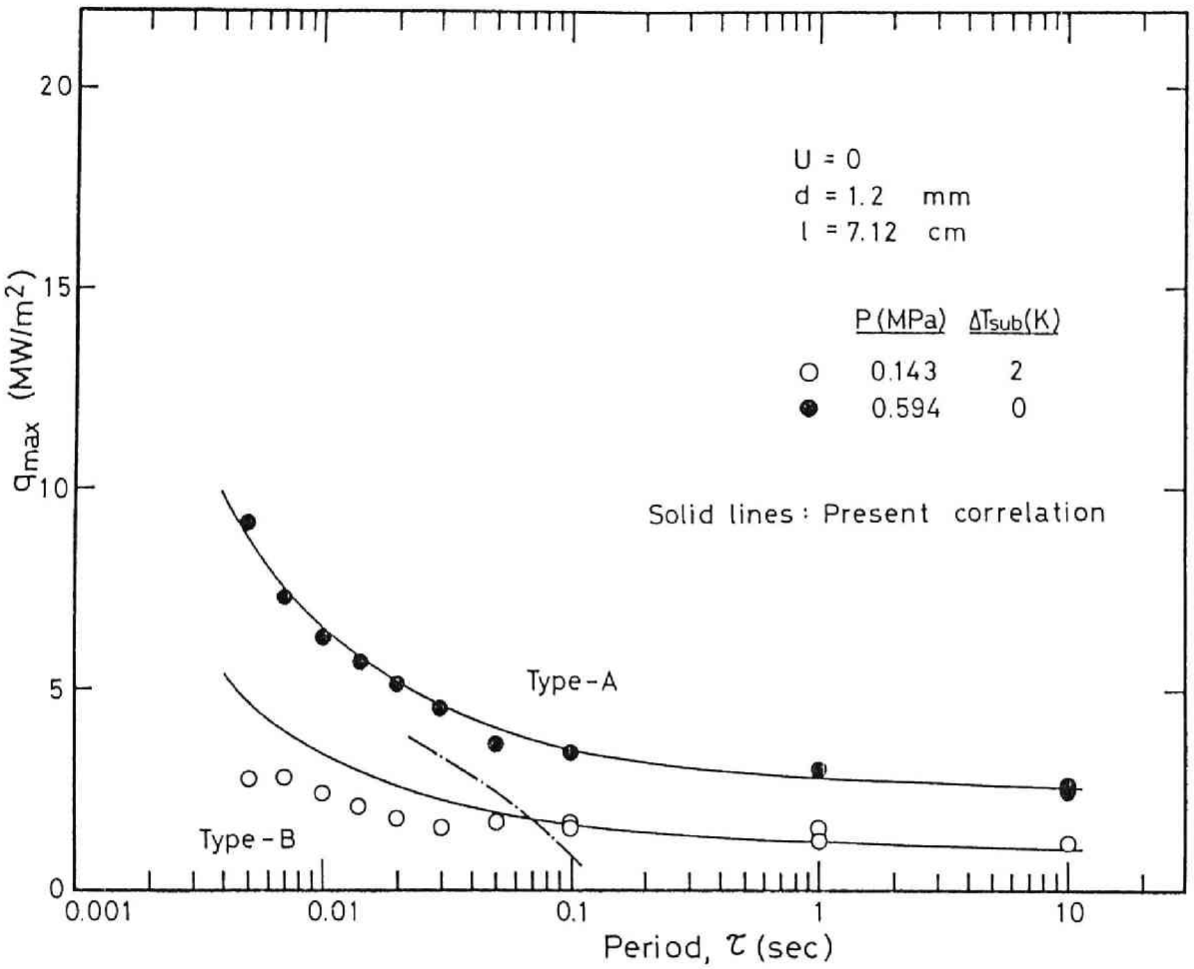

Fig.22 Transient maximum heat flux at zero flow.

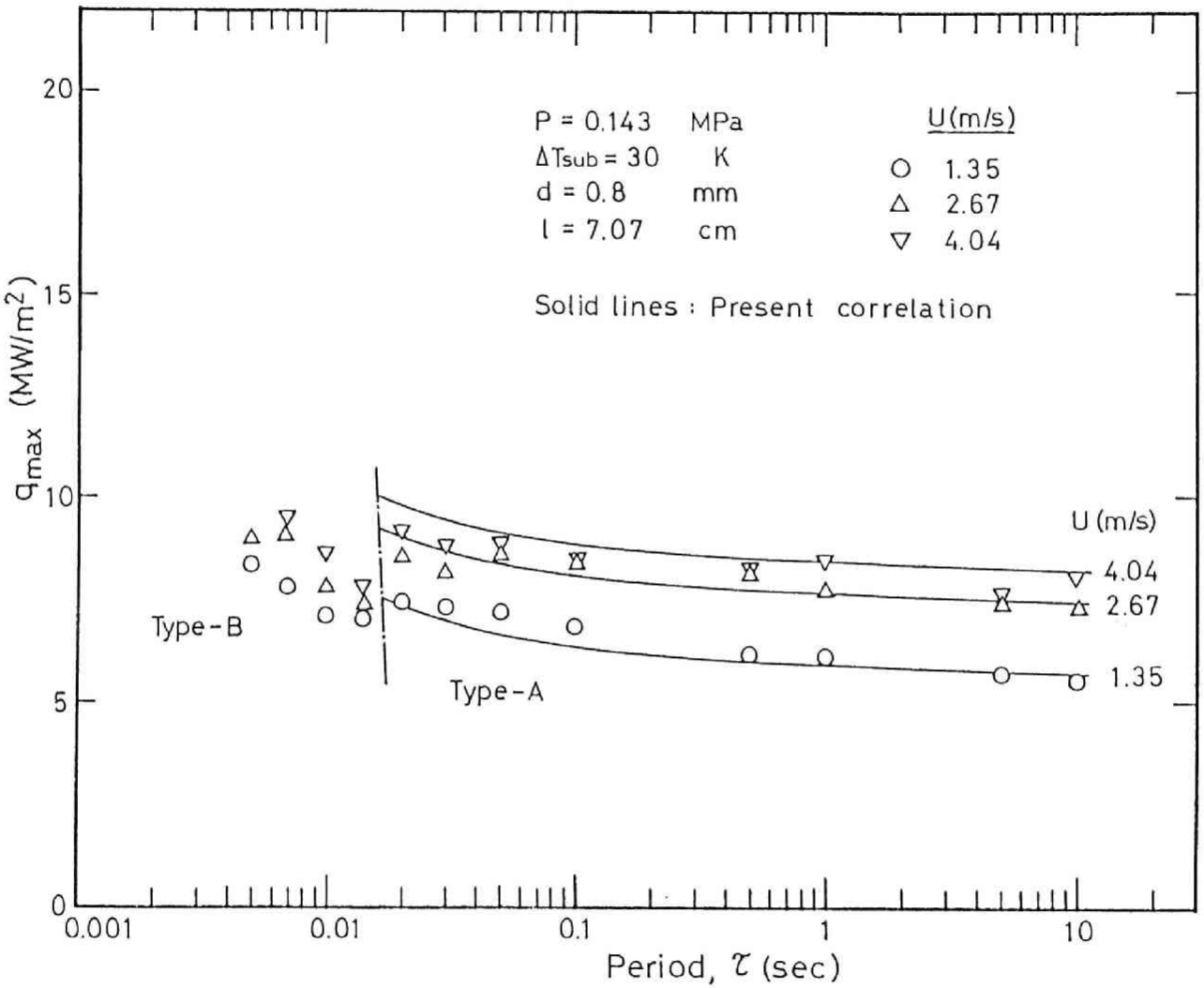

Fig.23(a) The variation of transient maximum heat flux with period and velocity at 0.143 MPA and 30 K subcooling (0.8 mm diam heater)

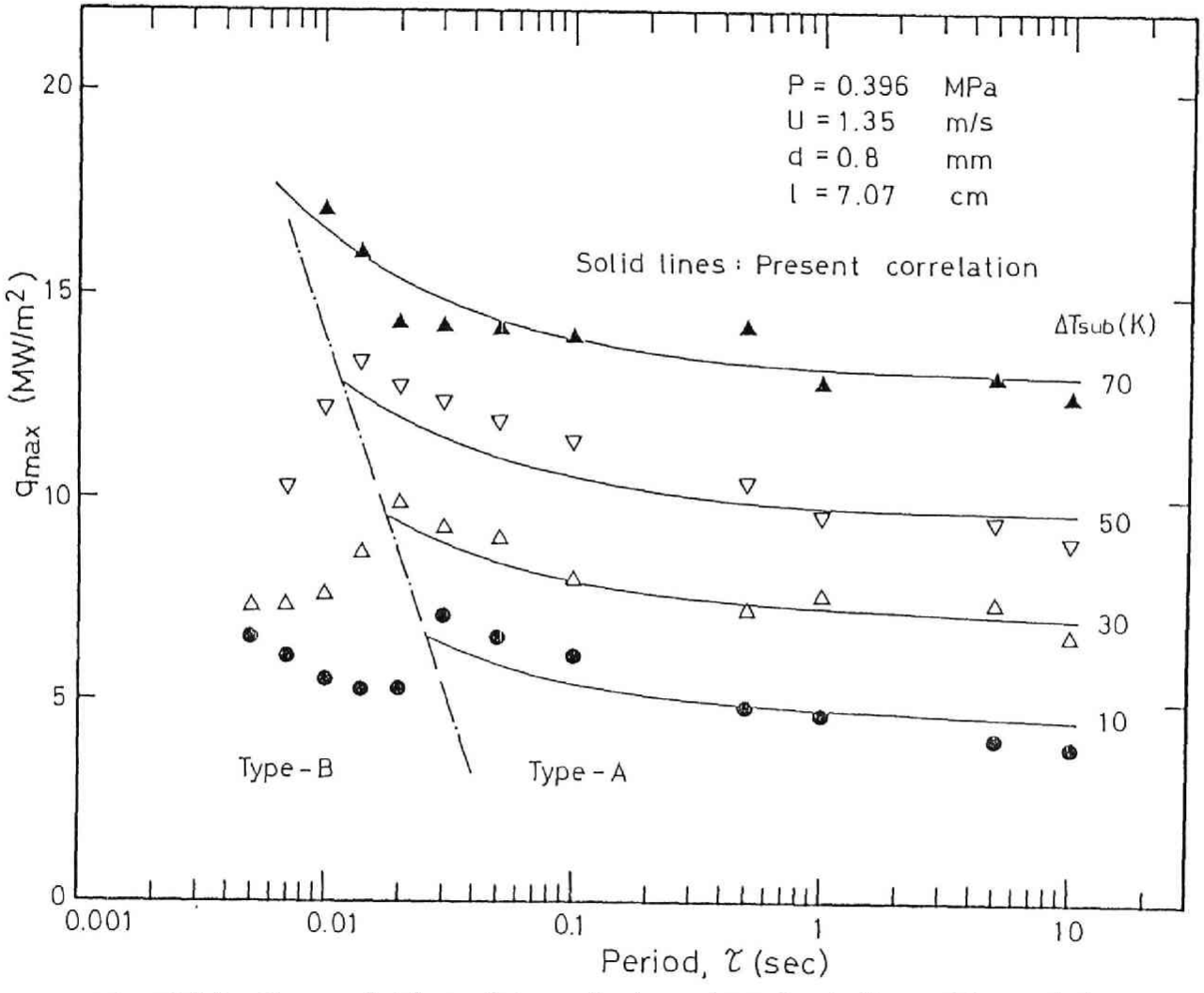

Fig.23(b) The variation of transient maximum heat flux with period and subcooling at 0.396 MPa and 1.35 m/s (0.8 mm diam heater)

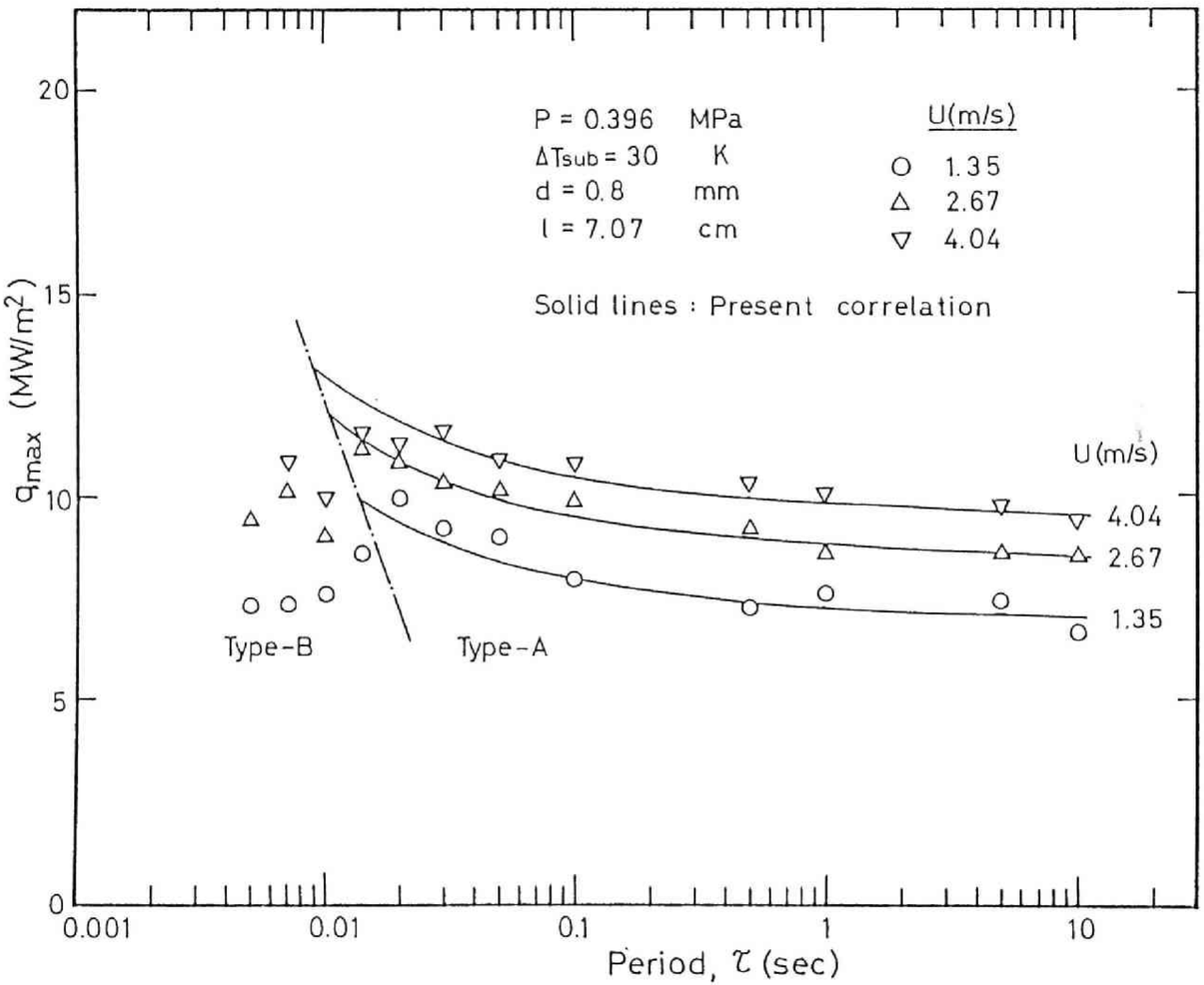

Fig.23(c) The variation of transient maximum heat flux with period and velocity at 0.396 MPa and 30 K subcooling (0.8 mm diam heater)

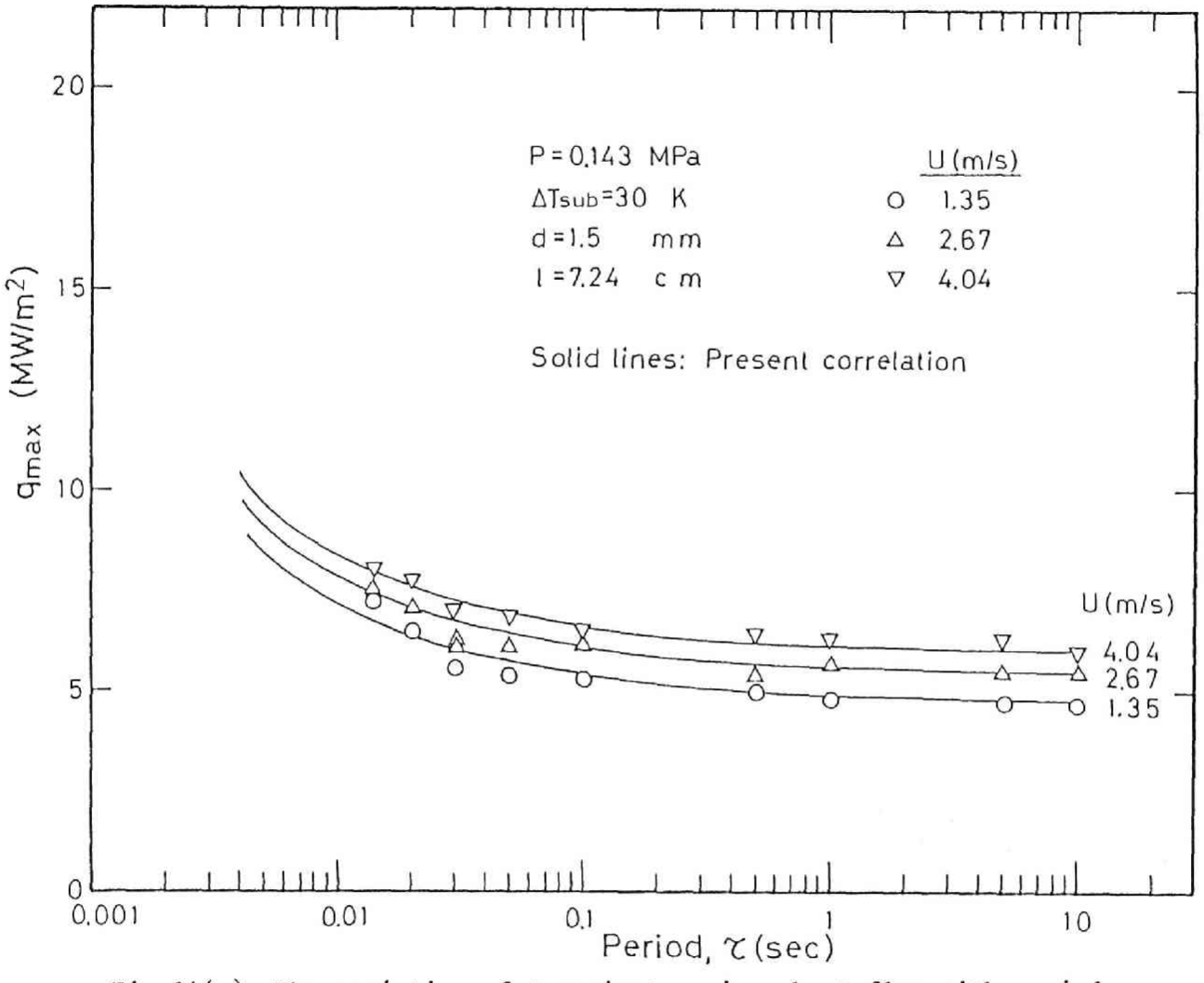

Fig.24(a) The variation of transient maximum heat flux with period and velocity at 0.143 MPa and 30 K subcooling (1.5 mm diam heater)

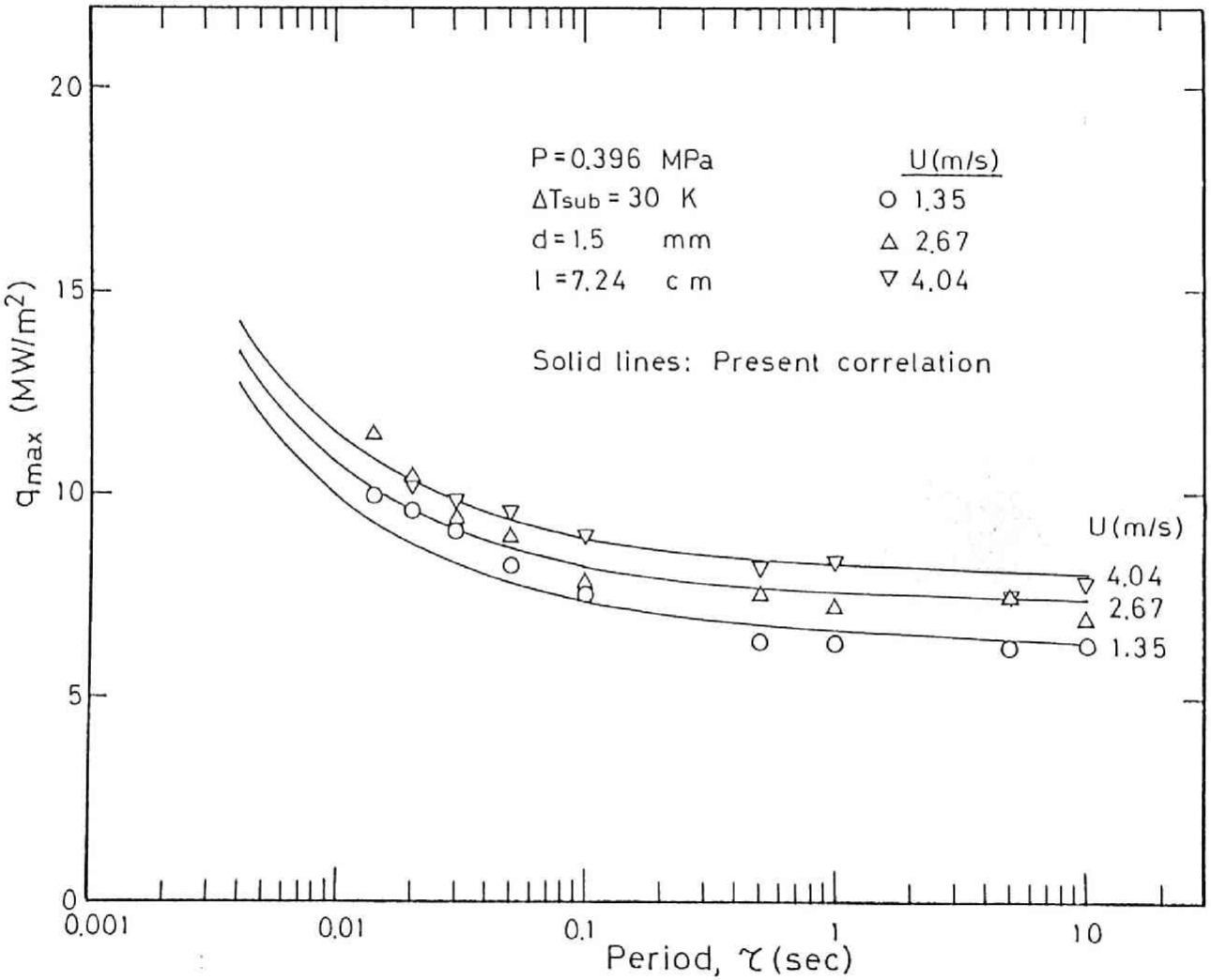

Fig.24(b) The variation of transient maximum heat flux with period and velocity at 0.396 MPa and 30 K subcooling (1.5 mm diam heater)

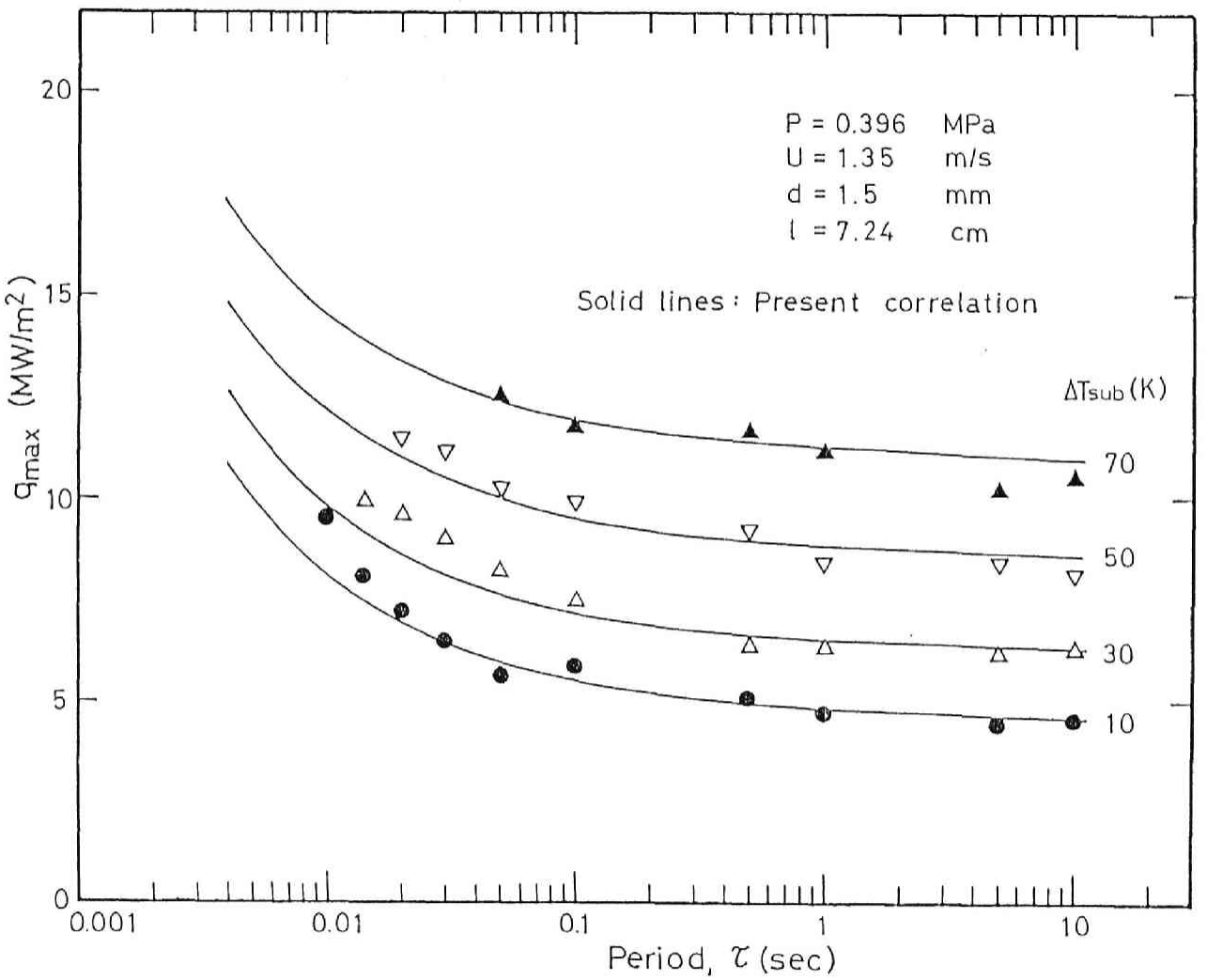

Fig.24(c) The variation of transient maximum heat flux with period and subcooling at 0.396 MPa and 1.35 m/s (1.5 mm diam heater)

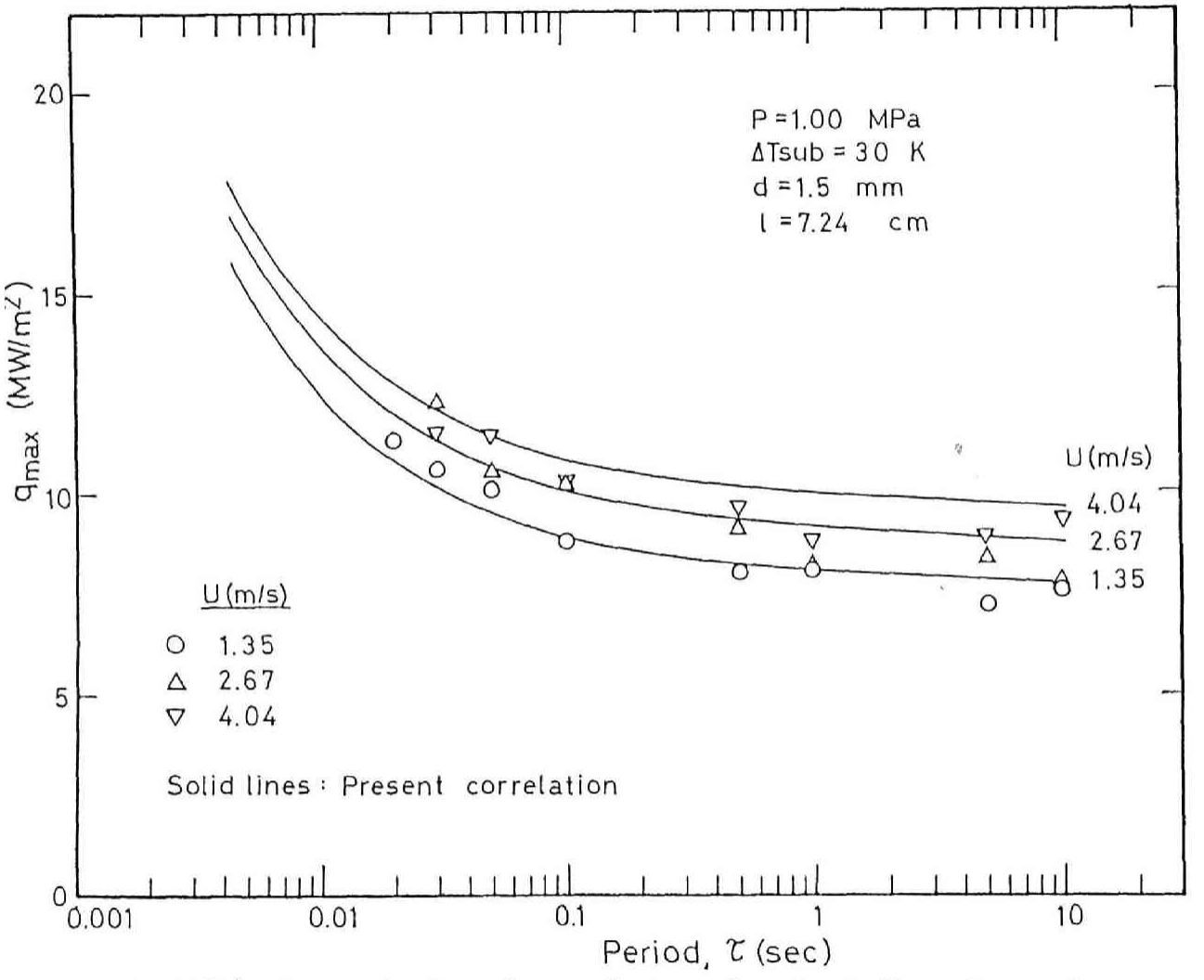

Fig.24(d) The variation of transient maximum heat flux with period and velocity at 1.00 MPa and 30 K subcooling (1.5 mm diam heater)

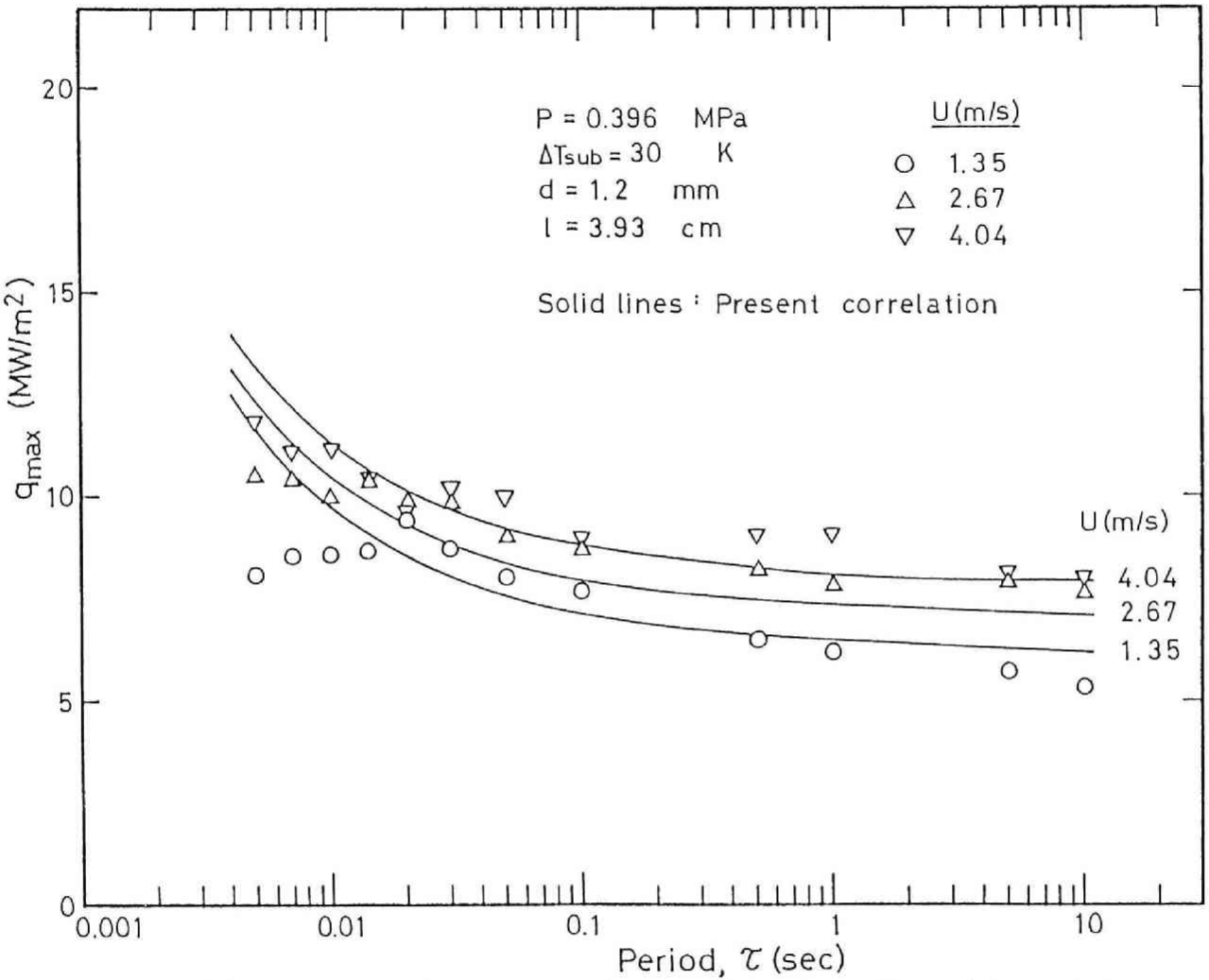

Fig.25(a) The variation of transient maximum heat flux with period and velocity at 0.396 MPa and 30 K subcooling (1.2 mm diam and 3.9. cm long heater)

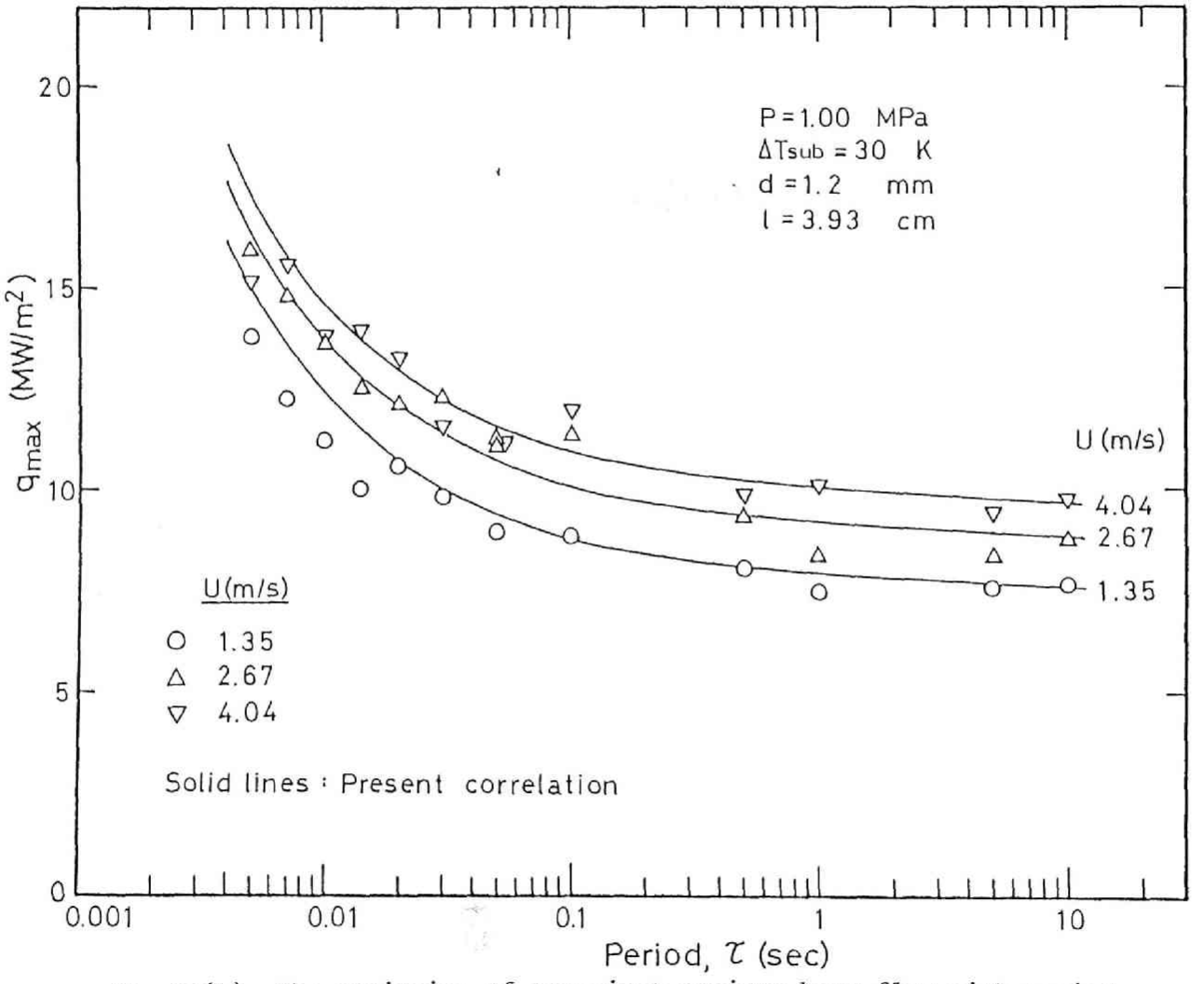

Fig.25(b) The variation of transient maximum heat flux with period and velocity at 1.00 MPa and 30 K subcooling (1.2 mm diam and 3.93 cm long heater)

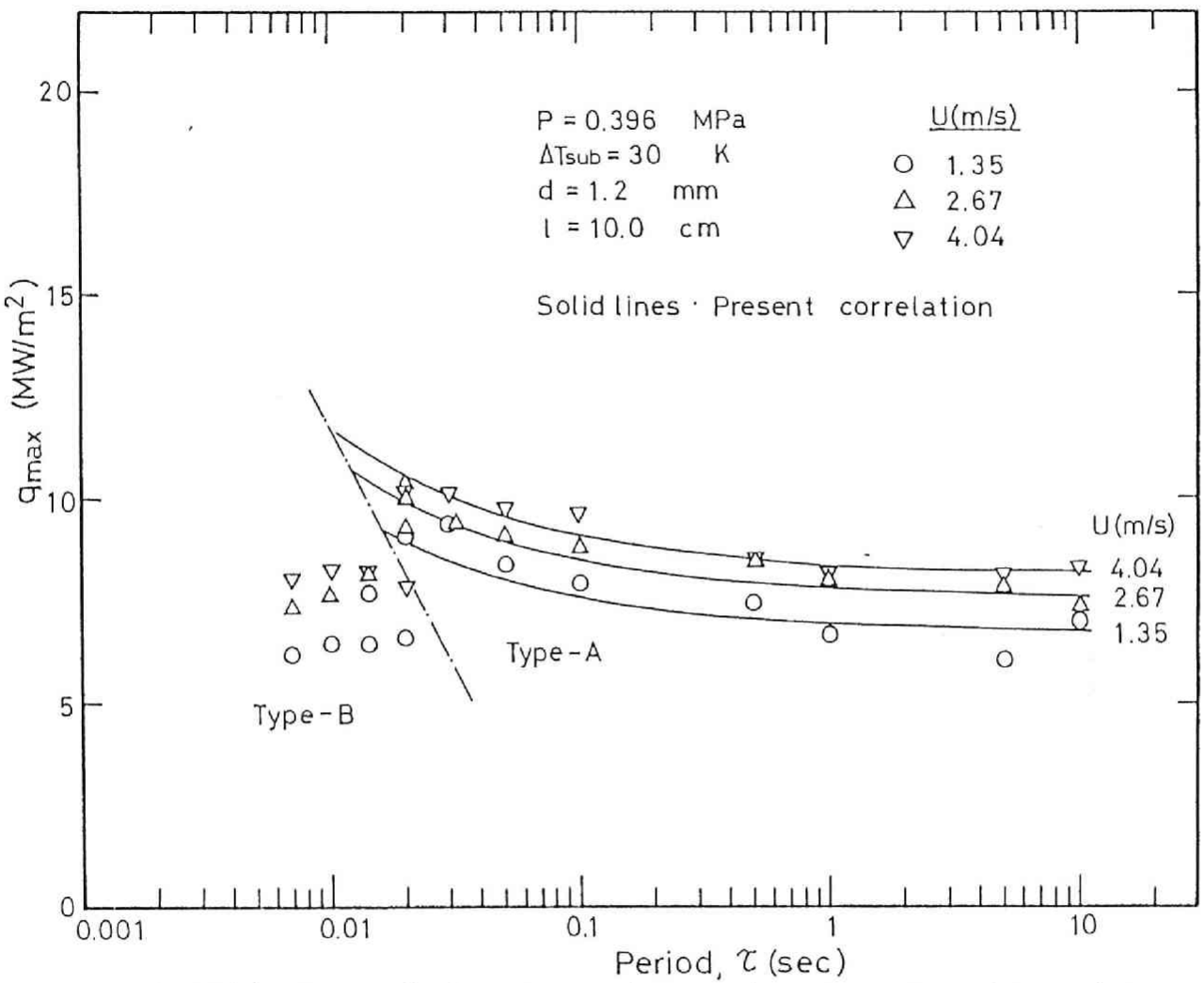

Fig.25(c) The variation of transient maximum heat flux with period and velocity at 0.396 MPa and 30 K subcooling(1.2 mm diam and 10.0 cm long heater)

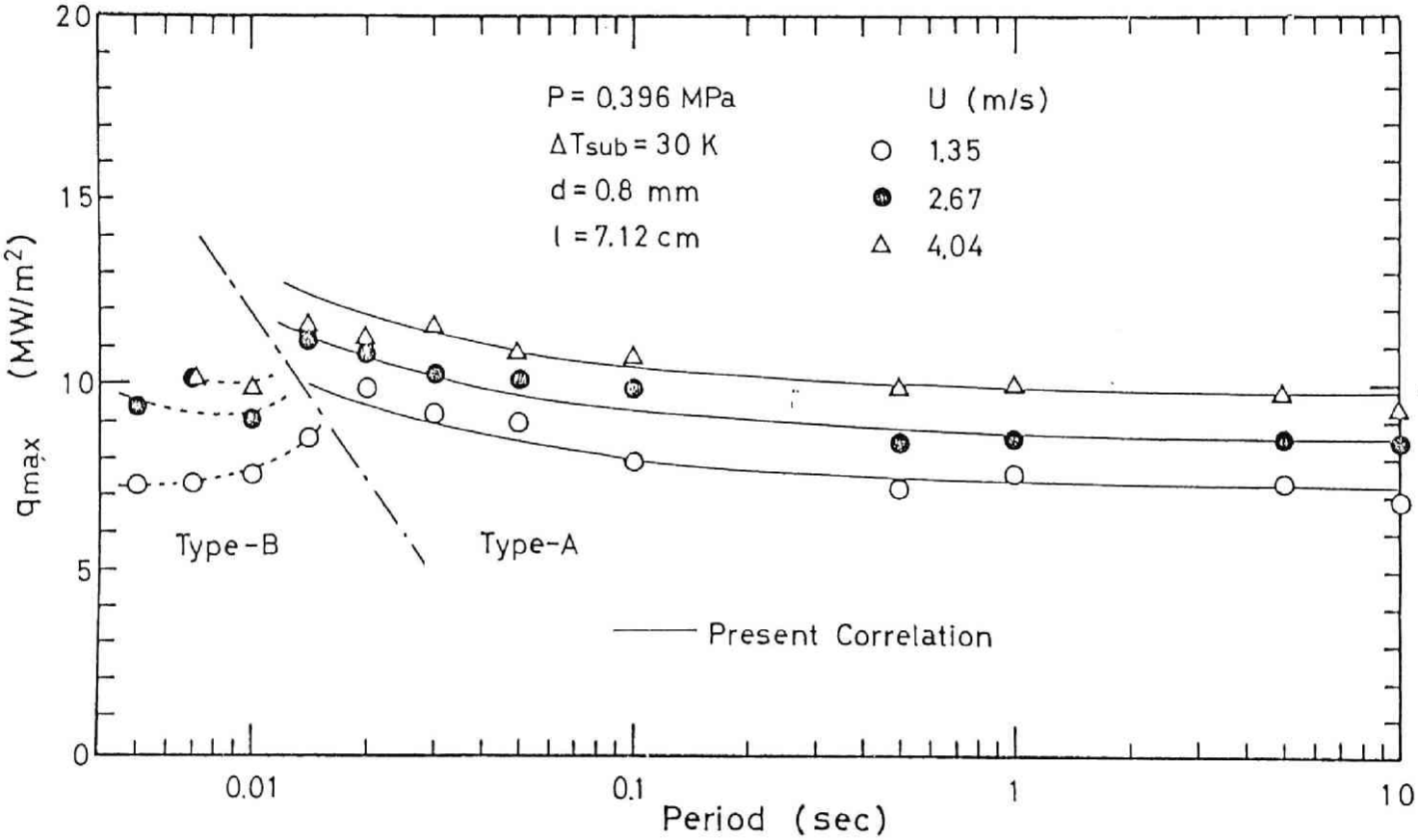

Fig.26(a) The variation of transient maximum heat flux with period and velocity at 0.396 MPa and 30 K subcooling (0.8 mm diam heater)

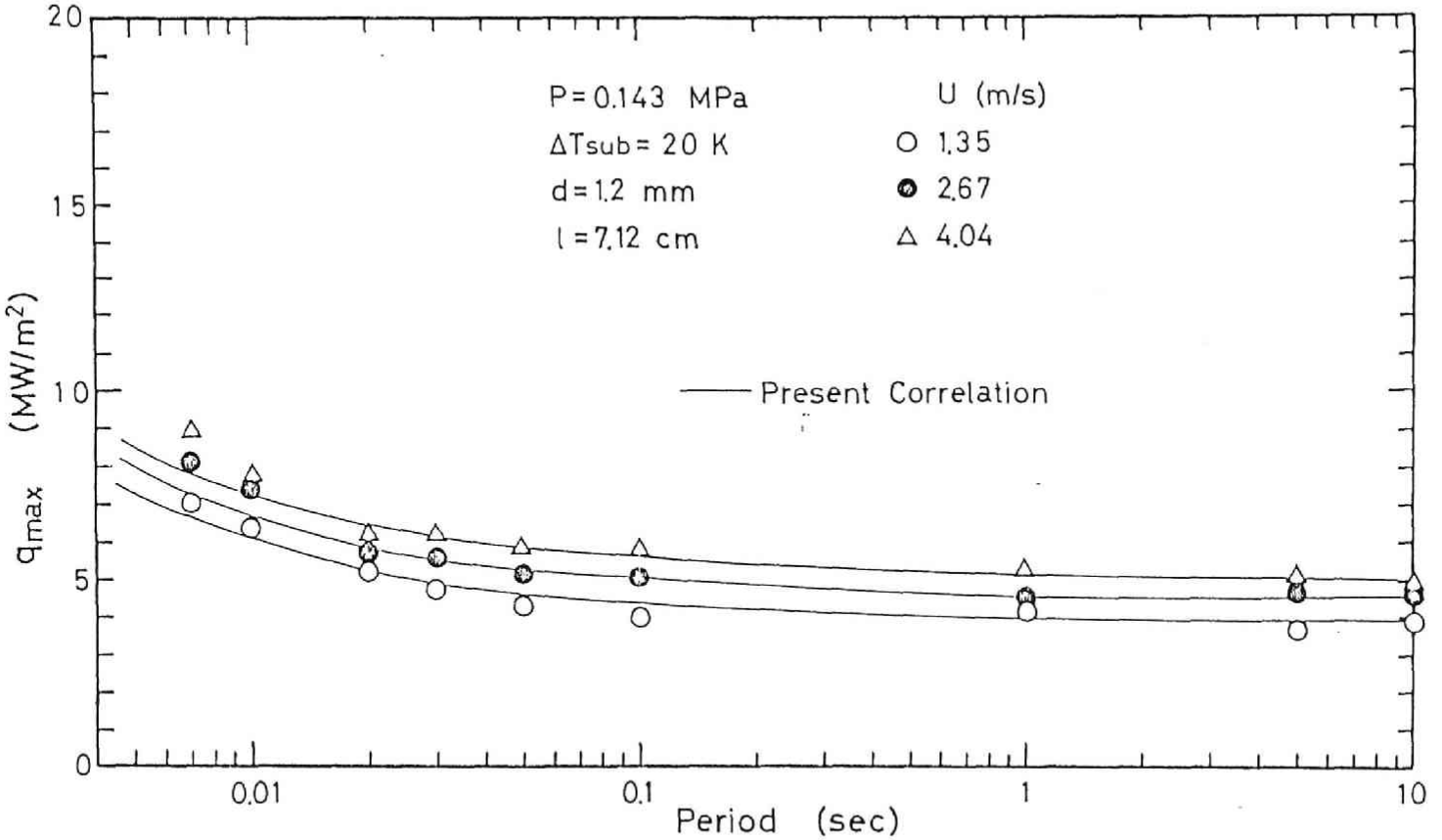

Fig.26(b) The variation of transient maximum heat flux with period and velocity at 0.143 MPa and 20 K subcooling (1.2 mm diam heater)

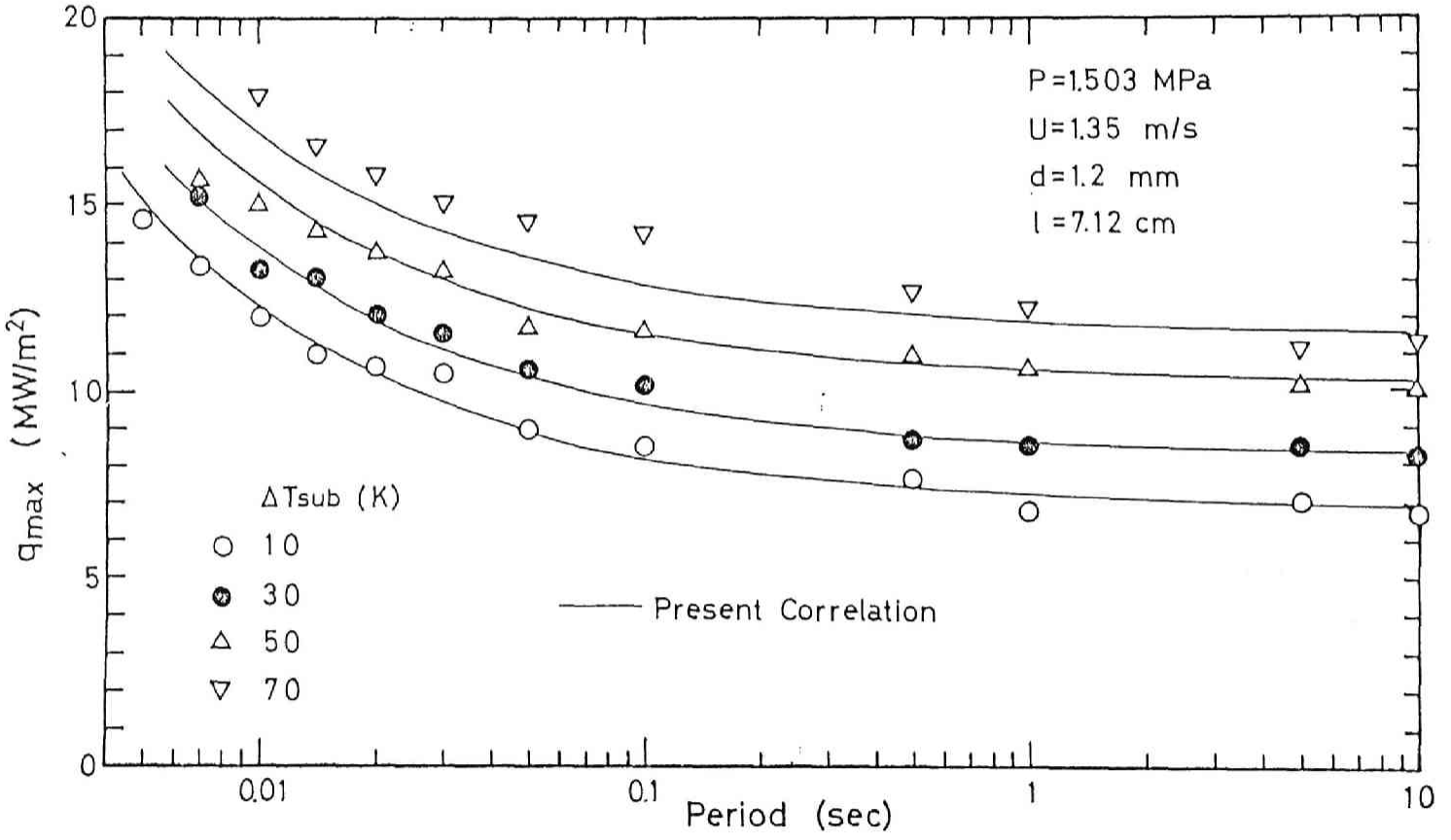

Fig.26(c) The variation of transient maximum heat flux with period and subcooling at 1.503 MPa and 1.35 m/s (1.2 mm diam heater)

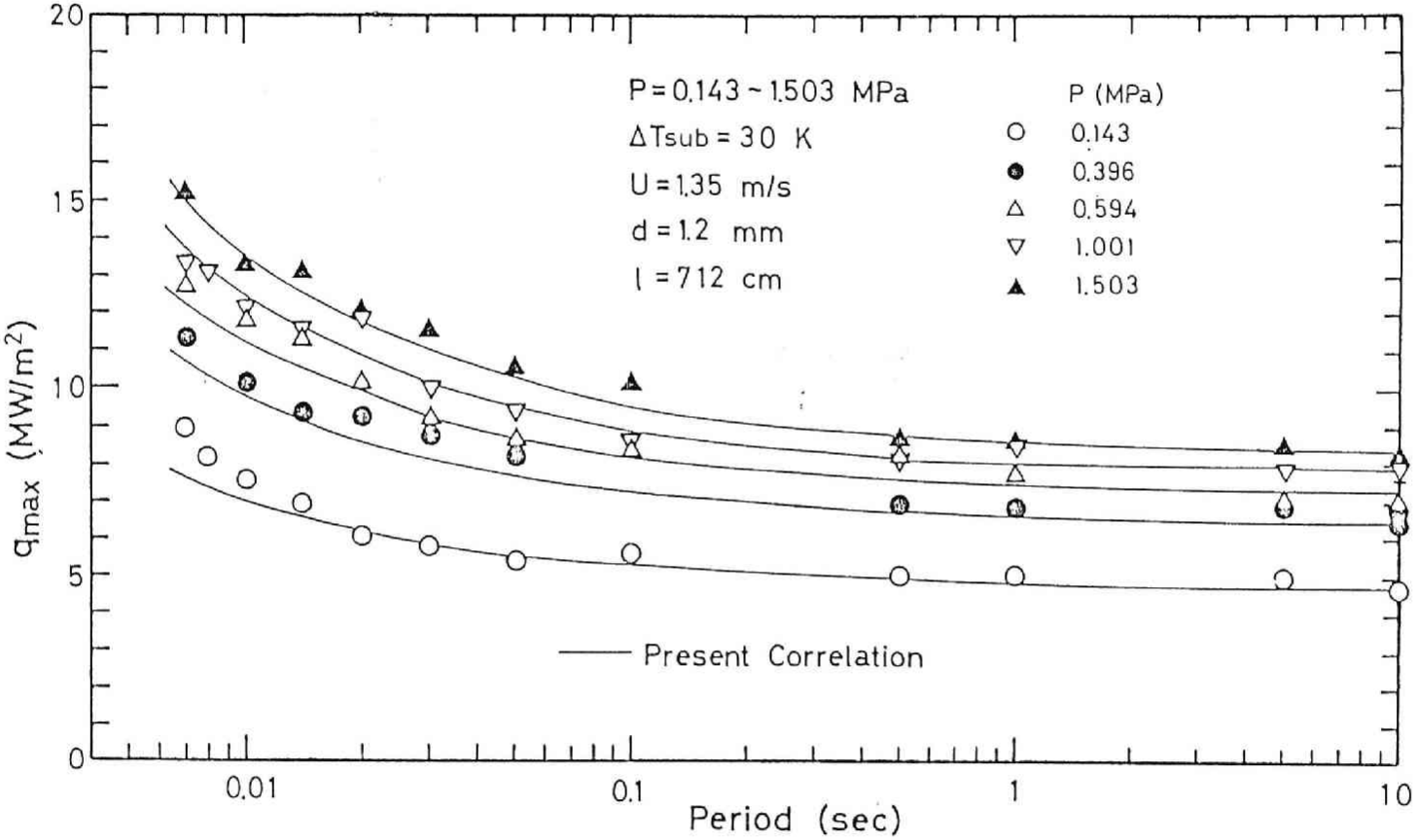

Fig. 26(d) The variation of transient maximum heat flux with period and presure at 1.35 m/s and 30 K subcooling (1.2 mm diam heater)

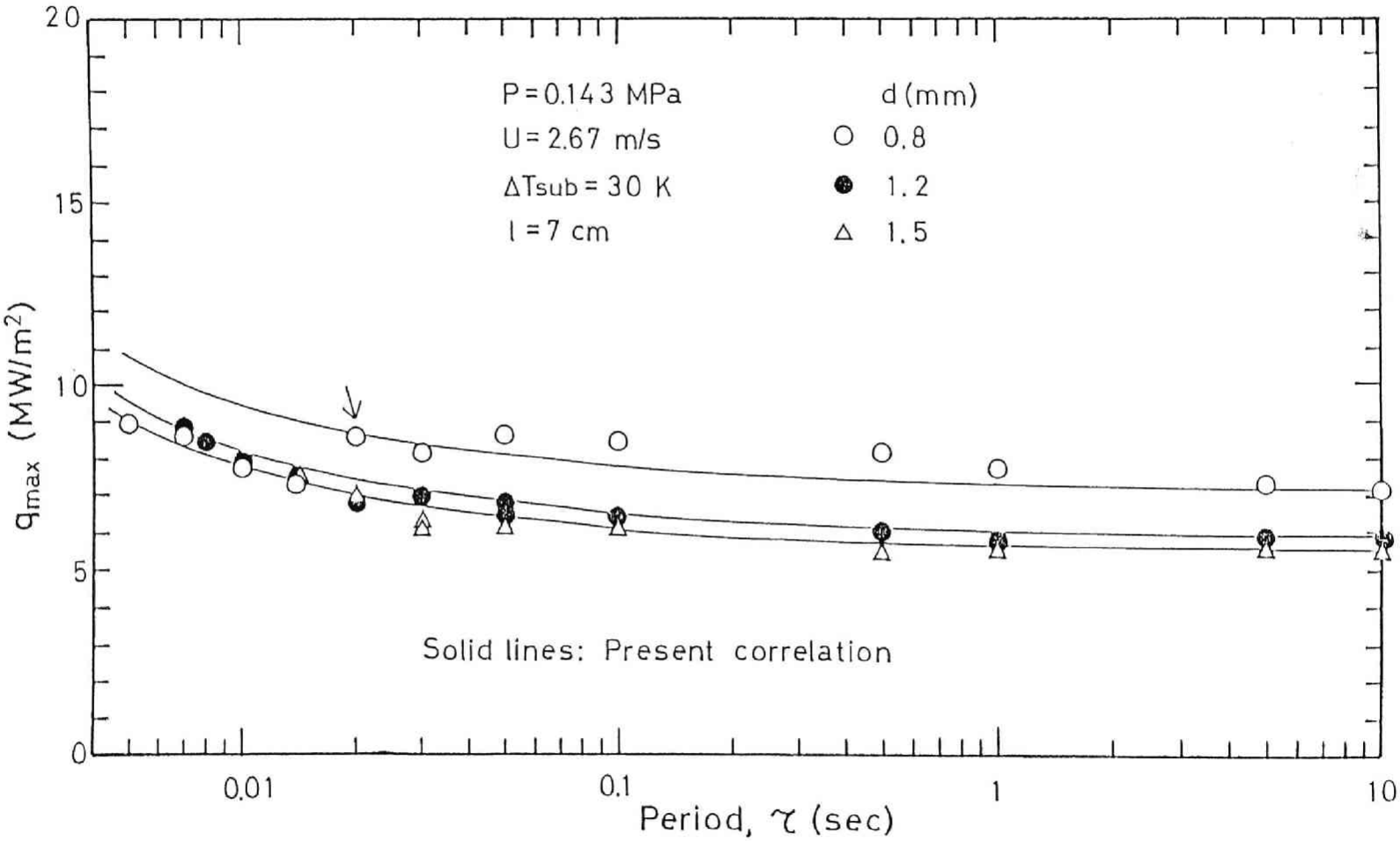

Fig.27(a) The variation of transient maximum heat flux with period and heater diameter at 0.143 MPa, 2.67 m/s and 30 K subcooling (7 cm long heater)

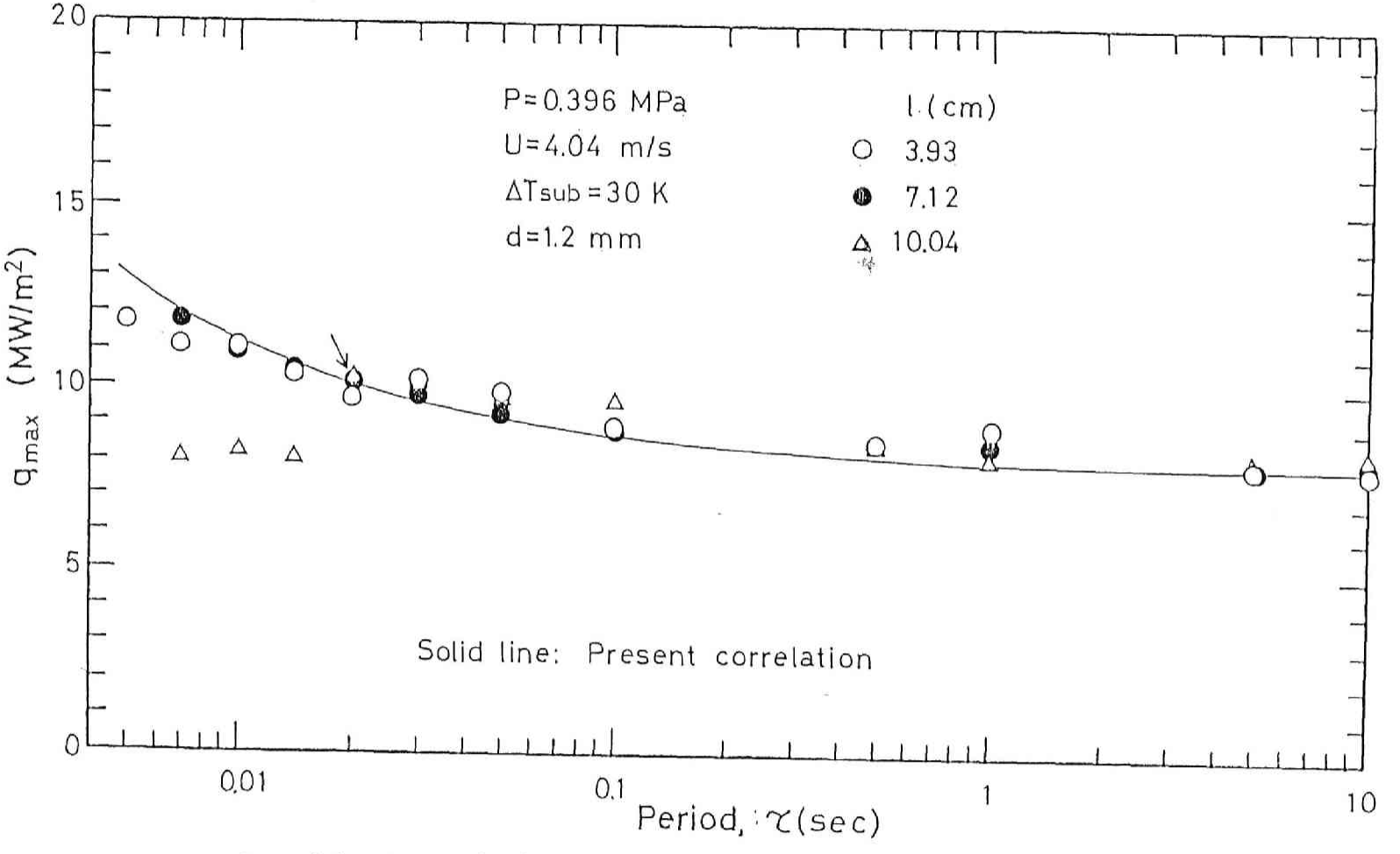

Fig.27(b) The variation of transient maximum heat flux with period and heater length at 0.396 MPa, 4.04 m/s and 30 K subcooling (1.2 mm diam heater)

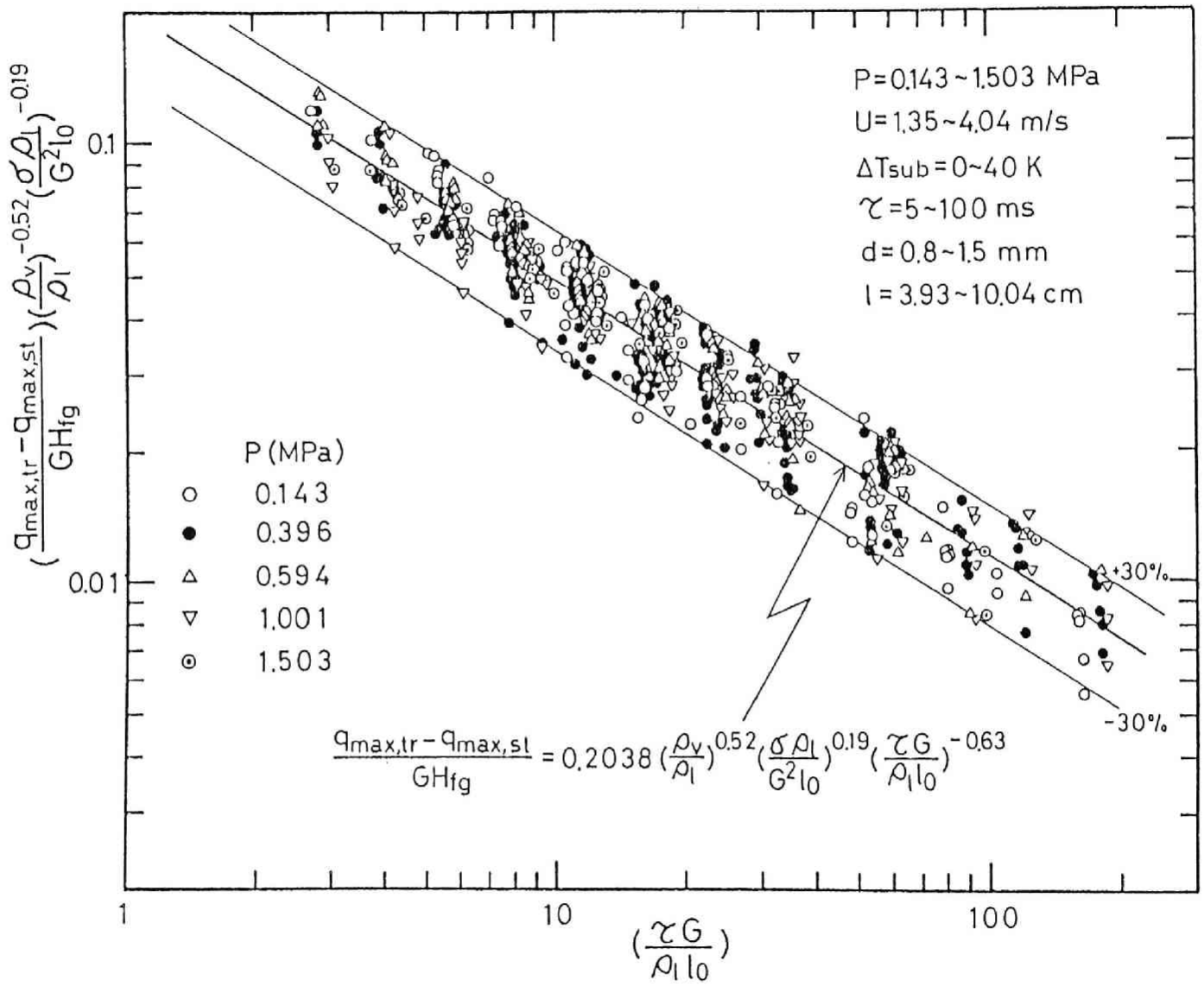

Fig.28 Comparative representation of transient maximum heat flux.

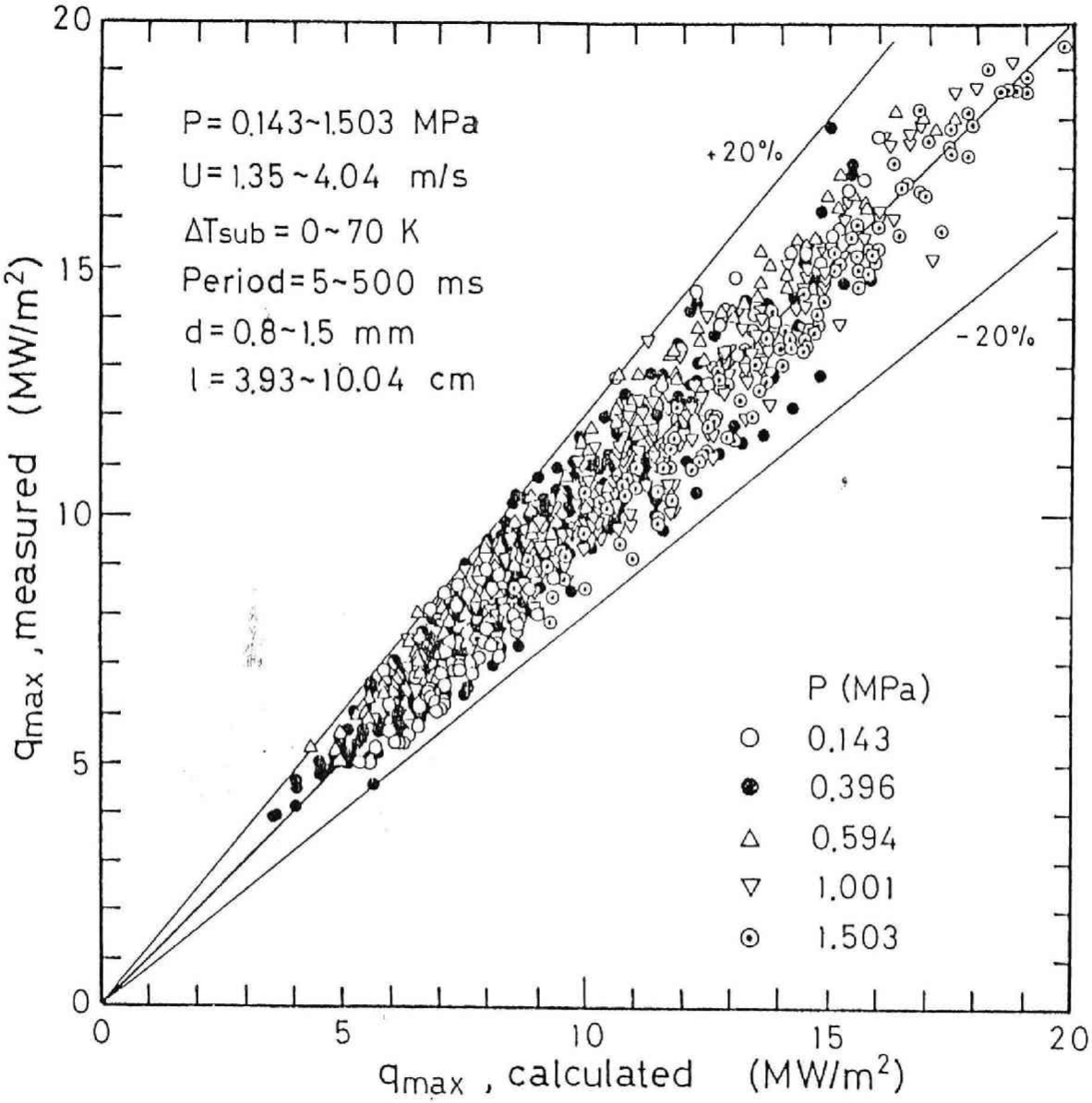

Fig.29 Comparison of Eq.(15) with the measured transient maximum heat flux.

CHAPTER II

ANALYSIS OF TRANSIENT FORCED CONVECTIVE HEAT TRANSFER BY BOUNDARY LAYER APPROXIMATION

II . 1 INTRODUCTION

As described in the previous chapter, heat transfer under exponential power increase is important in relation to reactivity accident in a nuclear reactor. Therefore, the transient boiling phenomena have been studied in detail. However, when the power transient accident occurs in a pressurized water reacter or in a liquid metal cooled reactor, the heat transfer process in an initial stage is considered to be of non-boiling forced convective transient heat transfer. Therefore, in analysing the problems associated with a reactivity accident, the knowledge of transient non-boiling heat transfer is also indespensable. In the previous chapter, some experimental results on non-boiling transient heat transfer coefficient have been reported. However, the obtained correlation was purely experimental one and not based on the detailed analysis of heat transfer mechanisms. Therefore, in this chapter, an analytical study has been carried out on the transient non-boiling forced convective heat transfer under exponentially increasing heat flux.

There have been some analytical and experimental works on transient non-boiling heat transfer [1]. Concerning the transient heat transfer analysis in flows in round tube, annulus and parallel plate, analytical and numerical analyses have been carried out by Siegel [2-5], Sparrow and Siegel [6], Perlmutter and Siegel [7], Siegel and Perlmutter [8], Namatame [9] and Kawamura et al. [10-12]. Kawamura et al. [10-12] also conducted experiments in annulus. On the other hand, several works have been carried out for flat plate by Cess [13], Goodman [14], Adams et al.[15], Soliman et al.[16-18], Chao et al.[19,20], Ishiguro et al.[21,22] and Hanawa [23-26]. In most

of these works, the transient heat transfer coefficients have been obtained for step changes in wall temperature or wall heat flux.

Concerning the transient non-boiling heat transfer under exponential power increase, there are a few analytical works and experimental works conducted by Siegel et al. [3], Soliman et al. [17,18] and Kataoka et al. [27]. However, reliable correlations based on a physical model have not been available due to the complexity of the phenomena.

One of the characteristic features of the transient non-boiling heat transfer coefficient for exponentially increasing heat flux is that the heat transfer coefficient attains asymptotic value after a certain time from the initiation of heating and remains constant until the inception of boiling (Fig. 1). The experimental data of Soliman et al. [17,18] and Kataoka et al. [27] show this tendency. Their results show that the ratio between the asymptotic value of transient heat transfer coefficient and the steady state one is approximately correlated in terms of one dimensionless parameter composed of velocity, heater length and exponentially increasing rate of heat flux, $(u/\ell\omega)$. Here, u is the velocity, ℓ is the representative heater length and ω is a parameter which represents the rate of exponentially increasing heat flux (or heat generation rate), $q = q_0 \exp(\omega t)$.

In recent years, the advances in numerical analysis for heat transfer process have made it possible to accurately predict the heat transfer coefficient for considerably complicated geometry. For the analysis of transient heat transfer, such techniques have been applied and numerical analyses have been carried out for step wall temperature rise or step heat flux rise [10-12, 21-26]. Basically, these techniques will be applied to the case for exponentially increasing heat flux. However, it

will take considerable time for computation. In case of safety analysis of nuclear reactor transients, it is neccessary to know the heat transfer characteristics for wide range of heat flux, pressure, velocity etc. Heat transfer process ranges from non-boiling to nucleate boiling and film boiling. Such being the case, it is not practical to consume much time of computation only for non-boiling heat transfer. Therefore, it will be useful to obtain simple and analytical correlations for transient non-boiling heat transfer coefficient, although they are approximate ones. These analytical correlations will also give a good understanding of the effects of various flow parameters on transient heat transfer processes.

In view of the above considerations, analyses have been made for transient non-boiling heat transfer coefficient under forced convection using boundary layer approximation (integral method) which is adopted by Goodman [14] and Adams et al. [15] for the analyses of heat transfer under step rise of wall temperature and heat flux. Approximate but simple and analytical correlations for transient non-boiling heat transfer coefficient have been obtained for flat plate located in uniform flow field with exponential increasing heat flux.

The results obtained in this chapter are also important in analysing a natural circulation problem which will be investigated in Chapter VI.

II. 2 BASIC EQUATIONS

The physical model under consideration is schematically shown in Fig.2. The coordinate parallel to a flat plate is defined x coordinate. The velocity in this direction is denoted by u. y is a coordinate per-

pendicular to the flat plate. v is the velocity in y coodinate. The flat plate is located in uniform flow field of which velocity is denoted by u_∞. The flat plate is parallel to the flow direction. Furthermore, it is assumed that steady state flow field around the flat plate is established. The temperature of bulk fluid is uniform and denoted by T_∞. The effects of compressibility of fluid and bouyancy force are neglected. At the time $t = 0$, exponentially increasing heat flux, $q = q_0 \exp(\omega t)$, is applied to the surface of the flat plate irrespective of x coordinate. In this case, the equations of continuity, momentum and energy are given by

Continuity;
$$\frac{\partial u}{\partial x} + \frac{\partial v}{\partial y} = 0 \tag{1}$$

Momemtum;
$$u\frac{\partial u}{\partial x} + v\frac{\partial u}{\partial y} = \nu\frac{\partial^2 u}{\partial y^2} \tag{2}$$

Energy;
$$\frac{\partial T}{\partial x} + u\frac{\partial T}{\partial x} + v\frac{\partial T}{\partial y} = a\frac{\partial^2 T}{\partial y^2} \tag{3}$$

The boundary conditions for these equations are given by

$$\mu\frac{\partial u}{\partial y}\Big|_{y=0} = \tau_w, \tag{4}$$

$$\lambda\frac{\partial T}{\partial y}\Big|_{y=0} = \begin{cases} 0 & (t \leqq 0) \\ q_0 e^{\omega t} & (t \geqq 0) \end{cases} \tag{5}$$

$$T\big|_{x=\infty} = T_\infty \tag{6}$$

$$T\big|_{x=0} = T_\infty \tag{7}$$

$$T\big|_{t=0} = T_\infty \tag{8}$$

Here, ν and a are kinematic viscosity and thermal diffusivity of fluid, μ and λ are viscosity and thermal conductivity of fluid, respectively.

q_0 is initial value of exponentially increasing heat flux and ω is a reciprocal of the period of exponetially increasing heat flux, respectively. In the momentum and energy equations (Eqs. (2) and (3)), the momentum transport in x direction, $\mu\frac{\partial^2 u}{\partial x^2}$, and energy transport in x direction, $\lambda\frac{\partial^2 T}{\partial x^2}$, are assumed to be negligible. Above equations are applied to laminar flow. For turbulent flow case, a and ν in above equations will be replaced by $(a+\varepsilon_H)$ and $(\nu+\varepsilon_M)$, respectively. Here, ε_H and ε_M are turbulent diffusivity of heat and momentum, respectively.

II. 3 LAMINAR FLOW FOR Pr << 1 (SLUG FLOW)

When the Prandtl number is much smaller than unity, the thickness of thermal boundary layer is much larger than velocity boundary layer. Therefore, velocity boundary layer has negligible contribution to heat transfer. Then velocity distribution in the thermal boundary layer can be regarded as uniform value, u_∞ (slug flow model). There are two extreme cases for Pr << 1. The one case is for very small viscosity of fluid, $\nu \to 0$, and the other case is for very large thermal diffusivity, $a \to \infty$, because of the definition of Prandtl number, $Pr = \nu/a$. For the former case, present slug flow model is consistent with the basic equations, Eqs. (1) through (3). On the other hand, for the latter case, where thermal diffudivity is very large, strictly speaking, the x direction energy transfer term, $\lambda\frac{\partial^2 T}{\partial x^2}$, may not be negligible in energy equation, Eq.(3). However, since temperature gradientin y direction is considered much larger than that of x direction, Eqs. (1) through (3) can be applied to the case of $a \to \infty$, as a first approximation.

One assumes temperature distribution within the thermal boundary layer is given by parabolic distribution, Eq. (10), Which is adopted by Adams et al. [15] for step heat flux change. This temperature distribution agrees well with experimental data under steady state condition

$$T - T_\infty = \frac{q_w \delta_t}{2\lambda} \left(1 - \frac{y}{\delta_t} \right)^2 \quad . \tag{10}$$

Here, δ_t represents the thickness of thermal boundary layer. Under transient state, the thickness of thermal boundary layer changes with time. In this analysis,it is assumed that temperature distribution is given by Eq. (10) even in transient state. Of course, as pointed out by Hanawa [23-26], this assumption may not be strictly accurate. However, in view of the success in step heat flux change [15], as a first approximation, above assumption can be applied to transient heat transfer with exponential heat flux increase without serious errors.

Integrating Eq.(3) from 0 to δ_t, and in view of Eqs.(1) and (2), one obtains,

$$\frac{\partial}{\partial t} \int_0^{\delta_t} T \, dy + \frac{\partial}{\partial x} \int_0^{\delta_t} uT \, dy = \frac{q_w}{C_p \rho} \quad . \tag{11}$$

Here, ρ and C_p are density and specific heat of fluid, respectively. Substituting Eqs.(9) and (10) into Eq.(11), one obtains,

$$\frac{1}{6\lambda} \frac{\partial}{\partial t} (\delta_t^2 q_w) + \frac{u_\infty}{6\lambda} \frac{\partial}{\partial x} (\delta_t^2 q_w) = \frac{q_w}{C_p \rho} \quad . \tag{12}$$

Considering $q_w = q_0 \exp(\omega t)$, Eq.(12) becomes,

$$\omega \delta_t^2 + \frac{\partial}{\partial t} (\delta_t^2) + u_\infty \frac{\partial}{\partial x} (\delta_t^2) = 6a \quad . \tag{13}$$

Introducing following dimensionless parameters,

$$\delta_t^* = \sqrt{\frac{\omega}{a}}\,\delta_t$$

$$t^* = t\omega \qquad (14)$$

$$x^* = \frac{x\omega}{u_\infty}$$

Equation (13) can be rewritten in dimensionless form by

$$\delta_t^{*2} + \frac{\partial}{\partial t^*}(\delta_t^{*2}) + \frac{\partial}{\partial x^*}(\delta_t^{*2}) = 6 \qquad (15)$$

The initial and boundary conditions are given by

$$\delta_t^*(x^*,0) = 0 \quad \text{for } x^* \geqq 0 \qquad (16)$$

$$\delta_t^*(0,t^*) = 0 \quad \text{for } t^* \geqq 0 \qquad (17)$$

The solution of Eq.(15) under the conditions of Eqs.(16) and (17) is solved by method of characteristic equation and given by

$$\text{for } x^* \leqq t^* \qquad \delta_t^* = \sqrt{6}\,\{1 - \exp(-x^*)\}^{\frac{1}{2}} \qquad (18)$$

$$\text{for } x^* \geqq t^* \qquad \delta_t^* = \sqrt{6}\,\{1 - \exp(-t^*)\}^{\frac{1}{2}} \qquad (19)$$

From Eq.(10), heat transfer coefficient is given by

$$h \equiv \frac{q_w}{T_w - T_\infty} = \frac{2\lambda}{\delta_t}, \qquad h^* \equiv h\frac{\sqrt{a/\omega}}{\lambda} \qquad (20)$$

Then the transient heat transfer coefficient for laminar and Pr << 1 is obtained from Eqs.(18), (19) and (20). It is shown in Fig. 3

$$\text{for } x^* \leqq t^* \qquad h^* = \frac{2}{\sqrt{6}\,\{1 - \exp(-x^*)\}^{\frac{1}{2}}}, \qquad (21)$$

$$\text{for } x^* \geqq t^* \qquad h^* = \frac{2}{\sqrt{6}\ \{\ 1 - \exp(-t^*)\}^{\frac{1}{2}}} \qquad (22)$$

Equations (21) and (22) indicate that for large time, heat transfer coefficient attains a asymptotic value, h_a^*, which is given by

$$h_a^* = \frac{2}{\sqrt{6}\ \{\ 1 - \exp(-x^*)\}^{\frac{1}{2}}} \qquad (23)$$

On the other hand, steady state heat transfer coefficient, h_{st}, can be obtained by putting $\omega \to 0$ in Eqs.(21)and (22), since for small value of ω heat flux increases slowly enough to be regarded as quasi-steady state. Then steady state heat transfer coefficient is given by

$$h_{st} = \frac{2}{\sqrt{6}}\ \lambda\ \left(\frac{u_\infty}{xa}\right)^{\frac{1}{2}} \qquad (24)$$

or in dimensionless form by

$$Nu_{st} = 0.82\ Pe_x^{\frac{1}{2}} \qquad (25)$$

Here, Nu_{st} and Pe_x are defined by

$$Nu_{st} \equiv \frac{h_{st}x}{\lambda}$$
$$Pe_x \equiv \frac{u_\infty x'}{a} \qquad (26)$$

From Eqs.(23) and (26), the ratio between asymptotic transient heat transfer coefficient and steady state one, h_a/h_{st}, can be obtained

$$\frac{h_a}{h_{st}}\ \left(\equiv \frac{Nu_a}{Nu_{st}}\right) = \frac{x^{*\frac{1}{2}}}{\{\ 1 - \exp(-x^*)\}^{\frac{1}{2}}} \qquad (27)$$

This ratio is expressed in term of dimensionless parameter, $x^*(\equiv x\omega/u_\infty)$, and shown in Fig. 4 in h_a/h_{st} vs. x^* plot. As shown in this figure, the

ratio increases with increasing x^*.

II. 4 LANIMAR FLOW FOR Pr >> 1

In this case, the velocity distribution in the thermal boundary layer must be considered. The velocity distribution near wall is given by Eq.(28) in term of wall shear stress, τ_w,

$$u = \frac{\tau_w}{\mu} y \quad . \tag{28}$$

When Prandtl number is very large, thermal boundary layer can be considered to be located in the velocity field which is represented by Eq.(28). Therefore, substituting Eqs,(10) and (28) into Eq.(11), one obtains

$$\frac{1}{6\lambda} \frac{\partial}{\partial t} (\delta_t^2 q_w) + \frac{1}{24\mu\lambda} \frac{\partial}{\partial x} (q_w \tau_w \delta_t^3) = \frac{q_w}{C_p \rho} \quad . \tag{29}$$

Considering $q_w = q_0 \exp(\omega t)$, one obtains

$$\omega\delta_t^2 + \frac{\partial}{\partial t} (\delta_t^2) + \frac{1}{4\mu} \frac{\partial}{\partial x} (\tau_w \delta_t^3) = 6a \quad . \tag{30}$$

For laminar flow, the wall shear stress is given by

$$\tau_w = 0.332 \, \rho u_\infty \sqrt{\frac{-\nu}{u_\infty x}} \quad . \tag{31}$$

Substituting Eq.(31) into Eq.(30), and nondimensionaling by Eq.(14), Eq.(30) becomes

$$\delta_t^{*2} + \frac{\partial}{\partial t^*} (\delta_t^{*2}) + 0.083 \frac{1}{\sqrt{Pr}} \frac{\partial}{\partial x^*} \left(\frac{\delta_t^{*3}}{\sqrt{x^*}}\right) = 6 \quad . \tag{32}$$

Initial and boundary conditions are same as Eqs.(16) and (17). One of the solutions of Eq.(32) which does not include t^*, can be considered to be a asymptotic

value of δ_t^* and is given by solving following differential equation

$$\delta_t^{*2} + 0.083 \frac{1}{\sqrt{Pr}} \frac{\partial}{\partial x^*} \left(\frac{\delta_t^{*3}}{\sqrt{x^*}} \right) = 6 \qquad (33)$$

$$(\delta_t^* = 0 \text{ at } x^* = 0)$$

It is difficult to express the solution of Eq.(33) in a analytical form. However it can be approximated by a simple analytical form by

$$\delta_t^* = \sqrt{6} \{ 1 - \exp(-4.91 \, Pr^{\frac{1}{2}} x^{*1.5}) \}^{0.33} \qquad (34)$$

In Fig.5, a comparison is made between Eq.(34) and numerical solution of Eq.(33) in δ_t^* vs. $Pr^{0.33}x^*$ plot. As shown in this figure, Eq.(34) can approximate the exact solution of Eq.(33) within 5 % errors.

On the other hand, for small time. the convection term in Eq.(32) can be neglected and Eq.(32)can be rewritten by

$$\delta_t^{*2} + \frac{\partial}{\partial t} (\delta_t^{*2}) = 6 \qquad (35)$$

$$(\delta_t^* = 0 \text{ at } t^* = 0)$$

The solution of this differential equation is easily obtained and given by

$$\delta_t^* = \sqrt{6} \{ 1 - \exp(-t^*) \}^{\frac{1}{2}} \qquad (36)$$

In view of Eqs.(34) and(36), the solution of the differential equation, Eq. (32) can be approximately given by

for $-\ln[1-\{1-\exp(-4.91 Pr^{\frac{1}{2}} x^{*1.5})\}^{0.67}] \leq t^*$

$$\delta_t^* = \sqrt{6} \{ 1 - \exp(-4.91 \, Pr^{\frac{1}{2}} x^{*1.5}) \}^{0.33} \qquad (37)$$

for $-\ln[1-\{1-\exp(-4.91 Pr^{\frac{1}{2}} x^{*1.5})\}^{0.67}] \geq t^*$

$$\delta_t^* = \sqrt{6} \{ 1 - \exp(-t^*) \}^{\frac{1}{2}} \qquad (38)$$

Then, from Eqs.(20), (37) and (38), heat transfer coefficient is given by

for $-\ln[1-\{1-\exp(-4.91Pr^{\frac{1}{2}}x^{*1.5})\}^{0.67}] \leqq t^*$

$$h^* = \frac{2}{\sqrt{6}\ \{\ 1\ -\ \exp(-4.91\ Pr^{\frac{1}{2}}x^{*1.5})\}^{0.33}} \tag{39}$$

for $-\ln[1-\{1-\exp(-4.91Pr^{\frac{1}{2}}x^{*1.5})\}^{0.67}] \geqq t^*$

$$h^* = \frac{2}{\sqrt{6}\ \{\ 1\ -\ \exp(-t^*)\}^{\frac{1}{2}}} \tag{40}$$

The transient heat transfer coefficient calculated by Eqs.(39) and (40) is shown in Fig.6 in h^* vs. $x^*Pr^{0.33}$ plot.

The steady state heat transfer coefficient can be obtained by $\omega \to 0$ in Eq.(39)

$$h_{st} = \frac{2}{\sqrt{6}}\lambda\ \frac{1}{(4.91)^{0.33}Pr^{0.17}(\frac{xa}{u_\infty})^{\frac{1}{2}}}\ , \tag{41}$$

or

$$Nu_{st} = 0.480\ Re_x^{\frac{1}{2}}Pr^{0.33}\ , \tag{42}$$

where

$$Re_x \equiv \frac{u_\infty x}{\nu}\ . \tag{43}$$

The asymptotic value of transient heat transfer coefficient is given by Eq.(39). Therefore, from Eqs.(39) and (43), The ratio between the asymptotic heat transfer coefficient and steady state one is given by

$$\frac{h_a}{h_{st}} \equiv \frac{Nu_a}{Nu_{st}} = 1.70\ \frac{Pr^{0.17}x^{*\frac{1}{2}}}{\{\ 1\ -\ \exp(-4.91\ Pr^{\frac{1}{2}}x^{*1.5})\}^{0.33}}\ . \tag{44}$$

The value of h_a/h_{st} calculated by Eq.(44) is shown in Fig.4.

II. 5 LAMINAR FLOW FOR Pr ≃ 1

When Prandtl number is order of unity or larger, The thickness of boundary layers for velocity and temperature are comparable. Therefore, velocity distribution given by Eq.(28), cannot be applied to this case. Then, one assumes the velocity distribution given by Eq.(45), which is typical in boundary layer analysis

$$\frac{u}{u_\infty} = \frac{3}{2}\left(\frac{y}{\delta_v}\right) - \frac{1}{2}\left(\frac{y}{\delta_v}\right)^3 \quad . \tag{45}$$

Here, δ_v is a thickness of velocity boundary layer and related to wall shear stress by

$$\tau_w = \mu\frac{\partial u}{\partial y}\Big|_{y=0} = \frac{3}{2}\,\mu\frac{u_\infty}{\delta_v} \quad . \tag{46}$$

Substituting Eqs.(10) and (45) into Eq.(11) and integrating,

for $Pr \geqq 1$

$$\frac{1}{6\lambda}\frac{\partial}{\partial t}(\delta_v^2 q_w) + \frac{u_\infty}{16\lambda}\frac{\partial}{\partial x}\left[q_w\delta_t^2\left\{\frac{\delta_t}{\delta_v} - \frac{1}{15}\left(\frac{\delta_t}{\delta_v}\right)^3\right\}\right] = \frac{q_w}{C_p\rho} \quad , \tag{47}$$

for $Pr \leqq 1$

$$\frac{1}{6\lambda}\frac{\partial}{\partial t}(\delta_t^2 q_w) + \frac{u_\infty}{16\lambda}\frac{\partial}{\partial x}\left[q_w\delta_t\delta_v\left\{\frac{5}{8} - \frac{4}{5}\left(\frac{\delta_t}{\delta_v}\right) + \frac{7}{24}\left(\frac{\delta_t}{\delta_v}\right)^2\right\}\right]$$
$$+ \frac{u_\infty}{6\lambda}\frac{\partial}{\partial x}\left\{q_w\,\delta_t^2\left(1 - \frac{\delta_v}{\delta_t}\right)^3\right\} = \frac{q_w}{C_p\rho} \quad . \tag{48}$$

As shown in Eq.(47) the contribution of (δ_t/δ_v) is considerably larger than that of $\frac{1}{15}(\delta_t/\delta_v)^3$ in the second term of the left hand side of Eq.(47), even if (δ_t/δ_v) is close to unity. As already shown in previous sections transient heat transfer coefficients are larger than those of steady state. This means the thickness of thermal boundary layer, δ_t, is thinner in transient case than in steady state case. Since velocity boundary layer, δ_v, is assumed to be steady state one in this analysis, (δ_t/δ_v) is smaller in transient case than in steady state case. Therefore, in transient case, the contribution of (δ_t/δ_v) is much greater than that of $\frac{1}{15}(\delta_t/\delta_v)^3$ in the second term of the left hand side of Eq.(47). In view of this, if one approximates $\{\delta_t/\delta_v - \frac{1}{15}(\delta_t/\delta_v)^3\}$ by (δ_t/δ_v) in Eq.(47), Eq.(47) becomes the same equation as Eq.(29) which is for $Pr >> 1$. Therefore, it may

not make serious errors when one assumes the approximate solution of Eq.(47) can be expressed in similar form to Eqs.(37) and (38) for Pr >> 1. In particular, when time, t, is small and convection terms can be neglected, Eq.(47) reduces to a same equation as Eq.(38). Therefore, for small time, the solution of Eq.(47) can be given by

$$\delta_t^* = \sqrt{6}\ \{\ 1 - \exp(-t^*)\}^{\frac{1}{2}} \quad . \tag{49}$$

On the other hand, the solution of Eq.(47) for large time can be approximated by Eq.(50) which is similar to Eq.(37) for Pr >> 1

$$\delta_t^* = \sqrt{6}\ \{\ 1 - \exp(-A\ Pr^{\frac{1}{2}} x^{*1.5})\}^{0.33} \quad . \tag{50}$$

It is well known that for Pr > 0.5, the steady state heat transfer coefficient for a flat plate is given by Eq.(51) under constant heat flux

$$Nu_{st} = 0.458\ Re_x^{\frac{1}{2}} Pr^{0.33} \quad . \tag{51}$$

On the other hand, one obtains the steady state heat transfer coefficient by putting $\omega \to 0$ in Eq.(50)

$$Nu_{st} = \frac{2}{\sqrt{6}}\ \frac{1}{A^{0.33}}\ Re_x^{\frac{1}{2}} Pr^{0.33} \quad . \tag{52}$$

From Eqs.(51) and (52), the value of A must be

$$A = 5.67 \quad . \tag{53}$$

Then one obtains approximate solution of Eq.(47) for large t

$$\delta_t^* = \sqrt{6}\ \{\ 1 - \exp(-5.67\ Pr^{\frac{1}{2}} x^{*1.5})\}^{0.33} \quad . \tag{54}$$

Therefore, the transient heat transfer coefficient for Pr > 0.5 can be approximated by Eqs.(55) and (56) in view of Eqs.(49) through (54)

for $-\ln[1-\{1-\exp(-5.67Pr^{\frac{1}{2}}x^{*1.5})\}^{0.67}] \leqq t^*$

$$h^* = \frac{2}{\sqrt{6}\ \{\ 1\ -\ \exp(-5.67\ Pr^{\frac{1}{2}}x^{*1.5})\}^{0.33}}\ , \tag{55}$$

for $-\ln[1-\{1-\exp(-5.67Pr^{\frac{1}{2}}x^{*1.5})\}^{0.67}] \geqq t^*$

$$h^* = \frac{2}{\sqrt{6}\ \{\ 1\ -\ \exp(-t^*)\}^{\frac{1}{2}}}\ . \tag{56}$$

The transient heat transfer coefficient calculated by Eqs.(55) and (56) is shown in Fig.7 in h^* vs $x^*Pr^{0.33}$ plot.

In view of Eqs.(52) and (55), the ratio between asymptotic transient heat transfer coefficient and steady state one is given by

$$\frac{h_a}{h_{st}} \equiv \frac{Nu_a}{Nu_{st}} = 1.78\ \frac{Pr^{0.17}x^{*\frac{1}{2}}}{\{\ 1\ -\ \exp(-5.67\ Pr^{\frac{1}{2}}x^{*1.5})\}^{0.33}}\ . \tag{57}$$

The value of h_a/h_{st} calculated by Eq.(57) for Pr = 1 is shown in Fig.4.

II. 6 TURBULENT FLOW FOR Pr << 1

As discussed in a laminar flow case, when Prandtl nuber is much smaller than unity, the conduction becomes dominant in heat transfer process. Therefore, slug flow model assumption can be applied. This assumption may be applicable to turbulent flow case, too. Therefore, the transient heat transfer coefficient can be given by Eqs.(21), (22) and (27) which are already derived for a laminar flow case.

II. 7 TURBULENT FLOW FOR Pr >> 1

For a turbulent flow, the velocity field is represented by turbulent

boundary layer. However, when Prandtl number is much larger than unity, thermal boundary layer is located in viscous sublayer. In this case, velocity and temperature distribution canbe given by Eqs.(10) and (28) which are those for a laminar flow for Pr >> 1. Therefore the energy equation which is integrated over thermal boundary layer, Eq.(30), can be also applied to present turbulent flow case for Pr >> 1. On the other hand, the wall shear stress for turbulent flow for a flat plate is given by

$$\tau_w = 0.0296\ \rho u_\infty^2 \left(\frac{\nu}{u_\infty x}\right)^{0.2} \quad (58)$$

Substituting Eq.(58) into Eq.(30) and nondimensionalizing by Eq.(14),

$$\delta_t^{*2} + \frac{\partial}{\partial t^*}(\delta_t^{*2}) + 0.0074\ Pr^{-\frac{1}{2}}\left(\frac{u_\infty^2}{\nu\omega}\right)^{0.3}\frac{\partial}{\partial x^*}\left(\frac{\delta_t^{*3}}{x^{*0.2}}\right) = 6 \quad (59)$$

The solution of Eq.(59) where δ_t^* is independent of time, t, or asymptotic value of δ_t^*, is given by a solution of following differential equation

$$\delta_t^{*2} + 0.0074\ Pr^{-\frac{1}{2}}\left(\frac{u_\infty^2}{\nu\omega}\right)^{0.3}\frac{\partial}{\partial x^*}\left(\frac{\delta_t^{*3}}{x^{*0.2}}\right) = 6 \quad (60)$$

$$\left(\delta_t^* = 0 \quad \text{at } x^* = 0\right)$$

It is difficult to give an analytical solution of Eq.(60). However, it can be approximated by following simple analytical expression

$$\delta_t^* = \sqrt{6}\ \left[1 - \exp\left(-46.0\{x^* Pr^{0.42}\left(\frac{\nu\omega}{u_\infty^2}\right)^{0.25}\}\right)\right]^{0.33} \quad (61)$$

In Fig.8, a comparison was made between the numerical solution of Eq.(60) and Eq.(61) in δ_t^* vs. $x^* Pr^{-0.42}(\nu\omega/u_\infty^2)^{0.25}$ plot. Agreement is fairly good.

On the other hand, when time is small, the convection contribution in Eq.(59) is negligible. Then δ_t^*can be given by Eq.(62) which is same as

previous cases

$$\delta_t^* = \sqrt{6}\ \{\ 1 - \exp(-t^*)\}^{\frac{1}{2}} . \tag{62}$$

From Eqs.(61) and (62), the approximate solution of Eq.(59) will be given by

$$\text{for}\quad -\ln[1-\{1-\exp(-46.0\{x^*Pr^{0.42}(\frac{\nu\omega}{u_\infty^2})^{0.25}\}^{1.2})\}^{0.67}] \leqq t^*$$

$$\delta_t^* = \sqrt{6}\ [\ 1 - \exp(-46.0\{x^*Pr^{0.42}(\frac{\nu\omega}{u_\infty^2})^{0.25}\}^{1.2})]^{0.33} , \tag{63}$$

$$\text{for}\quad -\ln[1-\{1-\exp(-46.0\{x^*Pr^{0.42}(\frac{\nu\omega}{u_\infty^2})^{0.25}\}^{1.2})\}^{0.67}] \geqq t^*$$

$$\delta_t^* = \sqrt{6}\ \{\ 1 - \exp(-t^*)\}^{\frac{1}{2}} . \tag{64}$$

Then, the transient heat transfer coefficient is given by

$$\text{for}\quad -\ln[1-\{1-\exp(-46.0\{x^*Pr^{0.42}(\frac{\nu\omega}{u_\infty^2})^{0.25}\}^{1.2})\}^{0.67}] \leqq t^*$$

$$h^* = \frac{2}{\sqrt{6}\ [\ 1 - \exp(-46.0\{x^*Pr^{0.42}(\frac{\nu\omega}{u_\infty^2})^{0.25}\}^{1.2})]^{0.33}} , \tag{65}$$

$$\text{for}\quad -\ln[1-\{1-\exp(-46.0\{x^*Pr^{0.42}(\frac{\nu\omega}{u_\infty^2})^{0.25}\}^{1.2})\}^{0.67}] \geqq t^*$$

$$h^* = \frac{2}{\sqrt{6}\ \{\ 1 - \exp(-t^*)\}^{\frac{1}{2}}} . \tag{66}$$

The transient heat transfer coefficient calculated by Eqs.(65) and (66) is shown in Fig.9 in h^* vs. $x^*(\nu\omega/u_\infty^2)^{0.25}Pr^{0.42}$ plot. The steady state heat transfer coefficient can be obtained by putting $\omega \to 0$ in Eq.(65)

$$Nu_{st} = 0.228\ Re_x^{0.6}Pr^{0.33} . \tag{66}$$

The ratio between asymptotic value of transient heat transfer coefficient and steady state one is derived from Eqs.(65) and (67)

$$\frac{h_a}{h_{st}} \equiv \frac{Nu_a}{Nu_{st}} = 3.58 \frac{x^{*0.42} Pr^{0.17} (\frac{\nu\omega}{u_\infty^2})^{0.1}}{[\,1 - \exp(-46.0\{x^* pr^{0.42} (\frac{\nu\omega}{u_\infty^2})^{0.25}\}^{1.2})]^{0.33}} \quad (68)$$

II. 8 TURBULENT FLOW FOR Pr ≃ 1

When Prandtl number is not so small, thermal boundary layer penetrates into turbulent boundary layer of velocity field. Under this circumstance, heat transfer process is dominated by turbulent heat diffusivity. For laminar flow, heat transfer process is characterized by thermal conductivity λ, which is unchanged for both transient and steady state. On the other hand, for turbulent flow, one faces the problem whether the turbulent diffusivity of heat, ε_H, for steady state can be applied to transient case. The turbulent diffusivity of heat for transient state may not be same as that for steady state, when the time scale of interest for transient heat transfer is of same order as time scale for turbulence, ℓ'/u', where ℓ' is a scale of eddy and u' is turbulent velocity. However, this time scale for turbulence is considered to be very small. Therefore for practical purpose, it can be postulated that the steady state turbulent diffusivity of heat can be applicable in analysing transient heat transfer without serious errors. In fact, for step rise of wall temperature or wall heat flux, the transient heat transfer coefficients calculated based on above assumption agree well with experimental data [10-12,21-26]. In present analysis, above assumption has been adopted.

As generally accepted for turbulent boundary layer analyses, the velocity and temperature distributions can be characterized by 1/7 th power law

$$\frac{u}{u_\infty} = \left(\frac{y}{\delta_v}\right)^{1/7} \tag{69}$$

$$\frac{T - T_\infty}{T_w - T_\infty} = 1 - \left(\frac{y}{\delta_t}\right)^{1/7} \tag{70}$$

Here, δ_v and δ_t are thicknesses of turbulent velocity boundary layer and turbulent thermal boundary layer repectively. The thickness of velocity boundary layer is related to the wall shear stress for turbulent flow which is given by Eq.(58). Then δ_v is given by

$$\delta_v = 0.380 \times Re_x^{-0.2} \tag{71}$$

On the other hand, the eddy diffusivity of momentum, ϵ_M, is defined by

$$\epsilon_M \rho = \frac{\tau}{\left(\frac{du}{dy}\right)} \tag{72}$$

Now, one considers the turbulent region near wall where Eq.(69) can be applicable. In this near wall region, one may approximate shear stress τ, by wall shear stress, τ_w. Based on this assumption, and substituting Eqs.(58) and (69) into Eq.(72), one obtains,

$$\frac{\epsilon_M}{(u_\infty x)} \simeq 0.545\left(\frac{\delta_v}{x}\right)\left(\frac{y}{\delta_v}\right)^{6/7} \tag{73}$$

On the other hand, turbulent diffusivity of heat is defined by

$$\epsilon_H C_p \rho = \frac{-q}{\left(\frac{dT}{dy}\right)} \tag{73}$$

Again, one considers the turbulent region near wall where Eq.(70) can be applicable. When the heat capacity of the viscous sublayer is much smaller than the heat capacity of turbulent thermal boundary layer, the heat flux q, in Eq.(74) can be approximated by wall heat flux, q_w, without serious

errors. In view of this, one can obtain Eq.(75) by substituting Eq.(70) into Eq.(74)

$$\varepsilon_H C_p \rho \simeq \frac{7q_w}{(T_w - T_\infty)\delta_t^{-1/7} y^{-6/7}} \quad . \tag{75}$$

This equation can be rewritten as

$$T_w - T_\infty = \frac{7q_w}{\varepsilon_H C_p \rho} \delta_t^{1/7} y^{6/7} \quad . \tag{76}$$

For the case of Pr ≃ 1, the turbulent diffusivity of heat, ε_H, can be approximated by the turbulent diffusivity of momentum, ε_M, that is,

$$\varepsilon_H \simeq \varepsilon_M \quad . \tag{77}$$

From Eqs.(73),(76) and (77), one obtains

$$T_w - T_\infty \simeq 33.82 \frac{q_w}{u_\infty C_p \rho} Re_x^{0.2} \left(\frac{\delta_t}{\delta_v}\right)^{1/7} \quad . \tag{78}$$

Under steady state condition and Pr ≃ 1, thermal boundary layer has approximately same thickness as velocity turbulent boundary layer, then (δ_t/δ_v) ≃ 1. Therefore, Eq.(78) gives, of course, the same result as Reynolds analogy.

Substituting Eqs.(60) and (61) into Eq.(3) and integrating from 0 to δ_t, one obtains,

$$\frac{1}{8} \frac{\partial}{\partial t}(T_w \delta_t) + \frac{7}{72} u \frac{\partial}{\partial x}\left(T_w \frac{\delta_t^{8/7}}{\delta_v^{1/7}}\right) = \frac{q_w}{C_p \rho} \quad . \tag{79}$$

In Eq.(3), thermal diffusivity, a, should be replaced by $(a+\varepsilon_H)$. However, in the limit of $y \to 0$, one obtains,

$$\lim_{y \to 0} (a + \varepsilon_H) \frac{\partial T}{\partial y} = \frac{q_w}{C_p \rho} \quad . \tag{80}$$

Equation (79) was derived based on above equation, Eq.(80). Substituting Eq.(78) into Eq.(79) and taking into consideration of $q_w = q_0 \exp(\omega t)$, one finally obtains a differential equation for boundary layers in dimensionless form,

$$x^*\left(\frac{\delta_t}{\delta_v}\right)^{8/7} + x^* \frac{\partial}{\partial t^*}\left(\frac{\delta_t}{\delta_v}\right)^{8/7} + \frac{7}{9}\frac{\partial}{\partial x^*}\left\{x^*\left(\frac{\delta_t}{\delta_v}\right)^{9/7}\right\} = 0.623 \quad (81)$$

Here, x^* and t^* are given by Eq.(14) and intial and boundary conditions are given by

$$\begin{aligned} \delta_t^*(x^*,0) &= 0 \quad \text{for } x^* \geq 0 \\ \delta_t^*(0,t^*) &= 0 \quad \text{for } t^* \leq 0 \end{aligned} \quad (82)$$

For small time, the convection term in Eq.(79) can be neglected and Eq.(79) reduces to

$$x^*\left(\frac{\delta_t}{\delta_v}\right)^{8/7} + x^* \frac{\partial}{\partial x^*}\left(\frac{\delta_t}{\delta_v}\right)^{8/7} = 0.623 \quad (83)$$

This differential equation is easily solved and the solution is given by

$$\left(\frac{\delta_t}{\delta_v}\right) = \left[\frac{0.623\{1 - \exp(-t^*)\}}{x^*}\right]^{7/8} \quad (84)$$

For large time, δ_t/δ_v will be independent of time and given by the solution of following differential equation

$$x^*\left(\frac{\delta_t}{\delta_v}\right)^{8/7} + \frac{7}{9}\frac{\partial}{\partial x^*}\left\{x^*\left(\frac{\delta_t}{\delta_v}\right)^{9/7}\right\} = 0.623 \quad (85)$$

Figure 10 shows the numerical solution of Eq.(85) in $(\delta_t/\delta_v)x^*$ vs. x^* plot. This solution can be approximated by the simple analytic function which is analogous to Eq.(84)

$$\frac{\delta_t}{\delta_v} = \left[\frac{0.623\{ 1 - \exp(-1.318\ x^*)\}}{x^*} \right]^{7/8} . \qquad (86)$$

In Fig.10, a comparison was made between the exact solution of Eq.(85) and the value calculated by Eq.(86), too. As shown in this figure, Eq.(86) can approximate the exact solution of Eq.(85) fairly well (within $\pm$ 5%).

In view of Eqs.(84) and (86), one finally obtains the approximate solution of Eq.(81).

for $1.318\ x^* \leqq t^*$

$$\frac{\delta_t}{\delta_v} = \left[\frac{0.623\{ 1 - \exp(-1.318\ x^*)\}}{x^*} \right]^{7/8} , \qquad (87)$$

for $1.318\ x^* \geqq t^*$

$$\frac{\delta_t}{\delta_v} = \left[\frac{0.623\{ 1 - \exp(-t^*)\}}{x^*} \right]^{7/8} . \qquad (88)$$

The transient heat transfer coefficient can be obtained by substituting Eqs.(87) and (88) into Eq.(78). It is given by

for $1.318\ x^* \leqq t^*$

$$St = 0.0296\ Re_x^{-0.2} \left[\frac{x^*}{0.623\ \{ 1 - \exp(-1.318x^*)\}} \right]^{1/8} , \qquad (89)$$

for $1.318\ x^* \geqq t^*$

$$St = 0.0296\ Re_x^{-0.2} \left[\frac{x^*}{0.623\ \{ 1 - \exp(-t^*)\}} \right]^{1/8} . \qquad (90)$$

Here, St is Stanton number ($St \equiv h/(u_\infty C_p \rho)$). The transient heat transfer coefficient calculated by Eqs.(89) and (90) is shown in Fig.11 in x^* vs. $St/(0.0296 x^{*0.125} Re_x^{-0.2})$ plot. The steady state heat transfer ciefficinet is obtained by putting $\omega \to 0$ in Eq.(89) and given by

$$St_{st} = 0.0288\ Re_x^{-0.2} . \qquad (91)$$

The asymptotic value of the transient heat transfer coefficient, h_a, is given by Eq.(89). Then the ratio between transient and steady state heat transfer coefficients is given by,

$$\frac{h_a}{h_{st}} \equiv \frac{St_a}{St_{st}} = \left[\frac{x^*}{0.623 \{ 1 - \exp(-1.318\, x^*)\}} \right]^{1/8} . \qquad (92)$$

The h_a/h_{st} calculated by Eq.(92) is shown in Fig.4, too.

II. 9 COMPARISON WITH EXPERIMENTAL DATA

Soliman et al. [16-18] carried out experiments on transient heat transfer with exponential increasing heat generation rate for a flat plate. Under turbulent flow condition, they have obtained experimental data of transient response of heater temperature averaged over the whole length of the flat plate, ℓ. They reported the transient heat transfer process can be predicted by quasi-steady state assumption with

$$\begin{aligned} &\text{for} \quad \ell^* \leqq 2 \qquad \frac{h_a}{h_{st}} = 1 \\ &\text{for} \quad \ell^* \geqq 2 \qquad \frac{h_a}{h_{st}} = 1.58 \end{aligned} \quad , \qquad (93)$$

where ℓ^* is dimensionless heater length ($\ell^* = \ell\omega/u_\infty$).

In their analysis, the comparison was made between heater temperatures obtained from their experiment and those calculated based on Eq.(93). Therefore, Eq.(93) can be regarded as very rough approximation of transient heat transfer coefficient, since there are considerable uncertainties in their experimental data. However it should be noted that experimental results of Soliman et al. [16-18] show general agreement with the results obtained in present analysis.

More precise measurements on transient heat transfer coefficient have been made by Kataoka et al. [27] for a cylindrical wire located parallel to turbulent water flow. In their experiment, the transient heat transfer coefficient averaged over the whole heater length, ℓ, with exponentially increasing heat generation rate has been measured. The result indicates that the transient heat transfer coefficient approaches a asymptotic value and it is correlated in term of ℓ^* by;

$$\frac{h_a}{h_{st}} = 1 + 0.1448\ \ell^{*0.97} . \tag{94}$$

On the other hand, present analysis shows that for small x^* and for turbulent flow and $Pr \simeq 1$, the ratio of h_a/h_{st} can be approximated by

$$\frac{h_a}{h_{st}} = 1 + 0.0824\ x^* , \tag{95}$$

Averaging Eq.(95) over heater length, ℓ, one obtains,

$$\frac{h_a}{h_{st}} = 1 + 0.0412\ \ell^* , \tag{96}$$

The difference of the proportionality constant between Eqs.(94) and (96) can be attributued to the difference of heater configuration (wire and plate). It is northworthy that turbulent boundary layer approximation in present analysis gives similar functional form to the exprimental correlation.

II. 10 CONCLUSIONS

Transient heat transfer coefficients for a flat plate with exponentially increasing heat flux under forced convection condition have been analysed by using boundary layer approximation. The results indicate that the

the transient heat flux attains the asymptotic value. The ratio between the asymptotic value of the transient heat transfer coefficient and steady state one is larger than unity. It increases with increasing x^*, a dimensionless parameter composed of distance from inlet, velocity and increasing rate of heat flux.

The transient heat transfer coefficient for laminar flow and Pr << 1 is given by Eqs.(21) and (22), for laminar flow and Pr >> 1 by Eqs.(39) and (40), for laminar flow and Pr≈1 by Eqs.(55) and (56). For turbulent flow and Pr << 1, it is given by Eqs.(21) and (22), for turbulent flow and Pr >> 1 by Eqs.(65) and(66), and for turbulent flow and Pr ≃ 1 by Eqs.(89) and (90).

The results for turbulent flow and Pr ≃ 1 can predict general trends and parametric dependence obtained in experiments for water using flat plate and cylindrical wire heaters.

More experimental data will be neccessary in order to acquire accurate knowledge for transinet heat transfer coefficient under forced convection condition along with analytical approaches carried out in present analysis.

NOMENCLATURES

a	Thermal diffusivity
A	Constant in Eq.(50)
h	Heat transfer coefficient
h^*	dimensionless heat transfer coefficient defined by Eq.(20)
ℓ	Heater length
ℓ'	Length scale for eddy
ℓ^*	Dimensionless heater length defined by Eq.(93).
Nu	Nusselt number ($\equiv hx/\lambda$)
Pe_x	Peclet number defined by Eq.(26)
Pr	Prandtl number ($\equiv \nu/a$)
q	Heat flux
q_w	Wall heat flux
q_0	Initial value of heat flux
Re_x	Reynolds number defined by Eq.(43)
St	Stanton number defined by Eq.(90)
t	Time
t^*	Dimensionless time defined by Eq.(14)
T	Temperature
u	Velocity in x direction
u'	Turbulent velocity
v	Velocity in y direction
x	Coordinate parallel to a flat plate
x^*	Dimensionless x coordinate defined by Eq.(14)

Greek Letters

δ_t	Thermal boundary layer
δ_t^*	Dimensionless thermal boundary layer defined by Eq.(14)
δ_v	Velocity boundary layer
ε_H	Turbulent diffusivity of heat
ε_M	Turbulent diffusivity of momentum
λ	Thermal conductivity
ν	Kinematic viscosity
τ	Shear stress
ω	Exponentially increasing rate of heat flux

Subscripts

a	Asymptotic
st	Steady state
w	Wall
∞	Ambient

REFERENCES

1. Kalinin, E. K. and Dreister, G. A., "Unsteady Convective Heat Transfer and Hydrodynamics in Channels", Adances in Heat Transfer, 6, p.367 Academic Press, NY. (1970)

2. Siegel, R., "Transient Heat Transfer for Laminar Slug Flow in Ducts", Trans. ASME, Ser. E, 81, p.140 (1959)

3. Siegel, R., "Forced Convection in Channel with Wall Heat Capacity and Wall Heating Variable with Axial Position and Time", Int. J. Heat Mass Transfer, 6, p.607 (1963)

4. Siegel, R. and Sparrow, E. M., "Transient Heat Transfer for Laminar Forced Convection in the Thermal Entrance Region of Flat Ducts", Trans.ASME, Ser. C, 81, p.29 (1959)

5. Siegel, R., "Heat Transfer for Laminar Flow in Ducts with Arbitrary Time Variations in Wall Temperature", Trans, ASME, Ser.E, 82, p.241 (1960)

6. Sparrow, E. M. and Siegel, R., "Unsteady turbulent Heat Transfer in Tubes", Trans. ASME, Ser. C, 82, p.170 (1960)

7. Perlmutter, M. and Siegel, R., "Two-Dimensional Unsteady Incompressible Laminar Duct Flow with a Step Change in Wall Temperature", Int. J. Heat Mass Transfer, 3, P. 94 (1961)

8. Siegel, R. and Perlmutter, M., "Laminar Heat Transfer in a Channel with Unsteady Flow and Wall Heating Varying with Position and Time", Trans. ASME, Ser. C, 85, p.358 (1963)

9. Namatame, K., "Transient Temperature Response of an Annular Flow with Step Change in Heat Generating Rod ", Nucl. Sci. Technol., 6, p.591

(1969)

10. Kawamura, H., "Analysis of Transient Heat Transfer for Turbulent Flow in Annuli, Part 1, Heating Element with a Finite Thermal Capacity and No Thermal Resistance", Trans. JSME, 39, p.2498 (1973)

11. Kawamura, H., "Analysis of Transient Heat Transfer for Turbulent Flow in Annuli, Part 2, Heating Element with a Finite Thermal Capacity and Finite Thermal Resistance", Trans. JSME, 42, p.1207 (1976)

12. Kawamura, H., and Iwahori, K., "Experiment of Transient Heat Transfer for Turbulent Flow in a Circular Tube", Trans. JSME, 42, p.2501 (1976)

13. Cess, R. D., "Heat Transfer to Laminar Flow across a Flat Plate with a Nonsteady Surface Temperature", Trans. ASME, Ser.C, 83, P.274 (1961)

14. Goodman, T. R., "Effects of Arbitrary Nonsteady Wall Temperature on Incompressible Heat Transfer", Trans. ASME, Ser. C, 84, P.347 (1962)

15. Adams, D. E. and Gebhart, B., "Transient Forced Convection from a Flat Plate Subjected to a Step Energy Input", Trans. ASME, Ser. C, 86, p.253 (1964)

16. Soliman, M., and Johnson, H. A., "Transient Heat Transfer for Turbulent Flow over a Flat Plate of Appreciable Thermal Capacity and Containing Time-Dependent Heat Source", Trans. ASME, 89, p.362 (1967)

17. Soliman, M. and Johnson, H. A., "Transient Heat Transfer for Forced Convection Flow over a Flat Plate of Appreciable Thermal Capacity and Containing an Exponential Time-Dependent Heat Source", Int. J. Heat Mass Transfer, 11, P.39 (1968)

18. Soliman, M., "Analytical and Experimental Study of Transient Heat Transfer External Forced Convection", USAEC Report, SAN-1010, (1963)

19. Chao, B. T. and Jeng, D. R., "Unsteady Stagnation Point Heat Transfer",

Trans. ASME, Ser. C, 87, p.221 (1965)

20. Chao, B. T. and Cheema, L. S., "Unsteady Heat Transfer in Laminar Boundary Layer over a Flat Plate", Int. J. Heat Mass Transfer. 11, p. 1311 (1968)

21. Ishiguro, R., "A Study of Turbulent Heat Transfer for Thermally Unsteady System", Proc. of 9th National Heat Transfer Symposium of Japan, A 205, p.315 (1972)

22. Mitazi, K. and Ishiguro, R., "Unsteady Forced Convective Heat Transfer", Proc. of 13th National Heat Transfer Symposium of Japan,A 209, p.67 (1976)

23. Hanawa, J., "Transient Heat Transfer to Laminar Flow from a Flat Plate with Heat Capacity (Numerical Solution)", Trans.JSME, 41, p.2119(1975)

24. Hanawa, J., "Transient Convective Heat Transfer to Laminar Flow from a Flat Plate with Constant Heat Capacity", Trans. JSME, 46, p.299 (1980)

25. Hanawa, J., "Transient Convective Heat Transfer to Turbulent Flow from a Flat Plate with Constant Heat Capacity", Trans. JSME, 46, p.927 (1980)

26. Hanawa, J., "Transient Convective Heat Transfer to Turbulent Flow from a Flat Plate with Constant Heat Capacity", Trans. JSME, 46, p.2348 (1980)

27. Kataoka, I. Serizawa, A. and Sakurai, A., "Transient Boiling Heat Transfer under Forced Convection", Int. J. Heat Mass Transfer, 24, p.583 (1983)

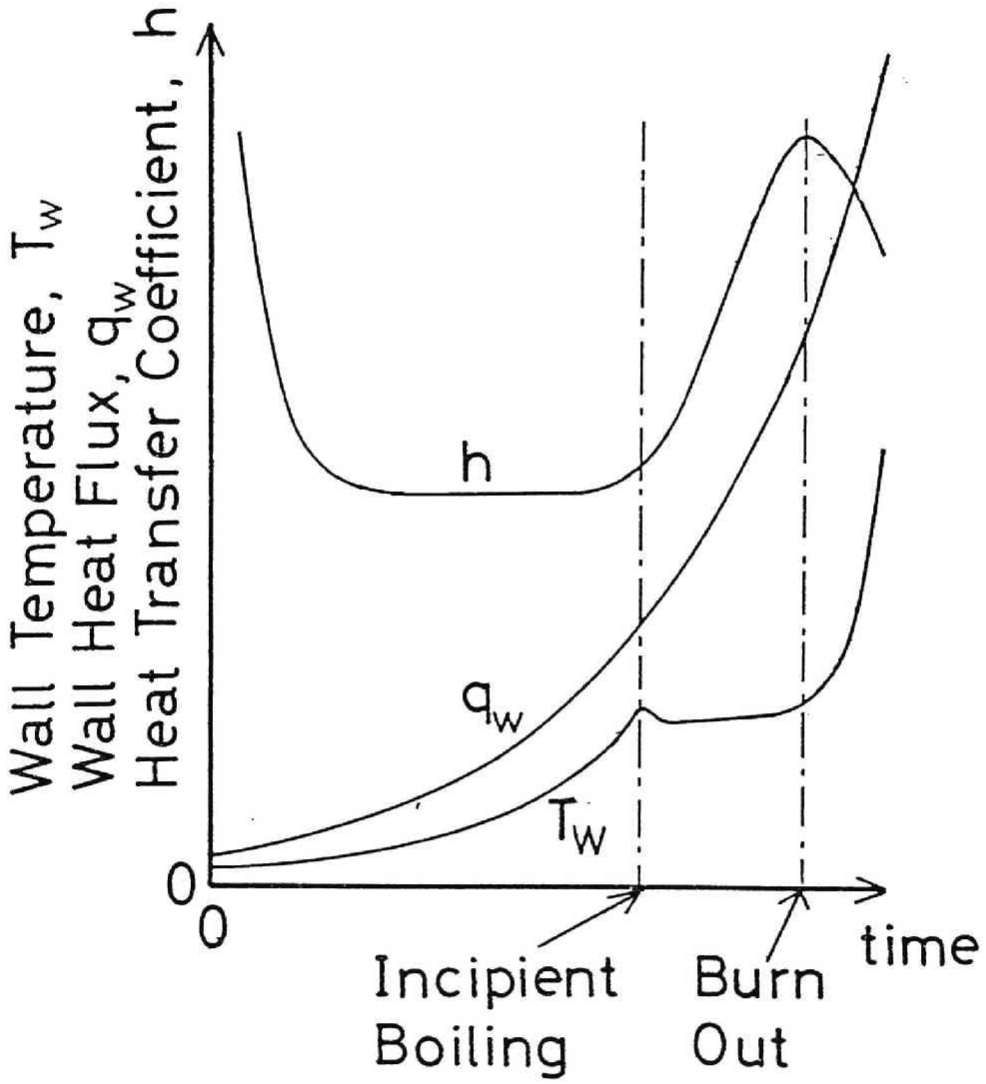

Fig.1 Transient heat transfer process under exponentially increasing heat flux

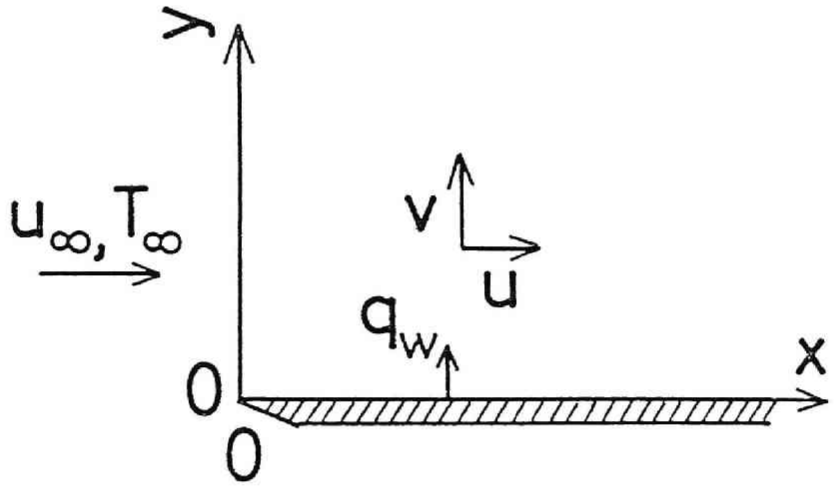

Fig.2 Schematic diagram of flow configuration

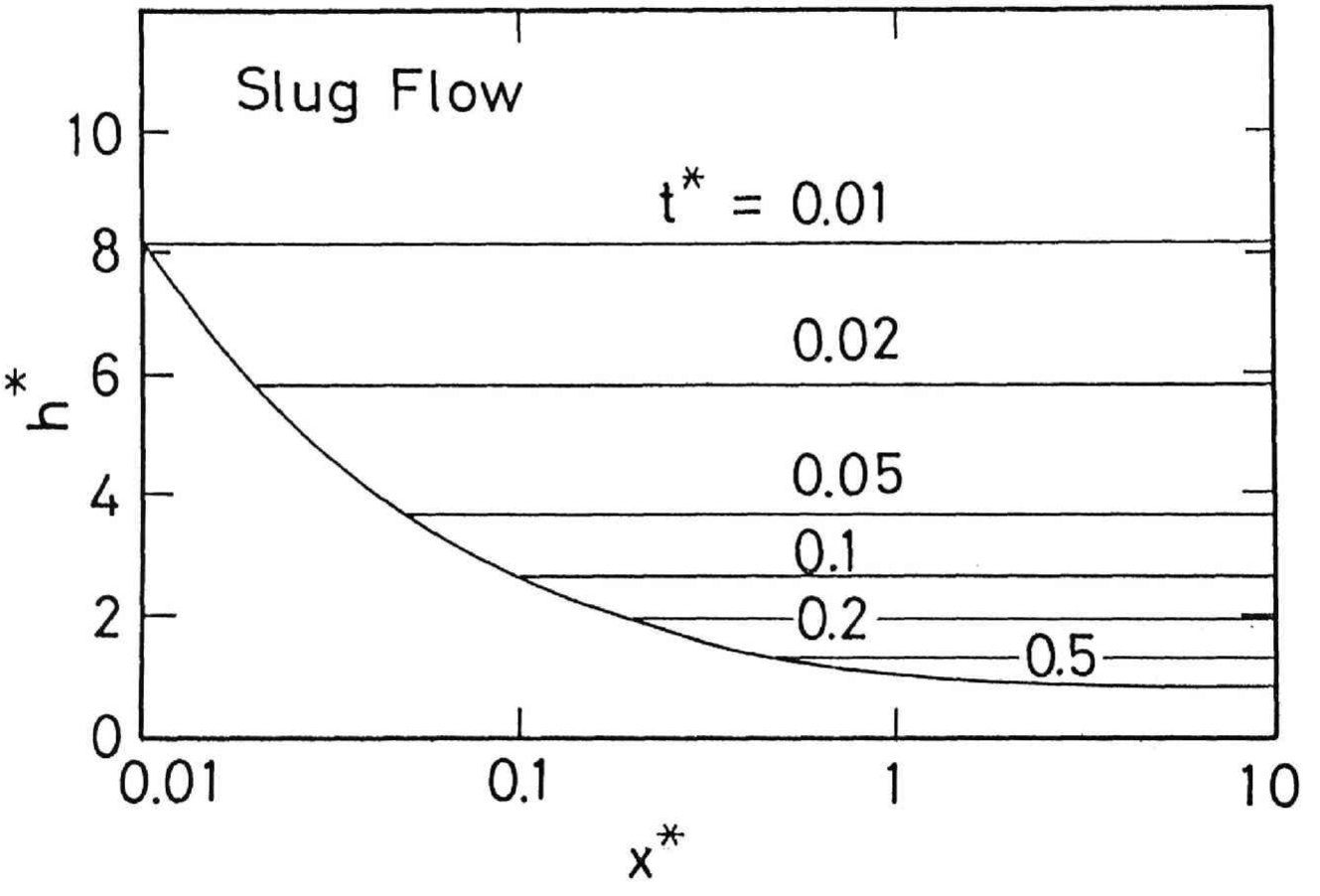

Fig.3 Transient heat transfer coefficient for slug flow

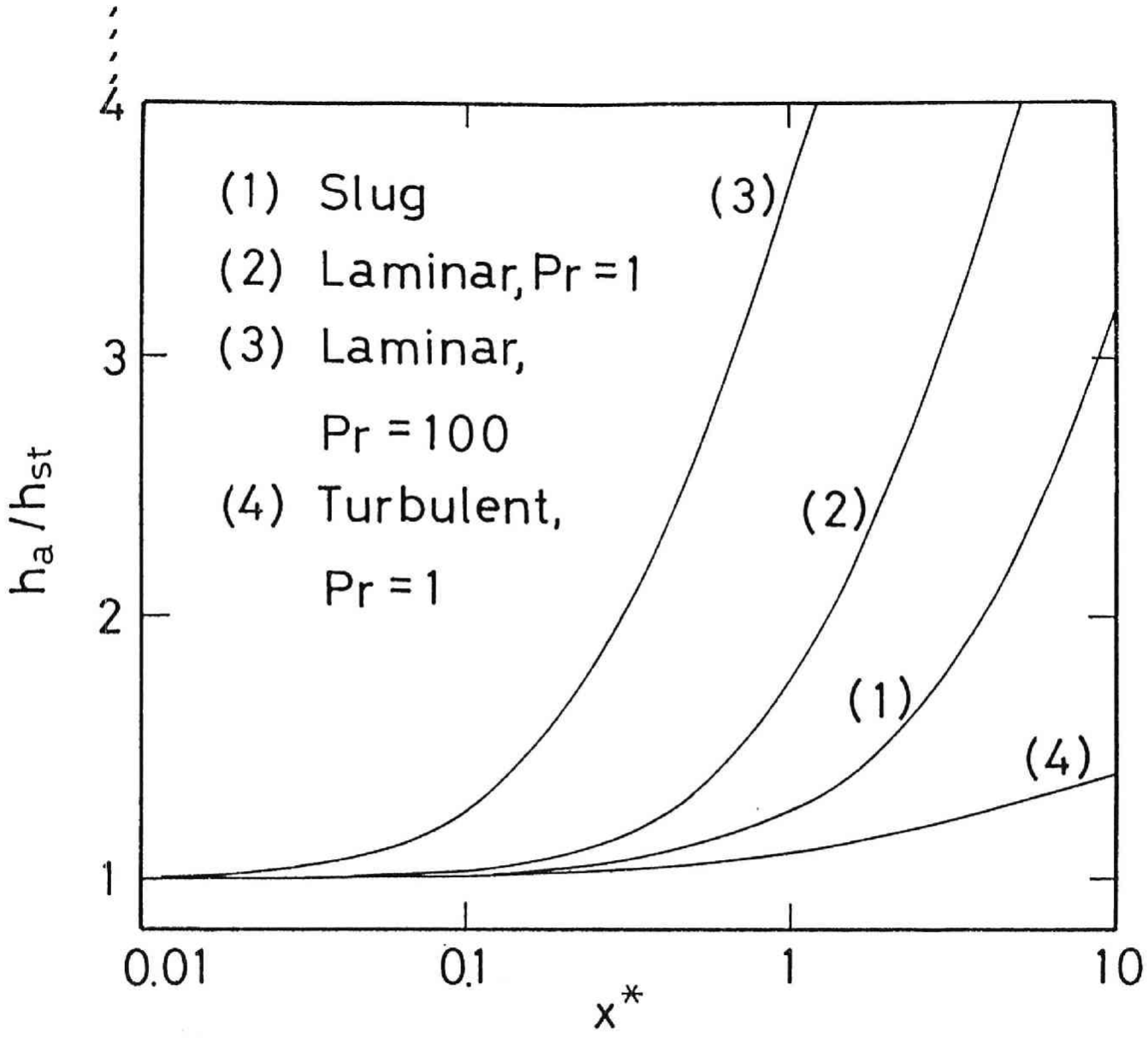

Fig.4 Ratio between transient heat transfer coefficient and steady staye one

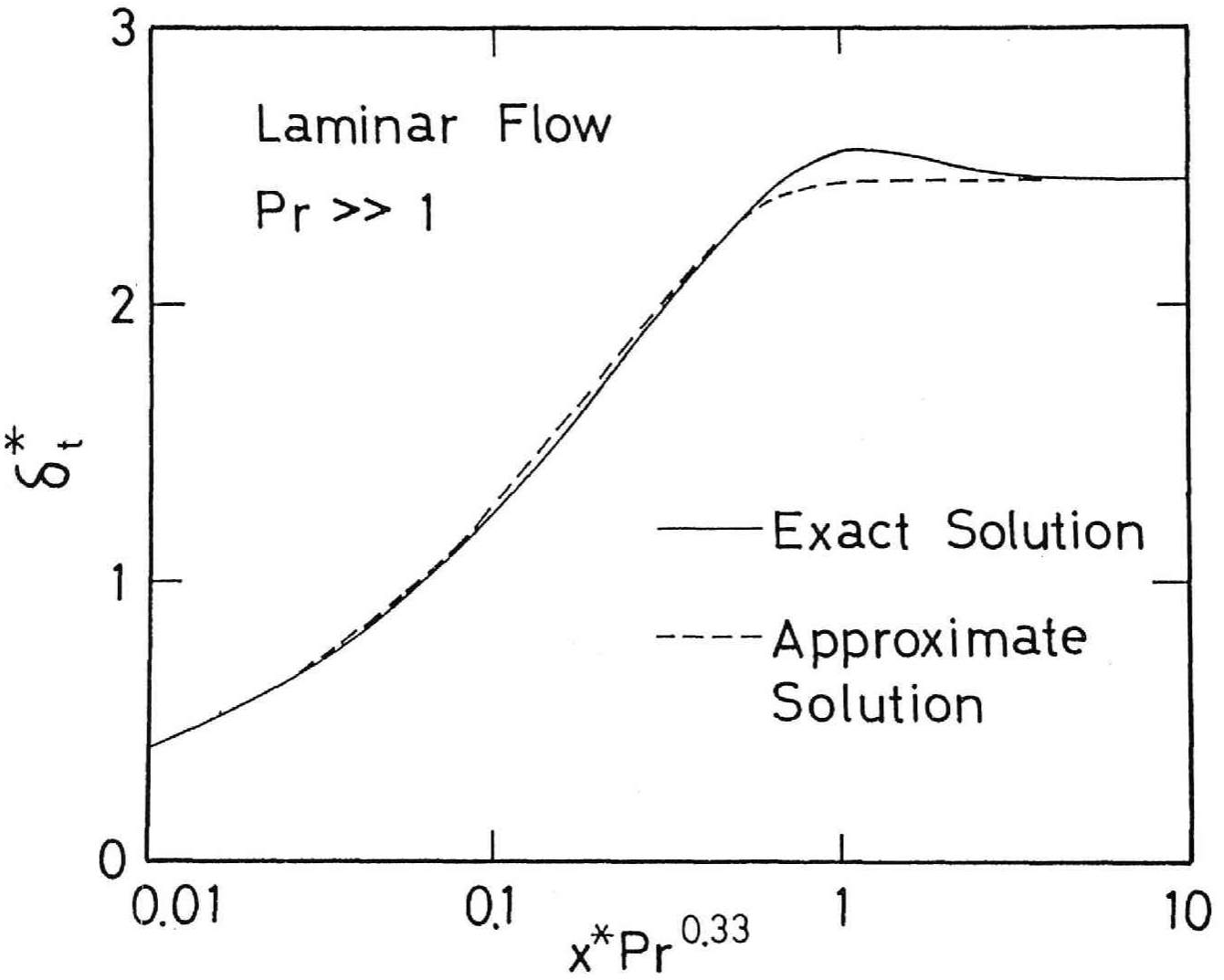

Fig.5 Thermal boundary layer for laminar flow and Pr >> 1

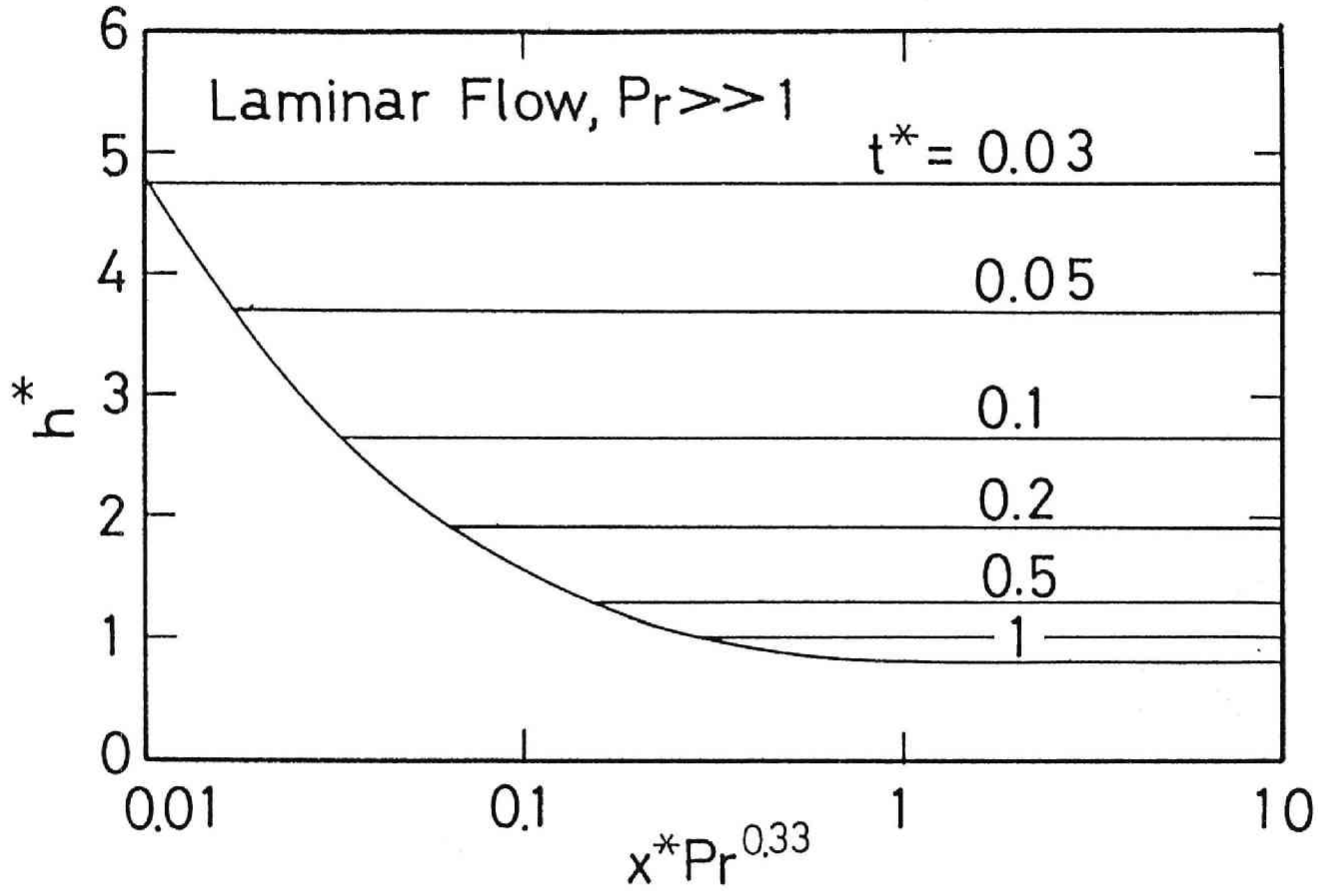

Fig.6 Transient heat transfer coefficient for laminar flow and Pr >> 1

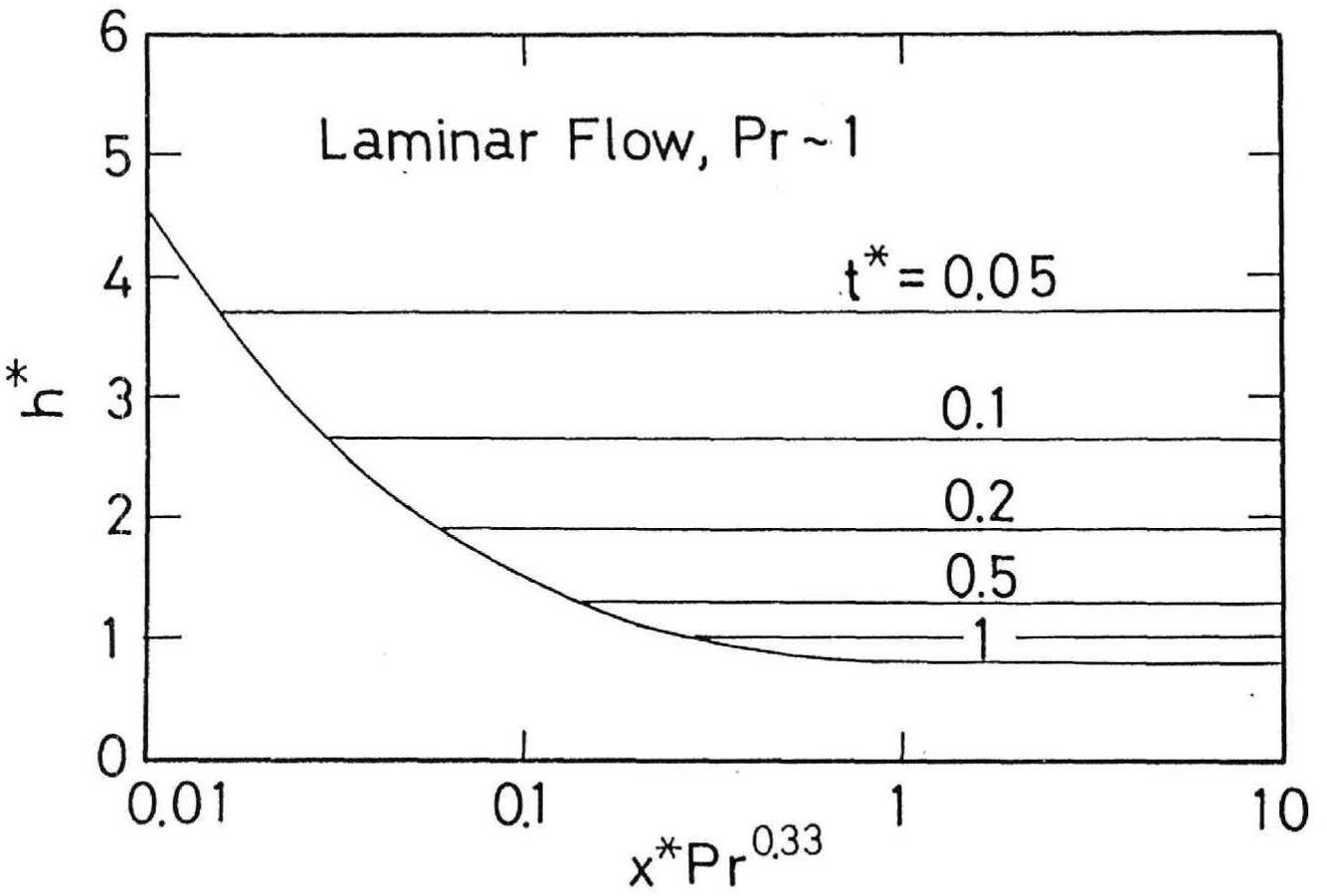

Fig.7 Transient heat transfer coefficient for laminar flow and Pr ≃ 1

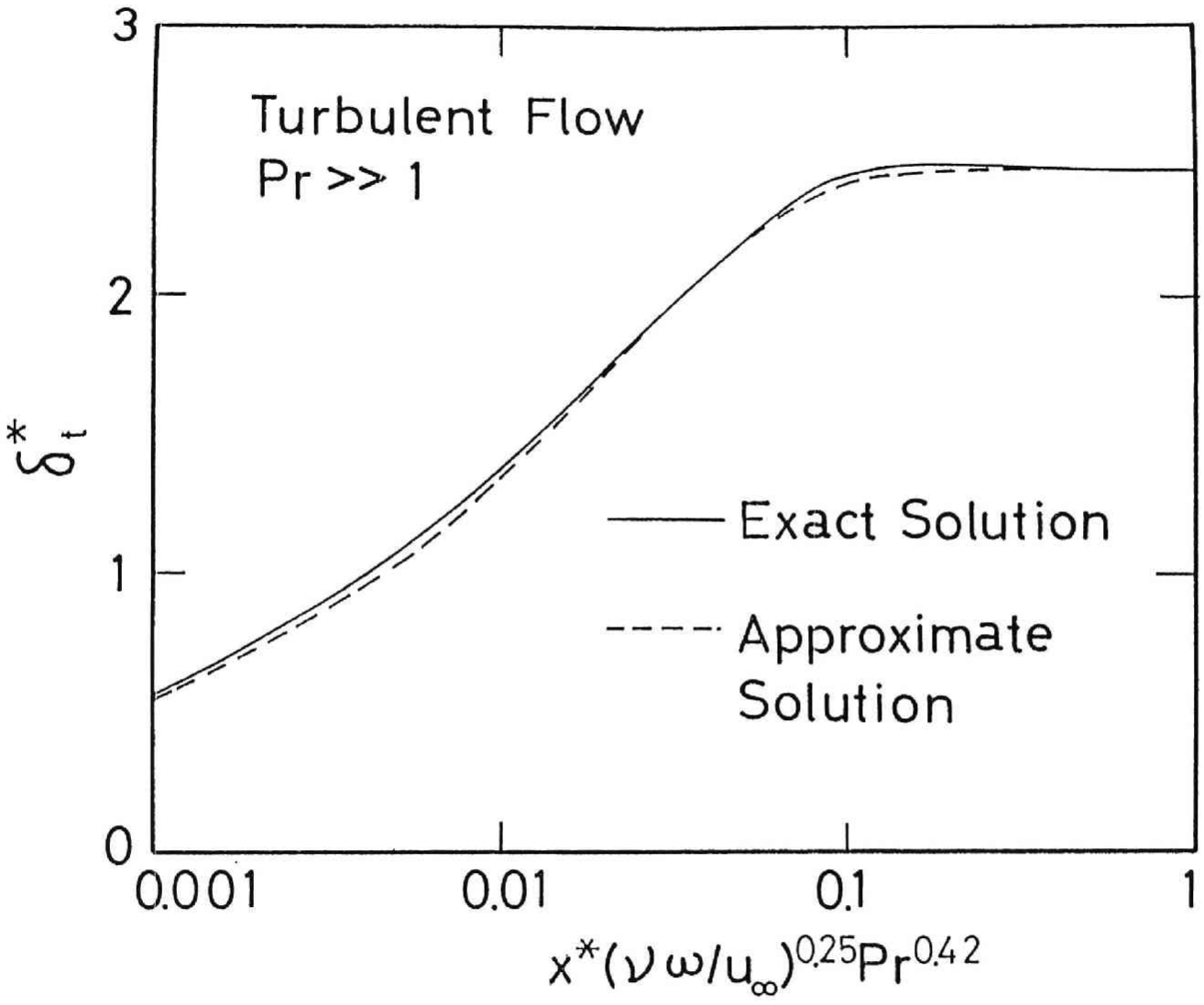

Fig.8 Thermal boundary layer for turbulent flow and Pr >> 1

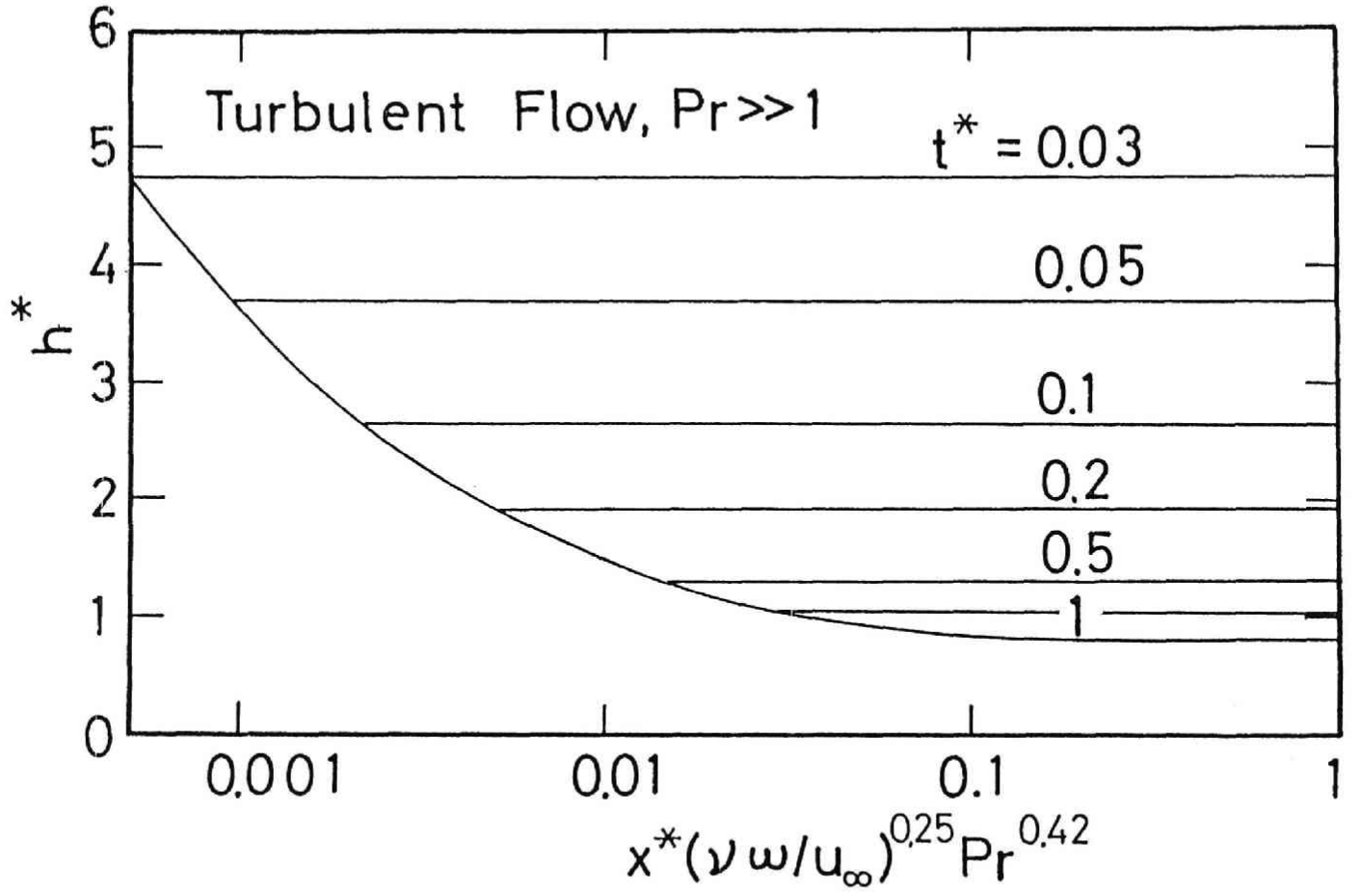

Fig.9 Transient heat transfer coefficient for turbulent flow and Pr >> 1

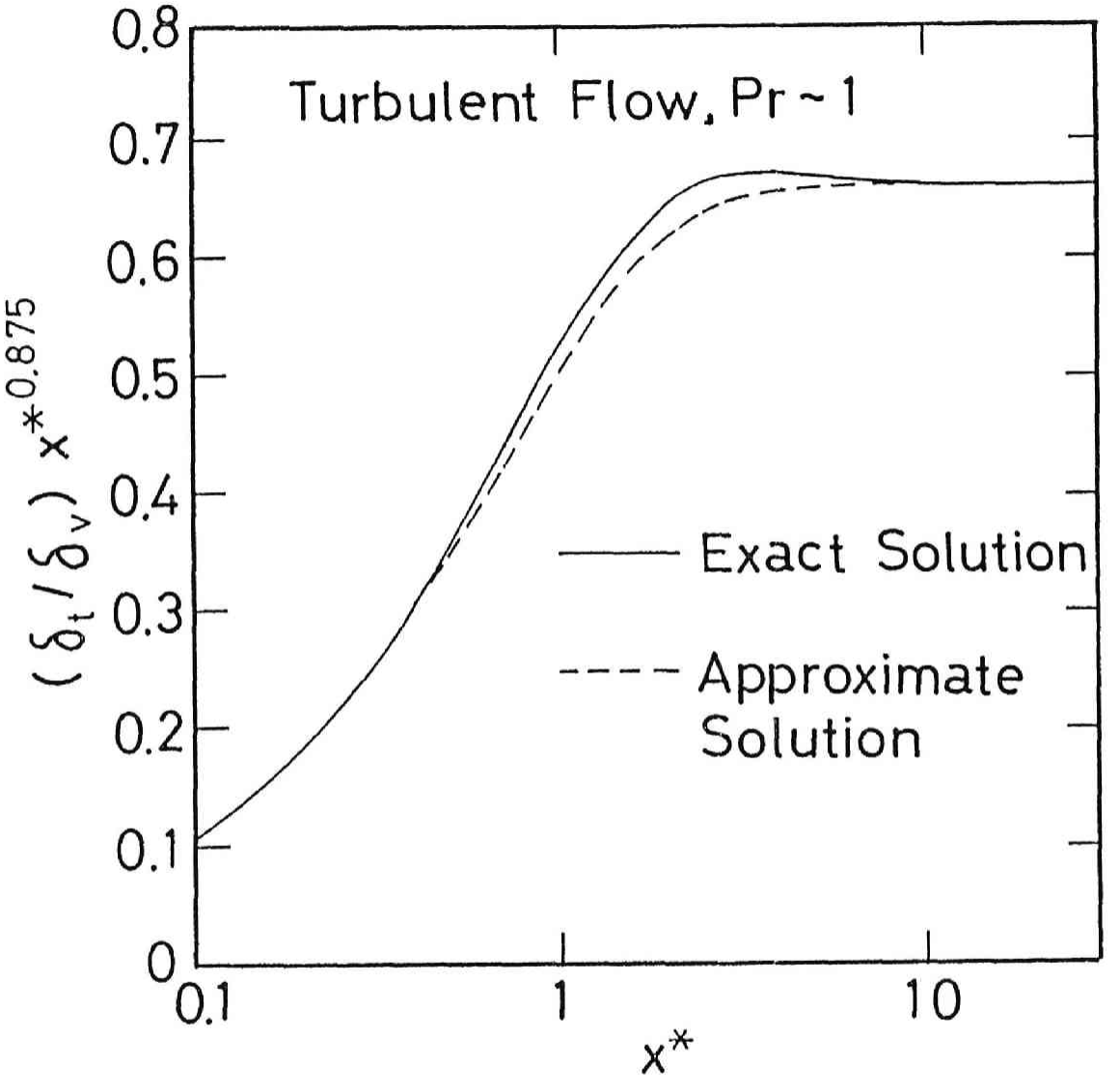

Fig.10 Thermal boundary layer for turbulent flow and Pr ≃ 1

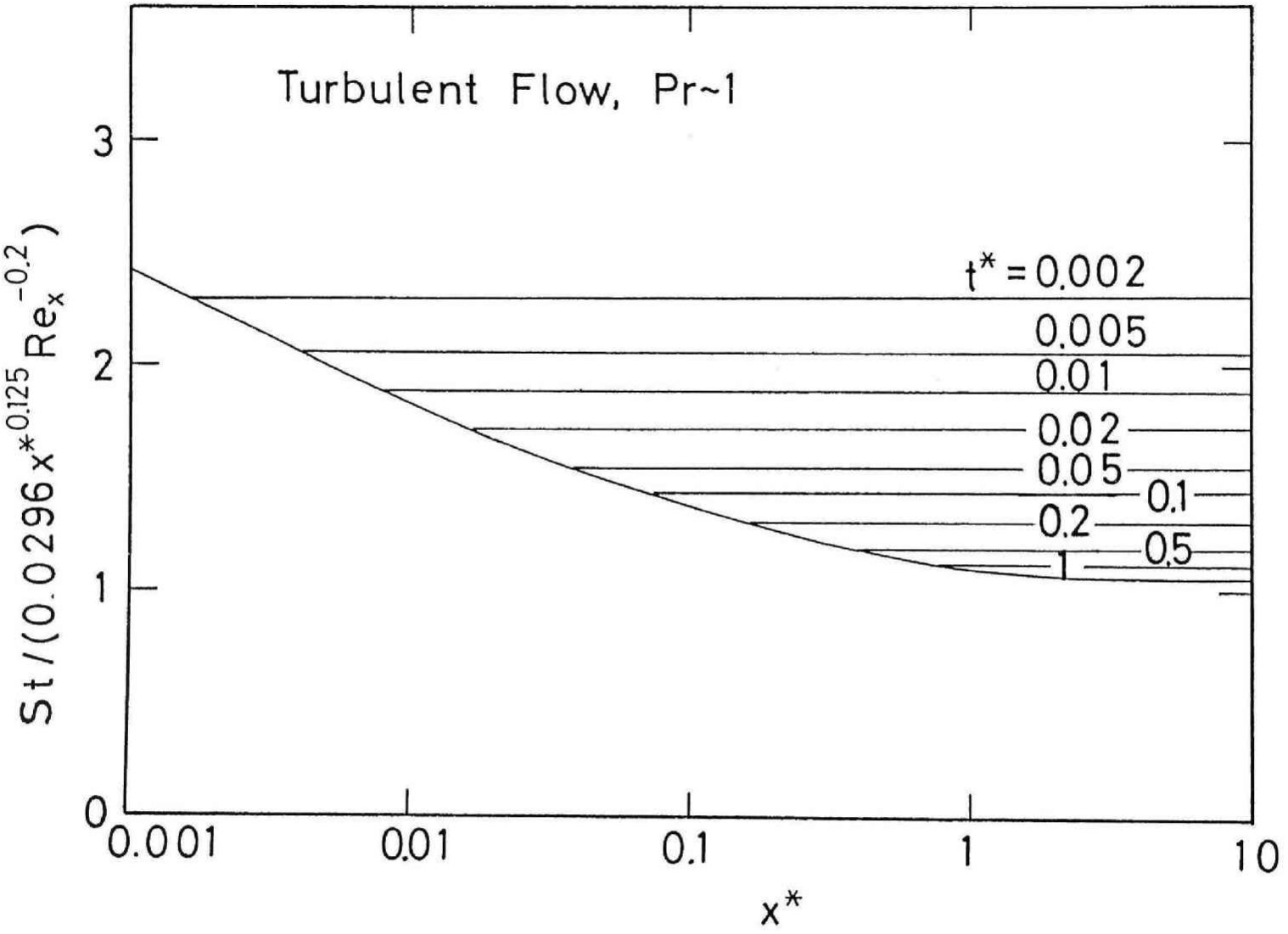

Fig.11 Transient heat transfer coefficient for turbulent flow and Pr ≃ 1

CHAPTER III

GENERATION AND SIZE DISTRIBUTION OF DROPLET IN GAS-LIQUID ANNULAR TWO-PHASE FLOW

Ⅲ. 1 INTRODUCTION

A loss of coolant accident (LOCA) and subsequent rewetting and reflooding phenomena in a nuclear reactor constitute another important phases of the nuclear reactor accident. In this case, large amount of vapor is generated and high quality two-phase flow often encountered. Power levels under these accidents are relatively low (decay heat level) and the transient process is slow. Under these circumstances, the boiling and two-phase flow phenomena are not localized , but depend on the upstream conditions. In the nuclear reactor core, the heated length is considerably long extending to several meters. Therefore, the boiling and two-phase flow phenomena involved are those for large length to diameter ratio, ℓ/d_{he}. The heat and mass transfer mechanisms are considered to be quite different from those for small ℓ/d_{he} which have been studied in the previous chapters.

The transient and steady state boiling phenomena under these large ℓ/d_{he} conditions are basically determined by the mass, momentum and energy transfer processes of annular or annular dispersed flows which are usually observed in high quality two-phase flow.

Therefore, in this chapter and succeeding two chapters (Chapter Ⅳ and Ⅴ), the hydrodynamic characteristics of annular or annular dispersed flow are studied. Several practical correlations which are necessary to the analyses of nuclear reactor accidents have been developed. Firstly, the droplet size and its distribution are analysed in this chapter.

An accurate knowledge of the mean droplet size and droplet size distribution is essential to the detailed analyses of droplet or annular dispersed flow. The inception of droplet entrainment from the liquid film significantly changes the mechanisms of mass, momentum and energy transfer [1,2]. The available interfacial area and droplet transport depend on the amount of entrainment and droplet size. Therefore, in order to accurately model and predict a number of important physical phenomena in annular dispersed flow, an understanding of mechanisms of entrainment, generation of droplets and size distribution are prerequisite. In particular, the relative velocity and droplet carryover, the dryout and post dryout heat transfer [3-7] and the effectiveness of the emergency core cooling in light water reactors [8-11] are signif-

icantly influenced by the amount of entrainment and droplet size.

In view of its importance, a detailed modeling of amount of entrained droplet has been carried out recently [2] by considering the entrainment mechanism of the shearing off of roll-wave crests by streaming gas flow. However, there have been no satisfactory correlations for the prediction of the mean droplet size and size distribution for annular dispersed flow. The lack of such a correlation has been one of the main difficulties of analyzing various important phenomena in annular flow. The principal objective of this study, therefore, is to develop a reliable and simple predictive method for the mean droplet size as well as the droplet size distribution. A certain mechanistic modeling which are consistent with the previously developed onset of entrainment criterion and correlation for the amount of entrainment has been adopted here to obtain a general correlation with wide ranges of applicability. Hence, the main mechanism of droplet generation considered here is the shearing off of the roll-wave crest by gas flow.

In addition to the present model based on entrainment mechanism, several existing droplet size criteria based on droplet disintegration have been reviewed in this study. As it becomes evident, the standard Weber number criterion expressed in terms of the relative velocity between gas and droplet gives far too large droplet sizes in annular flow. This also indicates that the droplet size in annular flow is mainly determined at the time of entrainment.

III. 2 DROPLET GENERATION MECHANISMS

Droplets can be generated by a number of different ways such as the liquid jet breakup, droplet disintegration and droplet entrainment from a body of liquid [1,12-14]. The former two mechanisms have been reviewed in detail by Brodkey [12]. A liquid jet or sheet disintegrates into small droplets due to interfacial instabilities [15,16].

Disintegration of droplets in gas stream has been studied by a number of researchers [12,13,17-23]. Several different mechanisms of droplet break-up have been recognized. The mode by which the disintegration occurs depends on the initial droplet size and the flow condition. A large free-falling drop initially becomes unstable due to the Taylor instability and then it is blown in by gas and disintegrates into fine droplets.

A criterion for droplet disintegration can be expressed in terms of the Weber number defined by

$$We \equiv \frac{\rho_g v^2 D}{\sigma} \quad , \tag{1}$$

where D is the droplet size. Then the criterion is given by a critical Weber number beyond which droplets disintegrate into smaller droplets.

In case of a falling drop, the critical Weber number is given [13,17,20] by

$$We_c \doteq 22 \qquad \text{(falling drop)} \quad . \tag{2}$$

However, direct observations of droplet sizes indicate that the critical diameter is approximately given [22,24] by

$$D_c \doteq (4 \sim 6)\sqrt{\sigma/g\Delta\rho} \quad . \tag{3}$$

This value can be also obtained from the consideration of the Taylor Instability [22]. On the other hand, the terminal velocity of a large drop [24,25] is about

$$v_\infty = (1.4 \sim 1.7)\left(\frac{\sigma g \Delta\rho}{\rho_g^2}\right)^{1/4} \quad . \tag{4}$$

Substituting Eqs. (3) and (4) into Eq. (1), one gets the critical Weber number to be

$$We_c = 8 \sim 17 \quad . \tag{5}$$

This value is much smaller than the one given by Eq. (2), however, it is considered to be a more reliable criterion for large drops.

When a droplet is suddenly exposed into a gas stream, violent shattering of droplets becomes possible. In this case, the critical Weber number is about 10 to 12 for low viscous fluids [13,18,20,21]. However, a significant effect of the liquid viscosity has been observed. Thus Hinze [13] correlated it in terms of the viscosity group $(\mu_f^2/\rho_f D\sigma)$ as

$$We_c = 12 \left[1 + \left(\frac{\mu_f^2}{\rho_f D\sigma} \right)^{0.36} \right] \quad . \tag{6}$$

Later some modification has been proposed [12] using the same dimensionless group as

$$We_c = 12 + 14 \left(\frac{\mu_f^2}{\rho_f D\sigma} \right)^{0.8} \quad . \tag{7}$$

In view of Eqs. (5) and (7), it may be concluded that the criterion given by Eq. (7) is a good general purpose correlation for droplet disintegrations in gas stream.

The third mechanism is the disintegration of fluid particles by strong turbulent motions of a continuous phase [13,17]. This occurs mainly in bubbly flow or droplet in liquid flow. For highly turbulent flow, the value of the critical Weber number is given approximately [13,17] by

$$We_c = 1.2 \sim 2.5 \quad . \tag{8}$$

It is noted that these critical Weber numbers are sensitive to flow conditions. For example, in a pulsating flow the value of We_c can be reduced by as much as 50% of the one given by Eq. (7).

Another important but quite different type of generation of droplets is associated with entrainment of droplets at gas-liquid interfaces [1,2,14]. In

this case, the entrainment mechanisms can be grouped into two main categories, i.e., film entrainment and pool entrainment. A wavy liquid film can be entrained into gas flow in several different ways such as roll-wave shearing off, wave under cutting, droplet impingement and liquid bridge disintegration. For annular flow shearing off of the roll-wave crests is the most important entrainment mechanism [2,14], see Fig. 1. The liquid bulge or bridge disintegration is similar to the large droplet disintegration discussed above in terms of the critical Weber number. This mechanism may be important in counter-current situations or near the churn to annular flow transition. The wave under cutting occurs at very high gas flow and at low Reynolds numbers. Therefore, for highly viscous fluids, this is an important mechanism to consider [14].

In the pool entrainment, droplets are generated by bubbles streaming through the horizontal pool level. Because of the bubble burst mechanism, droplets of two different size groups are produced and carried up by the gas flow. The entrainment often depends on the height from the pool level due to the existence of falling drops which cannot be suspended in the gas stream [26].

As mentioned above, most of the droplets in annular two-phase flow are produced by the entrainment. There is very strong experimental evidence indicating that the drops are too small to be generated by the standard droplet disintegration mechanism. In other words, the critical Weber number based on the relative velocity between gas and drops gives much larger drop sizes than experimentally observed. Therefore, the majority of droplets should have been generated at the time of entrainment and not during the flight as droplets in gas flow. This implies that the relative velocity between the gas core flow and liquid film flow is the governing factor in determining the droplet size. Furthermore, the dominant mechanism of entrainment in annular two-phase flow is shearing off of roll-wave crests by streaming gas flow. In view of these, a criterion for drop size in annular flow is derived by considering the roll-wave entrainment mechanism in the next section.

III. 3 DROPLET GENERATION BY ENTRAINMENT

Ishii and Grolmes [14] have developed a criterion for droplet entrainment based on the shearing off of roll-wave for film Reynolds number $\geq$ 160. At the gas velocity beyond the inception of entrainment, it can be considered that droplets are generated by the shearing off of roll-waves. Combined effects of entrainment and subsequent disintegration and coalescence of droplets produce a droplet size distribution. However, it is expected that droplet size distributions are mainly characterized by sizes of droplets which are entrained by the shearing off of roll-waves in annular flow.

Theoretical estimation of a droplet size based on this mechanism will be discussed below. In Fig. 1, the mechanism of the shearing off of roll-wave is illustrated. The force balance on the ligament, which is about to be torn off, is given by

$$\pi D\sigma = \frac{\pi}{4} D^2 C_D \frac{1}{2} \rho_g j_g^2 \quad . \tag{9}$$

Here D is the characteristic diameter and C_D is the drag coefficient at the wave crest. The term $\pi D\sigma$ is a surface tension force and the right hand side of Eq. (9) is a drag force acting on the ligament. Introducing Weber number, $We \left(\equiv \frac{\rho_g j_g^2 D}{\sigma} \right)$, Eq. (9) can be rewritten as

$$We = \frac{8}{C_D} \quad . \tag{10}$$

Now in what follows it will be shown that the drag coefficient, C_D, is related to interfacial shear stress, τ_i. In a droplet annular two-phase flow, interfacial force per unit volume acting on dispersed phase, M_{id}, is given (Ishii and Chawla [27]) by

$$M_{id} = \frac{F_D \alpha_d}{V_d} = \frac{\alpha_d A_d}{V_d} \left[-\frac{1}{2} C_D \rho_g v_r |v_r| \right] \quad , \tag{11}$$

where F_D, α_d, V_d and A_d are drag force, volume fraction, volume and projected area of a typical particle. Assuming that droplets are spheres, one obtains

$$\frac{\alpha_d A_d}{V_d} = \frac{a_i}{4} \quad , \tag{12}$$

where a_i is the interfacial area per unit volume. Then Eq. (11) becomes

$$M_{id} = \frac{a_i}{4} \left[-\frac{1}{2} C_D \rho_g v_r |v_r| \right] \quad . \tag{13}$$

By considering a neighborhood of a wave region as illustrated in Fig. 2, the shear force per unit volume, M_τ, is given by

$$M_\tau = \frac{A_{iw} \tau_i}{V_w}$$

$$= a_{iw} \tau_i \quad , \tag{14}$$

where a_{iw} is the wave area per unit volume. In a wave region, the interfacial force acting on semi-dispersed phase, M_{id}, is approximately equal to the shear force, M_τ. Therefore, from Eqs. (13) and (14) one obtains

$$\left[-\frac{1}{2} C_D \rho_g v_r |v_r| \right] = 4 \frac{a_{iw}}{a_i} \tau_i \quad . \tag{15}$$

When a liquid film on the wall is not so thick, the relative velocity between the mean gas flow and the film flow, v_r, can be approximated by the gas flux, j_g. Then the following simplification can be made;

$$\frac{1}{2} C_D \rho_g j_g^2 = 4 \frac{a_{iw}}{a_i} \tau_i \quad . \tag{16}$$

For the interfacial shear force for a rough wavy regime, Wallis [24] presented the following simple correlation:

$$\tau_i = 0.005 \left[1 + 300 \frac{\delta}{D_h} \right] \frac{1}{2} \rho_g j_g^2 \quad , \tag{17}$$

where δ is the average film thickness.

In the entrainment regime beyond the critical gas velocity for the onset of entrainment, the amplitude of the wave crest should be the most important parameter for the description of τ_i. Therefore, the above correlation is slightly modified by using the wave amplitude instead of the film thickness as

$$\tau_i = 0.005 \left[1 + C_g \frac{a}{D_h}\right] \frac{1}{2} \rho_g j_g^2$$

$$\simeq 0.005\, C_g \frac{a}{D_h} \cdot \frac{1}{2} \rho_g j_g^2 \quad . \tag{18}$$

The motion of the wave crest with respect to the film may be expressed by a shear flow model (Ishii and Grolmes [14]) as

$$\tau_i = C_w \mu_f \frac{v_f}{a} \quad . \tag{19}$$

On the other hand, interfacial shear force can also be expressed by the liquid friction factor as

$$\tau_i = f_i \frac{\rho_f v_f^2}{2} \quad . \tag{20}$$

From Eqs. (19) and (20) one can eliminate v_f and obtain an expression for the amplitude as

$$a = \sqrt{2}\, C_w \frac{\mu_f}{\rho_f} \sqrt{\frac{\rho_f}{\tau_i}} \frac{1}{\sqrt{f_i}} \quad . \tag{21}$$

A typical liquid friction factor can be obtained from the correlation for a film thickness given by Hughmark [28]. Thus for a relatively high Reynolds number regime of interest,

$$\sqrt{f_i} = 1.13\, Re_f^{-0.25} \quad . \tag{22}$$

Substituting Eqs. (21) and (22) into Eq. (18) a following expression for the interfacial shear force can be derived.

$$\tau_i = 0.005 C_g \left(\frac{2C_w}{1.13\sqrt{0.005 C_g}} \right)^{2/3} Re_f^{1/6} \, Re_g^{-2/3} \left(\frac{\rho_g}{\rho_f} \right)^{1/3} \left(\frac{\mu_g}{\mu_f} \right)^{-2/3} \frac{1}{2} \rho_g j_g^2 \quad . \tag{23}$$

Then in view of Eqs. (16) and (23) the expression for the drag coefficient, C_D, is obtained.

$$C_D = 0.02 \frac{a_{iw}}{a_i} C_g \left(\frac{2C_w}{1.13\sqrt{0.005 C_g}} \right)^{2/3} Re_f^{1/6} \, Re_g^{-2/3} \left(\frac{\rho_g}{\rho_f} \right)^{1/3} \left(\frac{\mu_g}{\mu_f} \right)^{-2/3} \quad . \tag{24}$$

By substituting Eq. (24) into Eq. (2), the critical Weber number for the droplets entrained from wave crests can be obtained.

$$We = 400 \frac{a_i}{a_{iw}} \frac{1}{C_g} \left(\frac{1.13\sqrt{0.005 C_g}}{2C_w} \right)^{2/3} Re_f^{-1/6} \, Re_g^{2/3} \left(\frac{\rho_g}{\rho_f} \right)^{-1/3} \left(\frac{\mu_g}{\mu_f} \right)^{2/3} \quad . \tag{25}$$

The above expression indicates the significant dependence of the critical Weber number on the gas flux which does not exist in the case of disintegration in gas stream. For practical applications, the proportionality constant in the above equation should be correlated in collaboration with experimental data.

III. 4 MEAN DROPLET SIZE AND SIZE DISTRIBUTION

Several experiments have been carried out to study droplet size distributions in annular two-phase flow. Among these available data, Wicks and Dukler [29,30], Cousins and Hewitt [31] and Lindsted et al. [32] are used for the correlation purpose, because in their experiments liquid velocity and gas velocity have been varied systematically. The conditions of their experiments are described in Table I.

Droplet distribution can be characterized by various representative diameters. In the present study, volume-median diameter, D_{vm}, is used as a representative diameter.

The experimental data listed in Table I indicates that the volume median diameter decreases with increasing gas flux, j_g, in a way $D_{vm} \sim j_g^{-n}$ where the power n is between 0.8 (Lindsted et al. [32]) and 1.2 (Wicks and Dukler [29,30] and Cousins and Hewitt [31]). This tendency is similar to that predicted by Eq. (25) where the droplet diameter decreases as the 4/3 power of the gas flux. Figure 3 shows experimental volume median diameter in $We(D_{vm})$ vs. $Re_f^{-1/6}\ Re_g^{2/3} \left(\frac{\rho_g}{\rho_f}\right)^{-1/3} \left(\frac{\mu_g}{\mu_f}\right)^{2/3}$ plot. Most of these data fall within ± 40% of the following correlation.

$$We(D_{vm}) = 0.028\ Re_f^{-1/6}\ Re_g^{2/3} \left(\frac{\rho_g}{\rho_f}\right)^{-1/3} \left(\frac{\mu_g}{\mu_f}\right)^{2/3}, \tag{26}$$

where $We(D_{vm})$ is the Weber number based on the volume median diameter.

$$We(D_{vm}) = \frac{\rho_g j_g^2 D_{vm}}{\sigma}. \tag{27}$$

The above Weber number criterion can be rewritten in terms of the volume median diameter as

$$D_{vm} = 0.028\ \frac{\sigma}{\rho_g j_g^2}\ Re_f^{-1/6}\ Re_g^{2/3} \left(\frac{\rho_g}{\rho_f}\right)^{-1/3} \left(\frac{\mu_g}{\mu_f}\right)^{2/3}. \tag{28}$$

This correlation indicates that the median diameter is proportional to $j_g^{-4/3}$. On the other hand, the standard Weber number criterion implies that D_{vm} is

proportional to j_g^{-2}. This difference arises from the inclusion of the interaction between the liquid film and gas core flow in the present model.

In Fig. 3, the data of Wicks and Dukler [29,30] for $Re_f \geq 7500$ (liquid flowrate $\geq$ 4000 lb/hr) are excluded because in these regions the liquid bridge extends across the channel width according to the authors. Tatterson et al. [33] measured droplet size distributions in an air-water annular flow in a horizontal rectangular channel. But their data show that volume median diameter increases with increasing gas flux. The mechanism of droplet formation should be quite different in this case. One possibility is that the entrainment at the inlet has been the main mechanism of droplet generation. In view of these, their data were not used in the present analysis.

Comparing Eqs. (25) and (26), one obtains

$$400 \frac{a_i}{a_{iw}} \frac{1}{C_g} \left(\frac{1.13\sqrt{0.005 C_g}}{2C_w} \right) = 0.028 \quad . \tag{29}$$

The order of magnitude of the interfacial area ratio a_i/a_{iw} can be estimated as follows. If the internal flow within the wave crest is laminar and similar to a pipe flow, then $C_w \simeq 8$. The value of C_g is approximately 300 or less in view of the correlation of Wallis [24]. Using these values, the interfacial area ratio can be calculated from Eq. (29) as

$$\frac{a_i}{a_{iw}} \simeq 0.11 \quad . \tag{30}$$

Equation (30) implies the interfacial area of wave region is about ten times as large as the interfacial area of the wave crests. Physically this indicates that the wave length is rather long in comparison with the film thickness.

Now that volume median diameters are correlated by Eq. (26), it is expected that droplet size distribution can be correlated in terms of the similar dimensionless groups as used in Eq. (26). Figures 4 through 13 show droplet size distributions in We/X vs. the volume fraction oversize, Δ, plot. Here the parameter X is given by

$$X = Re_f^{-1/6} \, Re_g^{2/3} \left(\frac{\rho_g}{\rho_f} \right)^{-1/3} \left(\frac{\mu_g}{\mu_f} \right)^{2/3} \quad , \tag{31}$$

and the volume fraction oversize Δ is defined as the volume fraction of droplets whose diameters are larger than D indicated by the Weber number We. Solid lines in Figs. 4 through 13 represent Eqs. (35) and (36) discussed below. Figures 4 through 7 show the data of Wicks and Dukler [29,30], Figs. 8 and 9 show the data of Cousins and Hewitt [31] and Figs. 10 through 12 show the data of Lindsted et al. [32]. Figure 13 shows all the data shown in Figs. 4 through 12 in one figure. As shown in these figures, most of the data for the examination of the droplet size distribution lie within ± 40% of the mean values in the We/X vs. Δ coordinate.

The mean values of the data in Fig. 13 are fitted to the upper limit log-normal distribution proposed by Mugele and Evance [34] and given by

$$\frac{d\Delta}{dy} = - \frac{\xi}{\sqrt{\pi}} e^{-(\xi y)^2} . \tag{32}$$

Here ξ is a distribution parameter, and y is defined in terms of the maximum diameter D_{max} and volume median diameter D_{vm} as

$$y = \ln \frac{kD}{D_{max} - D} , \tag{33}$$

$$k = \frac{D_{max} - D_{vm}}{D_{vm}} . \tag{34}$$

The experimental data in Fig. 13 give $\xi = 0.884$ and $k = 2.13$ (i.e. $\frac{D_{max}}{D_{vm}} = 3.13$). The value of D_{vm} has been correlated by Eq. (26).

Therefore, one obtains a correlation for droplet distribution as

$$\frac{d\Delta}{dy} = - \frac{0.884}{\sqrt{\pi}} e^{-0.781y^2} , \tag{35}$$

with

$$y = \ln \left(\frac{2.13\ D}{D_{max} - D} \right) . \tag{36}$$

Here D_{max} is related to D_{vm} by

$$D_{max} = 3.13\ D_{vm} \quad , \tag{37}$$

and D_{vm} is correlated by the Weber number correlation given by Eq. (26). By using Eq. (37) y can also be expressed in terms of D_{vm} as

$$y = \ln\left(\frac{2.13\ D}{3.13\ D_{vm} - D}\right) \quad . \tag{38}$$

The above correlation for the droplet size distribution implies that the distribution can be uniquely determined by knowing the volume median diameter. Furthermore, the median diameter is a function of the gas and liquid fluxes as indicated by the correlation for D_{vm} given by Eq. (28).

By knowing the size distribution the weighted mean diameter defined below can be calculated.

$$\bar{D}_{nm} = \left[\frac{\int_0^{D_{max}} D^n f(D)\,dD}{\int_0^{D_{max}} D^m f(D)\,dD}\right]^{\frac{1}{n-m}} \quad , \tag{39}$$

where f(D) is a number density distribution function and related to the volume oversize function as follows

$$f(D) = \frac{\frac{1}{D^3}\frac{d\Delta}{dD}}{\int_0^{D_{max}} \frac{1}{D^3}\frac{d\Delta}{dD}\,dD} \quad . \tag{40}$$

Ratios of various mean diameters and D_{vm} or D_{max} are listed in Table II.

As can be seen from Eq. (26) the Weber number is not a strong function of the liquid Reynolds number Re_f. Thus for simplicity, the dependency of We on Re_f may be dropped in the correlation provided Re_f does not vary too widely. The range of the experimental data used in this study is from 100 to 4700 and then $Re_f^{-1/6}$ ranges from 0.46 to 0.24. If we use the mean value i.e., 0.35 instead of $Re_f^{-1/6}$, Eq. (26) reduces to

$$We(D_{vm}) = 0.0099\ Re_g^{2/3} \left(\frac{\rho_g}{\rho_f}\right)^{-1/3} \left(\frac{\mu_g}{\mu_f}\right)^{2/3} \quad . \tag{41}$$

In Fig. 14, experimental data are plotted in $We\ Re_g^{2/3} \left(\frac{\rho_g}{\rho_f}\right)^{-1/3} \left(\frac{\mu_g}{\mu_f}\right)^{2/3}$ vs. volume fraction oversize plane. The solid line in this figure is Eq. (35) where D_{vm} is given by Eq. (41).

By comparing Figs. 13 and 14, it can be said that the simplified correlation given by Eq. (41) is as good as the one given by Eq. (26). This also justifies the simplification proposed above. In this case, the recommended volume median diameter becomes

$$D_{vm} = 0.0099 \frac{\sigma}{\rho_g j_g^2} Re_g^{2/3} \left(\frac{\rho_g}{\rho_f}\right)^{-1/3} \left(\frac{\mu_g}{\mu_f}\right)^{2/3} \quad . \tag{42}$$

Hence the average maximum droplet size is

$$D_{max} = 0.031 \frac{\sigma}{\rho_g j_g^2} Re_g^{2/3} \left(\frac{\rho_g}{\rho_f}\right)^{-1/3} \left(\frac{\mu_g}{\mu_f}\right)^{2/3} \quad . \tag{43}$$

The actual distribution of droplet size is expressed by Eqs. (35) and (36). These four equations describe the droplet size and size distribution in annular droplet flow.

III. 5 CONCLUSIONS

(1) Based on the mechanism of the shearing off of the roll-wave crests, the theoretical model given by Eq. (25) was obtained for the droplet size in annular gas-liquid two-phase flow.

(2) The experimental data of volume median diameters were correlated within ± 40% errors by Eq. (26) which is derived from theoretical Eq. (25) in collaboration with data.

(3) The experimental data of droplet size distributions were correlated within ± 40% errors in $We \Big/ \left[Re_f^{-1/6} \; Re_g^{2/3} \left(\frac{\rho_g}{\rho_f}\right)^{-1/3} \left(\frac{\mu_g}{\mu_f}\right)^{2/3} \right]$ vs. volume fraction oversize coordinate which is obtained from the correlation for the mean diameter and the upper limit log-normal distribution function.

(4) Upper limit log-normal distribution function fitted the experimental data with the distribution parameter $\xi = 0.884$ or the standard deviation of 0.800 and $D_{max}/D_{vm} = 3.13$.

(5) Simplified correlation for the volume median diameter given by $D_{vm} = 0.01 \frac{\sigma}{\rho_g j_g^2} Re_g^{2/3} \left(\frac{\rho_g}{\rho_f}\right)^{-1/3} \left(\frac{\mu_g}{\mu_f}\right)^{2/3}$ correlated the experimental data within ± 40% errors.

NOMENCLATURE

a	Roll wave amplitude
a_i	Interfacial area per unit volume
a_{iw}	Wave area per unit volume
A_d	Projected area of a particle
A_{iw}	Wave area
C_D	Drag coefficient
C_g	Coefficient in Eq. (18)
C_w	Coefficient for internal flow
D	Droplet diameter
D_c	Critical diameter
D_{max}	Maximum diameter
$\bar{D}_{nm}$	Mean diameter defined by Eq. (39)
D_{vm}	Volume median diameter
D_h	Hydraulic equivalent diameter of flow passage
$f(D)$	Number density distribution function
f_i	Liquid interfacial friction factor
F_D	Drag force
g	Acceleration due to gravity
j_f	Liquid volumetric flux (superficial velocity)
j_g	Gas volumetric flux (superficial velocity)
k	Factor in upper limit log-normal distribution
M_{id}	Interfacial force per volume
M_τ	Shear force per unit volume
Re_f	Liquid Reynolds number ($= \rho_f j_f D_h/\mu_f$)
Re_g	Gas Reynolds number ($= \rho_g j_g D_h/\mu_g$)
v_f	Liquid film velocity

v_g	Gas velocity
v_r	Relative velocity between phases
v_∞	Terminal velocity
V_d	Volume of a particle
V_w	Volume of wave regime
We	Weber number
We_c	Critical Weber number
$We(D_{vm})$	Weber number based on volume median diameter
X	Parameter defined by Eq. (31)
y	Parameter defined by Eq. (33)

Greek Symbols

α_d	Volume fraction of a particle
δ	Average film thickness
Δ	Volume fraction oversize
$\Delta\rho$	Density difference
μ_f	Liquid viscosity
μ_g	Gas viscosity
ξ	Distribution parameter in upper limit log-normal distribution
ρ_f	Liquid density
ρ_g	Gas density
σ	Surface tension
τ_i	Interfacial shear stress

Subscripts

d	Particle
D	Drag
i	Interface
f	Liquid
g	Gas
w	Wave

REFERENCES

1. Hewitt, G. F. and Hall-Taylor, N. S., "Annular Two-phase Flow," Pergamon Press, Oxford (1970).

2. Ishii, M. and Mishima, K., "Correlation for Liquid Entrainment in Annular Two-phase Flow of Low Viscous Fluid," Argonne National Laboratory report, ANL/RAS/LWR 80-3 (1980).

3. Collier, J. G., "Burnout in Liquid Cooled Reactors," Nuclear Power, 5, 61 (1961).

4. Petrovichev, V. I., Kokorev, L. S., Didenko, A. Ya. and Dubvrovskiy, G. P., "Droplet Entrainment in Boiling of Thin Liquid Film," Heat Transfer-Soviet Res., 3, 19 (1971).

5. Cousins, L. B., Denton, W. H. and Hewitt, G. E., "Liquid Mass Transfer in Annular Two-phase Flow," Sym. on Two-phase Flow, Vol. 1, paper C4, Exter, England (1965).

6. Tong, L. S., "Boiling Heat Transfer and Two-phase Flow," R. E. Krieger Publishing Co., NY (1975).

7. Hsu, Y. Y. and Graham, R. W., "Transport Process in Boiling and Two-phase Systems," Hemisphere Pub. Co., Washington (1976).

8. Yamanouchi, A., "Effects of Core Spray Cooling at Stationary State After Loss of Coolant Accident," J. Nuclear Sci. & Tech., 5(9), 498 (1968).

9. Semeria, R. and Martinet, "Calefaction Spots on a Heating Wall; Temperature Distribution and Resorption," Sym. on Boiling Heat Trans. in Steam Generating Unit and Heat Exchangers, Proc. Inst. Mech. Engs. 180, 192-205 (1965).

10. Duffey, R., "The Physics of Rewetting in Water Reactor Emergency Core Cooling," Nucl. Eng. Design, 25, 379 (1973).

11. Bennett, A., "The Wetting of Hot Surfaces by Water in a Steam Environment at High Pressure," Atomic Energy Research Establishment, Harwell, AERE-R5146 (1966).

12. Brodkey, R. S., "The Phenomena of Fluid Motion," Addison-Wesley, Reading, MA (1967).

13. Hinze, J. O., "Fundementals of the Hydrodynamic Mechanism of Splitting in Dispersion Process," AIChE J., 1, 289 (1955).

14. Ishii, M. and Grolmes, M. A., "Inception Criteria for Droplet Entrainment in Two-Phase Concurrent Film Flow," AIChE J., 21, 308 (1975).

15. Lamb. H., "Hydrodynamics," Dover, NY (1945).

16. Levich, V. G., "Physicochemical Hydrodynamics," Prentice-Hall, NY (1962).

17. Sevik, M. and Park, S. H., "The Splitting of Drops and Bubbles by Turbulent Fluid Flow," J. of Fluid Eng., 95, 53 (1973).

18. Hanson, A. R., Domich, E. G. and Adams, H. S., "Shock Tube Investigation of the Breakup of Drops by Air Blasts," Physics of Fluids, 6, 1070 (1963).

19. Sleicher, Jr., C. A., "Maximum Stable Drop Size in Turbulent Flow," AIChE J., 8, 471 (1962).

20. Hass, F. C., "Stability of Droplets Suddenly Exposed to a High Velocity Gas Stream," AIChE J., 10, 920 (1964).

21. Lane, W. R., "Shatter of Drops in Streams of Air," Ind. Eng. Chem., 43, 1312 (1951).

22. Taylor, G. I., "The shape and Acceleration of a Drop in a High-Speed Air Stream," paper written for the Advisory Council on Scientific Research and Technical Development, Minstry of Supply (1949).

23. Clift, R., Grace, J. R. and Weber, M. E., "Bubbles, Drops and Particles," Academic Press, NY (1978).

24. Wallis, G. B., "One Dimensional Two-phase Flow," McGraw-Hill, NY (1969).

25. Ishii, M., "One-dimensional Drift-flux Model and Constitutive Equations for Relative Motion between Phases in Various Two-phase Flow Regimes," Argonne National Laboratory report, ANL-77-47 (1977).

26. Yeh, G. C. Y. and Zuber, N., "On the Problem of Liquid Entrainment," Argonne National Laboratory report, ANL-6244 (1960).

27. Ishii, M. and Chawla, T. C., "Local Drag Laws in Dispersed Two-phase Flow," Argonne National Laboratory report, ANL-79-105 (1979).

28. Hughmark, G. A., "Film Thickness, Entrainment and Pressure Drop in Upward Annular and Dispersed Flow," AIChE J., 19, 1012 (1973).

29. Wicks, M. and Dukler, A. E., "In Situ Measurements of Drop Size Distribution in Two-phase Flow," Int. Heat Trans. Conf., Chicago (1966).

30. Wicks, M., "Liquid Film Structure and Drop Size Distribution in Two-phase Flow," Ph.D. Thesis, University of Houston (1967).

31. Cousins, L. B. and Hewitt, G. F., "Liquid Phase Mass Transfer in Annular Two-phase Flow: Droplet Deposition and Liquid Entrainment," AERE-R5657 (1968).

32. Lindsted, R. D., Evans, D. L., Gass, J. and Smith, R. V., "Droplet and Flow Pattern Data, Vertical Two-phase (Air-water) Flow Using Axial Photography," Wichita State University, Department of Mechanical Engineering (1978).

33. Tatterson, D. F., Dallman, J. C. and Hanratty, T. J., "Drop Size in Annular Gas-Liquid Flow," AIChE J., 23, 68 (1977).

34. Mugele, R. A. and Evans, H. D., "Droplet Size Distribution in Sprays," Ind. Eng. Chem., 43, 1317 (1951).

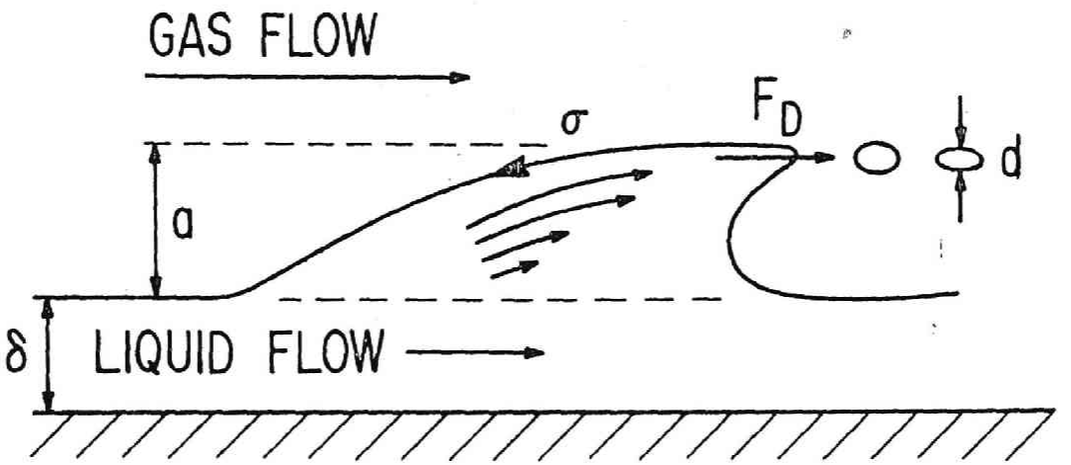

Fig. 1. Mechanism of the Shearing off of Roll-Wave

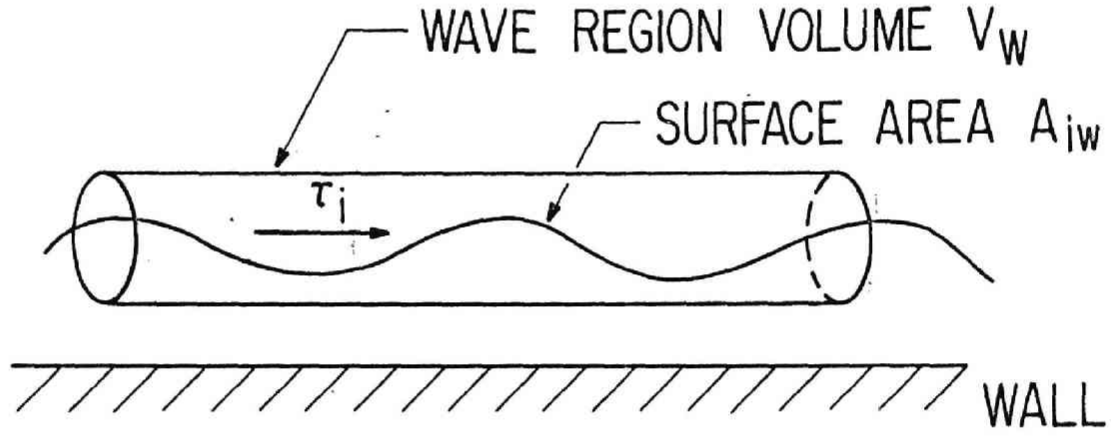

Fig. 2. Illustrative Figure of a Neighborhood of a Wave Region

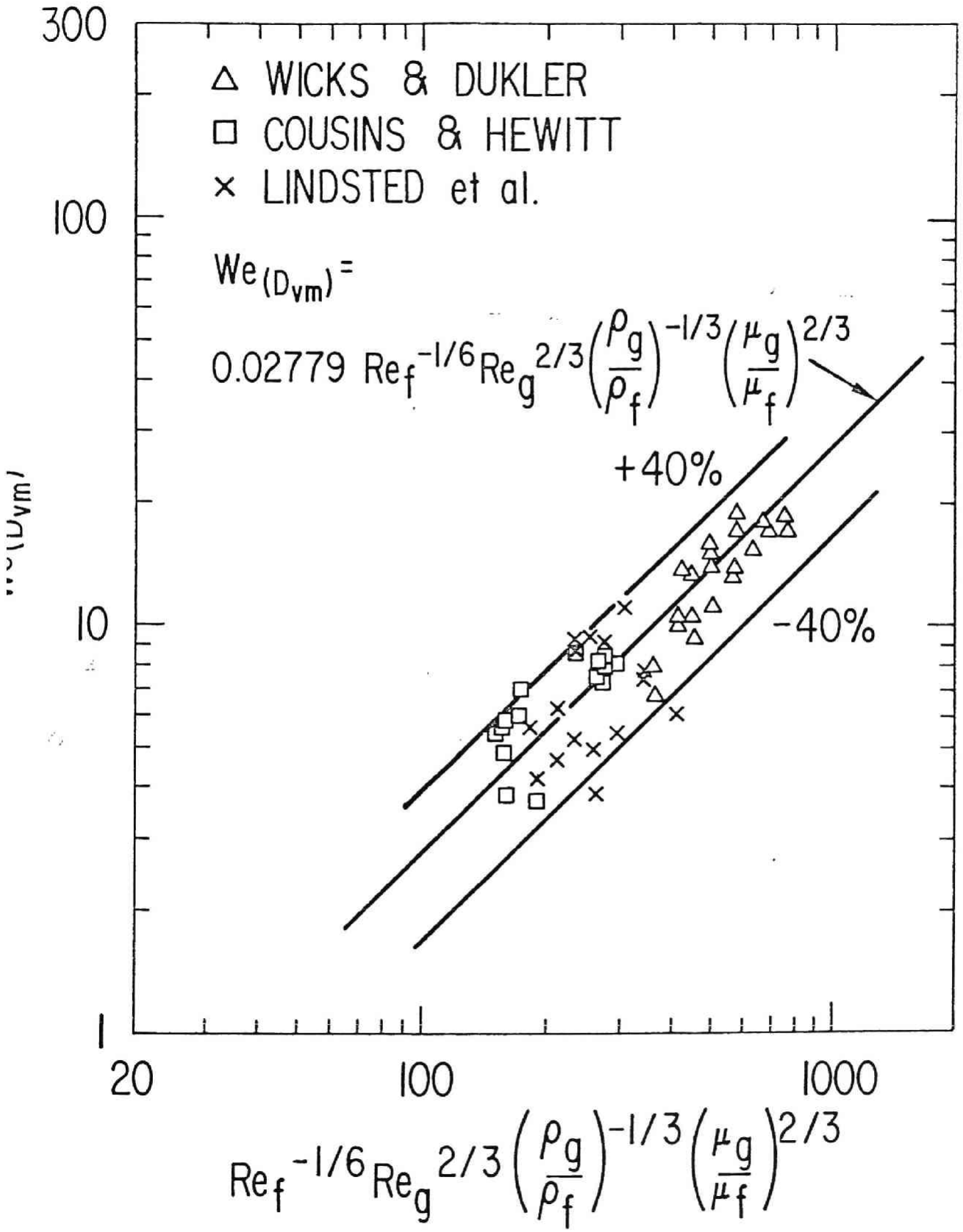

Fig. 3. Comparison of Volume Median Diameter Correlation to Various Data

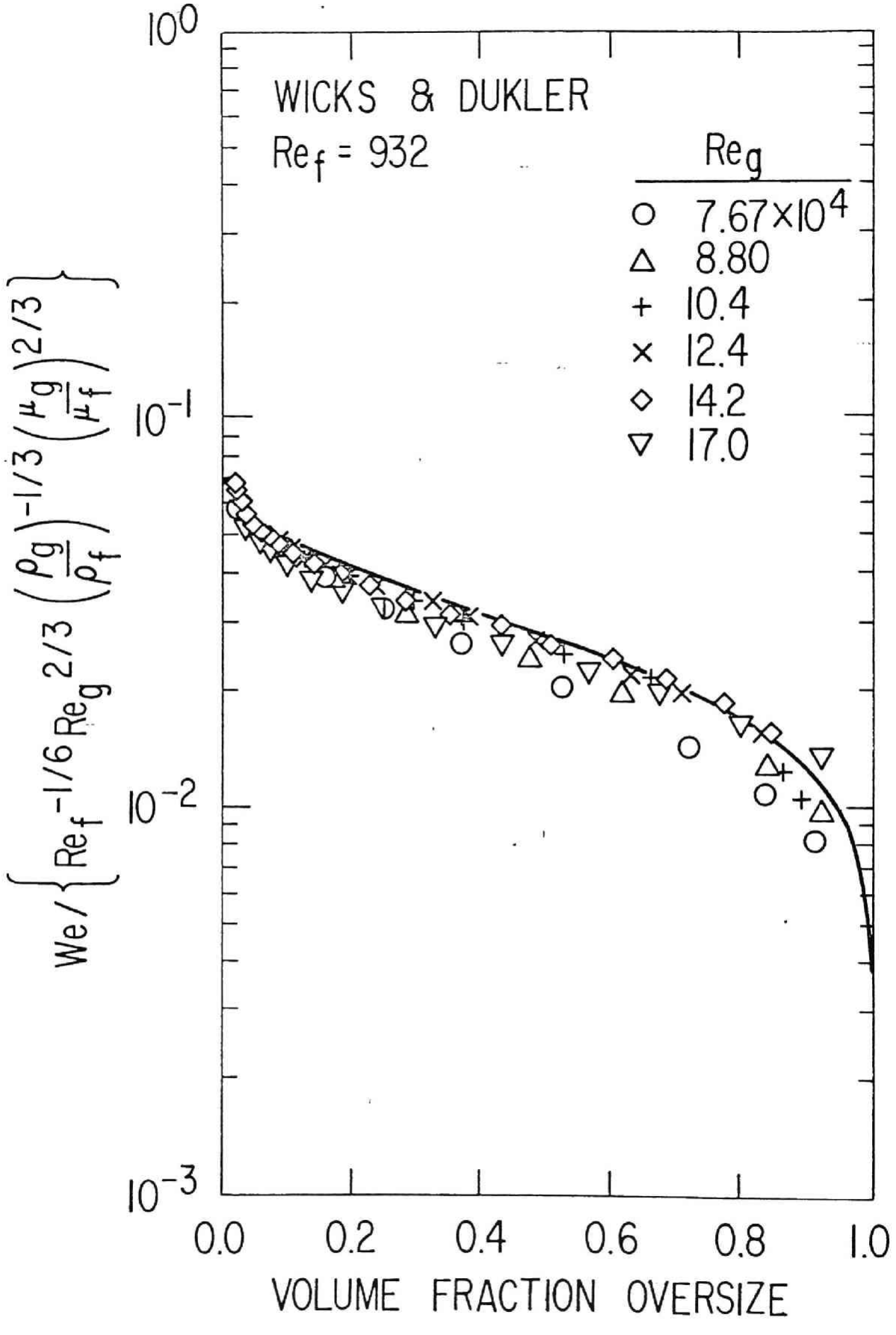

Fig. 4. Droplet Size Distributions at Re_f = 932 for Data of Wicks and Dukler [29,30]

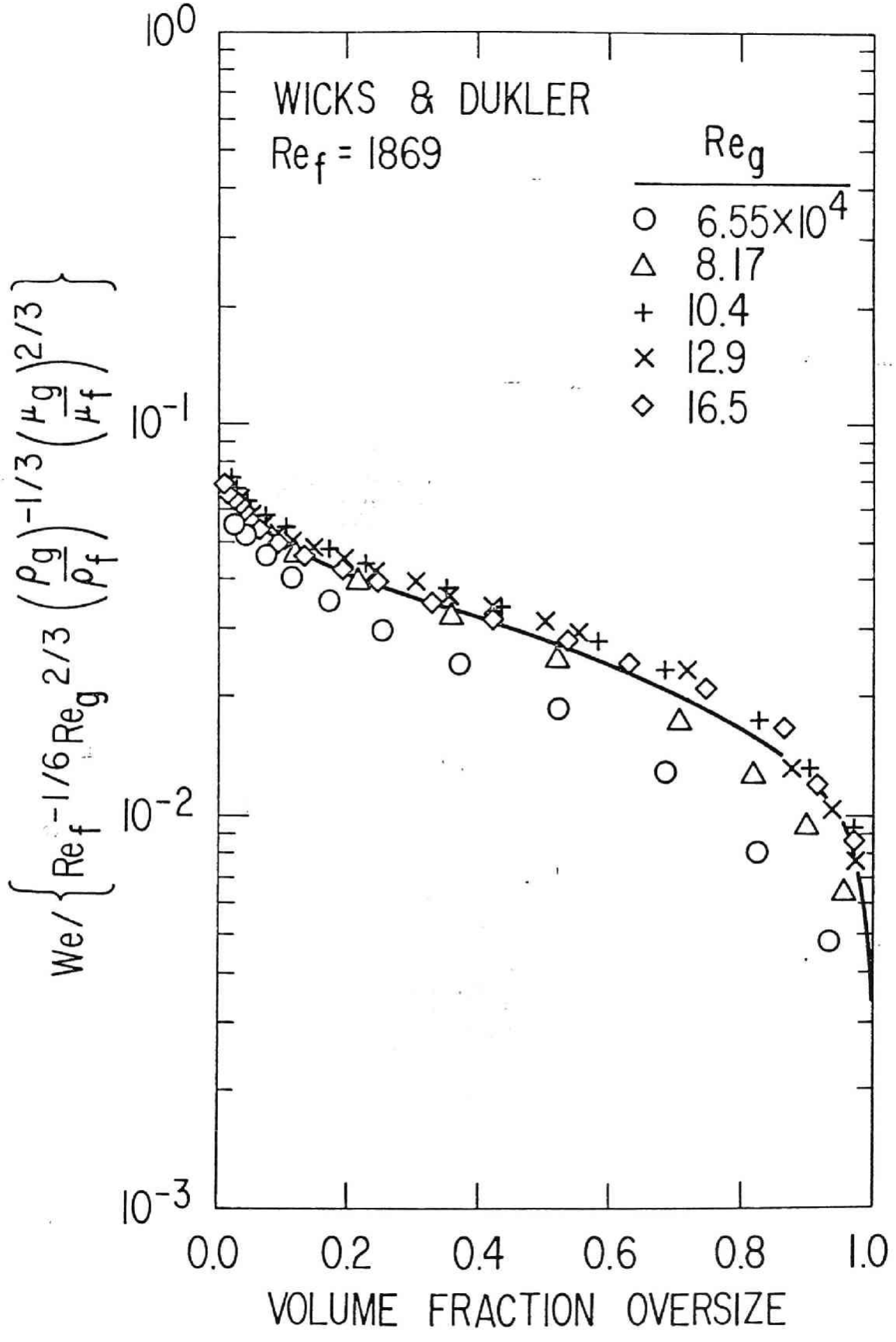

Fig. 5. Droplet Size Distributions at Re_f = 1869 for Data of Wicks and Dukler [29,30]

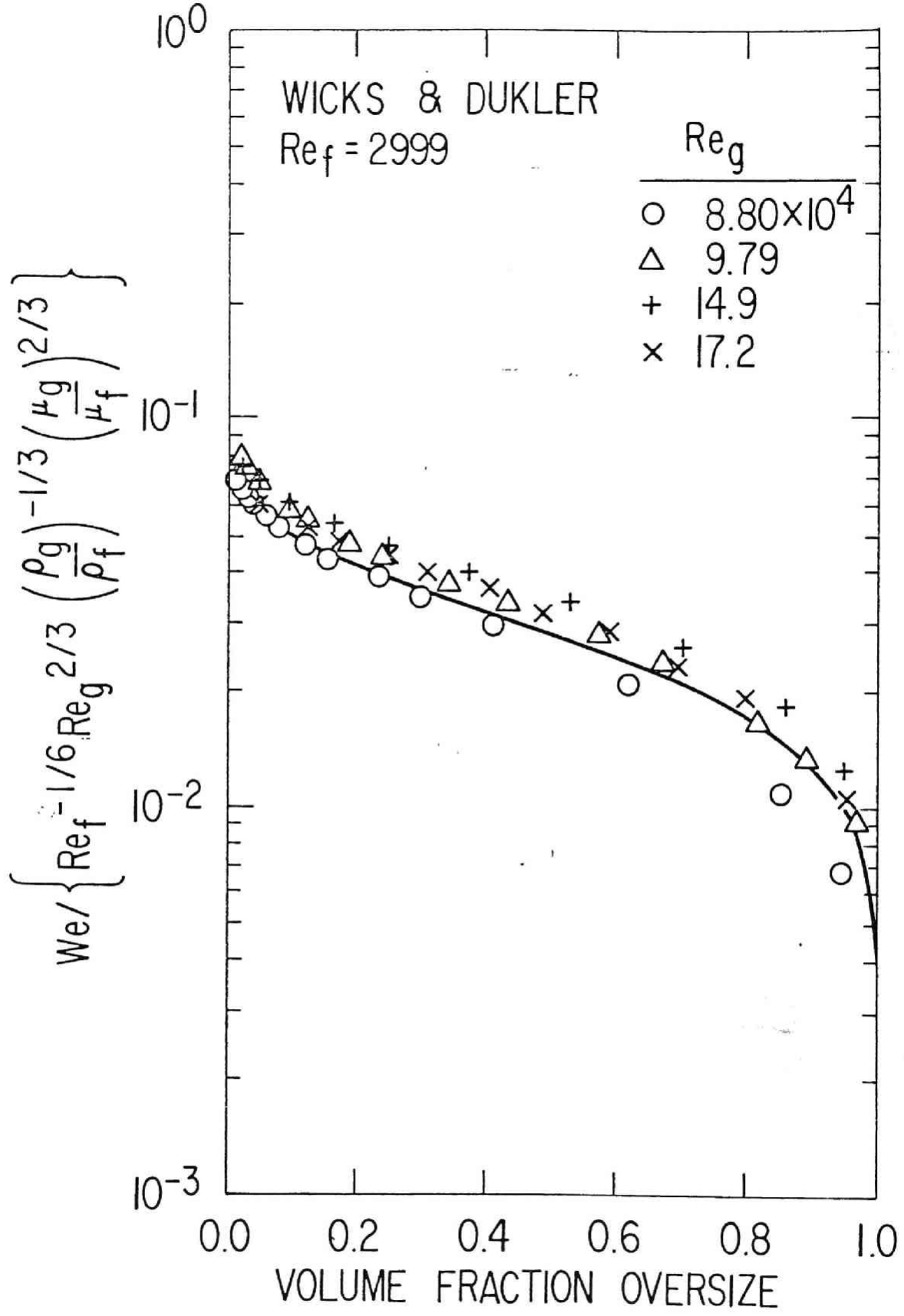

Fig. 6. Droplet Size Distributions at Re_f = 2999 for Data of Wicks and Dukler [29,30]

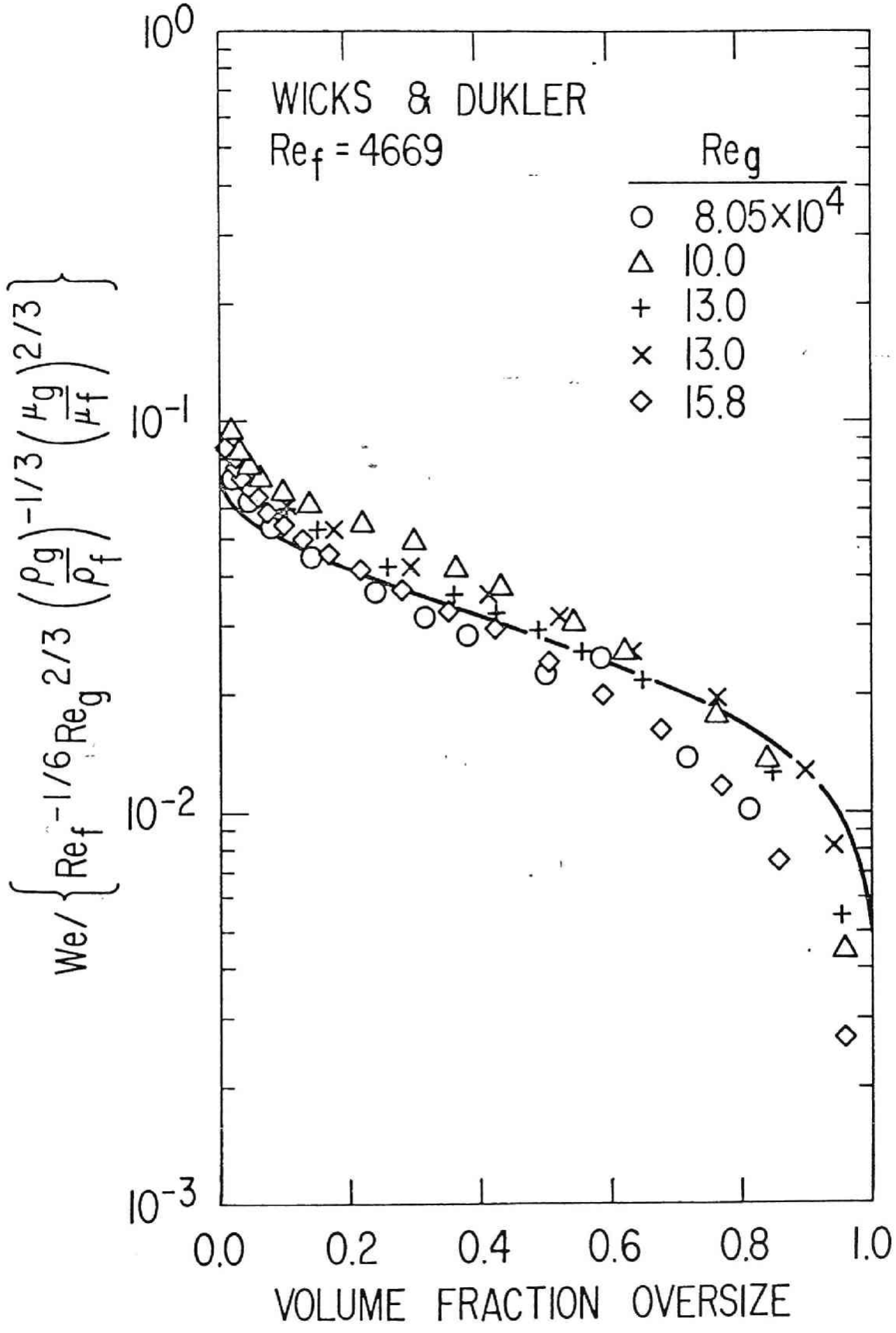

Fig. 7. Droplet Size Distributions at Re_f = 4669 for Data of Wicks and Dukler [29,30]

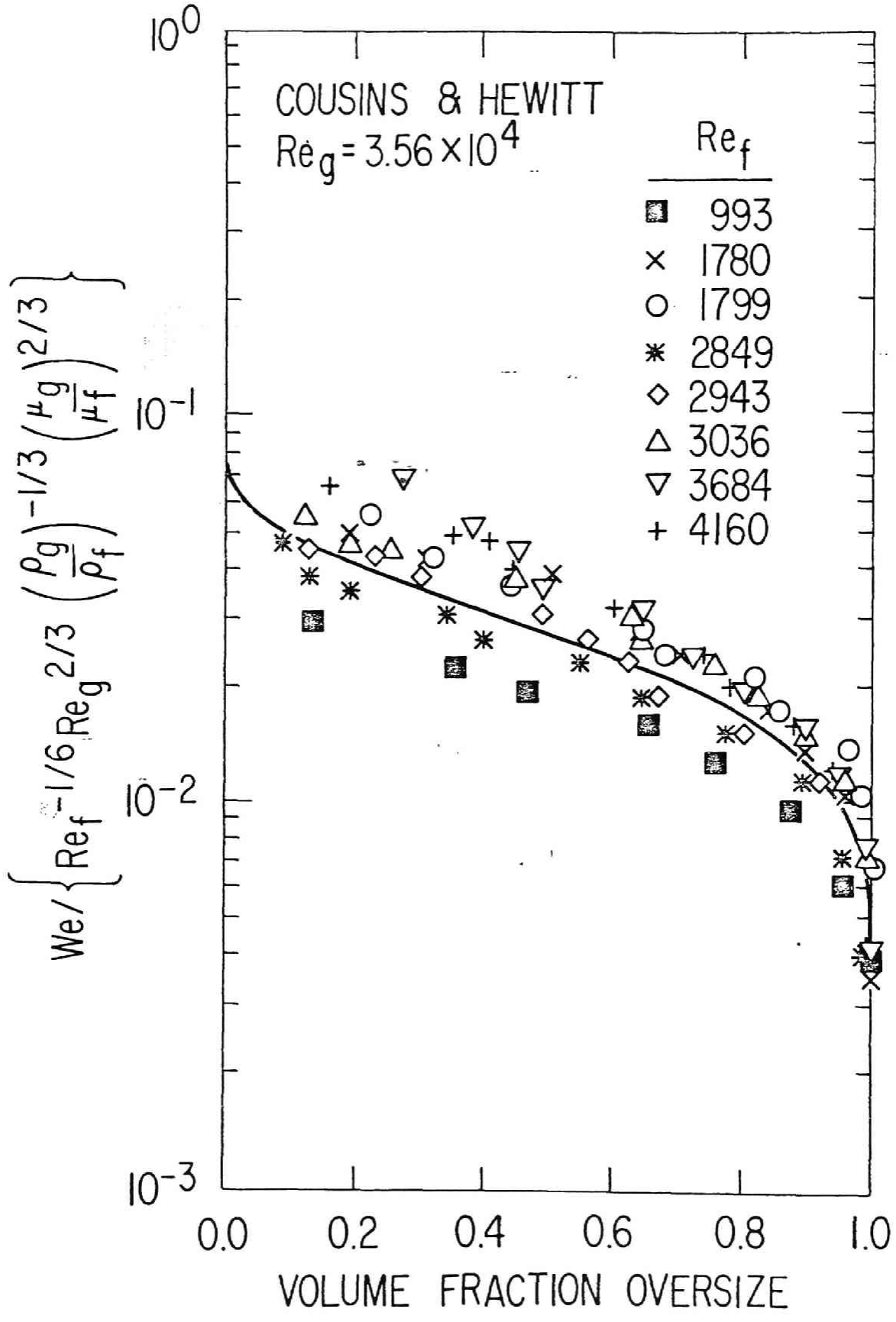

Fig. 8. Droplet Size Distributions at $Re_g = 3.56 \times 10^4$ for Data of Cousins and Hewitt [31]

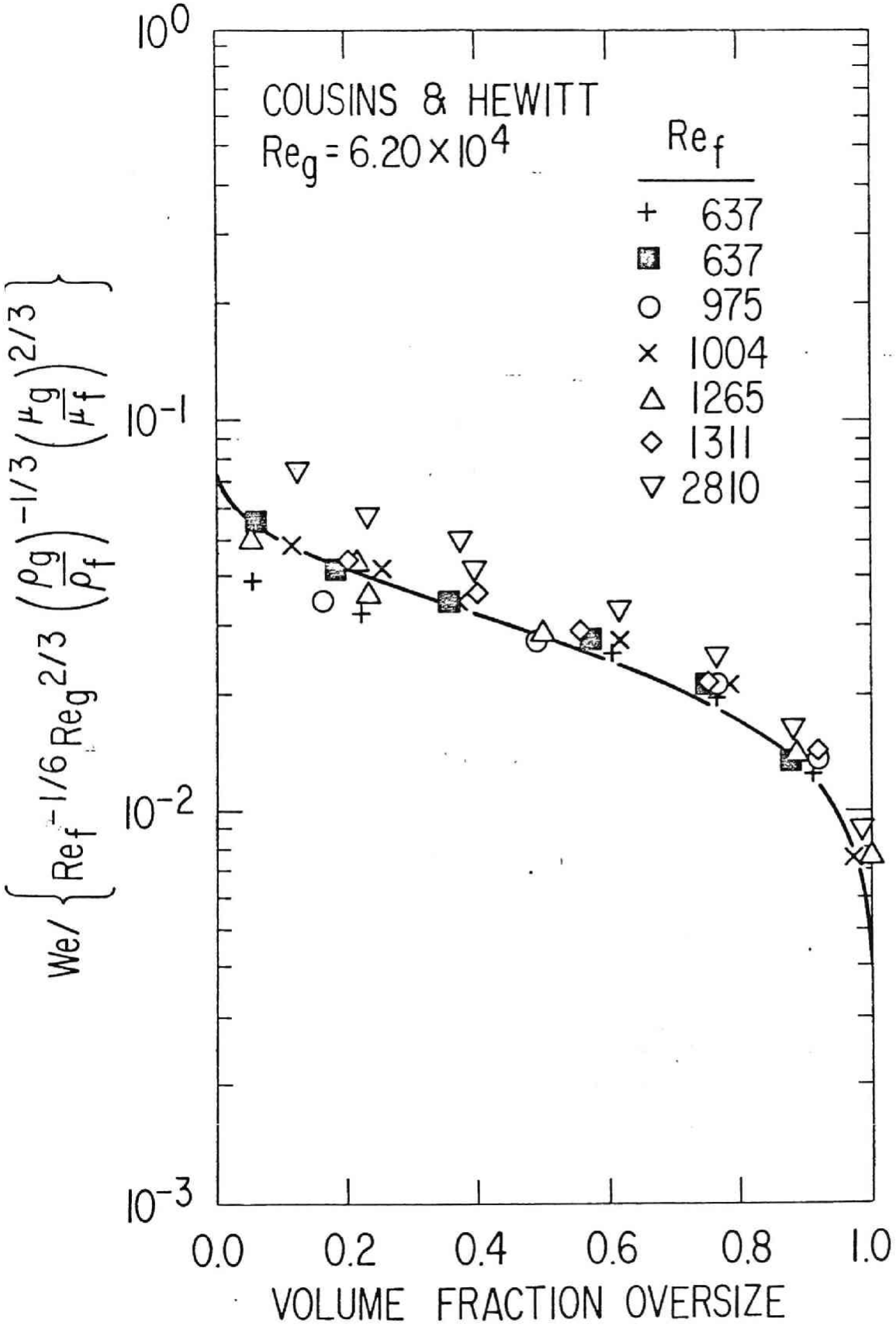

Fig. 9. Droplet Size Distributions at $Re_g = 6.20 \times 10^4$ for Data of Cousins and Hewitt [31]

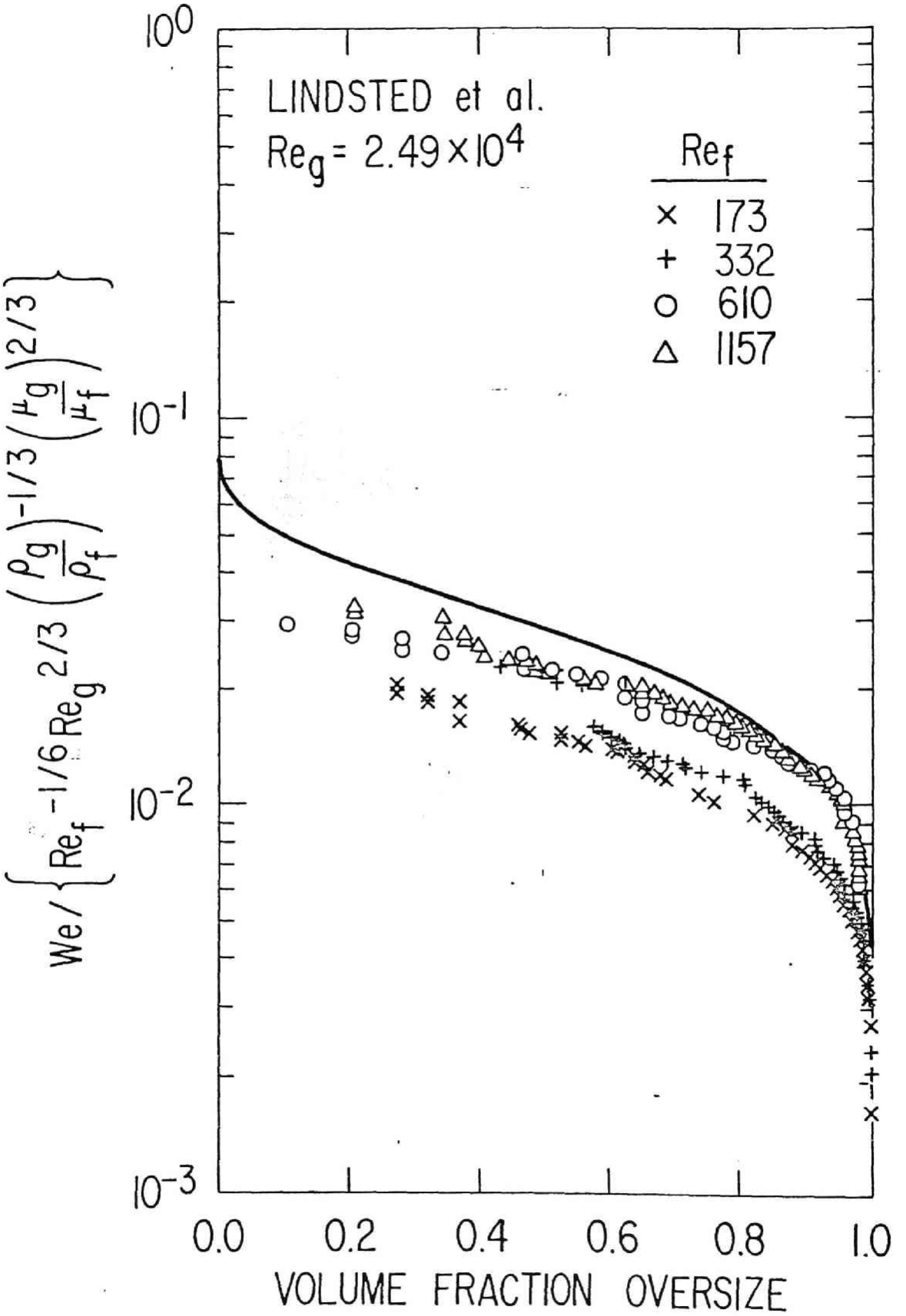

Fig. 10. Droplet Size Distributions at $Re_g = 2.49 \times 10^4$ for Data of Lindsted et al. [32]

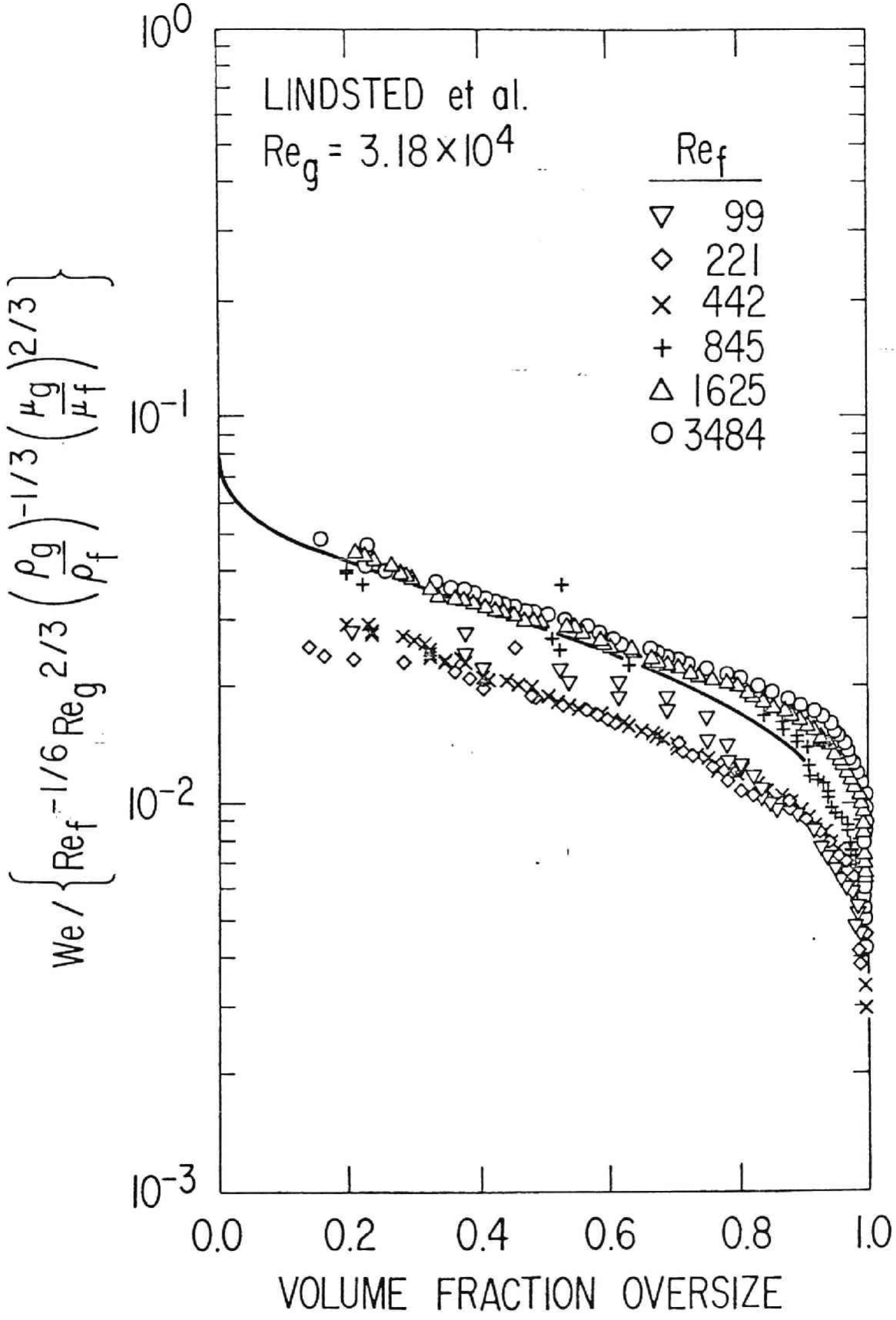

Fig. 11. Droplet Size Distributions at $Re_g = 3.18 \times 10^4$ for Data of Lindsted et al. [32]

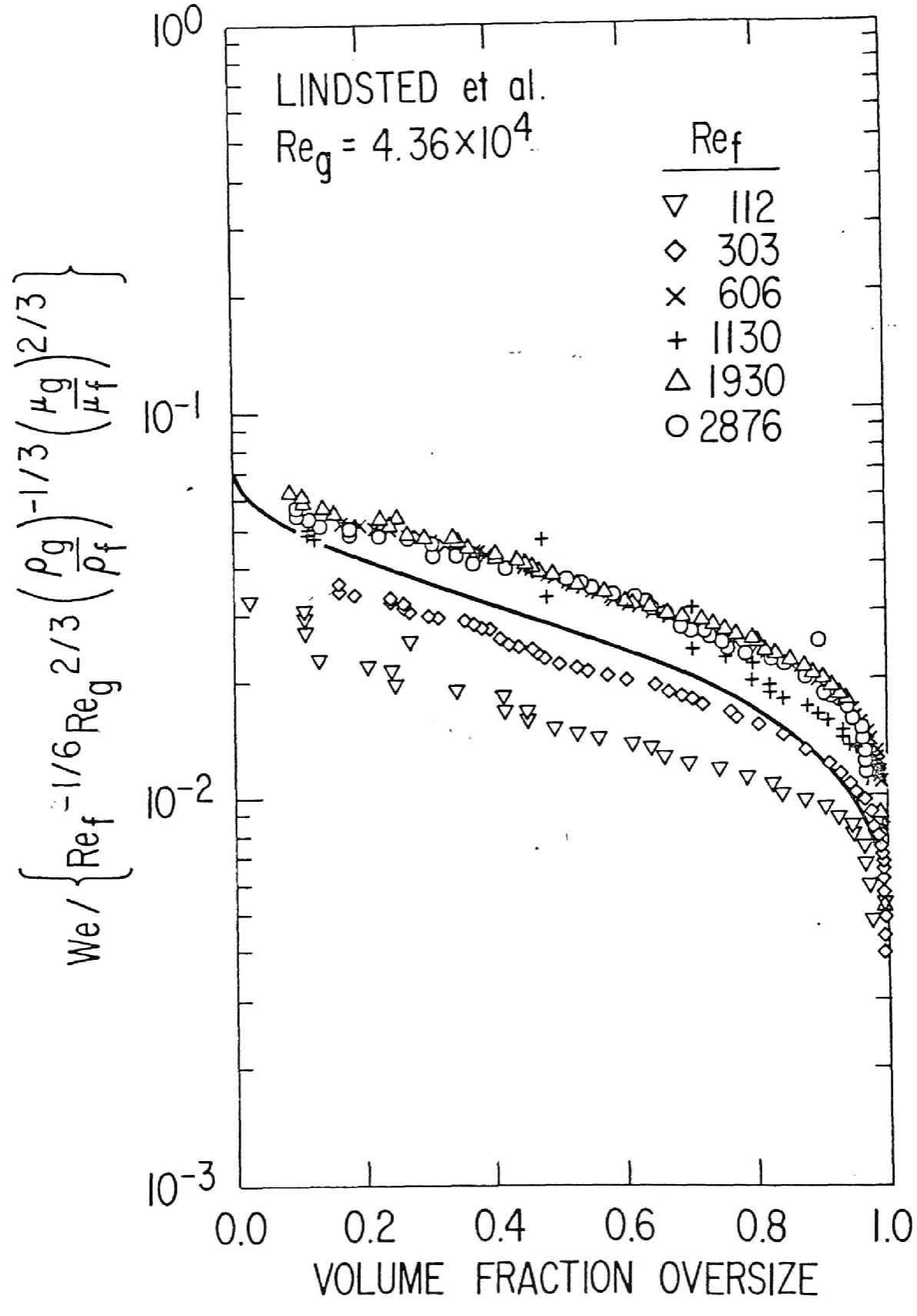

Fig. 12. Droplet Size Distributions at $Re_g = 4.36 \times 10^4$ for Data of Lindsted et al. [32]

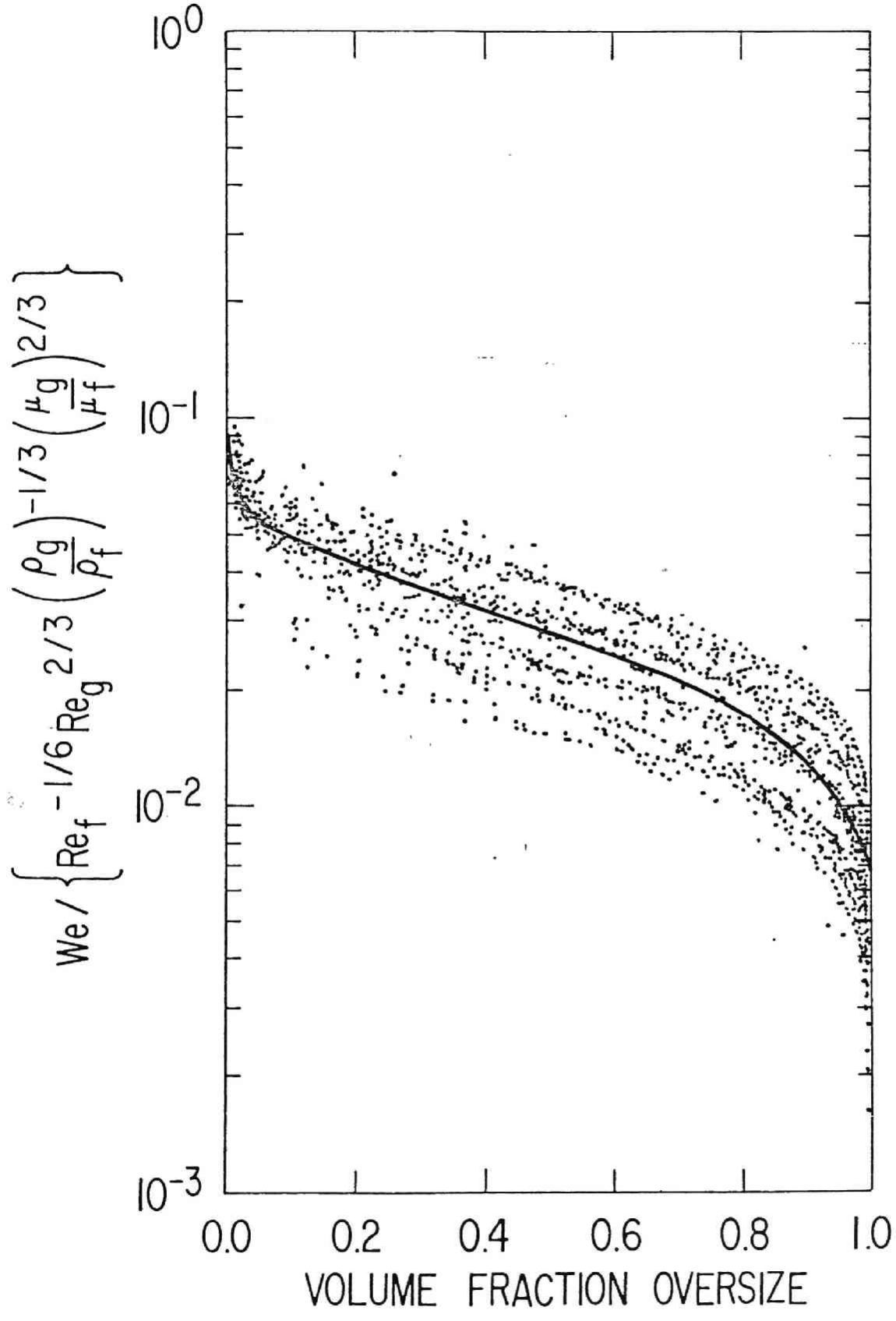

Fig. 13. Droplet Size Distributions in $We \Big/ \left[Re_f^{-1/6} \, Re_g^{2/3} \left(\frac{\rho_g}{\rho_f}\right)^{-1/3} \left(\frac{\mu_g}{\mu_f}\right)^{2/3} \right]$ vs. Volume Fraction Oversize Plot for Data of Wicks and Dukler [29,30], Cousins and Hewitt [31] and Lindsted et al. [32]

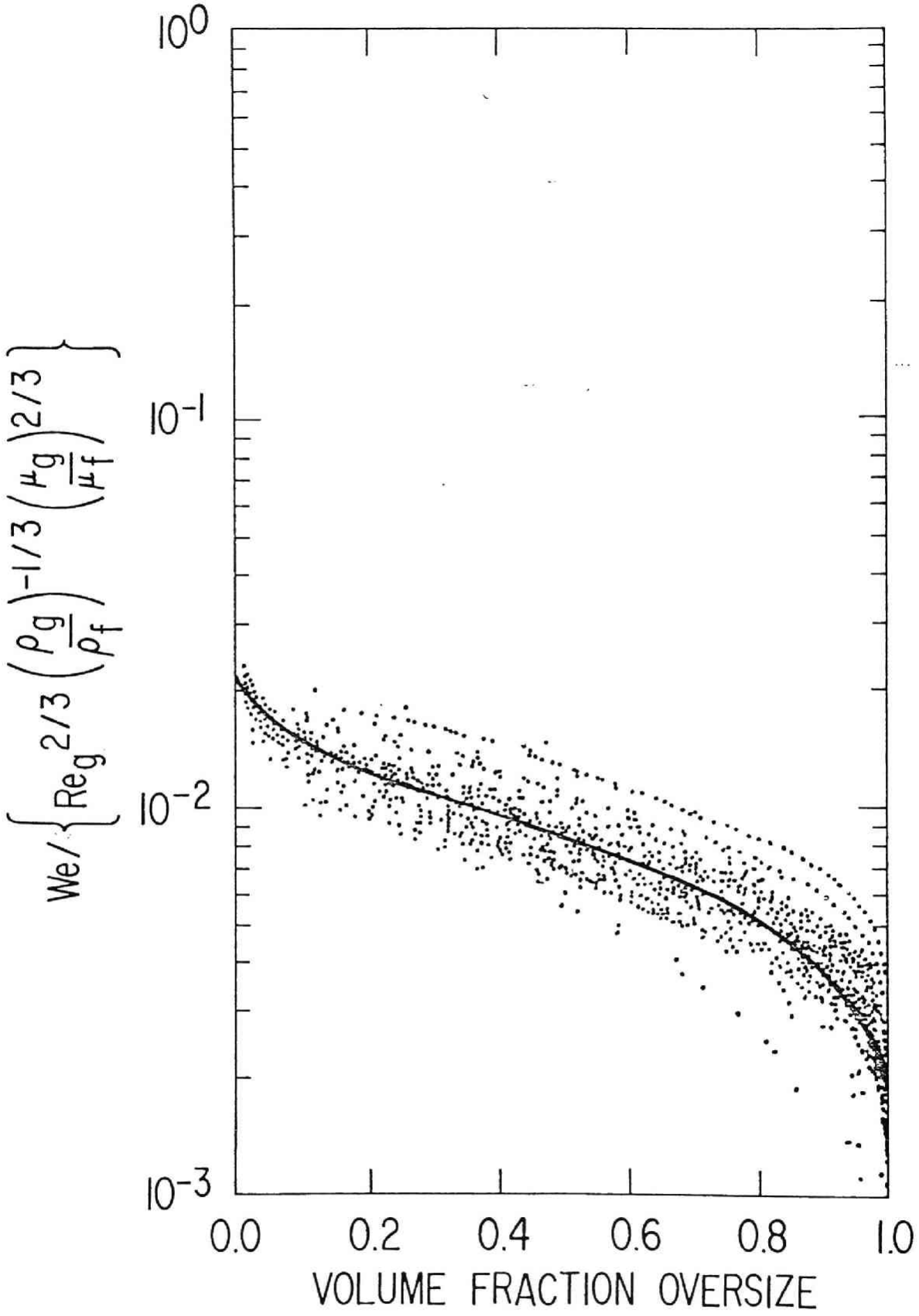

Fig. 14. Droplet Size Distributions in $We\Big/\left[Re_g^{2/3}\left(\frac{\rho_g}{\rho_f}\right)^{-1/3}\left(\frac{\mu_g}{\mu_f}\right)^{2/3}\right]$ vs. Volume Fraction Oversize Plot for Data of Wicks and Dukler [29,30], Cousins and Hewitt [31] and Lindsted et al. [32]

Table I. Summary of Various Experiments on Droplet Size Distribution

Reference	Fluids	Geometry	Flow Direction	Measurement	Operational Condition
Wicks and Dukler [29] (1966) Wicks [30] (1967)	Air-Water	1.9 × 15 cm Channel	Vertical Down	Electrical Conductance Probe	1 atm Re_f = 930 ∿ 9700 Re_g = 6.6 ∿ 17 × 10^4
Cousins and Hewitt [31] (1968)	Air-Water	0.95 cm Tube	Vertical Up	Photography	2 atm Re_f = 640 ∿ 4200 Re_g = 3.6 ∿ 6.2 × 10^4
Lindsted et al. [32] (1978)	Air-Water	3.2 cm Tube	Vertical Up	Photography	1 atm Re_f = 100 ∿ 3500 Re_g = 2.5 ∿ 4.4 × 10^4

Table II. Various Mean Diameters*

Ratio of diameter A and diameter B

A / B	$\bar{D}_{10}$	$\bar{D}_{20}$	$\bar{D}_{21}$	$\bar{D}_{30}$	$\bar{D}_{31}$	$\bar{D}_{32}$	$\bar{D}_{43}$	D_{vm}	D_{max}
D_{vm}	0.313	0.409	0.533	0.510	0.650	0.796	1.064	1.0	3.129
D_{max}	0.100	0.131	0.170	0.163	0.208	0.254	0.340	0.320	1.0

*$\bar{D}_{10}$; Linear mean diameter

$\bar{D}_{20}$; Surface mean diameter

$\bar{D}_{21}$; Surface diameter mean diameter

$\bar{D}_{30}$; Volume mean diameter

$\bar{D}_{31}$; Volume diameter mean diameter

$\bar{D}_{32}$; Sauter Mean diameter

$\bar{D}_{43}$; De Brouckere mean diameter

CHAPTER IV

ENTRAINMENT RATE IN ANNULAR TWO-PHASE FLOW

Ⅳ. 1 INTRODUCTION

As mentioned in the previous chapter, an accurate knowledge of the hydrodynamics of an annular and annular dispersed flow is the key factor in analysing the transient boiling and two-phase flow phenomena associated with a LOCA in a nuclear reactor. Mass, momentum and energy transfer processes in the annular and annular dispersed flow are strongly affected by the amount of droplet in the streaming gas flowing in the flow core [1,2]. In particular, an accurate knowledge of entrainment is indispensable for the prediction of dryout and post dryout heat transfer [3-8] and for the evaluation of the effectiveness of emergency core cooling in light water reactors [9-12].

Based on the mechanistic model of shearing off of roll-wave by the streaming gas, correlations are obtained for the inception of droplet entrainment [13], and for the amount of entrained droplet for a steady state flow condition [2]. The mean droplet size and its distribution [14] which are the important parameters in analysing the heat and mass transfer processes in boiling two-phase flow with high steam quality have been investigated in the previous chapter.

On the other hand, the liquid film flow rate on a heated surface is another important parameter in evaluating the heat and mass transfer and the dryout heat flux in annular and annular dispersed flow. The amount of the liquid film flow rate is determined by the integral balance between the droplet entrainment rate and the deposition rate. As for the deposition rate of droplet in a streaming gas, there have been many experimental and theoretical works and satisfactory correlations have been developed [1,15-28]. However, the process of the entrainment seems more complicated and thus the efforts to develop a reliable entrainment rate correlation have not been very successful. The lack of such a correlation has been the main difficulty of a detailed analysis of various phenomena in transient annular two-phase flow or in a post dryout regime. The main objective of this chapter is to develop a reliable correlation for entrainment rate from the liquid film. In the case of LWR transients and accidents, annular flow or droplet flow may be encountered under various conditions. Therefore, a general correlation covering a wide range of flow conditions including entrance effects is highly desirable. As a first step, an entrainment rate correlation has been developed for relatively low viscous fluid such as water where the entrainment of droplets is generated mainly by the shearing-off of roll wave crests.

IV. 2 PREVIOUS WORKS

In annular two-phase flow for low viscous fluid and for relatively high film Reynolds number ($Re_f \geq 160$), the mechanism of entrainment is basically the shearing-off of roll wave crests by a highly turbulent gas flow [13,29].

Based on the modeling of this mechanism, an onset of entrainment criterion [13] and a correlation for the amount of entrained droplet [2] have been developed. After establishing the basic parameters governing the entrainment process, the correlation has been obtained in collaboration with a large number of data. In addition to being accurate under steady state conditions, this correlation also indicated basic mechanisms of entrainment processes and parametric dependencies. A correlation for entrainment in the entrance region and for the necessary distance for the development of entrainment have also been obtained [2]. These supply valuable information on the process of entrainment. Detailed reviews of the other correlations for the amount of droplet entrainment have been given by Hewitt and Hall-Taylor [1] and Ishii and Mishima [2].

The amount of entrained drop represents the integral effects of the rate processes of entrainment and deposition. Therefore, it is considered that the amount of entrainment is a more stable parameter to measure and correlate than the entrainment rate. However, the above discussed correlation is suitable to quasi steady state conditions and under certain transient conditions its application can lead to considerable errors. From this point of view, Hutchinson and Whalley [31] and Whalley et al. [32] developed the entrainment rate correlation. The deposition rate $\dot{d}$ can be linearly related to the droplet concentration in the gas core by

$$\dot{d} = k\, C \ , \tag{1}$$

where k is the mass transfer coefficient and C is the droplet mass concentration in the gas core. Therefore, the entrainment rate has been related to the equilibrium concentration C_∞ by

$$\dot{\varepsilon} = k\, C_\infty \ . \tag{2}$$

Then the equilibrium concentration has been correlated by

$$C_{\infty} = C_{\infty}\left(\frac{\tau_i \delta}{\sigma}\right) , \tag{3}$$

where τ_i, δ and σ are the interfacial shear, film thickness, and surface tension, respectively.

Although this correlation method is conceptually right and it is more mechanistic than the correlation for the amount of entrainment, there are some difficulties associated with it. The first one is related to the development of the correlation for the equilibrium concentration C_{∞}. The data showed considerable scattering which can be up to more than one order of magnitude, particularly at small values of $\tau_i \delta/\sigma$. This suggests that a single dimensionless group used to correlate C_{∞} is not sufficient. Furthermore, in many entrainment experiments such parameters as C_{∞} and δ are not measured directly, thus some modeling to deduce data to useful forms has been necessary.

Ueda [33] presented the entrainment rate correlation in a similar manner as the above mentioned correlation. His correlation is dimensional and given by

$$\dot{\varepsilon} = 3.54 \times 10^{-3}\left[\frac{\tau_i}{\sigma}\left(\frac{j_f}{\sigma}\right)^{0.60}\right]^{0.57} , \tag{4}$$

for

$$\frac{\tau_i}{\sigma}\left(\frac{j_f}{\sigma}\right)^{0.6} \geq 120 , \tag{5}$$

where $\dot{\varepsilon}$ is in Kg/m^2S, τ_i in N/m^2, σ in N/m, and j_f in m/s. Although Eq. (4) correlates his experimental data, it is dimensional and parameter (j_f/σ) is not based on physical mechanisms of entrainment. Therefore, it is expected that the correlation may not apply to general cases.

It can be said that existing correlations for entrainment rate are not satisfactory. However, the entrainment rate are more mechanistic parameters representing the true transfer of mass at the wavy interfaces than the entrainment fraction. Particularly for analyzing the entrance and developing flow regions or transient flow, an accurate entrainment rate correlation is indispensable. In view of the highly reliable correlation for the amount of entrainment [2] which has been developed previously from a simple modeling,

it has been thought that a sufficient understanding of the entrainment mechanism exists to extend the model to the rate processes of entrainment. Thus an attempt has been made to develop an entrainment rate correlation based on physical modeling in this study.

IV. 3 BASIC EQUATION FOR ENTRAINMENT RATE

For annular dispersed two-phase flow one may write the following mass balance equation at the interface under steady state and without phase change conditions.

$$\dot{\varepsilon} = \frac{D\rho_f j_f}{4}\left(\frac{\partial E}{\partial z}\right) + \dot{d} \quad , \tag{6}$$

where $\dot{\varepsilon}$ and $\dot{d}$ are entrainment rate and deposition rate per unit interfacial area (in Kg/m^2sec), respectively, and z is a distance from inlet. E is the entrainment fraction defined as

$$E = \frac{W_{fe}}{W_f} = \frac{j_{fe}}{j_f} \quad , \tag{7}$$

where W_{fe}, W_f, j_{fe}, and j_f are droplet mass flow rate, total mass flow rate, droplet volumetric flux, and total liquid volumetric flux, respectively.

Deposition rate for the diffusion controlled deposition process may be given approximately by

$$\dot{d} \doteq k\, C \quad , \tag{8}$$

where C is the droplet concentration in the core and k is the mass transfer coefficient. There have been many theoretical and experimental works on the mass transfer coefficient k and several reliable correlations have been developed [15-28].

In the present analysis, Paleev and Fillipovich's correlation [19] is used. Their correlation is given by

$$\frac{k}{j_g} = 0.022\, Re_g^{-0.25}\left(\frac{C}{\rho_f}\right)^{-0.26}\left(\frac{\rho_g}{\rho_f}\right)^{0.26} \quad , \tag{9}$$

where $Re_g \equiv \rho_g\, j_g\, D/\mu_g$. On the other hand, the droplet mass concentration C, which is the droplet mass per unit mixture volume, is defined by the following expression (see Appendix A).

$$C = \rho_f \frac{j_{fe} v_g}{j_g v_{fe} + j_{fe} v_g} \quad , \tag{10}$$

or by introducing the entrainment fraction $E = j_{fe}/j_f$,

$$C = \frac{\rho_f E j_f v_g/(j_g v_{fe})}{1 + E j_f v_g/(j_g v_{fe})} \quad . \tag{11}$$

Assuming that the droplet velocity in the gas core is approximately equal to the gas velocity, Eq. (11) can be simplified to

$$C \doteq \rho_f \frac{E \frac{j_f}{j_g}}{1 + E \frac{j_f}{j_g}} \quad . \tag{12}$$

In annular two-phase flow, the liquid volumetric flux is much less than the gas volumetric flux, that is

$$\frac{j_f}{j_g} << 1 \quad . \tag{13}$$

Furthermore, since E is between 0 and 1,

$$E \frac{j_f}{j_g} << 1 \quad . \tag{14}$$

Then Eq. (12) is approximated by

$$C \doteq \rho_f E \frac{j_f}{j_g} \quad . \tag{15}$$

From Eqs. (8), (9), and (15), the deposition rate correlation can be simplified to

$$\frac{\dot{d}}{\rho_f j_f} = 0.022 \, Re_g^{-0.25} \left(E \frac{j_f}{j_g}\right)^{0.74} \left(\frac{j_g}{j_f}\right) \left(\frac{\rho_g}{\rho_f}\right)^{0.26} , \tag{16}$$

$$\doteq 0.022\ Re_f^{-0.26} \left(\frac{\mu_g}{\mu_f}\right)^{0.26} E^{0.74} \quad . \tag{17}$$

By substituting Eq. (17) into Eq. (6), the entrainment rate becomes

$$\dot{\varepsilon} = \frac{D\rho_f j_f}{4} \left(\frac{\partial E}{\partial z}\right) + 0.022\ \rho_f j_f\ Re_f^{-0.26} \left(\frac{\mu_g}{\mu_f}\right)^{0.26} E^{0.74} \quad . \tag{18}$$

Equation (18) indicates that knowing the entrainment fraction distribution along the flow direction, one can calculate the entrainment rate. In the following sections, entrainment rate is calculated from the existing entrainment fraction correlation in collaboration with experimental data.

IV. 4 ENTRAINMENT RATE CORRELATION

Ishii and Mishima [2] developed a correlation for entrainment fraction based on the mechanistic model of shearing-off of roll wave crest by a streaming gas. The fraction of liquid flux flowing as droplets, E, is correlated in terms of two dimensionless groups given by;

Weber Number for Entrainment

$$We = \frac{\rho_g j_g^2 D}{\sigma} \left(\frac{\Delta\rho}{\rho_g}\right)^{1/3} , \tag{19}$$

Total Liquid Reynolds Number

$$Re_f = \frac{\rho_f j_f D}{\mu_f} . \tag{20}$$

The entrained fraction reaches a quasi-equilibrium value, E_∞, at points far removed from the tube entrance where the entrainment and deposition processes attain an equilibrium condition. The distance necessary to reach this condition is given approximately by

$$z \simeq 440\ D\ We^{0.25}/Re_f^{0.5} , \tag{21}$$

for cases with smooth liquid injection. At this entrance length the entrainment has reached within about 2% of its ultimate value. Then for the region $z \gtrsim 440\ D\ We^{0.25}/Re_f^{0.5}$ the correlation becomes

$$E = E_\infty = \tanh\left(7.25 \times 10^{-7}\ We^{1.25}\ Re_f^{0.25}\right) . \tag{22}$$

This correlation has been compared to many experimental data for air-water systems in the ranges of $1 < p < 4$ atm, $0.95 < D < 3.2$ cm, $370 < Re_f < 6400$, and $j_g < 100$ m/sec, and the result has shown to be satisfactory. The various parametric dependencies have been explained in terms of physical mechanisms.

Some experimental data indicated the strong entrance effect as well as the gas expansion effect due to the axial pressure drop in a low pressure system. For the correlation development it was essential to use a local gas velocity or volumetric flux based on a local pressure in evaluating data. By separating these two effects, an additional correlation for the entrance

effect on entrainment have been developed. As mentioned above, the entrance region is given by $0 < z < 440\ D\ We^{0.25}/Re_f^{0.5}$. The correlation takes a typical form of an exponential relaxation, and it essentially reaches the quasi-equilibrium value given by E_∞ for large values of z. Thus for the case of liquid being injected smoothly as a film at inlet, the entrainment develops according to

$$E = (1 - e^{-1.87 \times 10^{-5}\ \zeta^2})E_\infty \quad . \tag{23}$$

Here ζ is the dimensionless distance given by

$$\zeta = \frac{z}{D} Re_f^{0.5}/We^{0.25} \quad . \tag{24}$$

Because of the nature of the above equation this correlation is not limited to the entrance region, but it can be used as a general correlation everywhere. A number of data from the entrance region have been successfully correlated by this expression.

The above entrainment fraction correlation can be used to evaluate the value of E as well as the dependency of E on z in Eq. (18). Thus by substituting Eq. (23) into Eq. (18), one obtains

$$\dot{\varepsilon} = 0.935 \times 10^{-5}\ \zeta\ e^{-1.87 \times 10^{-5}\ \zeta^2} \cdot \rho_f j_f Re_f^{0.5}\ We^{-0.25}\ E_\infty$$

$$+ 0.022\ \rho_f j_f Re_f^{-0.26} \left(\frac{\mu_g}{\mu_f}\right)^{0.26} E_\infty^{0.74} (1 - e^{-1.87 \times 10^{-5}\ \zeta^2})^{0.74} \tag{25}$$

Figure 1 shows entrainment rate calculated by Eq. (25) for air-water systems and We = 2000 and $Re_f = 100 \sim 10{,}000$. In the above correlation, the entrainment rate is expressed in terms of the operational conditions and the distance from the entrance. However, for a truely universal entrainment rate correlation, it is desirable that the $\dot{\varepsilon}$ is expressed by local flow conditions alone rather than by a combination of the operational conditions and the axial location. For this purpose several modifications are made on the above equation by taking account of some important limiting conditions.

By considering a quasi-equilibrium region where $\zeta >> 1$, the above equation can be reduced to the expression for equilibrium entrainment rate $\dot{\varepsilon}_\infty$ as

$$\dot{\varepsilon}_\infty = 0.022\ \rho_f j_f Re_f^{-0.26} \left(\frac{\mu_g}{\mu_f}\right)^{0.26} E_\infty^{0.74} \quad . \tag{26}$$

By rearranging the above equation, one can obtain

$$\frac{\dot{\varepsilon}_\infty D}{\mu_f} = 0.022\ Re_f^{0.74} \left(\frac{\mu_g}{\mu_f}\right)^{0.26} E_\infty^{0.74} \quad . \tag{27}$$

Since $\dot{\varepsilon}_\infty$ is the mass flux normal to an interface due to entrainment, $\dot{\varepsilon}_\infty D/\mu_f$ can be considered as the entrainment Reynolds number.

The above equation shows that the rate of entrainment depends on the total liquid Reynolds number, viscosity ratio, and entrainment fraction E_∞. The fraction of entrainment under a quasi-equilibrium condition is given by Eq. (22) which shows the dependence of E_∞ on We and total liquid Reynolds number Re_f. However, it is also possible to interpret the existence of E_∞ in Eq. (27) as representing the local dynamical condition at the interface. In that case, it is more meaningful to rewrite the expression for E_∞, Eq. (22), in terms of the local film Reynolds number defined by

$$Re_{ff} \equiv \frac{\rho_f j_{ff} D}{\mu_f} \quad , \tag{28}$$

where j_{ff} is the film liquid volumetric flux. Since by definition $j_f = j_{fe} + j_{ff}$, and $j_{ff} = (1 - E)j_f$, one obtains

$$Re_{ff\infty} = Re_f\ (1 - E_\infty) \quad , \tag{29}$$

and

$$Re_{ff} = Re_f\ (1 - E) \quad , \tag{30}$$

where ∞ denotes the equilibrium condition.

By substituting Eq. (29) into Eq. (22), one gets

$$E_\infty = \tanh \left[7.25 \times 10^{-7}\ We^{1.25}\ Re_{ff\infty}^{0.25}/(1 - E_\infty)^{0.25}\right] . \tag{31}$$

Thus

$$7.25 \times 10^{-7}\ We^{1.25}\ Re_{ff\infty}^{0.25} = \frac{1}{2}\,(1 - E_\infty)^{0.25}\ \ell n\left(\frac{1 + E_\infty}{1 - E_\infty}\right). \qquad (32)$$

However, it is easy to show that the right hand side of Eq. (32) can be approximated as

$$\frac{1}{2}\,(1 - E_\infty)^{0.25}\ \ell n\left(\frac{1 + E_\infty}{1 - E_\infty}\right) \simeq 0.9355\ E_\infty\ , \qquad (33)$$

for a wide range of E_∞ from 0 up to 0.97. Then, from Eqs. (32) and (33) one obtains

$$E_\infty \simeq 7.75 \times 10^{-7}\ We^{1.25}\ Re_{ff\infty}^{0.25}\ . \qquad (34)$$

By eliminating E_∞ between Eqs. (27) and (34), the rate of entrainment becomes

$$\frac{\dot{\varepsilon}_\infty D}{\mu_f} = 6.6 \times 10^{-7}\ Re_f^{0.74}\ Re_{ff\infty}^{0.185}\ We^{0.925}\left(\frac{\mu_g}{\mu_f}\right)^{0.26}\ . \qquad (35)$$

The above correlation shows that the entrainment rate depends on the total liquid Reynolds number, local film Reynolds number, local Weber number based on the hydraulic diameter, and the viscosity ratio. This correlation has been developed from the equilibrium entrainment fraction and deposition rate correlations. Although these correlations are based on steady state data, several observations can be made. Except at the entrance region, the entrainment and deposition processes may be considered as local phenomena which can be determined by the local parameters. Hence, if the rate correlations are expressed in terms of local parameters such as the local film Reynolds number and droplet mass concentration, it is expected that these correlations may be extended to nonequilibrium or unsteady conditions.

Based on this hypothesis which is commonly accepted except in very rapid transient situations, the equilibrium entrainment rate correlation is extended to more general case except at the entrance region. Thus replacing $\dot{\varepsilon}_\infty$ by ε in Eq. (35), the general entrainment rate correlation is given by

$$\frac{\dot{\varepsilon} D}{\mu_f} = 6.6 \times 10^{-7} \, Re_f^{0.74} \, Re_{ff}^{0.185} \, We^{0.925} \left(\frac{\mu_g}{\mu_f}\right)^{0.26}, \qquad (36)$$

for regions away from the entrance, i.e., $z \gtrsim 440 \, D \, We^{0.25}/Re_f^{0.5}$.

The above correlation indicates that the entrainment rate is roughly proportional to the effective Weber number based on the hydraulic diameter and to the liquid Reynolds number. These appear to correctly reflect the true physical mechanism of entrainment. The entrainment under consideration is caused by shearing-off of roll wave crests by gas core flow. Therefore, it is expected that the entrainment rate is proportional to an interfacial drag force or to j_g^2. The drag force is also proportional to roughness of the interface or the wave amplitude which may be related to the liquid Reynolds numbers. The correlation given by Eq. (36) indicates that $\dot{\varepsilon} \sim Re_f^{0.925}$ when the entrainment fraction is small. However, as the entrainment increases the liquid film Reynolds number Re_{ff} should decrease. The expected decrease in the entrainment rate as the film becomes thinner is reflected on the dependence of ε on Re_{ff}. At the limiting case of $Re_{ff} \to 0$, the correlation predicts the right limit of $\varepsilon \to 0$.

Although, as a first approximation, Eq. (36) can also be used in the entrance region, a more careful study on the transient and memory effects are needed. From this point of view, the entrainment rate in the entrance region and the validity of this correlation in the entrance region are studied in the next section.

IV. 5 ENTRAINMENT RATE IN ENTRANCE REGION

IV.5.1 General Formulation of Entrainment Rate

The correlation for entrainment at the entrance section given by Eq. (25) is developed for the case of the smooth injection of liquid as a film. In this particular case, the amount of entrainment gradually increases from zero to the equilibrium value with the distance from the inlet. From this entrainment correlation the rate of entrainment can be obtained. Although this rate applies only to the case with excess liquid on the film, compared to the equilibrium condition, the generalization of the model can be possible and will be discussed later.

From Eq. (23) the nondimensional distance parameter ζ can be expressed in terms of E/E_∞ as

$$\zeta = 231 \sqrt{\ell n[1/(1 - E/E_\infty)]} \quad . \tag{37}$$

By eliminating ζ in Eq. (25) in view of Eq. (37), and using Eq. (34), one obtains

$$\frac{\dot{\varepsilon} D}{\mu_f} = 1.67 \times 10^{-9} \, Re_f^{1.5} \, Re_{ff\infty}^{0.25} \, We \sqrt{\ell n \frac{1}{(1 - E/E_\infty)}} \left(1 - \frac{E}{E_\infty}\right)$$

$$+ 6.6 \times 10^{-7} \, Re_f^{0.74} \, Re_{ff\infty}^{0.185} \, We^{0.925} \left(\frac{\mu_g}{\mu_f}\right)^{0.26} \left(\frac{E}{E_\infty}\right)^{0.74} \quad . \tag{38}$$

As shown in Fig. 1, because of the existence of the first term on the right hand side, Eq. (38) gives much higher value of the entrainment rate than Eq. (36) for large Re_f and We in the entrance region where $E/E_\infty < 1$. The above rate correlation is a rather complicated function of E/E_∞, therefore, some modifications are made to obtain a simplified correlation in entrance region. By considering the entrainment rate in entrance region, where $E/E_\infty < 1$, as a function of E/E_∞, one can assume the following functional form for the entrainment rate

$$\frac{\dot{\varepsilon} D}{\mu_f} = f\,(E/E_\infty) + \left(\frac{\dot{\varepsilon} D}{\mu_f}\right)_\infty \quad , \tag{39}$$

where the equilibrium rate is given by Eq. (36).

Since $\dot{\varepsilon}$ approaches $\dot{\varepsilon}_\infty$ when $E/E_\infty \to 1$, $f(E/E_\infty)$ must approach zero as $E/E_\infty \to 1$. Furthermore, $f(E/E_\infty)$ is an additional term which should appear only for an entrance region where $E/E_\infty \leq 1$. In other words, $f(E/E_\infty)$ should be zero when the entrainment exceeds that of the equilibrium value. Hence

$$\begin{cases} f(E/E_\infty) = 0 & \text{for } E/E_\infty > 1 \\ f(1) = 0 \end{cases} , \quad (40)$$

The above two conditions can be explained in terms of the entrainment mechanisms as follows. When the liquid film flow is above the equilibrium value, i.e., $Re_{ff} > Re_{ff\infty}$, there is an extra entrainment force in addition to the equilibrium rate expressed by Eq. (36). The excess liquid flow in the film or $(Re_{ff} - Re_{ff\infty})$ acts as a driving force to promote the entrainment.

The exact form of the function $f(E/E_\infty)$ based on the entrainment correlation of Ishii and Mishima [2] is given by

$$f(E/E_\infty) = 1.67 \times 10^{-9}\, Re_f^{1.5}\, Re_{ff\infty}^{0.25}\, We \sqrt{\ell n \frac{1}{(1 - E/E_\infty)}} \left(1 - \frac{E}{E_\infty}\right) . \quad (41)$$

Several observations can be made with respect to Eq. (41). The function $f(E/E_\infty)$ is zero at $E = 0$ and E_∞ and has a maximum at $E/E_\infty \simeq 0.4$. Thus

$$Max(f) = 0.718 \times 10^{-9}\, Re_f^{1.5}\, Re_{ff\infty}^{0.25}\, We \quad . \quad (42)$$

This occurs at $\zeta \doteq 160$. It indicates that the extra entrainment force is very small for extremely low values of E. Some experimental data support the existence of this very small value of $f(E/E_\infty)$ at the very vicinity of the inlet as shown in the following discussion of experimental data. This low level of entrainment at high liquid film flow at the entrance may be attributed to the finite distance needed for the development of interfacial waves and entrainment. However, because of this, the entrainment mechanism in this region is strongly dependent on the geometry of the inlet itself.

In view of the above, this very vicinity of the inlet is neglected in the following simple model development. It is assumed that the function

$f(E/E_\infty)$ takes the maximum value at $E/E_\infty \to 0$ and the function is approximated by the following form.

$$f(E/E_\infty) = \begin{cases} 0.718 \times 10^{-9}\ Re_f^{1.5}\ Re_{ff\infty}^{0.25}\ We\ (1 - E/E_\infty)^2 & \text{for } E/E_\infty \leq 1 \\ 0 \quad \text{for } E/E_\infty > 1 \ . \end{cases} \tag{43}$$

This form indicates that the driving force for this extra entrainment is $(1 - E/E_\infty)^2$. Thus the value of $f(E/E_\infty)$ is higher for a larger deviation of E from the equilibrium value E_∞.

Substituting Eqs. (36) and (43) into Eq. (39), and using the relation $Re_{ff} = Re_f\ (1 - E)$, one finally obtains the entrainment rate correlation for $E/E_\infty \leq 1$ given by

$$\frac{\dot{\varepsilon} D}{\mu_f} = 0.72 \times 10^{-9}\ Re_f^{1.75}\ We\ (1 - E_\infty)^{0.25} \left(1 - \frac{E}{E_\infty}\right)^2 + 6.6 \times 10^{-7}\ (Re_f\ We)^{0.925} \left(\frac{\mu_g}{\mu_f}\right)^{0.26} (1 - E)^{0.185} , \tag{44}$$

and for $E/E_\infty > 1$ by

$$\frac{\dot{\varepsilon} D}{\mu_f} = 6.6 \times 10^{-7}\ (Re_f\ We)^{0.925} \left(\frac{\mu_g}{\mu_f}\right)^{0.26} (1 - E)^{0.185} , \tag{45}$$

where E_∞ is given by Eq. (31).

However, from Eqs. (29), (30), and (34) it can be shown that

$$\left(1 - \frac{E}{E_\infty}\right) = \frac{Re_{ff} - Re_{ff\infty}}{7.75 \times 10^{-7}\ We^{1.25}\ Re_{ff\infty}^{0.25}\ Re_f} , \tag{46}$$

where Re_{ff} and $Re_{ff\infty}$ are the local film Reynolds number and the equilibrium film Reynolds number, respectively. Hence by substituting Eq. (46) into Eq. (44) the entrainment rate correlations can be expressed in terms of the liquid film Reynolds numbers as follows. For $Re_{ff} \geq Re_{ff\infty}$

$$\frac{\dot{\varepsilon}D}{\mu_f} = 1.2 \times 10^3 \, Re_f^{-0.5} \, Re_{ff\infty}^{-0.25} \, We^{-1.5} \, (Re_{ff} - Re_{ff\infty})^2$$

$$+ 6.6 \times 10^{-7} \, Re_f^{0.74} \, Re_{ff}^{0.185} \, We^{0.925} \left(\frac{\mu_g}{\mu_f}\right)^{0.26} . \qquad (47)$$

And for $Re_{ff} < Re_{ff\infty}$

$$\frac{\dot{\varepsilon}D}{\mu_f} = 6.6 \times 10^{-7} \, Re_f^{0.74} \, Re_{ff}^{0.185} \, We^{0.925} \left(\frac{\mu_g}{\mu_f}\right)^{0.26} . \qquad (48)$$

The first expression applies to the case when the amount of entrainment is below the equilibrium value, whereas the second expression applies to the case for $E > E_\infty$. The extra entrainment rate over the equilibrium rate is given by the first term of the right hand side of Eq. (47). It is proportional to $(Re_{ff} - Re_{ff\infty})^2$, and, therefore, this quantity roughly represents the additional driving force for entrainment through the excess kinetic energy of the film over the equilibrium state. The results seem to be appropriate, since the more the excess kinetic energy is, the more intense the turbulent level at the interface. This should then lead to an increased entrainment rate when the excess liquid is flowing as a film, i.e., $Re_{ff} > Re_{ff\infty}$.

IV.5.2 Entrance Effect and Experimental Data

As indicated by Eq. (18), entrainment rate is obtained by knowing the entrainment amount as a function of the axial distance from the inlet. Cousins et al. [18], Gill and Hewitt [20], and Gill et al. [17] carried out the experiments in which amount of entrainment was measured at various positions from the inlet with relatively smooth injection of liquid as a film [17,18] and with injection of droplets through an axial jet [20]. The amount of entrainment was found to be very sensitive to the inlet conditions. Entrainment rate in the entrance region is considered to be quite different when inlet conditions are different. Because of the differences in the liquid film thickness, the development of the roll wave in the film are supposed to be considerably different with different inlet conditions.

In collaboration with the data of Cousins et al. [18] and Gill et al. [17], and Eq. (18) the entrainment rates with smooth injection of liquid

as a film are obtained. In calculating $\frac{\partial E}{\partial z}$, the gas expansion effect due to the axial pressure drop should be carefully distinguished from the entrance effect itself. Therefore, the following procedure of calculation was taken. The amount of entrainment is a function of z and j_g which is a function of z because of gas expansion effects. Then

$$E = E\,(z,\ j_g(z)) \quad . \tag{49}$$

Differentiating Eq. (49), one obtains

$$\frac{dE}{dz} = \frac{\partial E}{\partial z} + \frac{\partial E}{\partial j_g}\frac{dj_g}{dz} \quad . \tag{50}$$

Then $\frac{\partial E}{\partial z}$ is given

$$\frac{\partial E}{\partial z} = \frac{dE}{dz} - \frac{\partial E}{\partial j_g}\frac{dj_g}{dz} \quad . \tag{51}$$

The right hand side of Eq. (51) can be calculated by measured entrainment amount and measured pressure drop along the axial position.

Figure 2 shows $\frac{\partial E}{\partial z}$ calculated by numerically differentiating the data of Cousins et al. [18] and Gill et al. [17]. The solid line in Fig. 2 represents the derivative of Ishii and Mishima's correlation [2] which is given by

$$\frac{\left(\frac{\partial E}{\partial z}\right) D\ We^{0.25}}{E_\infty\ Re_f^{0.5}} = 3.74 \times 10^{-5}\ \zeta\ e^{-1.87 \times 10^{-5}\ \zeta^2} \quad . \tag{52}$$

Figures 3 through 7 show some of the entrainment rates obtained from the experimental data of Cousins et al. [18] and Gill et al. [17]. The entrainment rate increases with increasing liquid Reynolds number and with increasing effective Weber number. As for the entrance effects, the entrainment rate increasing with decreasing E/E_∞. This tendency is more eminent for larger Re_f and We. Solid lines in Figs. 3 through 7 represent Eq. (44) or (47). Although data scatters considerably due to the numerical differentiation, the present correlation well reproduces the experimental trends.

Figures 8 through 12 show the comparison of the entrainment rate obtained from the experimental data of Cousins et al. [18] and Gill et al. [17] with those predicted by Eq. (44). In the ranges of Re_f from 273 to 5041, We from 1414 to 9602, and diameter from 0.0095 m to 0.032 m, most of the data fall within $\pm$ 40% of Eq. (44) or (47).

Now that entrainment rate correlation Eq. (44) is obtained, one can calculate entrainment amount by integrating rate equation which is given by

$$\frac{\partial E}{\partial z} = \frac{4}{D\rho_f j_f}(\dot{\varepsilon} - \dot{d}) \quad . \tag{53}$$

Substituting Eqs. (17) and (47) into Eq. (53), one obtains for $Re_{ff} \geq Re_{ff\infty}$

$$\frac{\partial E}{\partial (z/D)} = 4.80 \times 10^3 \, Re_f^{-1.5} \, Re_{ff\infty}^{-0.25} \, We^{-1.5} \, (Re_{ff} - Re_{ff\infty})^2$$

$$+ 2.64 \times 10^{-6} \, Re_f^{-0.26} \, Re_{ff}^{0.185} \, We^{0.925} \left(\frac{\mu_g}{\mu_f}\right)^{0.26}$$

$$- 0.088 \, Re_f^{-0.26} \left(\frac{\mu_g}{\mu_f}\right)^{0.26} \left(1 - \frac{Re_{ff}}{Re_f}\right)^{0.74} \quad . \tag{54}$$

And for $Re_{ff} < Re_{ff\infty}$

$$\frac{\partial E}{\partial (z/D)} = 2.64 \times 10^{-6} \, Re_f^{-0.26} \, Re_{ff}^{0.185} \, We^{0.925} \left(\frac{\mu_g}{\mu_f}\right)^{0.26}$$

$$- 0.088 \, Re_f^{-0.26} \left(\frac{\mu_g}{\mu_f}\right)^{0.26} \left(1 - \frac{Re_{ff}}{Re_f}\right)^{0.74} \quad . \tag{55}$$

This equation can be rewritten in terms of E as follows. For $E/E_\infty \leq 1$

$$\frac{\partial E}{\partial (z/D)} = 2.87 \times 10^{-9} \, Re_f^{0.5} \, Re_{ff\infty}^{0.25} \, We \left(1 - \frac{E}{E_\infty}\right)^2$$

$$+ 2.64 \times 10^{-6} \, Re_f^{-0.075} \, We^{0.925} \left(\frac{\mu_g}{\mu_f}\right)^{0.26} (1 - E)^{0.185}$$

$$- 0.088\ Re_f^{-0.26} \left(\frac{\mu_g}{\mu_f}\right)^{0.26} E^{0.74} \quad . \qquad (56)$$

And for $E/E_\infty > 1$

$$\frac{\partial E}{\partial (z/D)} = 2.64 \times 10^{-6}\ Re_f^{-0.075}\ We^{0.925} \left(\frac{\mu_g}{\mu_f}\right)^{0.26} (1 - E)^{0.185}$$

$$- 0.088\ Re_f^{-0.26} \left(\frac{\mu_g}{\mu_f}\right)^{0.26} E^{0.74} \quad . \qquad (57)$$

Figures 13 through 28 show the comparison of experimental data of Cousins et al. [18] to the predicted amount of entrainment with the initial condition of $E = 0$ at $z/D = 0$. Except at small Reynolds numbers, the integration of Eq. (54) well reproduces the experimental data. For small Reynolds numbers, however, the experimental data show that it takes a certain distance to inception of entrainment. For the case with the smooth injection of liquid as a film, it should take a certain time for roll waves to grow sufficiently to reach the inception of entrainment. The time required should be related to the growth rate of roll wave and the growth rate to some power of $Re_f/\sqrt{We}$ as discussed previously [2]. Therefore, the distance from the inlet without entrainment should be inversely proportional to some power of $Re_f/\sqrt{We}$. The experimental data indicate this trend also at least in the turbulent film flow regime.

Figure 29 shows the comparison of the experimental data of Gill et al. [17,20] to the predicted amount of entrainment. In their experiment, liquid is introduced by smooth injection as a film ($E = 0$ at $z/D = 0$) or by injection of droplets through an axial jet ($E = 1$ at $z/D = 0$) under the same flow condition. In the case of the smooth injection of liquid, the experimental data agree well with the prediction shown as the solid line. However, in the case of droplet injection, there is a considerable discrepancy between experimental data and the prediction based on the boundary condition of $E = 1$ at $z/D = 0$, shown by the broken line. The experimental data shows there is an abrupt decrease in E between $z/D = 0$ and $z/D = 20$. In this very vicinity of the inlet, the deposition mechanism can be quite different from the diffusion process of droplets which is dominant in the down stream section. The direct

droplet impingements and deposition due to the initial droplet momentum at the inlet should play a very important roll in this section [34]. It appears that if the entire liquid is introduced in to a system as droplets, this initial deposition rate is very large. Furthermore, it is expected that the rate is strongly dependent on the geometry of the inlet. If this very vicinity of the inlet is excluded, the present model gives reasonable agreement with the data. This can be shown by changing the initial condition from $E = 1.0$ at $z = 0$ to $E = 0.711$ at $z/D = 20$. The result shown in Fig. 29 as a dotted line seems to be quite satisfactory.

The rough estimate of this geometry dependent inlet section can be obtained from the previously developed correlation for the amount of entrainment. It is thought that the full entrainment process is reached when the above mentioned entrainment rate function $f(E/E_{\infty})$ reaches to its maximum value (see Eq. (41)). From this, the geometry dependent inlet region is given by

$$0 \leq z \leq 160\ D\ We^{0.25}\ Re_f^{-0.5} \quad . \tag{58}$$

The comparison of the data to the above inequality indicates that it gives a reasonable criterion. However, at very small Reynolds numbers, the phenomena seems to be more complicated than that predicted by Eq. (58).

IV. 5 CONCLUSIONS

A correlation for the rate of entrainment in annular two-phase has been developed from a simple model and experimental data. The previously developed correlation for the amount of entrainment has been used as a basis of the present study. The amount of entrainment represents the integrated effect of the local rate processes of entrainment and deposition. The entrainment rate and deposition rate are more mechanistic parameters representing the true transfer of liquid mass at the wavy interfaces than the entrainment amount. However, because of that these rates are much more difficult parameters to measure and correlate.

It has been found that basically there are three regions of entrainment, namely, the geometry dependent inlet section, developing flow region, and fully developed region. The first region is roughly given by

$$0 < z < 160\ D\ We^{0.25}\ Re_f^{-0.5} \quad .$$

In this region, the entrainment rate seems to be quite small or

$$\dot{\varepsilon} \simeq 0 \quad .$$

On the other hand, the deposition rate for the case of the droplet injection at the inlet is very large. This rate is much larger than that predicted by the diffusion based correlation such as Eq. (17).

The developing entrainment region is defined by

$$\frac{E}{E_\infty} \leq 1 \text{ or } Re_{ff} \geq Re_{ff\infty} \quad .$$

For this region the entrainment rate is given by

$$\frac{\dot{\varepsilon} D}{\mu_f} = 0.72 \times 10^{-9}\ Re_f^{1.75}\ We\ (1 - E_\infty)^{0.25} \left(1 - \frac{E}{E_\infty}\right)^2$$

$$+ 6.6 \times 10^{-7}\ (Re_f\ We)^{0.925} \left(\frac{\mu_g}{\mu_f}\right)^{0.26} (1 - E)^{0.185} \quad ,$$

where E_∞ is given by

$$E_\infty = \tanh\left(7.25 \times 10^{-7}\ We^{1.25}\ Re_f^{0.25}\right) .$$

The fully developed or over entrained region is defined by

$$\frac{E}{E_\infty} > 1 \text{ or } Re_{ff} < Re_{ff\infty} .$$

For this region the entrainment rate becomes

$$\frac{\dot{\varepsilon} D}{\mu_f} = 6.6 \times 10^{-7}\ (Re_f\ We)^{0.925} \left(\frac{\mu_g}{\mu_f}\right)^{0.26} (1 - E)^{0.185} .$$

The diffusion based droplet deposition rate is

$$\frac{\dot{d} D}{\mu_f} = 0.022\ Re_f^{0.74} \left(\frac{\mu_g}{\mu_f}\right)^{0.26} E^{0.74} .$$

It should be noted that there is a cut off film Reynolds number below which the entrainment mechanism based on shearing-off of roll-wave crests stops. Thus one obtains

$$\dot{\varepsilon} = 0 \text{ for } Re_{ff} < 160 ,$$

for low viscous fluid such as water. At extremely high gas flux, another entrainment mechanism becomes possible, however, for most practical systems this can be considered as the entrainment shut off point.

The present correlation indicates that the entrainment rate depends on the total liquid Reynolds number, Weber number, equilibrium entrainment fraction E_∞ and entrainment fraction E or the local film Reynolds number Re_{ff}. These correlations are compared to a number of experimental data both in terms of the entrainment rate and entrainment fraction. The results are shown to be satisfactory both in the developing region and fully developed entrainment region.

The present model is based on the previously developed criteria for the onset of entrainment and the correlation for the entrainment fraction. Since these are developed from a simple model based on the force balance at the wavy interface, the present correlation for entrainment rate indicates basic mechanisms of entrainment processes and parametric dependencies in addition to being accurate. The entrainment rate correlation in the developing region is completely new. Therefore, the present results supply very variable information which has not been available previously.

NOMENCLATURE

C	Droplet concentration in gas core
C_∞	Equilibrium droplet concentration in gas core
$\dot{d}$	Droplet deposition rate
D	Hydraulic diameter
E	Fraction of liquid flux flowing as droplet ($= j_{fe}/j_f$)
E_∞	Equilibrium value of fraction entrained, E
g	Acceleration due to gravity
j_f	Volumetric flux of total liquid (superficial velocity)
j_{fe}	Volumetric flux of droplets
j_g	Volumetric flux of gas (superficial velocity)
k	Mass transfer coefficient
Re_f	Total liquid Reynolds number
Re_{ff}	Liquid film Reynolds number
$Re_{ff\infty}$	Equilibrium film Reynolds number
Re_g	Gas Reynolds number
v_{ff}	Liquid film velocity
$v_{ff\infty}$	Equilibrium liquid film velocity
v_{fe}	Velocity of droplets
v_g	Gas velocity
We	Weber number
W_f	Total liquid mass flow rate
W_{fe}	Droplet mass flow rate
z	Axial distance from inlet

Greek Symbols

α	Void fraction

α_{core}	Fraction of gas core
α_d	Droplet fraction in the gas core
δ	Film thickness
$\dot{\varepsilon}$	Entrainment rate
$\dot{\varepsilon}_\infty$	Equilibrium entrainment rate
ζ	Dimensionless distance given by Eq. (24)
μ_f	Viscosity of liquid
μ_g	Viscosity of gas
ρ_f	Liquid density
ρ_g	Gas density
$\Delta\rho$	Density difference between liquid and gas
σ	Surface tension
τ_i	Interfacial shear force

Subscripts

f	Liquid phase
fe	Liquid entrainment
ff	Liquid film
g	Gas phase
i	Interface
∞	Equilibrium

REFERENCES

1. Hewitt, G. F. and Hall-Taylor, N. S., "Annular Two-phase Flow," Pergamon Press, Oxford (1970).

2. Ishii, M. and Mishima, K., "Correlation for Liquid Entrainment in Annular Two-phase Flow of Low Viscous Fluid," Argonne National Laboratory Report, ANL/RAS/LWR 81-2 (1981).

3. Collier, J. G., "Burnout in Liquid Cooled Reactors," Nuclear Power, 5, 61 (1961).

4. Petrovichev, V. I., Kokorev, L. S., Didenko, A. Ya., and Dubvrovskiy, G. P., "Droplet Entrainment in Boiling of Thin Liquid Film," Heat Transfer-Soviet Res., 3, 19 (1971).

5. Cousins, L. B., Denton, W. H., and Hewitt, G. E., "Liquid Mass Transfer in Annular Two-phase Flow," Sym. on Two-phase Flow, Vol. 1, paper C4, Exter, England (1965).

6. Tong, L. S., "Boiling Heat Transfer and Two-phase Flow," R. E. Krieger Publishing Co., NY (1975).

7. Hsu, Y. Y. and Graham, R. W., "Transport Process in Boiling and Two-phase Systems," Hemisphere Publishing Co., WA (1976).

8. Hewitt, G. F., "Mechanism and Prediction of Burnout," NATO Advanced Study Institute on Two Phase Flows (1976).

9. Yamanouchi, A., "Effects of Core Spray Cooling at Stationary State After Loss of Coolant Accident," J. Nuc. Sci. & Tech., 5(9), 498 (1968).

10. Semeria, R. and Martinet, "Calefaction Spots on a Heating Wall; Temperature Distribution and Resorption," Sym. on Boiling Heat Trans. in Steam Generating Unit and Heat Exchangers, Proc. Inst. Mech. Engs. 180, 192-205 (1965).

11. Duffey, R., "The Physics of Rewetting in Water Reactor Emergency Core Cooling," Nucl. Eng. Design, 25, 379 (1973).

12. Bennett, A., "The Wetting of Hot Surfaces by Water in a Steam Environment at High Pressure," Atomic Energy Research Establishment, Harwell, AERE-R5146 (1966).

13. Ishii, M. and Grolmes, M. A., "Inception Criteria for Droplet Entrainment in Two-phase Concurrent Film Flow," AIChE J., 21, 308 (1975).

14. Kataoka, I., Ishii, M., and Mishima, K., "Generation and Size Distribution of Droplet in Annular Two-Phase Flow,"Trans. ASME, J. of Fluid Eng., Vol. 105, 230 (1983)

15. Alexander, L. G. and Coldren C. L., "Droplet Transfer from Suspending Air to Duct Walls," Ind. Eng. Chem., 43, 1325 (1951).

16. Goldmann, K., Firstenberg, H., and Lombardi, C., "Burnout in Turbulent Flow - A Droplet Diffusion Model," Trans. ASME J. Heat Trans., 83, 158 (1961).

17. Gill, L. E., Hewitt, G. F., and Hitchon, J. W., "Sampling Probe Studies of the Gas Core in Annular Two-phase Flow - Part I. The Effect of Length on Phase and Velocity Distribution," AERE-R3954 (1962).

18. Cousins, L. B., Denton, W. H., and Hewitt, G. F., "Liquid Mass Transfer in Annular Two-phase Flow," Sym. on Two-phase Flow, Vol. 1, paper C4, Exter, England (1965).

19. Paleev, I. I. and Filippovich, B. S., "Phenomena of Liquid Transfer in Two-phase Dispersed Annular Flow," Int. J. Heat Mass Trans., 9, 1089 (1966).

20. Gill, L. E. and Hewitt, G. F., "Sampling Probe Studies of the Gas Core in Annular Two-phase Flow - Part 3. Distribution of Velocity and Droplet Flowrate after Injection through an Axial Jet," AERE-M1202 (1967).

21. Gill, L. E. and Hewitt, G. F., "Sampling Probe Studies of the Gas Core in Annular Two-phase Flow - III; Distribution of Velocity and Droplet Flowrate after Injection through an Axial Jet," Chem. Eng. Sci., 23, 677 (1968).

22. Cousins, L. B. and Hewitt, G. F., "Liquid Phase Mass Transfer in Annular Two-phase Flow: Radial Liquid Mixing," AERE-R5693 (1968).

23. Cousins, L. B. and Hewitt, G. F., "Liquid Phase Mass Transfer in Annular Two-phase Flow: Droplet Deposition and Liquid Entrainment," AERE-R5657 (1968).

24. Hutchinson, P., Hewitt, G. F., and Dukler, A. E., "Deposition of Liquid or Solid Dispersion from Turbulent Gas Streams: A Stochastic Model," Chem. Eng. Sci., 26, 419 (1971).

25. Namie, S. and Ueda, T., "Droplet Transfer in Two-phase Annular Mist Flow, Part 1, Experiment of Droplet Transfer Rate and Distributions of Droplet Concentration and Velocity," Bulletin of JSME, 15, 1568 (1972).

26. Namie, S. and Ueda, T., "Droplet Transfer in Two-Phase Annular Mist Flow, Part 2, Prediction of Droplet Transfer Rate," Bulletin of JSME, 16, 752 (1973).

27. Hutchinson, P., Whalley, P. B., and Hewitt, G. F., "Transient Flow Redistribution in Annular Two-phase Flow," Int. J. Multiphase Flow, 1, 383 (1974).

28. Akagawa, K., Sakaguchi, T., Fujii, T., Nakatani, Y., Nakaseko, K., and Itoh, J., "Horizontal Liquid Film-mist Two-phase Flow - 1st Report, Concentration, Distribution and Diffusivity of Entrained Liquid Droplets," Bulletin of JSME, 23, 910 (1980).

29. Brodkey, R. S., "The Phenomena of Fluid Motion," Addison-Wesley, Reading, MA (1967).

30. M. Ishii, I. Kataoka, and G. Kocamustafaogullari, "Phenomenological Modeling of Two-phase Flow in Water Reactor at ANL: Two-fluid Model, Interfacial Area, Droplet Entrainment and Droplet Size," NRC 9th Water Reactor Safety Research Information Meeting, Gaitherburg, October (1981).

31. Hutchinson, P. and Whalley, P. B., "A Possible Characterization of Entrainment in Annular Flow," Chem. Eng. Sci., 28, 974 (1973).

32. Whalley, P. B. Hewitt, G. F., and Hutchinson, P., "Experimental Wave and Entrainment Measurement in Vertical Annular Two-phase Flow," Sym. on Multiphase Flow System, The Institute of Chemical Engineers, Sym. Ser. 38, paper A1 (1974).

33. Ueda, T., "Entrainment Rate and Size Distribution of Entrained Droplets in Annular Two-phase Flow," Bulletin of JSME, 22, 1258 (1979).

34. G. F. Hewitt, Personal communication, LWR Safety Information Meeting (Oct., 1981).

Appendix A

Derivation of Equation (10)

Equation (10) can be obtained by considering mass balance of liquid and gas phase. Volumetric flux of droplet is given by

$$j_{fe} = \alpha_{core}\, \alpha_d\, v_{fe} \quad . \tag{A.1}$$

α, α_{core}, and α_d are related by

$$\alpha = \alpha_{core}\, (1 - \alpha_d) \quad . \tag{A.2}$$

From (A.1) and (A.2) one gets

$$j_{fe} = \frac{\alpha}{1 - \alpha_d}\, \alpha_d\, v_{fe} \quad . \tag{A.3}$$

On the other hand,

$$\alpha = \frac{j_g}{v_g} \quad . \tag{A.4}$$

Substituting (A.4) into (A.3) and after some algebra

$$\alpha_d = \frac{j_{fe}\, v_g}{j_g v_{fe} + j_{fe} v_g} \quad . \tag{A.5}$$

Then one obtains

$$C = \rho_f\, \alpha_d \tag{A.6}$$

$$= \rho_f\, \frac{j_{fe}\, v_g}{j_g v_{fe} + j_{fe} v_g} \quad . \tag{A.7}$$

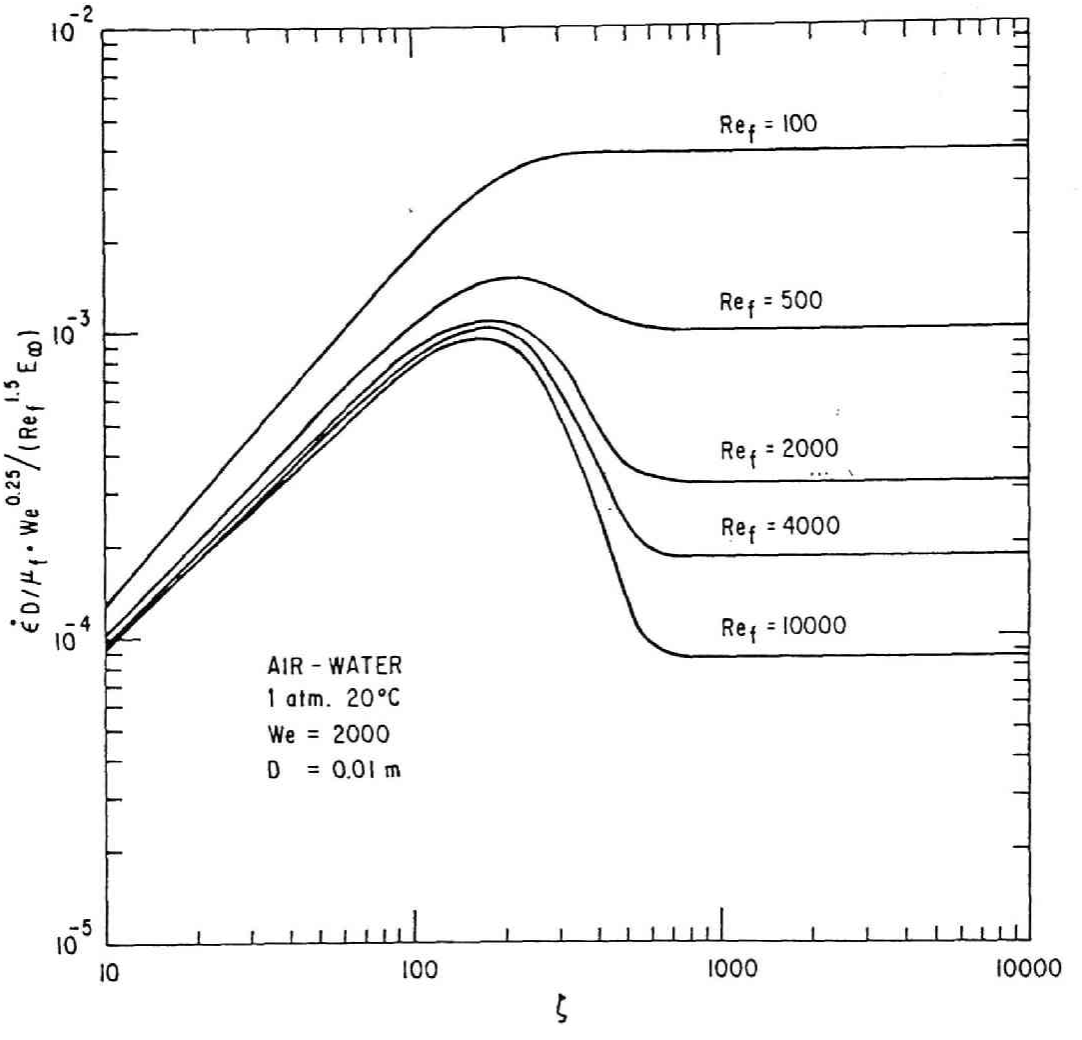

Fig. 1. Entrainment Rate Calculated by Eq. (25) for We = 2000, Re_f = 100 ∿ 10000, and D = 0.01 m in Air-Water System at 20°C, 1 atm

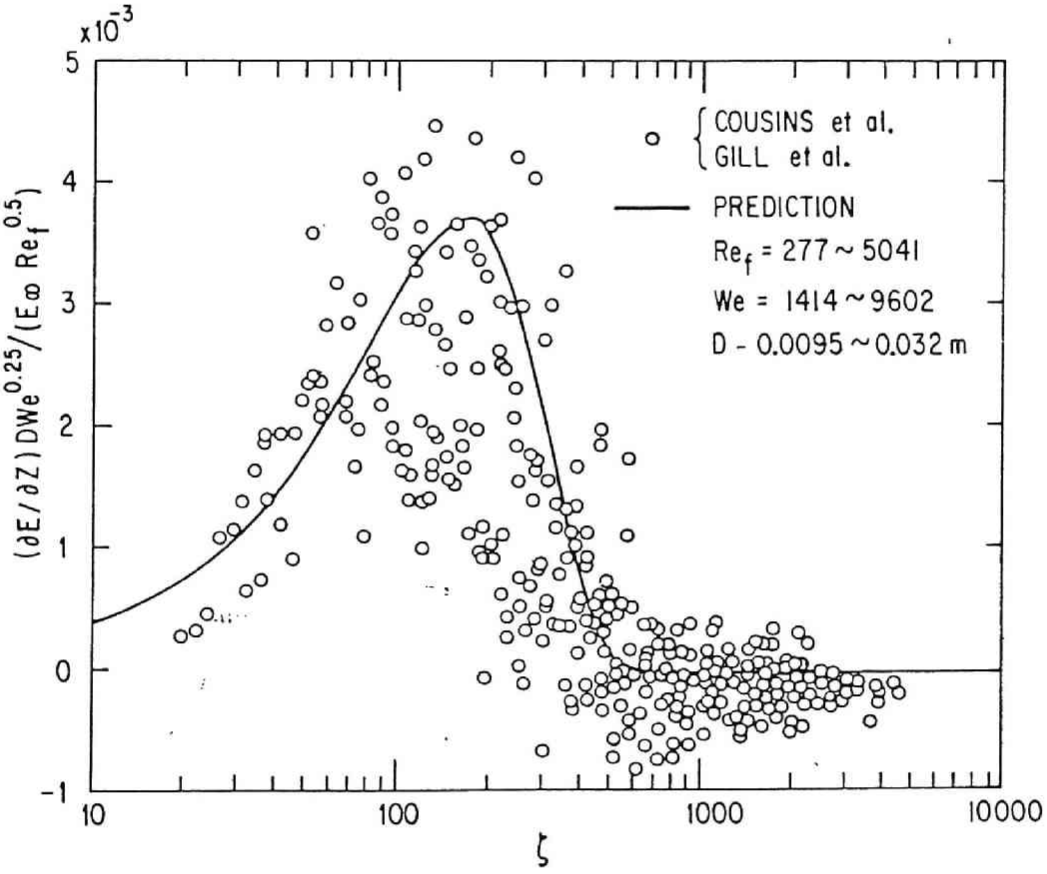

Fig. 2. $\left(\frac{\partial E}{\partial z}\right) D\ We^{0.25}/(E_\infty\ Re_f^{0.5})$ vs. ζ for the Data of Cousins et al. [18] and Gill et al. [17]

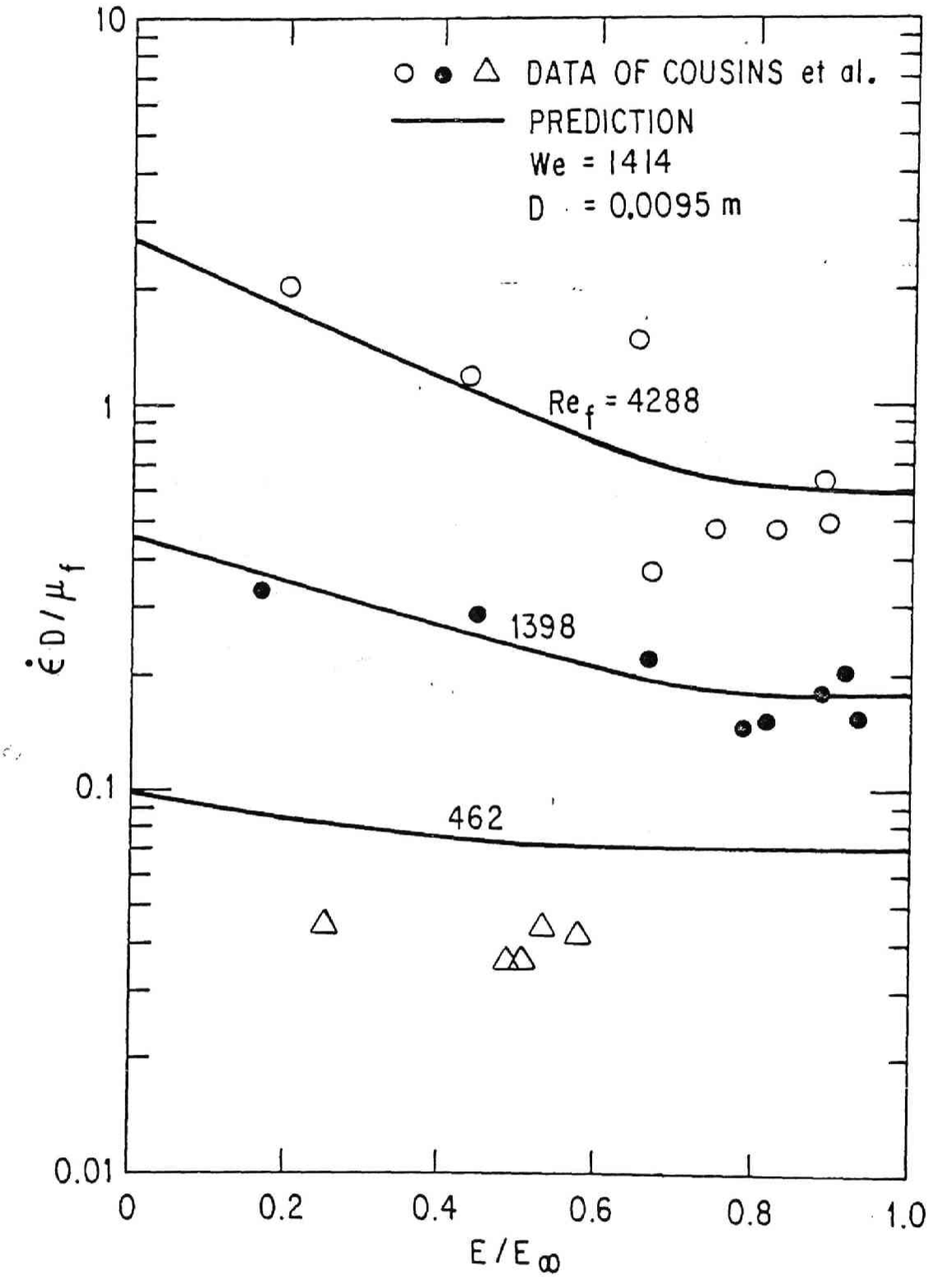

Fig. 3. Entrainment Rate for the Data of Cousins et al. [18] at We = 1414 and Re_f = 462 ~ 4288

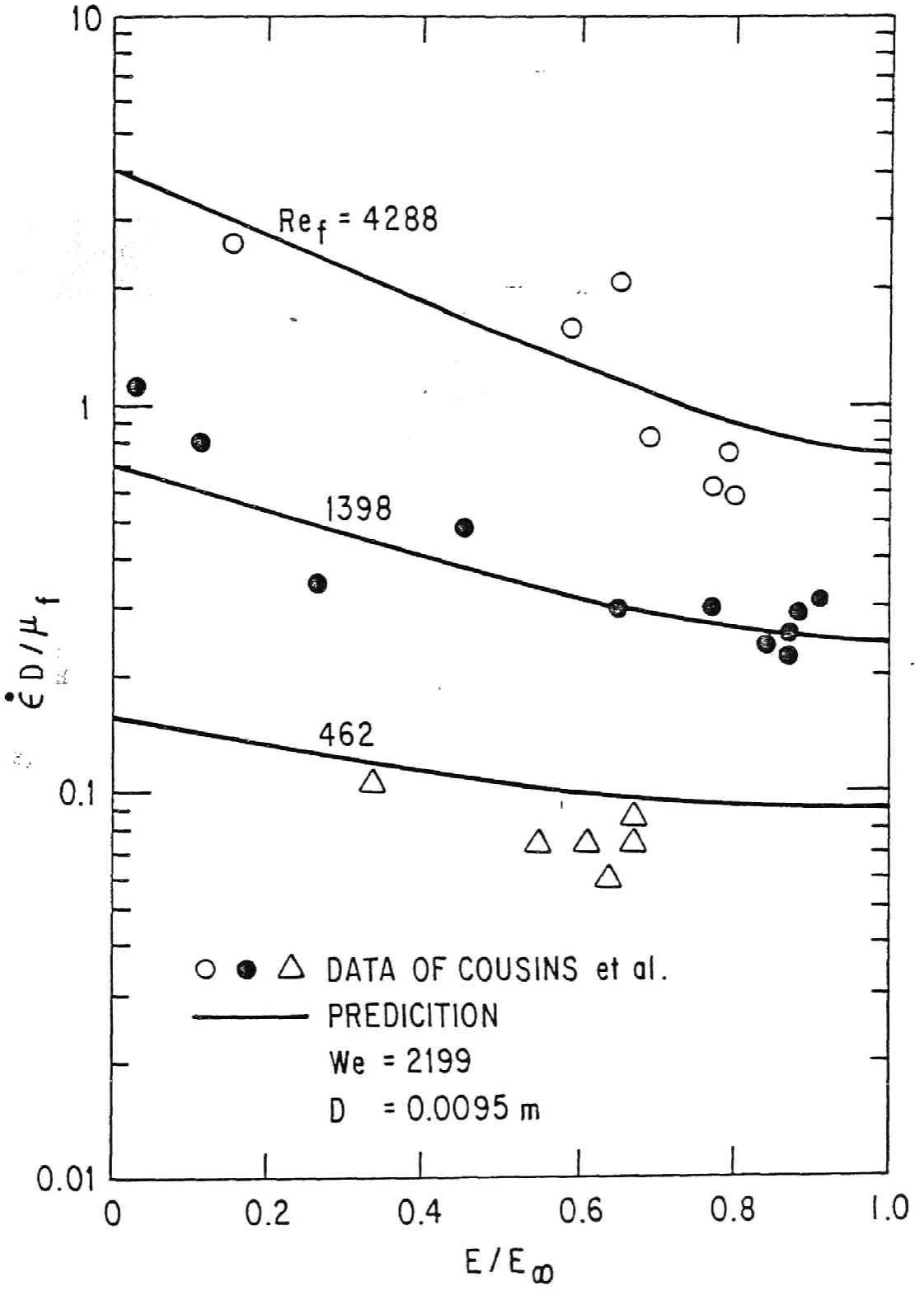

Fig. 4. Entrainment Rate for the Data of Cousins et al. [18] at We = 2199 and Re_f = 462 ~ 4288

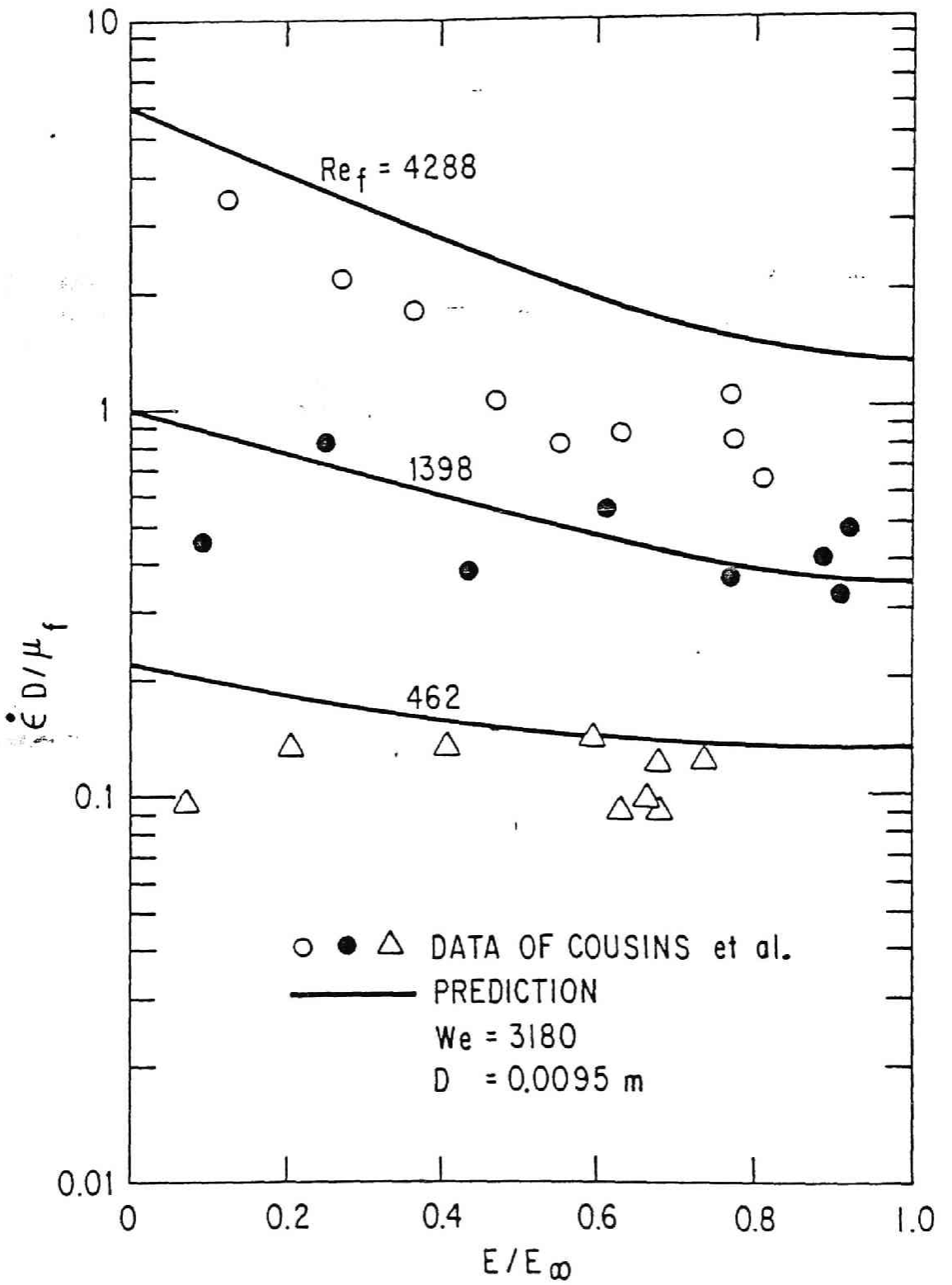

Fig. 5. Entrainment Rate for the Data of Cousins et al. [18] at We = 3180 and Re_f = 462 ~ 4288

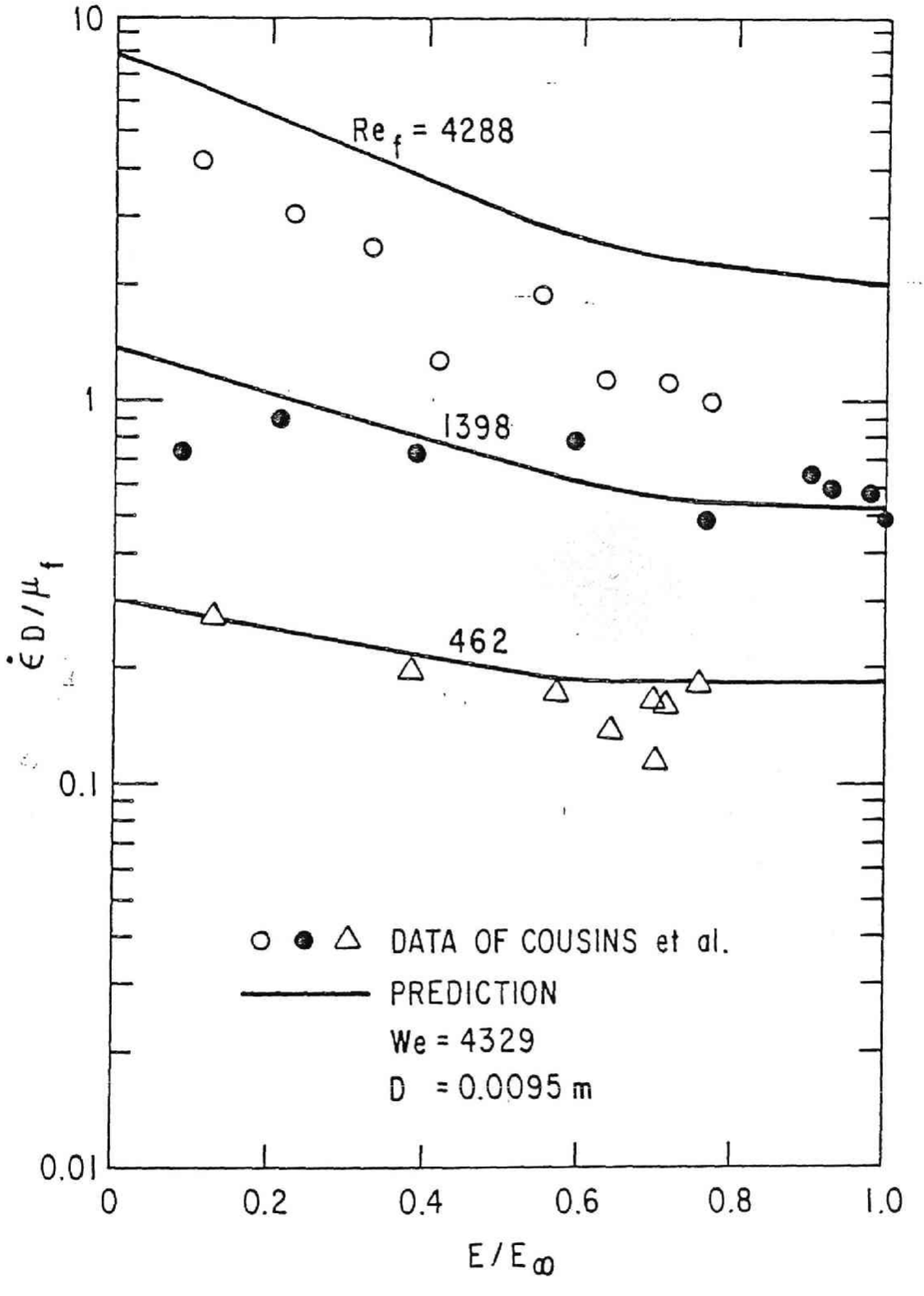

Fig. 6. Entrainment Rate for the Data of Cousins et al. [18] at We = 4329 and Re_f = 462 ~ 4288

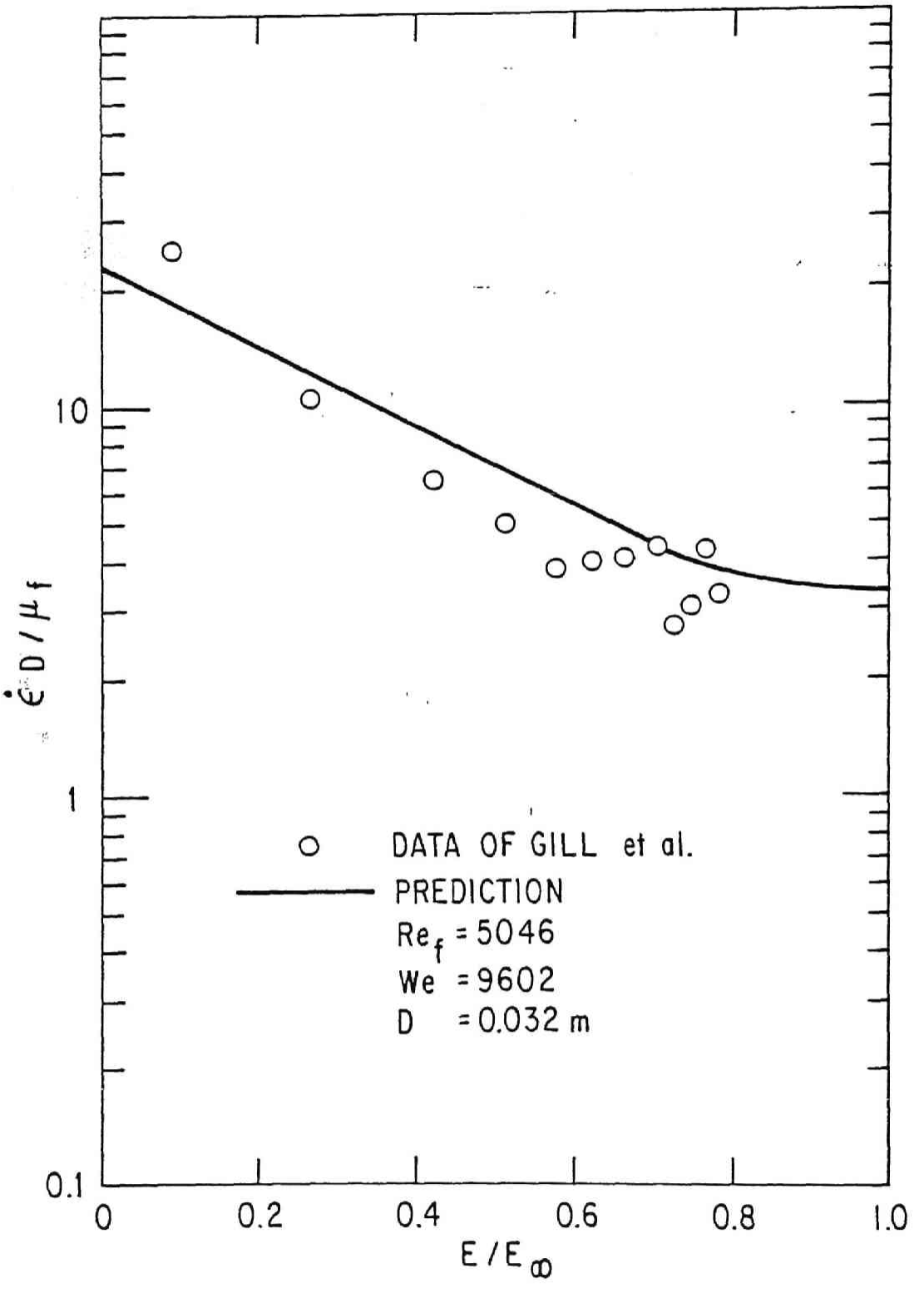

Fig. 7. Entrainment Rate for the Data of Gill et al. [17] at We = 9602 and Re_f = 5046

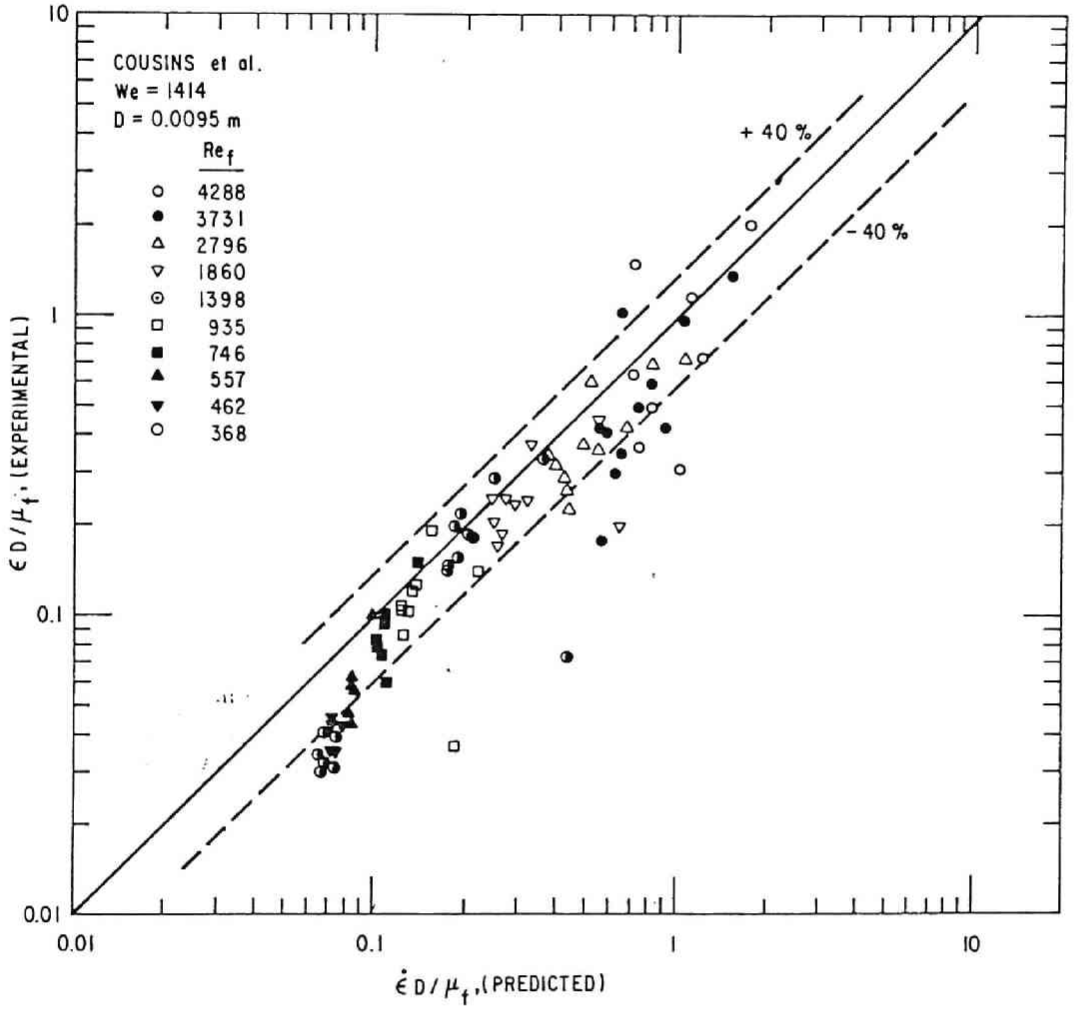

Fig. 8. Comparison of Experimental Entrainment Rate with Eq. (44) for the Data of Cousins et al. [18] at We = 1414 and Re_f = 368 ∿ 4288

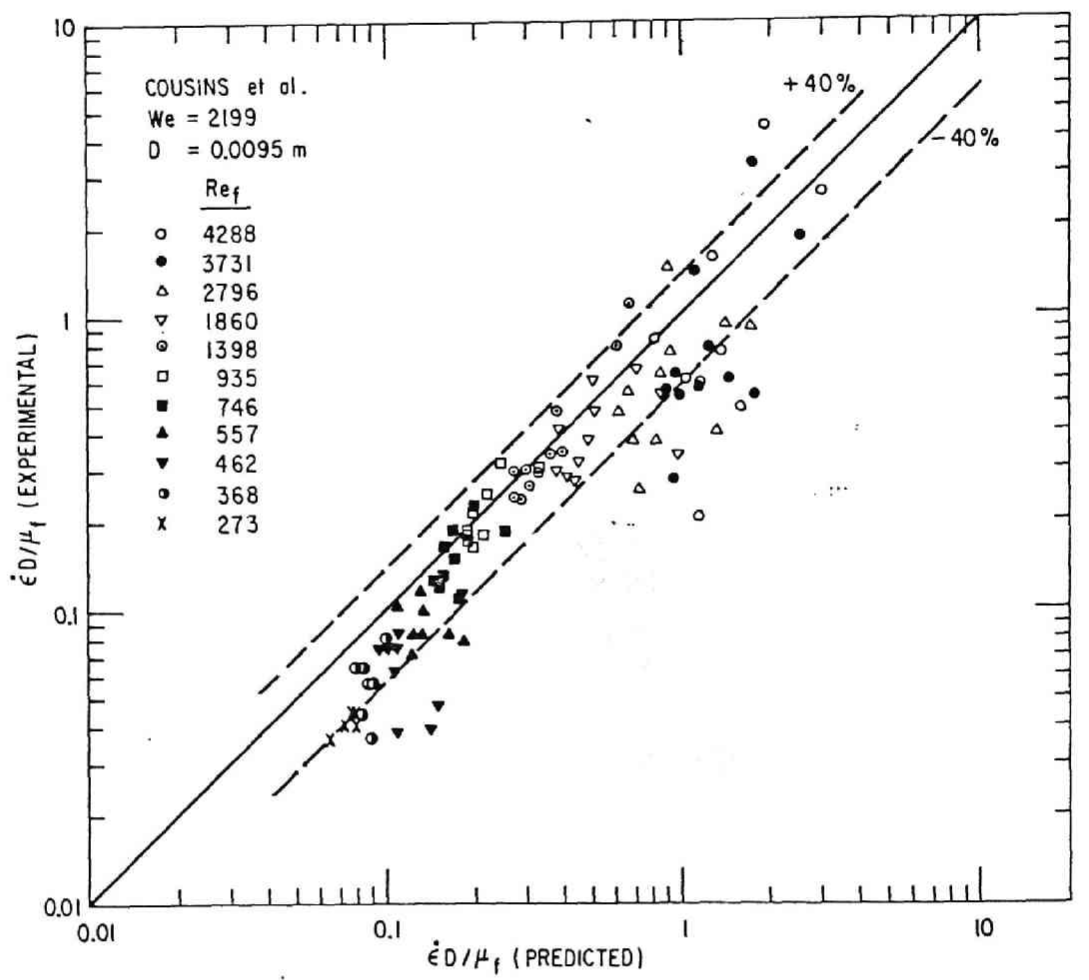

Fig. 9. Comparison of Experimental Entrainment Rate with Eq. (44) for the Data of Cousins et al. [18] at We = 2199 and Re_f = 273 ∿ 4288

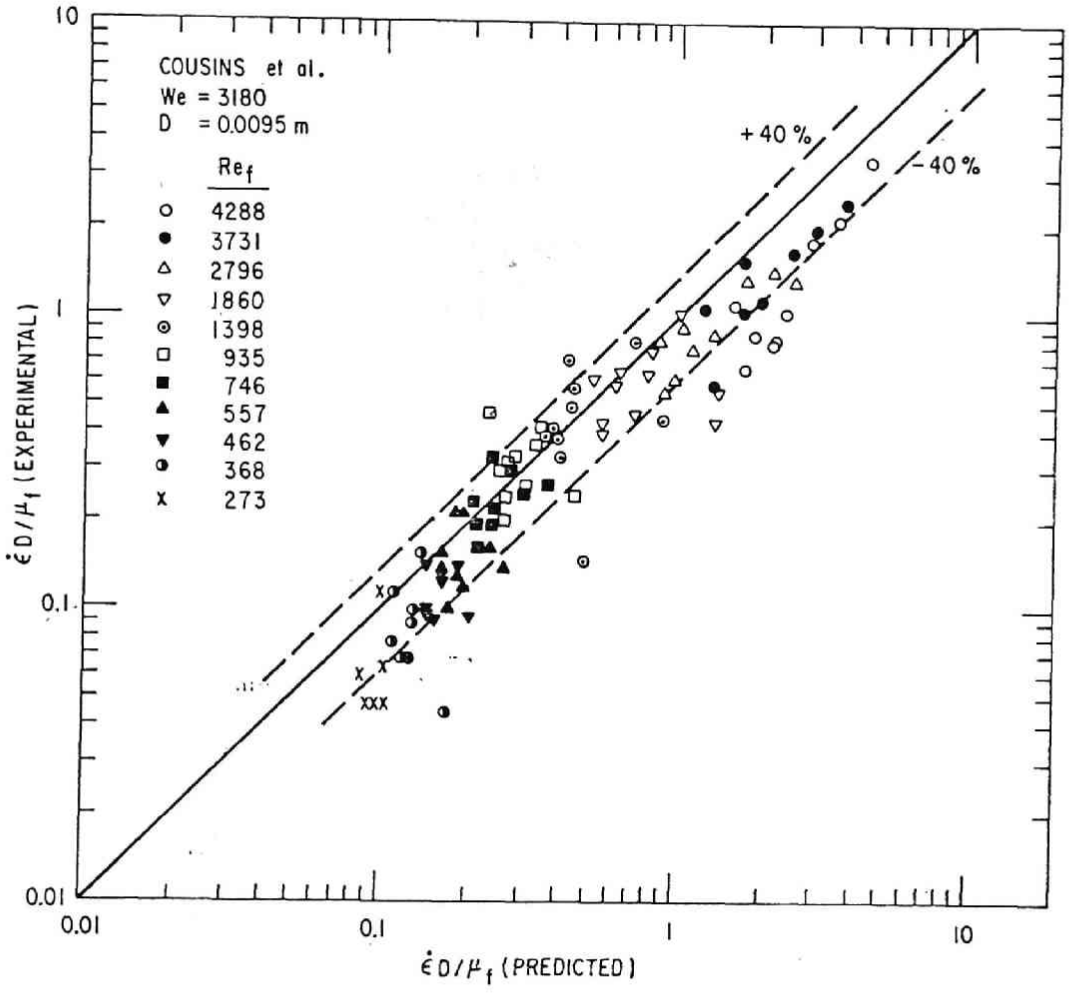

Fig. 10. Comparison of Experimental Entrainment Rate with Eq. (44) for the Data of Cousins et al. [18] at We = 3180 and Re_f = 273 ∿ 4288

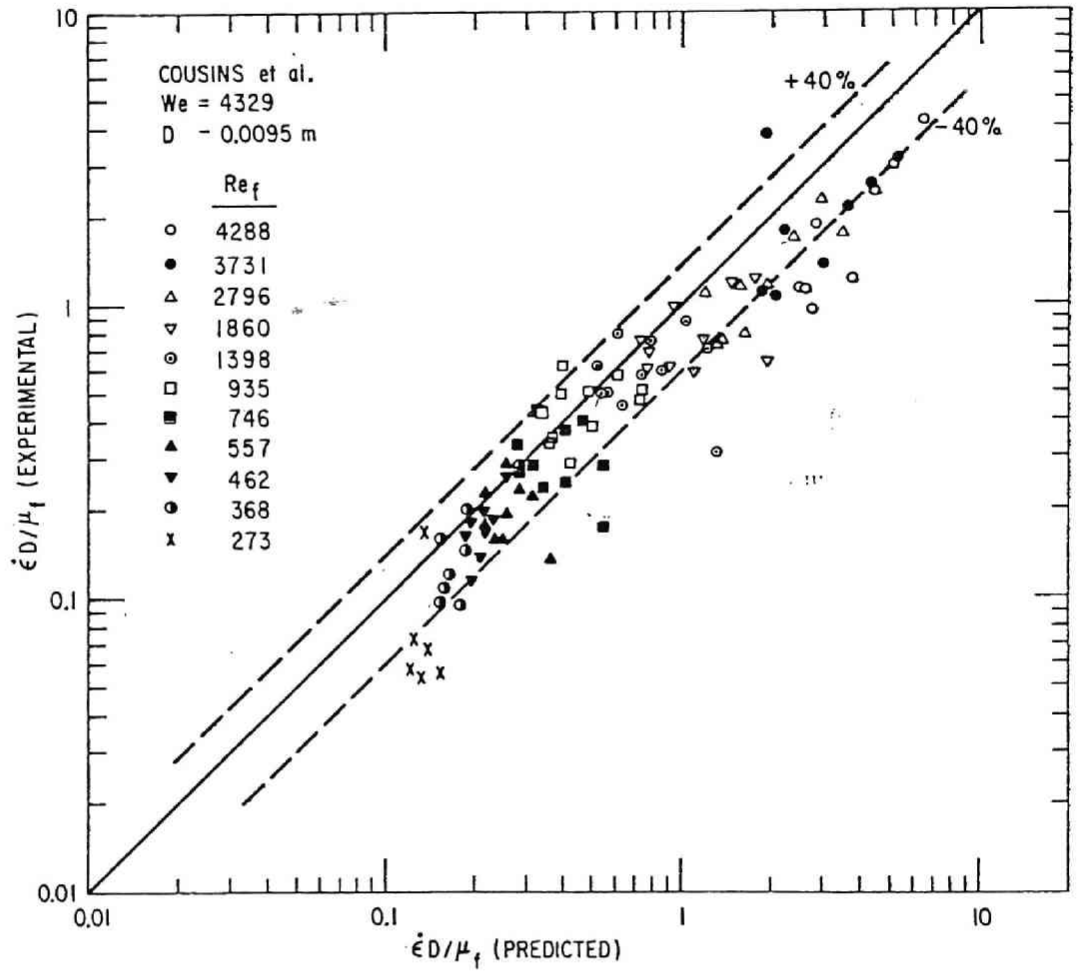

Fig. 11. Comparison of Experimental Entrainment Rate with Eq. (44) for the Data of Cousins et al. [18] at We = 4329 and Re_f = 273 ~ 4288

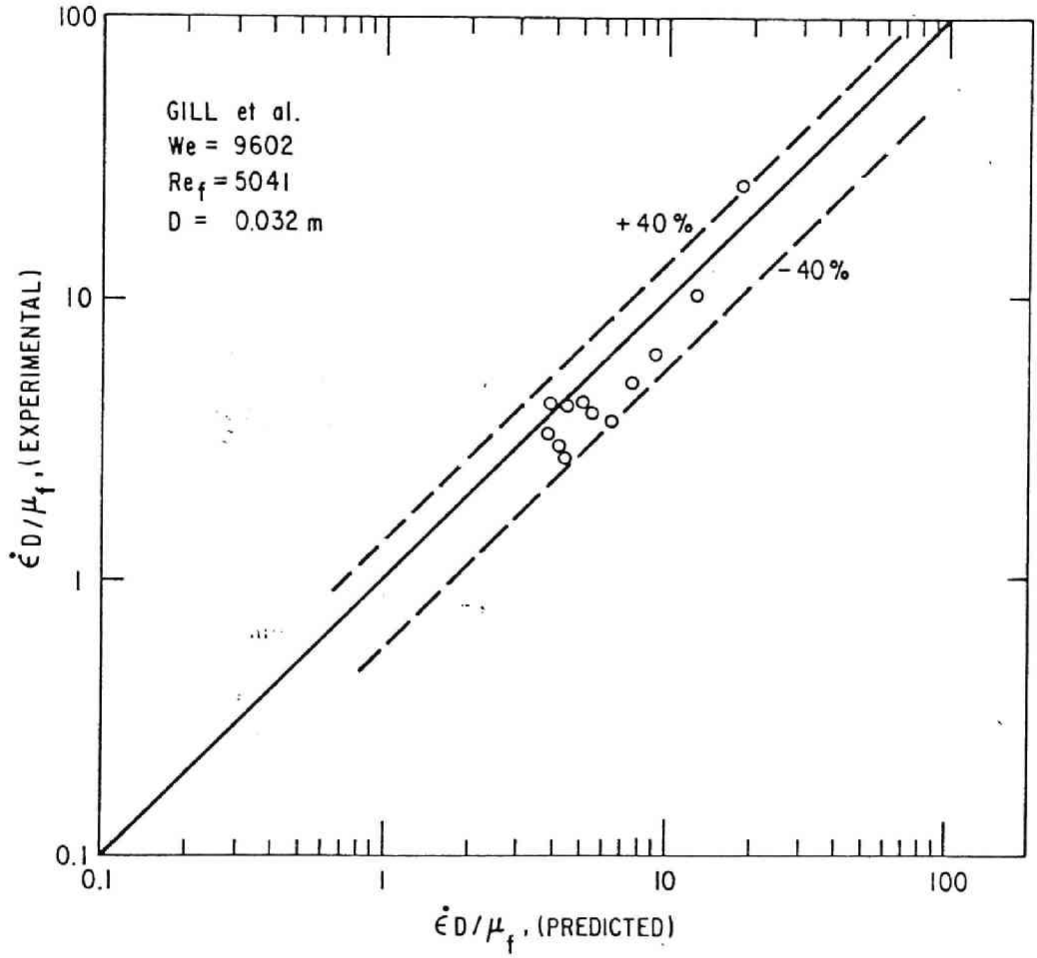

Fig. 12. Comparison of Experimental Entrainment Rate with Eq. (44) for the Data of Gill et al. [17] at We = 9602 and Re_f = 5041

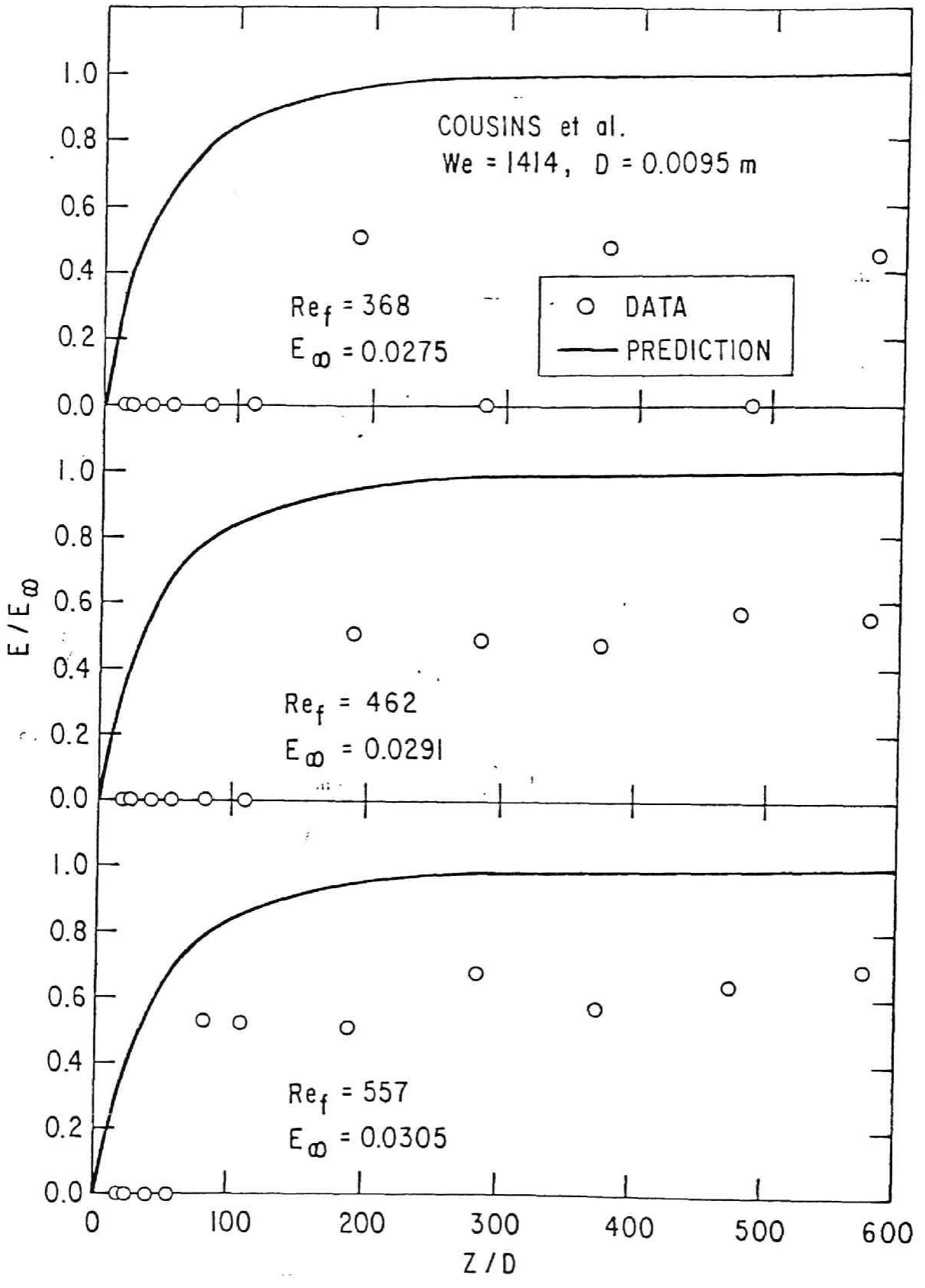

Fig. 13. Comparison of Experimental Data of Cousins et al. [18] with Predicted Amount of Entrainment at We = 1414 and Re_f = 368 ~ 557

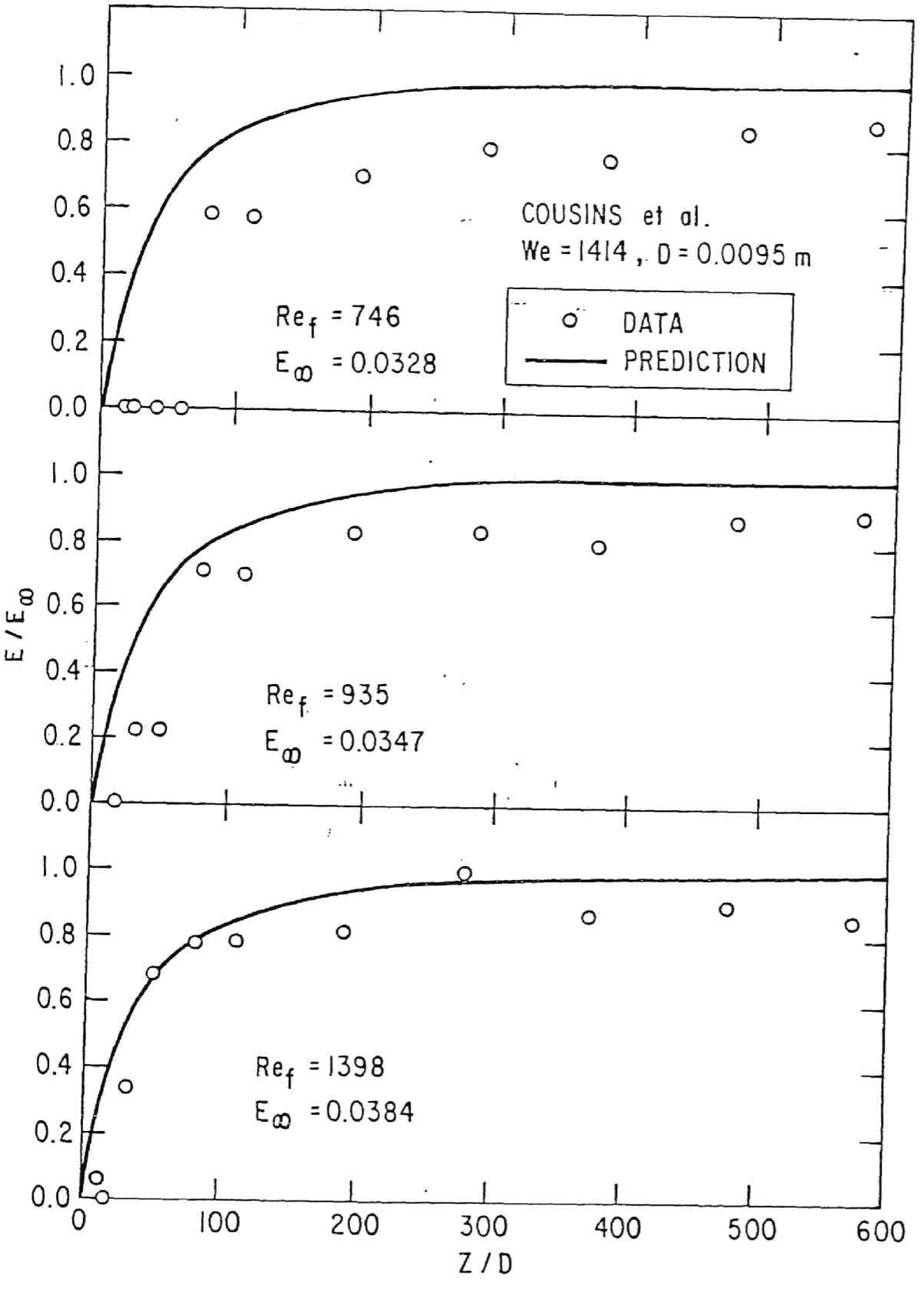

Fig. 14. Comparison of Experimental Data of Cousins et al. [18] with Predicted Amount of Entrainment at We = 1414 and Re_f = 746 ~ 1398.

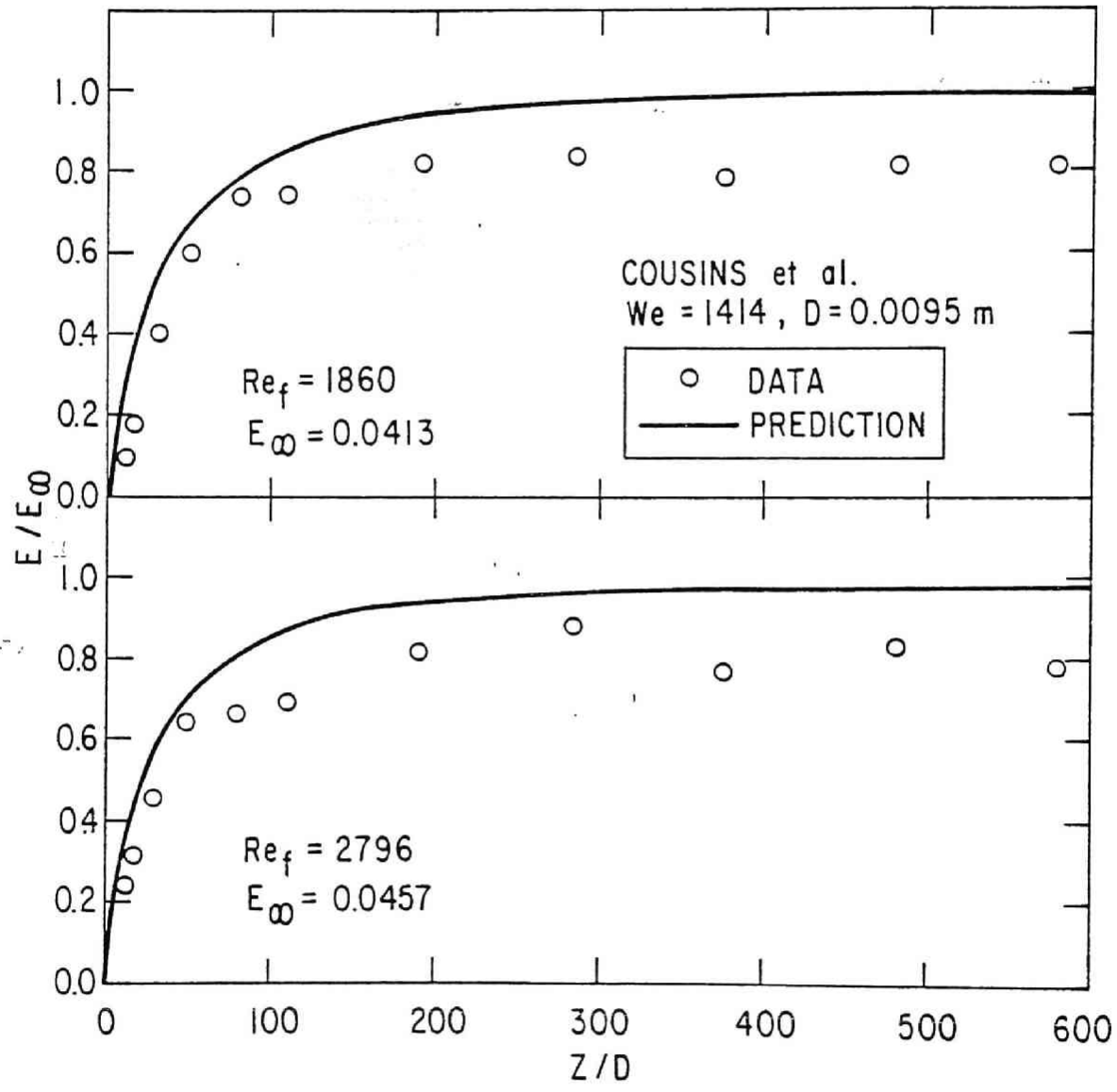

Fig. 15. Comparison of Experimental Data of Cousins et al. [18] with Predicted Amount of Entrainment at We = 1414 and Re_f = 1860 ~ 2796

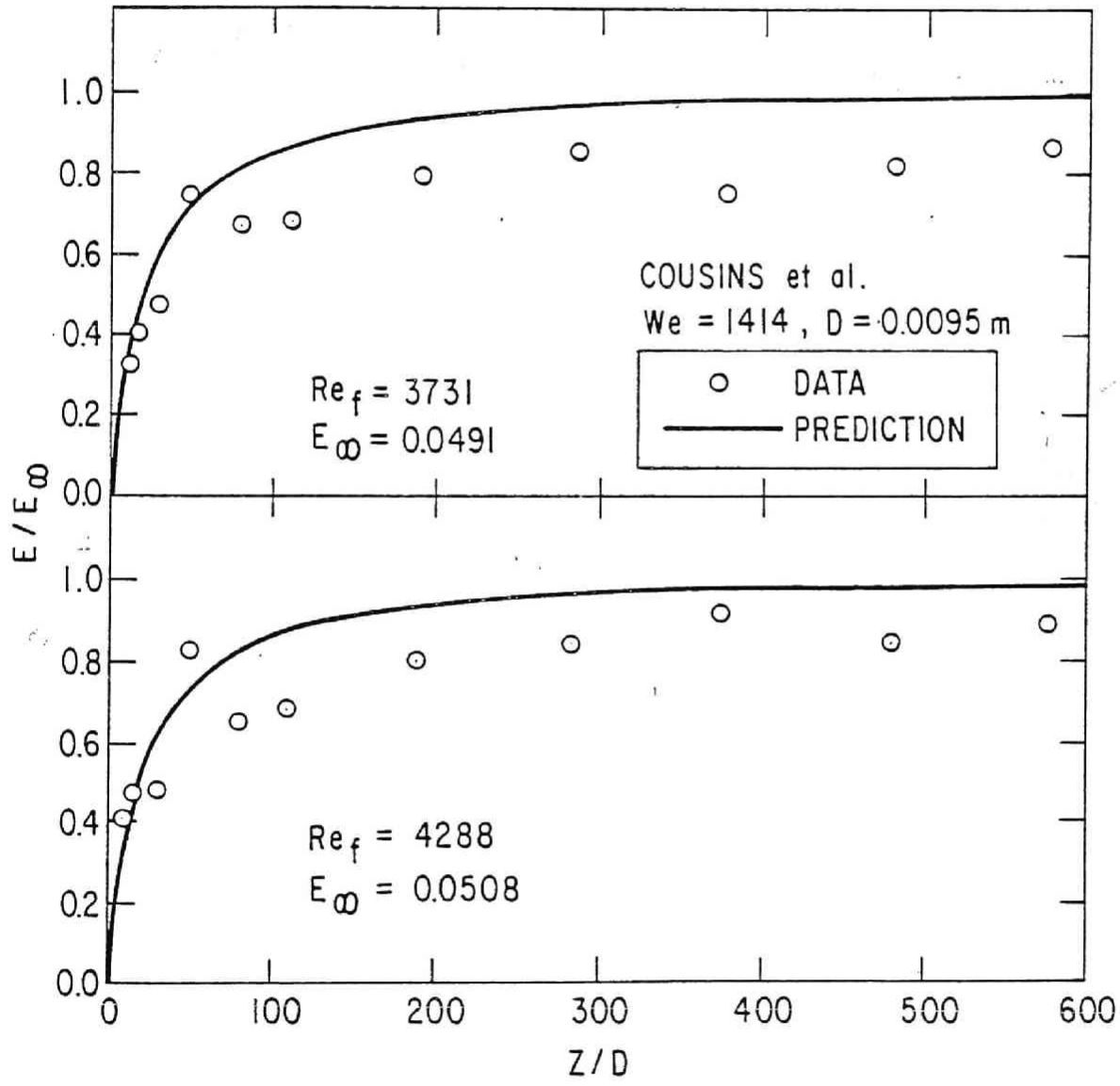

Fig. 16. Comparison of Experimental Data of Cousins et al. [18] with Predicted Amount of Entrainment at We = 1414 and Re_f = 3731 ~ 4288

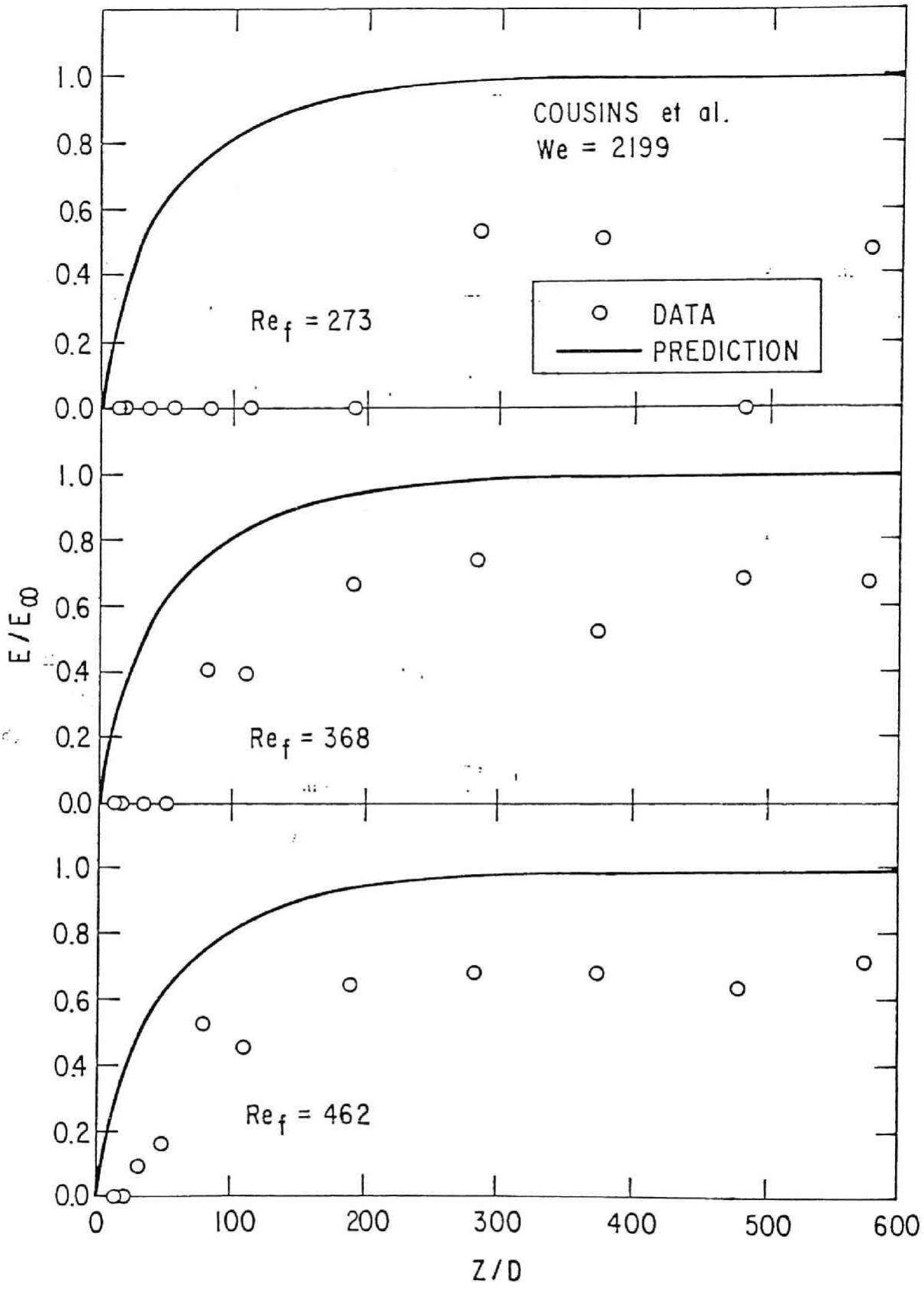

Fig. 17. Comparison of Experimental Data of Cousins et al. [18] with Predicted Amount of Entrainment at We = 2199 and Re_f = 273 ∿ 462

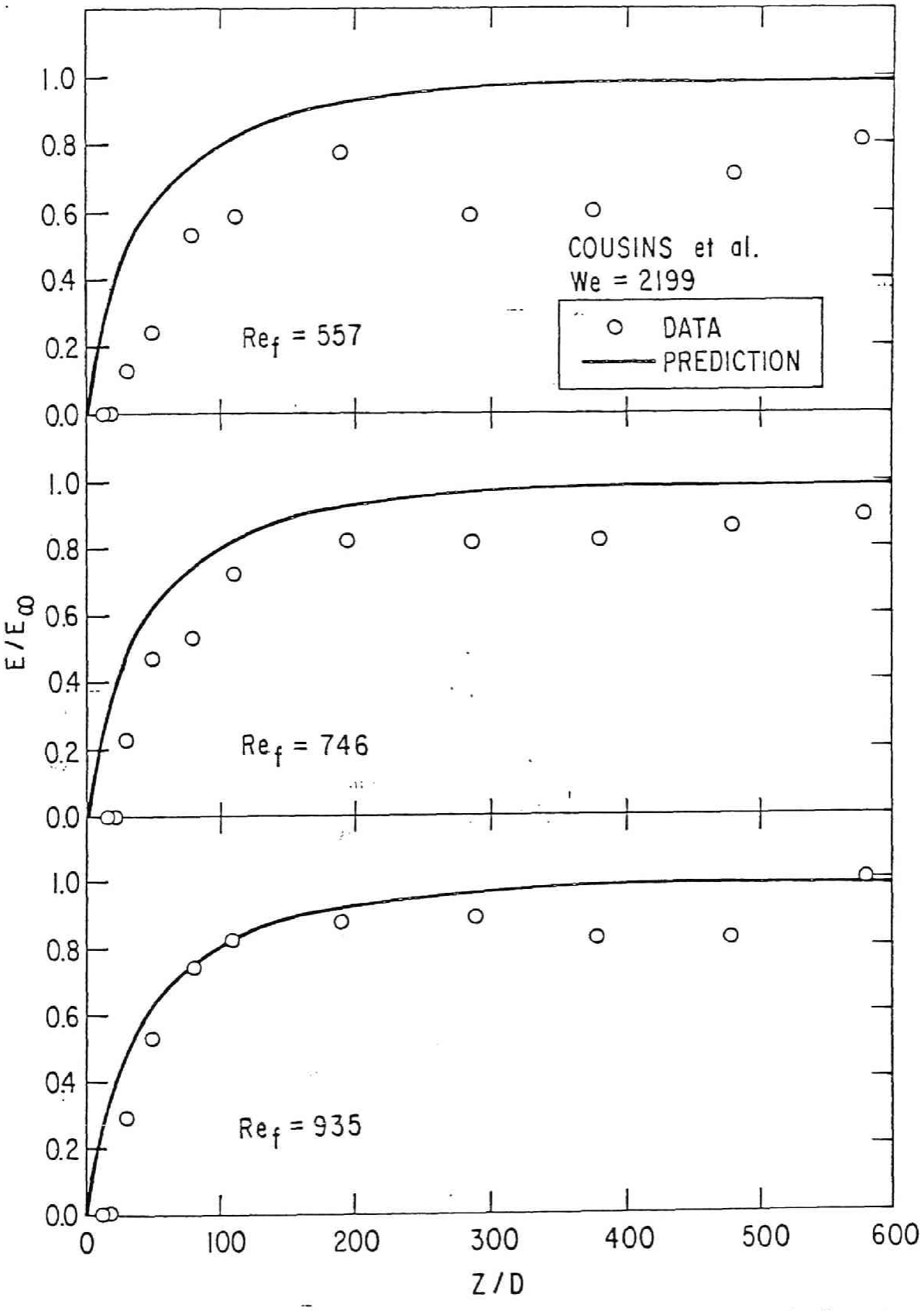

Fig. 18. Comparison of Experimental Data of Cousins et al. [18] with Predicted Amount of Entrainment at We = 2199 and Re_f = 557 ~ 935

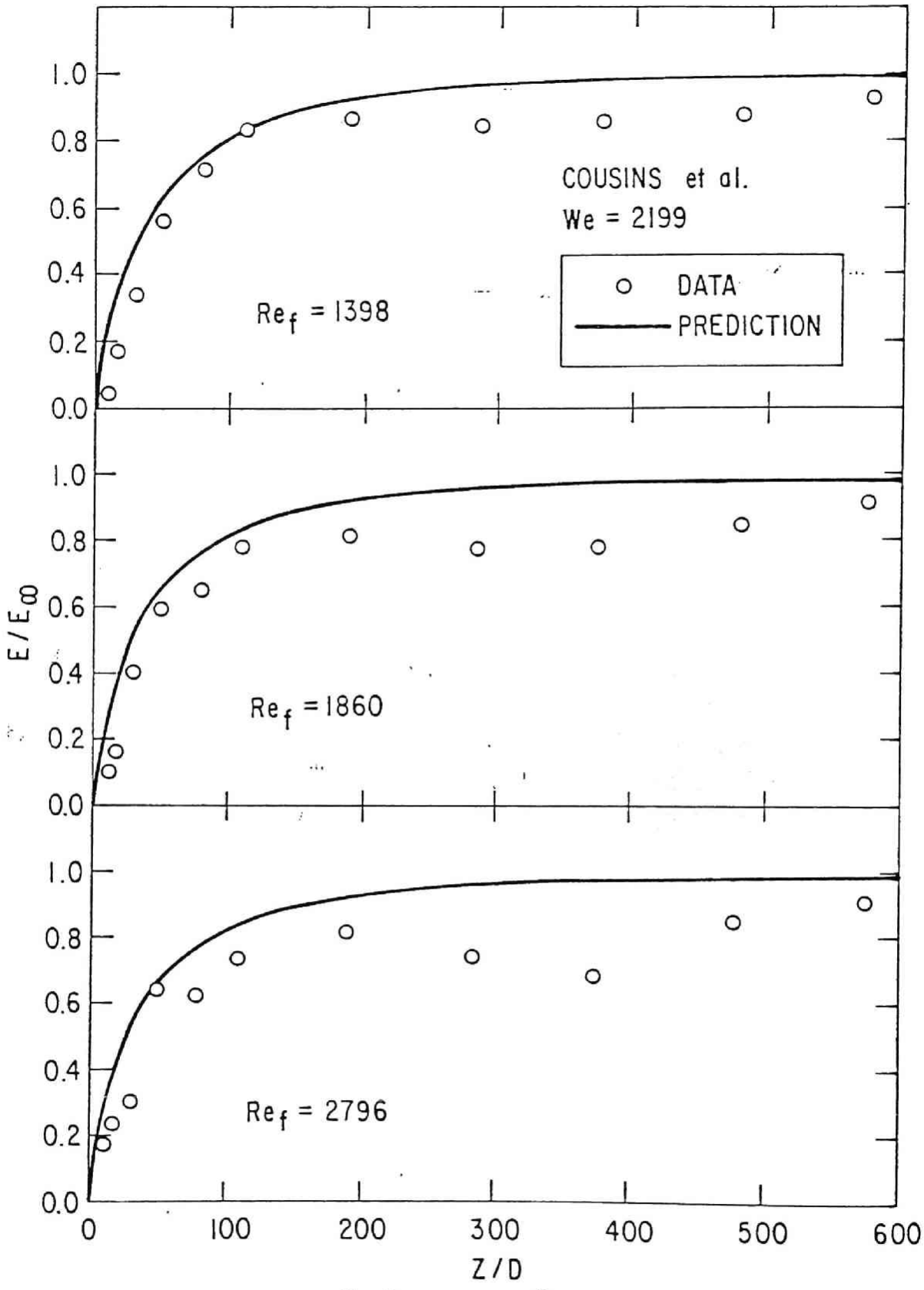

Fig. 19. Comparison of Experimental Data of Cousins et al. [18] with Predicted Amount of Entrainment at We = 2199 and Re_f = 1398 ~ 2796

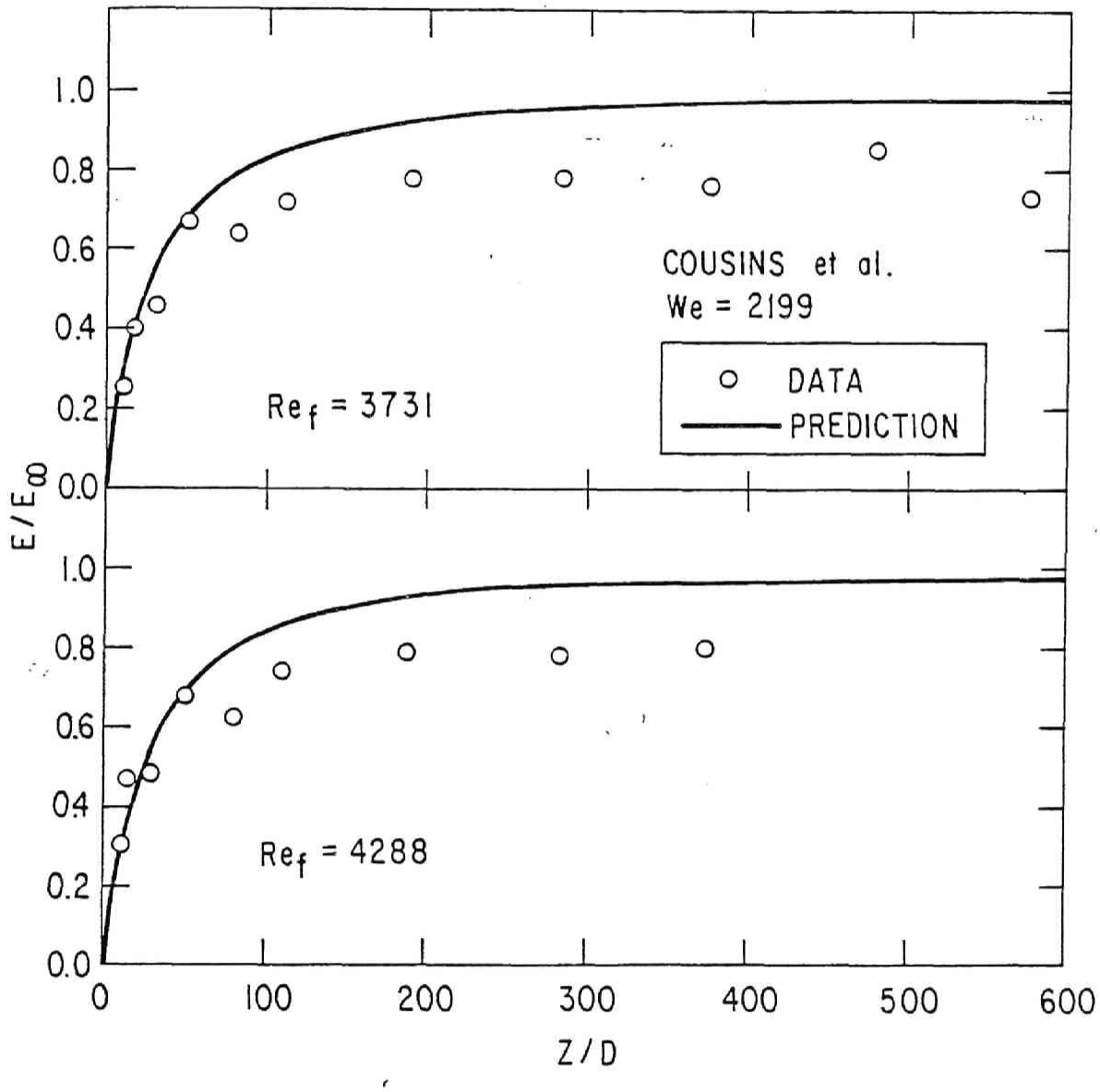

Fig. 20. Comparison of Experimental Data of Cousins et al. [18] with Predicted Amount of Entrainment at We = 2199 and Re_f = 3731 & 4288

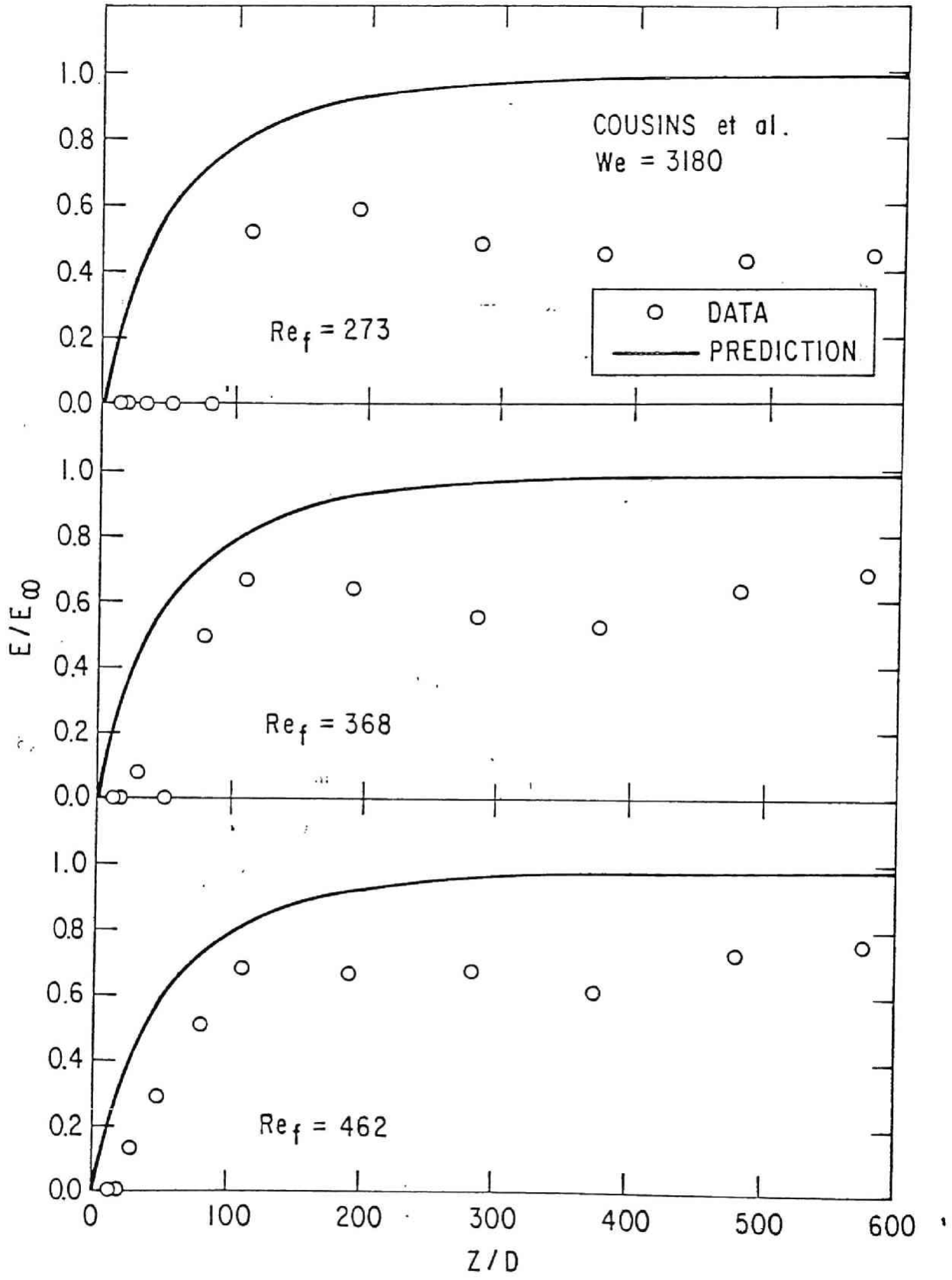

Fig. 21. Comparison of Experimental Data of Cousins et al. [18] with Predicted Amount of Entrainment at We = 3180 and Re_f = 273 ∿ 462

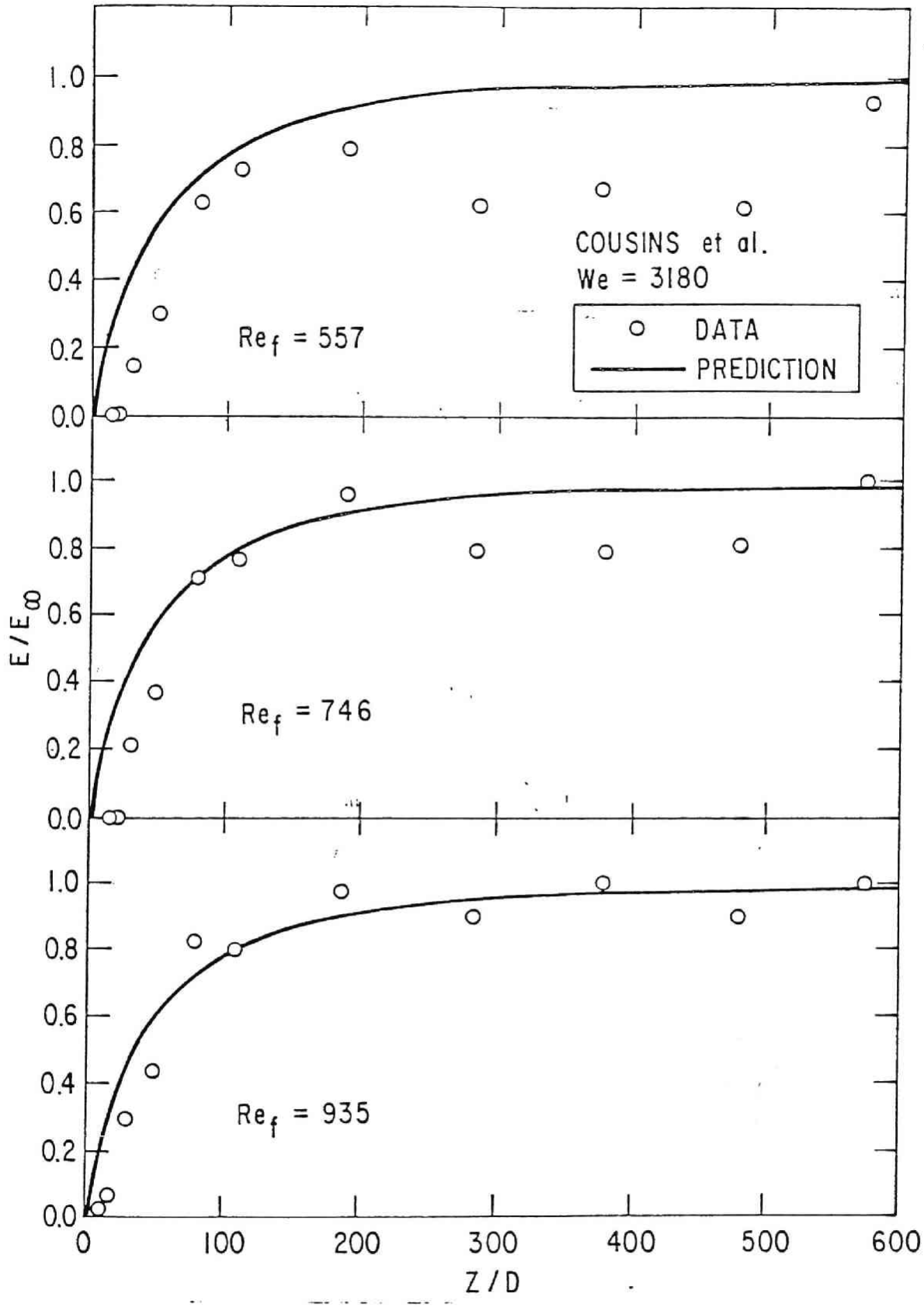

Fig. 22. Comparison of Experimental Data of Cousins et al. [18] with Predicted Amount of Entrainment at We = 3180 and Re_f = 557 ~ 935

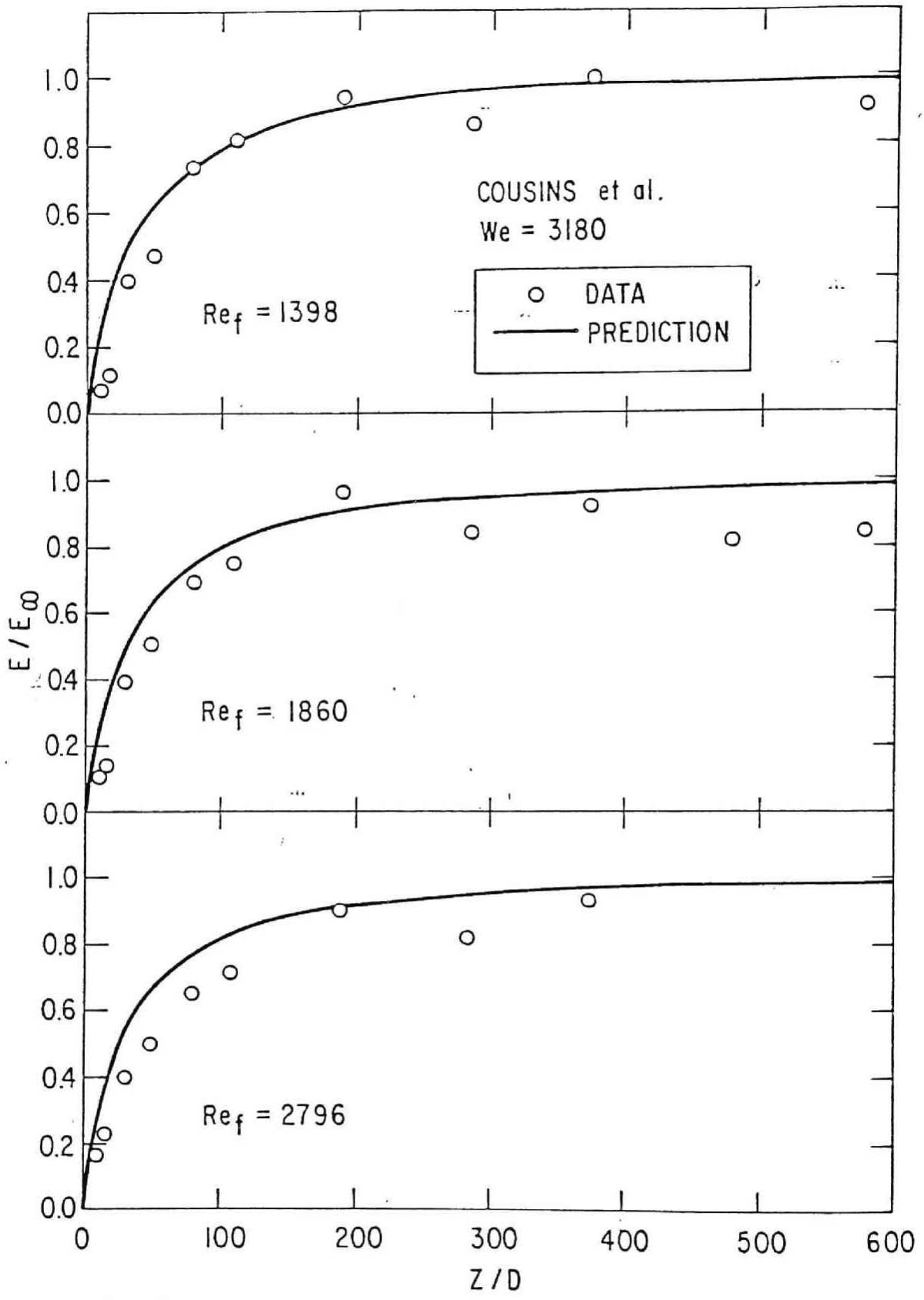

Fig. 23. Comparison of Experimental Data of Cousins et al. [18] with Predicted Amount of Entrainment at We = 3180 and Re_f = 1398 ~ 2796

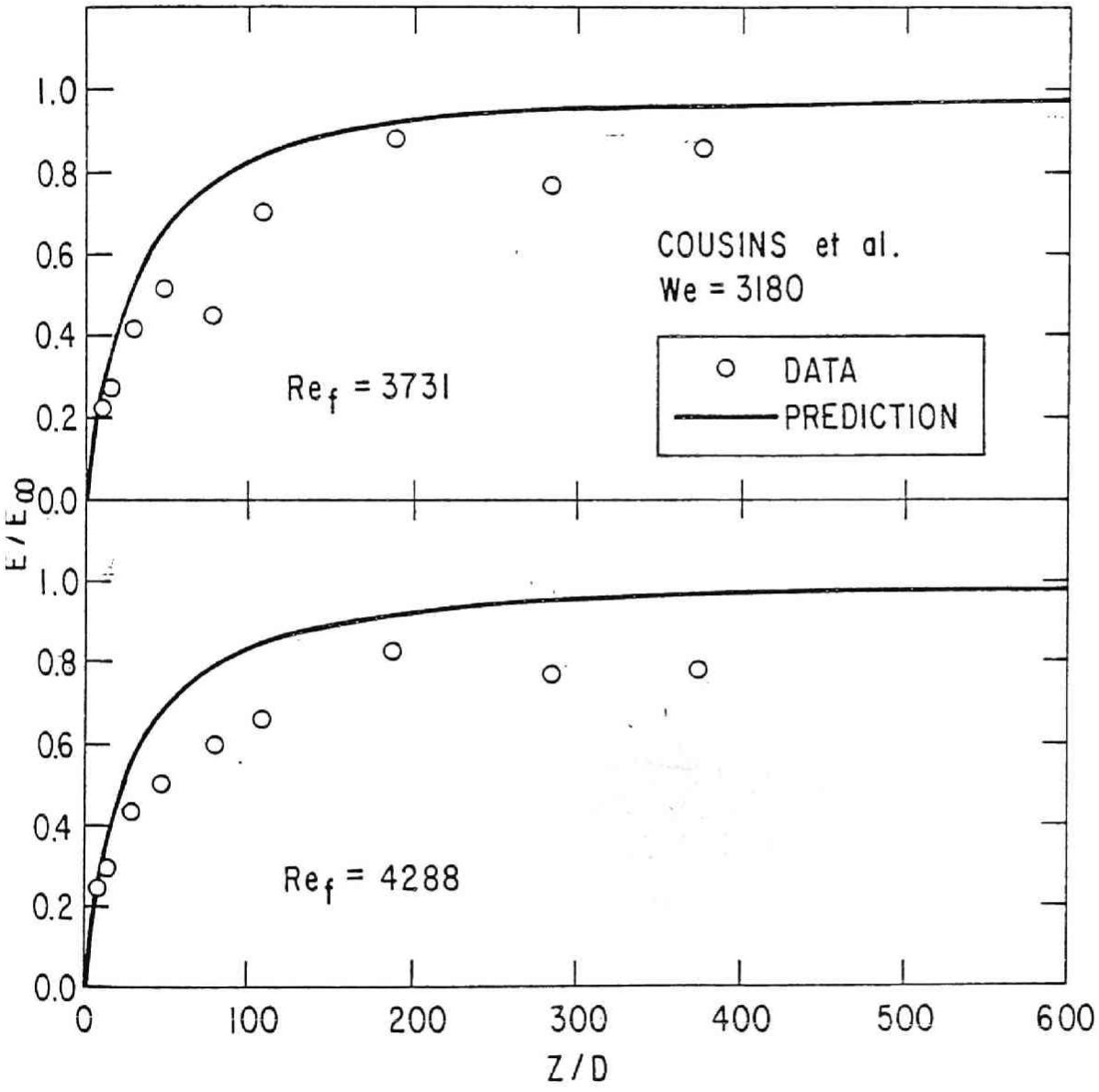

Fig. 24. Comparison of Experimental Data of Cousins et al. [18] with Predicted Amount of Entrainment at We = 3180 and Re_f = 3731 ∿ 4288

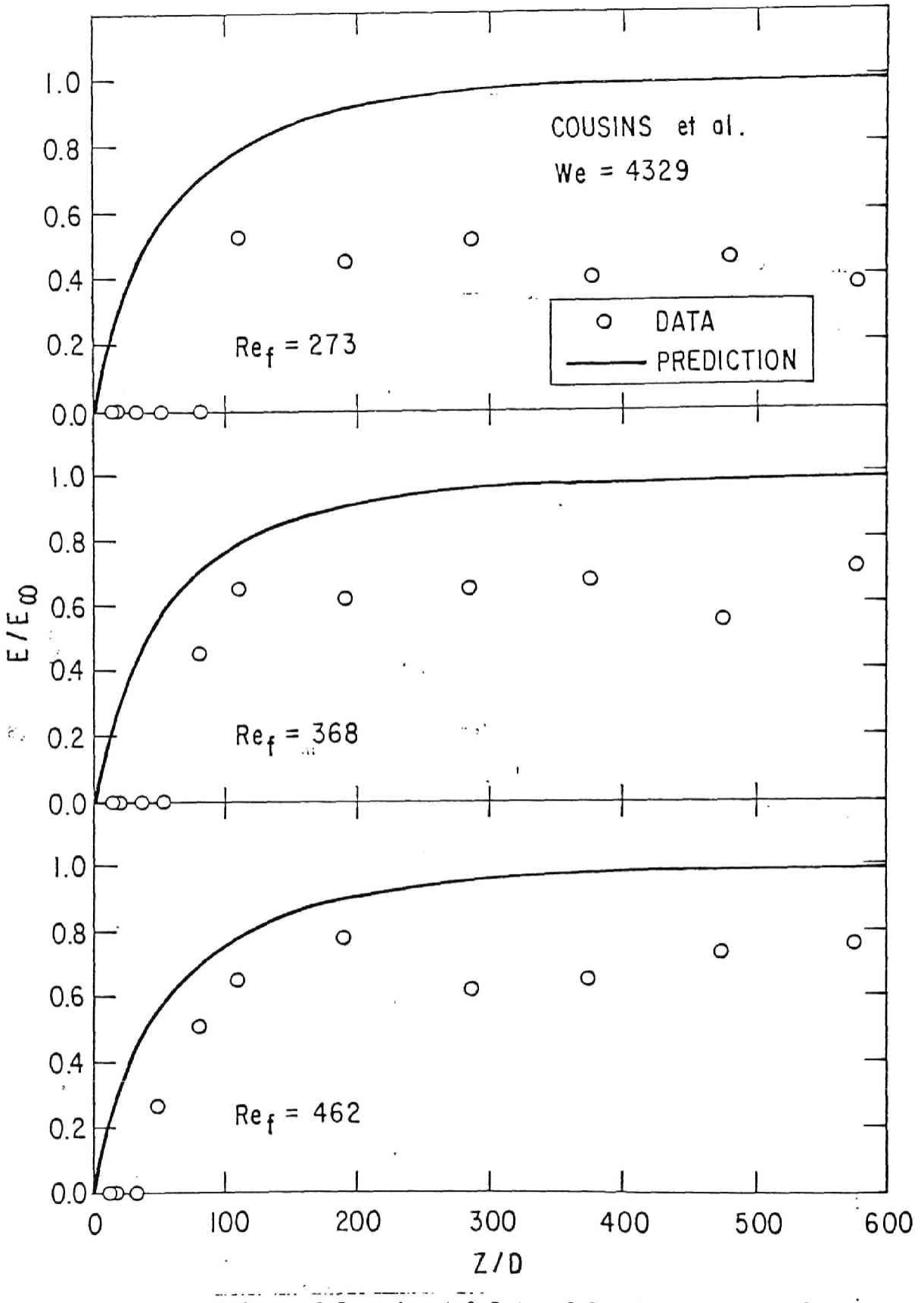

Fig. 25. Comparison of Experimental Data of Cousins et al. [18] with Predicted Amount of Entrainment at We = 4329 and Re_f = 273 ~ 462

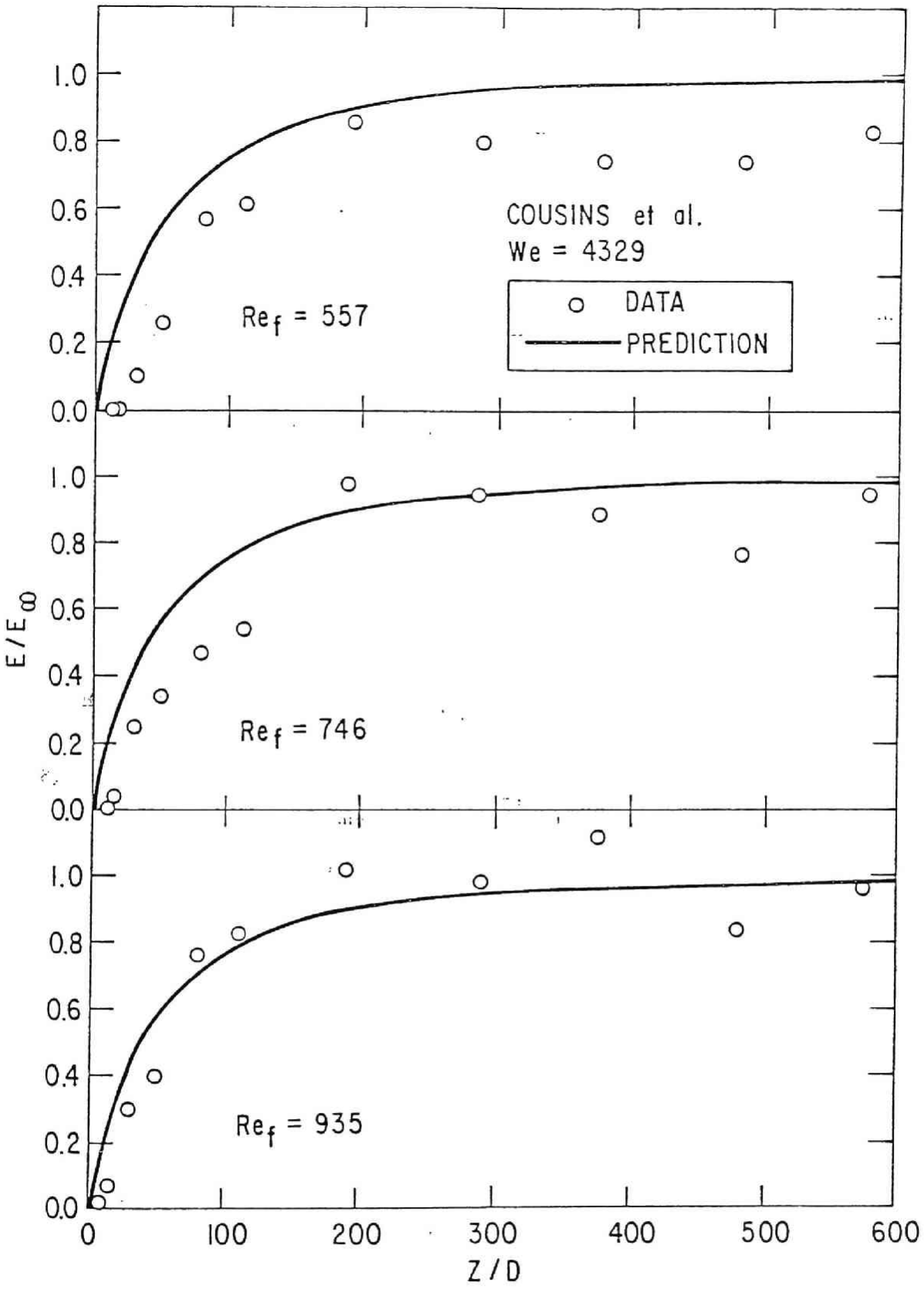

Fig. 26. Comparison of Experimental Data of Cousins et al. [18] with Predicted Amount of Entrainment at We = 4329 and Re_f = 557 ∿ 935

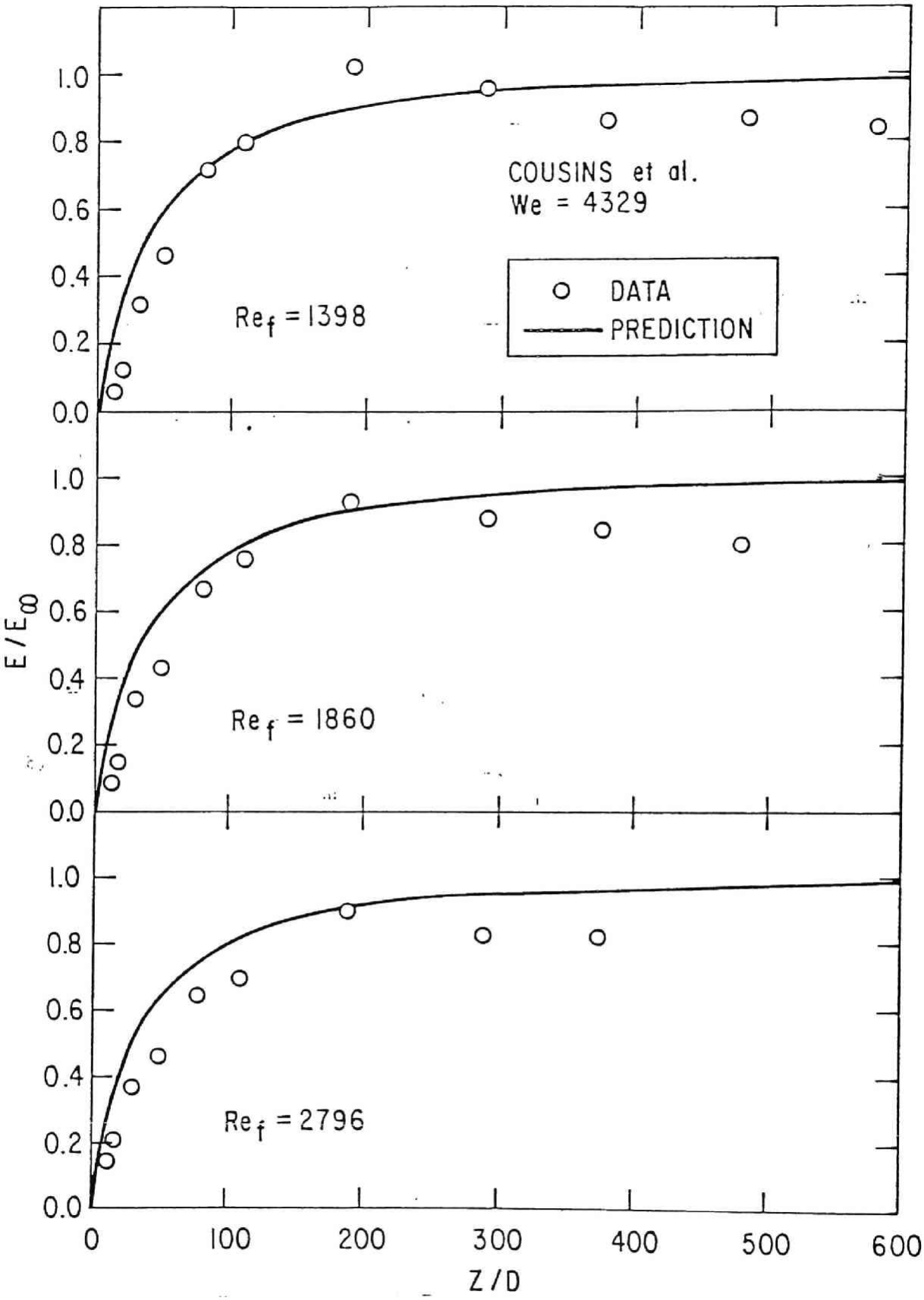

Fig. 27. Comparison of Experimental Data of Cousins et al. [18] with Predicted Amount of Entrainment at We = 4329 and Re_f = 1398 ~ 2796

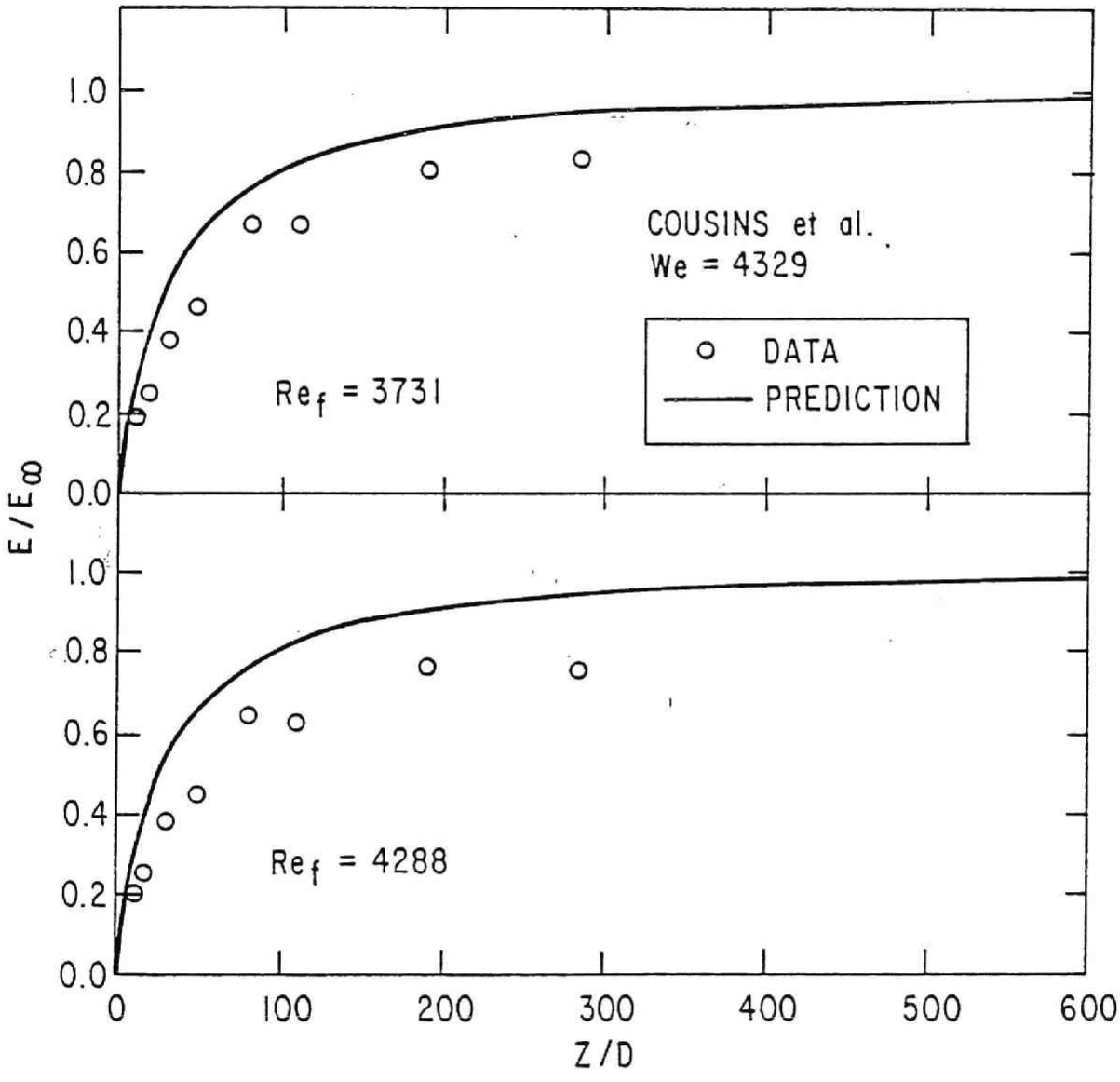

Fig. 28. Comparison of Experimental Data of Cousins et al. [18] with Predicted Amount of Entrainment at We = 4329 and Re_f = 3731 ∿ 4288

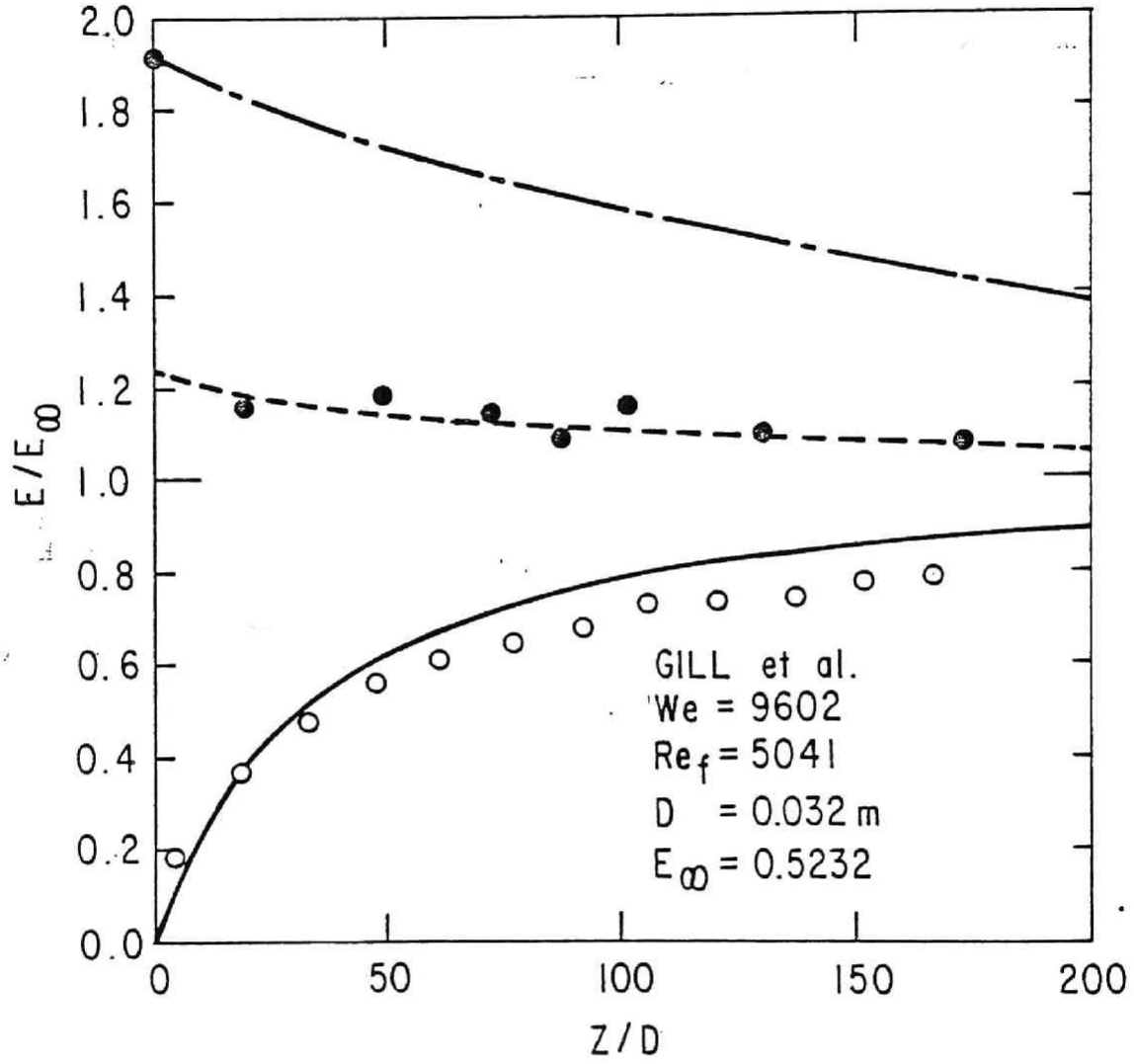

Fig. 29. Comparison of Experimental Data of Gill et al. [17] with Predicted Amount of Entrainment at We = 9602 and Re_f = 5041

Table I. Summary of Various Experiments on Entrainment Amount in Entrance Region

Reference	Fluids	Geometry	Flow Direction	Inlet Condition	Operational Condition
Cousins et al. [18] (1965)	Air-Water	0.0095 m Tube	Vertically Up	Smooth Injection as Liquid Film	0.28 MPa j_f = 0.026 ∿ 0.408 m/s j_g = 22.36 ∿ 39.12 m/s
Gill & Hewitt [20] (1967)	Air-Water	0.03175 m Tube	Vertically Up	Droplet Injection through Axial Jet	0.19 MPa j_f = 0.029 m/s j_g = 26.25 m/s
Gill et al. [17] (1962)	Air-Water	0.03175 m Tube	Vertically Up	Smooth Injection as Liquid Film	0.19 MPa j_f = 0.029 m/s j_g = 26.25 m/s

CHAPTER V

MECHANISTIC MODELING AND CORRELATION FOR POOL ENTRAINMENT PHENOMENA

V. 1 INTRODUCTION

As already described in the preceeding two chapters, annular and annular dispersed flows are the most important flow regimes involved in the safety evaluation of nuclear reactors under loss of coolant accident conditions. In these flow regimes, entrainment can play an important role on heat and mass transfer processes. There are several different entrainment mechanisms in annular dispersed flow [1,2]. Among these, the shearing off mechanism of roll-wave crests by a highly tubulent gas flow is the predominant mechanism [1,3]. Based on this mechanism, a criterion for the onset of entrainment [1], and a correlation for the amount of entrained droplets [4] have been recently developed. In Chapter III, a correlation of droplet size distribution [5], and in Chapter IV a correlation for entrainment rate [6], which are the key parameters for the annular dispersed flow, have been developed. Coupled with a theoretical formulation of two-fluid model [7], these correlations provide accurate predictions of thermohydraulics of annular dispersed flow. For example, the dryout heat flux, post dryout heat transfer coefficient [8-13], vapor superheat, and the effectiveness of the emergency core cooling in light water reactors [14-17] can be evaluated using these correlations in the formulation.

Besides the above mentioned phenomena, there is another important mechanism of entrainment. That is, the entrainment from a liquid pool by gas flow in boiling or bubbling. Earlier, in the field of nuclear engineering, this pool entrainment was studied in relation to radioactive carryover in a boiling water reactor [18], decontamination factors in evaporation of radioactive liquid waste in a natural circulation evaporator [19-22], and steam generator performance. In the above two cases, entrainment has detrimental effects on reduction of radioactivity.

Recently the importance of pool entrainment has been recognized associated with heat and mass transfer processes during loss-of-coolant accidents (LOCA), in particular, during the recovery phase of these accidents through reflooding of a core. In this case, pool entrainment may improve heat transfer, since droplets act as a heat sink through droplet evaporation. This will lead to lower vapor superheat and improved cooling of fuel pins which is quite important in terms of safety. Therefore, some researches have been carried out on pool entrainment during LOCA [23,24] and reflooding [25,26]. However, there have been no

satisfactory correlations which predict entrainment amount at given heat flux (or vapor velocity) and given distance from the free liquid surface.

In the field of chemical engineering, pool entrainment has been studied in relation to the efficiency of the gas liquid contacting equipments, e.g., plate columns, etc., [27-29] and fluidized beds [30,31]. Some correlations have been recommended [32] in this field. However, geometry and operational conditions of these chemical engineering equipments are quite different from those of boilers and nuclear reactor systems. Therefore, these correlations may not be directly applied to later cases.

As for the pool entrainment in boilers, some experimental works have been carried out and several empirical correlations have been proposed [33~49]. However, these correlations are not based on physical modeling, therefore their applicability may be limited.

In view of these, a correlation for the pool entrainment is developed here from a simple physical model by considering droplet size distribution, initial velocity of entrained droplets, droplet motion and droplet deposition. It is shown to correlate a number of data over a wide range of experimental conditions.

V.2 PREVIOUS WORKS

In boiling or bubbling pool systems, droplets are entrained by the mechanisms of bubble bursting, splashing and foaming near the top of a pool. Some part of these entrained droplets fall back to the surface of a pool and the other part is carried away by streaming gas. The entrainment E_{fg} which is the ratio of the droplet upward mass flux $\rho_f j_{fe}$ to the gas mass flux $\rho_g j_g$, has been measured experimentally by some researchers [34-49]. Here j_{fe} is the superficial velocity of liquid flowing as droplets, and j_g is the superficial velocity of gas. Thus the entrainment E_{fg} is defined by

$$E_{fg} \equiv \frac{\rho_f j_{fe}}{\rho_g j_g} \quad . \tag{1}$$

The experimental data show that the entrainment E_{fg} is a strong function of the gas superficial velocity j_g and the distance from the surface of a pool h. When the entrainment is plotted against the gas superficial velocity at a fixed distance h, at least three entrainment regimes can be observed [33,38,49]. In a low gas flux regime, the entrainment is small and entrained liquid consists of very fine droplets. In this regime, E_{fg} is approximately proportional to the gas flux. In an intermediate gas flux regime, larger drops are ejected from the pool and E_{fg} increases with $j_g^{3\sim4}$. At a higher gas flux, large gas slugs are formed and a pool is highly agitated. Then a considerable amount of liquid can be entrained by splashing. In this high gas flux regime, E_{fg} increases very rapidly with the gas flux, i.e., $E_{fg} \propto j_g^{7\sim20}$.

As for the effect of the distance from the surface of a pool, there are at least two distinct regions. In the first region (momentum controlled region), entrainment consists of larger droplets which rise due to their initial momentum at the surface and smaller droplets which are carried away by streaming gas. In this region, E_{fg} decreases rapidly with increasing distance, i.e., $E_{fg} \propto h^{-3}$. In the second region (deposition controlled region), entrainment consists only of small droplets whose terminal velocity is smaller than the gas velocity. Entrainment in this region decreases gradually due to the droplet depositions. This trend can be expressed as an exponential decay function of the height.

Although there have been no theoretical methods of predicting entrainment, several semi-empirical correlations [37,40,46] based on various data [35,38,39,41,44,49] and dimensional analyses have been proposed.

Kruzhilin [37] proposed a dimensionless correlation for the intermediate gas flux regime and momentum controlled region based on a dimensional analysis. With an assumption that the initial velocity of droplets at the interface is determined by the kinetic energy of vapor $\rho_g j_g^2/2$, he obtained

$$E_{fg} = C_K \, j_g^{*4} \sqrt{\frac{\Delta\rho}{\rho_g}} \sqrt{\frac{\Delta\rho}{\rho_f}} \quad . \tag{2}$$

Here j_g^* is the dimensionless gas flux defined by

$$j_g^* \equiv j_g \Big/ \left(\frac{\sigma g \Delta\rho}{\rho_g^2} \right)^{1/4} \quad , \tag{3}$$

where σ, g and $\Delta\rho$ are the surface tension, acceleration due to the gravity, and difference between the gas and liquid densities, respectively. In Eq. (2), C_K must be determined from experimental data. However, it has been found that the value of C_K depends on the distance from the interface. Although Eq. (2) shows the effects of velocity and pressure on E_{fg}, it does not give any information on the effect of height, which is important in the momentum controlled region.

Sterman [40] correlated the experimental data of entrainment for steam water systems at pressures from 0.1 MPa to 18 MPa, and proposed a dimensionless correlation. His correlation depends on the average void fraction in the pool, therefore, he has also proposed several void fraction correlations applicable to the problem. For a reasonably large vessel satisfying the condition given by

$$D_H^* \left(\frac{\Delta\rho}{\rho_g} \right)^{0.2} > 260 \quad , \tag{4}$$

where the dimensionless diameter of vessel D_H^* is given by

$$D_H^* \equiv D_H \Big/ \sqrt{\frac{\sigma}{g\Delta\rho}} \quad , \tag{5}$$

the Sterman correlation can be simplified to

$$E_{fg} = 6.09 \times 10^9 \; j_g^{*2.76} \; h^{*-2.3} \left(\frac{\rho_g}{\Delta\rho} \right)^{-0.26} N_{\mu f}^{2.2} \left(\frac{\Delta\rho}{\rho_f} \right)^{1.1} \quad . \tag{6}$$

Here the dimensionless height h^* is given by

$$h^* \equiv h \Big/ \sqrt{\frac{\sigma}{g\Delta\rho}} \quad , \tag{7}$$

and the liquid viscosity number $N_{\mu f}$ based on liquid viscosity μ_f is given by

$$N_{\mu f} \equiv \frac{\mu_f}{(\rho_f \sigma \sqrt{\sigma/g\Delta\rho})^{1/2}} \quad . \tag{8}$$

Equation (6) is applicable to the intermediate gas flux regime and momentum controlled region. The boundary between the intermediate and high gas flux regimes occurs at

$$j_g^* = 1.08 \times 10^{-5} \; h^{*0.83} \left(\frac{\Delta\rho}{\rho_g}\right)^{-0.2} N_{\mu f}^{-0.92} \left(\frac{\rho_f}{\Delta\rho}\right)^{0.46} \quad . \tag{9}$$

The Sterman correlation shows a strong dependence of E_{fg} on the liquid viscosity through the liquid viscosity number $N_{\mu f}$. According to this correlation, entrainment increases with the liquid viscosity as $E \propto \mu_f^{2.2}$. However, experimental data on the effect of the liquid viscosity on entrainment [42] does not show such a strong viscosity dependence. Furthermore, Eq. (6) fails to predict experimental data of air-water systems [41].

Rozen et al. [46] proposed a correlation for the deposition controlled region, which is given by

$$E_{fg} = 3.8 \times 10^{-5} \; [K^{0.5} + 530 \; K^{2.1}] \sqrt{\frac{\Delta\rho}{\rho_g}} \; e^{-0.23h/D_H} \quad , \tag{10}$$

where

$$K \equiv D_c^* \; j_g^* \quad , \tag{11}$$

with the dimensionless critical droplet diameter defined by

$$D_c^* \equiv D_c \Big/ \sqrt{\frac{\sigma}{g\Delta\rho}} \quad . \tag{12}$$

Here D_c is the critical droplet diameter whose terminal velocity is equal to gas velocity. Therefore, for this correlation the size of droplet should be specified. By matching the settling velocity of wake regime droplets [5,50] to the gas flux, the following correlation for a drop size can be obtained

$$D_c = \frac{4j_g}{\left[\frac{(g\Delta\rho)^2}{\mu_g \rho_g}\right]^{1/3}} \quad . \tag{13}$$

Then the K parameter can be specified as

$$K \equiv 4\, j_g^{*2}\, N_{\mu g}^{1/3} \quad , \tag{14}$$

where the gas viscosity number based on the gas viscosity μ_g is defined by

$$N_{\mu g} \equiv \frac{\mu_g}{(\rho_g \sigma \sqrt{\sigma/g\Delta\rho})^{1/2}} \quad . \tag{15}$$

In view of Eq. (14), the Rozen correlation can be modified to

$$E_{fg} = 7.6 \times 10^{-5} \{j_g^* N_{\mu g}^{1/6} + 4870\, j_g^{*4.2} N_{\mu g}^{0.7}\} \sqrt{\frac{\Delta\rho}{\rho_g}}\, e^{-0.23h/D_H} \quad . \tag{16}$$

The correlation given by Eq. (16) shows basically two regimes depending on the value of j_g^*. For small j_g^*, Eq. (16) can be approximated as

$$E_{fg} = 7.6 \times 10^{-5}\, j_g^*\, N_{\mu g}^{1/6} \sqrt{\frac{\Delta\rho}{\rho_g}}\, e^{-0.23h/D_H} \quad . \tag{17}$$

On the other hand, for large j_g^* Eq. (16) can be simplified to

$$E_{fg} = 0.37\, j_g^{*4.2}\, N_{\mu g}^{0.7} \sqrt{\frac{\Delta\rho}{\rho_g}}\, e^{-0.23h/D_H} \quad . \tag{18}$$

The transition occurs at

$$j_g^* = 0.071\, N_{\mu g}^{1/6} \quad . \tag{19}$$

As shown above, these semi-empirical correlations based on dimensional analyses are applicable to limited ranges of operational parameters. Furthermore, some parametric dependencies predicted by these correlations may not be correct if they are applied beyond the ranges of the data base. In view of the importance of entrainment from a liquid pool in safety analyses of nuclear reactors as well as various engineering problems, an accurate correlation applicable over wide ranges of operational parameters is highly desirable. For this general purpose, the correlation should be based on realistic modeling of droplet behaviors in the vapor space and at the liquid vapor interface.

Based on these observations, a correlation for pool entrainment is developed from mechanistic modeling in this study. It takes into account the droplet diameter distribution, initial velocity of droplets and droplet motion. Thus the present model reflects more realistic mechanisms of pool entrainment than those proposed previously.

V. 3 BASIC EQUATION

When boiling or bubbling occurs in a liquid pool, droplets are ejected from a pool surface by bursting of bubbles, splashing or foaming. These droplets have varying diameters and ejection velocities. Each droplet goes through its own trajectory depending on its mass, initial velocity, and drag force exerted by streaming gas. The entrained droplet flux is determined by the collective behavior of each droplet, which can be analyzed by solving an equation of motion of each droplet using initial condition at the interface. However, there are an enormous number of droplets ejected from the surface of a liquid pool, thus it is impractical to treat the movement of each droplet separately. Therefore, a statistical treatment has been adopted here.

In order to treat the entrainment problem statistically, one needs to introduce important physical parameters and distribution functions at the interface such as the entrainment rate at the interface, droplet size distribution function, droplet initial velocity distribution, and necessary initial velocity of a droplet to rise more than height, h. The entrainment rate at the interface, $\dot{\varepsilon}(j_g)$, is the mass flux of droplets at the interface and considered to be a function of the gas velocity.

Droplets ejected from the interface have various diameters represented by droplet size distribution function $f(D,j_g)$, which is the fraction of droplets whose diameter lies between D and D + dD. This function is considered to depend on the gas velocity. Furthermore, $f(D,j_g)$ satisfies the following relation.

$$\int_0^\infty f(D,j_g)dD = 1 \quad . \tag{20}$$

The initial velocity v_i which is the velocity of the droplet just ejected from the interface has its own distribution function, $g(v_i,D,j_g)$. This function represents the fraction of droplets whose velocity lies between v_i and $v_i + dv_i$ at the interface. It also satisfies

$$\int_0^\infty g(v_i,D,j_g)dv_i = 1 \quad . \tag{21}$$

In view of the mechanisms of the droplet ejection, this function is considered to depend on the droplet diameter and gas velocity.

The velocity of a droplet necessary to rise more than h, $v_h(D,j_g,h)$ can be obtained by solving the equation of motion of a single droplet with an appropriate drag coefficient. Thus it should be a function of the droplet diameter, gas velocity and height from the interface.

Using the above mentioned statistical parameters, the entrainment at distance h from the interface can be given by the following integral

$$E_{fg}(h,j_g) = \frac{\dot{\varepsilon}(j_g)}{\rho_g j_g} \int_0^\infty \int_{v_h(D,j_g,h)}^\infty g(v_i,D,j_g)f(D,j_g)dv_i dD \quad . \tag{22}$$

The entrainment given by Eq. (22) consists of two groups of droplets. The first group of droplets are the ones whose diameters are larger than the critical droplet diameter D_c. Here D_c is the diameter of a droplet whose

terminal velocity is equal to the gas velocity. Therefore, this group of droplets arrive at the height by the initial momentum gained at the ejection. The second group of droplets have their diameters less than the critical droplet diameter D_c. This group of droplets can be carried away by the streaming gas to any height unless they are deposited to the wall.

For large h, entrainment should consist only of those droplets having a diameter less than D_c. Then, for this case, one gets the limiting value of E_{fg} from Eq. (22) which is given by

$$\lim_{h\to\infty} E_{fg}(h,j_g) \equiv E_{fg\infty}(j_g) = \frac{\dot{\varepsilon}(j_g)}{\rho_g j_g} \int_0^{D_c} f(D,j_g)\,dD \quad . \tag{23}$$

Here $E_{fg\infty}$ gives the entrainment amount far from the pool surface with the negligible deposition effect. This value may be physically reached in a large diameter vessel. For a small diameter vessel some modification must be incorporated into the expression of $E_{fg\infty}$. This will be discussed later.

Using Eq. (23), one can rewrite Eq. (22) as

$$E_{fg}(h,j_g) = \frac{\dot{\varepsilon}(j_g)}{\rho_g j_g} \int_{D_c}^{\infty} \int_{v_h}^{\infty} g(D,j_g,v_i) f(D,j_g)\,dv_i\,dD + E_{fg\infty}(j_g) \quad . \tag{24}$$

The integral term of the right hand side of Eq. (24) represents the entrainment due to the first group of droplets with a diameter larger than D_c. The second term represents the droplets with a diameter smaller than D_c. Again, this equation is applicable to the system where the deposition is negligible. This formulation gives a more clear image of pool entrainment and is convenient in developing an entrainment correlation which is presented in the following sections.

V. 4 DROPLET DIAMETER DISTRIBUTION AND ENTRAINMENT RATE AT INTERFACE

The droplet diameter distribution function $f(D,j_g)$ and entrainment rate at interface $\dot{\varepsilon}(j_g)$ are key factors to determine entrainment at any

height from the pool surface. However, these two parameters are difficult quantities to analyze or measure directly. Thus one needs to consider through a more directly observable parameter. For this purpose the interface entrainment $E_o(D,j_g)$ is introduced. $E_o(D,j_g)$ represents the entrainment consisting of droplets whose diameters are less than the stated value D. Then it can be expressed as

$$E_o(D,j_g) = \frac{\dot{\varepsilon}(j_g)}{\rho_g j_g} \int_0^D f(D,j_g)dD \quad . \tag{25}$$

$E_o(D,j_g)$ is an observable parameter. For example, comparing Eq. (23) and Eq. (25) one immediately obtains that

$$E_o(D_c,j_g) = E_{fg\infty}(j_g) \quad . \tag{26}$$

Furthermore, the entrainment due to droplets with a diameter less than D denoted by $E_{fg}(h,j_g,D)$ can be related to this parameter $E_o(D,j_g)$ as shown below

$$E_{fg}(h,j_g,D) = \frac{\dot{\varepsilon}(j_g)}{\rho_g j_g} \int_0^D \int_{v_h(D,j_g,h)}^{\infty} g(v_i,D,j_g)f(D,j_g)dv_i dD \quad . \tag{27}$$

By considering the droplets with a diameter less than D_c and using the definition of $v_h(D,j_g,h)$, one gets

$$v_h(D,j_g,h) = 0 \qquad (D < D_c) \quad . \tag{28}$$

From Eqs. (21), (27) and (28), $E_{fg}(h,j_g,D)$ can be simplified to the following expression for $D < D_c$;

$$E_{fg}(h,j_g,D) = \frac{\dot{\varepsilon}(j_g)}{\rho_g j_g} \int_0^D f(D,j_g)dD \quad . \tag{29}$$

This implies that for $D < D_c$

$$E_o(D,j_g) = E_{fg}(h,j_g,D) \quad . \tag{30}$$

It is noted that Garner et al. [35] have measured $E_{fg}(h,j_g,D)$.

Now, instead of using a completely empirical correlation, a simple model for $E_o(D,j_g)$ is developed by considering the mechanisms of entrainment. By introducing the droplet site density N, mean frequency f_D, escape probability p and drag force F_D, the parameter $E_o(D,j_g)$ may be related to these by

$$E_o(D,j_g) \sim N\ f_D p\ F_D \quad . \tag{31}$$

The drag force F_D [50] is given by

$$F_D = -\frac{1}{2} C_D\ \rho_g\ v_r\ |v_r|\ A_d \ , \tag{32}$$

where C_D, v_r, and A_d are the drag coefficient, relative velocity, and projected area of a droplet, respectively. For a wake regime ($Re_D = 5 \sim 1000$), the drag coefficient C_D [5,50] is approximately given by

$$C_D = \frac{10.67}{Re_D^{0.5}} \quad . \tag{33}$$

Here Re_D is the droplet Reynolds number for a dilute suspension defined by

$$Re_D \equiv \frac{\rho_g v_r D}{\mu_g} \quad . \tag{34}$$

For a simple model, the following approximations may be used.

$$\begin{aligned} v_r\ |v_r| &\sim j_g^2 \\ A_d &\sim D^2 \end{aligned} \quad . \tag{35}$$

Substituting Eqs. (32) through (35) into Eq. (31) one obtains

$$E_o(D,j_g) \sim (j_g D)^{1.5} \quad . \tag{36}$$

In view of Eqs. (30) and (36), the experimental data of Garner et al. [35] for $E_{fg}(h,j_g,D)$ are plotted against $D^* j_g^*$ in Fig. 1. Here j_g^* is the nondimensional gas flux defined by Eq. (3) and D^* is the nondimensional drop diameter given by

$$D^* = D \Big/ \sqrt{\frac{\sigma}{g\Delta\rho}} \quad . \tag{37}$$

As predicted by Eq. (36), experimental data for $D \leqslant D_c$ can be well correlated by

$$E_{fg}(h,j_g,D) = 0.3975(D^* j_g^*)^{1.5} \quad . \tag{38}$$

From Eqs. (30), (25) and (38) one obtains for $D \leqslant D_c$ the following expression;

$$\frac{\dot{\varepsilon}(j_g)}{\rho_g j_g} \int_0^D f(D,j_g)dD = 0.3975(D^* j_g^*)^{1.5} \quad . \tag{39}$$

By differentiating Eq. (39) with respect to D,

$$\sqrt{\frac{\sigma}{g\Delta\rho}} \frac{\dot{\varepsilon}(j_g)}{\rho_g j_g} f(D,j_g) = 0.5963\ j_g^{*1.5}\ D^{*0.5} \quad . \tag{40}$$

This is an important correlation relating the entrainment rate and droplet diameter distribution function to the gas flux and droplet diameter. However, it should be noted that the correlation given by Eq. (38) is based on a data set taken at one pressure. As Eq. (2) indicates, there should be an additional pressure effect through the density ratio $\Delta\rho/\rho_g$ in Eqs. (38) and (40). This becomes clear in the latter analyses and some modifications on Eqs. (38) and (40) are made subsequently (see Section VIII).

V. 5 DROPLET VELOCITY AT INTERFACE

When the gas flux j_g is small, the flow regime in a pool is a bubbly flow. In this regime, discrete bubbles rise up to the surface of the pool and collapse there. This mechanism of the bubble burst and subsequent entrainment have been studied previously and an expression for the velocity of entrained droplets has been developed empirically or theoretically [51-57]. According to Newitt et al. [54], the initial velocity of entrained droplet due to bubble burst is given by

$$v_i = \frac{3}{2} \frac{t_B}{D_B \rho_f} \left(\frac{4\sigma}{D_B} + P_o \right) , \tag{41}$$

where t_B, D_B, and P_o are bubble burst time, bubble diameter, and pressure around the bubble.

However, for the pool entrainment, the bubbly flow regime is limited to a very small gas velocity. For example, in an air-water system at the atmospheric pressure, the flow regime transition from bubbly to churn turbulent flow occurs at j_g in the order of 10 cm/sec [58]. Applying the drift flux model [59] to a bubbling system and using the transition criterion from bubble to churn turbulent flow regime [60] given by $\alpha \approx 0.3$, the transition gas flux becomes

$$j_g^* = 0.325 \left(\frac{\rho_g}{\rho_f} \right)^{1/2} . \tag{42}$$

These indicate that the churn turbulent flow may be the most dominant flow regime in a bubbling pool. In case of the churn turbulent flow, the initial velocity of entrained droplets is not determined by the bubble burst mechanism, but by a momentum exchange mechanism suggested by Nielsen et al. [61].

This momentum exchange mechanism is shown schematically in Fig. 2. The equation of motion for an element of the liquid ligament is given by,

$$\rho_f D \frac{dv_f}{dt} = \tau_i - \Delta\rho g D \quad , \tag{43}$$

where v_f is the velocity of an element of a liquid ligament at z. And the interfacial shear stress τ_i is given in terms of interfacial friction factor f_i as

$$\tau_i = f_i \frac{1}{2} \rho_g v_g^2 \quad . \tag{44}$$

When the gravity term is negligible compared with the interfacial term, Eq. (43) can be rewritten as

$$\frac{dv_f}{\frac{1}{2} \frac{\rho_g}{\rho_f} \frac{1}{D} f_i v_g^2} = dt = \frac{dz}{v_f} \quad . \tag{45}$$

At $z = \ell$, this velocity is equal to the initial velocity of the droplet, that is

$$v_f(z=\ell) = v_i \quad . \tag{46}$$

Integrating Eq. (45) from z = 0 to $z = \ell$, one can obtain

$$\frac{1}{2} \rho_f v_i^2 D = \frac{1}{2} f_i \rho_g v_g^2 \ell \quad . \tag{47}$$

Equation (47) implies that the kinetic energy of the droplet entrained is equal to the work exerted on the element of a liquid ligament by gas flow.

The ligament of liquid at the pool interface, as shown in Fig. 2, can be regarded as a sequence of several droplets which are about to be entrained. Therefore, the interfacial shear stress may be related to the drag coefficient for a droplet in the wake regime, i.e., Eq. (33), thus

$$f_i \sim C_D \sim Re_D^{-0.5} \quad . \tag{48}$$

The length of the liquid ligament is assumed to be proportional to the width of the ligament which is on the order of the droplet diameter in analogy with the Rayleigh instability of a liquid jet. Then,

$$\ell \sim D \quad . \tag{49}$$

Substituting Eqs. (48) and (49) into Eq. (47), one obtains

$$v_i^* \sim v_g^{*3/4} \, N_{\mu g}^{1/4} \, D^{*-1/4} \left(\frac{\rho_g}{\rho_f}\right)^{1/2} \quad , \tag{50}$$

where

$$v_i^* \equiv v_i \Big/ \left(\frac{\sigma g \Delta\rho}{\rho_g^2}\right)^{1/4} \tag{51}$$

and

$$v_g^* \equiv v_g \Big/ \left(\frac{\sigma g \Delta\rho}{\rho_g^2}\right)^{1/4} \quad . \tag{52}$$

The gas velocity v_g is related to the superficial gas velocity j_g in terms of void fraction α in the liquid pool as

$$v_g = \frac{j_g}{\alpha} \quad . \tag{53}$$

Then Eq. (50) can be rewritten as

$$v_i^* \sim j_g^{*3/4} \, \alpha^{-3/4} \, N_{\mu g}^{1/4} \, D^{*-1/4} \left(\frac{\rho_g}{\rho_f}\right)^{1/2} \quad . \tag{54}$$

Equation (54) is derived from the consideration of the momentum exchange mechanism at the interface. However, there are some experimental data for v_i, which support the dependence of v_i on j_g and D as given by Eq. (54).

Akselrod et al. [62] and Cheng et al. [28] measured indirectly (calculated from the maximum height of a droplet) the droplet initial velocity in an air-water system at the atmospheric pressure. In their experiment, the

liquid level is very low, i.e., 5-6 mm for Akselrod et al. [62] and 38 mm for Cheng et al. [28]. Under these conditions, a steady gas jet should form at the pool interface as observed by Muller et al. [63]. For this case α is almost independent of j_g. Hence

$$v_i^* \sim j_g^{*3/4} \, N_{\mu g}^{1/4} \, D^{*-1/4} \left(\frac{\rho_g}{\rho_f}\right)^{1/2} \quad . \tag{55}$$

In Fig. 3, the experimental data of Akselrod et al. [62] and Cheng et al. [28] are plotted in $v_i^* \Big/ \left\{ j_g^{*3/4} \, N_{\mu g}^{1/4} \left(\frac{\rho_g}{\rho_f}\right)^{1/2} \right\}$ vs. D^* plane. It can be seen that the experimental data for the initial velocity of droplets are well correlated by

$$v_i^* = 205 \, j_g^{*3/4} \, N_{\mu g}^{1/4} \, D^{*-1/4} \left(\frac{\rho_g}{\rho_f}\right)^{1/2} \quad . \tag{56}$$

For a system with a much higher liquid level, which is of considerable practical importance, the void fraction is a function of the gas superficial velocity j_g. For this case a correlation between α and j_g is necessary. The void fraction in a liquid pool generally shows lower values than those predicted by the one-dimensional drift-flux model. This is mainly due to the recirculation of liquid in the pool. Some empirical correlations for the void fraction are available [64-67] for this kind of flow.

Margulova [64] proposed the following dimensional correlation for a steam water system;

$$\alpha = (0.576 + 0.00414 \, P) \, j_g^{0.75} \quad , \tag{57}$$

where P is pressure in atm and j_g in m/s. Kurbatov [65] presented a dimensionless correlation given by

$$\alpha = 0.67\ j_g^{*2/3} \left(\frac{\rho_g}{\rho_f}\right)^{-1/3} \left(\frac{\nu_g}{\nu_f}\right)^{-2/9} D_H^{*-1/6} \quad , \tag{58}$$

where D_H^* is the dimensionless hydraulic diameter of vessel defined by $D_H^* = D_H \Big/ \sqrt{\frac{\sigma}{g\Delta\rho}}$. The correlation of Sterman [66] is given by

$$\alpha = 1.07\ j_g^{*0.8}\ D_H^{*-0.25} \left(\frac{\rho_g}{\Delta\rho}\right)^{-0.23} \quad . \tag{59}$$

Wilson, et al. [67] proposed a dimensionless correlation similar to Sterman's;

$$\alpha = 0.68 \left(\frac{\rho_g}{\Delta\rho}\right)^{-0.14} D_H^{*-0.1}\ j_g^{*0.62} \quad . \tag{60}$$

These correlations indicate that the void fraction depends on the dimensionless velocity, hydraulic diameter and density ratio as

$$\alpha \sim j_g^{*n_1}\ D_H^{*-n_2} \left(\frac{\rho_g}{\Delta\rho}\right)^{-n_3} \quad , \tag{61}$$

where n_1, n_2, and n_3 have the ranges of

$$\begin{aligned} n_1 &= 0.62 \sim 0.8 \\ n_2 &= 0.1 \sim 0.25 \\ n_3 &= 0.14 \sim 0.23 \end{aligned} \quad . \tag{62}$$

Yeh and Zuber [33] recommend the value of $n_1 = 2/3$ which gives satisfactory agreements with a number of experimental data used in the above correlations. Then Eq. (61) becomes

$$\alpha \sim j_g^{*2/3}\ D_H^{*-n_2} \left(\frac{\rho_g}{\Delta\rho}\right)^{-n_3} \quad . \tag{63}$$

Substituting Eq. (63) into Eq. (54), one obtains

$$v_i^* = C\, j_g^{*1/4}\, N_{\mu g}^{1/4}\, D^{*-1/4} \left(\frac{\rho_g}{\rho_f}\right)^{1/2} D_H^{*3n_2/4} \left(\frac{\rho_g}{\Delta\rho}\right)^{3n_3/4} . \qquad (64)$$

Here C is a proportionality constant which should be determined in collaboration with experimental data.

It is noted here that actually the initial velocity of droplet at the pool interface should have its distribution as discussed in Section V.3. However, apparently no data are available due to experimental difficulties. Therefore, as a first approximation, only the mean value of the initial velocities expressed by the above correlation is used in this analysis. This may also be justified for the simplicity of the model which can be checked by experimental data. Then droplet velocity distribution function, $g(v_i,D,j_g)$ is given by the delta function in the following form

$$g(v_i,D,j_g)dv_i = \delta\left(v_i^* - Cj_g^{*1/4}N_{\mu g}^{1/4}D^{*-1/4} \times \left[\frac{\rho_g}{\rho_f}\right]^{1/2} D_H^{*3n_2/4} \left[\frac{\rho_g}{\Delta\rho}\right]^{3n_3/4}\right) dv_i^* , \qquad (65)$$

where

$$\left.\begin{aligned} &\int_{-\infty}^{\infty} \delta(x)dx = 1 \\ &\delta(x) = 0 \text{ for } x \neq 0 \end{aligned}\right\} . \qquad (66)$$

In others words, the initial velocity distribution over the same size droplets is neglected.

V. 6 MAXIMUM HEIGHT OF RISING DROPLET

The maximum height which can be attained by a rising droplet in gas flowing vertically upward can be calculated by solving the equation of motion of the droplet by specifying the drag coefficient [68,69]. In this study, an analytical solution for a practical range of the droplet Reynolds number (Re_D = 5 ~ 1000) has been obtained. From the maximum height of a rising droplet, the droplet velocity $v_h(D,j_g,h)$ necessary to rise more than height h can be calculated as an inverse function.

For the situation illustrated in Fig. 4, the equation of motion of a droplet in gas stream is formulated by

$$\frac{dv}{dt} = - \frac{\Delta\rho}{\rho_f} g - \frac{3}{4} C_D \frac{1}{D} \frac{\rho_g}{\rho_f} (v-v_g)|v-v_g| \tag{67}$$

and

$$\frac{dy}{dt} = v \quad . \tag{68}$$

Here v, t, and y are the droplet velocity, time, and height from the pool surface. In the above equations, it may be assumed that the droplet concentration is relatively small such that $v_g \simeq j_g$. This implies that the relative velocity can be given by

$$v_r = v - v_g \simeq v - j_g \quad . \tag{69}$$

Initial conditions are given by

$$\left.\begin{array}{l} v = v_i \\ y = 0 \end{array}\right\} \text{ at } t = 0 \quad . \tag{70}$$

Equations (67) and (68) can be rewritten in terms of the relative velocity and drag coefficient for wake regime given by Eq. (33) as

$$\frac{dv_r}{dt} = - \frac{\Delta\rho}{\rho_f} g - \frac{3}{4} \cdot \frac{10.67}{D} \left(\frac{\mu_g}{\rho_g D}\right)^{0.5} \frac{\rho_g}{\rho_f} v_r|v_r|^{0.5} \tag{71}$$

and

$$y = \int_0^t (v_r + j_g)dt \quad . \tag{72}$$

Equation (71) can be analytically solved and the maximum height of a rising droplet h_m can be obtained by integrating Eq. (72). Thus for $v_i > j_g$

$$h_m^+ = 2\sqrt{v_{ri}^+} + 2\sqrt{j_g^+} - \frac{1}{3}(1+j_g^+)\ \ell n \frac{(1+\sqrt{v_{ri}^+})^2}{(1-\sqrt{v_{ri}^+}+v_{ri}^+)}$$

$$+ \frac{1}{3}(1-j_g^+)\ \ell n \frac{(1-\sqrt{j_g^+})^2}{(1+\sqrt{j_g^+}+j_g^+)} - \frac{2}{\sqrt{3}}(1-j_g^+)\ \tan^{-1}\left(\frac{2\sqrt{v_{ri}^+}-1}{\sqrt{3}}\right)$$

$$- \frac{2}{\sqrt{3}}(1+j_g^+)\ \tan^{-1}\left(\frac{2\sqrt{j_g^+}+1}{\sqrt{3}}\right) + \frac{4}{\sqrt{3}} j_g^+ \tan^{-1}\frac{1}{\sqrt{3}} \quad . \tag{73}$$

For $v_i < j_g$

$$h_m^+ = 2(\sqrt{j_g^+}-\sqrt{-v_{ri}^+}) + \frac{2}{3}(1-j_g^+)\ \ell n \frac{(1-\sqrt{j_g^+})}{(1-\sqrt{-v_{ri}^+})}$$

$$- \frac{1}{3}(1-j_g^+)\ \ell n \frac{(1+\sqrt{j_g^+}+j_g^+)}{(1+\sqrt{-v_{ri}^+}-v_{ri}^+)}$$

$$- \frac{2}{\sqrt{3}}(1+j_g^+)\left\{\tan^{-1}\left(\frac{2\sqrt{j_g^+}+1}{\sqrt{3}}\right) - \tan^{-1}\left(\frac{2\sqrt{-v_{ri}^+}+1}{\sqrt{3}}\right)\right\} \quad . \tag{74}$$

where

$$h_m^+ \equiv \frac{h_m g}{v_{r\infty}^2} \frac{\Delta\rho}{\rho_f} \tag{75}$$

$$j_g^+ \equiv \frac{j_g}{v_{r\infty}} \tag{76}$$

$$v_{ri}^+ \equiv \frac{v_i - j_g}{v_{r\infty}} \quad . \tag{77}$$

Here $v_{r\infty}$ is the terminal velocity of a single droplet. For the wake regime it is given by [5,50]

$$v_{r\infty} = \frac{1}{4} D \left[\frac{(g\Delta\rho)^2}{\mu_g \rho_g} \right]^{1/3} \quad . \tag{78}$$

In Table I, the maximum height of a droplet for the Stokes regime and Newton's regime is also tabulated.

In Fig. 5, the maximum height calculated from Eq. (73) for $v_i/j_g = 1$, $v_i/j_g = 2$, and $v_i/j_g = 10$ is plotted against the diameter ratio D/D_c where D_c is the critical diameter having the terminal velocity equal to j_g.

As mentioned above, the initial velocity of a droplet necessary to rise more than height h is obtained as an inverse function of Eqs. (73) or (74). It is a complicated function of D, j_g, and h, therefore, the analytical solution is not presented here. However, calculations based on Eqs. (73) and (74) indicate that the effect of j_g is not so strong for the practical range of j_g. From this observation, therefore, $v_h(D,j_g,h)$ may be approximated by the following simple expression for the range of j_g corresponding to bubbly or churn turbulent flow.

$$\begin{aligned} v_h &= 0 && (D < D_c) \\ v_h &= \sqrt{2gh \frac{\Delta\rho}{\rho_f}} && (D \geq D_c) \end{aligned} \quad . \tag{79}$$

Equation (79) can be rewritten in a dimensionless form as

$$\begin{aligned} v_h^* &= 0 && (D^* < D_c^*) \\ v_h^* &= \sqrt{2h^*}\left(\frac{\rho_g}{\rho_f}\right)^{1/2} && (D^* \geq D_c^*) \end{aligned} \quad . \tag{80}$$

where

$$v_h^* \equiv v_h \Big/ \left(\frac{\sigma g \Delta\rho}{\rho_g^2}\right)^{1/4} \quad . \tag{81}$$

For the wake regime D_c^* is given by

$$D_c^* = 4\, j_g^*\, N_{\mu g}^{1/3} \quad . \tag{82}$$

V. 7 CORRELATION FOR ENTRAINMENT AMOUNT

In previous sections, the entrainment rate and droplet size distribution at the pool interface, initial droplet velocity, and velocity necessary to rise more than height h, are obtained. Now the amount of entrainment can be calculated using the basic expression for entrainment and these results. Hence by substituting Eqs. (40), (65), and (80) into Eq. (22) one obtains

$$E_{fg}(h,j_g) = \int_0^\infty \int_{v_h^*}^\infty \delta\left(v_i^* - Cj_g^{*1/4} N_{\mu g}^{1/4} D^{*-1/4}\left(\frac{\rho_g}{\rho_f}\right)^{1/2} D_H^{*3n_2/4}\left(\frac{\rho_g}{\Delta\rho}\right)^{3n_3/4}\right)$$

$$\times\, 0.5963\, j_g^{*1.5}\, D^{*0.5}\, dv_i^* dD^* \quad . \tag{83}$$

Using Eq. (24), the above equation can be rewritten as

$$E_{fg}(h,j_g) = 0.5963 \int_0^{D_c^*} j_g^{*1.5}\, D^{*0.5}\, dD^*$$

$$+ 0.5963 \int_{D_c^*}^{\infty} \int_{v_h^*}^{\infty} \delta\left(v_i^* - Cj_g^{*1/4} N_{\mu g}^{1/4} D^{*-1/4} \left(\frac{\rho_g}{\rho_f}\right)^{1/2} D_H^{*3n_2/4} \left(\frac{\rho_g}{\Delta\rho}\right)^{3n_3/4}\right)$$

$$\times\, j_g^{*1.5}\, D^{*0.5}\, dv_i^* dD^* \quad . \tag{84}$$

Droplets have finite diameters, therefore, the range of the integration over D^* will be limited by the maximum diameter of droplets D_{max}. D_{max} is often correlated in terms of the maximum droplet Weber number [70,4] defined by

$$We_{max} \equiv \frac{D_{max}\rho_g j_g^2}{\sigma} = D_{max}^* j_g^{*2} \quad , \tag{85}$$

where

$$D_{max}^* \equiv \frac{D_{max}}{\sqrt{\frac{\sigma}{g\Delta\rho}}} \quad . \tag{86}$$

For example, for falling droplets [70] the maximum droplet diameter is given by

$$We_{max} = 22 \quad . \tag{87}$$

This implies that

$$D_{max}^* = 22\, j_g^{*-2} \quad . \tag{88}$$

On the other hand, in annular-dispersed flow, the maximum droplet diameter is given by [4]

$$We_{max} = 0.031\ Re_g^{2/3} \left(\frac{\rho_g}{\rho_f}\right)^{-1/3} \left(\frac{\mu_g}{\mu_f}\right)^{2/3} , \tag{89}$$

where Re_g is the gas Reynolds number given by

$$Re_g \equiv \frac{\rho_g j_g D_H}{\mu_g} . \tag{90}$$

Equation (89) shows that D^*_{max} can be scaled by

$$D^*_{max} \sim j_g^{*-4/3} . \tag{91}$$

In view of the entrainment mechanism discussed in the previous sections, the maximum droplet diameter in pool entrainment is assumed to be given by a form similar to Eqs. (88) and (91). Thus

$$D^*_{max} = C_m\ j_g^{*-n_4} , \tag{92}$$

where C_m and n_4 should be determined in collaboration with experimental data in the absence of a detailed hydrodynamic model of the droplet generation.

Integrating Eq. (84) with Eq. (92), one obtains the following results:

$$\text{For } h^* \leq \frac{C^2}{2} \frac{1}{\sqrt{C_m}} j_g^{*\frac{n_4+1}{2}} N_{\mu g}^{1/2} D_H^{*3n_2/2} \left(\frac{\rho_g}{\Delta\rho}\right)^{3n_3/2}$$

$$E_{fg}(h,j_g) = 0.398\ C_m^{1.5}\ j_g^{*1.5-3n_4/2} \quad . \tag{93}$$

For $h^* \geq \frac{C^2}{4}\ N_{\mu g}^{1/3}\ D_H^{*3n_2/2} \left(\frac{\rho_g}{\Delta\rho}\right)^{3n_3/2}$

$$E_{fg}(h,j_g) = 3.18\ j_g^{*3}\ N_{\mu g}^{1/2} \quad . \tag{94}$$

For $\frac{C^2}{2} \frac{1}{\sqrt{C_m}}\ j_g^{*\frac{n_4+1}{2}}\ N_{\mu g}^{1/2}\ D_h^{*3n_2/2} \left(\frac{\rho_g}{\Delta\rho}\right)^{3n_3/2} \leq h^* \leq \frac{C^2}{4}\ N_{\mu g}^{1/3}\ D_H^{*3n_2/2} \left(\frac{\rho_g}{\Delta\rho}\right)^{3n_3/2}$

$$E_{fg}(h,j_g) = 0.0497\ C^6\ j_g^{*3}\ h^{*-3}\ N_{\mu g}^{1.5}\ D_H^{*4.5n_2} \left(\frac{\rho_g}{\Delta\rho}\right)^{4.5n_3} \quad . \tag{95}$$

Equations (93) through (95) show that there are three regions in terms of the height from the pool interface. The first region (near surface region) is limited to small h. The entrainment and limit on height are given by Eq. (93). In this region, entrainment consists of all droplets which are entrained at the pool interface. The second region (momentum controlled region) is limited to intermediate h. In this region, entrainment consists of droplets which can attain height h due to the initial momentum of droplets. As the correlation given by Eq. (95) indicates, the entrainment amount increases with increasing gas velocity and with decreasing height in the second region. The third region (deposition controlled region) applies to large h. In this region, entrainment consists of droplets whose terminal velocity is less than gas velocity. Equation (94) indicates that E_{fg} is independent of h. In actual system, droplets can deposit on the vessel wall and thus E_{fg} should decrease gradually with increasing height.

In Fig. 6, the general trend of the entrainment E_{fg} is shown schematically. Indeed, the same trend is also observed in various experiments [43,44]. Equations (93) through (95) indicate significant dependence of the entrainment amount on the height above the pool surface and gas velocity. For practical applications the proportionality constants and effects of physical properties of liquid and gas reflected in exponents n_2, n_3 and n_4 should be correlated in collaboration with experimental data.

V. 8 ENTRAINMENT AMOUNT IN MOMENTUM CONTROLLED REGIME

Several experiments have been carried out to study entrainment amount in a bubbling or boiling pool. Most of the experimental data fall in the momentum controlled region which is most important in view of practical applications. It is also noted that in this region the entrainment is a very strong function of the height, whereas in the other two regimes the effects of the height is not very important. In view of these, the entrainment in this region will be discussed first.

Among available data, those of Kolokoltsev [49] (steam-water, 0.129 MPa), Garner et al. [35] (steam-water 0.101 MPa), Sterman et al. [39,40] (steam-water 1.72 ~ 18.7 MPa), Golub [44] (air-water 0.101 MPa) and Styrikovich et al. [41] (air-water 0.11 ~ 5.0 MPa) are used for the present correlation purpose because in these experiments the gas velocity and measurement location above the pool surface have been varied systematically. The key parameters of these experiments are summarized in Table II.

In Figs. 7 through 17, experimental data for the entrainment are plotted against a parameter j_g^*/h^*. However, Fig. 18 shows the data of Golub [44] in E_{fg}/j_g^{*3} vs. h^* plane. This is because in his experiments h^* has been varied extensively, and in this plot the dependence of E_{fg} on h^* can be easily examined. It is noted that his data also include the entrainment amount in the deposition controlled region. Figure 18 verifies the dependence of the entrainment on the height above the pool surface as predicted by Eqs. (93) through (95) and indicated schematically in Fig. 6.

As shown in Figs. 7 through 17, the entrainment amount increases with the third power of j_g^*/h^*, which is also predicted by the present model by Eq. (95). In collaboration with these experimental data, the proportionality constant C, and exponents n_2 and n_3 in Eq. (95) are determined. Then the final form of the correlation for the entrainment in the momentum controlled region is given by

$$E_{fg}(h,j_g) = 5.417 \times 10^6 \; j_g^{*3} \; h^{*-3} \; N_{\mu g}^{1.5} \; D_H^{*1.25} \left(\frac{\rho_g}{\Delta\rho}\right)^{-0.31} \quad . \qquad (96)$$

Figure 19 shows the comparison of various data to the above correlation in $E_{fg} \Big/ \left\{ N_{\mu g}^{1.5} \; D_H^{*1.25} \left(\frac{\rho_g}{\Delta\rho}\right)^{-0.31} \right\}$ vs. j_g^*/h^* plane. As can be seen from this comparison, Eq. (96) satisfactorily correlates the wide range of experimental data for entrainment in the momentum controlled region. Further comparisons of data to the correlation are shown in Figs. 7 through 18. This correlation applies to the intermediate gas flux regime.

Figure 19 shows that at low values of j_g^*/h^*, the dependence of the entrainment on j_g^*/h^* changes. This change is caused by the flow regime transition in a liquid pool. As mentioned in Section V, when the gas velocity is small, the flow regime becomes bubbly flow. The discrete bubbles rise up to the pool interface and collapse there. This is different from the mechanisms under which Eq. (96) is derived. In this bubbly flow regime, the droplet size distribution and initial velocity distribution may be quite different from those predicted by Eqs. (40) and (65). This regime corresponds to the low gas flux regime previously mentioned. Indeed, the change from the low to intermediate gas flux regime occurs approximately at j_g^* predicted by Eq. (42) which is derived from the criteria of flow regime transition from bubbly to churn turbulent flow in a pool.

Although data are scarce and considerable scattering is observed, the entrainment in the low gas flux regime may be correlated by

$$E_{fg}(h,j_g) = 2.213\ N_{\mu g}^{1.5}\ D_H^{*1.25} \left(\frac{\rho_g}{\Delta\rho}\right)^{-0.31}\ j_g^*\ h^{*-1} \quad . \tag{97}$$

In Fig. 19, overall comparisons between the various experimental data and the above correlations are shown.

From Eqs. (96) and (97) the transition criterion between the low and intermediate gas flux regimes can be obtained, thus

$$\frac{j_g^*}{h^*} = 6.39 \times 10^{-4} \quad . \tag{98}$$

This criterion gives a higher value of j_g^* than that predicted by Eq. (42) over the range of h^* appeared in the experimental data. This is because in a boiling or bubbling pool system, the void fraction is generally lower than those predicted by the standard drift flux model due to the significant internal circulation of liquid in the pool. Here h^* appears in the criterion due to the fact that the information at the interface to reach h^* requires a certain gas flux.

Figure 20 shows the various experimental data for entrainment in E_{fg} vs. $(j_g^*/h^*)\ N_{\mu g}^{0.5}\ D_H^{*0.42} \left(\frac{\rho_g}{\Delta\rho}\right)^{-0.10}$ plane. The solid line in this figure represents the correlation given by Eq. (96). This figure indicates that the correlation generally agrees well with the data, however, there is a systematic deviation at high values of j_g^*/h^*. This actually signifies the appearance of the high gas flux regime. This transition occurs approximately at

$$\left(\frac{j_g^*}{h^*}\right) = 5.7 \times 10^{-4}\ N_{\mu g}^{-0.5}\ D_H^{*-0.42} \left(\frac{\rho_g}{\Delta\rho}\right)^{0.10} \tag{99}$$

or at

$$E_{fg} \simeq 1.0 \times 10^{-3} \quad . \tag{100}$$

In the regime where (j_g^*/h^*) exceeds the value given by Eq. (99), the entrainment increases with (j_g^*/h^*) very rapidly as given by

$$E_{fg} \propto (j_g^*/h^*)^{7\sim20} \quad . \tag{101}$$

The transition from the intermediate to high gas flux regime may be attributed to a flow regime transition in the liquid pool. The transition from churn-turbulent to annular, pseudo jet or fountain flow [2,73,74] is indicated.

Now, based on the above analysis and correlation development, some of the underlining assumptions are reexamined. First, from Eqs. (95) and (96), the various constants in the correlation are now identified as

$$C = 21.86 \tag{102}$$

$$n_2 = 0.279 \tag{103}$$

and

$$n_3 = -0.0693 \quad . \tag{104}$$

When these values are compared to the results from the void fraction correlations given by Eq. (62), interesting observations can be made. The value of n_2 from Eq. (103) almost coincides with that given in Eq. (62), whereas the value of n_3 is quite different from that given in Eq. (62). This discrepancy should come from neglecting the effect of the density ratio $(\rho_g/\Delta\rho)$ in some of the correlations used to develop Eq. (95).

A careful reexamination of Eqs. (40), (65), and (80) leading to Eq. (95), indicates that Eq. (40) should have an additional $(\rho_g/\Delta\rho)$ term which reflects the effects of the pressure. Note that Eq. (40) is obtained from a simple model and the experimental data of steam-water system at 1 atm. There are no experimental data available at elevated pressures for this correlation. Thus Eq. (40) should be modified to account for the pressure effects as

$$\sqrt{\frac{\sigma}{g\Delta\rho}}\frac{\dot{\varepsilon}(j_g)}{\rho_g j_g} f(D,j_g) = C_1\left(\frac{\rho_g}{\Delta\rho}\right)^{n_5} j_g^{*1.5}\, D^{*0.5} \quad . \tag{105}$$

From Eqs. (62), (95), and (96) C_1 and n_5 can be determined. Therefore, Eq. (105) becomes

$$\sqrt{\frac{\sigma}{g\Delta\rho}}\frac{\dot{\varepsilon}(j_g)}{\rho_g j_g} f(D,j_g) = 3.72 \times 10^{-4}\left(\frac{\rho_g}{\Delta\rho}\right)^{-1.0} j_g^{*1.5}\, D^{*0.5} \quad . \tag{106}$$

This correlation is used instead of Eq. (40) in analysis of the entrainment for the deposition controlled region and near surface region which is discussed in the following section. With these modifications, there are no inconsistencies between the present entrainment correlation and previously developed void fraction correlations for a bubbling pool.

V. 9 ENTRAINMENT AMOUNT IN DEPOSITION CONTROLLED REGION

As shown in Section VII, beyond a certain height from the pool surface the entrainment consists only of the droplets having the terminal velocity less than the gas velocity. This phenomenon is also observed in some experiments [43,44]. By neglecting the effect of the droplet deposition, the upper limit of the entrainment in this region can be expressed by the following equation

$$E_{fg}(h,j_g) = 1.99 \times 10^{-3}\, j_g^{*3}\, N_{\mu g}^{0.5}\left(\frac{\rho_g}{\Delta\rho}\right)^{-1.0} \quad . \tag{107}$$

This is the modified form of Eq. (94) in view of Eq. (106).

In an actual system, the entrainment amount decreases gradually with height h due to the deposition. The mass balance equation in the deposition controlled region is given by Eq. (108) assuming that there are no phase changes between liquid and gas, and no additional entrainment from the liquid film.

$$\frac{dE_{fg}}{dh} = -\frac{4}{D_H}\frac{\dot{d}}{\rho_g j_g} \quad . \tag{108}$$

Here $\dot{d}$ is the deposition rate of droplets ($K_g/m^2/s$) and related to the mass concentration of droplets in the gas $C_E(K_g/m^3)$ by

$$\dot{d} = k_d C_E \quad , \tag{109}$$

where k_d is droplet deposition coefficient (m/s) [2,5]. When the velocity of droplets is approximately equal to the gas velocity (Appendix A), the droplet concentration C_E is given in terms of E_{fg} as

$$C_E = \rho_g E_{fg} \quad . \tag{110}$$

Substituting Eqs. (109) and (110) into Eq. (108) one obtains

$$\frac{dE_{fg}}{d(h/D_H)} = -4\left(\frac{k_d}{j_g}\right)E_{fg} \quad . \tag{111}$$

Integration of Eq. (111) leads to an exponential decay characteristic given by

$$E_{fg} \propto e^{-\beta(h/D_H)} \quad , \tag{112}$$

with

$$\beta \equiv 4\, k_d/j_g \quad . \tag{113}$$

In view of Eqs. (107) and (112) experimental data of entrainment for the deposition controlled region [35,44] are plotted in $E_{fg} \Big/ \left\{ j_g^{*3}\, N_{\mu g}^{0.5} \left(\frac{\rho_g}{\Delta\rho}\right)^{-1.0} \right\}$ vs. h/D_H plane in Fig. 21. Although the data scatter considerably due to experimental uncertainties, they can be correlated by

$$E_{fg}(h,j_g) = 7.13 \times 10^{-4}\ j_g^{*3}\ N_{\mu g}^{0.5} \left(\frac{\rho_g}{\Delta\rho}\right)^{-1.0} \exp\left(-0.205(h/D_H)\right) \quad (114)$$

and $k_d = 0.051\ j_g$.

The deposition coefficient calculated from Eqs. (113) and (114) gives higher values of k_d than those observed in normal annular dispersed flow [75]. It is considered that droplets entrained from a bubbling or boiling pool have higher random velocity in the lateral direction when they are entrained. The deposition coefficient should increase due to this initial random momentum in the lateral direction. This situation is similar to the case where droplets are injected from a nozzle [76] into a pipe. In the latter case, the very high deposition rate near the injection nozzle is well known [2,5,76].

Comparing Eqs. (96) and (114) the height above the pool surface at which the momentum controlled region changes to deposition controlled regime is given by

$$h^* \exp\left(-0.068(h^*/D_H^*)\right) = 1.97 \times 10^3\ N_{\mu g}^{0.33}\ D_H^{*0.42} \left(\frac{\rho_g}{\Delta\rho}\right)^{0.23} . \quad (115)$$

When the droplet deposition is small, Eq. (115) can be approximated by

$$h^* \simeq 1.97 \times 10^3\ N_{\mu g}^{0.33}\ D_H^{*0.42} \left(\frac{\rho_g}{\Delta\rho}\right)^{0.23} . \quad (116)$$

V. 10 ENTRAINMENT AMOUNT NEAR SURFACE REGION

In the near surface region, entrainment consists of all the entrained droplets from the pool surface. It is given by Eq. (93), which should be rewritten as follows in view of Eq. (106).

$$E_{fg}(h,j_g) = 2.48 \times 10^{-4}\ C_m^{1.5}\ j_g^{*1.5-3n_4/2} \left(\frac{\rho_g}{\Delta\rho}\right)^{-1.0} . \quad (117)$$

Measuring the entrainment amount in this region is difficult because the pool surface is highly agitated. Therefore, the discrimination of entrained droplets from the agitated pool is quite difficult. The only data available in this near surface region are those of Rozen et al. [45,46] who have obtained the data by extrapolating the measured entrainment in the momentum controlled region. The data are for an air-water system at the atmospheric pressure. Their results show no dependence of E_{fg} on j_g and are given by

$$E_{fg} \simeq 4 \quad . \tag{118}$$

In view of Eqs. (117) and (118), one obtains the correlation for the near surface region as

$$E_{fg}(h,j_g) = 4.84 \times 10^{-3} \left(\frac{\rho_g}{\Delta\rho}\right)^{-1.0} \quad . \tag{119}$$

Equation (119) indicates that C_m and n_4 in Eq. (93) are given by

$$C_m = 7.24 \tag{120}$$

$$n_4 = 1 \quad . \tag{121}$$

From the above results, the maximum drop size correlation given by Eq. (92) can be rewritten as

$$D^*_{max} = 7.24\ j_g^{*-1} \quad . \tag{122}$$

Equation (122) implies that the maximum droplet size is fairly large, however, such large droplets only exist in the near surface region and their life time is considered to be very short.

From Eqs. (96) and (119), the transition point between the near surface and momentum controlled regions is given by

$$h^* = 1.038 \times 10^3 \, j_g^* \, N_{\mu g}^{0.5} \, D_H^{*0.42} \left(\frac{\rho_g}{\Delta\rho}\right)^{0.23} \quad . \tag{123}$$

Since Eq. (119) is obtained from a limited number of experimental data, further experimental works may be needed to verify the validity of the correlation given by Eq. (119) at high pressures.

V. 11 CONCLUSIONS

Correlations for the droplet entrainment and carryover from a bubbling or boiling pool by streaming gas have been developed based on a simple mechanistic model of entrainment in collaboration with experimental data.

The analysis reveals that there are three regions of entrainment depending on the height above the pool surface. For each region the correlation for the entrainment amount has been developed in terms of the dimensionless gas velocity j_g^*, height above surface h^*, gas viscosity number $N_{\mu g}$, vessel diameter D_H^*, and density ratio $\left(\frac{\rho_g}{\Delta\rho}\right)$. These are defined by

$$j_g^* \equiv j_g \Big/ \left(\frac{\sigma g \Delta\rho}{\rho_g^2}\right)^{1/4}$$

$$h^* \equiv h \Big/ \sqrt{\frac{\sigma}{g\Delta\rho}}$$

$$N_{\mu g} \equiv \mu_g / (\rho_g \sigma \sqrt{\sigma / g\Delta\rho})^{1/2}$$

and

$$D_H^* \equiv D_H \Big/ \sqrt{\frac{\sigma}{g\Delta\rho}} \quad .$$

The results for the entrainment amount are summarized below:

(1) Near Surface Region

This region is limited to the viscinity of the pool surface given by

$$0 \leqq h^* \leqq 1.038 \times 10^3 \, j_g^* \, N_{\mu g}^{0.5} \, D_H^{*0.42} \left(\frac{\rho_g}{\Delta\rho}\right)^{0.23} .$$

In this region, entrainment consists of all droplets entrained at the pool surface and given by Eq. (119) as

$$E_{fg}(h,j_g) = 4.84 \times 10^{-3} \left(\frac{\rho_g}{\Delta\rho}\right)^{-1.0} .$$

(2) Momentum Controlled Region

This region is limited to the intermediate height range given by

$$1.038 \times 10^3 \, j_g^* \, N_{\mu g}^{0.5} \, D_H^{*0.42} \left(\frac{\rho_g}{\Delta\rho}\right)^{0.23} \leqq h^*$$

$$\lesssim 1.97 \times 10^3 \, N_{\mu g}^{0.33} \, D_H^{*0.42} \left(\frac{\rho_g}{\Delta\rho}\right)^{0.23} .$$

In this regime, entrainment consists partly of the droplets which attain height h due to the initial momentum and partly of the droplets whose terminal velocity is less than the gas velocity. This region is subdivided into three regimes, depending on the gas velocity:

(2-1) For the low gas flux regime limited to

$$j_g^*/h^* \lesssim 6.39 \times 10^{-4}$$

the entrainment is given by Eq. (97) as

$$E_{fg}(h,j_g) = 2.213\ N_{\mu g}^{1.5}\ D_H^{*1.25} \left(\frac{\rho_g}{\Delta\rho}\right)^{-0.31}\ j_g^*\ h^{*-1} \quad .$$

(2-2) For the intermediate gas flux regime bounded by

$$6.39 \times 10^{-4} \lesssim j_g^*/h^* \lesssim 5.7 \times 10^{-4}\ N_{\mu g}^{-0.5}\ D_H^{*-0.42} \left(\frac{\rho_g}{\Delta\rho}\right)^{0.10}$$

the entrainment is given by Eq. (96) as

$$E_{fg}(h,j_g) = 5.417 \times 10^6\ j_g^{*3}\ h^{*-3}\ N_{\mu g}^{1.5}\ D_H^{*1.25} \left(\frac{\rho_g}{\Delta\rho}\right)^{-0.31} \quad .$$

(2-3) For the high gas flux regime limited to

$$j_g^*/h^* \gtrsim 5.7 \times 10^{-4}\ N_{\mu g}^{-0.5}\ D_H^{*-0.42} \left(\frac{\rho_g}{\Delta\rho}\right)^{0.10}$$

the entrainment amount increases very rapidly as

$$E_{fg} \propto (j_g^*/h^*)^{7\sim20} \quad .$$

(3) Deposition Controlled Region

Above the height given by

$$h^* \gtrsim 1.97 \times 10^3\ N_{\mu g}^{0.33}\ D_H^{*0.42} \left(\frac{\rho_g}{\Delta\rho}\right)^{0.23}$$

the deposition becomes the main factor determining the amount of entrainment. In this regime, the entrainment consists of droplets whose

terminal velocity is less than the gas velocity. E_{fg} decreases gradually with h due to deposition and is given by Eq. (114) as

$$E_{fg}(h,j_g) = 7.13 \times 10^{-4}\ j_g^{*3}\ N_{\mu g}^{0.5} \left(\frac{\rho_g}{\Delta\rho}\right)^{-1.0} \exp\left(-0.205(h/D_H)\right) \quad .$$

(4) Entrainment rate and droplet size distribution.

From the above development for entrainment, now it is possible to obtain the entrainment rate and droplet size distribution at the pool surface. By integrating Eq. (106) over D with the limit given by Eq. (122), one gets

$$\frac{\dot{\varepsilon}(j_g)}{\rho_g j_g} \int_0^\infty f(D,j_g)dD = 4.84 \times 10^{-3} \left(\frac{\rho_g}{\Delta\rho}\right)^{-1.0} \quad . \tag{124}$$

In view of Eq. (20), the entrainment rate becomes

$$\dot{\varepsilon}(j_g) = 4.84 \times 10^{-3}\ \rho_g\ j_g \left(\frac{\rho_g}{\Delta\rho}\right)^{-1.0} \quad . \tag{125}$$

Thus the droplet size distribution becomes

$$f(D,j_g) = 0.077\ j_g^{*1.5}\ D^{*0.5} \sqrt{\frac{g\Delta\rho}{\sigma}} \tag{126}$$

which applies to $D^* \leq D^*_{max}$ where $D^*_{max} = 7.24\ j_g^{*-1}$.

V. 12 SUPPLEMENTARY REMARKS ON APPLICATION TO PRACTICAL CASES

When the correlations developed here are applied to a practical system, additional considerations may be necessary for each case. Some of the important cases are discussed below.

(1) Total Droplet Flux

In this work, the entrainment is correlated in terms of the upward droplet flux j_{fe}. This parameter itself is very important in studying the carryover droplet mass. However, it is noted that the total liquid volumetric flux j_f may be different from the upward droplet flux j_{fe} due to the droplets and liquid film which are falling back to the pool. For quasi-steady state conditions, it is straight forward to extend the present analysis to obtain the total liquid flux as discussed below.

For simplicity, the effect of the deposition is neglected. In this case, it can easily be shown from the continuity relation that the total liquid flux can be given by the droplet flux at the end of the momentum controlled region, thus from Eq. (107)

$$\frac{\rho_f j_f}{\rho_g j_g} = 2.0 \times 10^{-3} \; j_g^{*3} \; N_{\mu g}^{0.5} \left(\frac{\rho_g}{\Delta\rho}\right)^{-1.0} \quad . \tag{127}$$

This is because all the droplets arriving at the end of momentum controlled region are fully suspended and cannot fall back without the deposition. Then the droplet volumetric flux of the falling drops are given by

$$j_{fd} = j_f - j_{fe} \tag{128}$$

which is generally negative in the near surface or momentum controlled regions. this indicates that there are a definite number of droplets falling downward in these regions.

(2) Burnout in Steady State

In the case where vapor is produced by pool boiling, the critical heat flux (CHF) gives an additional limit for j_g^*. The pool boiling CHF criterion developed by Zuber [77] or Kutateladze [78] is given by

$$\frac{q_c}{\rho_g \Delta H_{fg}} = 0.16 \left[\frac{\sigma g \Delta\rho}{\rho_g^2}\right]^{1/4} \quad . \tag{129}$$

Here q_c is the critical heat flux and ΔH_{fg} is the latent heat of vaporization. Then the superficial gas velocity at CHF j_{gc} is given by

$$j_{gc} = \frac{q_c}{\rho_g \Delta H_{fg}} \frac{A_H}{A_V} \quad , \tag{130}$$

where A_H is the heated area and A_V is the cross sectional area of a vessel. From Eqs. (129) and (130), one obtains

$$j^*_{gc} = 0.16 \left(\frac{A_H}{A_V} \right) \quad , \tag{131}$$

where j^*_{gc} is defined by

$$j^*_{gc} \equiv j_{gc} \Big/ \left(\frac{\sigma g \Delta \rho}{\rho_g^2} \right)^{1/4} \quad . \tag{132}$$

(3) Flooding

When the gas flux increases up to a certain value, the flooding can occur and all the liquid is expelled from the vessel. This forms another upper limit for j^*_g. From the standard flooding correlations [58,79,80] for pool boiling or bubbling one obtains for $D^*_H > 30$

$$j^*_g \sim 4 \quad , \tag{133}$$

and for $3 < D^*_H < 20$

$$j^*_g \sim (0.5 \sim 1) \sqrt{D^*_H} \quad . \tag{134}$$

It is noted that usually the value of j^*_g given by Eqs. (133) or (134) is much larger than the upper limits of j^*_g such as the boundary between the low and

intermediate gas flux regimes given by Eq. (98) or the limit due to CHF given by Eq. (131).

(4) Entrainment amount in high gas flux regime

At a high gas flux in momentum controlled region, the entrainment increases rapidly with j_g, as given by $E_{fg} \propto j_g^{7\sim20}$. It may be possible to make a dimensionless correlation based on experimental data for this case. However, such correlation is not very useful because it may give an unreasonably high value of entrainment at large j_g^* due to its high power dependence on j_g^*. Although no data are available, there should be an upper limit for entrainment in this regime. Here, as a first approximation, it is assumed that all the droplets produced at the pool surface are carried away. This limit is also predicted by the basic formulation given by Eq. (83) at $j_g^* \to \infty$ with the condition given by Eq. (122). Thus, the limit is obtained as

$$E_{fg}(h,j_g) \sim \lim_{j_g^* \to \infty} \int_0^{8.45\, j_g^{*-1}} \int_{v_h^*}^{\infty} \delta \left(v_i^* - 22 j_g^{*1/4} N_{\mu g}^{1/4} D^{*-1/4} \left[\frac{\rho_g}{\rho_f}\right]^{1/2} D_H^{*0.21} \left[\frac{\rho_g}{\Delta\rho}\right]^{0.17} \right)$$

$$\times\, 3.72 \times 10^{-4} \left(\frac{\rho_g}{\Delta\rho}\right)^{-1.0} j_g^{*1.5}\, D^{*0.5}\, d\, v_i^*\, dD^*$$

$$= 4.84 \times 10^{-3} \left(\frac{\rho_g}{\Delta\rho}\right)^{-1.0} . \qquad (135)$$

This value is identical to that in the near surface regime which is given by Eq. (119). Therefore, for practical purposes, the entrainment amount in the high gas flux might well be estimated by the correlation for the near surface region.

NOMENCLATURE

A_d	Projected area of droplet
A_H	Heated Area (heated perimeter times heated length)
A_v	Cross sectional area of vessel
C_D	Drag coefficient of droplet
C	Coefficient in Eq. (64)
C_E	Droplet concentration in gas space (Kg/m^3)
C_K	Coefficient in Eq. (2)
C_m	Coefficient in Eq. (92)
C_1	Coefficient in Eq. (105)
$\dot{d}$	Deposition rate of droplets ($Kg/m^2/s$)
D	Droplet diameter
D^*	Dimensionless droplet diameter defined by Eq. (37)
D_B	Bubble diameter
D_c	Critical droplet diameter whose terminal velocity is equal to gas velocity
D_c^*	Dimensionless critical droplet diameter defined by Eq. (12)
D_H	Hydraulic diameter of vessel
D_H^*	Dimensionless hydraulic diameter of vessel defined by Eq. (5)
D_{max}	Maximum droplet diameter
D_{max}^*	Dimensionless maximum droplet diameter defined by Eq. (86)
E_{fg}	Entrainment defined by Eq. (1)
$E_{fg}(h,j_g)$	Entrainment at height h and gas velocity j_g
$E_{fg}(h,j_g,D)$	Entrainment at height h and gas velocity j_g which consists of droplets whose diameter is less than D (given by Eq. (27))
$E_{fg\infty}(j_g)$	Limiting value of $E_{fg}(h,j_g)$ for $h \to \infty$
$E_o(D,j_g)$	Entrainment at interface which consists of droplets whose diameter are less than D (given by Eq. (25))
$f(D,j_g)$	Droplet size distribution function for j_g
f_D	Frequency of entrained droplet (in Eq. (31))
f_i	Interfacial friction factor between gas and liquid ligament
F_D	Drag force acting on droplet
g	Acceleration due to gravity

NOMENCLATURE (Cont'd)

$g(v_i,D,j_g)$	Initial velocity distribution function for diameter D and gas velocity j_g
h	Height above the pool surface
h^*	Dimensionless height above the pool surface defined by Eq. (7)
h_m	Maximum height of rising droplet
h_m^+	Dimensionless maximum height of rising droplet defined by Eq. (75)
j_{gc}	Superficial gas velocity at burnout
j_{gc}^*	Dimensionless superficial gas velocity at burnout defined by Eq. (132)
j_{fe}	Superficial velocity of liquid flowing upward as droplet
j_f	Total liquid volumetric flux
j_{fd}	Droplet volumetric flux (superficial velocity) of falling drops
j_g	Superficial gas velocity
j_g^*	Dimensionless superficial gas velocity defined by Eq. (3)
j_g^+	Dimensionless superficial gas velocity defined by Eq. (76)
k_d	Deposition coefficient of droplet (m/s)
K	Parameter defined by Eq. (11)
ℓ	Length of liquid ligament
n_1~n_3	Exponents in Eq. (61)
n_4	Exponent in Eq. (92)
n_5	Exponent in Eq. (105)
N	Site density of entrained droplet (in Eq. (31))
$N_{\mu g}$	Gas viscosity number defined by Eq. (15)
$N_{\mu f}$	Liquid viscosity number defined by Eq. (8)
p	Escape probability of entrained droplet (in Eq. (31))
P	System pressure
P_o	Pressure around the bubble
q_c	Critical heat flux
Re_D	Droplet Reynolds number defined by Eq. (34)
Re_g	Gas Reynolds number defined by Eq. (90)
S	Velocity ratio between gas and liquid defined by Eq. (A.5)
t	Time
t_B	Bubble burst time

NOMENCLATURE (Cont'd)

v	Velocity
v_f	Velocity of element of liquid ligament
v_{fe}	Droplet velocity
v_g	Gas velocity
v_g^*	Dimensionless gas velocity defined by Eq. (52)
$v_h(D,j_g,h)$	Initial velocity of droplet (diameter D) necessary to rise more than height h under gas velocity j_g
v_h^*	Dimensionless form of v_h defined by Eq. (81)
v_i	Initial velocity of droplet at pool surface
v_i^*	Dimensionless initial velocity defined by Eq. (51)
v_r	Relative velocity between droplet and gas defined by Eq. (69)
$v_{r\infty}$	Terminal velocity of droplet given by Eq. (78)
v_{ri}^+	Dimensionless initial relative velocity of droplet defined by Eq. (77)
We_{max}	Weber number based on maximum droplet diameter defined by Eq. (85)
y	Vertical position above pool surface
z	Vertical coordinate attached to the liquid ligament

Greek Symbols

α	Void fraction in liquid pool
α_E	Liquid fraction of droplet in gas space
β	Parameter defined by Eq. (113)
$\delta(x)$	Delta function defined by Eq. (66)
ΔH_{fg}	Latent heat of vaporization
$\Delta\rho$	Density difference between gas and liquid
$\dot{\varepsilon}(j_g)$	Entrainment rate at pool surface for j_g ($Kg/m^2/s$)
μ_f	Viscosity of liquid
μ_g	Viscosity of gas
ν_f	Kinematic viscosity of liquid
ν_g	Kinematic viscosity of gas
ρ_f	Density of liquid
ρ_g	Density of gas
σ	Surface tension
τ_i	Interfacial shear stress between gas and liquid ligament

REFERENCES

1. Ishii, M. and Grolmes, M. A., "Inception Criteria for Droplet Entrainment in Two-Phase Cocurrent Film Flow," AIChE J. 21, 308 (1975).

2. Hewitt, G. F. and Hall-Taylor, N. S., "Annular Two-Phase Flow," Pergamon Press, Oxford (1970).

3. Brodkey, R. S., "The Phenomena of Fluid Motion," Addison-Wesley, Reading, MA (1967).

4. Ishii, M. and Mishima, K., "Liquid Transfer and Entrainment Correlation for Droplet-Annular Flow," Proc. 7th Intl. Heat Trans. Conf., TF 20, Munich (1982)

5. Kataoka, I., Ishii, M., and Mishima, K., "Generation and Size Distribution of Droplet in Annular Two-Phase Flow,"Trans. ASME, J. of Fluid Eng., Vol. 105, 230 (1983)

6. Kataoka, I., and Ishii, M., "Mechanism and Correlation of Droplet Entrainment and Deposition in Annular Two-Phase Flow," ANL 82-44, NUREG/CR-2885 (1982)

7. Ishii, M., "Thermo-fluid Dynamic Theory of Two-phase Flow," Eyrolles, Paris, Scientific and Medical Publication of France, NY (1975).

8. Collier, J. G., "Burnout in Liquid Cooled Reactors," Nuclear Power 5, 61 (1961).

9. Petrovichev, V. I., Kokorev, L. S., Didenko, A. Ya., and Dubvrovskiy, G. P., "Droplet Entrainment in Boiling of Thin Liquid Film," Heat Transfer-Soviet Res. 3, 19 (1971).

10. Cousins, L. B., Denton, W. H., and Hewitt, G. E., "Liquid Mass Transfer in Annular Two-phase Flow," Sym. on Two-phase Flow, Vol. 1, paper C4, Exter, England (1965).

11. Tong, L. S., "Boiling Heat Transfer and Two-phase Flow," R. E. Krieger Publishing Co., NY (1975).

12. Hsu, Y. Y. and Graham, R. W., "Transport Process in Boiling and Two-phase Systems," Hemisphere Publishing Co., WA (1976).

13. Hewitt, G. F., "Mechanism and Prediction of Burnout," NATO Advanced Study Institute on Two Phase Flows (1976).

14. Yamanouchi, A., "Effects of Core Spray Cooling at Stationary State After Loss of Coolant Accident," J. Nuc. Sci. & Tech. 5(9), 498 (1968).

15. Semeria, R. and Martinet, "Calefaction Spots on a Heating Wall; Temperature Distribution and Resorption," Sym. on Boiling Heat Trans. in Steam Generating Unit and Heat Exchangers, Proc. Inst. Mech. Engs. 180, 192-205 (1965).

16. Duffey, R., "The Physics of Rewetting in Water Reactor Emergency Core Cooling," Nucl. Eng. Design 25, 379 (1973).

17. Bennett, A., "The Wetting of Hot Surfaces by Water in a Steam Environment at High Pressure," Atomic Energy Research Establishment, Harwell, AERE-R5146 (1966).

18. Shor, A. J., Ward, H. T., Miller, D., and Rodger, W. A., "Radioactive Carry-over from Borax-III and Test Systems," Nucl. Sci. Eng. 2, 126-142 (1957).

19. Manowitz, B., Bretton, R. H., and Horrigan, R. V., "Entrainment in Evaporators," Chem. Eng. Progress 51(7), 313 (1955).

20. Mitsuishi, N., Sakata, S., Matsuda, Y., and Yamamoto, Y., "The Liquid Entrainment and Its Removal of Large Scale Evaporation Unit - Evaporation of Radioactive Liquid Waste," J. of Atomic Energy Soc. of Japan 1(6), 363, (1959).

21. Mitsuishi, N., "The Liquid Entrainment and Its Prevention," J. of Chem. Eng. Soc. of Japan 23(1), 34 (1959).

22. Mitsuishi, N., Yamamoto, Y., and Oyama, Y., "On the Liquid Entrainment and Its Removal - Decontamination Characteristic of Evaporation Unit," J. of Chem. Eng. Soc. of Japan 23(10), 648 (1959).

23. Viecenz, H. J. and Mayinger, F., "Comparison of Phase Separation Models by Use of Own Experimental Data," Proc. of NATO Advanced Study Institute on Two-phase Flow and Heat Transfer, 1383, Instanbuhl (1976).

24. Langner, H., Viecenz, H. J., and Zetzmann, K., "Some Special Investigations of Fluid Behavior in Two-Phase Flow at Steady State and Blowdown Conditions: Flow Pattern, Entrainment of Annular Flow and Phase Separation," Two-phase Transport and Reactor Safety, Proc. of Two-phase Flow and Heat Transfer Symposium Workshop, Vol. 1, p. 225, Fort Lauderdale, FL (1976).

25. Lee, H. M. and McCarthy, G. E., "Liquid Carry-over in Air-water Countercurrent Flooding," Proc. 7th Intl. Heat Trans. Conf., TF-7, Munich (1982).

26. Iguchi, T., "Carryover from a Liquid Pool with Vertical Air Flow,"Trans. Japan Chem. Eng. Soc. 8(3), 225 (1982).

27. Hunt, C. D., Hanson, D. N., and Wilke, C. R., "Capacity Factors in the Performance of Perforated-plate Column," AIChE J. 1(4), 441 (1955).

28. Cheng, S. I. and Teller, A. J., "Free Entrainment Behavior in Sieve Trays," AIChE J. 7(2), 283 (1961).

29. Bain, J. L. and Winkle, M. V., "A Study of Entrainment, Perforated Plate Column - Air-Water System," AIChE J. 7(3), 363 (1961).

30. Zenz, F. A. and Weil, N. A., "A Theoretical-Empirical Approach to the Mechanism of Particle Entrainment from Fluidized Beds," AIChE J. 4(4), 473 (1958).

31. Andrews, J. M., "Kinetic Study of Fluidized Solids Entrainment," Ind. Eng. Chem. 52(1), 85 (1960).

32. Perry, R. H. and Chilton, C. H., Chemical Engineers Handbook, 5th edition, McGraw-Hill Publishing Co., NY (1973).

33. Yeh, G. C. K. and Zuber, N., "On the Problem of Liquid Entrainment," ANL-6244 (1960).

34. O'connell, H. E. and Pettyjohn, E. S., "Liquid Carry Over in a Horizontal Tube Evaporator," Trans. AIChE 42, 795 (1946).

35. Garner, F. H., Ellis, S. R. M., and Lacey, J. A., "The Size Distribution and Entrainment of Droplets," Trans. Inst. Chem. Engs. 32, 222 (1954).

36. Garner, F. H., Ellis, S. R. M., and Shearn, D. B., "Entrainment in Evaporators," Trans. Inst. Chem. Engs. 37, 247 (1959).

37. Kruzhilin, G. N., "The Dependence of the Permissible Vapor Load upon the Pressure," Izv. Akad, Nauk. Otd. Tekh, Nauk., No. 7, 1106 (1951).

38. Styrikovich, M. A., Sterman, L. S., and Surnov, A. V., "An Investigation of Carry Over of Salt by Using Radioactive Isotopes," Teploenergetika 2(2), 43 (1955).

39. Sterman, L. S., Antonov, A. I., and Surnov, A. V., "An Investigation of Steam Quality at 185 atm," Teploenergetika 4(3), 17 (1957).

40. Sterman, L. S., "On the Theory of Steam Separation," J. of Tech. Physics 28(7), 1562 (1958).

41. Styrikovich, M. A., Petukhov, V. I., and Kolokoltsev, V. A., "The Effect of Gas Phases Density on the Extent of Droplet Entrainment," Teploenergetika 11(11), 50 (1964).

42. Petukhov, V. I. and Kolokoltsev, V. A., "Effect of Liquid Viscosity on Droplet Entrainment and Volumetric Air Content," Teploenergetika 12(9), 30 (1965).

43. Rozen, A. M., Golub, S. I., Davydov, I. F., and Gostinin, G. I., "Some Law Governing Drop Carry Over," Soviet Physics-Doklady 14(7), 648 (1970).

44. Golub, S. I., "Investigation of Moisture Carryover and Separation in Evaporation Apparatus," Candidates Dissertation, MEI (1970) (quoted from Ref. 46).

45. Rozen, A. M., Golub, S. I., and Davydov, I. F., "Entrainment of Moisture at Small Distance from a Bubbling Surface," Soviet Physics-Doklady 19(6), 338 (1974).

46. Rozen, A. M., Golub, S. I., and Votintseva, T. I., "Calculating Droplet Carryover with Bubbling," Teploenergetika 23(11), 59 (1976).

47. Rozen, A. M., Golub, S. I., and Votintseva, T. I., "On the Nature of Degree of Dependence of Transported Carryover on Vapor Velocity with Bubbling," Teploenergetika 23(9), 55 (1976).

48. Rozen, A. M., Gostinin, G. I., Davydov, I. F., Golub, S. I., and Krasikov, A. N., "On the Problem of Effects of Salt Content in Water on Moisture Carryover with Bubbling," Izv. Akad. Nauk, Energetika and Transport, No. 6, p. 164 (1973).

49. Kolokoltsev, V. A., "Investigation of the Operation of the Steam Space of ISV Evaporator," Trudy MEI (1952) (quoted from Ref. 40).

50. Ishii, M. and Zuber, N., "Drag Coefficient and Relative Velocity in Bubbly, Droplet or Particulate Flows," AIChE J. 25, 843 (1979).

51. Davis, R. F., "The Physical Aspect of Steam Generation at High Pressure and Problem of Steam Contamination," Proc. Inst. Mech. Engs., Vol. 144, p. 198 (1940).

52. Woodcock, A. H., Kientzler, C. F., Arons, A. B., and Blanchard, D. C., "Giant Condensation Nuclei from Bursting Bubbles," Nature 172(4390), 1144 (1953).

53. Knelman, F., Dombrowski, N., and Newitt, D. M., "Mechanism of the Bursting of Bubbles," Nature 173(4397), 261 (1954).

54. Newitt, D. M., Dombrowski, N., and Knelman, F. M., "Liquid Entrainment, 1. The Mechanism of Drop Formation from Gas or Vapor Bubble," Trans. Inst. Chem. Engs. 32, 245 (1954).

55. Gleim, V. G., "On the Problem for General Theory on Moisture Entrainment from Boiling Mixture," Zhurnal Prikladnoi Khimii 28(1), 12 (1955).

56. Gleim, V. G., Shelomov, I. K., and Shidlovskii, B. R., "Process Leading to Generation of Droplets in Rupture of Bubbles at Liquid-Gas Interface," J. of Applied Chem. USSR 32(1), 222 (1959).

57. Aiba, S. and Yamada, T., "Studies on Entrainment," AIChE J. 5(4), 506 (1959).

58. Wallis, G. B., "One Dimensional Two-Phase Flow," McGraw-Hill Publishing Co., NY, 261-263 (1969).

59. Ishii, M., "One-Dimensional Drift-Flux Model and Constitutive Equations for Relative Motion between Phases in Various Flow Regimes," ANL-77-47 (1977).

60. Ishii, M. and Mishima, K., "Study of Two-Fluid Model and Interfacial Area," ANL-80-111, NUREG/CR-1873 (1980).

61. Nielsen, R. D., Tek, M. R., and York, J. L., "Mechanism of Entrainment Formation in Distillation Columns," University of Michigan, Ann Arbor, MI.

62. Akselrod, L. S. and Yusova, G. M., "Dispersity of the Liquid in the Interplate Space in Bubble Tower," J. of Applied Chem. USSR 30, 739 (1959).

63. Muller, R. L. and Prince, R. G. H., "Regimes of Bubbling and Jetting from Submerged Orifices," Chem. Eng. Sci. 27, 1583 (1972).

64. Margulova, T. H., "An Experimental Investigation of the Relative Velocity of Vapor in Bubbling through a Layer of Water at High Pressures," Trans. of Power Inst., M. V. Molotov, Vol. 11 Moscow (1953) (quoted from Ref. 33).

65. Kurbatov, A. V., "The Bubbling and the Problem of Critical Load in Steam Separation," Trans. of the Power Inst., M. V. Molotov, Vol. 11, Moscow (1953) (quoted from Ref. 33).

66. Sterman, L. S., "The Generalization of Experimental Data Concerning the Bubbling of Vapor Through Liquid," Soviet Physics - Technical Physics, 1479 (1957).

67. Wilson, J. F., Grenda, R. J., and Patterson, J. F., "Steam Volume Fraction in a Bubbling Two-Phase Mixture," Trans. ANS 5 Ser. 25, 151 (1962).

68. Lapple, C. E. and Shepherd, C. B., "Calculation of Particle Trajectory," Ind. Eng. Chem. 32(5), 605 (1940).

69. Golub, S. I., Rozen, A. M., Vaislat, M. B., and Votintseva, T. I., "On the Height of Thrown Liquid Droplet under Vertical Gas Flow," Teor. Osnovy Khim. Tekhnol. 6(3), 484 (1972).

70. Hinze, J. O., "Fundamentals of the Hydrodynamic Mechanism of Splitting in Dispersion Process," AIChE J. 1, 289 (1955).

71. Antonov, A. I. and Panasenko, M. D., "The Influence of the Vapor Volume Fraction upon the Critical Height of Vapor Space in Boiler," Teploenergetika 4(8), 39 (1957).

72. Panasenko, M. D. and Antonov, A. I., "Correlation of Mechanical Carryover by Steam," Teploenergetika 6(10), 44 (1959).

73. Zuber, N. and Findley, J. A., "Average Volumetric Concentration in Two-phase Flow Systems," J. Heat Trans. 87, 453 (1965).

74. Orth, K. W., Epstein, M., Linehan, J. H., Lambert, G. A., and Stachyra, L. J., "Hydrodynamic Aspects of Volume Boiling," ANL/RAS 80-6 (1980).

75. Paleev, I. I. and Filipovich, B. S., "Phenomena of Liquid Transfer in Two-Phase Dispersed Annular Flow," Int. J. Heat Mass Trans. 9, 1089 (1966).

76. Gill, L. E. and Hewitt, G. F., "Sampling Probe Studies of the Gas Core in Annular Two-phase Flow - Part 3. Distribution of Velocity and Droplet Flowrate after Injection through Axial Jet," AERE-M1202 (1967).

77. Zuber, N., "On the Stability of Boiling Heat Transfer," Trans. ASME 80, 711 (1958).

78. Kutateladze, S. S., "Heat Transfer During Condensation and Boiling," AEC-tr-3770 (1952).

79. Tien, C. L., "A Simple Analytical Model for Counter-current Flow Limiting Phenomena with Vapor Condensation," Letters in Heat and Mass Transfer 4, 231 (1977).

80. Bankoff, S. G., Tankin, R. S., Yuen, M. C., and Hsieh, C. L., "Countercurrent Flow of Air/Water and Steam/Water through a Horizontal Perforated Plate," Intl. J. Heat Mass Trans. 24, 1381 (1981).

APPENDIX A

Derivation of Eq. (110)

Equation (110) can be obtained by considering mass balance of liquid and gas phase. The mass concentration of droplet C_E is given by

$$C_E = \rho_f \alpha_E \quad . \tag{A.1}$$

Here α_E is the droplet volumetric fraction in the gas space above the pool. On the other hand, in the deposition controlled region

$$j_{fe} = v_{fe}\ \alpha_E \tag{A.2}$$

and

$$j_g = v_g\ (1-\alpha_E) \quad . \tag{A.3}$$

Here v_{fe} and v_g are the velocity of droplets and gas in gas space.

From Eqs. (A.2) and (A.3) one obtains

$$\alpha_E = \frac{j_{fe}}{j_{fe} + S j_g} \quad . \tag{A.4}$$

Here S is the velocity ratio between droplet and gas

$$S = \frac{v_{fe}}{v_g} \quad . \tag{A.5}$$

When $j_g >> j_{fe}$ and S = 1, which may be applicable in the present analysis, Eq. (A.4) can be rewritten as

$$\alpha_E = \frac{j_{fe}}{j_g} \quad . \tag{A.6}$$

Substituting Eq. (A.6) into Eq. (A.1) one finally obtains

$$C_E \doteq \rho_f \frac{j_{fe}}{j_g} = \rho_g E_{fg} \quad . \tag{A.7}$$

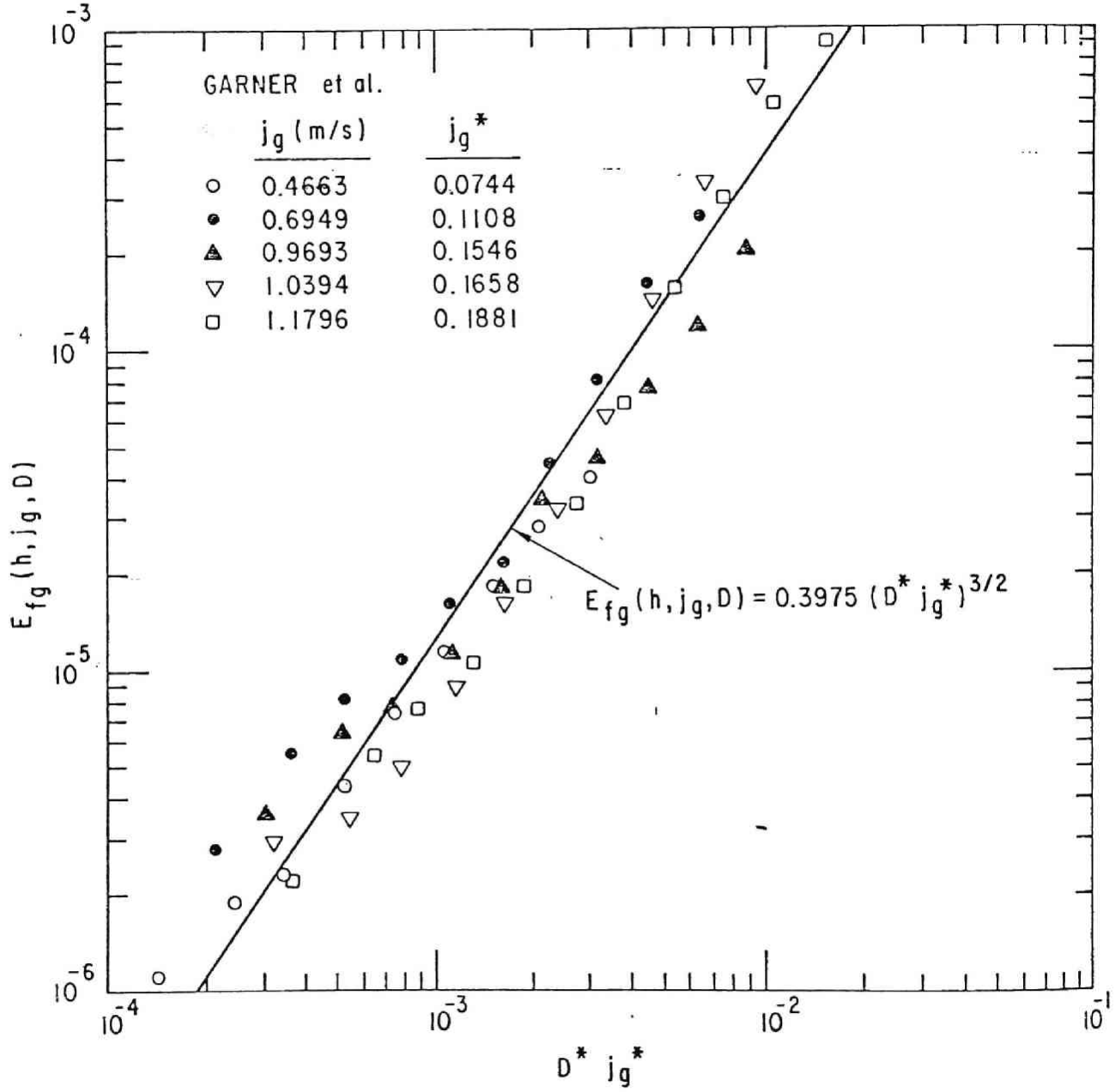

Fig. 1. Entrainment below Stated Value $E_{fg}(h,j_g D)$ vs. Dimensionless Diameter $D^* j_g^*$ for the Data of Garner et al. [35]

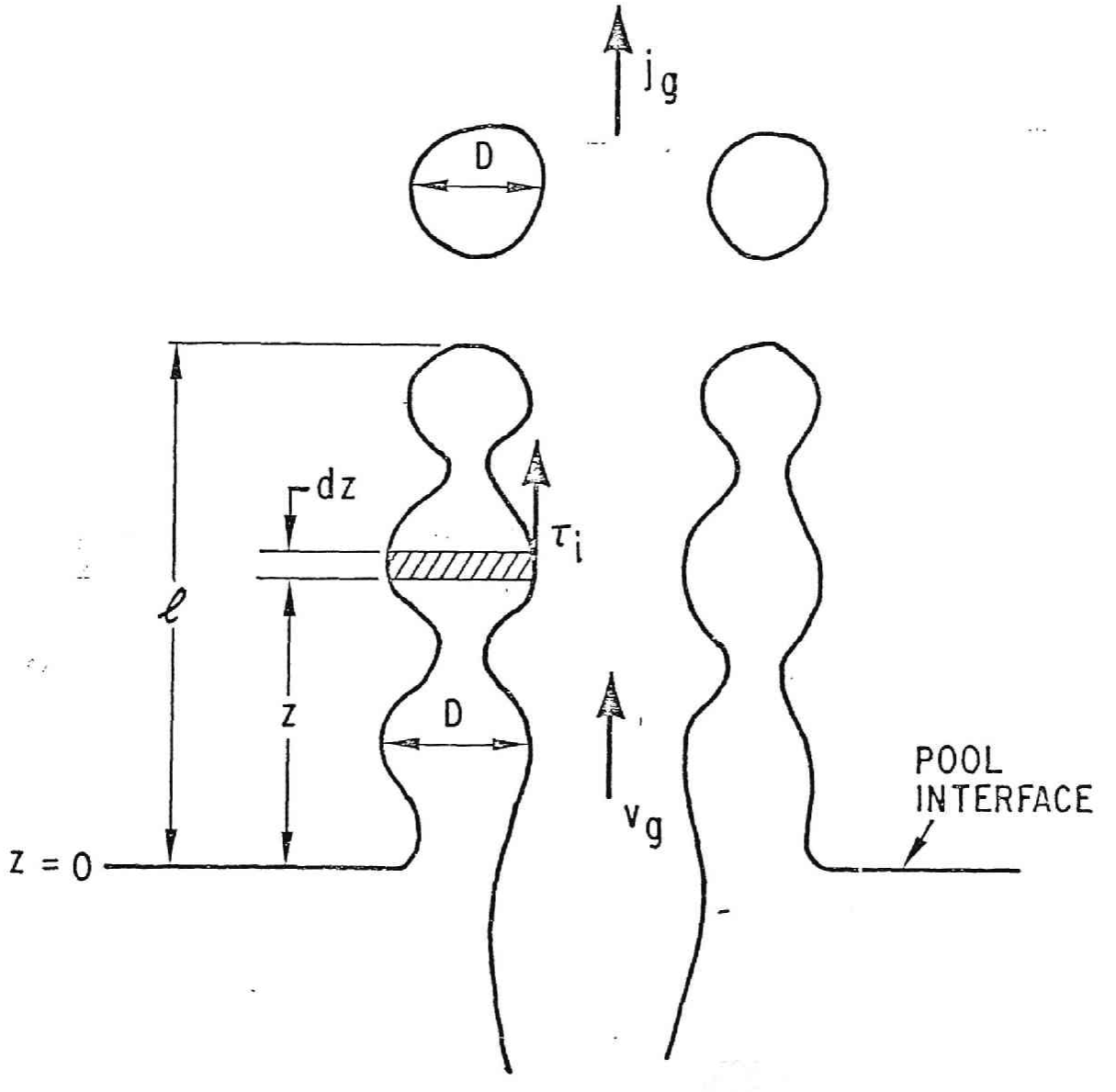

Fig. 2. Schematic Diagram of Droplet Entrainment

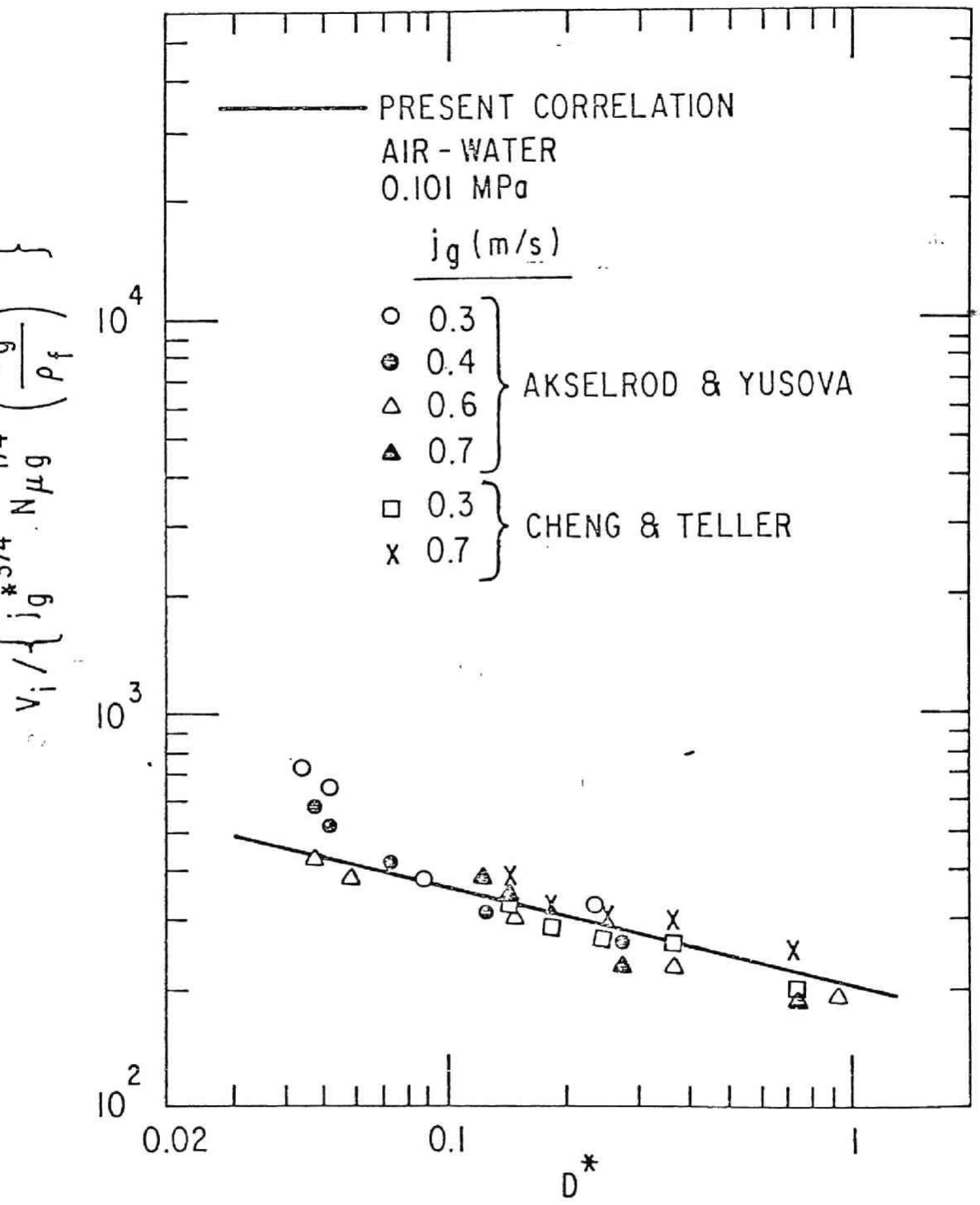

Fig. 3. Initial Velocity of Droplet in $v_i^* \Big/ \left\{ j_g^{*3/4} N_{\mu g}^{*1/4} \left(\frac{\rho_g}{\rho_f} \right)^{1/2} \right\}$ vs. D^* Plane for the Data of Akselrod et al. [62] and Cheng et al. [28]

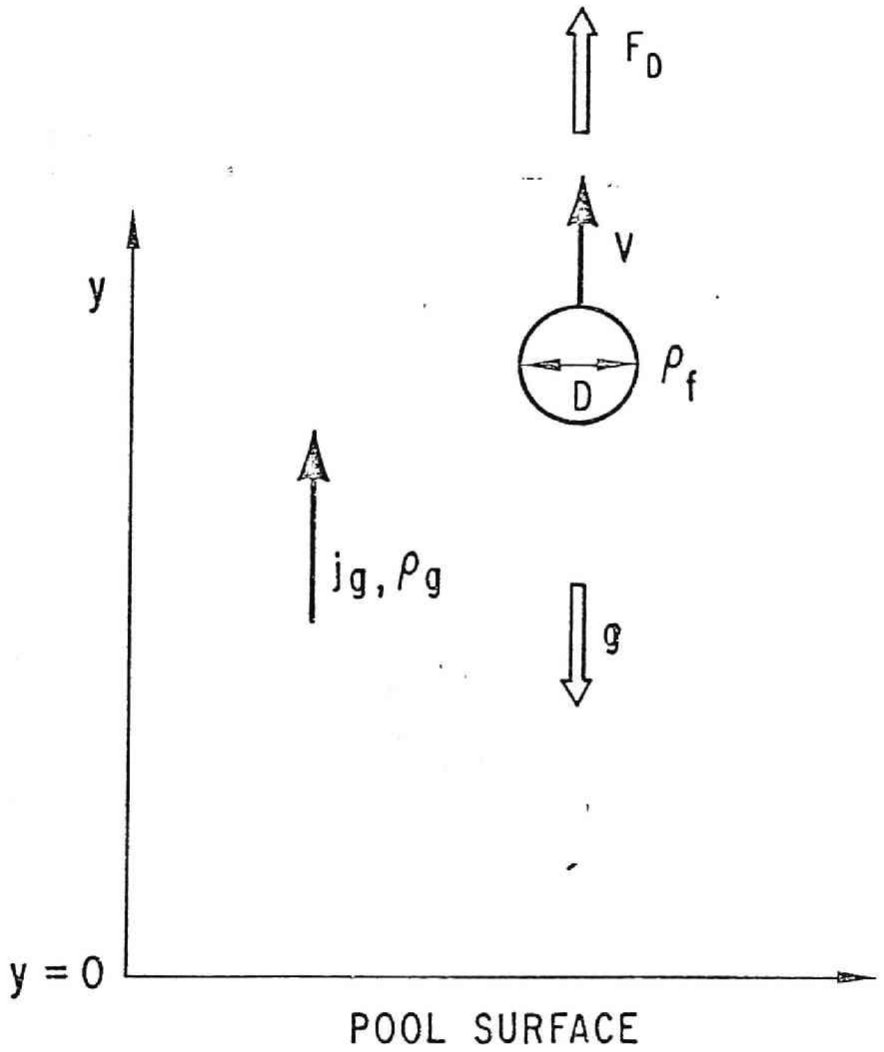

Fig. 4. Schematic Diagram of Droplet Motion in Gas Stream

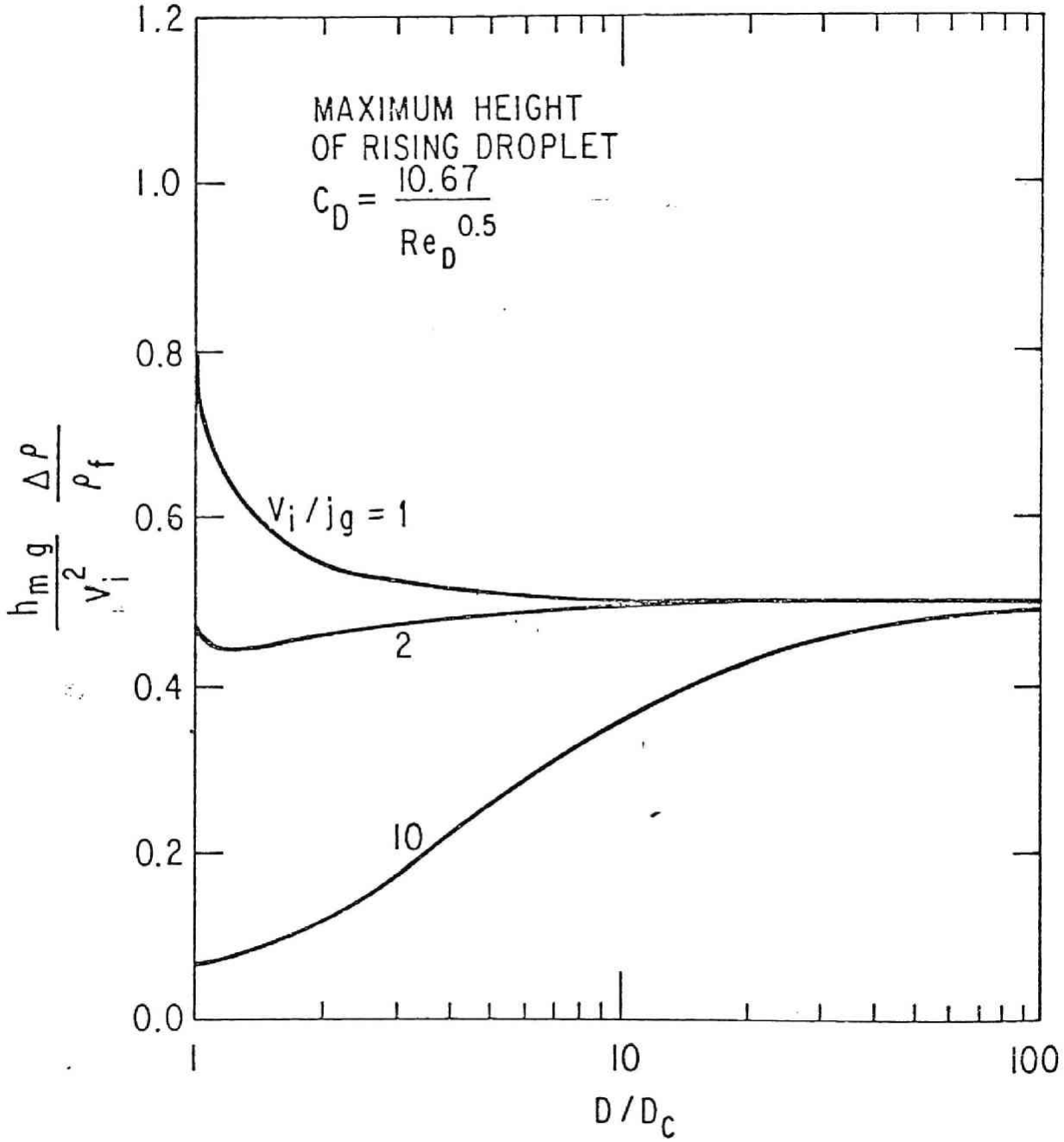

Fig. 5. Maximum Height of Rising Droplet Calculated by Eq. (73) for Wake Regime

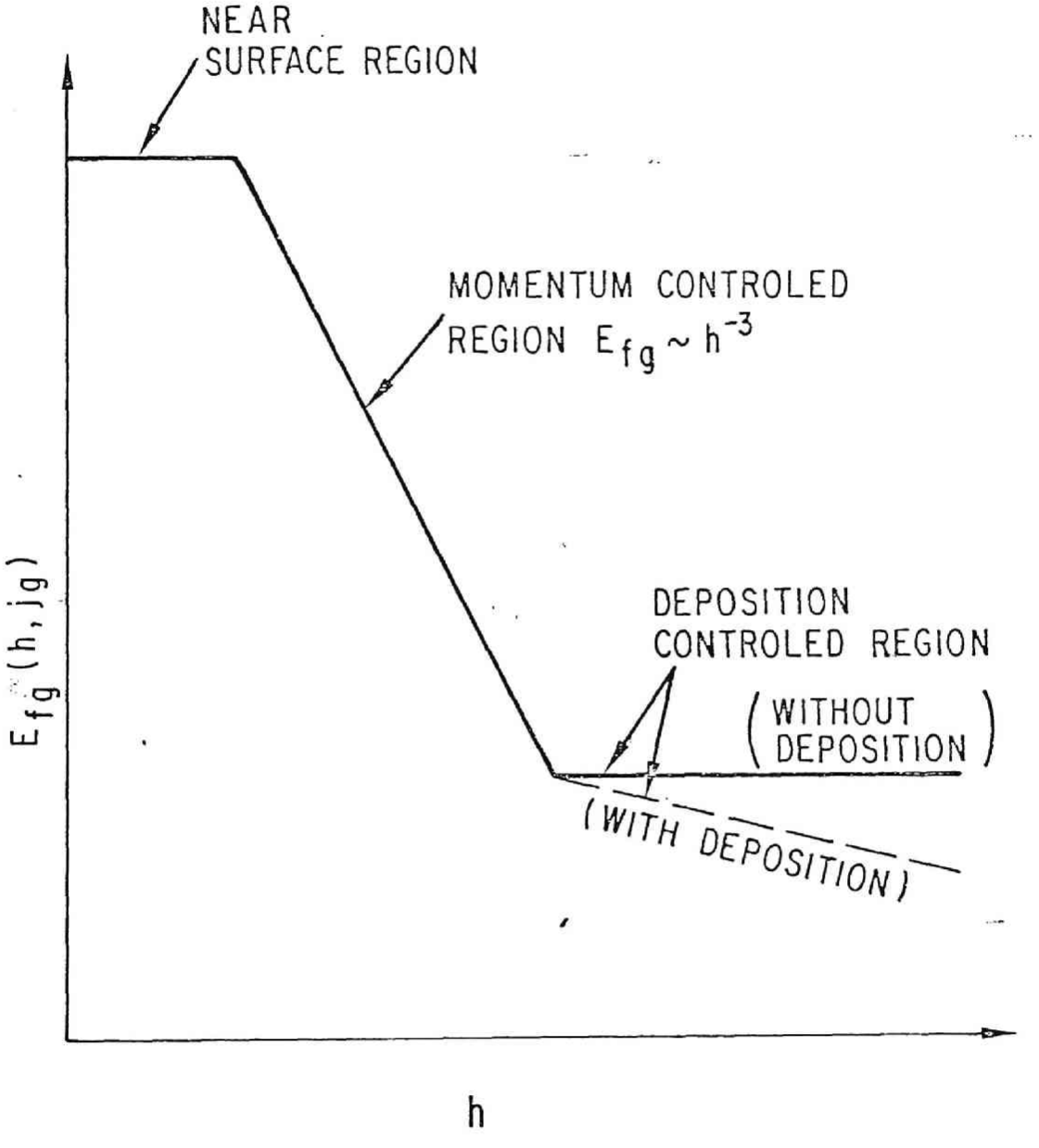

Fig. 6. General Trend of Effects of Height, h, on Entrainment E_{fg}

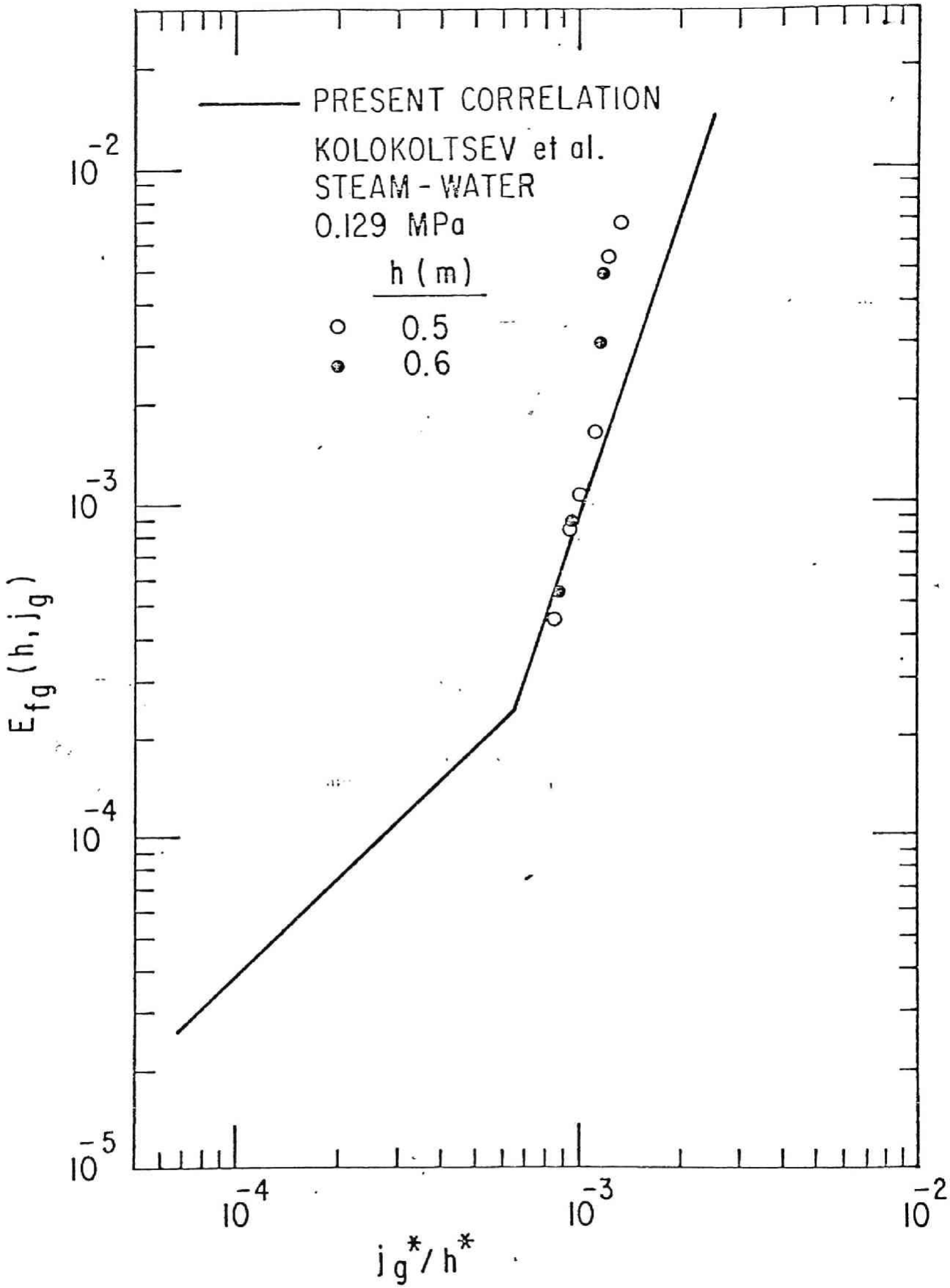

Fig. 7. Comparison of Experimental Data of Kolokoltsev [49] with Predicted Entrainment at 0.129 MPa

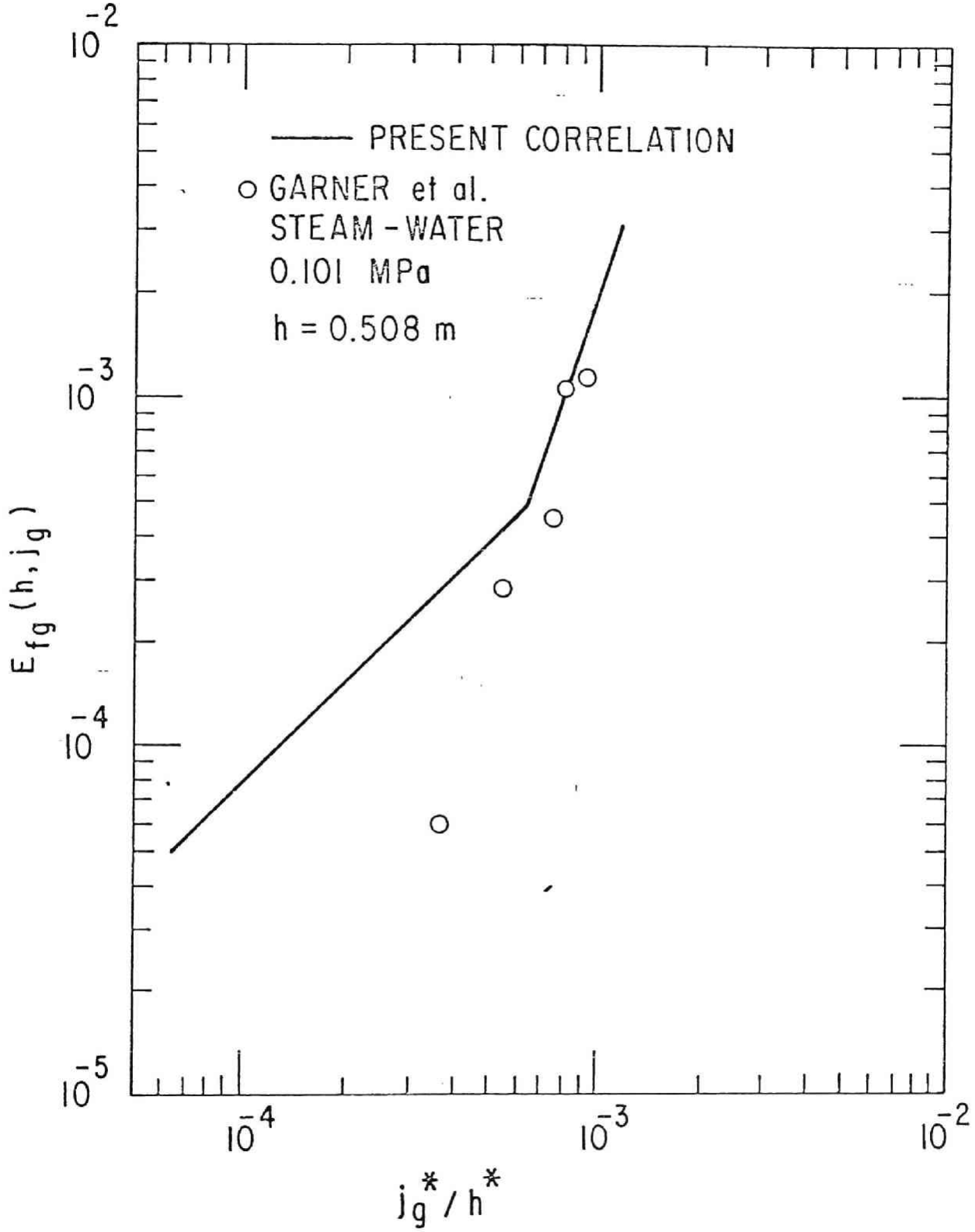

Fig. 8. Comparison of Experimental Data of Garner et al. [35] with Predicted Entrainment at 0.101 MPa

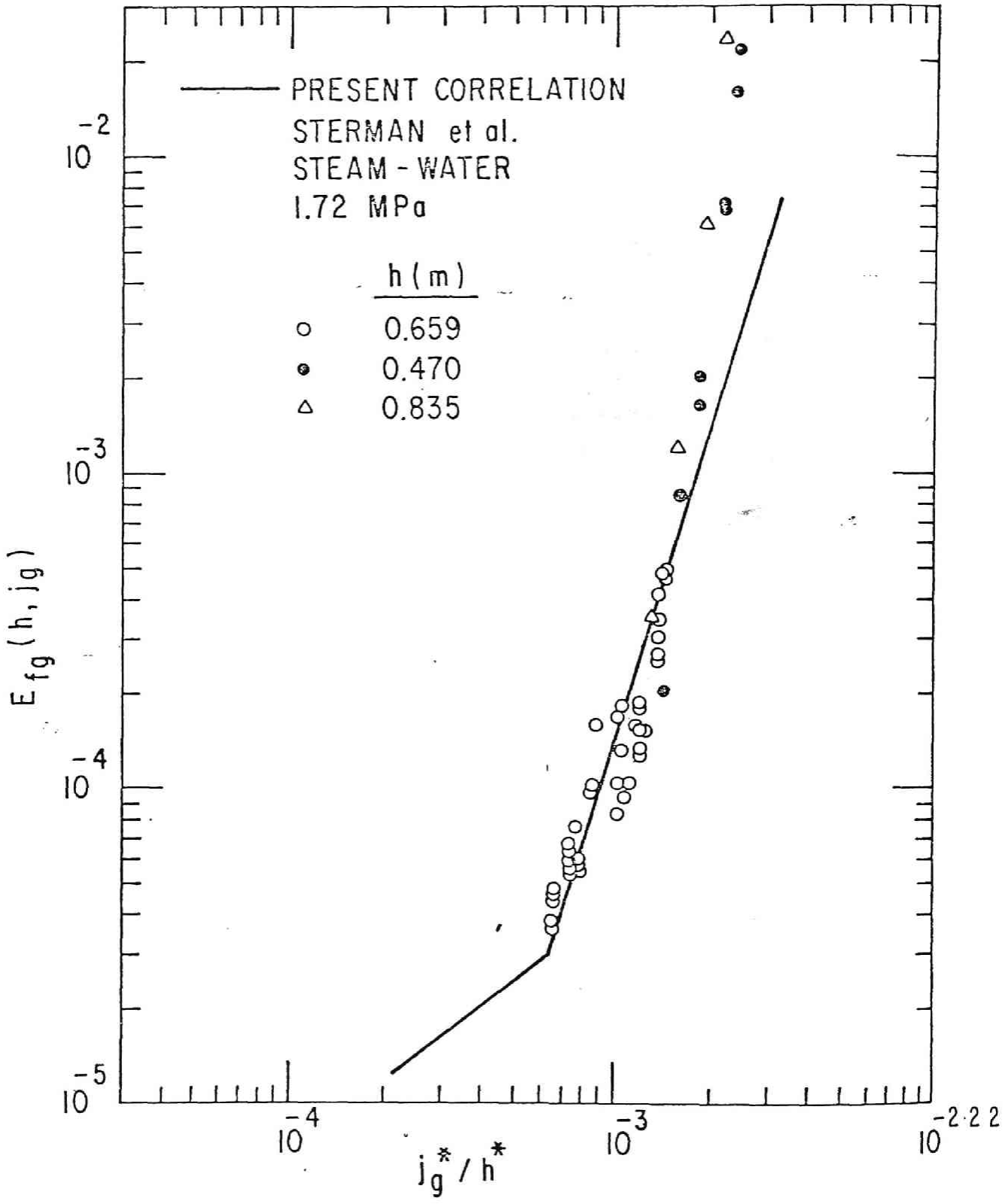

Fig. 9. Comparison of Experimental Data of Sterman et al. [39,40] with Predicted Entrainment at 1.72 MPa

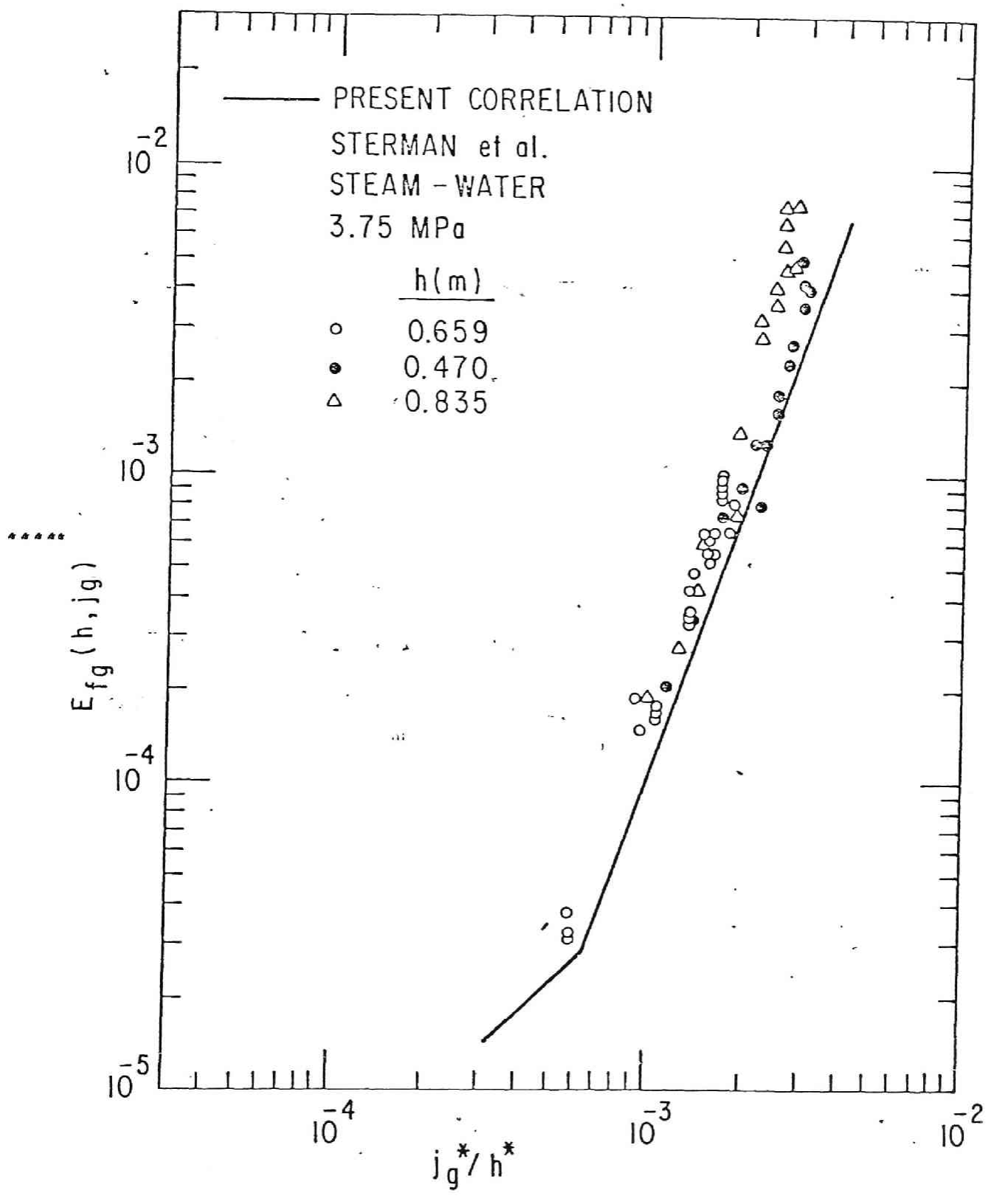

Fig. 10. Comparison of Experimental Data of Sterman et al. [39,40] with Predicted Entrainment at 3.75 MPa

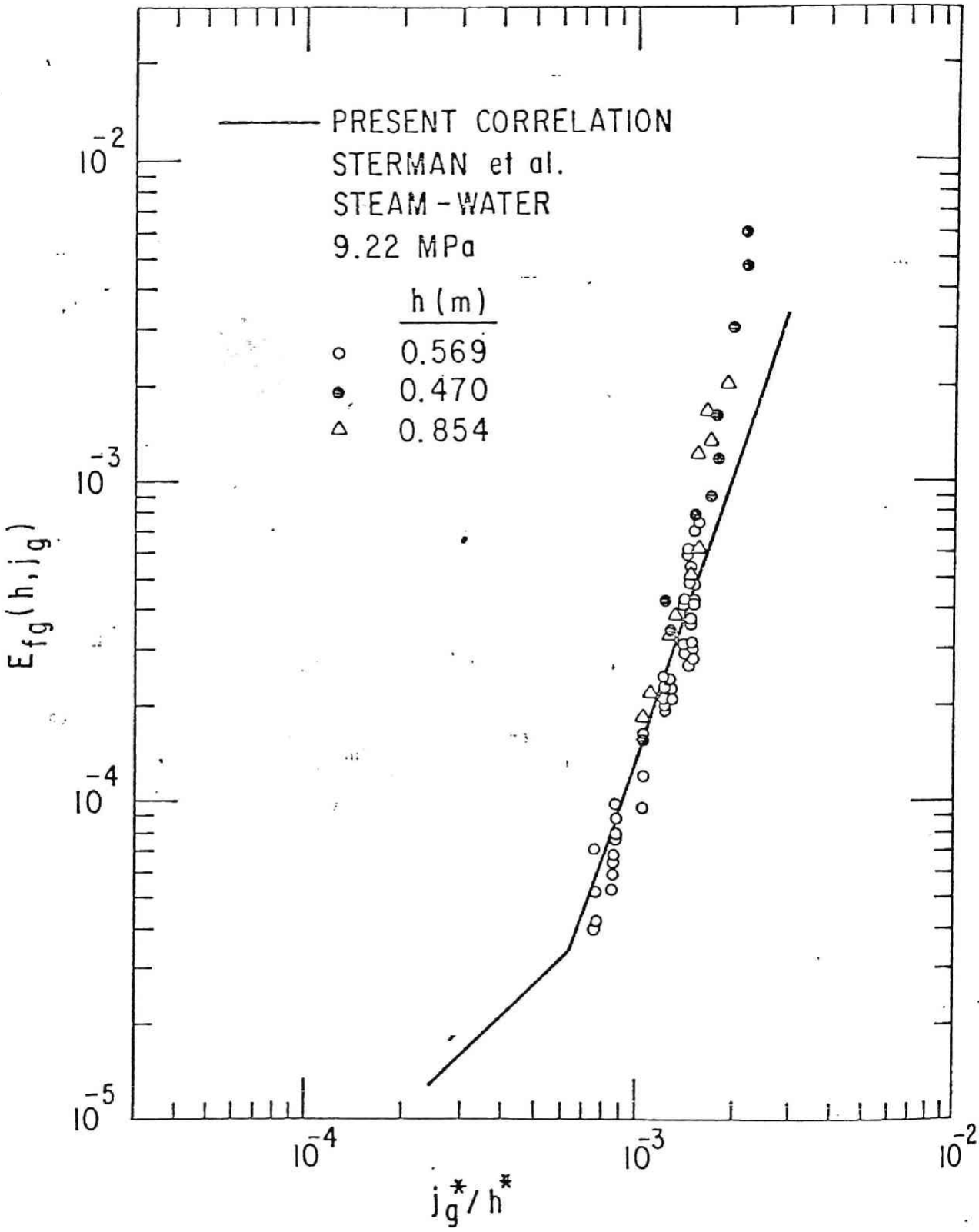

Fig. 11. Comparison of Experimental Data of Sterman et al. [39,40] with Predicted Entrainment at 9.22 MPa

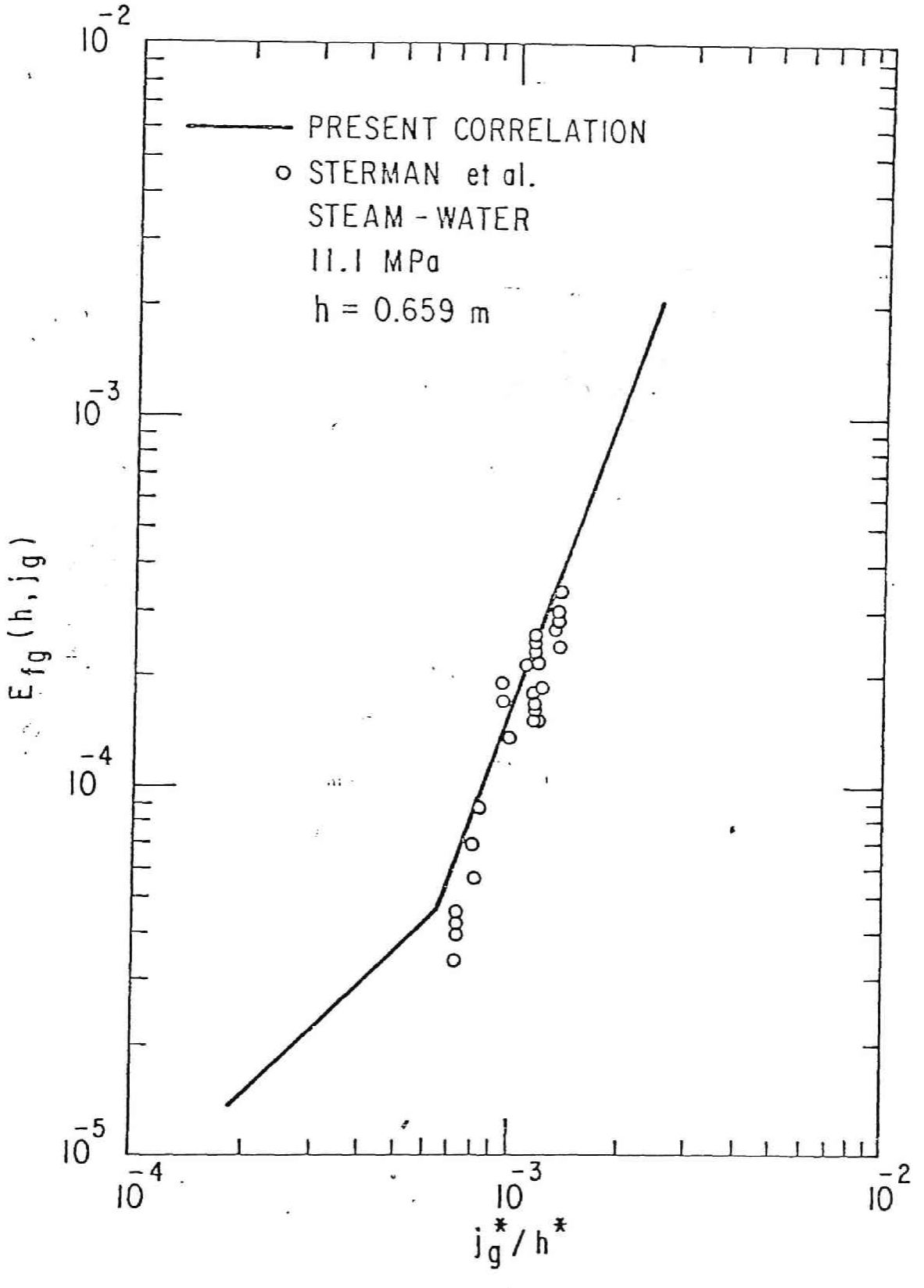

Fig. 12. Comparison of Experimental Data of Sterman et al. [39,40] with Predicted Entrainment at 11.1 MPa

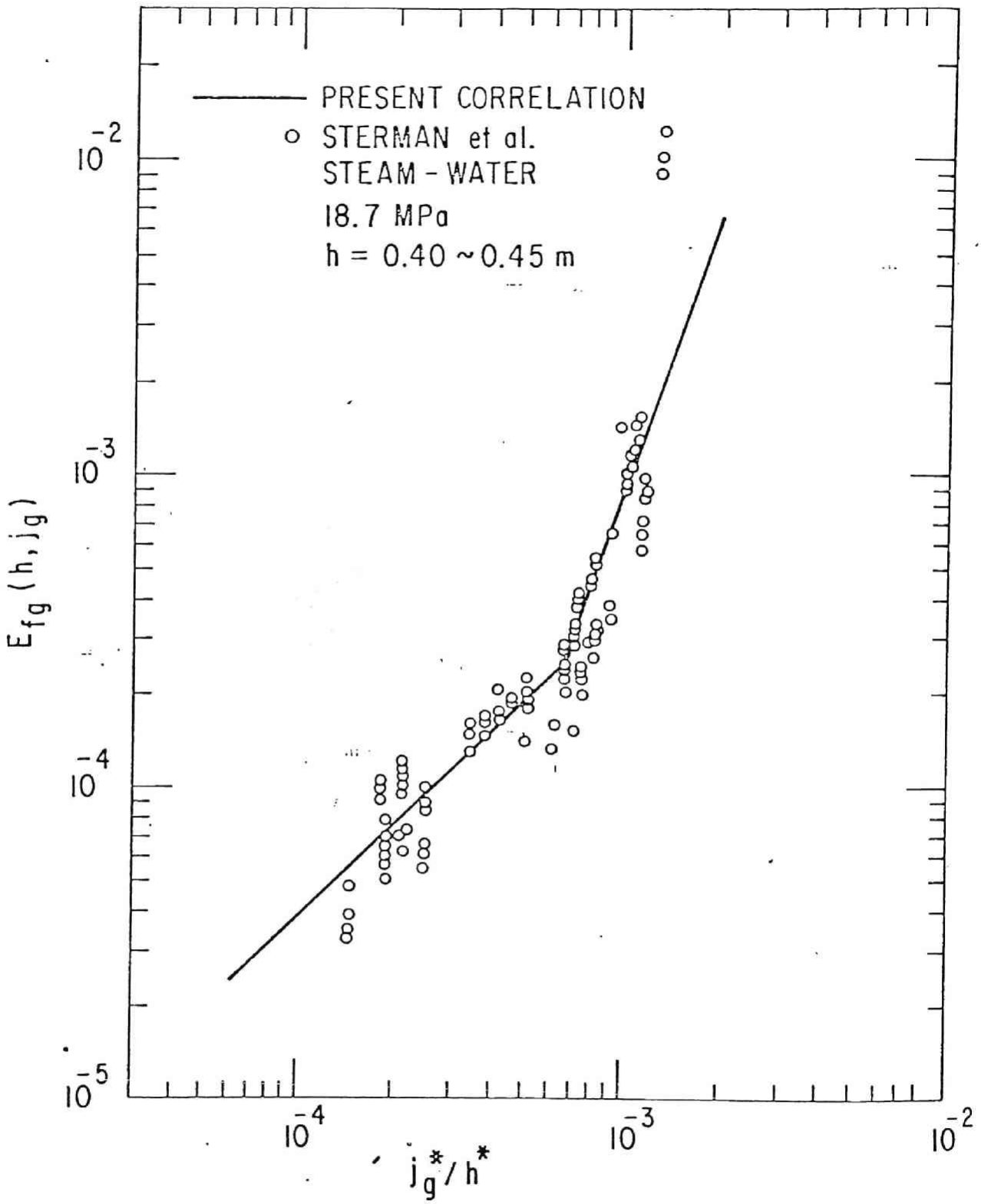

Fig. 13. Comparison of Experimental Data of Sterman et al. [39,40] with Predicted Entrainment at 18.7 MPa

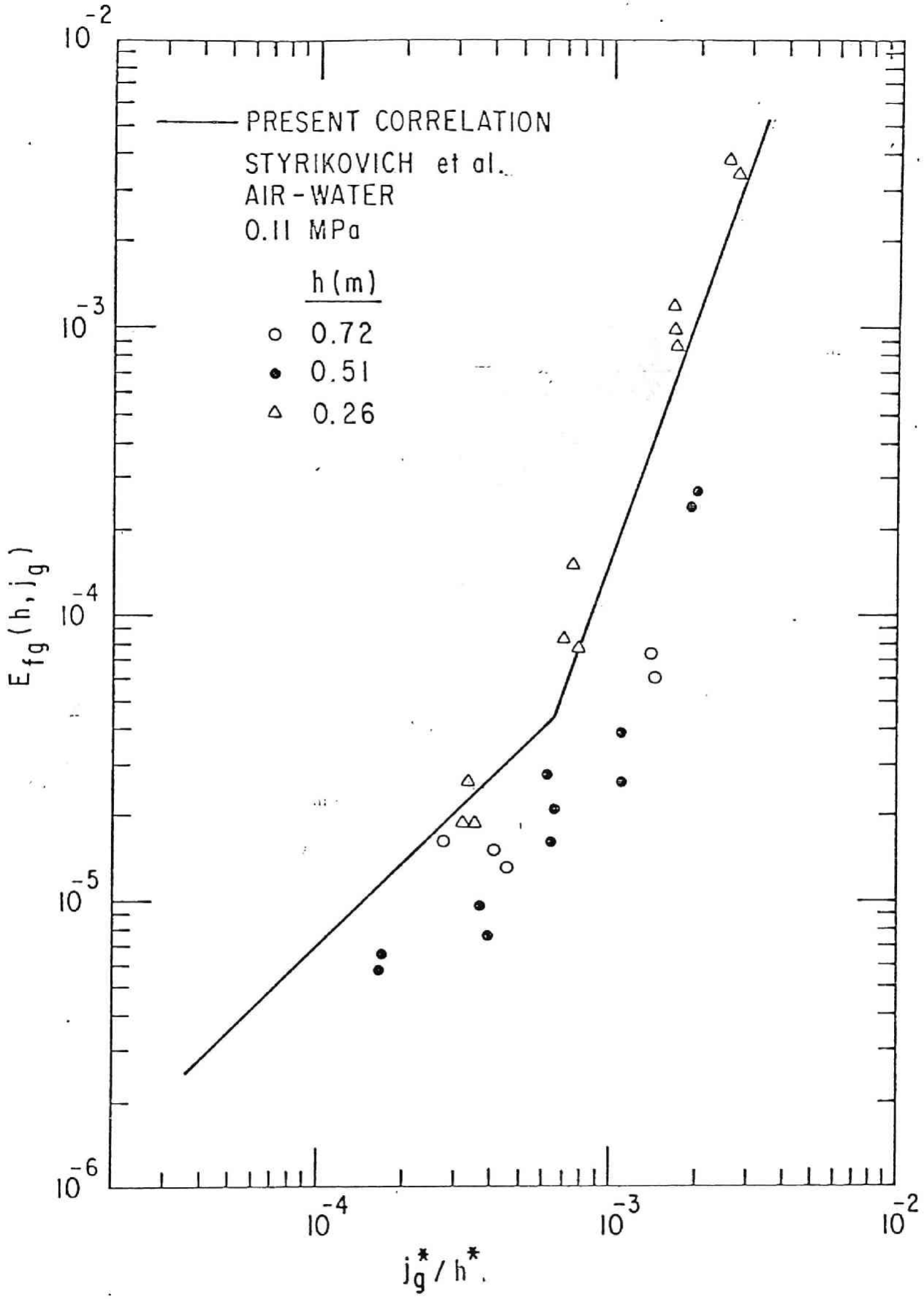

Fig. 14. Comparison of Experimental Data of Styrikovich et al. [41] with Predicted Entrainment at 0.11 MPa

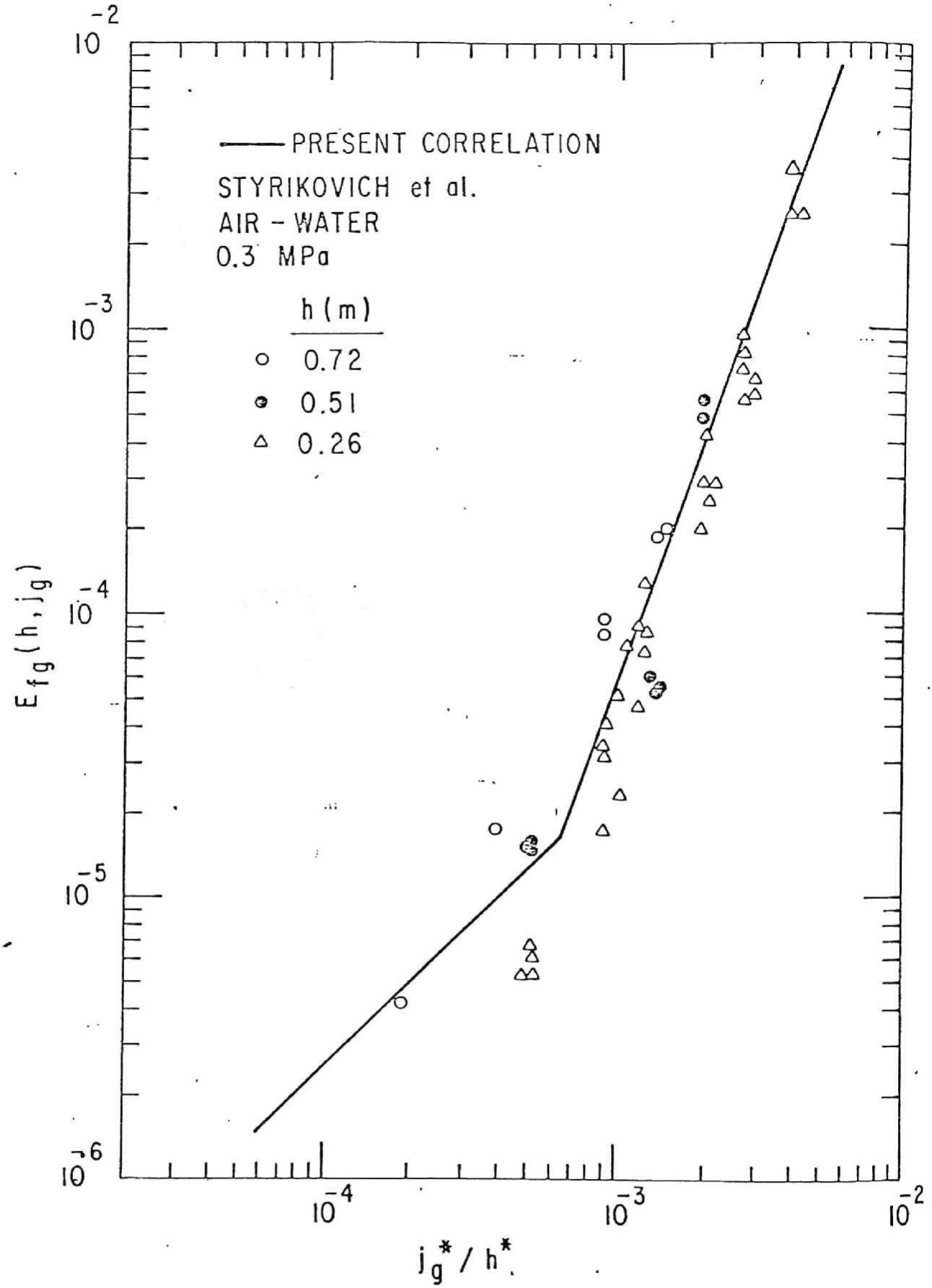

Fig. 15. Comparison of Experimental Data of Styrikovich et al. [41] with Predicted Entrainment at 0.3 MPa

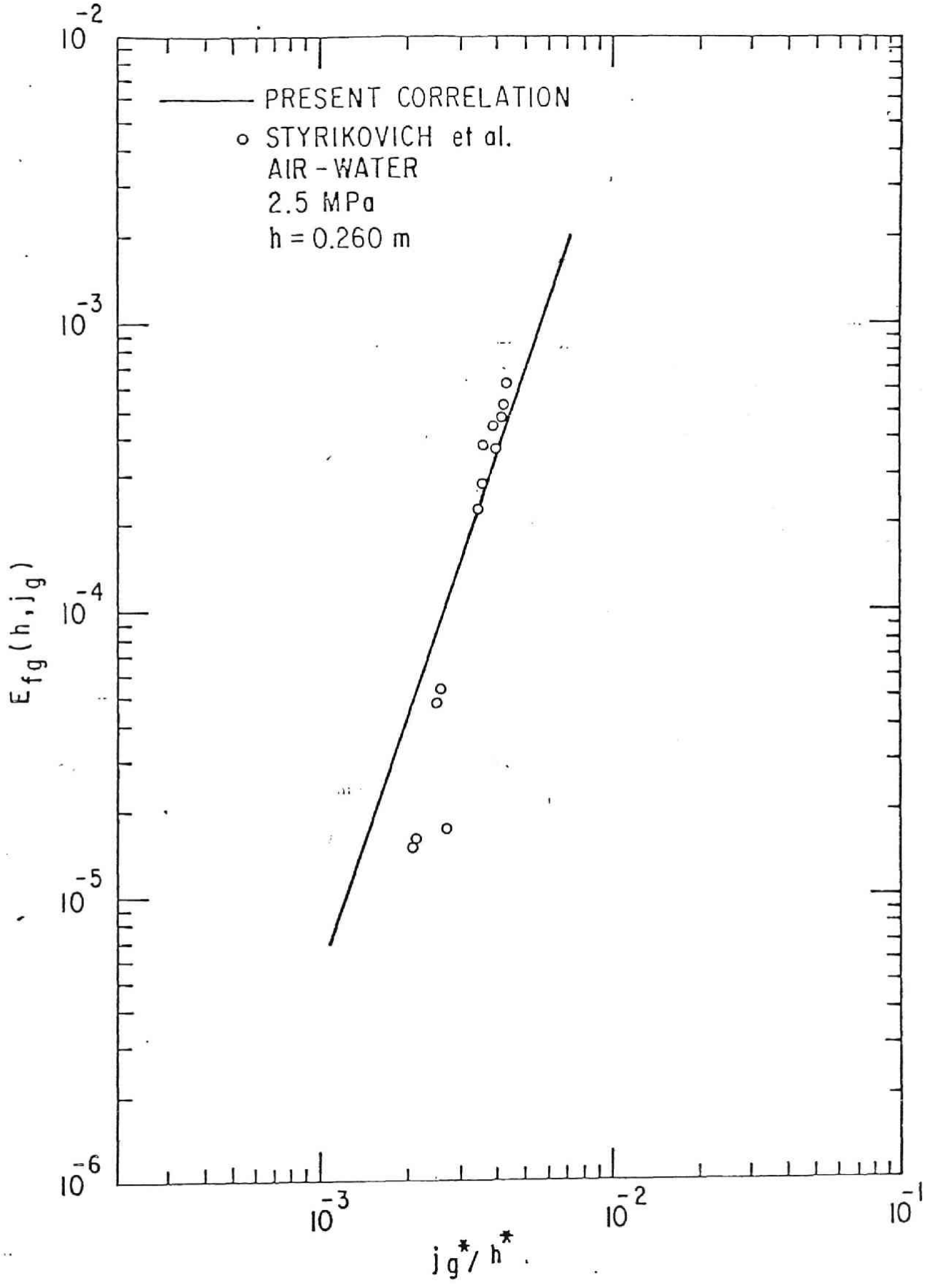

Fig. 16. Comparison of Experimental Data of Styrikovich et al. [41] with Predicted Entrainment at 2.5 MPa

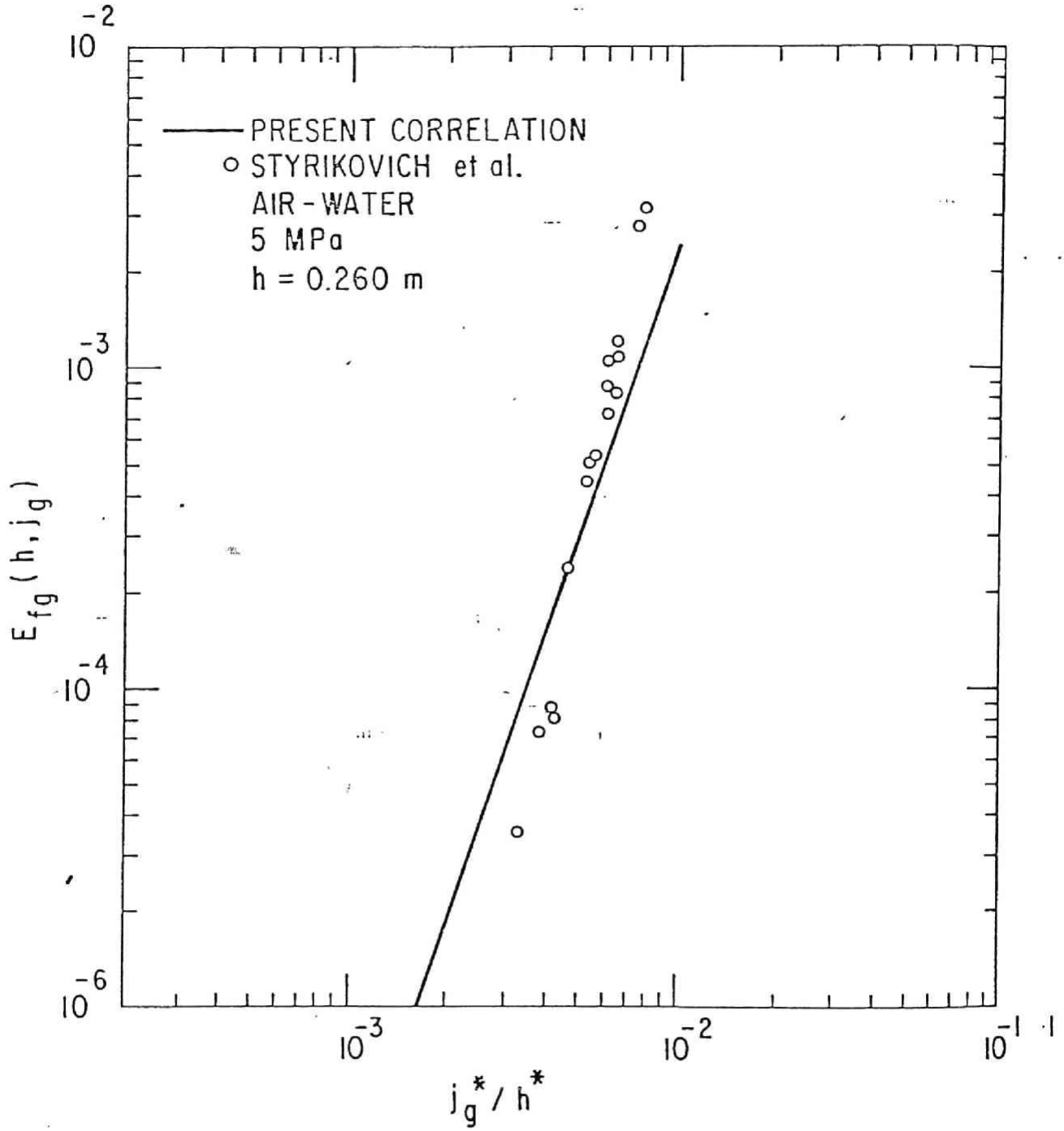

Fig. 17. Comparison of Experimental Data of Styrikovich et al. [41] with Predicted Entrainment at 5.0 MPa

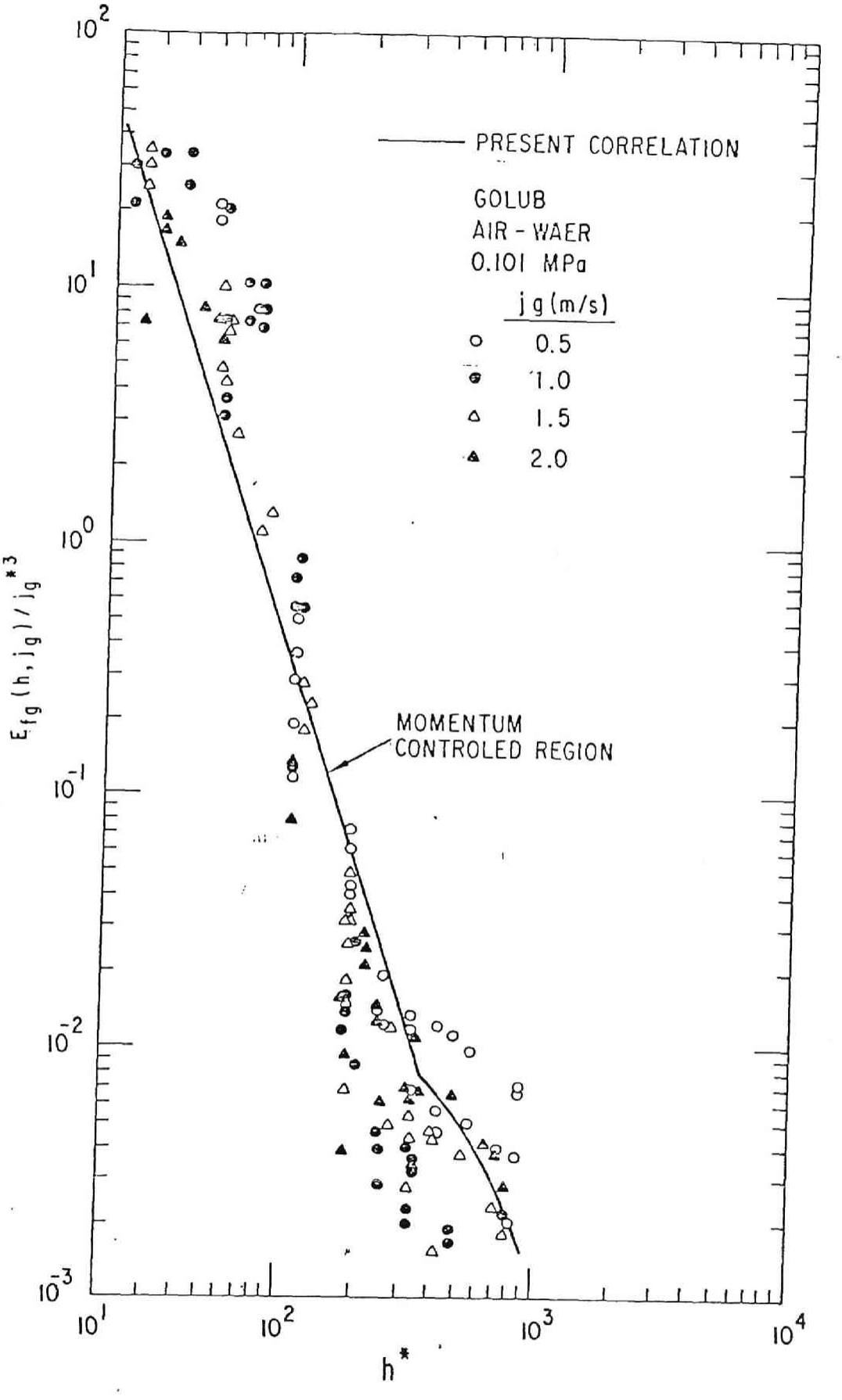

Fig. 18. . Comparison of Experimental Data of Golub [44] with Predicted · Entrainment at 0.101 MPa

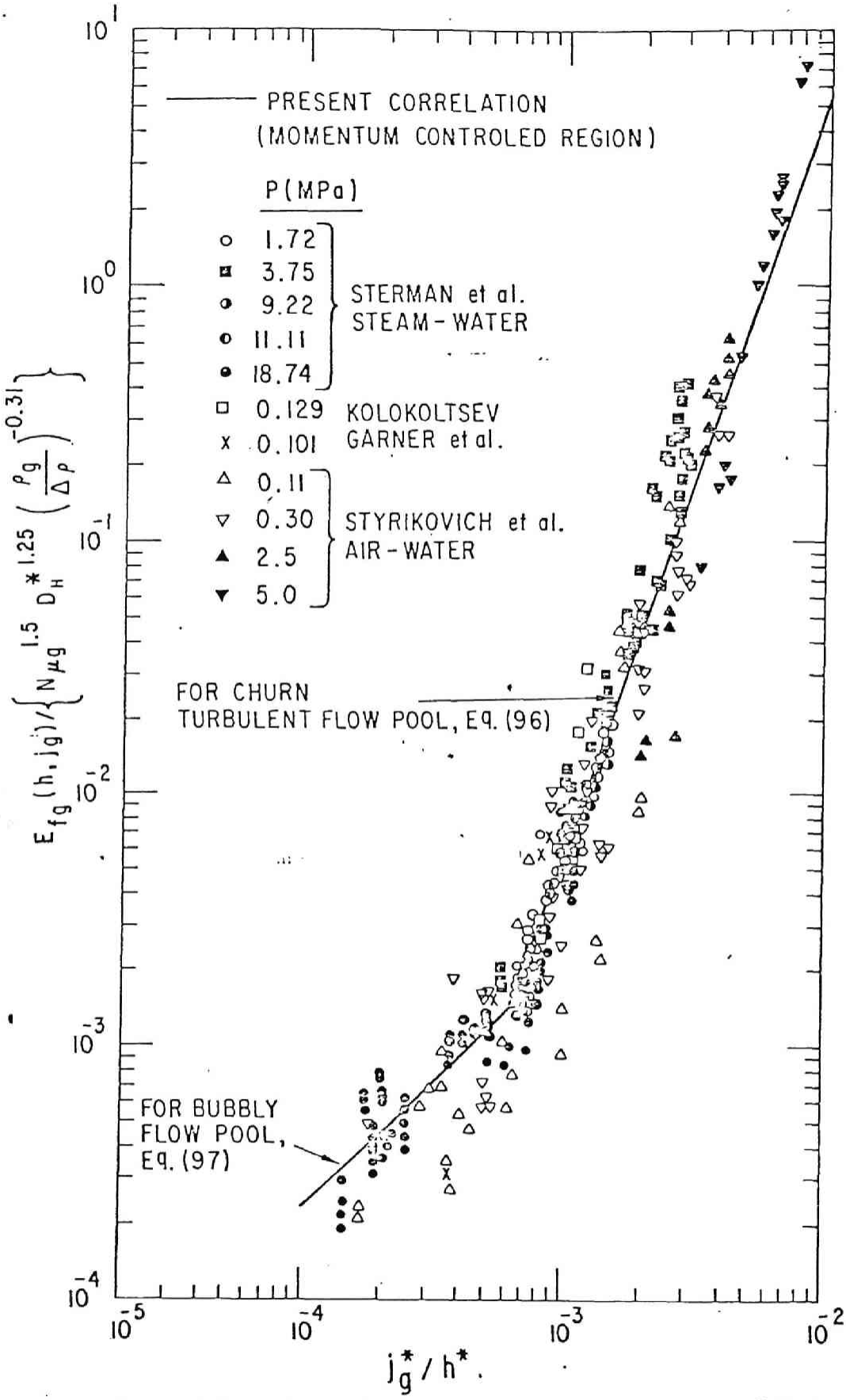

Fig. 19. Comparison of Experimental Data of Various Researchers [35,39,40, 41,49] with Predicted Entrainment in $E_{fg} \Big/ \left\{N_{\mu g}^{1.5} D_H^{*1.25} \left(\frac{\rho_a}{\Delta\rho}\right)^{-0.31}\right\}$ vs. j_a^*/h^* Plane

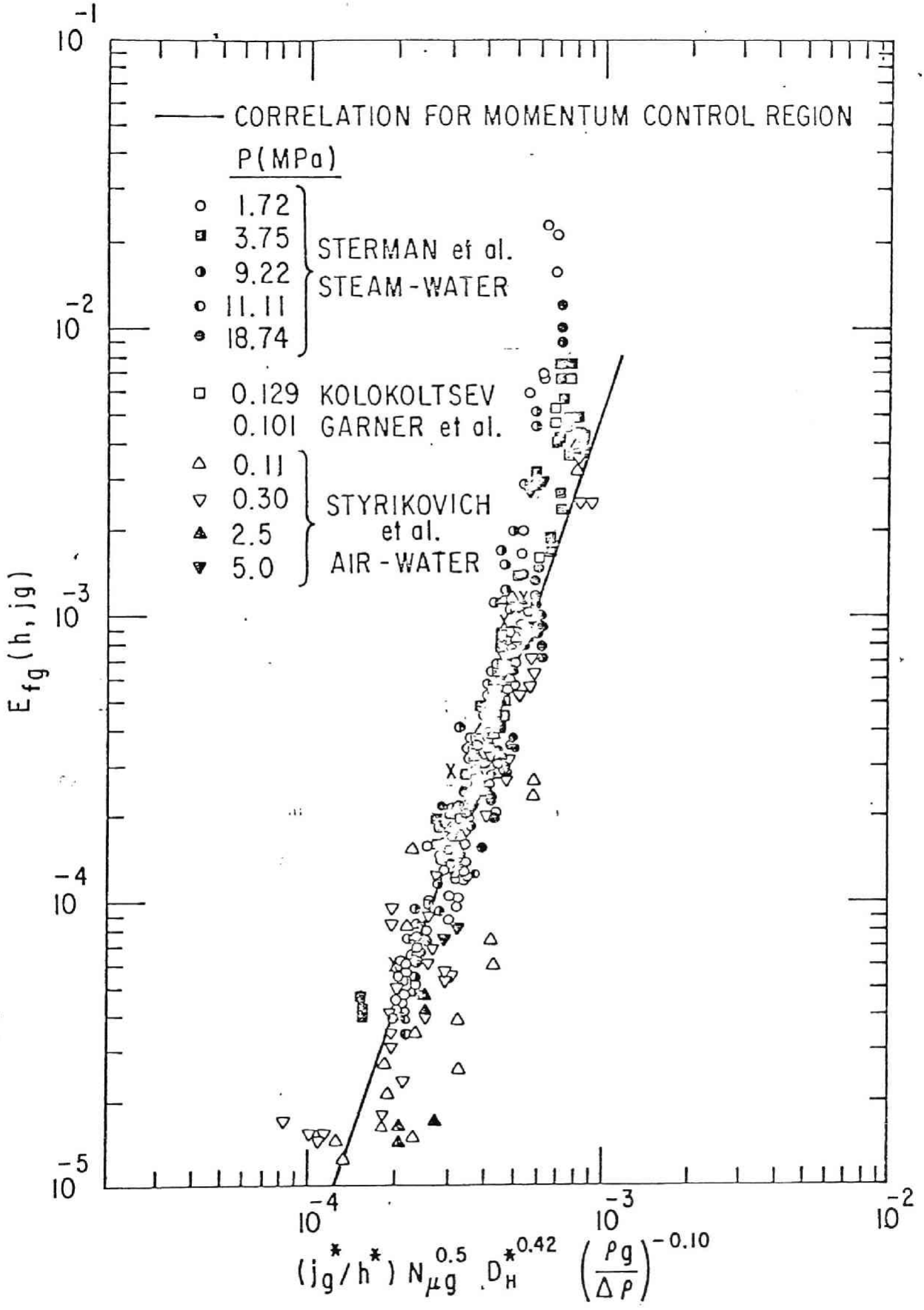

Fig. 20. Comparison of Experimental Data of Various Researchers [35,39,40, 41,49] with Predicted Entrainment in E_{fg} vs. $(j_g^*/h^*)N_{\mu g}^{0.5}\, D_H^{*0.42} \left(\frac{\rho_g}{\Delta\rho}\right)^{-0.10}$ Plane

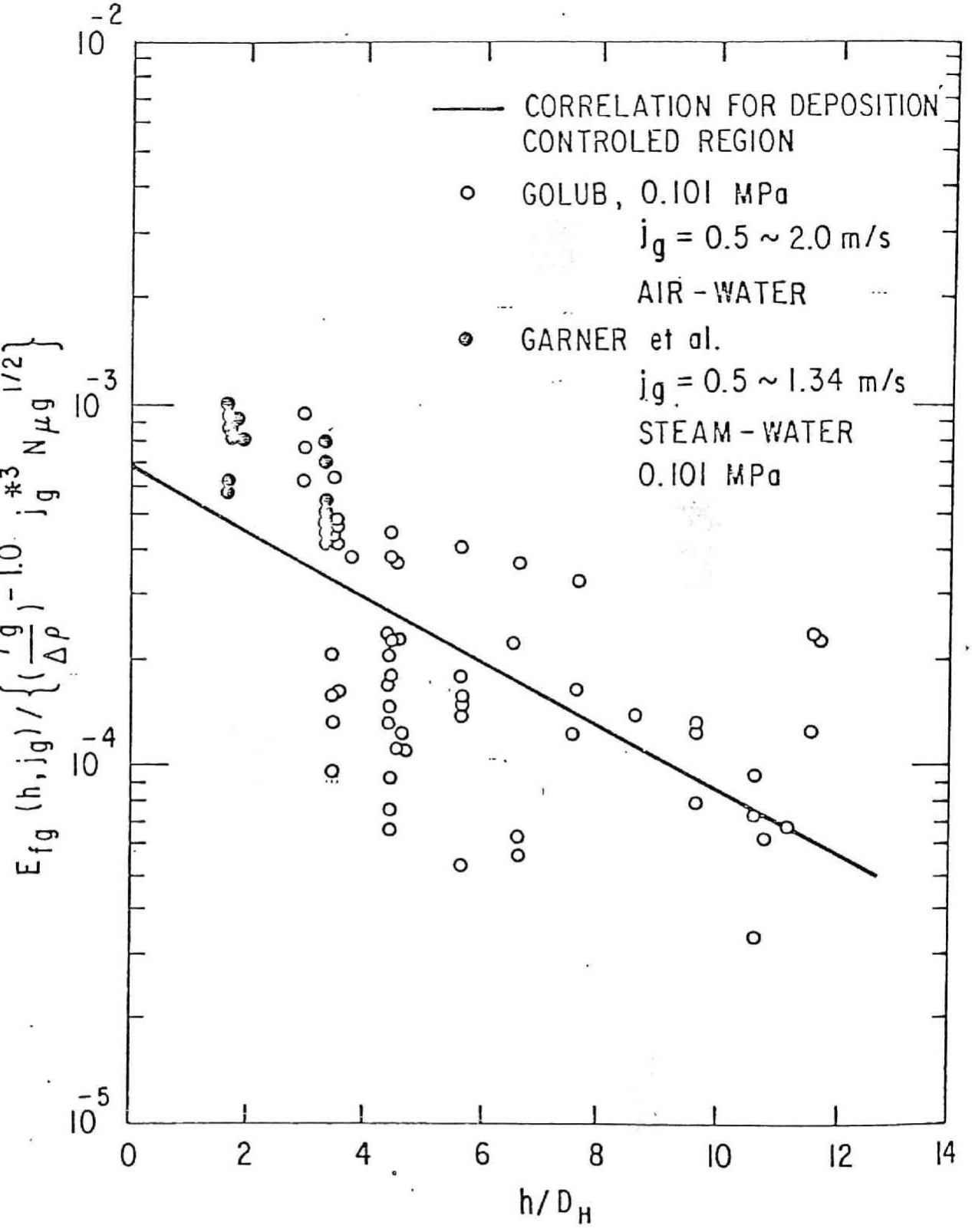

Fig. 21. Experimental Data of Entrainment in Deposition Controlled Region [35,44]

Table I. Maximum Height of Rising Droplet for Various Regimes

Regime	Range of Reynolds Number	C_D	$V_{r\infty}$	h_m^+
Stokes	$Re_D < 5$	$\frac{24}{Re_d}$	$\frac{1}{18}\frac{D^2 \Delta\rho g}{\mu_g}$	$v_{rf}^+ + j_g^+ - (1-j_g^+) \ln \frac{(1+v_{rf}^+)}{(1-j_g^+)}$
Wake	$5 < Re_D < 1000$	$\frac{10.67}{Re_d^{0.5}}$	$\frac{D}{4}\left[\frac{(g\Delta\rho)^2}{\mu_g \rho_g}\right]^{1/3}$	For $v_f > j_g$
				$2\sqrt{v_{rf}^+} + 2\sqrt{j_g^+} - \frac{1}{3}(1+j_g^+) \ln \frac{(1+\sqrt{v_{rf}^+})^2}{(1-\sqrt{v_{rf}^+ + v_{rf}^+})}$
				$+ \frac{1}{3}(1-j_g^+) \ln \frac{(1-\sqrt{j_g^+})^2}{(1+\sqrt{j_g^+ + j_g^+})} - \frac{2}{\sqrt{3}}(1-j_g^+) \tan^{-1}\left(\frac{2\sqrt{v_{rf}^+}-1}{\sqrt{3}}\right)$
				$- \frac{2}{\sqrt{3}}(1+j_g^+) \tan^{-1}\left(\frac{2\sqrt{j_g^+}+1}{\sqrt{3}}\right) + \frac{4}{\sqrt{3}} j_g^+ \tan^{-1}\frac{1}{\sqrt{3}}$
				For $v_f < j_g$
				$2\left(\sqrt{j_g^+} - \sqrt{-v_{rf}^+}\right) + \frac{2}{3}(1-j_g^+) \ln \frac{(1-\sqrt{j_g^+})}{(1-\sqrt{-v_{rf}^+})}$
				$- \frac{1}{3}(1-j_g^+) \ln \frac{(1+\sqrt{j_g^+ + j_g^+})}{(1+\sqrt{-v_{rf}^+ - v_{rf}^+})}$
				$- \frac{2}{\sqrt{3}}(1+j_g^+)\left\{\tan^{-1}\left(\frac{2\sqrt{j_g^+}+1}{\sqrt{3}}\right) - \tan^{-1}\left(\frac{2\sqrt{-v_{rf}^+}+1}{\sqrt{3}}\right)\right\}$
Newton's	$1000 < Re_D$	0.45	$1.72\sqrt{gD\frac{\Delta\rho}{\rho_g}}$	For $v_f > j_g$
				$\frac{1}{2} \ln (1+v_{rf}^{+2})(1-j_g^{+2}) + j_g^+ (\tan^{-1} v_{rf}^+ + \tanh^{-1} j_g^+)$
				For $v_f < j_g$
				$- \frac{1}{2} \ln \frac{(1-v_{rf}^{+2})}{(1-j_g^{+2})} + j_g^+ (\tanh^{-1} v_{rf}^+ + \tanh^{-1} j_g^+)$

Table II. Summary of Various Experiments on Entrainment Amount from Liquid Pool

Reference	Fluid	Vessel Diameter D_H (m)	Height above Pool Surface, h (m)	Pressure (MPa)	j_g (m/s)
Kolokoltsev [49]	Steam-Water	0.30	0.5 ~ 0.6	0.129	1.0 ~ 1.7
Garner et al. [35]	Steam-Water	0.30	0.5 ~ 1.0	0.101	0.3 ~ 1.3
Sterman et al. [39,40]	Steam-Water	0.24	0.5 ~ 0.9	1.72 ~ 18.7	0.01 ~ 1.3
Styrikovich et al. [41]	Air-Water	0.10	0.26 ~ 0.72	0.11 ~ 5.0	0.1 ~ 1.7
Golub [44]	Air-Water	0.20	0.1 ~ 2.2	0.101	0.5 ~ 2.0
Rozen [47]	Air-Water	0.20	0 ~ 0.35	0.101	0.6 ~ 3.0

CHAPTER VI

SCALING CRITERIA FOR LWR'S UNDER SINGLE PHASE AND TWO-PHASE NATURAL CIRCULATION

VI. 1 INTRODUCTION

In the preceeding chapters, the transient boiling and two-phase flow phenomena for various ℓ/d_{he}, steam quality and liquid velocity are investigated. The separate effects of the various operational parameters on heat and mass transfer processes associated with nuclear reactor safety have been made clear. Along with the separate effects, the overall characteristics of transient boiling and two-phase flow for a nuclear reactor are also important. The phenomena correspond to the boiling and two-phase flow for extremely large ℓ/d_{he}.

One of the most important problems in this category is natural circulation cooling. It is quite important associated with a small break LOCA and subsequent pump trip. In natural circulation, the driving force is determined by the density difference between the hot and cold sections in the nuclear reactor. Investigations for the natural circulation are often carried out using a scale model which simulates a prototype reactor. In designing the scale model it is quite important to know accurate scaling laws. Therefore, in this chapter, the scaling laws for the natural circulation under single and two-phase flow are investigated.

The scaling laws for forced convection single phase flow have been well established and modeling using these criteria has long been an accepted practice. Similar reasons exist for the desire to model natural circulation single and two-phase flows. However, the similarity analysis for a natural circulation system is much more complicated due to the coupling of the driving force and heat transfer processes. The flow condition can only be determined by the integral effect of the thermo-hydraulic processes along the entire loop. Therefore, in order to develop meaningful similarity criteria, it is necessary to consider these integral effects through some forms of simplified solutions.

There are some publications on a simulation of a single phase natural circulation system. For example, Heisler and Singer [1] and Heisler [2] have analyzed the simulation of a liquid metal natural circulation system. The similarity analysis for a two-phase flow system has been carried out by Ishii and Zuber [3], Ishii and Jones [4], and Zuber [5] among others. The determination of scaling criteria for single phase flow is achieved through appropriate non-dimensionalization of the well established balance and constitutive

equations. However, the same approach for two-phase flow encounters considerable difficulties due to the existing uncertainties in the basic formulation related to balance equations, two-phase flow correlations, and flow regime transition criteria.

The available methods to develop similarity criteria for two-phase flow systems have been reviewed by Ishii and Jones [4]. In the present analysis, the results based on the local conservation equations and ones based on the perturbation method are utilized. The extension of the similarity analysis to a natural circulation system is achieved by considering the scaling criteria from a small perturbation method and the steady state solution. For this purpose, the relatively well established drift-flux model and constitutive relations [6,7] are used.

The above results are applied to the simulation of a natural circulation in pressurized light water reactors by the LOFT facility [8]. It is noted that the single phase and two-phase heat transfer under a natural circulation pattern is particularly important for LWR's. Accidents which lead to the decay heat removal by natural circulation have much higher probability than those of the severe accidents extensively studied recently. However, the breakdown of the natural circulation boiling which leads to dryout and burnout of heated surface in these conditions have significant consequences. A detailed study of the critical heat flux under these conditions has been carried out by Mishima and Ishii [9]. This result is used to analyze the requirements for the simulation of the critical heat flux phenomena in addition to the general thermo-hydraulic simulation.

VI.2 SINGLE PHASE SIMILARITY LAWS

VI.2.1 Similarity Parameters for Single Phase Natural Circulation

The similarity criteria for a natural circulation system can be obtained from the integral effects of the local balance equations along the entire loop. A typical system under consideration is shown in Fig. 1. This system consists of the heat source, heat sink, connecting piping system, and flow resistances such as orifices. For a single phase flow case, a method similar to that used by Heisler and Singer [1] and Heisler [2] for a liquid metal system is applied to develop similarity criteria.

In the following analysis, subscripts o and r denote the reference constant value and representative variable of a system. The ith component and solid are denoted by subscripts i and s. Using the Boussinesq assumption for a single phase natural convection system, the fluid is considered incompressible, except in the gravitational term in the momentum equation. Then the conservation laws can be expressed by the following set of simplified balance equations based on a one-dimensional formulation.

Continuity Equation

$$u_i = \frac{a_o}{a_i} u_r \quad . \tag{1}$$

Integral Momentum Equation

$$\rho \frac{du_r}{dt} \sum_i \frac{a_o}{a_i} \ell_i = \beta g \rho \Delta T \ell_h - \frac{\rho u_r^2}{2} \sum_i \left(\frac{f\ell}{d} + K \right)_i \left(\frac{a_o}{a_i} \right)^2 \quad . \tag{2}$$

Fluid Energy Equation for ith Section

$$\rho C_p \left\{ \frac{\partial T}{\partial t} + u \frac{\partial T}{\partial z} \right\} = \frac{4h}{d} (T_s - T) \quad . \tag{3}$$

Solid Energy Equation for ith Section

$$\rho_s C_{ps} \frac{\partial T_s}{\partial t} + k_s \nabla^2 T_s - \dot{q}_s = 0 \quad . \tag{4}$$

The boundary condition between the ith section fluid and structure is given by

$$- k_s \frac{\partial T_s}{\partial y} = h (T_s - T) \quad . \tag{5}$$

In the above equations, u_r is the representative velocity of the system corresponding to the velocity of the section having cross sectional area a_o. ℓ_h is the equivalent total length of the hot fluid sections. The above set of equations can be non-dimensionalized by introducing the following dimensionless parameters:

$$U_i = u_i/u_o \quad , \quad U_r = u_r/u_o$$

$$L_i = \ell_i/\ell_o \quad , \quad L_h = \ell_h/\ell_o \quad , \quad Z = z/\ell_o$$

$$\tau = t\, u_o/\ell_o$$

$$\theta = \Delta T/\Delta T_o \qquad (6)$$

$$A_i = a_i/a_o$$

$$\nabla^{*2} = \delta^2 \nabla^2 \quad , \quad Y = y/\delta$$

The dimensionless balance equations can be given by the following expressions.

Continuity Equation

$$U_i = U_r/A_i \quad . \qquad (7)$$

Momentum Balance

$$\frac{dU_r}{d\tau}\left(\sum_i \frac{L_i}{A_i}\right) = R\,(\theta_h-\theta_c)\,L_h - \frac{U_r^2}{2}\sum_i \left(F_i\,\frac{1}{A_i^2}\right). \qquad (8)$$

Fluid Energy Equation (ith Section)

$$\frac{\partial\theta_i}{\partial\tau} + \frac{U_r}{A_i}\frac{\partial\theta_i}{\partial Z} = St_i\,(\theta_{si}-\theta_i) \quad . \qquad (9)$$

Solid Energy Equation (ith Section)

$$\frac{\partial\theta_{si}}{\partial\tau} + T^*\,\nabla_i^{*2}\,\theta_{si} - Q_{si} = 0 \quad . \qquad (10)$$

Fluid-Solid Boundary Condition (ith Section)

$$\frac{\partial\theta_{si}}{\partial Y_i} = B_i\,(\theta_{si}-\theta_i) \quad . \qquad (11)$$

The similarity groups appeared in the above equations are defined below.

$$\text{Richardson No.} \quad ; \; R \equiv \frac{g\beta\Delta T_o \ell_o}{u_o^2} = \frac{\text{Buoyancy}}{\text{Inertia Force}}$$

$$\text{Friction No.} \quad ; \; F_i \equiv \left(\frac{f\ell}{d} + K\right)_i = \frac{\text{Friction}}{\text{Inertia Force}}$$

$$\text{Modified Stanton No.} ; \; St_i \equiv \left(\frac{4h\ell_o}{\rho C_p u_o d}\right)_i = \frac{\text{Wall Convection}}{\text{Axial Convection}}$$

$$\text{Time Ratio No.} \quad ; \; T_i^* \equiv \left(\frac{\alpha_s}{\delta^2}\frac{\ell_o}{u_o}\right)_i = \frac{\text{Transport Time}}{\text{Conduction Time}} \qquad (12)$$

$$\text{Biot No.} \quad ; \; B_i \equiv \left(\frac{h\delta}{k_s}\right)_i = \frac{\text{Wall Convection}}{\text{Conduction}}$$

$$\text{Heat Source No.} \quad ; \; Q_{si} \equiv \left(\frac{\dot{q}_s \ell_o}{\rho_s C_{ps} u_o \Delta T_o}\right)_i = \frac{\text{Heat Source}}{\text{Axial Energy Change}}$$

In addition to the above defined physical similarity groups, several geometrical similarity groups are obtained. These are;

$$\text{Axial Scale} \quad ; \; L_i = \ell_i/\ell_o \qquad (L_h = \ell_h/\ell_o)$$

$$\text{Flow Area Scale;} \; A_i = a_i/a_o \qquad (13)$$

It is noted here that the hydraulic diameter d_i and the conduction depth δ_i are defined by

$$d_i = 4a_i/\xi_i \quad , \qquad (14)$$

and

$$\delta_i = a_{si}/\xi_i \quad , \qquad (15)$$

where a_i, a_{si}, and ξ_i are the flow area, solid cross sectional area, and wetted perimeter of ith section, respectively. Hence, d_i and δ_i are related by

$$d_i = 4\delta_i \left(\frac{a}{a_s}\right)_i \quad . \tag{16}$$

In the above development, the reference scales for the velocity and temperature change have been used. The simplest way to obtain these scales are to use the steady state solutions. By taking the heated section as a representative section, one can obtain the following solution for temperature rise.

$$\Delta T_o = \frac{\dot{q}_o \ell_o}{\rho C_p u_o}\left(\frac{a_{so}}{a_o}\right) \quad , \tag{17}$$

where subscript o denotes the heated section. Substituting the above expression into the steady state momentum integral equation, the solution for the velocity becomes

$$u_o = \left\{ \frac{2\beta \left(\frac{\dot{q}_o \ell_o}{\rho C_p}\right) \ell_h \left(\frac{a_{so}}{a_o}\right)}{\frac{1}{2g}\sum_i (F_i/A_i^2)} \right\}^{1/3} \tag{18}$$

VI.2.2 General Similarity Laws

The similarity criteria between two different systems can be obtained from a detailed consideration of the similarity groups developed above together with necessary constitutive relations. In the following analysis, subcript R denotes the ratio between the model and prototype. Thus

$$\psi_R \equiv \frac{\psi_m}{\psi_p} = \frac{\psi \text{ for model}}{\psi \text{ for prototype}} \quad . \tag{19}$$

In general, the solid materials need not be the same between the model and prototype. However, for simplicity the use of the same materials for structures is assumed in the present analysis. This implies that

$$\rho_{sR} = C_{psR} = k_{sR} = \alpha_{sR} = 1 \quad . \tag{20}$$

The most fundamental requirement for the similarity is concerned with the geometrical similarity criteria. It is evident from the continuity relation that for a complete kinematic similarity the geometrical similarity for the flow area

$$A_{iR} = \frac{(a_i/a_o)_m}{(a_i/a_o)_p} = 1 \quad , \tag{22}$$

should be satisfied. On the other hand, from the dynamic similarity, it is necessary that

$$\left(\sum_i L_i/A_i\right)_R = 1$$

$$L_{hR} = 1 \tag{23}$$

These are somewhat weaker restrictions than the complete axial geometrical similarity given by

$$L_{iR} = \frac{(\ell_i/\ell_o)_m}{(\ell_i/\ell_o)_p} = 1 \quad . \tag{24}$$

However, for simplicity both the transverse area and axial length similarities are assumed at least where the energy transfer is important.

From the dynamical similarity condition one obtains that

$$\left(\sum_i F_i/A_i^2\right)_R = 1 \quad . \tag{25}$$

This requirement can be easily satisfied by using appropriate orifices, thus this restriction on the friction number is assumed to be satisfied unconditionally.

From the steady state condition given by Eqs. (18) to (25), the ratio of the reference velocities becomes

$$u_{oR} = \frac{u_{om}}{u_{op}} = \left\{ \dot{q}_{oR} \left(\frac{\beta}{\rho C_p} \right)_R \frac{\delta_{oR}}{d_{oR}} \ell_{oR}^2 \right\}^{1/3} , \tag{26}$$

where $\dot{q}_{oR} = \dot{q}_{om}/\dot{q}_{op}$ and $\ell_R = \ell_{om}/\ell_{op}$. Thus the temperature rise ratio is given by

$$\Delta T_{oR} = \frac{\Delta T_{om}}{\Delta T_{op}} = \dot{q}_{oR} \left(\frac{1}{\rho C_p} \right)_R \frac{\ell_{oR}}{u_{oR}} \frac{\delta_{oR}}{d_{oR}} . \tag{27}$$

By substituting Eq. (27) into the definition of the Richardson number, it can be shown that $R_R = 1$ is equivalent to Eq. (26). Therefore, the correct scaling of velocity satisfies the Richardson number requirement automatically. Then

$$R_R = 1 \text{ equivalent to Eq. (26)} . \tag{28}$$

On the other hand, the energy similarity conditions require that

$$\begin{aligned} St_{iR} &= 1 \\ T^*_{iR} &= 1 \\ B_{iR} &= 1 \\ Q_{soR} &= 1 \end{aligned} \tag{29}$$

It is noted here that the Stanton number and Biot number involve a heat transfer coefficient. Thus a form of the constitutive relation for h becomes important. Under the conditions of

$$\left\{ \begin{array}{l} \text{same solid materials, Eq. (20),} \\ \text{transverse flow area similarity, Eq. (22), and} \\ \text{axial length similarity, Eq. (24),} \end{array} \right.$$

the above energy similarity conditions reduce to

$$T^*_{iR} = \ell_R/(u_R \delta^2_{iR}) = 1 . \tag{30}$$

$$B_{iR} = h_R \delta_{iR} = 1 \quad . \tag{31}$$

$$Q_{soR} = (\rho C_p)_R \frac{d_{oR}}{\delta_{oR}} = 1 \quad . \tag{32}$$

For the last relation, the velocity scaling criteria, Eq. (26), and geometrical relation given by Eq. (16) have also been used. An important point is that the Stanton number requirement is satisfied automatically if the above three similarity criteria can be achieved.

Physically the time ratio scales the speed of transport processes in fluid and solid. The Biot number is the ratio of the thermal conductances in fluid and solid. Thus it is the scale for the boundary layer temperature drop and thermal gradient in solid. The heat source number is important for the temperature in solid and for the overall energy level of the system. The Stanton and Biot numbers are related to the boundary condition at the fluid-solid interface. Thus they contain a heat transfer coefficient. Under a natural circulation condition, relatively slow transients are anticipated. For these cases, the similarity requirement from these two numbers mainly contribute to the simulation of the temperature drop in the boundary layer and the interfacial temperature.

The requirements from the time constant ratio and heat source number lead to additional geometrical restrictions. Thus the conduction depth ($\sim$ wall thickness) should be

$$\delta_{iR} = \delta_R = \sqrt{\frac{\ell_R}{u_R}} \quad , \tag{33}$$

whereas the hydraulic diameter should be

$$d_{oR} = d_{iR} = d_R = \frac{\delta_R}{(\rho C_p)_R} = \frac{1}{(\rho C_p)_R} \sqrt{\frac{\ell_R}{u_R}} \quad . \tag{34}$$

Furthermore, the Biot number similarity requires

$$h_{iR} = h_R = \sqrt{\frac{u_R}{\ell_R}} \quad . \tag{35}$$

In contrast to the design parameters such as δ_i and d_i, the heat transfer coefficient cannot be determined independent of a flow field and fluid properties. Thus Eq. (35) imposes an additional constraint on the flow field.

In general the heat transfer coefficient depends on the fluid properties and flow conditions. It is customary to represent a correlation for h in terms of the Nusselt number defined by

$$Nu \equiv \frac{hd}{k} \quad , \tag{36}$$

where d and k are the hydraulic diameter and fluid conductivity. There are a number of correlations for Nu for a flow in a relatively long tube, however, the following three correlations typically represent the three important groups

$$\begin{cases} \text{Laminar Flow (q given)} & Nu = 4.36 \\ \text{Turbulent Flow } (1 < Pr < 20) & Nu = 0.0155\ Re^{0.83}\ Pr^{0.5} \\ \text{Liquid Metals } (Pr < 0.1) & Nu = 4.82 + 0.0185\ (RePr)^{0.83} \end{cases} \tag{37}$$

This shows that the Nusselt number depends on the Reynolds number and fluid properties.

On the other hand, in a free convection range, Nu depends on the length of a heated surface and the Grashof number defined by

$$Gr \equiv \frac{g\beta(T_s - T)\ell^3}{(\mu/\rho)^2} \quad . \tag{38}$$

Then for a wide range of Gr, the Nusselt number may be correlated by

$$Nu = 0.3\ (GrPr)^{0.3} \left(\frac{d}{\ell}\right) \quad . \tag{39}$$

These different constitutive relations for h indicate that the similarity requirements from the Stanton and Biot numbers are not easy to meet,

particularly in the case of a fluid to fluid simulation. The correlation for forced convection flow given by Eq. (37) shows that it is desirable to use a fluid with a similar Prandtl number.

In a laminar flow range, the heat transfer correlation gives

$$h_R = \frac{k_R}{d_R} \quad , \tag{40}$$

whereas for turbulent flow of fluid such as water

$$h_R = \frac{k_R}{d_R}\left(\frac{\rho_R u_R d_R}{\mu_R}\right)^{0.83} Pr_R \quad . \tag{41}$$

It is evident that Eqs. (40) and (41) impose quite different constraints on operational and design parameters with respect to Eq. (35). Furthermore, Eqs. (34), (35), and (41) require that the ratio of the Reynolds number to be close to one. For a scale model this may result in higher model velocity and very high model power. Because of this, the similarity condition based on the Biot or Stanton number should be carefully evaluated.

VI.2.3 Scale Model with Same Fluid

A special case of a scale model with the same fluid is now examined. For this case all the property ratio groups can be set as unity. Thus

$$\rho_R = \left(\frac{\beta}{\rho C_p}\right)_R = (\rho C_p)_R = k_R = \mu_R = Pr_R = 1 \quad . \tag{42}$$

Then the similarity laws developed above reduce to the following equations.

Reference Velocity Ratio

$$u_R = \left\{\dot{q}_{oR}\,\frac{\delta_R}{d_R}\,\ell_R^2\right\}^{1/3} \quad . \tag{43}$$

Wall Conduction Depth Ratio

$$\delta_{iR} = \delta_R = \sqrt{\frac{\ell_R}{u_R}} \quad . \tag{44}$$

Hydraulic Diameter Ratio

$$d_{iR} = d_R = \sqrt{\frac{\ell_R}{u_R}} \quad . \tag{45}$$

Biot Number Similarity

$$h_R = \sqrt{\frac{u_R}{\ell_R}} \quad . \tag{46}$$

Heat Transfer Laws

$$\begin{cases} \text{Laminar} & h_R = \dfrac{1}{d_R} \quad . & (47) \\ \text{Turbulent (}\sim\text{Water)} & h_R = \dfrac{1}{d_R}\,(u_R d_R)^{0.83} \quad . & (48) \\ \text{Liquid Metals (}\sim\text{Low Velocity)} & h_R \doteq \dfrac{1}{d_R} \quad . & (49) \end{cases}$$

The Biot and Stanton number similarity conditions with the constitutive laws for the heat transfer coefficient mainly simulate the boundary layer temperature drop. When the heat transfer mechanism is not completely simulated, the system would adjust to a different temperature drop in the boundary layer. However, the overall flow and energy distribution will not be strongly affected in slow transients typical of a natural circulation system. The violation of the Biot or Stanton number similarity within the liquid flow condition should not cause a major problem except at very rapid power transients.

In view of the above, the first three conditions are of prime importance. The substitution of Eq. (44) and (45) gives

$$u_R = (\dot{q}_{oR}\ell_R^2)^{1/3} \quad . \tag{50}$$

Hence

$$\delta_R = d_R = (\ell_R/\dot{q}_{oR})^{1/6} \quad . \tag{51}$$

From Eq. (16), this implies that

$$\left(\frac{a}{a_s}\right)_R = 1 \quad . \tag{52}$$

In addition to these conditions, the friction number similarity and geometrical similarity conditions should be satisfied. Thus

$$\left[\sum_i \left(\frac{f\ell}{d} + K\right)\left(\frac{a_o}{a_i}\right)^2\right]_R = 1 \quad , \tag{53}$$

and

$$\left(\frac{\ell_i}{\ell_o}\right)_R = 1 \quad , \quad \left(\frac{a_i}{a_o}\right)_R = 1 \quad . \tag{54}$$

The last geometrical similarity condition can be relaxed depending on the degree of similarity required. For example, the transverse area condition is important only where the heat transfer is significant because the velocity simulation in adiabatic sections is not important. In terms of the axial length similarity condition, it is important that Eq. (54) is satisfied in the hot leg section such that the driving head is well simulated. When Eq. (54) is partially violated, it is very important that Eq. (23) is satisfied such that the fluid transient time over the entire loop is correctly simulated. Hence

$$\left(\sum_i L_i/A_i\right)_R = 1$$

$$L_{hR} = 1 \tag{55}$$

In view of Eqs. (46) to (49), it becomes clear that a laminar flow or liquid metal flow at moderate Reynolds number can automatically satisfy the similarity criteria for solid-liquid boundary conditions, i.e., the Biot and Stanton number criteria. On the other hand, for a turbulent flow of water, it is almost impossible to satisfy them in a scale model due to the very much increased power demand in a model.

A scale model can be designed by first determining the size of the model or ℓ_R. This factor and the available power determine the velocity scale from Eq. (50). It is important to note that the time scale will be shifted by the factor

$$t_R = \frac{\ell_R}{u_R} \quad . \tag{56}$$

Therefore, for a real time simulation an additional condition of

$$t_R \simeq 1 \text{ or } \frac{\ell_R}{u_R} \simeq 1 \tag{57}$$

should be imposed. In this case, the power level can be uniquely determined by

$$\dot{q}_{oR} = \ell_R \quad . \tag{58}$$

Then one obtains

$$\delta_R = d_R = 1 \quad . \tag{59}$$

VI.2.4 Sample Calculations (Real Time Scale)

As an example, a simulation of natural circulation flow in a typical light water reactor by the LOFT facility is considered. The representative geometry of PWR relevant to the natural circulation study is shown in Fig. 2 and that of LOFT facility [8] in Fig. 3. Here the PWR geometry is that of CE System 80. Some of the important design parameters are listed in Table I.

In view of the elevation AF and AB, the axial length ratio ℓ_R is in the range of

$$\ell_R = 0.4 \sim 0.44 \quad . \tag{60}$$

For a real time simulation, the velocity should be reduced by the same factor as given by Eq. (57). Then

$$u_R = 0.4 \sim 0.44$$

$$q_R = 0.4 \sim 0.44 \qquad (61)$$

On the other hand, the hydraulic diameter and the conduction depth in the important heat transfer sections, i.e., the core and steam generator, should satisfy Eq. (59). From Table I it is clear that these conditions are satisfied. Hence, the single phase natural circulation can be easily simulated by the LOFT facility by installing appropriate offices and using proper length pipes in a horizontal section. In case of a turbulent flow, the boundary layer temperature drop cannot be simulated well due to unrealistic demand on the necessary power in the model. However, it is considered that this discrepancy may have little effect on the overall similarity of the systems.

Another major difference is the relative length of the steam generator tubes. The length ratio here is only 0.26. Thus the axial length in the cooling region is much shorter in the model in relation to other sections. This may be a problem in case of rapidly changing power.

Ⅵ.3 TWO-PHASE SIMILARITY LAWS

Ⅵ.3.1 Basic Formulation for Two-Phase Natural Circulation

The similarity parameters for a natural circulation system under a two-phase condition can be obtained from the integral effects of the local two-phase flow balance equations along the entire loop. Under a natural circulation condition, the majority of transients are expected to be relatively slow. Furthermore, for developing system similarity laws, the response of the whole mixture is important rather than the detailed responses of each phase and phase interactions

The basic concept of the drift flux model is to consider the motion and energy of mixture as a whole, rather than those of two phases separately. However, the drift flux model requires some additional constitutive assumptions on the phase interactions [7,10,11]. For the derivation of system similarity criteria under a natural circulation condition, the drift-flux model is appropriate [3,4,12]. This is because the drift-flux model can properly describe the mixture-structure interactions over a wide range of flow conditions. The overall similarity of two different systems in terms of mixture properties can be analyzed effectively by using the drift-flux model.

The similarity criteria based on the drift flux model have been developed by Ishii and Zuber [3] and Ishii and Jones [4]. Two different methods have been used. The first method is based on the one-dimensional drift-flux model by choosing proper scales for various parameters. Since it is obtained from the differential equations, it has the characteristics of local scales. The second method is based on the small perturbation technique and consideration of the whole system responses. The local responses of main variables are obtained by solving the differential equations, then the integral effects are found. The resulting transfer functions are nondimensionalized. From these, the governing similarity parameters are obtained [3].

The first method based on the balance equations of the drift-flux model is useful in evaluating the relative importance of various physical effects and mechanisms existing in the system. However, there are certain shortcomings in this method when it is applied to a system similarity analysis. In developing the similarity criteria, the most important aspect is to choose proper scales for various variables. However, this may not always be simple or easy, because in a natural circulation system the variables change over wide ranges. Therefore, the scaling parameters obtained from this method are more locally oriented than system oriented.

The second method requires that the field and constitutive equations are firmly established and that the solutions to the small perturbations can be obtained analytically for the system under consideration. When these conditions are met, it gives quite useful similarity laws. In what follows, the combination of the results from the above two methods will be used to develop practical similarity criteria for a natural circulation system.

The drift-flux model obtained from the temporal and area averaging [6,7, 10] is given below.

Mixture Continuity Equation

$$\frac{\partial \rho_m}{\partial t} + \frac{\partial}{\partial z}(\rho_m u_m) = 0 \quad . \tag{62}$$

Continuity Equation for Vapor

$$\frac{\partial \alpha \rho_g}{\partial t} + \frac{\partial}{\partial z}(\alpha \rho_g u_m) = \Gamma_g - \frac{\partial}{\partial z}\left(\frac{\alpha \rho_g \rho}{\rho_m} V_{gj}\right) \quad . \tag{63}$$

Mixture Momentum Equation

$$\frac{\partial \rho_m u_m}{\partial t} + \frac{\partial}{\partial z}(\rho_m u_m^2) = -\frac{\partial p_m}{\partial z} - \rho_m g - \frac{\partial}{\partial z}\left[\frac{\alpha\rho_g\rho}{(1-\alpha)\rho_m} V_{gj}^2\right]$$

$$-\left[\frac{fm}{2D} + K\,\delta(z-z_i)\right]\rho_m u_m|u_m| \quad . \tag{64}$$

Mixture Enthalpy Energy Equation (ith Section)

$$\frac{\partial \rho_m H_m}{\partial t} + \frac{\partial}{\partial z}(\rho_m u_m H_m) = \frac{4h_m}{d}(T_s - T_{sat}) - \frac{\partial}{\partial z}\left[\frac{\alpha\rho_g\rho}{\rho_m}\Delta H_{fg}\, V_{gj}\right] \quad . \tag{65}$$

Solid Energy Equation (ith Section)

$$\rho_s C_{ps}\frac{\partial T_s}{\partial t} + k_s\nabla^2 T_s - \dot{q}_s = 0 \quad . \tag{66}$$

Solid-Fluid Boundary Condition (ith Section)

$$-k_s\frac{\partial T_s}{\partial y} = h_m(T_s - T_{sat}) \quad . \tag{67}$$

Here V_{gj} is the drift velocity given by $V_{gj} = (1-\alpha)(u_g - u_f)$. The mixture friction factor and heat transfer coefficient are denoted by f_m and h_m, respectively. The constitutive relations for the drift velocity, V_{gj}, and the vapor source term Γ_g should be specified in the above formulation. Under the thermal equilibrium condition, it can be shown [3] that

$$\Gamma_g = \frac{4h_m(T_s - T_{sat})}{d\Delta H_{fg}} \quad . \tag{68}$$

For water at relatively high pressure and under natural circulation conditions, the assumption of the thermal equilibrium is reasonable. The representative constitutive equation [7] for the drift velocity is given by

$$V_{gj} = 0.2\,(1 - \sqrt{\rho_g/\rho})\,j + 1.4\left(\frac{\sigma g\Delta\rho}{\rho^2}\right)^{1/4} , \tag{69}$$

where the total flux j is given by

$$j = u_m + \frac{\alpha\Delta\rho}{\rho_m} V_{gj} \quad . \tag{70}$$

The relative motion between phases can be specified by a number of different forms. For example, the classical void-quality correlation which gives

$$\alpha = f(x) \tag{71}$$

is mathematically equivalent to Eq. (69).

The heat transfer coefficient can be given by the standard correlations [13,14]. The boiling heat transfer is rather efficient, and the value of h_m is generally very high. In normal conditions the wall superheat, $T_s - T_{sat}$ is relatively small. However, the occurrence of the critical heat flux (CHF) is significant, because the heat transfer coefficient is drastically reduced at CHF. Therefore, in two-phase flow the simulation of the CHF condition is much more important than that of the thermal boundary layer. The occurrence of CHF can be considered as a flow regime transition due to a change in heat transfer mechanisms.

In view of the above, the conduction in solid may be decoupled from the fluid convection for the purpose of the similarity analysis. Thus the boundary condition, Eq. (67), may be changed to

$$T_s \doteq T_{sat} \text{ (at solid-fluid boundary)} \quad , \tag{72}$$

which is applicable from the boiling inception point to the CHF point.

The CHF condition at low flow has been reviewed by Leung [15], Katto [16], and Mishima and Ishii [9]. The modified Zuber correlation [17] for low flow is given by

$$q''_c = 0.14\,(1-\alpha)\,\rho_g \Delta H_{fg} \left(\frac{\sigma g \Delta\rho}{\rho_g^2} \right)^{1/4} \quad . \tag{73}$$

Based on the limited data on blowdown experiments it is recommended [15] for the mass velocity range of -24 to 10 g/cm^2 sec. It is evident that this correlation is based on a pool boiling CHF mechanism. Thus it may apply only for transients involving flow reversal.

Katto's correlation [16] for low flow is given by

$$q''_c = \frac{1}{4} \Delta H_{fg} G \frac{d_o}{\ell_o} \left[\left(\frac{\sigma\rho}{G^2 \ell_o} \right)^{0.043} + \frac{\Delta H_{sub}}{\Delta H_{fg}} \right] , \tag{74}$$

which implies that the critical quality is $x_c = (\sigma\rho/G^2\ell_o)^{0.043}$. Here G and ΔH_{sub} are the mass velocity and inlet subcooling. The typical value of x_c is 0.5 - 0.8, thus the underlining mechanism should be the annular flow film dryout. This correlation can be applied to most slow transient situations at low flow.

However, there is a possibility [9] that the critical heat flux may occur at much lower exit quality than that given above due to a change in two-phase flow regimes. In a natural circulation system with very small flow fluctuations, the occurrences of CHF have been observed at the transition between the churn-turbulent to annular flows. Beyond this transition, the lack of large disturbance waves eliminated the preexisting rewetting of dry patches. This leads to the formation of permanent dry patches and CHF. The criteria developed by Mishima and Ishii [9] for this case is given by

$$q''_c = \frac{d_o}{4\ell_o} \left\{ \left(\frac{1}{C_o} - 1 \right) \Delta H_{fg} \sqrt{\rho_g \Delta\rho g d_o} + G\Delta H_{sub} \right\} . \tag{75}$$

Here C_o is the distribution parameter for the drift-flux model [7] and given by

$$C_o = 1.2 - 0.2 \sqrt{\rho_g/\rho} . \tag{76}$$

These CHF criteria should be used to develop a similarity criterion for the fluid-solid boundary instead of the heat transfer coefficient. This ensures that the critical heat flux occurs under the similar condition in a simulated system.

VI.3.2 Steady State Formulation for Two-Phase Flow

As has been shown in the case of a single phase flow, the steady-state solutions are very important in obtaining scales for thermo-hydraulic parameters. Therefore, a brief summary of a steady-state formulation is presented below.

By assuming an axially uniform heat flux for simplicity of the analysis, the nonboiling length ℓ_{nb} of the heated section is given by

$$\ell_{nb} = \frac{\Delta H_{sub} \rho u_o d_o}{4q''_o} \quad . \tag{77}$$

However, in steady-state the heat flux is related to the heat generation rate by

$$q''_o = \delta \dot{q}_{so} \quad . \tag{78}$$

The vapor quality at the exit of the heated section is given by

$$x_e = \frac{4q''_o \ell_o}{\rho u_o \Delta H_{fg} d_o} - \frac{\Delta H_{sub}}{\Delta H_{fg}} \quad , \tag{79}$$

and the volumetric flux in the heated section by

$$j = (1 + \Delta\rho x/\rho_g) u_o \quad . \tag{80}$$

The pressure drop in the heated section can be given approximately by

$$\Delta p_o \simeq \rho u_o^2 \left\{ K_{in} + \frac{f\ell_{nb}}{2d_o} + \frac{f}{2d_o} \left[\frac{1 + \frac{\Delta\rho}{\rho_g} \frac{x_e}{2}}{\left(1 + \frac{\Delta\mu}{\mu_g} \frac{x_e}{2}\right)^{0.25}} \right] (\ell_o - \ell_{nb}) \right.$$
$$\left. + \left[\frac{x_e^2}{\alpha_e} \frac{\rho}{\rho_g} + \frac{(1-x_e)^2}{(1-\alpha_e)} - 1 \right] + K_e \left(1 + \frac{\Delta\rho}{\rho_g} x_e^{1.5} \right) \right\}$$
$$+ g\rho_o \ell_o - \Delta\rho g \left[\langle\alpha\rangle_o (\ell_o - \ell_{nb}) \right] \quad . \tag{81}$$

Here the homogeneous two-phase friction factor model and outlet orifice pressure drop model have been used [18]. Furthermore, the average quality have been used for calculating the pressure drop along the heated section. Hence the mean void fraction is given approximately by

$$\langle\alpha\rangle_o = f\left(\frac{x_e}{2}\right) . \tag{82}$$

A similar pressure drop equation can be written for the other two-phase sections, i.e., the upper plenum and condensation section. From this formulation, it is clear that the density ratio, viscosity ratio, exit quality, and void-quality (or drift velocity) correlations are very important for the similarity of two-phase systems in addition to the similarity conditions for single phase flow. In essence, the exit quality corresponds to the temperature rise ΔT in a single phase flow. Furthermore, the frictional, convective, and gravitational pressure drops depend strongly on the exit quality, property ratios and void-quality correlation. These dependencies make the similarity requirement for two-phase flow much more severe than that for single phase flow.

For a natural circulation system, the total driving force can be written as

$$\Delta p_{dr} = \beta g \rho \Delta T \left(\frac{\ell_{nb}}{2} + \frac{\ell_{nc}}{2}\right) + \sum_{TP} (\Delta \rho g \langle\alpha\rangle \ell)_i . \tag{83}$$

On the other hand, the resistance to the flow is given by

$$\Delta p_{fr} = \frac{\rho u_o^2}{2}\left\{\sum_{SP}\left(\frac{f\ell}{d} + K\right)_i \left(\frac{a_o}{a_i}\right)^2 + \sum_{TP}\left(\frac{f\ell}{d}\right)_i \left[\frac{1 + \Delta\rho x/\rho_g}{(1 + \Delta\mu x/\mu_g)^{0.25}}\right]_i \left(\frac{a_o}{a_i}\right)^2 + \sum_{TP} K_i (1 + \Delta\rho x^{1.5}/\rho_g)_i \left(\frac{a_o}{a_i}\right)^2\right\} . \tag{84}$$

Here SP and TP denote the single phase and two-phase regions. The net convective acceleration term has been neglected because the large part of it should cancel out between the boiling and condensation processes. The right hand side of Eq. (83) represents the single phase and two-phase driving force due

to density change. In two-phase flow, the second term should dominate because the density change by boiling is very large. It is evident from the above two expressions that reference velocity u_o can be obtained from the solution for the quality given by Eq. (79) and the force balance. However, since this involves a void-quality correlation, it is not straight forward as in the case of single phase flow.

VI.3.3 Similarity Criteriafor Two-Phase Flow

The similarity groups for two-phase flow can be obtained from the set of balance equations directly [4] or from the perturbation analysis [3]. The results obtained from the latter method are summarized below.

$$\text{Phase Change No. } N_{pch} = \frac{4q''_o \ell_o}{du_o \Delta H_{fg} \rho} \frac{\Delta\rho}{\rho_g} = \frac{\text{Flux due to Phase Change}}{\text{Inlet Flux}}$$

$$\text{Subcooling No. } N_{sub} = \frac{\Delta H_{sub}}{\Delta H_{fg}} \frac{\Delta\rho}{\rho_g} = \frac{\text{Subcooling}}{\text{Latent Heat}}$$

$$\text{Froude No. } N_{Fr} = \frac{u_o^2}{g\ell_o \langle\alpha\rangle_o} \frac{\Delta\rho}{\rho} = \frac{\text{Inertia}}{\text{Gravity Force}}$$

$$\text{Drift Flux No. } N_d = \frac{V_{gj}}{u_o} \text{ (or Void Quality Relation)}$$

$$\text{Density Ratio } N_\rho = \rho_g/\rho$$

$$\text{Friction No. } N_f = \frac{f\ell}{d}\left[\frac{1 + \Delta\rho x/\rho_g}{(1 + \Delta\mu x/\mu_g)^{0.25}}\right]\left(\frac{a_o}{a_i}\right)^2$$

$$\text{Orifice No. } N_o = K(1 + \Delta\rho x^{1.5}/\rho_g)\left(\frac{a_o}{a_i}\right)^2 \quad . \tag{85}$$

In addition to the above, the single phase similarity groups given in Eq. (12) can be obtained. In case of a two-phase natural circulation, the temperature rise can be replaced by subcooling as

$$\Delta T_o = \frac{\Delta H_{sub}}{C_p} \quad . \tag{86}$$

In view of Eqs. (12), (85), and (86), the additional groups are

$$\text{Time Ratio} \qquad T_i^* = \left(\frac{\alpha_s}{\delta^2}\frac{\ell_o}{u_o}\right)_i$$

$$\text{Heat Source No.} \qquad Q_{si} = \left(\frac{\dot{q}_s \ell_o C_p}{\rho_s C_{ps} u_o \Delta H_{sub}}\right) \tag{87}$$

The groups related to the thermal boundary layer should be replaced by the one based on the critical heat flux. Thus

$$\text{CHF No.} \qquad N_q = \frac{q''_c}{q''_o} \quad , \tag{88}$$

where q''_c is given by Eqs. (73), (74) or (75) depending on the CHF mechanisms.

In view of Eqs. (78) and (85), the phase change number can be modified to

$$N_{pch} = \frac{4\delta \dot{q}_o \ell_o}{d u_o \Delta H_{fg} \rho} \frac{\Delta\rho}{\rho_g} \quad . \tag{89}$$

On the other hand, the relative velocity scale based on the drift velocity correlation is

$$N_d = 0.2\,(1 - \sqrt{\rho_g/\rho})(1 + \Delta\rho x/\rho_g) + \frac{1.41}{u_o}\left(\frac{\sigma g \Delta\rho}{\rho^2}\right)^{1/4} \quad , \tag{90}$$

or it should have the same void quality correlation

$$\alpha = f(x,\ \rho_g/\rho,\ \mu_g/\mu,\ \text{etc.}) \quad . \tag{91}$$

The original similarity parameters and the modified ones given above indicate that the similarity criteria for different fluids at different pressures are extremely complicated. However, if the following conditions are met, significant simplifications can be made.

Negligible Effects of Viscosity Ratio on Two-phase Friction

Relatively Small Exit Orificing

Relatively Small Local Slip

In general, it can be shown from Eqs. (79) and (85),

$$\Delta\rho X_e/\rho_g = (N_{pch} - N_{sub}) \quad . \tag{92}$$

Therefore, the similarity based on the phase change number and subcooling number can satisfy N_d, N_f and N_o approximately. For a natural circulation the Froude number and thus the void fraction plays a very important roll at the low quality. However, at relatively high quality, the void fraction is very close to unity and, therefore, the driving force becomes only dependent on the length of the two-phase region.

Physically, the phase change number is the scale for the amount of heating and phase change, whereas the subcooling number is the scale for the cooling in the condensation section. The subcooled liquid temperature is mainly determined by the excess cooling in this section. The similarity analysis becomes much more complicated when there is not sufficient cooling to condense all of the steam or the subcooling cannot be well controlled by the condensation section. In such a case, detailed modeling of condensation process and the analysis of the secondary loop may become necessary to determine the exit quality or subcooling at the condensation section.

VI.3.4 Scale Model with Same Fluid

A special case of a scale model with same fluid under same pressure is now examined because of its obvious importance. In this case, all the fluid properties can be considered the same between the model and prototype, thus

$$\rho_R = \rho_{gR} = \beta_R = C_{pR} = k_R = \mu_R = \mu_{gR} = \Delta H_{fgR} = 1 \quad . \tag{93}$$

Under the above condition, the similarity criteria become

$$(N_{pch})_R = \frac{\delta_R q_R \ell_R}{d_R u_R} = 1 \quad . \tag{94}$$

$$(N_{sub})_R = (\Delta H_{sub})_R = 1 \quad . \tag{95}$$

$$(N_{Fr})_R = \frac{u_R^2}{\ell_R \langle\alpha\rangle_R} = 1 \quad . \tag{96}$$

$$(N_f)_R = \left(\frac{f\ell}{d}\right)_R \left(\frac{a_o}{a_i}\right)_R^2 = 1 \quad . \tag{97}$$

$$(N_o)_R = K_R \left(\frac{a_o}{a_i}\right)_R^2 = 1 \quad . \tag{98}$$

The drift flux number can be automatically satisfied, if the contribution of the local slip is small in comparison with the slip due to the transverse velocity and void profiles. When the local slip, i.e., the second term on R.H.S. of Eq. (90), is the dominant factor for the relative motion, the similarity requirement is $u_R = 1$ which is a rather severe restriction. Hence from $(N_d)_R = 1$ one obtains,

$$\begin{cases} \text{Distribution Controlled Slip} \rightarrow \text{Automatically Satisfied} \\ \text{Local Slip Controlled} \rightarrow u_R = 1 \end{cases} \quad . \tag{99}$$

For most cases the first condition applies. Even in the second case, the distortion of the velocity will introduce limited changes in the void-quality relation. Therefore, in the following analysis the first condition will be assumed.

From Eqs. (92) to (93), it is evident that basically the similarity in terms of the vapor quality is satisfied. Thus

$$x_R = 1 \quad . \tag{100}$$

And from Eq. (99) this implies that the void similarity also exists,

$$\alpha_R = 1 \quad . \tag{101}$$

Hence, excluding the friction similarity conditions, it is required that

$$\frac{\delta_R}{d_R}\frac{q_R \ell_R}{u_R} = 1$$

$$(\Delta H_{sub})_R = 1 \quad . \tag{102}$$

$$u_R^2/\ell_R = 1$$

In addition to the above, the critical heat flux similarity requires

$$\left(\frac{q_c''}{q''}\right)_R = 1 \quad . \tag{103}$$

Using the Katto CHF criterion given by Eq. (74) and N_{pch} similarity criteria, it can be shown that Eq. (103) becomes

$$(x_c)_R = \left(\frac{1}{u_R^2 \ell_R}\right)^{0.043} = 1 \quad . \tag{104}$$

It is noted that the exponent of the above expression is very small at 0.043. This implies that the x_c is in the range of $0.6 \sim 0.8$. Therefore, it may safely be assumed that Eq. (104) is approximately satisfied if the quality similarity given by Eq. (100) holds.

From the single phase scaling criteria on geometry given by Eqs. (44) and (45), it is necessary that

$$u_R = \sqrt{\ell_R} \quad ,$$

and $\tag{105}$

$$q_R = \frac{1}{\sqrt{\ell_R}} \quad .$$

These requirements also satisfy the single phase scaling criteria on the velocity given by Eq. (43). However, the real time simulation cannot be achieved in case of two-phase flow due to the additional conditions imposed on the system. Furthermore, Eq. (105) implies that the power to the system should be increased in a model. Additional caution should be paid to the simulation of

the CHF under natural circulation conditions. For example, if the CHF occurs due to the local condition such as given by Eq. (73), it cannot be simulated by the above scaling criteria.

VI.3.5 Sample Calculations

As an example, a preliminary consideration on the simulation of LWR by the LOFT facility is presented. In this case, as stated above it is not possible to operate in the real time scale. Therefore, the time scale should be distorted in order to have a meaningful simulation.

From Eqs. (60) and (105)

$$\ell_R = 0.4 \sim 0.44$$

$$u_R = 0.63 \sim 0.66 \quad . \tag{106}$$

$$q_R = 1.58 \sim 1.51$$

The geometrical similarity criteria given by Eqs. (44) and (45) requires that

$$\delta_R = d_R \doteq 0.8 \quad . \tag{107}$$

The subcooling or the secondary loop temperature is limited by

$$(\Delta H_{sub})_R = 1 \quad . \tag{108}$$

Furthermore, for an accurate simulation, it is necessary that in two-phase sections the friction and orifice number satisfy

$$\left(\frac{f\ell}{d}\right)_R = 1 \qquad \text{or} \qquad f_R = 2 \sim 1.8 \quad ,$$

and $\tag{109}$

$$K_R = 1 \quad ,$$

where it was assumed that $(a_i/a_o)_R = 1$ based on d_R = constant. On the other hand, for single phase sections the overall friction similarity is sufficient.

It is noted that the above conditions also satisfies the single phase natural circulation requirements. The exception is the simulation of the turbulent boundary layer. As mentioned above the time scale is distorted by

$$t_R \doteq \frac{\ell_R}{u_R} = 0.63 \sim 0.66 \quad . \tag{110}$$

Therefore, the time events will be accelerated in the model.

The above similarity requirement can be compared to the parameters given in Table I. It is clear that the geometrical condition given by Eq. (107) is only met approximately. Furthermore, Eq. (106) shows that the power should be higher in the LOFT facility by 50% or more. It is necessary to adjust the frictional pressure drop coefficients by installing several orifices in the two-phase flow sections. For modifications of the facility or designing experiments, much more detailed analysis may be needed. In the present analysis only the general similarity criteria and the feasibility of using the LOFT facility are examined.

VI. 4 CONCLUSIONS

Scaling criteria for a natural circulation loop under single phase and two-phase flow conditions have been derived from the fluid balance equations, boundary conditions, and solid energy equations. For a single phase case the continuity, integral momentum, and energy equations in one-dimensional area averaged forms have been used. The solid heat conduction is considered only in a direction normal to the flow, therefore, the effect of axial conduction has been neglected. For a two-phase natural convection case the one-dimensional drift-flux model obtained from the short time temporal averaging the sectional area averaging has been used.

The set of balance equations and boundary conditions is nondimensionalized by using reference scales and steady state solutions. From this, important similarity groups have been identified. The natural circulation in a closed loop is induced by the density changes due to heating up of liquid and due to boiling. Therefore, special attention has been paid to the driving head of the gravitational term in the differential and integral momentum equations. The coupling of this gravitational driving force with the solution of the fluid energy equation is the particular characteristic of a natural circulation loop.

The above similarity analysis shows that for a single phase case the geometrical similarity group, friction number, Richardson number, characteristic time constant ratio, Biot number, and heat source number are important. It can be shown that the Stanton number, obtainable from the fluid energy equation, is redundant in terms of the above similarity groups. The geometrical similarity group consists of the axial length and flow area ratio of various sections. The Biot number involves the constitutive relation for the heat transfer coefficient. This will cause some difficulties in case of a fluid to fluid simulation, however, the relaxation of the Biot number similarity condition influences the boundary layer temperature drop only, and, therefore, it may not be very significant in the single phase case.

In the case of two-phase natural circulation, the dimensional analysis shows that the phase change number, drift-flux number, friction number, density ratio, and two-phase Froude number are the important similarity groups. The physical significances and conditions imposed by these similarity parameters are discussed. These are interpreted into the conditions on the operational parameters and standard two-phase flow parameters such as the void fraction and quality. In the two-phase case, the critical heat flux is one of the important transients which should be simulated in a scale model. This additional condition is also discussed in detail in terms of the standard high quality CHF and the newly discovered low quality CHF.

The above results are applied to the LOFT facility in case of a natural circulation simulation. The fluid and pressure levels are assumed to be the same between the model and prototype. Therefore, the similarity criteria are evaluated with respect to the operational conditions and system geometry. In particular, the feasibility of the real time simulation which imposes an additional constraint is discussed. The results show that the real time simulation is only possible in the case of a single phase flow. The similarity criteria for two-phase natural circulation basically requires the similarity in terms of the steam quality and void fraction. Because of this, the power requirement for a scale model should be considerably higher than in the prototype. The detailed geometrical similarity in the two-phase region is quite important due to the strong dependence of the frictional and gravitational pressure drops on the steam quality or void fraction. It appears that some modification of the LOFT facility by installing several orifices in the hot legs is necessary.

In the present study, only general similarity criteria and the feasibility of using the LOFT facility for PWR natural circulation simulations have been examined. A more detailed study may be necessary for optimum modifications of the facility or designing experimental programs.

NOMENCLATURE

a	Flow area
a_s	Wall cross sectional area
A	Non-dimensional area
B	Biot number
C_p	Fluid heat capacity
C_{ps}	Solid heat capacity
C_o	Distribution parameter
d	Hydraulic diameter
f	Friction factor
F	Friction number
$f(x)$	Void-quality relation
g	Gravity
Gr	Grashof number
G	Mass velocity
h	Heat transfer coefficient
H_m	Enthalpy of mixture
j	Total volumetric flux
k	Conductivity of liquid
k_s	Conductivity of solid
K	Orifice coefficient
ℓ	Axial length
ℓ_h	Length of hot fluid section
L	Non-dimensional length
ℓ_{nb}	Non boiling length (heated section)
ℓ_{nc}	Non boiling head (cooled section)
Nu	Nusselt number
N_{pch}	Phase change number
N_{sub}	Subcooling number
N_{Fr}	Froude number
N_d	Drift flux number
N_ρ	Density ratio
N_f	Friction number (two-phase)
N_o	Orifice number (two-phase)
N_q	Critical heat flux number

Pr	Prandtl number
p	Pressure
$\dot{q}_s$	Heat generation in solid
Q_s	Heat source number
q''	Heat flux
q''_c	Critical heat flux
R	Richardson number
Re	Reynolds number
St	Stanton number
t	Time
T	Fluid temperature
T_s	Solid temperature
T_{sat}	Saturation temperature
T^*	Characteristic time ratio
u	Velocity (liquid)
u_r	Representative velocity
u_f	Liquid velocity
u_g	Vapor velocity
u_m	Mixture velocity
U	Non-dimensional velocity
V_{gj}	Drift velocity
x	Vapor quality
xe	Exit quality
y	transverse distance
Y	Non-dimensional transverse distance
z	Axial distance
Z	Non-dimensional axial distance

Greek Symbols

α	Void fraction
α_e	Exit void fraction
α_s	Solid thermal diffusivity
β	Thermal expansion coefficient
Γ_g	Vapor mass source
δ	Conduction thickness

$\delta(z)$	Delta function
ΔT	Characteristic temperature rise
ΔH_{fg}	Latent heat
ΔH_{sub}	Subcooling
Δp	Pressure drop
$\Delta \rho$	Density difference
$\Delta \mu$	Viscosity difference
θ	Non-dimensional temperature
μ	Viscosity of liquid
ξ	Wetted (heated) perimeter
ρ	Density of liquid
ρ_s	Density of solid
σ	Surface tension
τ	Non-dimensional time

Subscripts

i	ith section
o	Reference constant (heated section)
r	Representative variable
s	Solid
h	Hot
c	Cold
R	Model to prototype ratio
in	Inlet
ex	Exit
m	Mixture
g	Vapor
$(\ )_m$	Model
$(\ )_p$	Prototype

REFERENCES

1. M. P. Heisler and R. M. Singer, "Facility Requirements for Natural Convection Shutdown Heat Removal System Testing," Decay Heat Removal and Natural Convection in Fast Breeder Reactors, Hemisphere, p. 113 (1981).

2. M. P. Heisler, "Development of Scaling Requirements for Natural Convection Liquid-Metal Fast Breeder Reactor Shutdown Heat Removal Test Facilities," Nucl. Sci. Eng. 80, p. 347 (1982).

3. M. Ishii and N. Zuber, "Thermally Induced Flow Instabilities in Two-phase Mixtures," 4th Int. Heat Trans. Conf., Paris, paper B5.11 (1970).

4. M. Ishii and O. C. Jones, Jr., "Derivation and Application of Scaling Criteria for Two-phase Flows," Two-phase Flows and Heat Transfer, Proc. NATO Advanced Study Institute, Istanbul, Turkey, Vol. 1, p. 163 (1976).

5. N. Zuber, "Problems in Modeling of Small Break LOCA," NRC NUREG-0724 Report (1980).

6. N. Zuber and J. A. Findlay, "Average Volumetric Concentration in Two-phase Flow Systems," J. Heat Trans. 87, p. 453 (1965).

7. M. Ishii, "One-dimensional Drift-flux Model and Constitutive Equations for Relative Motion between Phases in Various Two-phase Flow Regimes," Argonne Report ANL-77-47 (1977).

8. D. L. Reeder, "LOFT System and Test Description," NUREG/CR-0247, TREE-1208 (1978).

9. K. Mishima and M. Ishii, "Critical Heat Flux Experiments under Low Flow Conditions in a Vertical Annulus," NUREG/CR-2647, ANL-82-6 (1982).

10. M. Ishii, "Thermo-fluid Dynamic Theory of Two-phase Flow," Eyrolles, Paris (1975).

11. M. Ishii and N. Zuber, "Drag Coefficient and Relative Velocity in Bubbly, Droplet or Particulate Flows," AIChE J. 25, p. 843 (1979).

12. M. Ishii, "Foundation of Various Two-phase Flow Models and Their Limitations," NRC-EPRI Joint Conf. on Simulation Methods for Nuclear Power Systems, EPRI WS-81-212, p. 3-47 (1981).

13. L. S. Tong, "Boiling Heat Transfer and Two-phase Flow," R. E. Krieger, NY (1975).

14. Y. Y. Hsu and R. W. Graham, "Transport Processes in Boiling and Two-phase Systems," Hemisphere, WA (1976).

15. J. C. M. Leung, "Occurrence of Critical Heat Flux during Blowdown with Flow Reversal," ANL-77-4 (1977).

16. Y. Katto, "A Generalized Correlation of Critical Heat Flux for Forced Convection Boiling in Vertical Uniformly Heated Round Tube," Int. J. Heat Mass Trans., Vol. 21, p. 1527 (1978).

17. P. Griffith, J. F. Pearson, and R. J. Lepkowski, "Critical Heat Flux During a Loss-of-Coolant Accident," Nucl. Saf. 18(3), p. 298 (1977).

18. J. G. Collier, "Convective Boiling and Condensation," McGraw-Hill, NY (1972).

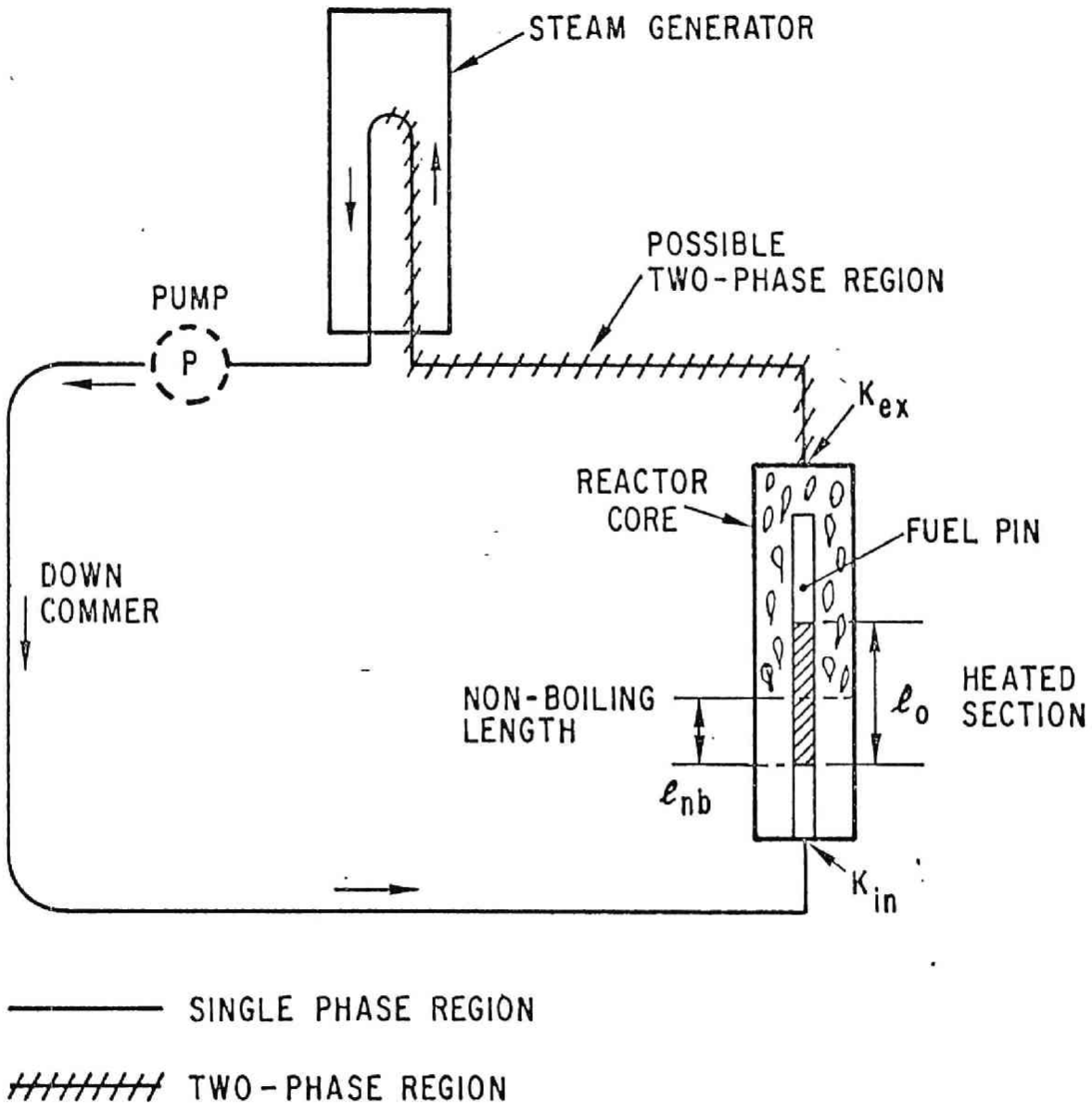

Fig. 1. Schematics of Natural Circulation in LWR

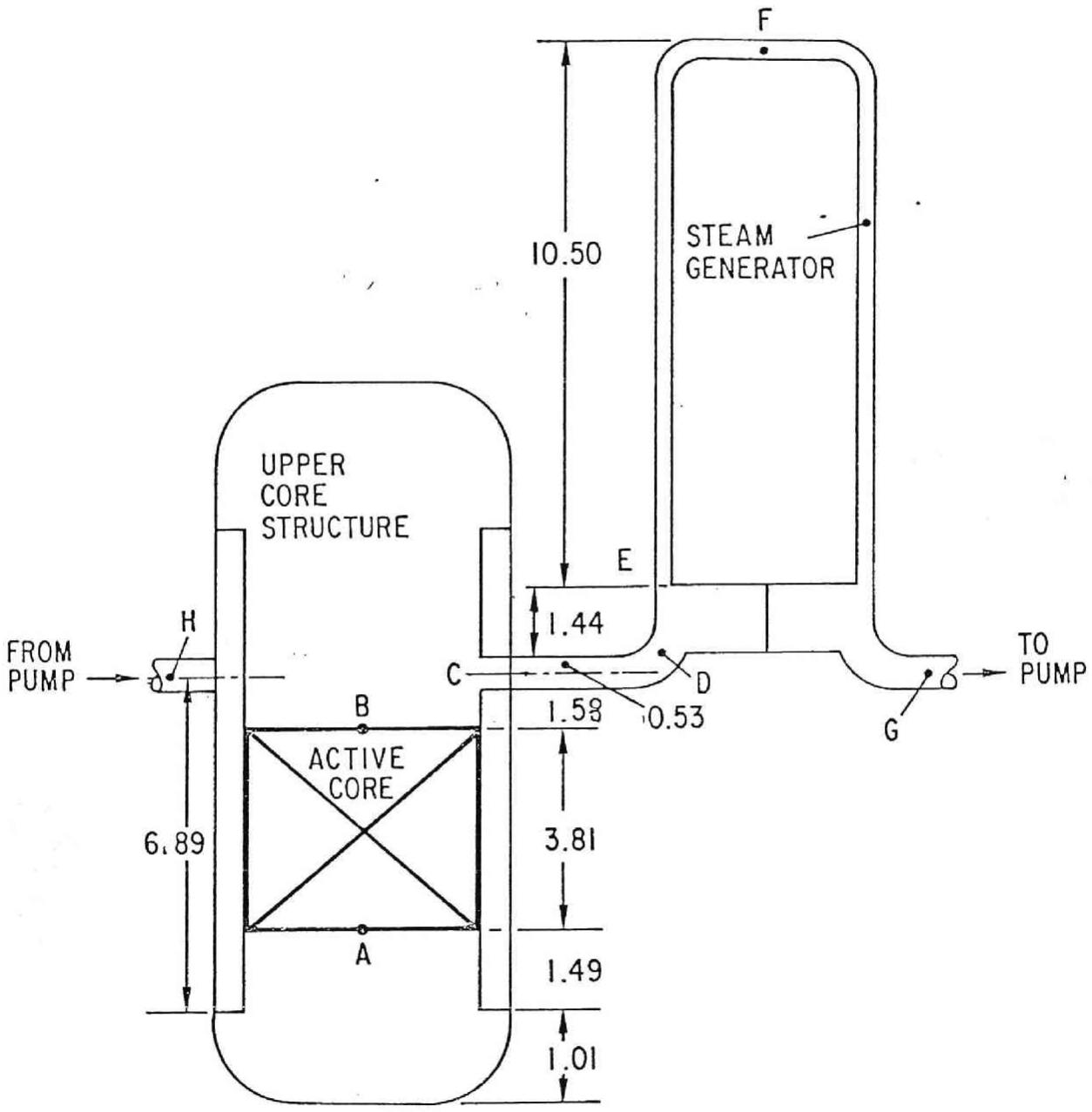

Fig. 2. Simplified LWR Geometry Relevant to Natural Circulation (Dimensions in m)

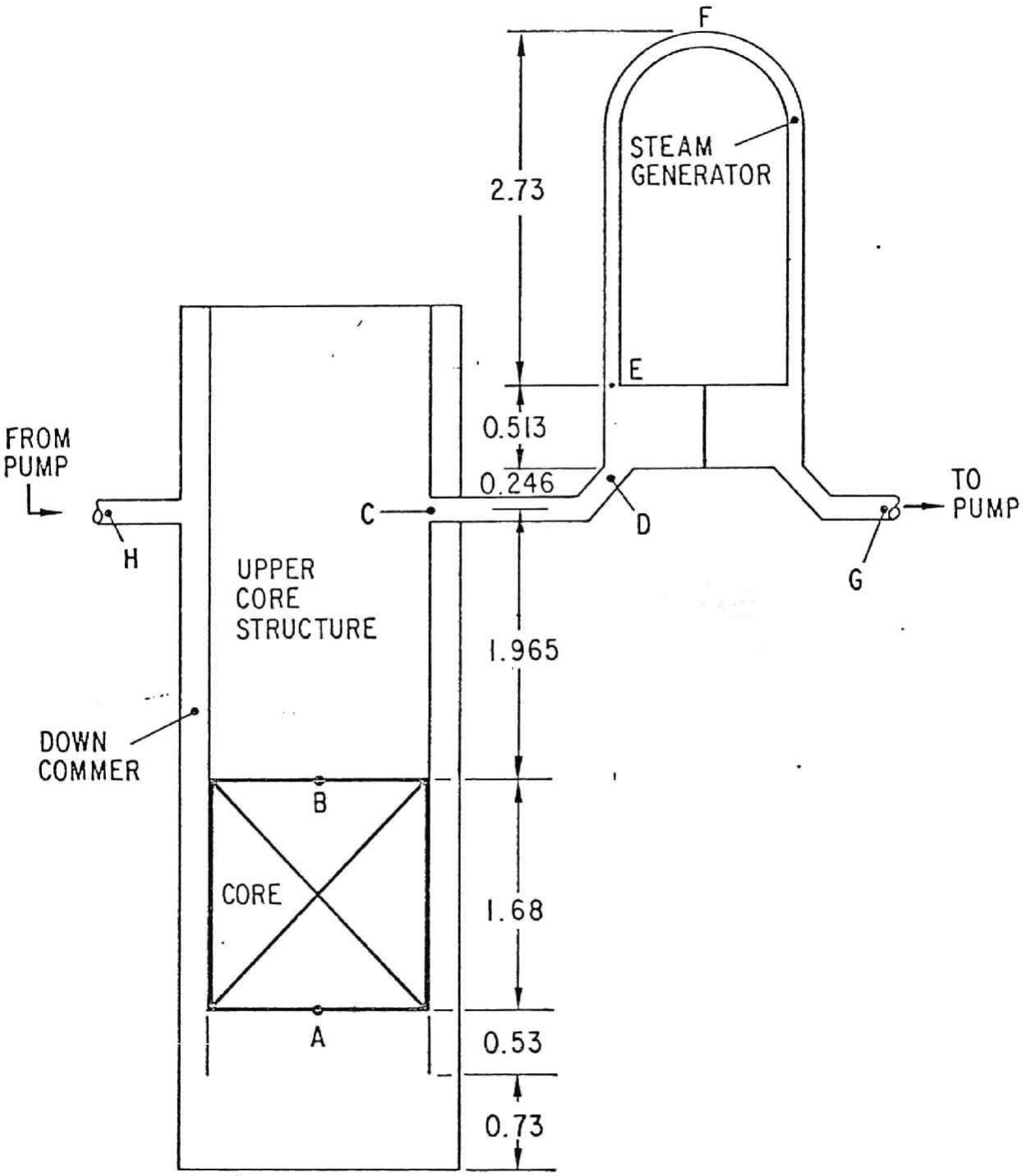

Fig. 3. Simplified LOFT Facility Geometry Relevant to Natural Circulation (Dimensions in m)

Table I. Basic Geometrical Parameters for PWR and LOFT Facility [8]

System / Item	PWR	LOFT
Fuel Rod O.D., cm	0.97	1.07
Length (AB), cm	381	168
Pitch, cm	1.29	1.43
Hydraulic Diameter, cm	1.2	1.363
No. of Rod	~55000	1300
Elevation BC, cm	158	196.5
Elevation CE, cm	197	75.9
Elevation EF, cm	1050	273
SG Tube I.D., cm	1.69	1.02
Wall Thickness, cm	0.107	0.124
No. of Tube	~11000	1845

SUMMARY AND CONCLUSIONS

The thermohydraulic characteristics of transient boiling and two-phase flow have been studied experimantally and analytically. The main objectives of the study are to provide an accurate knowledge for the various thermohydraulic phenomena encountered under the accidental conditions of a nuclear reactor.

In relation to the reactivity accident of a nuclear reactor, the transient boiling phenomena under rapid power increase have been studied experimentally. In this case, transient boiling and two-phase flow phenomena under small ℓ/d_{he} and low steam quality are particularly important and the boiling phenomena are considered to be localized. Experiments were conducted by exponentially increasing heat input to a platinum wire in water flowing vertically upward in a round tube, under mean water velocity from 1.35 to 4.04 m/s, inlet subcooling from 0 to 70 K, system pressure from 0.143 to 1.503 MPa, exponential period from 5 ms to 10 s, heater diameter from 0.8 to 1.5 mm and heater length from 3.93 to 10.04 cm. In most cases, the transient boiling curve after temperature overshoot coincided with the steady state boiling curve and/or its extrapolation. In these cases, the transient maximum heat flux increased with increasing velocity, subcooling and pressure, and with decreasing period and heater diameter, independently of heater length. The difference between the transient maximum heat flux and the steady state maximum heat flux was satisfactorily correlated by the exponential period.

Incidental to the transient boiling phenomena, the transient non-boiling heat transfer has been analysed. Based on integral method (boundary layer approximation), transient non-boiling heat transfer coefficients are obtained for a flat plate. The approximate but simple and analytic correlations obtained in this analysis cover various flow regimes (laminar, turbulent) and a wide range of Prandtl number of a fluid. These transient heat transfer coefficients attain the asymptotic values. The ratio between the asymptotic heat transfer coefficient and the steady state one is correlated in terms of dimensionless parameter including a heat flux increasing rate.

Concerning a LOCA and subsequent rewetting and reflooding phenomena in a nuclear reactor, the transient boiling and two-phase flow under large ℓ/d_{he} and high steam quality are considerably important. In analysing the phenomena, an accurate knowledge of an annular and annular dispersed flow is essential.

In an earlier stage of the LOCA and reflooding, the most important flow regime involved is counter-current annular dispersed flow where liquid flow rate is positive. Associated with the annular dispersed flow in the above case, droplet size and entrainment rate have been analyzed.

The mean droplet size and size distribution are important for detailed mechanistic modeling of annular two-phase flow. A large number of experimental data indicate that the standard Weber number criterion based on the relative velocity between droplets and gas flow predicts far large droplet sizes. Therefore, it was postulated that the majority of the droplets were generated at the time of entrainment and the size distribution was the direct reflection of the droplet entrainment mechanism based in roll-wave shearing off. A detailed model of the droplet size in annular flow was then developed based on the above assumption. The correlations for the volume mean diameter as well as the size distrinution were obtained in collaboration with a large number of experimental data. A comparison with experimental data indicated that indeed the postulated mechanism has been the dominant factor in determining the droplet size. Furthermore, a large number of data can be successfully correlated by the present model. These correlations can supply accurate information on droplet size in annular flow which has not been available previously.

As for the entrainment rate in annular dispersed flow, the correlations for entrainment rate covering both entrance region and equilibrium region have been developed from a simple model in collaboration with data. Results show that the entrainment rate varies considerably in the entrainment development region, however, at a certain distance from an inlet it attains an equilibrium state where entrainment rate and deposition rate becomes equal. The result indicates that the equilibrium entrainment rate is proportional to the Weber number based on the hydraulic diameter of the tube.....

On the other hand, in a later stage of the LOCA and reflooding where liquid flow rate is extremely low, the pool entrainment phenomena play important roles in heat and mass transfer processes. Therefore, these phenomena were studied. Droplets which are suspended from a free surface are partly carried away by streaming gas and partly returned back to the free surface by gravity. A correlation is developed for the pool entrainment amount based on simple mechanistic modeling and a number of data. This analysis reveals that there exist three regions of entrainment in the axial direction from a pool surface. In the first region (near surface region), entrainment is independent of height and gas velocity. In the second region (momentum controlled region), the amount of entrainment decreases with increasing height from the free surface and increases with increasing gas velocity. In the third region (deposition controlled region), the entrainment increases with increasing gas velocity and decreases with increasing height due to deposition of droplets. The present correlation agrees well with a large number of experimental data over a wide range of pressure for air-water and steam-water systems.

Along with the separate effects of the transient boiling and two-phase flow on the thermohydraulic characteristics of a nuclear reactor, the overrall characteristics throughout the entire loop of a nuclear reactor comprise another set of important problems. The phenomena correspond to the transient boiling and two-phase flow under extremely large ℓ/d_{he} where ℓ covers the entire loop. One of the most important applications of the above problems is the natural circulation coolability. The phenomena are particularly important associated with small break LOCA and subsequent pump trip in a nuclear reactor. A model facility is often used in evaluating the natural circulation coolability. In designing the model facility which simulates a prototype reactor, scaling laws are impotant. Therefore, scaling criteria for a natural circulation loop under single phase and two-phase flow conditions have been derived. For a single phase case the continuity, integral momentum, and energy equations in one-dimensional area average forms have been used. From this, the geometrical similarity groups, friction number, Richardson number, characteristic time constant ratio, Biot number, and heat source number are obtained. The Biot number involves the heat transfer coefficient which may cause some difficulties in simulating the

turbulent flow regime. For a two-phase flow case, the similarity groups obtained from a perturbation analysis based on the one-dimensional drift-flux model have been used. The physical significance of the phase change number, subcooling number, drift-flux number, friction number are discussed and conditions imposed by these groups are evaluated. In the two-phase flow case, the critical heat flux is one of the most important transients which should be simulated in a scale model. The above results are applied to the LOFT facility in case of a natural circulation simulation. Some preliminary conclusions on the feasibility of the facility have been obtained.

Some of the results of this study on the transient boiling and two-phase flow have been incorporated into a large scale computor code such as TRAC which is commonly used to evaluate the safety of a nuclear reactor accident. The author believes that this study will make some contribution to the improvement of such safety analyses of the nuclear reactor accidents.

However, it is needless to say that much more research efforts on the transient boiling and two-phase flow phenomena should be done in order to acquire accurate understandings of the themohydraulics of nuclear power plants under normal and off-normal operational conditions.